



# Geological Fieldwork 2020

## A Summary of Field Activities and Current Research



Ministry of  
Energy, Mines and  
Low Carbon Innovation

Paper 2021-01



Ministry of  
Energy, Mines and  
Low Carbon Innovation



# Geological Fieldwork 2020

A Summary of Field Activities and Current Research

Ministry of Energy, Mines and Low Carbon Innovation  
British Columbia Geological Survey

Paper 2021-01

# Ministry of Energy, Mines and Low Carbon Innovation

## Mines, Competitiveness, and Authorizations Division

### British Columbia Geological Survey

Recommended citation format for individual papers:

Schiarizza, P., and Friedman, R.M., 2021. U-Pb zircon date for Eocene volcanic rocks on Mount Timothy, south-central British Columbia. In: Geological Fieldwork 2020, British Columbia Ministry of Energy, Mines and Low Carbon Innovation, British Columbia Geological Survey Paper 2021-01, pp. 15-21.

#### Front Cover:

Flat-lying volcanic flows of the Sloko Group (Eocene; ca. 54 Ma). Intermediate at base, felsic in middle, mafic at top. At right, upper flows are columnar, indicating subaerial volcanism. View to the northeast from the Llewellyn glacier, near Atlin Lake. See Van Wagoner, N., Ootes, L., and Thomson-Gladish, J., 2021. Volcanism and geochemistry of the Kamloops Group, south-central British Columbia, this volume. **Photo by L. Ootes.**

#### Back Cover:

Pervasively foliated and sericite- and iron carbonate-altered lapilli tuff to tuff breccia of the Stuhini Group, between the Saddle South and Saddle North deposits. See Greig, C.J., Dudek, N.P., ver Hoeve, T.J., Quinn, T.D.M., Newton, G., and Greig, R.E., 2021. Geology of the Tatogga property: Geologic framework for the Saddle North porphyry Cu-Au deposit and the Saddle South epithermal Au-Ag vein system, northwestern British Columbia, this volume. **Photo by C.J. Greig.**

This publication is available, free of charge, from the British Columbia Geological Survey website:

<https://www2.gov.bc.ca/gov/content/industry/mineral-exploration-mining/british-columbia-geological-survey/publications>

#### British Columbia Cataloguing in Publication Data

Main entry under title:

Geological Fieldwork: - 1974 -

Annual.

Issuing body varies

Vols. for 1978-1996 issued in series: Paper / British Columbia. Ministry of Energy, Mines and Petroleum Resources; vols. for 1997 - 1998, Paper / British Columbia. Ministry of Employment and Investment; vols. for 1999-2004, Paper / British Columbia. Ministry of Energy and Mines; vols. for 2005-2009, Paper / British Columbia. Ministry of Energy, Mines and Petroleum Resources; vols. for 2010, Paper / British Columbia. Ministry of Forests, Mines and Lands; vols. for 2011, Paper / British Columbia. Ministry of Energy and Mines; vols. for 2012-, Paper / British Columbia. Ministry of Energy, Mines and Natural Gas; vols. for 2014-, Paper / British Columbia. Ministry of Energy and Mines; vols. for 2018-, Paper / British Columbia. Ministry of Energy, Mines and Petroleum Resources; vols. for 2021-, Paper / British Columbia. Ministry of Energy, Mines and Low Carbon Innovation.

Includes Bibliographical references.

ISSN 0381-243X=Geological Fieldwork

1. Geology - British Columbia - Periodicals. 2. Mines and mineral resources - British Columbia - Periodicals. 3. Geology - Fieldwork - Periodicals. 4. Geology, Economic - British Columbia - Periodicals. 5. British Columbia. Geological Survey Branch - Periodicals. I. British Columbia. Geological Division. II. British Columbia. Geological Survey Branch. III. British Columbia. Geological Survey Branch. IV. British Columbia. Dept. of Mines and Petroleum Resources. V. British Columbia. Ministry of Energy, Mines and Petroleum Resources. VI. British Columbia. Ministry of Employment and Investment. VII. British Columbia Ministry of Energy and Mines. VIII. Series: Paper (British Columbia. Ministry of Energy, Mines and Petroleum Resources). IX. Series: Paper (British Columbia. Ministry of Employment and Investment). X. Series: Paper (British Columbia Ministry of Energy and Mines). XI. Series: Paper (British Columbia Ministry of Energy, Mines and Petroleum Resources). XII. Series: Paper (British Columbia Ministry of Forests, Mines and Lands). XIII. Series: Paper (British Columbia Ministry of Energy and Mines). XIV. Series: Paper (British Columbia Ministry of Energy, Mines and Natural Gas). XV. Series: Paper (British Columbia Ministry of Energy and Mines). XVI. Series: Paper (British Columbia Ministry of Energy, Mines and Petroleum Resources). XVII. Series: Paper (British Columbia Ministry of Energy, Mines and Low Carbon Innovation).

QE187.46 622.1'09711 C76-083084-3 (Rev.)

Victoria  
British Columbia  
Canada

January 2021

# Message from the Assistant Deputy Minister

## The British Columbia Geological Survey: 125 years of public geoscience

Exploration and mining are cornerstones of British Columbia's economy and have been an integral part of our history. Indigenous groups used and traded rocks and minerals for thousands of years before coal was discovered on Vancouver Island in 1835. The gold rushes of the mid-1800s drew prospectors from across North America and Europe, opening up significant parts of the province. Our mineral wealth was an important factor in British Columbia joining confederation in 1871, and throughout our history, exploration and mining have provided jobs and government revenues to help the people of British Columbia prosper.

Through most of our history as a Province, the British Columbia Geological Survey (BCGS) has faithfully served the people of British Columbia. Since 1895, BCGS has provided the geoscience knowledge that connects government, the minerals industry, and communities to the geology and mineral resources of the province. Survey work is used for effective mineral exploration, sound land use management, and responsible governance, enabling decisions that balance the economy, the environment, and community interests.

In 2020, the BCGS celebrated 125 years of service. Although the pandemic has limited our opportunities to acknowledge the long history of the Survey, I would like to recognize BCGS staff and alumni for their contributions to our understanding of the geology and mineral wealth of the province and the opportunities it brings all British Columbians.



Peter Robb  
Assistant Deputy Minister  
Mines, Competitiveness, and Authorization Division  
Ministry of Energy, Mines and Low Carbon Innovation

# Preface

## Geological Fieldwork 2020

Geological Fieldwork 2020 is the forty-sixth edition of the annual volume that presents peer-reviewed papers detailing the results of British Columbia Geological Survey (BCGS) geoscience activities. In addition to this volume, the Survey published other reports, maps and databases and made contributions to peer-reviewed journals and partners publications (i.e., Geological Survey of Canada and Geoscience BC). BCGS also publishes two other annual publications, the Provincial Overview of Exploration and Mining in British Columbia and the Coal Industry Overview.

Geological Fieldwork 2020 includes nine papers. Wildgust et al. provide an overview of Survey activities in the past year. The first of two papers by Schiarizza et al. conclude that volcanic rocks on Mount Timothy in central British Columbia are part of the Skull Hill Formation (early Eocene) rather than the Nicola Group (Triassic). The second paper examines new U-Pb ages for intrusive rocks of the Granite Mountain batholith (Late Triassic) including the Burgess Creek and Sheridan Creek stocks. Jones et al. is a contribution to ongoing studies in the Hogem Batholith. Their work provides geochronological data that sequences the intrusions of the Thane Creek, Duckling Creek, Osilinka and Mesilinka intrusive suites. Also in the Hogem Batholith area, Ferbey and Elia describe the Late Wisconsinan ice-flow history and surficial geology. A paper by Van Wagoner et al. examines the Challis-Kamloops belt (early Eocene) in central British Columbia. Greig et al. contribute new U-Pb and Re-Os geochronology and explain the geological framework and context of the Tatogga property in northwestern British Columbia. Rukhlov et al. describe preliminary endeavours by BCGS in using natural emissions of Hg vapour into the atmosphere as an exploration tool. The final paper in the volume, by Lett et al., re-examines unpublished surface sediment geochemical data from a massive sulphide and gold-quartz vein mineralization at the Ace property, near Likely.

2020 will be remembered as an historic year during which the Covid-19 pandemic impacted all aspects of society worldwide. Like many other countries, Canada shifted to remote working as public health orders limited in-person social interactions. In British Columbia, exploration and mining were declared essential services, enabling the industry to continue operating by adhering to strict public health and safety guidelines. These measures were largely successful, and explorers continued to work, surpassing 2019 expenditures by \$93 million, reaching \$422 million by the end of 2020. The sector showed its resiliency and economic importance while most other parts of the provincial economy struggled. At BCGS, staff were encouraged to work from home. Although staff maintained a full workload and publication output, health and work safe requirements and travel restrictions curtailed summer field activity.

BCGS celebrated 125 years of service in 2020 and, even though the pandemic limited opportunities to recognize this milestone, we are proud to be British Columbia's oldest government science agency. The Survey continues to respond to change while continuing to fulfil its traditional role. The Survey remains committed to modernization and adaptation to digital transformation of infrastructure and products. Staff renewal continues to be a focus as the Survey replaces venerable staff who have made significant contributions to the understanding of Cordilleran geology. The Survey would also like to welcome back the Regional Geologists who are now part of the BCGS Mineral Development Office.



Adrian S. Hickin  
Chief Geologist and Executive Director  
British Columbia Geological Survey

# Table of Contents

---

<b>Wildgust, N., Jones, L.D., Clarke, G., and Hickin, A.S.:</b> British Columbia Geological Survey annual program review 2020-2021 .....	1
<b>Schiarizza, P., and Friedman, R.M.:</b> U-Pb zircon date for Eocene volcanic rocks on Mount Timothy, south-central British Columbia .....	15
<b>Schiarizza, P., and Friedman, R.M.:</b> U-Pb zircon dates for the Granite Mountain batholith, Burgess Creek stock, and Sheridan Creek stock, Gibraltar Mine area, south-central British Columbia .....	23
<b>Jones, G., Ootes, L., Milidragovic, D., Friedman, R., Camacho, A., Luo, Y., Vezinet, A., Pearson, D.G., and Schiarizza, P.:</b> Geochronology of northern Hogem batholith, Quesnel terrane, north-central British Columbia .....	37
<b>Ferbey, T., and Elia, E.A.:</b> Preliminary surficial geology of the northern Hogem batholith area, north-central British Columbia .....	57
<b>Van Wagoner, N., Ootes, L., and Thomson-Gladish, J.:</b> Volcanism and geochemistry of the Kamloops Group, south-central British Columbia .....	65
<b>Greig, C.J., Dudek, N.P., ver Hoeve, T.J., Quinn, T.D.M., Newton, G., Makin, S.A., and Greig, R.E.:</b> Geology of the Tatogga property: Geologic framework for the Saddle North porphyry Cu-Au deposit and the Saddle South epithermal Au-Ag vein system, Iskut district, northwestern British Columbia .....	89
<b>Rukhlov, A.S., Ootes, L., Hickin, A.S., and Mashyanov, N.R.:</b> Near-surface mercury vapour haloes in air above ore deposits and faults on Vancouver Island: Insights into buried materials in real-time? .....	113
<b>Lett, R.E., and Paulen, R.C.:</b> Soil and till geochemical surveys at the Ace mineral property, central British Columbia .....	145
<b>Appendix:</b> British Columbia Geological Survey publications and peer-reviewed journal papers authored by BCGS staff and released in 2020 .....	167



# British Columbia Geological Survey annual program review 2020-2021



Neil Wildgust<sup>1, a</sup>, Larry D. Jones<sup>1</sup>, Gordon Clarke<sup>2</sup>, and Adrian S. Hickin<sup>1</sup>

<sup>1</sup> British Columbia Geological Survey, Ministry of Energy, Mines and Low Carbon Innovation, Victoria, BC, V8W 9N3

<sup>2</sup> British Columbia Geological Survey, Ministry of Energy, Mines and Low Carbon Innovation, Vancouver, BC, V6Z 2G3

<sup>a</sup> corresponding author: Neil.Wildgust@gov.bc.ca

Recommended citation: Wildgust, N., Jones, L.D., Clarke, G., and Hickin, A.S., 2021. British Columbia Geological Survey annual program review 2020-2021. In: Geological Fieldwork 2020, Ministry of Energy, Mines and Low Carbon Innovation, British Columbia Geological Survey Paper 2021-01, pp. 1-14.

---

## Executive Summary

The British Columbia Geological Survey, as the steward of provincial geoscience and mineral resource information, conducts research to define the geological evolution and natural resources of British Columbia. Part of the Ministry of Energy, Mines and Low Carbon Innovation, the Survey generates geoscience knowledge and data to inform land use and resource management decisions, and to support the growth of British Columbia as a competitive jurisdiction for mineral exploration. This paper summarizes current research activity and 2020 highlights from a year that, despite the impacts of the global pandemic, realized just under 50 publications, in line with typical annual output.

The Cordilleran Geoscience Section of the Survey conducts field and desk-based research activities including bedrock and surficial geology mapping programs, regional geochemical surveys, and targeted mineral deposit studies. Despite field activity in 2020 being confined to targeted studies on Vancouver Island due to Covid-19 health restrictions and related concerns, multi-year mapping and research programs in both northwest, central, and southern British Columbia were advanced with desk-based work and laboratory analyses. Integrated bedrock mapping updates for the provincial database and MapPlace (the BCGS geospatial web service) are in preparation for several areas of the province, including: southern Quesnellia, Bonaparte Lake to Quesnel River, Hagem, Polaris, Decar, Turnagain and Tulameen. Plans are also being developed to initiate a multi-year project, starting in 2021, to integrate detailed surficial geological mapping across the province into a seamless database and MapPlace.

Responsible for maintaining and developing provincial geoscience databases, the Resource Information Section disseminates data online through MapPlace. Information managed by the team includes traditional geological maps together with thematic studies and reports, geochemical, geophysical, and geological databases, plus information such as MINFILE, COALFILE, Mineral Assessment Reports (ARIS), and Property File. These databases also support development of next-generation mineral potential assessments using machine learning, which is now a major focus for the Survey to support land use and resource planning initiatives.

The Mineral Development Office (MDO) provides investment intelligence to government and global business, publishing the annual Provincial Overview of Exploration and Mining in British Columbia volume, and includes three Regional Geologists who track minerals activity across the province.

---

## 1. Introduction

The British Columbia Geological Survey, as the oldest scientific agency in the province, has provided public geoscience services to the people of British Columbia since 1895. The province is endowed with significant natural resources including metallurgical coal, base and precious metals, and industrial minerals. These deposits are intimately tied to the tectonic evolution of the Canadian Cordillera, which continued from protracted supercontinent breakup starting about 1600 million years ago to accretionary processes that operate today as Pacific Ocean crust slides beneath Vancouver Island. In the northeast of the province, the Western Canadian Sedimentary basin hosts significant petroleum hydrocarbon resources. As the steward of geoscience and mineral resource information in the province, the Survey has an important role in stimulating activity, attracting investment, informing decisions through technical information, and providing continuous research based on more than a century of corporate memory. The purpose of this paper is to provide a concise overview of current Survey

research activities and highlight key findings in 2020.

Active Survey research programs (Fig. 1) continue to define the geological evolution and natural resources of the province, generating knowledge and data to support land use and resource management decisions that balance economic, environmental, and community interests. A particular focus is providing public geoscience to support the growth of British Columbia as a competitive jurisdiction for mineral exploration. Not only does this include supporting industry, but also providing mineral resource information that is essential for informed land use decisions by government and, increasingly, from communities. The Survey is the primary repository for provincial geoscience knowledge. Maps, reports, and databases are freely available online, serving the interests of stakeholder groups including First Nations, local communities, the minerals industry, public safety agencies, environmental scientists, research organizations, and government agencies. Despite the extensive knowledge base provided by Survey products and archives, much work remains. The remote, rugged terrain

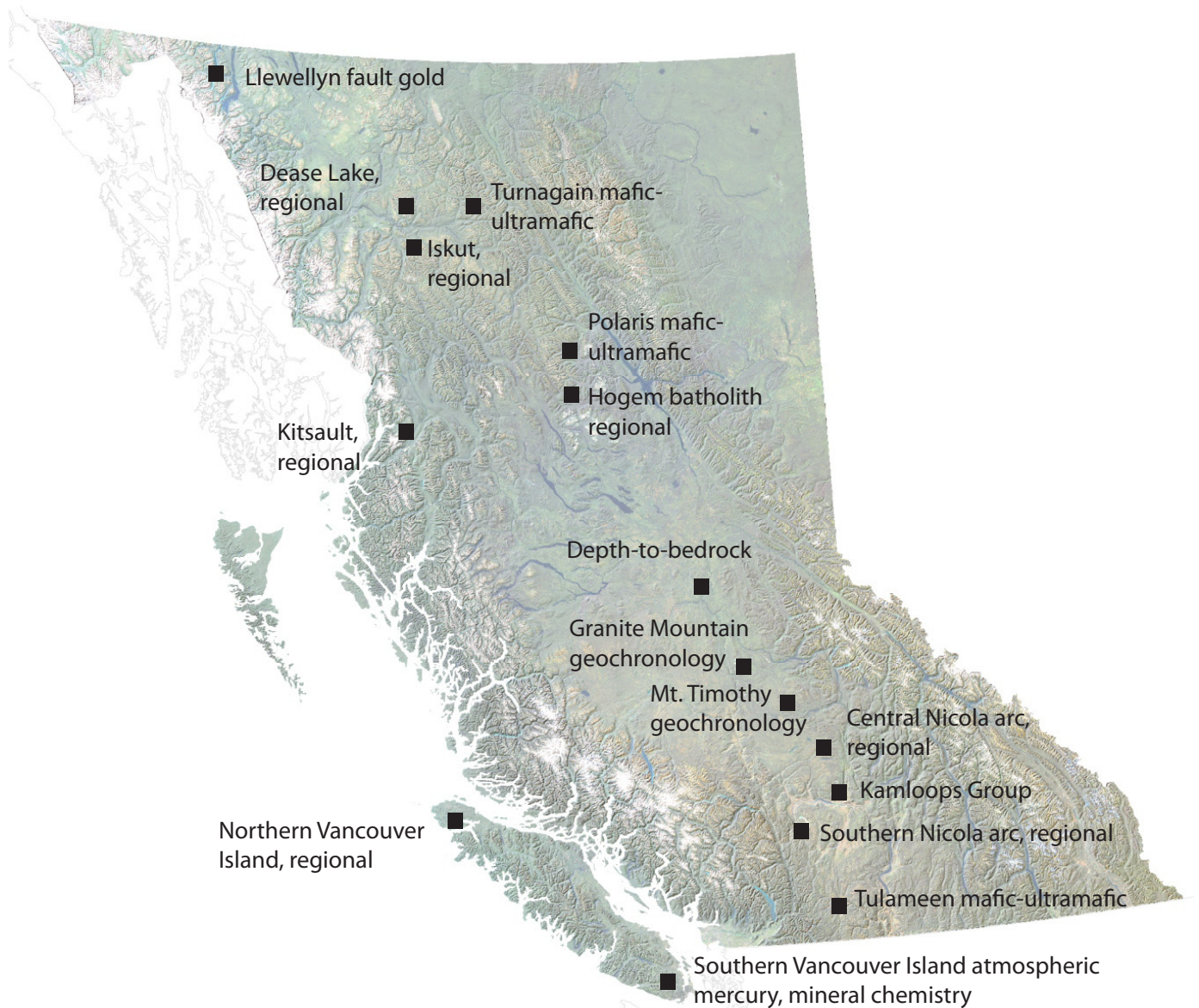


**Fig. 1.** British Columbia Geological Survey projects in 2020.

with harsh climatic conditions across much of the province has historically constrained Survey fieldwork. However, modern mapping techniques and technology advancements help improve the breadth and depth of geological understanding. Transformation of historic geoscience information to digital formats and databases will require coordinated effort as a multi-year initiative.

Headquartered in Victoria, the Survey is part of the Mines, Competitiveness, and Authorizations Division in the British Columbia Ministry of Energy, Mines and Low Carbon Innovation. Staffed by 35 employees, the BCGS consists of three sections: 1) Cordilleran Geoscience; 2) Resource Information and 3) the Mineral Development Office (based in a Vancouver satellite office and with Regional Geologists across the province). The Cordilleran Geoscience Section generates

new knowledge through field- and desk-based research activities including bedrock and surficial geology mapping programs, regional geochemical surveys, and targeted mineral deposit studies. Section team members manage in-house laboratory facilities, curate the provincial sample archive, and build capacity through contract employment and training of geoscience assistants (typically undergraduate and graduate students). The Resource Information Section is responsible for maintaining and developing provincial geoscience databases and disseminating data online through MapPlace, the BCGS geospatial web service. The Resource Information Section is also responsible for collecting, evaluating, approving, and archiving mineral and coal exploration assessment reports submitted by industry to maintain titles in good standing. The Mineral Development Office (MDO) provides investment

intelligence to government and global business, publishing the annual Provincial Overview of Exploration and Mining in British Columbia volume (e.g., Clarke et al., 2021), and includes three Regional Geologists who track minerals activity across the province (two positions are currently vacant).

The Survey welcomed the following new staff during 2020: Neil Wildgust (Director, Cordilleran Geoscience), replacing Fil Ferri who retired after 32 years with the Ministry; Evan Orovan, Mineral Potential Geoscientist; Bronwen Wallace, Mineral Assessment Geoscientist; Easton Elia, Geomatics Geoscientist; and Jenny Boulet, Project and Branch Coordinator. In addition, two Regional Geologists transferred from other parts of the Ministry to the Survey: Sean Tombe (Northwest Region) and Fiona Katay (Southeast Region). The past 12 months also saw Dejan Milidragovic and Pierre Landry leave the Survey ranks to pursue geoscience opportunities elsewhere in the province.

The global Covid-19 pandemic inevitably affected Survey operations in 2020. Staff were encouraged to work from home for much of the year and public health and social distancing requirements restricted summer field activity, exacerbated by concerns about local community interactions. External laboratory services were also affected in many cases, leading to delays in analytical testing and processing of results. Nonetheless, projects continued and the Survey staff maintained a full workload and publication output (Fig. 2).

## 2. Partnerships

The Survey adopts a collaborative approach wherever possible, extending the scope and content of public geoscience while also minimizing the risk of duplicative work. The Geological Survey of Canada (GSC) is an established partner; the two surveys have collaborated recently through the Geomapping for Energy and Minerals (GEM 2) and Targeted Geoscience Initiative 5 (TGI-5) programs, both completed in 2020. Research completed under these programs included: mapping of Cache Creek and Stikine terranes near Atlin (Zagorevski et al., 2021; and see section 3.1.1.); examining specialty metal deposits that host rare earth elements, lithium, tantalum, and niobium (Simandl et al., 2021; Paradis et al., 2021a, b; and see section 3.2.1.); defining a new mineral deposit model for orogenic Ni-Cu-PGE mineralization in Alaskan-type ultramafic-mafic intrusions (Nixon et al., 2020a, b); and investigating gold deposits related to the Llewellyn fault and Tally Ho shear zone in northwestern British Columbia and southern Yukon (Castonguay et al., 2020). The GSC is currently launching new multi-year phases of these programs (TGI-6 and GEM-GeoNorth) and seeking active collaboration with provincial and territorial surveys across Canada.

In collaboration with GSC, the Yukon Geological Survey (YGS) and the Geological Association of Canada (Pacific section), the Survey hosted an online workshop ‘Cordilleran Geoscience: a 2020 Perspective’ in October. This event included a historic perspective on the development of Cordilleran Geoscience and terrane tectonics, followed by recent research focussed on Cordilleran evolution. The workshop attracted

more than 400 registrants, with at least 240 participants logged on throughout the day and contributing to lively Q&A sessions.

## 3. Cordilleran Geoscience Section

Section geologists collect fundamental geoscience data through single and multi-year field-based programs complemented by laboratory and desk-based studies, including regional-scale mapping, mineral deposit studies, and development of new mineral exploration methods. Expertise encompasses tectonics and structural geology, stratigraphy, petrology, metallogeny, coal deposits, Quaternary and surficial geology, critical minerals, and geochemistry. The following sections highlight ongoing and recently completed research activities, which progressed significantly in 2020 despite fieldwork being limited to Vancouver Island by pandemic concerns and associated public health orders.

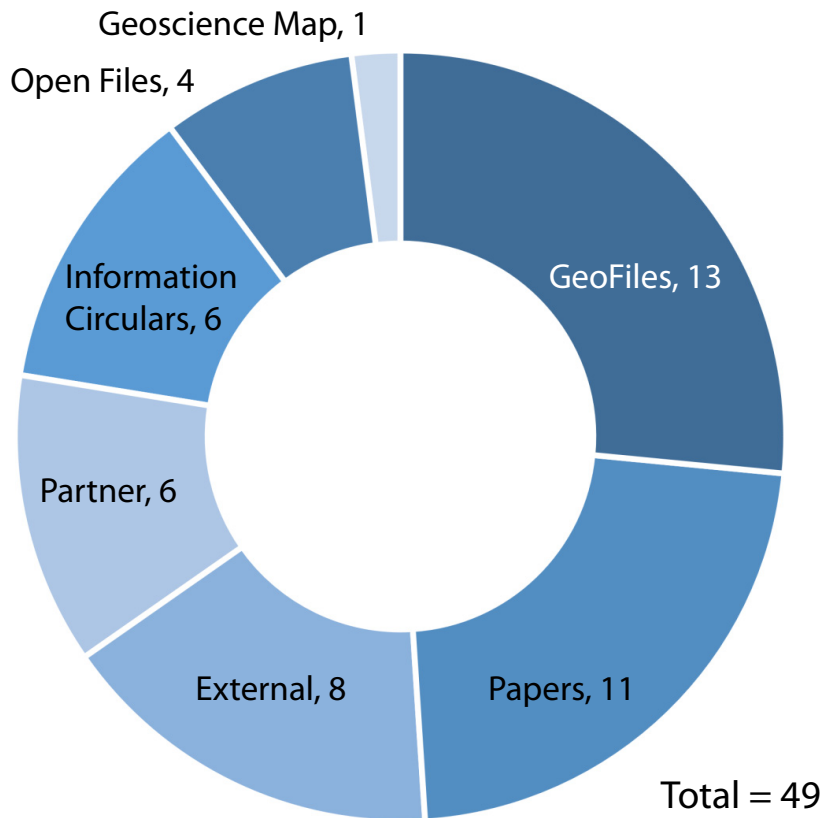
### 3.1. Mapping, regional synthesis and compilation

Mapping is a core element of Survey and Cordilleran Section programs, delivering two key products: updates to the provincial digital geology database that ultimately feed into MapPlace, and more traditional published maps in the form of PDF files with accompanying research papers. Both products stem from common processes including desk-based review of previous work and aerial and satellite imagery, field mapping, laboratory analyses, geological interpretation, and synthesis of these information sources into digital data formats. The resulting datasets form an essential component of modern mineral potential assessment methods being developed by the Survey to inform land use planning policies within the provincial government (see section 3.2.).

Integrated regional bedrock map updates for the provincial database and MapPlace are listed in the sections below. Plans are also being developed to initiate a multi-year project, starting in 2021, to integrate detailed surficial geological mapping across the province into MapPlace.

#### 3.1.1. Northwest British Columbia

Northwest British Columbia hosts significant base and precious metals mineral deposits, including in an area colloquially referred to as the ‘Golden Triangle’ between Iskut and Stewart. An ongoing multi-year Survey program will continue to expand regional bedrock mapping coverage to support mineral exploration activity. Understanding the stratigraphic, magmatic, structural, metallogenic, and tectonic framework of this region, as recently summarized by Colpron and Nelson (2021), continues to advance through Survey research. Nelson and van Straaten (2020) described how mineralization in the Stikine volcanic island arc terrane aligns with deep crustal corridors that probably originated as fundamental zones of weakness in the pre-Devonian basement of north-central Stikinia, concluding that the exceptional mineral endowment of this region is due to a location intersecting sets of long-lived trans-crustal (probably trans-lithospheric) lineaments that provided conduits for magmas



**Papers\*:** This series is reserved for reviews and final thematic or regional works. Geological Fieldwork, our annual review of field activities and current research, is released as the first Paper of each year.

**Geoscience Maps:** This series is the BCGS vehicle for publishing final maps.

**Open Files:** These maps and reports present the interim results of ongoing research, particularly mapping projects.

**GeoFiles:** These publications enable rapid release of extensive data tables from ongoing geochemical, geochronologic, and geophysical work. As such, they serve the same function as data repositories provided by many journals, providing immediate access to raw data from specific projects.

**Information Circulars:** These publications provide accessible geoscience information to a broad audience in government, industry, and the general public. Included in the Information Circular series are the annual Provincial Overview of Mining and Exploration, \*\*Exploration and Mining in British Columbia, and the Coal Industry Overview.

**Contributions to partner publications:** This category includes reports, maps, and other products published by another agency such as the Geological Survey of Canada or Geoscience BC, but have received contributions from British Columbia Geological Survey staff.

**External publications:** These are contributions to the peer reviewed literature and published in a recognized national or international scientific journal.

\*The count refers to the total number of articles authored by BCGS personnel in a volume.

\*\*Although five articles are included in Exploration and Mining in British Columbia, it is counted as a single volume.

**Fig. 2.** Types and numbers of publications produced by the British Columbia Geological Survey in 2020.

and fluids during a succession of arc, back-arc, and post-arc tectonic regimes. George et al. (2021) provide new U-Pb zircon geochronologic and Lu-Hf isotopic data to address the timing of latest Triassic-Early Jurassic accretion in Stikinia, attributing

regional shortening to variable along-strike interactions during end-on collision with the Yukon-Tanana terrane such that the northern apex of Stikinia saw significant crustal thickening that is lacking farther south. Pre-Devonian zircon populations,

likely multi-cyclic, differ from those of northern Yukon-Tanana terrane but resemble those of southern Wrangell terrane, and George et al. (2021) suggest that Stikinia was an independent crustal block before the onset of latest Triassic collision.

Integrated bedrock mapping updates for the provincial database and MapPlace are currently in preparation for significant areas (Fig. 3). For the Dease Lake area, ongoing activities are geared towards publication of a 1:100,000 scale Geoscience Map, a final update to the provincial database and a GeoFile incorporating geochronological, paleontological, petrographic, lithogeochemical, structural and petrophysical data. Lang et al. (2020) detailed the geology of the Gnat Pass porphyry copper deposit.

Field mapping in the Kitsault River area commenced in 2019 (Hunter and van Straaten, 2020), and a further season of mapping will be undertaken in 2021 or as soon as pandemic

restrictions allow. The area is largely underlain by porphyry-epithermal- and VMS-prospective volcanosedimentary rocks of the Stuhini and Hazelton groups (Late Triassic to Middle Jurassic). To complement future regional mapping, a desktop lithogeochemical study is currently focussed on the Hazelton Group with analyses of 2015 and 2019 Survey field samples and using available exploration lithogeochemistry data from sampling in the Dolly Varden, Brucejack (Bowser Property) and Eskay Creek VMS-related deposit areas. The results of this study will be published in 2021 to identify geochemical characteristics of rock units that host VMS-style mineralization and resolve key stratigraphic questions. This project also builds on concurrent research nearby at Kinskuch Lake by Miller et al. (2020).

Included in this edition of Fieldwork is a guest paper by Greig et al. (2021), which summarizes the results of recent

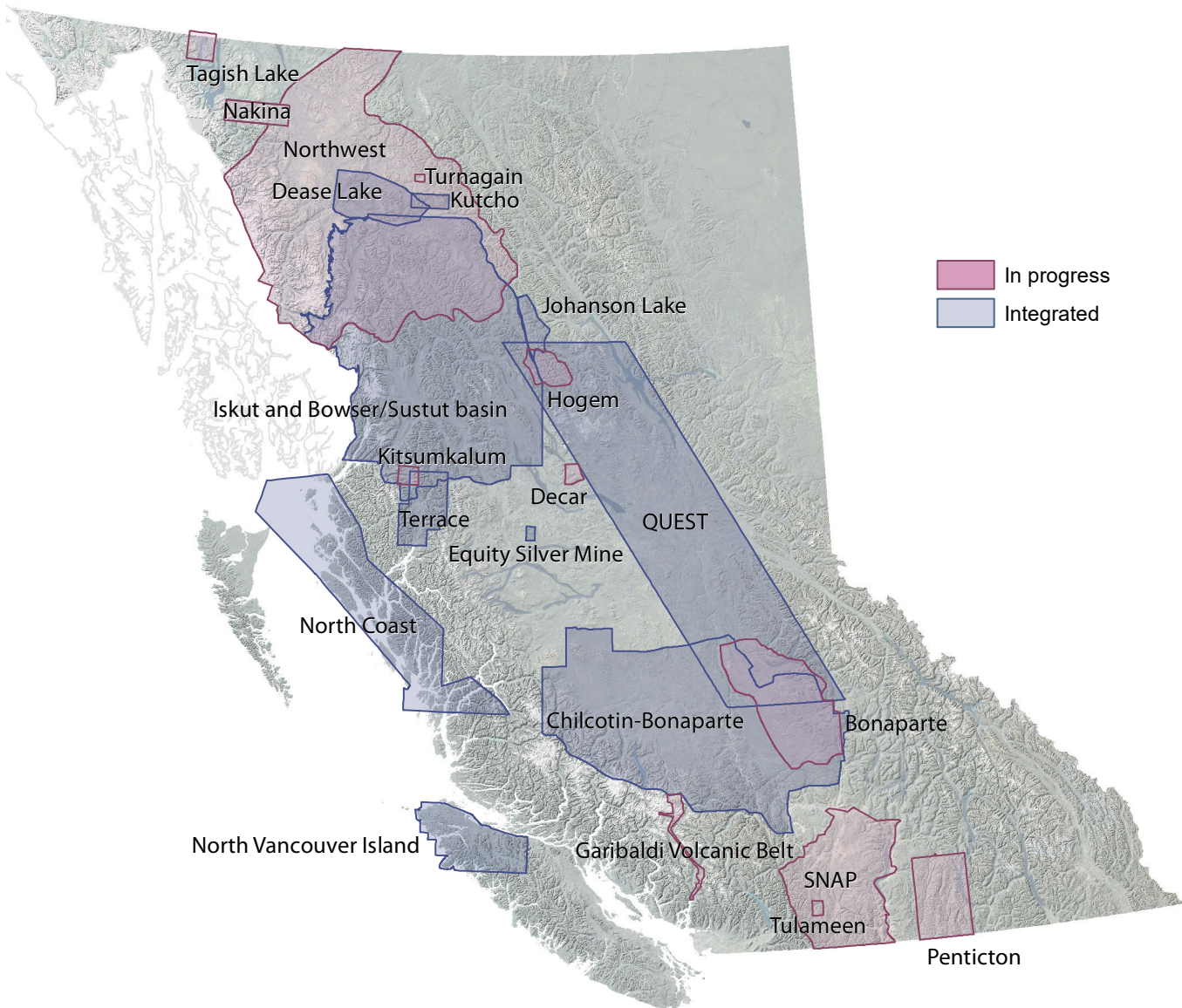


Fig. 3. Recent and planned digital geology compilation updates.

geologic mapping, new U-Pb zircon and Re-Os molybdenum geochronology, and drilling at the Tatogga property in the Iskut district. The data obtained establish the geological framework of mineralization and the timing of contraction that led to Stuhini Group deformation, uplift, and erosional stripping before deposition of the Hazelton Group (Fig. 4).



**Fig. 4.** Gently northwest-dipping Hazelton Group rocks underlying Tsazia Mountain, viewing west from Mount Poelzer; see Greig et al. (2021).

### 3.1.2. Central and southern British Columbia

Integrated bedrock mapping updates for the provincial database and MapPlace (Fig. 3) are currently in preparation for several areas of central and southern British Columbia as a result of Survey mapping and compilation projects: southern Nicola Arc, southern Quesnellia, Bonaparte Lake to Quesnel River, Hagem, Polaris, Decar, Turnagain and Tulameen. An update based on mapping outside of Survey programs in the Penticton area of southern BC is planned.

A multi-year mapping project was initiated in 2018 targeting the northern Hagem batholith and adjacent intrusive, volcanic and sedimentary rocks of the Stikine and Cache Creek terranes. New and previously unpublished geochronological data that complement bedrock mapping and geochemical studies indicate punctuated emplacement of four distinct intrusive suites during a protracted (ca. 80 Ma) interval, from 207 to 128 Ma (Fig. 5; Ootes et al., 2020; Jones et al., 2021). Bedrock mapping and geochronologic results from this study indicate that the northern Hagem batholith contains prospective rocks comparable to those that host the Lorraine and other deposits south of the present study area. Surficial geologic mapping integrated with the bedrock component indicates that the Cordilleran Ice Sheet covered the Hagem batholith area during the Late Wisconsinan glacial maximum when ice flowed east and southeast across the region (Ferbey and Elia, 2021). For most of the Late Wisconsinan, ice flow was controlled by topography, as recorded by glacially streamlined or eroded landform- and outcrop-scale indicators which are commonly aligned parallel to valleys. Valley glaciers were not entirely

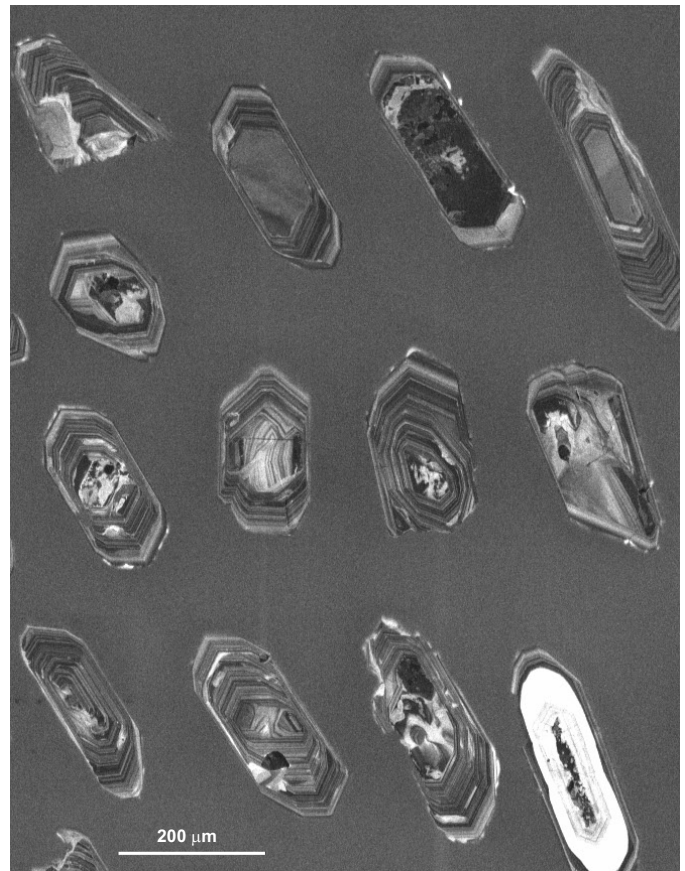


**Fig. 5.** Cathodoluminescent images of zircons from the Mesilinka plutonic suite (Cretaceous), Hagem batholith. All show typical prismatic igneous zircon morphology, but some show cores with rim overgrowths. The bright interior of the zircon at the bottom right reflects a relatively high U content. See Ootes et al. (2020) and Jones et al. (2021).

controlled by local topography and were thick enough to flow over low-elevation, through-valley, topographic divides transporting glacial debris into adjacent drainages. Significant volumes of glacial meltwater flowed through the valleys during deglaciation, transporting coarse-grained sands and gravels. Colluvial deposits are common along the base of steep slopes and are now vegetated and stable, but talus aprons and cones are still actively being constructed. Organic deposits occur throughout the study area, mostly as narrow transition zones between tree stands and water bodies. Subglacial till (Fig. 6), the ideal sample medium for till geochemistry and mineralogy surveys, is common in valley bottoms and lower hillslopes. Surficial geology maps of the Hagem batholith are in preparation for publication in 2021. In addition to the current mapping, Logan et al. (2020) reviewed the geology, structural setting, and porphyry deposits of the Hagem batholith.

Summarizing a long-term project in the southern Nicola arc, a region endowed with significant porphyry Cu-Au-Mo-Ag and other deposits, Mihalynuk and Diakow (2020) completed a 1:50,000 scale map depicting the geology of a 2000 km<sup>2</sup> area extending from southeast of Merritt to Princeton. Friedman



**Fig. 6.** A blocky, massive, overconsolidated subglacial till with a silty-sand matrix exposed on the north side of Mesilinka River valley, east of Aiken Lake; see Ferbey and Elia (2021).

et al. (2020) reported two new U-Pb zircon ages from the Nicola Group, one the oldest dated thus far (CA-TIMS,  $239.99 \pm 0.16$  Ma), the other the youngest (LA-ICPS detrital,  $200.2 \pm 1.1$  Ma; Fig. 7). van Straaten et al. (2020) reviewed the mined Gibraltar porphyry copper-molybdenum deposit and Schiarizza and Friedman (2021a) report new chronological data for the Granite Mountain batholith (Late Triassic), host to the mine. Three samples from the Granite Mountain batholith yield Late Triassic dates of  $217.15 \pm 0.37$  Ma (Granite Mountain phase leucocratic tonalite),  $215.71 \pm 0.36$  Ma (Mine phase tonalite), and  $214.98 \pm 0.38$  Ma (quartz-plagioclase porphyry dike cutting Mine phase tonalite). The Burgess Creek stock, on the northeast margin of the Granite Mountain batholith, provides dates of  $222.71 \pm 0.39$  Ma (tonalite) and  $221.25 \pm 0.39$  Ma (quartz diorite), demonstrating that it is also Late Triassic, but several million years older than the Granite Mountain batholith. To the south, the Sheridan Creek stock contains a foliation with the same orientation and characteristics as a prominent foliation in the southern part of the batholith (Fig. 8). Tonalite from the Sheridan Creek stock returns an Early Cretaceous date of  $108.57 \pm 0.18$  Ma, demonstrating that the foliation is mid-Cretaceous or younger. Work continues on the final compilation of a study (e.g., Schiarizza, 2019) in the central part of the Nicola arc.

Working in the type area of the Kamloops Group in south-central British Columbia, Van Wagoner et al. (2021) examined the physical volcanology and geochemistry of Eocene rocks that form part of the Challis-Kamloops belt which, extending for 2000 km along the length of Cordillera, records orogen-scale extension, graben formation, volcanism, and sedimentation. The area is underlain by rocks indicating subaerial to subaqueous (lacustrine) volcanism, with volcanic facies including mega pillows, hyaloclastites, pahoehoe and aa flows, domes and phreatomagmatic cones (Fig. 9). A preliminary comparison of Kamloops Group geochemistry and data from other nearby Eocene units (Princeton and Penticton groups) indicates distinct geographic differences. The Kamloops and



**Fig. 7.** Geochronologic sampling, Nicola Group; see Friedman et al. (2020) and Mihalyuk and Diakow (2020).



**Fig. 8.** Foliated Mine phase tonalite, Granite Mountain batholith, west of Gibraltar Mine; see Schiarizza and Friedman (2021a).



**Fig. 9.** The ridge top exposes Eocene andesitic breccias (Kissick member, Dewdrop Flats Formation, Kamloops Group) representing a dome or sub-volcanic intrusion. In the foreground are Quaternary gravel deposits. See Van Wagoner et al. (2021).

Princeton group melts may have been derived from the spinel-garnet transition zone in the subcontinental lithospheric mantle and influenced by slab-derived fluids, whereas the Pentiction Group shows trends toward anhydrous enrichment and may have been derived from a different source. Farther north, Schiarizza and Friedman (2021b) resolved the age of volcanic rocks exposed on the southern slope of Mount Timothy that previously had been considered part of the Nicola Group. A sample of plagioclase-hornblende-pyroxene-phyric andesite yielded an Eocene U-Pb zircon age of  $50.84 \pm 0.04$  Ma (CA-TIMS), significantly younger than the Nicola Group.

To help steer future exploration efforts, the BCGS is continuing a regional depth-to-bedrock study in the drift-covered area of the Central Interior Plateau between the Mount Polley and Mount Milligan Cu-Au porphyry deposits. This project is using published data, including drill hole, bedrock, and surficial maps to establish the geometry of the bedrock-drift interface. Final reporting is anticipated in early 2021. The Survey is also planning to undertake remotely piloted aircraft system surveying in this region (see section 3.2.2.).

Field activity on northern Vancouver Island focussed on collecting samples of Neogene rocks for geochronology and geochemistry to better understand the spatial and temporal distribution of porphyry Cu-Mo mineralization. High-precision dating reported by Nixon et al. (2020c) linked the Klaskish Plutonic Suite (ca. 7 to 4.6 Ma) emplacement and crystallization to porphyry Cu-Mo magmatic-hydrothermal systems, representing an extensive and underexplored metalotect. Analytical results and reporting are anticipated in the first half of 2021.

### 3.2. Targeted deposit studies and exploration methods

Regional mapping programs as described above are complemented by more specific or thematic studies, typically selected to develop public geoscience knowledge and datasets in key topics that support minerals exploration or land use policy within government. Survey geoscientists are able to trial innovative technologies that can support future regional mapping and mineral exploration activities.

#### 3.2.1. Deposit studies

In anticipation of the next generation of mineral deposit profiles which, aided by machine learning, will guide modern mineral potential assessments, Lefebure and Jones (2020) compiled all deposit profiles developed between 1995 and 2012 into a single volume. The Survey is well positioned to advance such new methods with established databases supporting MapPlace and other applications (see section 4); 2020 saw significant effort to frame and develop mineral potential assessment for the Tahltan traditional territory in the northwestern part of the province to support land use policy discussions.

Although Alaskan-type ultramafic-mafic intrusions are gaining recognition as a global class formed at convergent margins and are also gaining global importance as an economic resource, they remain poorly understood and underexplored. Nixon et al. (2020a) reviewed magmatic Ni-Cu-PGE deposits hosted by Alaskan-type intrusions in the Canadian Cordillera, including Tulameen in south-central British Columbia and Polaris and Turnagain in the northwest. Nixon et al. (2020b) reported new U-Pb zircon and  $^{40}\text{Ar}/^{39}\text{Ar}$  ages from the Turnagain intrusion, and Nott et al. (2020) published a detailed (1:15,000)

map of the Polaris intrusion that refined internal and external geological relationships. Research directed toward developing an emplacement framework for the Polaris intrusion continues.

As part of ongoing work devoted to specialty metals in southern British Columbia, Simandl et al. (2021) reported on rare earth elements in carbonates from sediment-hosted lead-zinc deposits, Paradis et al. (2021a) summarized carbonate-hosted mineral deposits (Mississippi Valley-type, magnesite, and REE-F-Ba), and Paradis et al. (2021b) examined the distribution of trace elements in pyrite from carbonate-hosted sulphide deposits. Work continues on the geochemistry of the main mineralized zone at the Rock Canyon Creek REE-Ba-F deposit and reviewing opportunities and risks associated with exploration and development of critical magnet, battery, and photovoltaics materials.

Riddell (2020) evaluated coal ash chemistry indices for predicting CSR (coke strength after reaction with  $\text{CO}_2$ ) for coking coals of the Rocky Mountains (Fig. 10), concluding that correlations between measured CSR and the most commonly used predictive index (Base-Acid Ratio) are moderate to strong and thus can provide a timely and inexpensive first-order prediction for CSR, although not accurate enough for feasibility studies or product marketing. A new mineral characterization study of metallurgical coals by the Survey was initiated in 2020, beginning with sampling of the Gething Formation in the Peace River coalfield. Samples will be analyzed using an automated scanning electron microscope (SEM) to determine the mineral content, including abundance, speciation, contact association and grain size. The method is used to help design the most effective methods of processing raw coal. The data produced can also be used at the exploration phase of a project, to improve coal quality prediction.



**Fig. 10.** Coal core from the Gething Formation, Carbon Creek, northern British Columbia; see Riddell (2020).

### 3.2.2. Exploration methods

Regional geochemistry remains a major focus for the Survey. Indicator mineral chemistry enhances the provincial

geochemical database by typifying potential ore deposits in prospective drainage basins. As an example and a focus during 2020, re-analysis of the archive heavy-mineral concentrate (HMC) samples using scanning electron microscopy, electron probe micro-analysis (EPMA), laser ablation inductively coupled plasma mass spectrometry (LA-ICP-MS) and quantitative mineralogy (Rukhlov et al., 2021a) confirmed the findings of Rukhlov et al. (2020a) that yttrium-rich garnet associated with placer gold deposits at Loss Creek in the southern Vancouver Island area is the main host of ‘strategic’ and ‘critical’ heavy rare earth elements (HREE) and Ge in the HMC samples. Concentrations of up to 0.53% REE (mostly HREE) in the garnet are comparable with the top grade of the world’s largest HREE producers such as the ion-adsorption clay deposits (0.05-0.5% REE) in southern China, and with eudialyte-hosted REE deposits (1.6% REE) associated with peralkaline massifs such as Ilímaussaq in southern Greenland. The significant geochemical resources of HREE, Mn, and Ge in the Loss Creek catchment basin (Rukhlov et al., 2020a) suggest that the Y-rich garnet could be a potentially source of the low-carbon energy and high-technology metals. A suite of indicator minerals, including apatite, magnetite, and epidote, recovered from samples collected in the northern Vancouver Island area in 2019 have been also analyzed for major- and trace-element concentrations using in situ EPMA and LA-ICP-MS.

Continuing long-standing Survey geochemical and mineralogical studies to define glacial dispersal systems down-ice of buried mineral deposits (e.g., Hickin and Plouffe, 2017), Lett and Paulen (2021) re-examined surface sediment and till geochemistry at the Ace mineral property using data from Survey fieldwork conducted in 2000. Much of the bedrock on the property is concealed by lodgement (basal) till, which was deposited by a southeast to northwest ice movement. The trace element dispersal profiles suggest a massive sulphide source for the anomalous metals in bedrock beneath the till at the east end of the dispersal train. Potentially, other till and soil Au and As anomalies in the western and southern parts of the survey area could have been derived from unmapped, northeast-trending gold-quartz veins.

Mercury vapour surveys have been used in geochemical exploration because Hg occurs in most types of endogenic ore deposits and is highly mobile. Rukhlov et al. (2020b, 2021b) measured atmospheric mercury vapour (Fig. 11) at 15 sites on Vancouver Island. To evaluate the effectiveness of the method across a range of settings, these sites include different types of known mineralized zones, barren rocks, and faults, both buried and exposed. The highest Hg concentration was above tailings at the Bentley Au occurrence, possibly due to the amalgamation technique used for fine gold extraction between the late 1800s and early 1900s. Prominent Hg vapour haloes mark shear-hosted Cu-Ag-Au sulphides at Mount Skirt (13.4x background Hg), epithermal Au-Ag-Cu at Mount Washington (8.9x background Hg), and sediment-covered polymetallic volcanogenic massive sulphide at the Lara-Coronation occurrence (4.2 to 6.6x background Hg). Basalt-hosted Cu-



**Fig. 11.** Simultaneous measurement of meteorological conditions (on tripod) and direct measurement of atmospheric Hg vapour concentrations using a portable RA-915M analyzer along a terrane boundary at Harling Point, Municipality of Oak Bay, Victoria; see Rukhlov et al. (2020b, 2021b).

Ag-Au sulphide zones at the Sunro past producer are marked by weak Hg vapour anomalies relative to local background. Faults, including the Leech River fault, which was active in the Quaternary, are also marked by weak Hg vapour anomalies. The study confirms that, although the Hg level is influenced by weather, the real-time Hg vapour measurement of near-surface air can delineate mineralized zones and fault structures that are buried under overburden 10s of m thick. In contrast to soil gas sampling, this simple and rapid technique can be applied to mineral exploration and geological mapping under overburden above any type of surface, including outcrops, talus, bogs, water bodies, snow, and permafrost.

Remotely piloted aircraft system (RPAS)-mountable gamma ray spectrometers are now commercially available, allowing inexpensive acquisition of K, U, and Th data above till-covered areas. The Survey is planning to use this technique to help characterize mineral potential in the Central Interior Plateau region. Phase 1 (scheduled for 2021) of this project would be a case study to prove the RPAS-borne radiometric method, in the context of till provenance and drift prospecting. The Mount Polley porphyry Cu-Au mine area is an ideal field laboratory for this case study, with mapping control on bedrock and surficial geology supplemented by matrix till geochemical and mineralogical data; forestry clear-cuts are well located for enabling RPAS surveys to be flown over subglacial tills of different provenance.

#### 4. Resource Information Section

The Survey is the custodian of all provincial public geoscience data. This entails regularly upgrading databases and making this information, and its derivatives, easily accessible through web portals. Survey geoscientists collect fundamental geoscience information that is transferred into these online databases and used by industry to develop projects

and help search for new discoveries. This information includes traditional geological maps together with thematic studies and reports, geochemical, geophysical, and geological databases, plus information such as MINFILE, COALFILE, Mineral Assessment Reports (ARIS), and Property File. All these data products are accessible through the Digital Geoscience Data page of the Survey website. Besides providing improved access to geoscience data and functionality for a range of applications and stakeholders, the availability of databases supports developing machine learning methods for future applications including mineral potential assessment.

#### 4.1. MapPlace

MapPlace <[www.MapPlace.ca](http://www.MapPlace.ca)> is the BCGS geospatial web service to efficiently visualize, search, report, and generate custom results and maps from province-wide geoscience databases. Some of the advanced applications and user interfaces are specifically designed to enable research and analytics for mineral exploration and prospecting. Easy access to, and analysis of, geoscience data and maps are fundamental to inform decisions on mineral exploration, mining, environmental protection, and land use management. MapPlace provides a platform to facilitate the discovery, display, search, and analysis of geoscience in the context of all other relevant data such as mineral titles, assessment reports, land ownership, linear infrastructure, aquifers, topography and satellite imagery. Recent additions to MapPlace include: a light version for mobile devices; enhancement of topographic features; assessment report-sourced surface sediment geochemical data; and a layer to display bedrock map footprints with links to publication details and downloads.

#### 4.2. ARIS reports and database

Results of mineral exploration programs are submitted by industry in assessment reports to the government in compliance with the Mineral Tenure Act. After a one-year confidentiality period, the reports become an open resource for mineral exploration, investment, research, land-use, and resource management. The Survey maintains these reports in the Assessment Report Indexing System (ARIS) database. This database provides information about the location, mineral occurrences, commodities, claims, work types, and expenditures as documented in the assessment reports. ARIS contains more than 38,000 reports dating from 1947. All reports are available online as PDF documents through the British Columbia Geological Survey website. Digital data, in formats that can be readily used such as spreadsheets rather than .PDF files, from 620 assessment reports are available through the ARIS search application. A version of the ARIS database is available in Microsoft Access format (.mdb) from the digital geoscience data webpage <<https://www2.gov.bc.ca/gov/content/industry/mineral-exploration-mining/british-columbia-geological-survey/publications/digital-geoscience-data>>.

Following the 2019 release of the assessment report-sourced surface sediment geochemical (ARSSG) database

(Norris and Fortin, 2019) work continues beyond the Interior Plateau. The database currently contains more than 5.75 million determinations from over 143,000 samples across the province. The data are incorporated into MapPlace and the ARSSG application <[http://webmap.em.gov.bc.ca/arssg/arssg\\_home.asp](http://webmap.em.gov.bc.ca/arssg/arssg_home.asp)>, which includes sample details and a location map. Development of an assessment report-sourced drillhole database is ongoing.

#### 4.2.1. ARIS digital data submission

Traditionally, data in assessment reports have been embedded in paper or non-digital electronic files, such as PDF, making them difficult to extract and use. The Survey is encouraging digital data submission, which will benefit users because digital data can be easily retrieved, integrated, processed, recalculated, and recast for specific needs. Digital submission will also enable the Survey to better maintain province-wide databases and create derivative products that use past results to guide future exploration. The ARIS Data portal is now available for clients to submit both assessment reports and digital data files (up to 2 GB), such as spreadsheets, databases, maps, grids describing technical work in an assessment report. Data can be uploaded through the ARIS data submission page <[http://webmap.em.gov.bc.ca/mapplace/ar\\_digital\\_submission.html](http://webmap.em.gov.bc.ca/mapplace/ar_digital_submission.html)>. Archives of previous assessment report data are accepted and encouraged for submission.

#### 4.3. Other databases

COALFILE includes a collection of 1030 coal assessment reports, dating from 1900. Associated data include 16,100 boreholes, 550 bulk samples, 5400 maps, 3650 trenches, 484 coal ash chemistry analyses and links to MINFILE. COALFILE data are integrated with MapPlace.

MINFILE is a database for mineral, coal, and industrial mineral occurrences and associated details on geology and economic information for more than 15,300 records. In the last year, more than 200 new occurrences and 1250 updates were added to the database. The web-enabled MINFILE search application interacts with MapPlace, ARIS, and Property File. The MINFILE bibliography now links more than 9500 MINFILE records directly to Property File.

Property File is a collection of more than 85,000 archived reports, maps, photos, and technical notes documenting mineral exploration activities in British Columbia from the late 1800s. These documents are accessible in a full-text, searchable, online database. The records are spatially linked to MINFILE. The Survey accepts donations to Property File.

The provincial geochemical databases hold field and geochemical data from multi-media surveys by the Geological Survey of Canada, the BCGS, and Geoscience BC. The databases are updated regularly and contain results from: 1) the Regional Geochemical Survey program (RGS) including analyses from more than 66,000 stream-sediment, lake sediment, moss, and water samples (Han and Rukhlov, 2020a);

2) 10,500 till surveys (Bustard et al., 2017, 2019); and 3) 11,000 litho-geochemical samples (Han and Rukhlov, 2020b). An updated geochronology database (Han et al., 2020) is anticipated to be launched in 2021. A surficial geology index map for the province (Arnold and Ferbey, 2019) is regularly updated as is an ice-flow indicator database for British Columbia and Yukon (Arnold and Ferbey, 2020).

#### 4.4. British Columbia digital geology

The BCGS offers a province-wide digital coverage of bedrock geology including details from field mapping at any scale, with a typical regional compilation at a scale of 1:50,000. BC Digital Geology regularly integrates new regional compilations. Bedrock geology is standardized with consistent stratigraphic coding, ages, and rock types to enable computations and is available for download in GeoPackage and Esri shapefile formats. Customized bedrock geological maps and legends can be explored, and data downloaded as KML by spatial and non-spatial queries via MapPlace. The BCGS has transformed the digital geology to the GeoSciML Lite schema and mapped the contents using the vocabularies adopted by the IUGS Commission for the Management and Application of Geoscience Information (CGI). The GeoSciML Lite-compliant digital geology is accessible via the OneGeology portal and open standard-based interface such as WMS and WFS, to enable interoperation and analytics of the Survey database to the exploration and mining industry. The Survey is currently focussing on integrating various compilations (see section 3) and progressing a compilation of field stations and structural measurements that will be part of the BC Digital Geology database; preliminary results will be released in 2021.

#### 5. Mineral Development Office

The Mineral Development Office (MDO) is the Vancouver base of the British Columbia Geological Survey. It links the more than 800 exploration and mining companies headquartered in Vancouver to provincial mineral and coal information. The MDO distributes Survey data and provides technical information and expertise about mineral opportunities to the domestic and international investment community. The MDO monitors the activities of the mining and exploration sectors and produces the ‘Provincial Overview of Exploration and Mining in British Columbia’, an annual volume that summarizes activities in the different regions of the province (see e.g., Clarke et al., 2021).

The British Columbia Regional Geologists (Table 1) represent the provincial government on geological matters at a regional level and capture information on industry activity in their jurisdictions. Within their communities, they provide information on exploration trends, possible investment opportunities, land use processes, First Nation capacity building, and public outreach. Since 1993, the Regional Geologists reported to regional office directors. In 2020, the Regional Geologists were repatriated to the BCGS as part of the MDO.

**Table 1.** British Columbia Regional Geologists.

Regional Geologist	Office	Region
Sean Tombe	Smithers	Northwest
Vacant	Prince George	Northeast and North Central
Vacant	Kamloops	South Central
Fiona Katay	Cranbrook	Southeast
Bruce Northcote	Vancouver	Southwest

### Acknowledgment

We thank George Owsiacski of Total Earth Science Services (Victoria) for the desktop publishing of this volume.

### References cited

- Arnold, H., and Ferbey, T., 2019. British Columbia surficial geology map index, British Columbia Ministry of Energy, Mines and Petroleum Resources, British Columbia Geological Survey Open File 2019-03, Data version 2020-01.
- Arnold, H., and Ferbey, T., 2020. Ice-flow indicator database, British Columbia and Yukon. British Columbia Ministry of Energy and Mines and Petroleum Resources, British Columbia Geological Survey Open File 2020-03, 1 p.
- Bustard, A.L., Han, T., and Ferbey, T., 2017. Compiled till geochemical data for British Columbia. British Columbia Ministry of Energy, Mines and Petroleum Resources, British Columbia Geological Survey GeoFile 2017-09, 7 p.
- Bustard, A.L., Ferbey, T., and Arnold, H., 2019. Regional- to property-scale till geochemical and mineralogical surveys in British Columbia for base and precious metals. British Columbia Ministry of Energy and Mines and Petroleum Resources, British Columbia Geological Survey Open File 2019-04 version 2020-01.
- Castonguay, S., Ootes, L., Devine, F., and Friedman, R., 2020. Superimposed Late Cretaceous and earliest Eocene gold mineralization and deformation events along the Llewellyn-Tally Ho deformation corridor in northwest British Columbia and southern Yukon. In: Mercier-Langevin, P., Lawley, C.J.M., and Castonguay, S., (Eds.), Targeted Geoscience Initiative 5: Contributions to the Understanding of Canadian Gold Systems. Geological Survey of Canada Open File 8712, pp. 223-236.
- Clarke, G., Northcote, B., Katay, F., and Tombe, S.P., 2021. Exploration and Mining in British Columbia, 2020: A summary. In: Provincial Overview of Exploration and Mining in British Columbia, 2020. British Columbia Ministry of Energy, Mines and Low Carbon Innovation, British Columbia Geological Survey, Information Circular 2021-01, in press.
- Colpron, M., and Nelson, J.L., 2021. Northern Cordillera: Canada and Alaska. In: Elias, S., and Alderton, D., (Eds.), Encyclopedia of Geology, Second Edition. Academic Press, pp. 93-106.
- Ferbey, T., and Elia, E.A., 2021. Preliminary surficial geology of the northern Hogen batholith area, north-central British Columbia. In: Geological Fieldwork 2020, British Columbia Ministry of Energy, Mines and Low Carbon Innovation, British Columbia Geological Survey Paper 2021-01, pp. 57-64.
- Friedman, R.M., Mihalynuk, M.G., and Diakow, L.J., 2020. Geochronologic data from samples collected near Pothole Lake and Pennask Mountain (NTS 92H/15, 16) as part of the Southern Nicola Arc Project. British Columbia Ministry of Energy, Mines and Low Carbon Innovation, British Columbia Geological Survey GeoFile 2020-12, 6 p.
- George, S.W.M., Nelson, J.L., Alberts, D., Greig, C.J., and Gehrels, G.E., 2021. Triassic-Jurassic accretionary history and tectonic origin of Stikinia from U-Pb geochronology and Lu-Hf isotope analysis, British Columbia. Tectonics, in press.
- Greig, C.J., Dudek, N.P., van Hoeve, T.J., Quinn, T.D.M., Newton, G., Makin, S.A., and Greig, R.E., 2021. Geology of the Tatogga property: Geologic framework for the Saddle North porphyry Cu-Au deposit and the Saddle South epithermal Au-Ag vein system, Iskut district, northwestern British Columbia. In: Geological Fieldwork 2020, British Columbia Ministry of Energy, Mines and Low Carbon Innovation, British Columbia Geological Survey Paper 2021-01, pp. 89-111.
- Han, T., and Rukhlov, A.S., 2020a. Update of the provincial Regional Geochemical Survey (RGS) database at the British Columbia Geological Survey. British Columbia Ministry of Energy, Mines and Petroleum Resources, British Columbia Geological Survey GeoFile 2020-08, 3 p.
- Han, T., and Rukhlov, A.S., 2020b. Update of rock geochemical database at the British Columbia Geological Survey. British Columbia Ministry of Energy, Mines and Petroleum Resources, British Columbia Geological Survey GeoFile 2020-02, 4 p.
- Han, T., Ootes, L., and Yun, K., 2020. The British Columbia Geological Survey geochronologic database: Preliminary release of ages. British Columbia Ministry of Energy, Mines and Low Carbon Innovation, British Columbia Geological Survey GeoFile 2020-10, 4 p.
- Hickin, A.S., and Plouffe, A., 2017. Sampling and interpreting stream, lake and glacial sediments for mineral exploration in the Canadian Cordillera, a review. In: Ferbey, T., Plouffe, A., and Hickin, A.S., (Eds.), Indicator Minerals in Till and Stream Sediment of the Canadian Cordillera. Geological Association of Canada Special Paper 50, pp. 27-52.
- Hunter, R.C., and van Straaten, B.I., 2020. Preliminary stratigraphy and geochronology of the Hazelton Group, Kitsault River area, Stikine terrane, northwest British Columbia. In: Geological Fieldwork 2019, British Columbia Ministry of Energy, Mines and Petroleum Resources, British Columbia Geological Survey Paper 2020-01, pp. 101-118.
- Jones, G., Ootes, L., Milidragovic, D., Friedman, R., Camacho, A., Luo, Y., Vezinet, A., Pearson, D.G., and Schiarizza, P., 2021. Geochronology of northern Hogen batholith, Quesnel terrane, north-central British Columbia. In: Geological Fieldwork 2020, British Columbia Ministry of Energy, Mines and Low Carbon Innovation, British Columbia Geological Survey Paper 2021-01, pp. 37-56.
- Lang, J.R., Roberts, K., Galicki, M., van Straaten, B.I., and Bui, P.V., 2020. Magmatic, hydrothermal, and structural features of the Gnat

- Pass porphyry copper deposit, British Columbia. In: Sharman, E.R., Lang, J.R., and Chapman, J.B., (Eds.), *Porphyry Deposits of the Northwestern Cordillera of North America: A 25-Year Update*. Canadian Institute of Mining and Metallurgy Special Volume 57, pp. 324-340.
- Lefebure, D.V., and Jones, L.D., (compilers) 2020. British Columbia Geological Survey mineral deposit profiles, 1995 to 2012. British Columbia Ministry of Energy, Mines and Low Carbon Innovation, British Columbia Geological Survey GeoFile 2020-11, 580 p.
- Lett, R.E., and Paulen, R.C., 2021. Soil and till geochemical surveys at the Ace mineral property, central British Columbia. In: *Geological Fieldwork 2020*, British Columbia Ministry of Energy, Mines and Low Carbon Innovation, British Columbia Geological Survey Paper 2021-01, pp. 145-165.
- Logan, J.M., Schiarizza, P., and Devine, F., 2020. Geology, structural setting, and porphyry deposits of the Hagem batholith, northeast British Columbia. In: Sharman, E.R., Lang, J.R., and Chapman, J.B., (Eds.), *Porphyry Deposits of the Northwestern Cordillera of North America: A 25-Year Update*. Canadian Institute of Mining and Metallurgy Special Volume 57, pp. 212-227.
- Mihalynuk, M.G., and Diakow, L.J., 2020. Southern Nicola arc geology. British Columbia Ministry of Energy, Mines and Low Carbon Innovation, British Columbia Geological Survey Geoscience Map 2020-01, 1:50,000 scale, two sheets.
- Miller, E.A., Kennedy, L.A., and van Straaten, B.I., 2020. Geology of the Kinskuch Lake area and Big Bulk porphyry prospect, northwestern British Columbia: Syndepositional faulting and basin formation during the Rhaetian (latest Triassic) transition from the Stuhini to the Hazelton Group. In: *Geological Fieldwork 2019*, British Columbia Ministry of Energy, Mines and Petroleum Resources, British Columbia Geological Survey Paper 2020-01, pp. 77-99.
- Nelson, J.L., and van Straaten, B., 2020. Recurrent syn- to post-subduction mineralization along deep crustal corridors in the Iskut-Stewart-Kitsault region of western Stikinia, northwestern British Columbia. In: Sharman, E.R., Lang, J.R., and Chapman, J.B., (Eds.), *Porphyry Deposits of the Northwestern Cordillera of North America: A 25-Year Update*. Canadian Institute of Mining and Metallurgy Special Volume 57, pp. 194-211.
- Nixon, G.T., Scoates, J.S., Milidragovic, D., Nott, J., Moerhuis, N., ver Hoeve, T.J., Manor, M.J., and Kjarsgaard, I.M., 2020a. Convergent margin Ni-Cu-PGE-Cr ore systems: U-Pb petrochronology and environments of Cu-PGE vs. Cr-PGE mineralization in Alaskan-type intrusions. In: Bleeker, W., and Houlé, M.G., (Eds.), *Targeted Geoscience Initiative 5: Advances in the understanding of Canadian Ni-Cu-PGE and Cr ore systems-Examples from the Midcontinent Rift, the Circum-Superior Belt, the Archean Superior Province, and Cordilleran Alaskan-type intrusions*. Geological Survey of Canada Open File 8722, pp. 197-218.
- Nixon, G.T., Scheel, J.E., Scoates, J.S., Friedman, R.M., Wall, C.J., Gabites, J., and Jackson-Brown, S., 2020b. Syn-accretionary multistage assembly of an Early Jurassic Alaskan-type intrusion in the Canadian Cordillera: U-Pb and <sup>40</sup>Ar/<sup>39</sup>Ar geochronology of the Turnagain ultramafic-mafic intrusive complex, Yukon-Tanana terrane. *Canadian Journal of Earth Sciences*, 57, 575-600.
- Nixon, G.T., Friedman, R.M., and Creaser, R.A., 2020c. Late Neogene porphyry Cu-Mo(±Au-Ag) mineralization in British Columbia: the Klaskish Plutonic Suite, northern Vancouver Island. In: *Geological Fieldwork 2019*, British Columbia Ministry of Energy, Mines and Petroleum Resources, British Columbia Geological Survey Paper 2020-01, pp. 119-132.
- Norris, J., and Fortin, G., 2019. Assessment report-sourced surface sediment geochemical database: Development and initial data release from the Interior Plateau. British Columbia Ministry of Energy, Mines and Petroleum Resources, British Columbia Geological Survey GeoFile 2019-04, 10 p.
- Nott, J., Milidragovic, D., Nixon, G.T., and Scoates, J.S., 2020. Geology of the Polaris ultramafic-mafic Alaskan-type intrusion, north-central British Columbia. British Columbia Ministry of Energy, Mines and Petroleum Resources, Geological Survey Open File 2020-04, scale 1:15,000.
- Ootes, L., Jones, G.O., Schiarizza, P., Milidragovic, D., Friedman, R., Camacho, A., Luo, Y., Vezinet, A., Pearson, D.G., and Zhang, S., 2020. Geochronologic and geochemical data from northern Hagem batholith and its surroundings, north-central British Columbia. British Columbia Ministry of Energy, Mines and Low Carbon Innovation, British Columbia Geological Survey GeoFile 2020-01, 21 p.
- Paradis, S., Simandl, G.J., Drage, N., D'Souza, R.J., Kontak, D.J., and Waller, Z., 2021a. Carbonate-hosted deposits (Mississippi Valley-type, magnesite, and REE-F-Ba) of the southeastern Canadian Cordillera: A review and isotopic data comparison. In: Peter, J. M., and Gadd, M.G., (Eds.), *TG15 Volcanic- and Sedimentary-Hosted Base Metals Ore Systems*. Geological Survey of Canada Bulletin, in press.
- Paradis, S., Jackson, S.E., Petts, D., Simandl, G.J., D'Souza, R.J., and Hamilton, T., 2021b. Distribution of trace elements in pyrite from carbonate-hosted sulfide deposits of southern British Columbia, Canada. In: Peter, J.M., and Gadd, M.G., (Eds.), *Targeted Geoscience Initiative: 2019 report of activities*. Geological Survey of Canada Bulletin, in press.
- Riddell, J., 2020. Evaluation of coal ash chemistry indices for predicting CSR (coke strength after reaction with CO<sub>2</sub>) for coking coals of the Rocky Mountains, British Columbia. British Columbia Ministry of Energy, Mines and Petroleum Resources British Columbia Geological Survey GeoFile 2020-06, 18 p.
- Rukhlov, A.S., Fortin, G., Kaplenkov, G.N., Lett, R.E., Lai, V. W.-M., and Weis, D., 2020a. Multi-media geochemical and Pb isotopic evaluation of modern drainages on Vancouver Island. In: *Geological Fieldwork 2019*, British Columbia Ministry of Energy, Mines and Petroleum Resources, British Columbia Geological Survey Paper 2020-01, pp. 133-167.
- Rukhlov, A.S., Ootes, L., Hickin, A.S., and Mashyanov, N.R., 2020b. Supplementary data for near-surface mercury vapour haloes in air above ore deposits and faults on Vancouver Island: Insights into buried materials in real-time? British Columbia Ministry of Energy, Mines and Low Carbon Innovation, British Columbia Geological Survey GeoFile 2020-13, 1 p.
- Rukhlov, A.S., Spence, J., LaForge, N., Czech, E., Kabel, J., and Kaplenkov, G.N., 2021a. Yttrium-rich garnet: a source of HREE? British Columbia Ministry of Energy, Mines and Low Carbon Innovation, British Columbia Geological Survey GeoFile 2021-08 (poster).
- Rukhlov, A.S., Ootes, L., Hickin, A.S., and Mashyanov, N.R., 2021b. Near-surface mercury vapour haloes in air above ore deposits and faults on Vancouver Island: Insights into buried materials in real-time? In: *Geological Fieldwork 2020*, British Columbia Ministry of Energy, Mines and Low Carbon Innovation, British Columbia Geological Survey Paper 2021-01, pp. 113-143.
- Schiarizza, P., 2019. Geology of the Nicola Group in the Bridge Lake-Quesnel River area, south central British Columbia. In: *Geological Fieldwork 2018*, British Columbia Ministry of Energy, Mines and Petroleum Resources, British Columbia Geological Survey Paper 2019-01, pp. 15-30.
- Schiarizza, P., and Friedman, R.M., 2021a. U-Pb zircon dates for the Granite Mountain batholith, Burgess Creek stock, and Sheridan Creek stock, Gibraltar Mine area, south-central British Columbia. In: *Geological Fieldwork 2020*, British Columbia Ministry of Energy, Mines and Low Carbon Innovation, British Columbia Geological Survey Paper 2021-01, pp. 23-35.
- Schiarizza, P., and Friedman, R.M., 2021b. U-Pb zircon date for Eocene volcanic rocks on Mount Timothy, south-central British Columbia. In: *Geological Fieldwork 2020*, British Columbia

- Ministry of Energy, Mines and Low Carbon Innovation, British Columbia Geological Survey Paper 2021-01, pp. 15-21.
- Simandl, G.J., D'Souza, R.J., Paradis, S., and Spence, J., 2021. REE content of carbonate minerals in sediment-hosted Pb-Zn deposits, Canadian southern Rocky Mountains. In: Peter, J.M., and Gadd, M.G., (Eds.), Targeted Geoscience Initiative: 2019 report of activities. Geological Survey of Canada, Bulletin, in press.
- van Straaten, B.I., Mostaghimi, N., Kennedy, L., Gallagher, C., Schiarizza, P., and Smith, S., 2020. The deformed Gibraltar porphyry copper-molybdenum deposit, south-central British Columbia, Canada. In: Sharman, E.R., Lang, J.R., and Chapman, J.B., (Eds.), Porphyry Deposits of the Northwestern Cordillera of North America: A 25-Year Update. Canadian Institute of Mining and Metallurgy Special Volume 57, pp. 547-567.
- Van Wagoner, N., Ootes, L., and Thomson-Gladish, J., 2021. Volcanism and geochemistry of the Kamloops Group, south-central British Columbia. In: Geological Fieldwork 2020, British Columbia Ministry of Energy, Mines and Low Carbon Innovation, British Columbia Geological Survey Paper 2021-01, pp. 65-88.
- Zagorevski, A., van Staal, C.R., Bédard, J.H., Bogatu, A., Canil, D., Coleman, M., Golding, M., Joyce, N., Lawley, C., McGoldrick, S., Mihalyuk, M., Milidragovic, D., Parsons, A., and Schiarizza, P., 2021. Paper 1: Overview of Cordilleran oceanic terranes and their significance for the tectonic evolution of the northern Cordillera. Geological Survey of Canada Bulletin 610, in press.

# U-Pb zircon date for Eocene volcanic rocks on Mount Timothy, south-central British Columbia



Paul Schiarizza<sup>1, a</sup>, and Richard M. Friedman<sup>2</sup>

<sup>1</sup> British Columbia Geological Survey, Ministry of Energy, Mines and Low Carbon Innovation, 300-865 Hornby Street, Vancouver, BC V6Z 2G3

<sup>2</sup> Pacific Centre for Isotopic and Geochemical Research, Department of Earth, Ocean and Atmospheric Sciences, The University of British Columbia, Vancouver, BC, V6T 1Z4

<sup>a</sup> corresponding author: Paul.Schiarizza@gov.bc.ca

Recommended citation: Schiarizza, P., and Friedman, R.M., 2021. U-Pb zircon date for Eocene volcanic rocks on Mount Timothy, south-central British Columbia. In: Geological Fieldwork 2020, British Columbia Ministry of Energy, Mines and Low Carbon Innovation, British Columbia Geological Survey Paper 2021-01, pp. 15-21.

## Abstract

Mount Timothy, near the eastern edge of the Fraser Plateau in south-central British Columbia, is in a belt of Late Triassic-Early Jurassic volcanic, sedimentary, and plutonic rocks belonging to Quesnel terrane. The mountain is also in a belt of Eocene volcanic rocks that unconformably overlies rocks of Quesnel terrane. Volcanic rocks on Mount Timothy have previously been assigned to either the Nicola Group (Triassic, Quesnel terrane) or the Skull Hill Formation (Eocene). In order to resolve this uncertainty, a sample of plagioclase-hornblende-pyroxene-phyric andesite collected from the south slope of the mountain was dated using the U-Pb zircon chemical abrasion thermal ionization mass spectrometry method (CA-TIMS). Five zircon grains yield a weighted mean  $^{206}\text{Pb}/^{238}\text{U}$  date of  $50.84 \pm 0.04$  Ma, interpreted as the crystallization age of the andesite. This date shows that the volcanic rocks are part of the Skull Hill Formation and, together with the few K-Ar dates obtained elsewhere in the region, indicates a predominantly early Eocene age for the unit.

**Keywords:** Eocene, Skull Hill Formation, Kamloops Group, Mount Timothy, U-Pb, zircon, CA-TIMS

## 1. Introduction

Mount Timothy is near the eastern edge of the Fraser Plateau, 18 km northeast of the community of Lac La Hache and Highway 97, within the traditional territories of the Secwepemc and Esk'etemc First Nations. It is in a belt of Triassic and Early Jurassic volcanic, sedimentary and plutonic rocks included in Quesnel terrane, and also in a younger belt of Eocene volcanic rocks that overlies Quesnel terrane and extends northwestward into the Chilcotin and Nechako plateaus, where it overlies Cache Creek and Stikine terranes (Fig. 1). Volcanic and volcanoclastic rocks near Mount Timothy were included in the Nicola Group (Triassic) by Campbell and Tipper (1971) but were assigned to the Skull Hill Formation (Eocene) by Schiarizza and Bligh (2008). However, Schiarizza (2016) questioned the Eocene assignment because a distinctive plagioclase-phyric andesite in the upper part of the volcanic package is lithologically similar to Late Triassic andesite (U-Pb zircon date of  $203.9 \pm 0.4$  Ma) in the upper part of the Nicola Group near Woodjam Creek, 36 km north of Mount Timothy (Schiarizza et al., 2013). To resolve this uncertainty, a sample from the Mount Timothy andesite, collected in 2015, was dated using the U-Pb zircon CA-TIMS method. The crystallization age of  $50.84 \pm 0.04$  Ma that we report herein demonstrates that the andesite from Mount Timothy is early Eocene and part of the Skull Hill Formation, as inferred by Schiarizza and Bligh (2008).

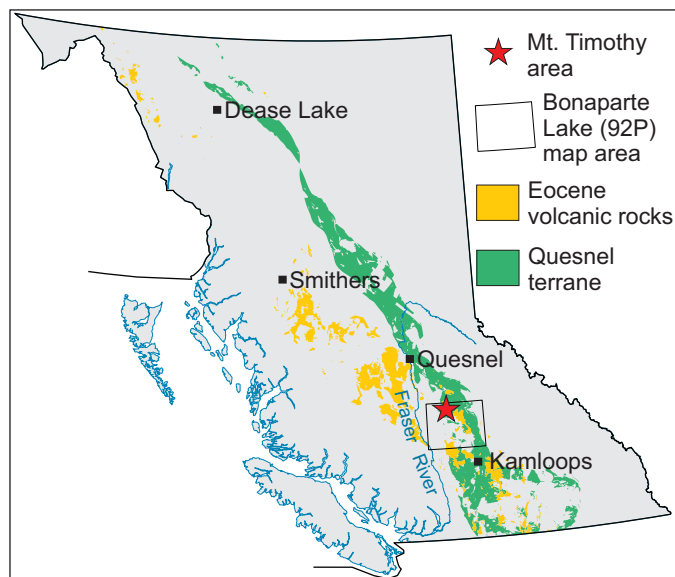


**Fig. 1.** Location of the Mount Timothy area; main exposures of Quesnel terrane rocks and the belt of Eocene volcanic rocks that cuts across Quesnel terrane. Lower Eocene volcanic rocks east of the Fraser River are in the Kamloops, Princeton and Penticton groups, those to the west are mainly in the Ootsa Lake and Endako groups.

## 2. Geology of the Mount Timothy area

The Mount Timothy area is underlain by Late Triassic and Early Jurassic sedimentary, volcanic and plutonic rocks of

Quesnel terrane, and unconformably overlying Eocene volcanic rocks. The youngest rocks are Pleistocene basalts, commonly with mantle-derived xenoliths of spinel ilmenite, that locally overlie the Mesozoic and Eocene rocks (Fig. 2).

The oldest rocks of Quesnel terrane are sedimentary and volcanic rocks of the Nicola Group, which includes two separate units. The oldest Nicola unit is exposed in the southern part of the area and is separated from adjacent rocks by east- and north-trending faults. This unit (assemblage two of Schiarizza, 2019) consists mainly of green to grey volcanic sandstone and conglomerate, dated regionally as Carnian and lower Norian. The second Nicola unit (assemblage four of Schiarizza, 2019) is exposed mainly north of Mount Timothy. It consists of red, purple and green polymictic conglomerate and feldspathic sandstone, but also includes a mappable body of pyroxene-plagioclase-phyric basalt and basalt breccia (Fig. 2). Assemblage four (mainly late Norian and Rhaetian) is the uppermost component of the Nicola Group in the region and is separated from older parts of the group by an unconformity or disconformity (Schiarizza, 2019).

Plutonic rocks of Quesnel terrane include several small stocks of Late Triassic monzodiorite and diorite that cut assemblage four of the Nicola Group, mainly north of Mount Timothy, and a large body of Early Jurassic hornblende-biotite granodiorite, which forms part of the western margin of the Takomkane batholith, in the eastern part of the area (Schiarizza et al., 2013).

Campbell and Tipper (1971) applied the name Skull Hill Formation (originally defined by Uglow, 1922) to Eocene volcanic rocks in the Mount Timothy area, considering the unit as part of the Kamloops Group. The Skull Hill Formation, as mapped by Schiarizza and Bligh (2008) and confirmed by the U-Pb zircon date of the present study, covers a large area near Mount Timothy, where it overlies the Nicola Group and the adjacent Takomkane batholith; it also forms several small outliers that overlie the Nicola Group farther north (Fig. 2). The formation consists mainly of andesitic to basaltic flows, but also includes volcanic breccias and minor amounts of arkosic wacke. Basalt flows are dark grey, massive, and commonly include sparse to abundant phenocrysts of pyroxene±plagioclase. Andesitic flows are grey to brown, commonly friable, and characterized by phenocryst assemblages of plagioclase-hornblende-pyroxene or plagioclase-hornblende-biotite. These flows, in part, form a mappable unit on the south and east flanks of Mount Timothy that contains abundant large (5-12 mm) plagioclase phenocrysts, commonly accompanied by smaller and less abundant hornblende and pyroxene phenocrysts. Volcanic breccias of uncertain origin are mainly near the top of Mount Timothy; together with basaltic and andesitic flows, these breccias are beneath the mappable coarse plagioclase-phyric andesite unit. The breccias comprise purple, green and grey volcanic fragments (1-10 cm, with various combinations of plagioclase, hornblende and pyroxene phenocrysts) in a friable matrix that contains abundant plagioclase grains.

Grey, fine- to medium-grained, equigranular diorite forms

two small plugs that intrude volcanic flows and breccias of the Skull Hill Formation on the east flank of Mount Timothy. The diorite consists of plagioclase, traces of K-feldspar, and 25 to 35% mafic minerals that include hornblende, clinopyroxene and biotite. This composition is very similar to that of Late Triassic monzodiorite-diorite stocks that intrude the Nicola Group north of Mount Timothy. Nevertheless, Schiarizza and Bligh (2008) considered them Eocene or younger because they intrude rocks that they mapped as Skull Hill Formation. The early Eocene U-Pb zircon date presented here confirms this interpretation.

### 3. Geochronology

Here we present U-Pb zircon isotopic dating results obtained by the chemical abrasion thermal ionization mass spectrometry method (CA-TIMS) for a sample collected from the coarse plagioclase-phyric andesite unit that is exposed on the south and east flanks of Mount Timothy. Sample preparation and analytical work was conducted at the Pacific Centre for Isotopic and Geochemical Research (PCIGR), the Department of Earth, Ocean and Atmospheric Sciences, the University of British Columbia.

#### 3.1. Analytical procedures

CA-TIMS procedures described here are modified from Mundil et al. (2004), Mattinson (2005) and Scoates and Friedman (2008). After the rock sample underwent standard mineral separation procedures, zircons were handpicked in alcohol. The clearest, crack- and inclusion-free grains were selected, photographed and then annealed in quartz glass crucibles at 900°C for 60 hours. Annealed grains were transferred into 3.5 mL PFA screwtop beakers, ultrapure HF (up to 50% strength, 500 µL) and HNO<sub>3</sub> (up to 14 N, 50 µL) were added and caps were closed finger tight. The beakers were placed in 125 mL PTFE liners (up to four per liner) and about 2 mL HF and 0.2 mL HNO<sub>3</sub>, of the same strength as the acid in the beakers containing the samples, were added to the liners. The liners were then slid into stainless steel Parr™ high-pressure dissolution devices, which were sealed and brought to a maximum of 200°C for 8-16 hours (typically 175°C for 12 hours). Beakers were removed from the liners and zircon was separated from the leachate. Zircons were rinsed with >18 MΩ.cm water and subboiled acetone. Then 2 mL of subboiled 6N HCl was added and beakers were set on a hotplate at 80-130°C for 30 minutes and again rinsed with water and acetone. Masses were estimated from the dimensions (volumes) of grains. Single grains were transferred into clean 300 µL PFA microcapsules (crucibles), and 50 µL 50% HF and 5 µL 14 N HNO<sub>3</sub> were added. Each was spiked with a <sup>233-235</sup>U-<sup>205</sup>Pb tracer solution (EARTHTIME ET535), capped and again placed in a Parr liner (8-15 microcapsules per liner). HF and nitric acids, in a 10:1 ratio, were added to the liner, which was then placed in a Parr high-pressure device and dissolution was achieved at 240°C for 40 hours. The resulting solutions were dried on a hotplate at 130°C, 50 µL 6N HCl was added to microcapsules and fluorides were dissolved in high-pressure

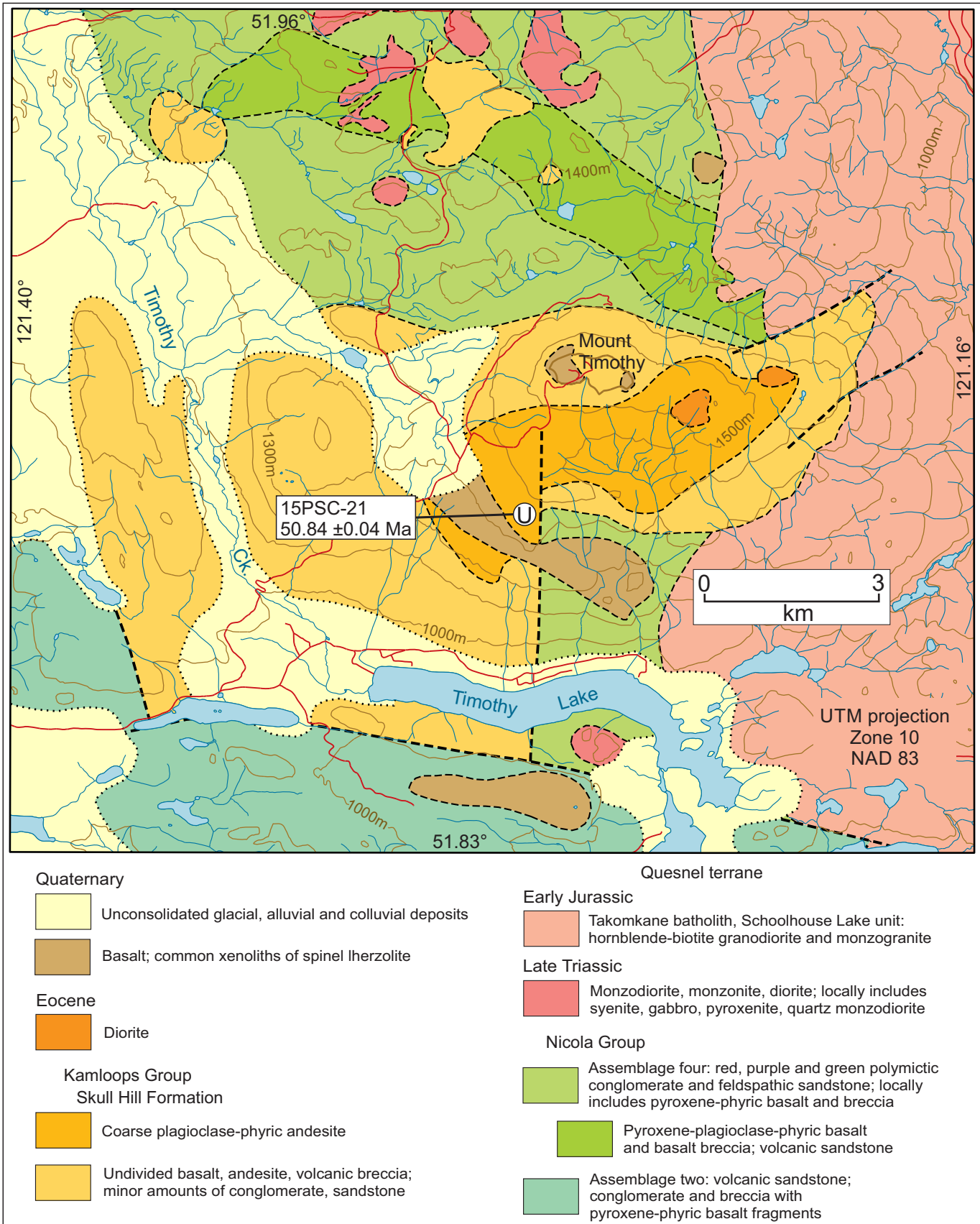


Fig. 2. Geology of the Mount Timothy area showing the location of sample 15PSC-21. Geology modified from Schiarizza et al. (2013), with Nicola subdivisions from Schiarizza (2019).

Parr devices for 12 hours at 210°C. HCl solutions were transferred into clean 7 mL PFA beakers and dried with 2  $\mu\text{L}$  of 0.5 N  $\text{H}_3\text{PO}_4$ . Samples were loaded onto degassed, zone-refined Re filaments in 2  $\mu\text{L}$  of silicic acid emitter (Gerstenberger and Haase, 1997).

Isotopic ratios were measured by a modified single collector VG-54R or 354S (with Sector 54 electronics) thermal ionization mass spectrometer equipped with analogue Daly photomultipliers. Analytical blanks were 0.2 pg for U and up to 1 pg for Pb. U fractionation was determined directly on individual runs using the EARTHTIME ET535 mixed  $^{233}\text{-}^{235}\text{U-}^{205}\text{Pb}$  isotopic tracer. Pb isotopic ratios were corrected for fractionation of  $0.25 \pm 0.03\%$ /amu, based on replicate analyses of NBS-982 reference material and the values recommended by Thirlwall (2000). Data reduction employed the Excel-based program of Schmitz and Schoene (2007). Standard concordia diagrams were constructed and regression intercepts and weighted averages calculated with Isoplot (Ludwig, 2003). Unless otherwise noted all errors are quoted at the 2 sigma or 95% level of confidence. Isotopic dates are calculated with the decay constants  $\lambda_{238} = 1.55125\text{E-}10$  and  $\lambda_{235} = 9.8485\text{E-}10$  (Jaffey et al., 1971). EARTHTIME U-Pb synthetic solutions were analyzed on an on-going basis to monitor the accuracy of results.

### 3.2. U-Pb zircon CA-TIMS results for sample 15PSC-21

Sample 15PSC-21 was collected from an exposure along an abandoned logging road (618939E, 5749330N, UTM Zone 10, NAD 83), 2.6 km south-southwest of Mount Timothy (Fig. 2). It is a grey andesite with abundant large plagioclase phenocrysts, and smaller and less abundant hornblende and pyroxene phenocrysts (Fig. 3). A moderate quantity of anhedral and subhedral zircon grains were extracted from the sample (Fig. 4), and five of these were selected for CA-TIMS processing and analysis (Table 1). Results for the five grains are mutually overlapping on concordia, with a weighted mean  $^{206}\text{Pb}/^{238}\text{U}$  date of  $50.84 \pm 0.04$  Ma (MSWD=1.35), interpreted as the crystallization age of the andesite (Fig. 5).



**Fig. 3.** Plagioclase-hornblende-pyroxene-phyric andesite of sample 15PSC-21, collected 2.6 km south-southwest of Mount Timothy.

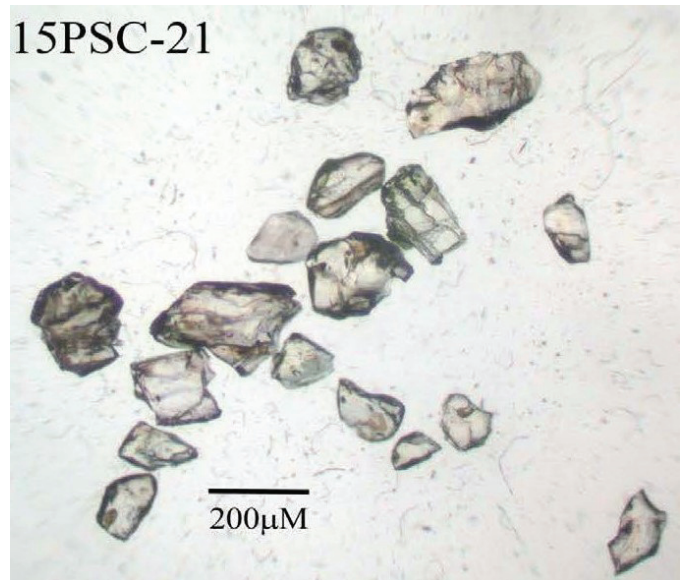


**Fig. 4.** Zircon grains extracted from sample 15PSC-21.

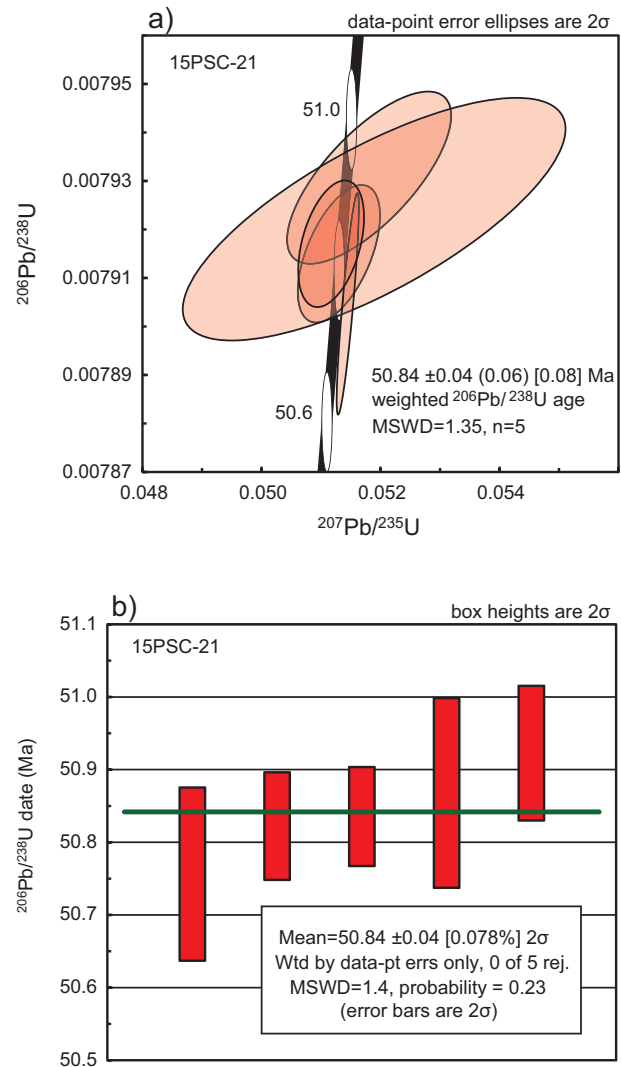


**Fig. 5. a)** Concordia plot of zircons analyzed from sample 15PSC-21. **b)**  $^{206}\text{Pb}/^{238}\text{U}$  ages and calculated weighted mean age.

**Table 1.** U-Th-Pb analytical results for sample 15PSC-21.

Sample	Compositional Parameters										Radiogenic Isotope Ratios						Isotopic Ages							
	Wt.	U	Pb	Th	<sup>206</sup> Pb*	mol %	Pb*	Pb <sub>c</sub>	<sup>206</sup> Pb	<sup>208</sup> Pb	<sup>207</sup> Pb	<sup>206</sup> Pb	<sup>207</sup> Pb	<sup>206</sup> Pb	<sup>207</sup> Pb	<sup>206</sup> Pb	<sup>207</sup> Pb	<sup>206</sup> Pb	<sup>207</sup> Pb	<sup>206</sup> Pb	<sup>207</sup> Pb			
	mg	ppm	ppm	U	x10 <sup>-13</sup> mol	<sup>206</sup> Pb*	Pb <sub>c</sub>	(pg)	<sup>204</sup> Pb	<sup>206</sup> Pb	<sup>206</sup> Pb	<sup>206</sup> Pb	<sup>206</sup> Pb	<sup>206</sup> Pb	<sup>206</sup> Pb	<sup>206</sup> Pb	<sup>206</sup> Pb	<sup>206</sup> Pb	<sup>206</sup> Pb	<sup>206</sup> Pb	<sup>206</sup> Pb	<sup>206</sup> Pb	<sup>206</sup> Pb	
(a)	(b)	(c)	(c)	(d)	(e)	(e)	(e)	(e)	(f)	(g)	(g)	(g)	(g)	(g)	(g)	(g)	(g)	(g)	(g)	(g)	(g)	(g)	(g)	(g)
A	0.0042	466	4.6	0.934	0.6522	97.34%	12	1.46	696	0.299	0.047005	1.027	0.051297	1.101	0.007915	0.147	0.554	49.46	24.51	50.79	0.55	50.82	0.07	
B	0.0033	383	3.8	0.522	0.4196	94.23%	5	2.11	321	0.169	0.047376	2.048	0.051805	2.176	0.007931	0.183	0.719	68.22	48.70	51.28	1.09	50.92	0.09	
G	0.0029	79	0.8	0.415	0.0760	91.53%	3	0.57	218	0.134	0.047505	4.880	0.051889	5.069	0.007922	0.258	0.744	74.68	115.9	51.37	2.54	50.87	0.13	
H	0.0127	796	7.0	0.765	3.3346	99.76%	135	0.66	7681	0.246	0.047203	0.146	0.051446	0.296	0.007905	0.236	0.872	59.51	3.49	50.94	0.15	50.76	0.12	
I	0.0046	280	2.4	0.524	0.4290	98.44%	19	0.55	1189	0.168	0.046873	0.836	0.051166	0.883	0.007917	0.135	0.417	42.74	19.97	50.67	0.44	50.84	0.07	

(a) A, B etc. are labels for fractions composed of single zircon grains or fragments; all fractions annealed and chemically abraded after Mattinson (2005) and Scoates and Friedman (2008).  
 (b) Nominal fraction weights estimated from photomicrographic grain dimensions, adjusted for partial dissolution during chemical abrasion.  
 (c) Nominal U and total Pb concentrations subject to uncertainty in photomicrographic estimation of weight and partial dissolution during chemical abrasion.  
 (d) Model Th/U ratio calculated from radiogenic <sup>208</sup>Pb/<sup>206</sup>Pb ratio and <sup>207</sup>Pb/<sup>235</sup>U age.  
 (e) Pb\* and Pb<sub>c</sub> represent radiogenic and common Pb, respectively; mol % <sup>206</sup>Pb\* with respect to radiogenic, blank and initial common Pb.  
 (f) Measured ratio corrected for spike and fractionation only. Mass discrimination of 0.25±0.03‰/amu based on analysis of NBS-982; all Daly analyses.  
 (g) Corrected for fractionation, spike, and common Pb; up to 2.1 pg of common Pb was assumed to be procedural blank: <sup>206</sup>Pb/<sup>204</sup>Pb = 18.50 ± 1.0%; <sup>207</sup>Pb/<sup>204</sup>Pb = 15.50 ± 1.0%; <sup>208</sup>Pb/<sup>204</sup>Pb = 38.40 ± 1.0% (all uncertainties 1-sigma).  
 (h) Errors are 2-sigma, propagated using the algorithms of Schmitz and Schoene (2007) and Crowley et al. (2007).  
 (i) Calculations are based on the decay constants of Jaffey et al. (1971). <sup>206</sup>Pb/<sup>238</sup>U and <sup>207</sup>Pb/<sup>235</sup>U ages corrected for initial disequilibrium in <sup>230</sup>Th/<sup>238</sup>U using Th/U [magma] = 3.

#### 4. Discussion

Campbell and Tipper (1971) mapped the rocks near Mount Timothy as Nicola Group (Triassic), but mapped volcanic rocks farther west, on the ridge west of Timothy Creek, as Skull Hill Formation (Eocene). Schiarizza and Bligh (2008) inferred that the Eocene rocks were much more extensive, and that they continued eastward from Timothy Creek beyond Mount Timothy, where they overlapped the contact between the Nicola Group and the Takomkane batholith (as shown on Fig. 2). Schiarizza (2016) subdivided the Nicola Group regionally into four assemblages and assigned the Nicola rocks north of Mount Timothy to the uppermost part of the group (assemblage four). He suggested that the volcanic rocks on and south of Mount Timothy, mapped as Eocene by Schiarizza and Bligh (2008), were also part of assemblage four because: 1) the plagioclase-phyric andesite unit exposed south and east of Mount Timothy is lithologically similar to Late Triassic andesite in assemblage four near Woodjam Creek, 36 km north of Mount Timothy (Schiarizza et al., 2013); and 2) the two small diorite plugs that intrude the plagioclase-phyric andesite unit east of Mount Timothy are markedly similar to the Late Triassic monzodiorite stocks that intrude assemblage four north of Mount Timothy, and might likewise be Late Triassic. The  $50.84 \pm 0.04$  Ma date obtained for the Mount Timothy andesite in this study confirms the Eocene interpretation of Schiarizza and Bligh (2008) and allows us to reject the Triassic interpretation proposed by Schiarizza (2016).

Uglow (1922) introduced the name Skull Hill Formation for undated volcanic rocks of suspected Tertiary age along the North Thompson River valley, and Campbell and Tipper (1971) adopted the name for volcanic rocks of probable Eocene age across the entire Bonaparte Lake map area (Fig. 1). Campbell and Tipper (1971) assigned the formation to the Kamloops Group, a term applied to Tertiary rocks in the Kamloops area by Drysdale (1914) and Cockfield (1948), and later redefined to include only Lower and Middle Eocene rocks (Mathews, 1964; Ewing, 1981). Before the present study, an early Eocene age for the Skull Hill Formation had been confirmed by only a few scattered K-Ar age determinations, including whole rock K-Ar dates of  $52.1 \pm 1.8$  Ma and  $50.9 \pm 1.8$  Ma for two separate basalt flows north of the Bonaparte River, 74 km south of Mount Timothy (Read, 2000), and a K-Ar date of  $52.2 \pm 1.8$  Ma on biotite separated from a trachyandesite flow near Antoine Lake, 56 km north-northwest of Mount Timothy (Panteleyev et al., 1996). The  $50.84 \pm 0.04$  Ma date obtained for the Mount Timothy andesite in this study corroborates these K-Ar dates and confirms that the Skull Hill Formation is, at least in part, early Eocene.

#### 5. Conclusions

Plagioclase-hornblende-pyroxene-phyric andesite exposed on the south and east slopes of Mount Timothy was dated with the U-Pb zircon CA-TIMS method and yields a weighted mean  $^{206}\text{Pb}/^{238}\text{U}$  date of  $50.84 \pm 0.04$  Ma, interpreted as the crystallization age of the andesite. This date confirms that the

volcanic succession on Mount Timothy is part of the Skull Hill Formation, as proposed by Schiarizza and Bligh (2008). It shows that the Skull Hill Formation is, at least in part, early Eocene, as also indicated by the few K-Ar dates obtained elsewhere in the region.

#### Acknowledgments

Jessica Norris helped collect sample 15PSC-21 (and correctly inferred its Eocene age). H. Lin, T. Ockerman, C. Wall, and N. Moerhous assisted with mineral separation, sample preparation and mass spectrometry at PCIQR. Lawrence Aspler reviewed the paper and made suggestions that improved it.

#### References cited

- Campbell, R.B., and Tipper, H.W., 1971. Bonaparte Lake map area, British Columbia. Geological Survey of Canada, Memoir 363, 100 p.
- Cockfield, W.E., 1948. Geology and mineral deposits of Nicola map area, British Columbia. Geological Survey of Canada, Memoir 249, 164 p.
- Crowley, J.L., Schoene, B., and Bowring, S.A., 2007. U-Pb dating of zircon in the Bishop Tuff at the millennial scale. *Geology*, 35, 1123-1126.
- Drysdale, C.W., 1914. Geology of the Thompson River valley below Kamloops Lake, B.C. Geological Survey of Canada, Summary Report for 1912, pp. 115-150.
- Ewing, T.E., 1981. Regional stratigraphy and structural setting of the Kamloops Group, south-central British Columbia. *Canadian Journal of Earth Sciences*, 18, 1464-1477.
- Gerstenberger, H., and Haase, G., 1997. A highly effective emitter substance for mass spectrometric Pb isotopic ratio determinations. *Chemical Geology*, 136, 309-312.
- Jaffey, A.H., Flynn, K.F., Glendenin, L.E., Bentley, W.C., and Essling, A.M., 1971. Precision measurement of half-lives and specific activities of  $^{235}\text{U}$  and  $^{238}\text{U}$ . *Physics Review*, C4, 1889-1906.
- Ludwig, K.R., 2003. Isoplot 3.09-A Geochronological toolkit for Microsoft Excel. Berkeley Geochronology Center, The University of California at Berkeley, Special Publication No. 4.
- Mathews, W.H., 1964. Potassium-argon age determination of Cenozoic volcanic rocks from British Columbia. *Geological Society of America Bulletin*, 75, 465-468.
- Mattinson, J.M., 2005. Zircon U-Pb chemical abrasion ("CA-TIMS") method: Combined annealing and multi-step partial dissolution analysis for improved precision and accuracy of zircon ages. *Chemical Geology*, 220, 47-66.
- Mundil, R., Ludwig, K.R., Metcalfe, I., and Renne, P.R., 2004. Age and timing of the Permian Mass Extinctions: U/Pb Dating of Closed-System Zircons. *Science*, 305, 1760-1763.
- Panteleyev, A., Bailey, D.G., Bloodgood, M.A., and Hancock, K.D., 1996. Geology and mineral deposits of the Quesnel River-Horsefly map area, central Quesnel Trough, British Columbia. British Columbia Ministry of Employment and Investment, British Columbia Geological Survey Bulletin 97, 155 p.
- Read, P.B., 2000. Geology and industrial minerals of the Tertiary basins, south-central British Columbia. British Columbia Ministry of Energy and Mines, British Columbia Geological Survey GeoFile 2000-3, 109 p.
- Schiarizza, P., 2016. Toward a regional stratigraphic framework for the Nicola Group: Preliminary results from the Bridge Lake-Quesnel River area. In: *Geological Fieldwork 2015*, British Columbia Ministry of Energy and Mines, British Columbia Geological Survey Paper 2016-1, pp. 13-30.
- Schiarizza, P., 2019. Geology of the Nicola Group in the Bridge Lake-Quesnel River area, south-central British Columbia. In:

- Geological Fieldwork 2018, British Columbia Ministry of Energy, Mines and Petroleum Resources, British Columbia Geological Survey Paper 2019-01, pp. 15-30.
- Scharizza, P., and Bligh, J.S., 2008. Geology and mineral occurrences of the Timothy Lake area, south-central British Columbia (NTS 092P/14). In: Geological Fieldwork 2007, British Columbia Ministry of Energy, Mines and Petroleum Resources, British Columbia Geological Survey Paper 2008-1, pp. 191-211.
- Scharizza, P., Israel, S., Heffernan, S., Boulton, A., Bligh, J., Bell, K., Bayliss, S., Macauley, J., Bluemel, B., Zuber, J., Friedman, R.M., Orchard, M.J., and Poulton, T.P., 2013. Bedrock geology between Thuya and Woodjam creeks, south-central British Columbia, NTS 92P/7, 8, 9, 10, 14, 15, 16; 93A/2, 3, 6. British Columbia Ministry of Energy, Mines and Natural Gas, British Columbia Geological Survey Open File 2013-05; 4 sheets, scale 1:100,000.
- Schmitz, M.D., and Schoene, B., 2007. Derivation of isotope ratios, errors, and error correlations for U-Pb geochronology using  $^{205}\text{Pb}$ - $^{235}\text{U}$ -( $^{233}\text{U}$ )-spiked isotope dilution thermal ionization mass spectrometric data. *Geochemistry, Geophysics, Geosystems*, 8, Q08006, doi:10.1029/2006GC001492.
- Scoates, J.S., and Friedman, R.M., 2008. Precise age of the platiniferous Merensky Reef, Bushveld Complex, South Africa, by the U-Pb zircon chemical abrasion ID-TIMS technique. *Economic Geology*, 103, 465-471.
- Stacey, J.S., and Kramers, J.D., 1975. Approximation of terrestrial lead isotopic evolution by a two-stage model. *Earth and Planetary Science Letters*, 26, 207-221.
- Thirlwall, M.F., 2000. Inter-laboratory and other errors in Pb isotope analyses investigated using a  $^{207}\text{Pb}$ - $^{204}\text{Pb}$  double spike. *Chemical Geology*, 163, 299-322.
- Uglove, W.L., 1922. Geology of the North Thompson Valley map area, British Columbia. Geological Survey of Canada, Summary Report for 1921, Part A, pp. 72A-106A.



# U-Pb zircon dates for the Granite Mountain batholith, Burgess Creek stock, and Sheridan Creek stock, Gibraltar Mine area, south-central British Columbia



Paul Schiarizza<sup>1, a</sup>, and Richard M. Friedman<sup>2</sup>

<sup>1</sup> British Columbia Geological Survey, Ministry of Energy, Mines and Low Carbon Innovation, 300-865 Hornby Street, Vancouver, BC, V6Z 2G3

<sup>2</sup> Pacific Centre for Isotopic and Geochemical Research, Department of Earth, Ocean and Atmospheric Sciences, The University of British Columbia, Vancouver, BC, V6T 1Z4

<sup>a</sup> corresponding author: Paul.Schiarizza@gov.bc.ca

Recommended citation: Schiarizza, P., and Friedman, R.M., 2021. U-Pb zircon dates for the Granite Mountain batholith, Burgess Creek stock, and Sheridan Creek stock, Gibraltar Mine area, south-central British Columbia. In: Geological Fieldwork 2020, British Columbia Ministry of Energy, Mines and Low Carbon Innovation, British Columbia Geological Survey Paper 2021-01, pp. 23-35.

## Abstract

The Granite Mountain batholith (Late Triassic), host to the Gibraltar porphyry Cu-Mo deposit, is east of the Fraser River between Williams Lake and Quesnel. Previously considered part of Cache Creek terrane, the batholith is in a panel of Quesnel terrane rocks that is faulted against Cache Creek terrane to the east and south, as established by mapping carried out in 2013 and 2014. Samples collected during this mapping, dated using the U-Pb zircon chemical abrasion thermal ionization mass spectrometry method (CA-TIMS), provide crystallization ages for the batholith and two adjacent plutonic units. Three samples from the Granite Mountain batholith yield Late Triassic dates of 217.15 ± 0.37 Ma (Granite Mountain phase leucocratic tonalite), 215.71 ± 0.36 Ma (Mine phase tonalite), and 214.98 ± 0.38 Ma (quartz-plagioclase porphyry dike cutting Mine phase tonalite). The Burgess Creek stock, on the northeast margin of the Granite Mountain batholith, provides dates of 222.71 ± 0.39 Ma (tonalite) and 221.25 ± 0.39 Ma (quartz diorite), demonstrating that it is also Late Triassic, but several million years older than the Granite Mountain batholith. Tonalite from the Sheridan Creek stock, south of the Granite Mountain batholith, returns an Early Cretaceous date of 108.57 ± 0.18 Ma. The Sheridan Creek contains a foliation with the same orientation and characteristics as a prominent foliation in the southern part of the Granite Mountain batholith, demonstrating that deformation of both is mid-Cretaceous or younger.

**Keywords:** Triassic, Granite Mountain batholith, Burgess Creek stock, Cretaceous, Sheridan Creek stock, Quesnel terrane, U-Pb, zircon, CA-TIMS

## 1. Introduction

The Granite Mountain batholith (Late Triassic), host to the Gibraltar porphyry Cu-Mo deposit, is on the Fraser Plateau, about 18 km east of the Fraser River, in the traditional territories of the Secwepemc, Tsilhqot'in, and Lhtako Dené First Nations (Fig. 1). Schiarizza (2014, 2015) carried out geological mapping of the batholith and surrounding rocks to better understand its geologic setting and terrane affinity. This work established that the batholith, previously included in Cache Creek terrane, is part of Quesnel terrane, and forms the south end of a panel of Quesnel rocks that is in fault contact with Cache Creek terrane to the east and south. Supporting this mapping we conducted isotopic dating (U-Pb zircon CA-TIMS method) at the University of British Columbia. Herein we present the geochronologic data and age interpretations for six samples: three from the Granite Mountain batholith (Late Triassic); two from the Burgess Creek stock (Late Triassic); and one from the Sheridan Creek stock (Early Cretaceous).

## 2. Geology of the Granite Mountain area

The Granite Mountain area (Fig. 2) is underlain by a north-

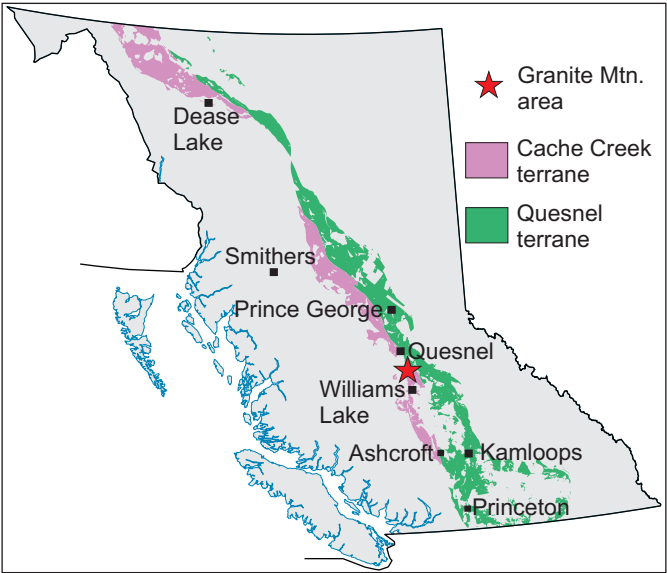


Fig. 1. Location of the Granite Mountain area and the main exposures of Quesnel and Cache Creek terranes in British Columbia.

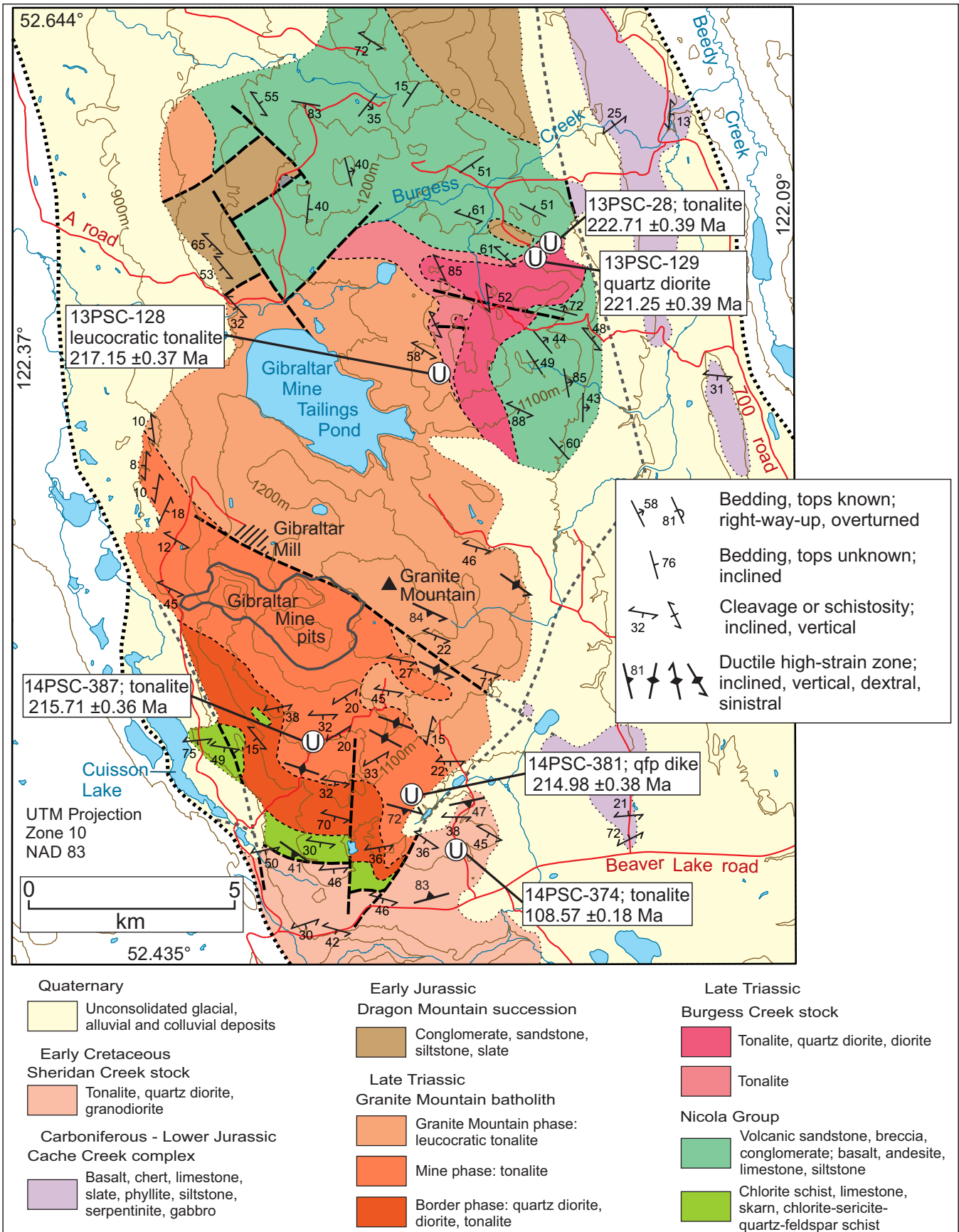


Fig. 2. Geology of the Granite Mountain area, showing the locations of samples dated in this study. Geology modified from Schiarizza (2015).

trending belt of rocks assigned to Quesnel terrane, including the Nicola Group (Upper Triassic), the Burgess Creek stock (Late Triassic), the Granite Mountain batholith (Late Triassic) and the Dragon Mountain succession (Lower Jurassic). This panel of Quesnel terrane rocks is in fault contact with the Cache Creek complex (Cache Creek terrane) to the east, and with Early Cretaceous tonalite of the Sheridan Creek stock to the south.

The Nicola Group is exposed mainly in the northern part of the area, where it is cut by the Burgess Creek stock and, locally, the north end of the Granite Mountain batholith. It consists of feldspathic volcanic sandstone and gritty to pebbly sandstone, with local intercalations of conglomerate, mafic and felsic volcanic breccia, siltstone, limestone and basalt (Schiarizza, 2014). These rocks are dated at one locality, 4 km north of the Gibraltar tailings pond, where a limestone lens intercalated with volcanic sandstone yielded a conodont of probable Lower Norian age (M.J. Orchard in Schiarizza, 2015).

Rocks assigned to the Nicola Group also form a narrow belt of feldspathic chlorite schists, foliated limestones and skarns along the southwest margin of the Granite Mountain batholith (Fig. 2). These rocks were included in the Cache Creek complex by Drummond et al. (1976), Panteleyev (1978), Bysouth et al. (1995), and Ash and Riveros (2001), but Schiarizza (2015) inferred a protolith of feldspathic volcanoclastic rocks, mafic volcanic rocks, and limestones that is more likely correlated with the Nicola Group. Narrow units of sericite-chlorite-quartz-plagioclase schist in the northern part of the succession may have been derived from quartz diorite dikes related to the adjacent Granite Mountain batholith (Schiarizza, 2015).

The Burgess Creek stock intrudes the Nicola Group on the northeast margin of the Granite Mountain batholith (Fig. 2). It comprises two mappable units (Schiarizza, 2015): a mixed unit that includes hornblende-biotite tonalite, hornblende-biotite quartz diorite, and hornblende diorite; and a tonalite unit consisting mainly of leucocratic hornblende-biotite tonalite. Panteleyev (1978) and Bysouth et al. (1995) thought that the Burgess Creek stock was younger than the Granite Mountain batholith, whereas Ash et al. (1999a, b) considered it a border phase of the batholith. The U-Pb zircon dates presented here show that it is Late Triassic, and several million years older than the Granite Mountain batholith.

The Granite Mountain batholith is exposed across an area measuring up to 20 km north-south by 10 km east-west. It is subdivided into three northwest-trending map units that show a trend of decreasing mafic content and increasing quartz content from southwest to northeast (Fig. 2). The Border phase, in the south, consists of medium- to coarse-grained quartz diorite, diorite and mafic tonalite. The Mine phase, which hosts the orebodies at the Gibraltar mine, is mainly medium- to coarse-grained tonalite with 15-25% chloritized mafic grains (mainly or entirely hornblende) and 25-35% quartz. The Granite Mountain phase, which forms most of the batholith, is predominantly coarse-grained leucocratic tonalite with 5-10% mafic minerals (hornblende and biotite) and 45-55% quartz.

Fine- to coarse-grained leucotonalite (0-5% mafic minerals) and quartz-plagioclase porphyry occur as dikes in all three units. The dikes are commonly a few cm to tens of cm wide, but range to several tens of m in the Border phase and Mine phase. Contacts between phases of the Granite Mountain batholith and adjacent map units are not well exposed, but the Granite Mountain phase apparently intrudes the Burgess Creek stock and Nicola Group on the northeast margin of the batholith, and the Border phase intrudes Nicola rocks along the batholith's southwest margin.

Lower Jurassic sedimentary rocks in the Granite Mountain area are assigned to the Dragon Mountain succession (Logan and Moynihan, 2009; Schiarizza, 2015). These include a small outlier of thin-bedded slate, siltstone, and sandstone that overlies the Nicola Group 200 m north of the Burgess Creek stock, and a larger, mainly fault-bounded outlier to the west, consisting of slate, sandstone, and polymictic pebble conglomerate, that in part sits directly above the Granite Mountain batholith (Barker and Grubisa, 1994, diamond-drill hole 94-3). The succession also includes a northeast-dipping panel of polymictic conglomerates and sandstones that overlies the Nicola Group near the northern boundary of the area (Fig. 2). The conglomerates, here and to the north, include pebbles and cobbles of tonalite that are very similar to tonalites of the Granite Mountain batholith (Tipper, 1978; Schiarizza, 2015).

The Cache Creek complex is represented by scattered exposures of mainly chert, argillite, slate, limestone, and basalt east of the Triassic and Jurassic rocks of Quesnel terrane, from which they are separated by an inferred north-northwest trending fault (Fig. 2). These Cache Creek rocks are undated, but a limestone unit 10 km east of the southern part of the Granite Mountain batholith has yielded Permian fossils (Tipper, 1978).

The Sheridan Creek stock (Early Cretaceous) crops out in the southern part of the Granite Mountain area and consists mainly of massive to well-foliated medium-grained hornblende tonalite. It is in fault contact with the Quesnel terrane rocks to the north (Nicola Group and Granite Mountain batholith), and apparently intrudes the Cache Creek complex to the south (Ash et al., 1999a, b).

Rocks of the Granite Mountain batholith commonly display a tectonic foliation that dips at gentle to moderate angles to the south, and which shows a general increase in intensity from north to south. A foliation with the same orientation and characteristics in the Sheridan Creek stock is parallel to a well-developed schistosity in the narrow belt of Nicola rocks that separates the two plutonic units. The foliation in all three of these units is locally cut by a crenulation cleavage that strikes east-southeast and dips steeply, mainly to the south-southwest, and by narrow shear zones of similar orientation (Schiarizza, 2015). At the Gibraltar mine the foliation (S1) is ascribed to a period of deformation (D1) that also produced south-dipping top-to-the-north ductile shear zones that host or bound ore zones (Mostaghimi, 2016; van Straaten et al., 2020). A south-

dipping fault is also inferred to form the contact between the Nicola Group and the Sheridan Creek stock because the foliation in both units becomes progressively stronger, and is locally mylonitic, as the contact is approached (Schiarizza, 2015).

### 3. Geochronology

Here we present U-Pb zircon isotopic dating results obtained by the chemical abrasion thermal ionization mass spectrometry method (CA-TIMS) for samples collected from the Granite Mountain batholith, the Burgess Creek stock and the Sheridan Creek stock (Table 1). Samples were collected in 2013 and 2014. Soon thereafter sample preparation and analytical work was conducted at the Pacific Centre for Isotopic and Geochemical Research (PCIGR), the Department of Earth, Ocean and Atmospheric Sciences, the University of British Columbia.

#### 3.1. Analytical procedures

CA-TIMS procedures described here are modified from Mundil et al. (2004), Mattinson (2005) and Scoates and Friedman (2008). After rock samples underwent standard mineral separation procedures, zircons were handpicked in alcohol. The clearest, crack- and inclusion-free grains were selected, photographed and then annealed in quartz glass crucibles at 900°C for 60 hours. Annealed grains were transferred into 3.5 mL PFA screwtop beakers, ultrapure HF (up to 50% strength, 500 µL) and HNO<sub>3</sub> (up to 14 N, 50 µL) were added and caps were closed finger tight. The beakers were placed in 125 mL PTFE liners (up to four per liner) and about 2 mL HF and 0.2 mL HNO<sub>3</sub>, of the same strength as the acid in the beakers containing the samples, were added to the liners. The liners were then slid into stainless steel Parr™ high-pressure dissolution devices, which were sealed and brought to a maximum of 200°C for 8-16 hours (typically 175°C for 12 hours). Beakers were removed from the liners and zircon was separated from the leachate. Zircons were rinsed with >18 MΩ.m water and subboiled acetone. Then 2 mL of subboiled 6N HCl was added and beakers were set on a hotplate at 80-130°C for 30 minutes and again rinsed with water and acetone. Masses were estimated from the dimensions (volumes) of grains. Single grains were transferred into clean 300 µL PFA microcapsules (crucibles), and 50 µL 50% HF and 5 µL 14 N HNO<sub>3</sub> were added. Each was spiked with a <sup>233-235</sup>U-<sup>205</sup>Pb tracer solution (EARTHTIME ET535), capped and again placed in a

Parr liner (8-15 microcapsules per liner). HF and nitric acids, in a 10:1 ratio, were added to the liner, which was then placed in a Parr high-pressure device and dissolution was achieved at 240°C for 40 hours. The resulting solutions were dried on a hotplate at 130°C, 50 µL 6N HCl was added to microcapsules and fluorides were dissolved in high-pressure Parr devices for 12 hours at 210°C. HCl solutions were transferred into clean 7 mL PFA beakers and dried with 2 µL of 0.5 N H<sub>3</sub>PO<sub>4</sub>. Samples were loaded onto degassed, zone-refined Re filaments in 2 µL of silicic acid emitter (Gerstenberger and Haase, 1997).

Isotopic ratios were measured by a modified single collector VG-54R or 354S (with Sector 54 electronics) thermal ionization mass spectrometer equipped with analogue Daly photomultipliers. Analytical blanks were 0.2 pg for U and up to 1 pg for Pb. U fractionation was determined directly on individual runs using the EARTHTIME ET535 mixed <sup>233-235</sup>U-<sup>205</sup>Pb isotopic tracer. Pb isotopic ratios were corrected for fractionation of 0.25 ± 0.03%/amu, based on replicate analyses of NBS-982 reference material and the values recommended by Thirlwall (2000). Data reduction employed the Excel-based program of Schmitz and Schoene (2007). Standard concordia diagrams were constructed and weighted averages calculated with Isoplot (Ludwig, 2003). Interpreted ages for all samples are based on weighted <sup>206</sup>Pb/<sup>238</sup>U dates reported at the 2 sigma confidence level in the three error, ±X (Y) [Z] format of Schoene et al. (2006), where X includes internal errors only, largely comprised of analytical (counting statistics), mass fractionation and common lead composition uncertainties. The (Y) error includes X plus isotopic tracer calibration uncertainty and [Z] additionally includes uranium decay constant errors. Isotopic dates are calculated with the decay constants  $\lambda_{U238}=1.55125E^{-10}$  and  $\lambda_{U235}=9.8485E^{-10}$  (Jaffey et al., 1971). EARTHTIME U-Pb synthetic solutions were analyzed on an on-going basis to monitor the accuracy of results.

#### 3.2. Granite Mountain batholith

Three samples from the Granite Mountain batholith were dated: one from the Granite Mountain phase, one from the Mine phase, and one from a quartz-feldspar porphyry dike that cuts the Mine phase.

##### 3.2.1. Sample 13PSC-128, Granite Mountain phase

Sample 13PSC-128 was collected from the Granite Mountain phase near the northeast margin of the batholith, 1.8 km east of the Gibraltar mine tailings pond and about 150 m west of the

**Table 1.** Summary of samples dated in this study. Locations given by Easting and Northing for UTM Zone 10, NAD 83.

Sample	Easting	Northing	Rock Type	Unit	Age (Ma)
13PSC-128	553132	5824059	leucocratic tonalite	Granite Mountain batholith, Granite Mountain phase	217.15 ± 0.37
14PSC-387	550105	5815070	tonalite	Granite Mountain batholith, Mine phase	215.71 ± 0.36
14PSC-381	552439	5813890	quartz-plagioclase porphyry	Granite Mountain batholith, dike cutting Mine phase	214.98 ± 0.38
13PSC-028	555635	5827248	tonalite	Burgess Creek stock, tonalite unit	222.71 ± 0.39
13PSC-129	555392	5827019	quartz diorite	Burgess Creek stock, mixed unit	221.25 ± 0.39
14PSC-374	553598	5812478	tonalite	Sheridan Creek stock	108.57 ± 0.18

(unexposed) contact with the Burgess Creek stock (Fig. 2). It is a coarse-grained equigranular tonalite consisting of subequal proportions of plagioclase and quartz, and less than 10% chloritized mafic grains (Fig. 3). Three of the four zircon grains analyzed (Table 2) are mutually overlapping on concordia, with a weighted mean  $^{206}\text{Pb}/^{238}\text{U}$  date of  $217.15 \pm 0.20$  (0.29) [0.37] Ma (MSWD=0.45), interpreted as the crystallization age of the tonalite at this locality (Fig. 4). The fourth grain plots slightly below concordia near 215 Ma, possibly due to minor Pb loss.



**Fig. 3.** Leucocratic quartz-rich tonalite, Granite Mountain phase of the Granite Mountain batholith, sample site 13PSC-128.

### 3.2.2. Sample 14PSC-387, Mine phase

Sample 14PSC-387 was collected from the Mine phase about 2 km south of the Gibraltar mine pits (Fig. 2). It is a coarse-grained, moderately foliated tonalite containing 15-20% chloritized mafic grains, 30-35% quartz, and 50% saussuritic plagioclase (Fig. 5). Five zircon grains were analyzed. Three are mutually overlapping on concordia and yield a weighted mean  $^{206}\text{Pb}/^{238}\text{U}$  date of  $215.71 \pm 0.17$  (0.27) [0.36] Ma (MSWD=1.2), interpreted as the best estimate of the crystallization age of this tonalite (Table 2, Fig. 4). The other two grains give slightly older  $^{206}\text{Pb}/^{238}\text{U}$  results (216.56 and 217.17 Ma) and may include inherited zircon components.

### 3.2.3. Sample 14PSC-381, quartz-feldspar porphyry dike

Sample 14PSC-381 is from the southeastern part of the Granite Mountain batholith, about 900 m west of the fault contact with the Sheridan Creek stock (Fig. 2). Here, a quartz-feldspar porphyry dike, 10-20 m wide, cuts Mine phase tonalite and was traced for 80 m along a west-northwest trend (contacts not exposed). The sample, representative of most of the dike, comprises 30% quartz and plagioclase phenocrysts (2-8 mm) in a fine-grained crystalline groundmass consisting of quartz, plagioclase, and minor amounts of chloritized hornblende. Locally however, the dike is highly strained and the groundmass has been converted to quartz-plagioclase-sericite schist (Fig. 6).

Three of four zircon grains analyzed from sample 14PSC-381 are mutually overlapping on concordia and yield a weighted mean  $^{206}\text{Pb}/^{238}\text{U}$  date of  $214.98 \pm 0.22$  (0.30) [0.38] Ma (MSWD=0.28), interpreted as the crystallization age of the dike (Table 2, Fig. 4). The fourth grain yields an older  $^{206}\text{Pb}/^{238}\text{U}$  date of  $220.44 \pm 0.93$  Ma and may include an inherited zircon component.

## 3.3. Burgess Creek stock

Two samples from the Burgess Creek stock were dated: a tonalite from the tonalite unit, and a quartz diorite from the mixed unit.

### 3.3.1. Sample 13PSC-28, tonalite unit

Sample 13PSC-28 was collected from the tonalite unit along the northern margin of the Burgess Creek stock, 900 m west of the fault inferred to mark the eastern limit of Quesnel terrane (Fig. 2). It is a medium-grained equigranular tonalite estimated to contain 10% mafic minerals (hornblende>biotite), 35% quartz, and 55% plagioclase (Fig. 7). Three of six zircon grains analyzed from sample 13PSC-28 are mutually overlapping on concordia and yield a weighted mean  $^{206}\text{Pb}/^{238}\text{U}$  date of  $222.71 \pm 0.22$  (0.31) [0.39] Ma (MSWD=1.5), interpreted as the crystallization age of the tonalite at this locality (Table 3, Fig. 8). Two other grains overlap concordia at slightly younger ages ( $^{206}\text{Pb}/^{238}\text{U}$  dates of  $221.84 \pm 0.33$  Ma and  $220.51 \pm 0.44$  Ma), and the sixth grain plots below concordia near 209.5 Ma, probably due to Pb loss.

### 3.3.2. Sample 13PSC-129, mixed unit

Sample 13PSC-129 was collected from the mixed unit in the northeastern part of the Burgess Creek stock, 350 m southwest of sample site 13PSC-28 (Fig. 2). It is a coarse-grained quartz diorite (Fig. 9) with 30-35% mafic minerals (hornblende>biotite>magnetite). The five zircon grains analyzed form a cluster on or very near concordia, with  $^{206}\text{Pb}/^{238}\text{U}$  dates ranging from  $221.06 \pm 0.45$  Ma to  $221.93 \pm 0.31$  Ma (Table 3, Fig. 8). The three youngest grains, mutually overlapping on concordia, yield a weighted mean  $^{206}\text{Pb}/^{238}\text{U}$  date of  $221.25 \pm 0.20$  (0.30) [0.39] Ma (MSWD=0.60), interpreted as the crystallization age of the quartz diorite.

## 3.4. Sheridan Creek stock, Sample 14PSC-374

Sample 14PSC-374 was collected from the northeastern part of the Sheridan Creek stock, about 1 km east of its fault contact with the Granite Mountain batholith (Fig. 2). It is a medium-grained, equigranular, weakly to moderately foliated tonalite with 20% mafic grains (hornblende>biotite), 30% quartz, and 50% plagioclase (Fig. 10). Five zircon grains were analyzed, all of which fall on concordia, with  $^{206}\text{Pb}/^{238}\text{U}$  dates ranging from  $108.43 \pm 0.22$  Ma to  $108.95 \pm 0.16$  Ma (Table 3, Fig. 8). The four youngest grains form a very tight overlapping cluster that yields a weighted mean  $^{206}\text{Pb}/^{238}\text{U}$  date of  $108.57 \pm 0.09$  (0.14) [0.18] Ma (MSWD=1.0), interpreted as the best estimate of the crystallization age.

**Table 2.** U-Th-Pb analytical results for samples from the Granite Mountain batholith.

Sample (a)	Compositional Parameters										Radiogenic Isotope Ratios						Isotopic Ages										
	Wt. mg	U ppm	Pb ppm	Th U	$^{206}\text{Pb}^*$ x 10 <sup>-13</sup> mol	mol % $^{206}\text{Pb}^*$	Pb* Pb <sub>c</sub> (pg)	Pb <sub>c</sub> Pb <sub>c</sub> (pg)	$^{206}\text{Pb}$ $^{204}\text{Pb}$	$^{208}\text{Pb}$ $^{206}\text{Pb}$	$^{207}\text{Pb}$ $^{206}\text{Pb}$	% err (h)	$^{207}\text{Pb}$ $^{235}\text{U}$	% err (h)	$^{206}\text{Pb}$ $^{238}\text{U}$	% err (g)	corr. coef.	$^{207}\text{Pb}$ $^{206}\text{Pb}$	± (i)	$^{235}\text{U}$ (i)	± (h)	$^{206}\text{Pb}$ $^{238}\text{U}$	± (i)	± (h)			
<b>13PSC-128</b>																											
A	0.0196	58	1.9	0.200	1.5950	99.67%	83	0.44	5534	0.064	0.0507	0.410	0.2370	0.446	0.03390	0.138	0.410	227.4	9.5	215.96	0.87	214.91	0.29				
C	0.0145	55	1.9	0.273	1.1287	98.97%	27	0.97	1803	0.087	0.0505	0.497	0.2386	0.546	0.03424	0.135	0.471	219	12	217.2	1.1	217.05	0.29				
D	0.0136	20	0.7	0.290	0.3873	98.69%	22	0.42	1411	0.093	0.0508	0.881	0.2403	0.935	0.03428	0.169	0.400	234	20	218.7	1.8	217.26	0.36				
F	0.0037	39	1.4	0.307	0.2062	97.48%	11	0.44	733	0.098	0.0509	1.413	0.2403	1.500	0.03427	0.211	0.471	234	33	218.7	3.0	217.20	0.45				
<b>14PSC-387</b>																											
A	0.0033	88	3.1	0.222	0.4123	97.65%	12	0.81	788	0.071	0.0507	0.865	0.2376	0.937	0.03401	0.160	0.516	225	20	216.4	1.8	215.60	0.34				
B	0.0030	104	4.5	0.225	0.4419	91.83%	3	3.24	225	0.072	0.0507	1.041	0.2376	1.121	0.03400	0.193	0.485	227	24	216.4	2.2	215.51	0.41				
C	0.0021	81	3.0	0.178	0.2440	96.48%	8	0.73	526	0.056	0.0503	1.718	0.2377	1.793	0.03426	0.174	0.470	210	40	216.6	3.5	217.17	0.37				
D	0.0027	80	2.8	0.260	0.3072	98.10%	15	0.49	976	0.083	0.0508	0.736	0.2393	0.803	0.03416	0.165	0.489	232	17	217.8	1.6	216.56	0.35				
E	0.0025	405	13.8	0.277	1.4355	99.42%	49	0.69	3171	0.088	0.0504	0.219	0.2364	0.273	0.03405	0.110	0.642	211.6	5.1	215.48	0.53	215.83	0.23				
<b>14PSC-381</b>																											
B	0.0030	25	1.0	0.278	0.1084	94.48%	5	0.52	335	0.087	0.0499	2.322	0.2394	2.496	0.03479	0.430	0.478	191	54	217.9	4.9	220.44	0.93				
C	0.0025	52	2.0	0.264	0.1841	95.76%	6	0.67	436	0.084	0.0502	1.562	0.2348	1.668	0.03393	0.185	0.606	203	36	214.1	3.2	215.10	0.39				
D	0.0044	75	2.9	0.314	0.4681	96.00%	7	1.61	461	0.100	0.0507	0.959	0.2370	1.041	0.03390	0.172	0.541	227	22	216.0	2.0	214.94	0.36				
E	0.0025	52	1.9	0.264	0.1851	96.77%	8	0.51	572	0.084	0.0509	1.407	0.2378	1.494	0.03390	0.173	0.551	235	32	216.6	2.9	214.91	0.37				

(a) Letters are labels for fractions composed of single zircon grains or fragments; all fractions annealed and chemically abraded after Mattinson (2005) and Scoates and Friedman (2008).

(b) Nominal fraction weights estimated from photomicrographic grain dimensions, adjusted for partial dissolution during chemical abrasion.

(c) Nominal U and total Pb concentrations subject to uncertainty in photomicrographic estimation of weight and partial dissolution during chemical abrasion.

(d) Model Th/U ratio calculated from radiogenic  $^{208}\text{Pb}/^{206}\text{Pb}$  ratio and  $^{206}\text{Pb}/^{238}\text{U}$  date.

(e) Pb\* and Pb<sub>c</sub> represent radiogenic and common Pb, respectively; mol %  $^{206}\text{Pb}^*$  with respect to radiogenic, blank and initial common Pb.

(f) Measured ratio corrected for spike and fractionation only. Mass discrimination of 0.25 ± 0.03%/amu, based on analysis of NBS-982; all Daly analyses.

(g) Corrected for fractionation, spike, and common Pb; up to 1 pg common Pb was assumed to be procedural blank:  $^{206}\text{Pb}/^{204}\text{Pb} = 18.50 \pm 1.0\%$ ;  $^{207}\text{Pb}/^{204}\text{Pb} = 15.50 \pm 1.0\%$ ;

(h) Errors are 2-sigma, propagated using the algorithms of Schmitz and Schoene (2007) and Crowley et al. (2007).

(i) Calculations are based on the decay constants of Jaffey et al. (1971).  $^{206}\text{Pb}/^{238}\text{U}$  and  $^{207}\text{Pb}/^{235}\text{U}$  ages corrected for initial disequilibrium in  $^{230}\text{Th}/^{238}\text{U}$  using Th/U [magma] = 3.

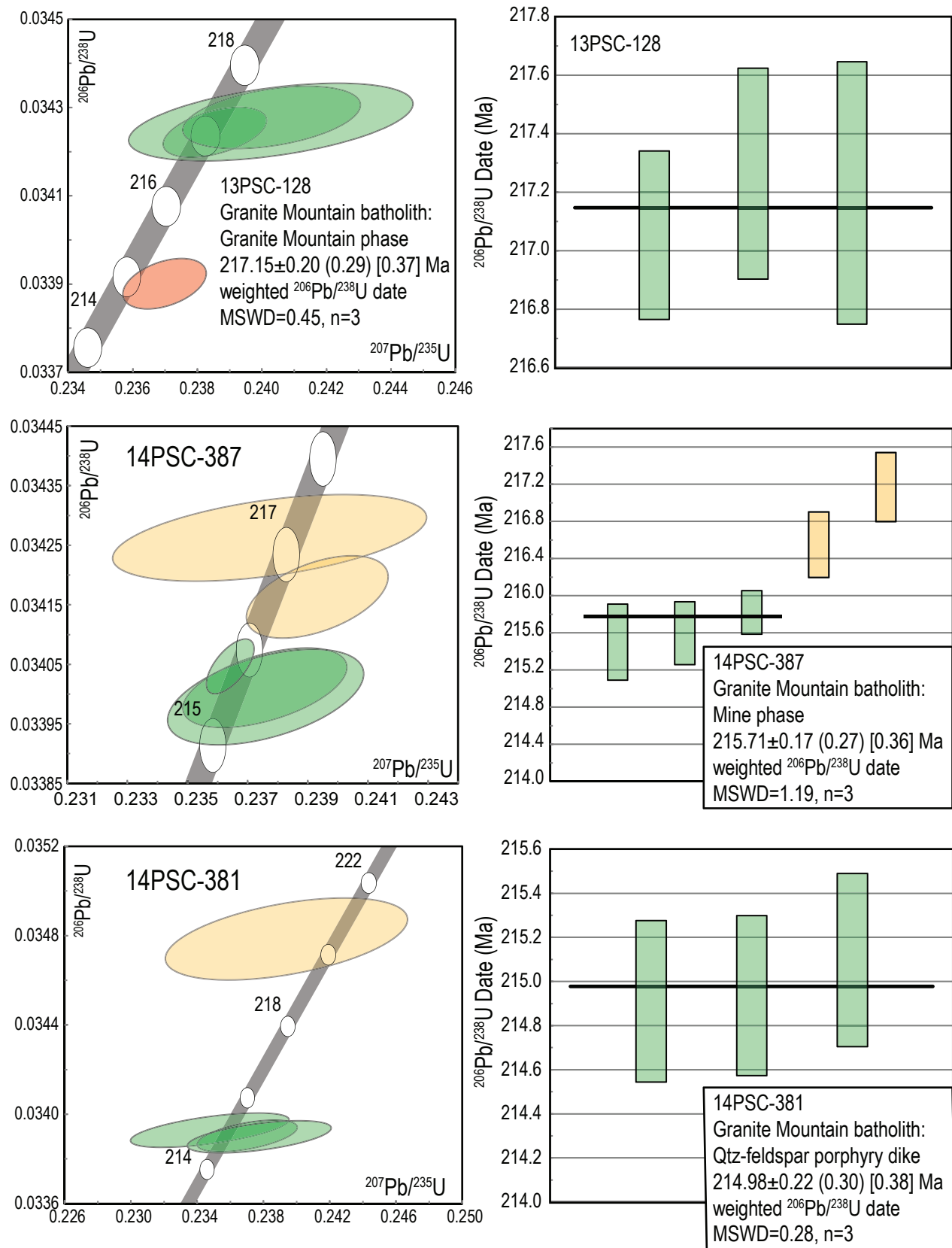


**Fig. 4.** Concordia plots and  $^{206}\text{Pb}/^{238}\text{U}$  weighted mean age diagrams for samples from different units in the Granite Mountain batholith. Green ellipses are zircons used for the  $^{206}\text{Pb}/^{238}\text{U}$  weighted mean calculation. Yellow are zircons that may have inherited components; red are zircons with lead loss.



**Fig. 5.** Foliated tonalite, Mine phase of the Granite Mountain batholith, sample site 14PSC-387.



**Fig. 6.** Foliated quartz-feldspar porphyry, from high-strain zone in dike cutting Mine phase tonalite, near sample site 14PSC-381.

#### 4. Discussion

Samples dated in this study provide Late Triassic crystallization ages for parts of the Burgess Creek stock and Granite Mountain batholith. The dates from the Burgess Creek stock ( $222.71 \pm 0.39$  Ma and  $221.25 \pm 0.39$  Ma) are the only isotopic dates available for this unit and demonstrate that it is, at least in part, several million years older than the oldest dated rocks in the Granite Mountain batholith. The three dates from the Granite



**Fig. 7.** Hornblende-biotite tonalite, tonalite unit of the Burgess Creek stock, sample site 13PSC-28.

Mountain batholith ( $217.15 \pm 0.37$  Ma,  $215.71 \pm 0.36$  Ma, and  $214.98 \pm 0.38$  Ma) demonstrate magmatic crystallization over a  $\sim 3$  million-year period. A number of previously reported U-Pb zircon dates from the Granite Mountain batholith fall within this same time window, including: 1) a U-Pb zircon CA-TIMS date of  $216.17 \pm 0.39$  Ma reported by Mostaghimi (2016) for Mine phase tonalite from the Gibraltar mine; 2) a  $215 \pm 0.8$  Ma U-Pb zircon date reported by Ash and Riveros (2001), from a Granite Mountain phase sample collected 1.5 km north-northeast of the Gibraltar mill (Ash et al., 1999a); and 3) U-Pb zircon LA-ICP-MS dates of  $211.9 \pm 4.3$  Ma (Mine phase) and  $209.6 \pm 6.3$  Ma (Granite Mountain phase) reported by Oliver et al. (2009) for samples from the Gibraltar mine. However, younger intrusive rocks in the batholith are indicated by a recent study that included U-Pb zircon LA-ICP-MS dating of six samples, all mapped as Mine phase tonalite, from the Gibraltar mine area (Kobylinski et al., 2018). Two of the dates ( $218.9 \pm 3.1$  Ma and  $213.2 \pm 2.4$  Ma) are within error of previous dates, but the other four, ranging from  $201.9 \pm 5.0$  Ma to  $206.8 \pm 4.0$  Ma, document a younger, latest Triassic, intrusive phase.

The Granite Mountain batholith and Burgess Creek stock are included in Quesnel terrane because they intrude Triassic rocks of the Nicola Group, the most widespread component of the terrane. They are inferred to be part of a belt of Late Triassic calcalkaline plutons that is restricted to the western part of Quesnel terrane in southern British Columbia (Schiarizza, 2014), although this belt is not exposed between the Granite Mountain area and Ashcroft, mainly due to extensive Neogene and Quaternary cover. The belt is best represented by Late Triassic granitic to tonalitic plutons between Ashcroft and Princeton (Fig. 1), including the Guichon Creek batholith ( $211$ – $207$  Ma, D'Angelo et al., 2017), the Allison pluton ( $223$  Ma, Mihalynuk et al., 2016), and the Coldwater pluton ( $210$  Ma, Mihalynuk et al., 2016).

The  $108.57 \pm 0.18$  Ma date for the Sheridan Creek stock demonstrates that the deformation that produced the foliations

**Table 3.** U-Th-Pb analytical results for samples from the Burgess Creek stock and Sheridan Creek stock.

Sample	Compositional Parameters										Radiogenic Isotope Ratios						Isotopic Ages							
	Wt. mg	U ppm	Pb ppm	Th U	$^{206}\text{Pb}^*$ mol $\times 10^{-13}$	mol % $^{206}\text{Pb}^*$	Pb <sub>c</sub> (pg)	$\frac{^{206}\text{Pb}}{^{204}\text{Pb}}$	$\frac{^{207}\text{Pb}}{^{206}\text{Pb}}$	$\frac{^{208}\text{Pb}}{^{206}\text{Pb}}$	$\frac{^{207}\text{Pb}}{^{206}\text{Pb}}$	$\frac{^{207}\text{Pb}}{^{235}\text{U}}$	$\frac{^{206}\text{Pb}}{^{238}\text{U}}$	corr. coef.	$\frac{^{207}\text{Pb}}{^{235}\text{U}}$	$\frac{^{206}\text{Pb}}{^{238}\text{U}}$	$\frac{^{207}\text{Pb}}{^{235}\text{U}}$	$\frac{^{206}\text{Pb}}{^{238}\text{U}}$						
<b>13PSC-28</b>																								
A	0.008	100	3.6	0.323	1.2078	99.00%	29	1.01	1843	0.103	0.0505	0.700	0.2425	0.773	0.03480	0.204	0.474	220	16	220.5	1.5	220.51	0.44	
B	0.008	129	4.2	0.273	1.4687	99.58%	68	0.51	4435	0.088	0.0509	0.838	0.2317	0.885	0.03303	0.261	0.323	236	19	211.6	1.7	209.47	0.54	
C	0.005	184	6.6	0.398	1.2943	99.58%	69	0.46	4435	0.127	0.0508	0.741	0.2462	0.775	0.03512	0.163	0.311	234	17	223.5	1.6	222.53	0.36	
D	0.006	45	1.7	0.428	0.4113	98.07%	15	0.67	957	0.136	0.0507	1.101	0.2456	1.170	0.03513	0.204	0.416	227	25	223.0	2.3	222.60	0.45	
E	0.007	139	4.9	0.369	1.3625	99.72%	103	0.32	6676	0.117	0.0508	0.474	0.2450	0.524	0.03501	0.152	0.454	230	11	222.5	1.0	221.84	0.33	
F	0.003	154	5.8	0.541	0.6996	99.34%	46	0.38	2814	0.172	0.0508	0.554	0.2462	0.605	0.03519	0.157	0.443	230	13	223.5	1.2	222.94	0.34	
<b>13PSC-129</b>																								
B	0.003	167	5.8	0.309	0.7525	99.54%	62	0.29	4022	0.098	0.0507	0.433	0.2442	0.475	0.03492	0.122	0.460	228	10	221.81	0.95	221.26	0.26	
D	0.005	420	17.9	0.424	2.8736	94.54%	5	13.77	337	0.135	0.0505	1.312	0.2435	1.374	0.03494	0.208	0.368	220	30	221.2	2.7	221.41	0.45	
E	0.002	178	6.4	0.380	0.5712	99.20%	36	0.38	2304	0.120	0.0505	0.644	0.2436	0.688	0.03501	0.137	0.412	217	15	221.4	1.4	221.80	0.30	
F	0.004	258	9.1	0.347	1.3902	99.63%	77	0.44	4942	0.111	0.0510	0.740	0.2452	0.817	0.03489	0.205	0.486	240	17	222.7	1.6	221.06	0.45	
G	0.002	1063	37.5	0.359	2.7931	99.84%	182	0.37	11524	0.115	0.0509	0.275	0.2456	0.319	0.03503	0.143	0.511	235	6	223.0	0.6	221.93	0.31	
<b>14PSC-374</b>																								
A	0.003	224	4.1	0.466	0.4589	98.46%	20	0.58	1205	0.148	0.0479	1.537	0.1122	1.563	0.01698	0.155	0.216	96	36	108.0	1.6	108.53	0.17	
B	0.025	18	0.3	0.503	0.3145	97.60%	12	0.63	770	0.161	0.0482	1.164	0.1131	1.224	0.01700	0.145	0.459	112	27	108.8	1.3	108.65	0.16	
C	0.004	178	3.9	0.283	0.4394	91.21%	3	3.48	211	0.090	0.0479	1.582	0.1120	1.655	0.01696	0.201	0.414	94	37	107.8	1.7	108.43	0.22	
D	0.003	124	2.4	0.449	0.2289	96.83%	9	0.61	584	0.144	0.0483	1.548	0.1132	1.625	0.01699	0.206	0.430	114	36	108.8	1.7	108.61	0.22	
E	0.003	260	4.7	0.398	0.4617	98.37%	18	0.63	1134	0.127	0.0482	0.762	0.1133	0.810	0.01705	0.144	0.415	111	18	109.0	0.8	108.95	0.16	

(a) Letters are labels for fractions composed of single zircon grains or fragments; all fractions annealed and chemically abraded after Mattinson (2005) and Scoates and Friedman (2008).  
 (b) Nominal fraction weights estimated from photomicrographic grain dimensions; adjusted for partial dissolution during chemical abrasion.  
 (c) Nominal U and total Pb concentrations subject to uncertainty in photomicrographic estimation of weight and partial dissolution during chemical abrasion.  
 (d) Model Th/U ratio calculated from radiogenic  $^{208}\text{Pb}/^{206}\text{Pb}$  ratio and  $^{206}\text{Pb}/^{238}\text{U}$  date.  
 (e) Pb\* and Pb<sub>c</sub> represent radiogenic and common Pb, respectively; mol %  $^{206}\text{Pb}^*$  with respect to radiogenic, blank and initial common Pb.  
 (f) Measured ratio corrected for spike and fractionation only. Mass discrimination of  $0.25 \pm 0.03\%$  amu, based on analysis of NBS-982; all Daly analyses.  
 (g) Corrected for fractionation, spike, and common Pb; up to 1 pg common Pb was assumed to be procedural blank;  $^{206}\text{Pb}/^{204}\text{Pb} = 18.50 \pm 1.0\%$ ;  $^{207}\text{Pb}/^{204}\text{Pb} = 15.50 \pm 1.0\%$ ;  $^{206}\text{Pb}/^{204}\text{Pb} = 38.40 \pm 1.0\%$  (all uncertainties 1-sigma). Excess over blank was assigned to initial common Pb with Stacey and Kramers (1975) model Pb composition at interpreted age of sample.  
 (h) Errors are 2-sigma, propagated using the algorithms of Schmitz and Schoene (2007) and Crowley et al. (2007).  
 (i) Calculations are based on the decay constants of Jaffey et al. (1971).  $^{206}\text{Pb}/^{238}\text{U}$  and  $^{207}\text{Pb}/^{238}\text{U}$  ages corrected for initial disequilibrium in  $^{230}\text{Th}/^{238}\text{U}$  using  $[\text{Th}/\text{U}]_{\text{magma}} = 3$ .

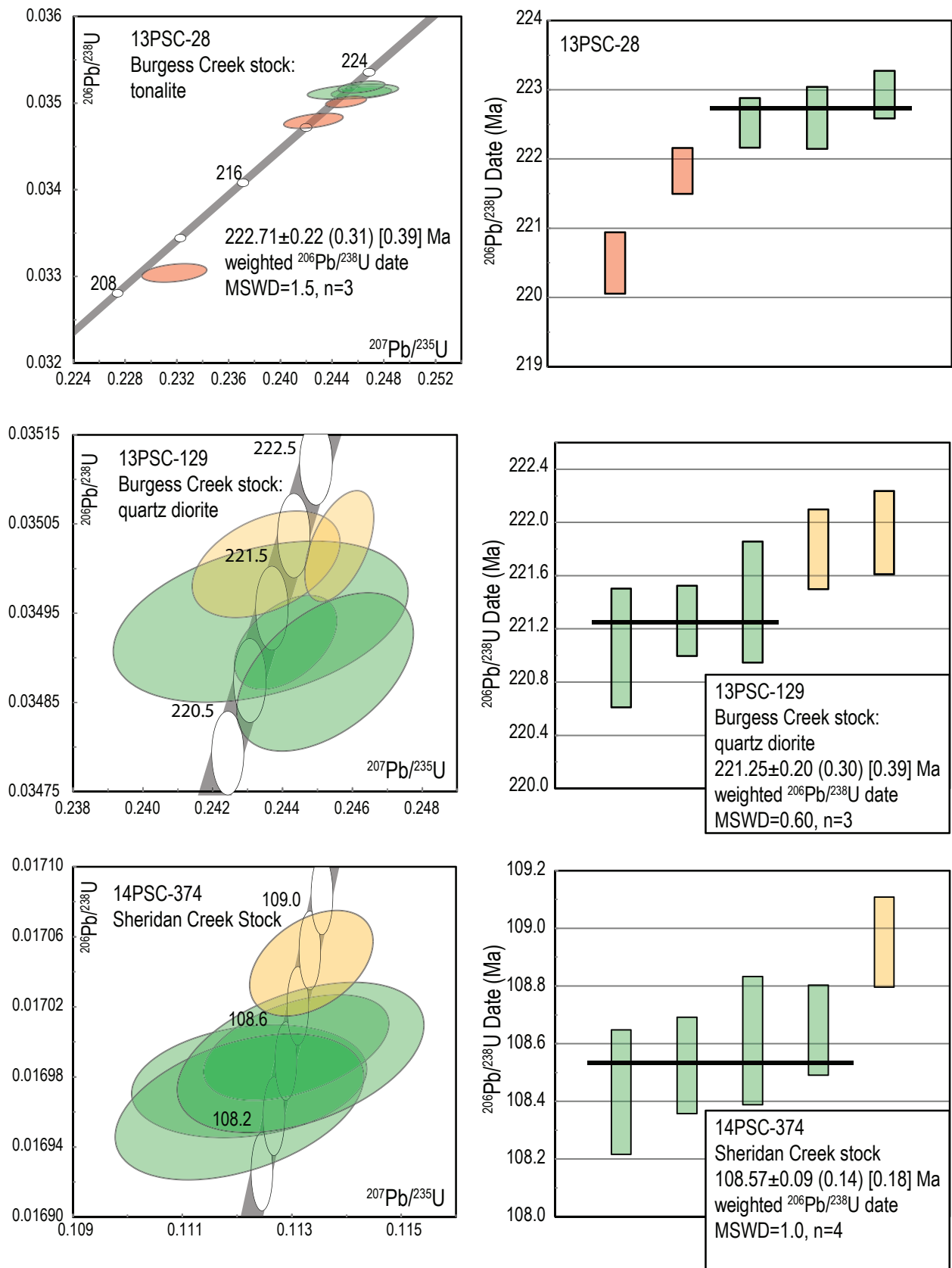


**Fig. 8.** Concordia plots and  $^{206}\text{Pb}/^{238}\text{U}$  weighted mean age diagrams for samples from the Burgess Creek stock and Sheridan Creek stock. Green ellipses are zircons used for the  $^{206}\text{Pb}/^{238}\text{U}$  weighted mean calculation. Yellow are zircons that may have inherited components; red are zircons with lead loss.



**Fig. 9.** Hornblende-biotite quartz diorite, mixed unit of the Burgess Creek stock, near sample site 13PSC-129. Leucotonalite veins and epidote-altered fractures, such as those in this photo, were avoided during sampling.



**Fig. 10.** Weakly foliated hornblende-biotite tonalite, Sheridan Creek stock, sample site 14PSC-374.

common to the Sheridan Creek stock, Nicola Group, and Granite Mountain batholith was mid-Cretaceous or younger. Based on the orientations of structures, and  $^{40}\text{Ar}$ - $^{39}\text{Ar}$  dates ranging from 54 to 36 Ma on white mica from fault zones at the Gibraltar mine, Mostaghimi (2016) linked development of the foliation and related north-directed thrust faults to northwest-striking Eocene dextral strike-slip faults. These structures were then offset by, and rotated between, faults related to the younger north-striking Fraser fault system. A northwest-striking fault mapped by Ash et al. (1999a, b) to the south of the Granite Mountain batholith (Fig. 11, fault PFE) may be the specific structure to which the south-dipping foliations and

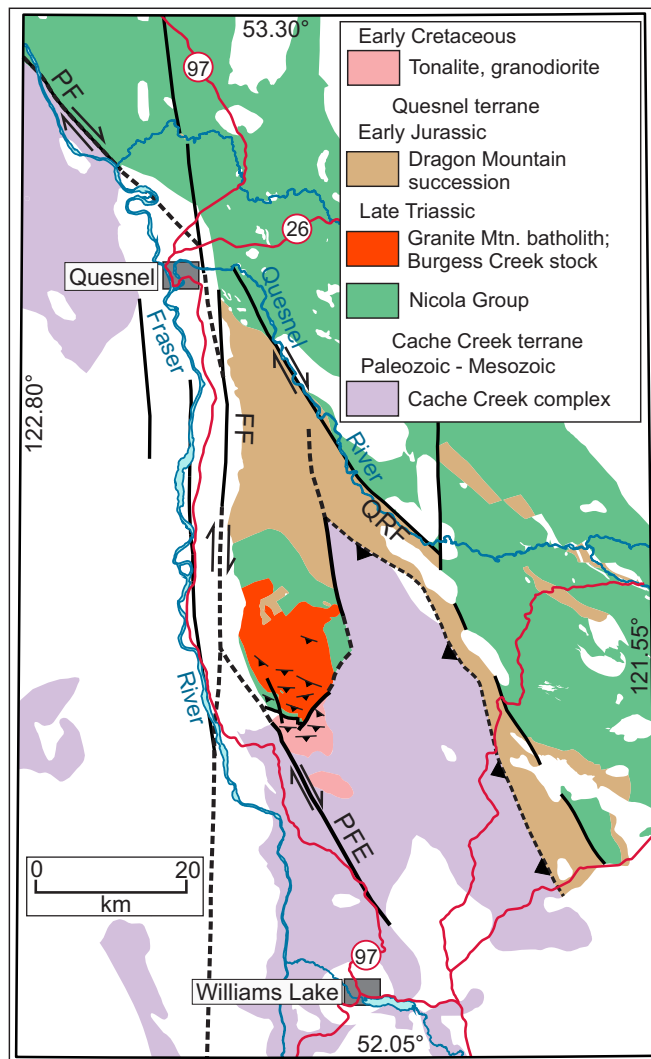


**Fig. 11.** Map of selected geologic units and structures in the Williams Lake-Quesnel area, showing location of the Granite Mountain batholith with respect to known and inferred dextral strike-slip faults. Geology from Cui et al. (2017). FF-Fraser fault; PF-Pinchi fault; PFE-inferred Pinchi fault extension; QRF-Quesnel River fault.

contractional faults are linked, and this fault may be a southern extension (offset by the Fraser fault system) of the Pinchi fault, which extends 400 km northwest from Quesnel, marking the contact between Cache Creek and Quesnel terranes for most of this length (Struik et al., 2001; Gabrielse et al., 2006).

The panel of Quesnel terrane rocks that includes the Granite Mountain batholith is juxtaposed against Cache Creek terrane to the east across an unexposed northerly trending fault (Figs. 2, 11). Schiarizza (2015) suggested that this fault might record mid-Cretaceous sinistral strike-slip movement. An alternative explanation is that the fault is an Eocene east-side-down normal fault that accommodated uplift of the Granite Mountain batholith and associated rocks as they were being deformed along the Pinchi and/or Fraser fault systems. This would imply that the Cache Creek rocks to the east and southeast of the

Granite Mountain batholith form a relatively thin thrust sheet that overlies the western part of Quesnel terrane (Fig. 11), including the belt of Late Triassic calcalkaline plutons.

## 5. Summary

Samples collected during mapping of the Granite Mountain area in 2013 and 2014 were dated using the U-Pb zircon chemical abrasion thermal ionization mass spectrometry method (CA-TIMS), providing crystallization ages for the Granite Mountain batholith, the Burgess Creek stock, and the Sheridan Creek stock. Leucocratic tonalite from the Granite Mountain phase of the batholith yields a Late Triassic date of  $217.15 \pm 0.37$  Ma; Mine phase tonalite is dated at  $215.71 \pm 0.36$  Ma; and a quartz-plagioclase porphyry dike cutting Mine phase tonalite is  $214.98 \pm 0.38$  Ma. The Burgess Creek stock, on the northeast margin of the batholith, is also Late Triassic, but several million years older than the Granite Mountain batholith. A tonalite sample from the stock yields a date of  $222.71 \pm 0.39$  Ma, and a sample of quartz diorite is dated at  $221.25 \pm 0.39$  Ma. The Sheridan Creek stock, south of the Granite Mountain batholith, is Early Cretaceous, based on a date of  $108.57 \pm 0.18$  Ma obtained from a tonalite sample collected from the stock.

## Acknowledgments

Wes Harman, Mark Ralph, Lori Kennedy, and Adrian Hickin assisted with fieldwork and collecting samples for U-Pb dating. H. Lin, D. Newton, and C. Wall assisted with mineral separation, sample preparation, and mass spectrometry at PCIGR. Lawrence Aspler reviewed the paper and made suggestions that improved it.

## References cited

- Ash, C.H., Rydman, M.O., Payne, C.W., and Panteleyev, A., 1999a. Geological setting of the Gibraltar mine, south-central British Columbia (93B/8, 9). In: *Exploration and Mining in British Columbia 1998*, British Columbia Ministry of Energy and Mines, pp. A1-A15.
- Ash, C.H., Panteleyev, A., MacLennan, K.L., Payne, C.W., and Rydman, M.O., 1999b. Geology of the Gibraltar mine area, NTS 93B/8, 9. British Columbia Ministry of Energy and Mines, British Columbia Geological Survey Open File 1999-7; scale 1:50,000.
- Ash, C.H., and Riveros, C.P., 2001. Geology of the Gibraltar copper-molybdenite deposit, east-central British Columbia (93B/9). In: *Geological Fieldwork 2000*, British Columbia Ministry of Energy and Mines, British Columbia Geological Survey Paper 2001-1, pp. 119-133.
- Barker, G.E., and Grubisa, G.G., 1994. Diamond drill report on the Ze claim group, Cariboo Mining Division, 93B/9W. British Columbia Ministry of Energy and Mines, British Columbia Geological Survey Assessment Report 23,496, 69 p.
- Bysouth, G.D., Campbell, K.V., Barker, G.E., and Gagnier, G.K., 1995. Tonalite-trondhjemite fractionation of peraluminous magma and the formation of syntectonic porphyry copper mineralization, Gibraltar mine, central British Columbia. In: Schroeter, T.G., (Ed.), *Porphyry deposits of the northwestern cordillera of North America*, Canadian Institute of Mining, Metallurgy and Petroleum, Special Volume 46, pp. 201-213.
- Crowley, J.L., Schoene, B., and Bowring, S.A., 2007. U-Pb dating of zircon in the Bishop Tuff at the millennial scale. *Geology*, 35, 1123-1126.
- Cui, Y., Miller, D., Schiarizza, P., and Diakow, L.J., 2017. British Columbia digital geology. British Columbia Ministry of Energy, Mines and Petroleum Resources, British Columbia Geological Survey Open File 2017-08, 9 p.
- D'Angelo, M., Alfaro, M., Hollings, P., Byrne, K., Piercey, S., and Creaser, R.A., 2017. Petrogenesis and magmatic evolution of the Guichon Creek batholith: Highland Valley porphyry Cu  $\pm$ (Mo) district, south-central British Columbia. *Economic Geology*, 112, 1857-1888.
- Drummond, A.D., Sutherland Brown, A., Young, R.J., and Tennant, S.J., 1976. Gibraltar-regional metamorphism, mineralization, hydrothermal alteration and structural development. In: Sutherland Brown, A., (Ed.), *Porphyry deposits of the Canadian Cordillera*, Canadian Institute of Mining and Metallurgy, Special Volume 15, pp. 195-205.
- Gabrielse, H., Murphy, D.C., and Mortensen, J.K., 2006. Cretaceous and Cenozoic dextral orogen-parallel displacements, magmatism, and paleogeography, north-central Canadian Cordillera. In: Haggart, J.W., Enkin, R.J., and Monger, J.W.H., (Eds.), *Paleogeography of the North American Cordillera: Evidence for and against large-scale displacements*, Geological Association of Canada, Special Paper 46, pp. 255-276.
- Gerstenberger, H., and Haase, G., 1997. A highly effective emitter substance for mass spectrometric Pb isotopic ratio determinations. *Chemical Geology*, 136, 309-312.
- Jaffey, A.H., Flynn, K.F., Glendenin, L.E., Bentley, W.C., and Essling, A.M., 1971. Precision measurement of half-lives and specific activities of  $^{235}\text{U}$  and  $^{238}\text{U}$ . *Physics Review*, C4, 1889-1906.
- Kobylinski, C.H., Hattori, K., Smith, S.W., and Plouffe, A., 2018. High cerium anomalies in zircon from intrusions associated with porphyry copper mineralization in the Gibraltar deposit, south-central British Columbia. *Geological Survey of Canada*, Open File 8430, 19 p.
- Logan, J.M., and Moynihan, D.P., 2009. Geology and mineral occurrences of the Quesnel River map area, central British Columbia (NTS 093B/16). In: *Geological Fieldwork 2008*, British Columbia Ministry of Energy, Mines and Petroleum Resources, British Columbia Geological Survey Paper 2009-1, pp. 127-152.
- Ludwig, K.R., 2003. Isoplot 3.09-A Geochronological toolkit for Microsoft Excel. Berkley Geochronology Center, The University of California at Berkeley, Special Publication No. 4.
- Mattinson, J.M., 2005. Zircon U-Pb chemical abrasion ("CA-TIMS") method: Combined annealing and multi-step partial dissolution analysis for improved precision and accuracy of zircon ages. *Chemical Geology*, 220, 47-66.
- Mihalynuk, M.G., Diakow, L.J., Friedman, R.M., and Logan, J.M., 2016. Chronology of southern Nicola arc stratigraphy and deformation. In: *Geological Fieldwork 2015*, British Columbia Ministry of Energy and Mines, British Columbia Geological Survey Paper 2016-1, pp. 31-63.
- Mostaghimi, N., 2016. Structural geology and timing of deformation at the Gibraltar copper-molybdenum porphyry deposit, south-central British Columbia. Unpublished M.Sc. thesis, The University of British Columbia, 358 p.
- Mundil, R., Ludwig, K.R., Metcalfe, I., and Renne, P.R., 2004. Age and timing of the Permian Mass Extinctions: U/Pb Dating of Closed-System Zircons. *Science*, 305, 1760-1763.
- Oliver, J., Crozier, J., Kamionko, M., and Fleming, J., 2009. The Gibraltar Mine, British Columbia. A billion tonne deep copper-molybdenum porphyry system: structural style, patterns of mineralization and rock alteration. In: *Association for Mineral Exploration British Columbia, 2009 Mineral Exploration Roundup*, program with abstracts, pp. 35-36.
- Panteleyev, A., 1978. Granite Mountain project (93B/8). In: *Geological Fieldwork 1977*, British Columbia Ministry of Energy, Mines and Petroleum Resources, British Columbia Geological Survey Paper 1978-1, pp. 39-42.

- Schiarizza, P., 2014. Geological setting of the Granite Mountain batholith, host to the Gibraltar Cu-Mo porphyry deposit, south-central British Columbia. In: Geological Fieldwork 2013, British Columbia Ministry of Energy and Mines, British Columbia Geological Survey Paper 2014-1, pp. 95-110.
- Schiarizza, P., 2015. Geological setting of the Granite Mountain batholith, south-central British Columbia. In: Geological Fieldwork 2014, British Columbia Ministry of Energy and Mines, British Columbia Geological Survey Paper 2015-1, pp. 19-39.
- Schmitz, M.D., and Schoene, B., 2007. Derivation of isotope ratios, errors, and error correlations for U-Pb geochronology using  $^{205}\text{Pb}$ - $^{235}\text{U}$ -( $^{233}\text{U}$ )-spiked isotope dilution thermal ionization mass spectrometric data. *Geochemistry, Geophysics, Geosystems*, 8, Q08006, doi:10.1029/2006GC001492.
- Schoene, B.A., Crowley, J.L., Condon, D.J., Schmitz, M.D., and Bowring, S.A., 2006. Reassessing the uranium decay constants for geochronology using ID-TIMS U-Pb data. *Geochimica et Cosmochimica Acta*, 70, 426-445.
- Scoates, J.S., and Friedman, R.M., 2008. Precise age of the platinumiferous Merensky Reef, Bushveld Complex, South Africa, by the U-Pb zircon chemical abrasion ID-TIMS technique. *Economic Geology*, 103, 465-471.
- Stacey, J.S., and Kramers, J.D., 1975. Approximation of terrestrial lead isotopic evolution by a two-stage model. *Earth and Planetary Science Letters*, 26, 207-221.
- Struik, L.C., Schiarizza, P., Orchard, M.J., Cordey, F., Sano, H., MacIntyre, D.G., Lapierre, H., and Tardy, M., 2001. Imbricate architecture of the upper Paleozoic to Jurassic oceanic Cache Creek Terrane, central British Columbia. *Canadian Journal of Earth Sciences*, 38, 495-514.
- Thirlwall, M.F., 2000. Inter-laboratory and other errors in Pb isotope analyses investigated using a  $^{207}\text{Pb}$ - $^{204}\text{Pb}$  double spike. *Chemical Geology*, 163, 299-322.
- Tipper, H.W., 1978. Northeastern part of Quesnel (93B) map-area, British Columbia. In: Current Research, Part A, Geological Survey of Canada, Paper 78-1A, pp. 67-68.
- van Straaten, B.I., Mostaghimi, N., Kennedy, L., Gallagher, C., Schiarizza, P., and Smith, S., 2020. The deformed Gibraltar porphyry copper-molybdenum deposit, south-central British Columbia, Canada. In: Sharman, E.R., Lang, J.R., and Chapman, J.B., (Eds.), *Porphyry deposits of the northwestern cordillera of North America: A 25-year update*. Canadian Institute of Mining, Metallurgy and Petroleum, Special Volume 57, pp. 547-567.





# Geochronology of northern Hogem batholith, Quesnel terrane, north-central British Columbia

Jones, G.<sup>1,2</sup>, Ootes, L.<sup>1,a</sup>, Milidragovic, D.<sup>1,3</sup>, Friedman, R.<sup>4</sup>, Camacho, A.<sup>5</sup>, Luo, Y.<sup>2</sup>, Vezinet, A.<sup>2</sup>, Pearson, D.G.<sup>2</sup>, and Schiarizza, P.<sup>1</sup>

<sup>1</sup>British Columbia Geological Survey, Ministry of Energy, Mines and Low Carbon Innovation, Victoria, BC, V8W 9N3

<sup>2</sup>Department of Earth & Atmospheric Sciences, University of Alberta, Edmonton, AB, T6G 2E3

<sup>3</sup>Geological Survey of Canada, Natural Resources Canada, Vancouver, BC, V6B 5J3

<sup>4</sup>Pacific Centre for Geochemical and Isotopic Research, University of British Columbia, Vancouver, BC, V6T 1Z4

<sup>5</sup>Department of Geological Sciences, University of Manitoba, Winnipeg, MB R3T 2N2

<sup>a</sup>corresponding author: Luke.Ootes@gov.bc.ca

Recommended citation: Jones, G., Ootes, L., Milidragovic, D., Friedman, R., Camacho, A., Luo, Y., Vezinet, A., Pearson, D.G., and Schiarizza, P., 2021. Geochronology of northern Hogem batholith, Quesnel terrane, north-central British Columbia. In: Geological Fieldwork 2020, British Columbia Ministry of Energy, Mines and Low Carbon Innovation, British Columbia Geological Survey Paper 2021-01, pp. 37-56.

## Abstract

New and previously unpublished geochronological data that complement bedrock mapping and geochemical studies in northern Hogem batholith indicate punctuated emplacement of four distinct intrusive suites during a protracted (ca. 80 Ma) interval, from 207 to 128 Ma. U-Pb crystallization ages include new zircon (by LA-ICP-MS), previously unpublished legacy zircon and titanite (by ID-TIMS), and published zircon (by CA-TIMS). Amphibole, biotite, and muscovite <sup>40</sup>Ar/<sup>39</sup>Ar step-heating results provide magmatic cooling ages and post-deformation cooling ages. The Thane Creek suite, composed of mostly metaluminous diorite to quartz monzodiorite with lesser hornblende, intruded host Nicola Group strata between 207 and 194 Ma. The Duckling Creek suite consists of alkaline biotite clinopyroxene and syenite that intruded the Thane Creek suite between 182 and 175 Ma. The Osilinka suite, represented by a weakly peraluminous leucocratic granite body, yielded a maximum emplacement age of ca. 160 Ma. The Mesilinka suite consists of metaluminous tonalite and weakly peraluminous granodiorite to granite, with interpreted crystallization ages ranging from 135 to 128 Ma. Bedrock mapping and geochronologic results from this study indicate that northern Hogem batholith contains prospective rocks comparable to those that host the Lorraine and other deposits south of the present study area. The Hogem batholith is relatively unique in the Canadian Cordillera because it contains a remarkable evolution of punctuated Upper Triassic to Lower Cretaceous intrusive suites that are compositionally and chemically diverse. A new discovery is that the Mesilinka suite (Lower Cretaceous) intruded during a Cordilleran-wide magmatic lull.

**Keywords:** Hogem batholith, Quesnel terrane, Stikine terrane, geochemistry, U-Pb zircon crystallization ages, CA-TIMS, ID-TIMS, LA-ICP-MS

## 1. Introduction

In 2018, the British Columbia Geological Survey initiated a three-year mapping project in the Omineca Mountains of north-central British Columbia (Figs. 1, 2; Ootes et al., 2019, 2020a-c). The project aims to better understand the bedrock and surficial geology and associated base- and precious-metal mineralization in the northern part of Hogem batholith and surroundings, through detailed 1:50,000-scale mapping and geochemical studies (Fig. 2; Ootes et al., 2020a). Herein we summarize the results of new U-Pb zircon, legacy U-Pb zircon and titanite, and <sup>40</sup>Ar/<sup>39</sup>Ar biotite, hornblende, and muscovite geochronology for northern Hogem batholith. Full details, including locations, data tables, zircon descriptions, and cathodoluminescence (CL) imagery are presented in Ootes et al. (2020c).

## 2. Geologic setting and previous work

### 2.1. Geology

In Quesnel terrane, Hogem batholith is bounded to the north

and east by volcanic and sedimentary rocks of the Nicola Group (Triassic) along fault and intrusive contacts (Fig. 1). To the west, the batholith and Nicola Group are juxtaposed against Cache Creek and Stikine terranes across the Pinchi-Ingenika dextral strike-slip fault system (Figs. 1, 2).

Hogem batholith is subdivided into four petrologically distinct intrusive units; from oldest to youngest these are the Thane Creek, Duckling Creek, Osilinka, and Mesilinka suites (Figs. 3, 4; Woodsworth, 1976; Schiarizza and Tan, 2005a, b; Devine et al., 2014; Ootes et al., 2019, 2020a-c). Full unit descriptions can be found in Ootes et al. (2019) and supporting geochemical data are in Ootes et al. (2020c). The intrusive suites span a range of compositions from ultramafic to highly silicic (SiO<sub>2</sub>=34.3-77.0 wt.%, on LOI-free anhydrous basis; Figs. 3, 4). In general, the metaluminous (Fig. 4) Thane Creek suite contains relatively small pockets (<0.01 km<sup>2</sup>) of coarse-grained hornblende that was intruded and co-mingled with medium-grained diorite to quartz monzodiorite (Fig. 3). The suite ranges from undeformed to strongly deformed, including

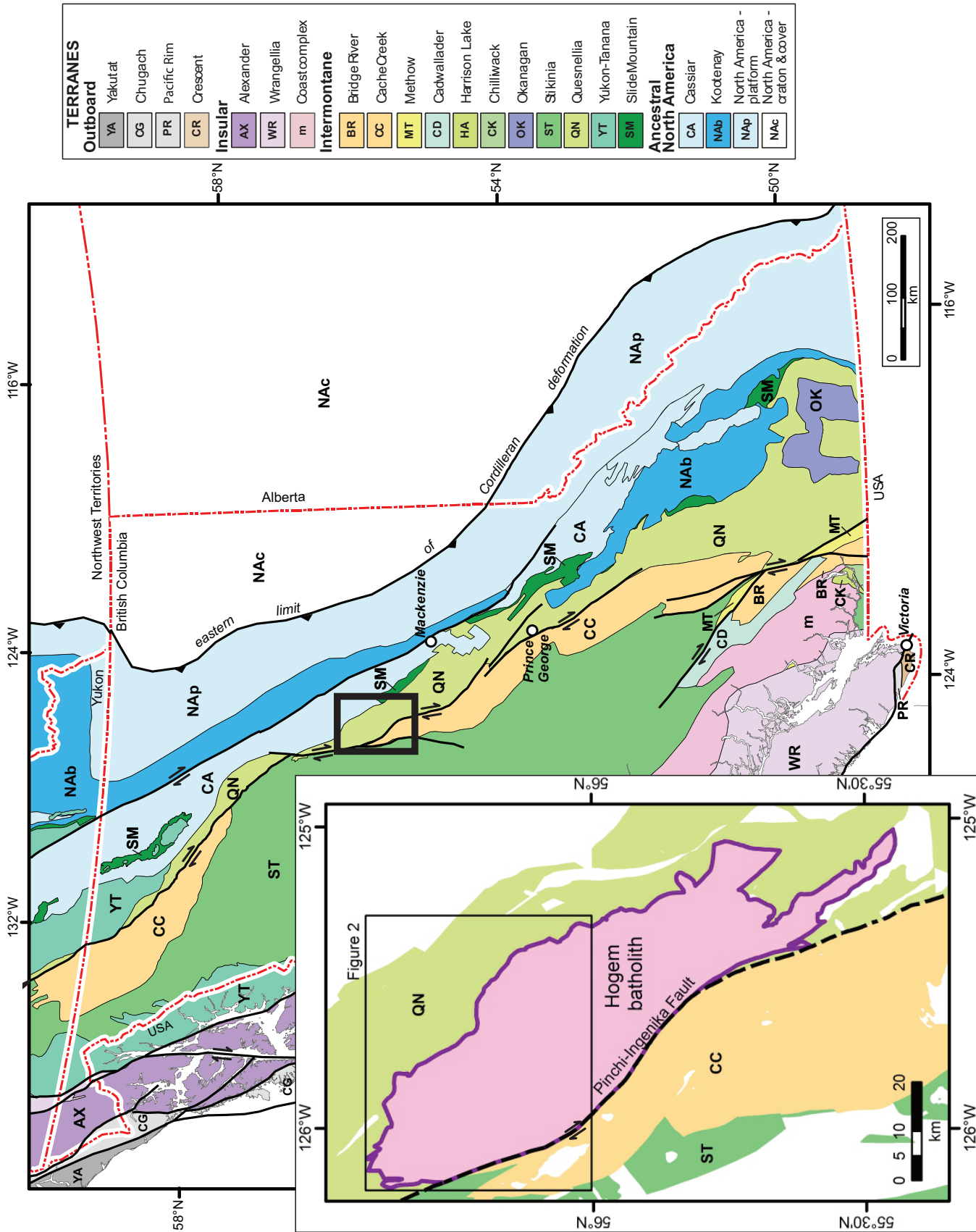


Fig. 1. Terrane map of British Columbia. Modified after Nelson et al. (2013). Inset map shows the Hogem batholith within Quesnel terrane.

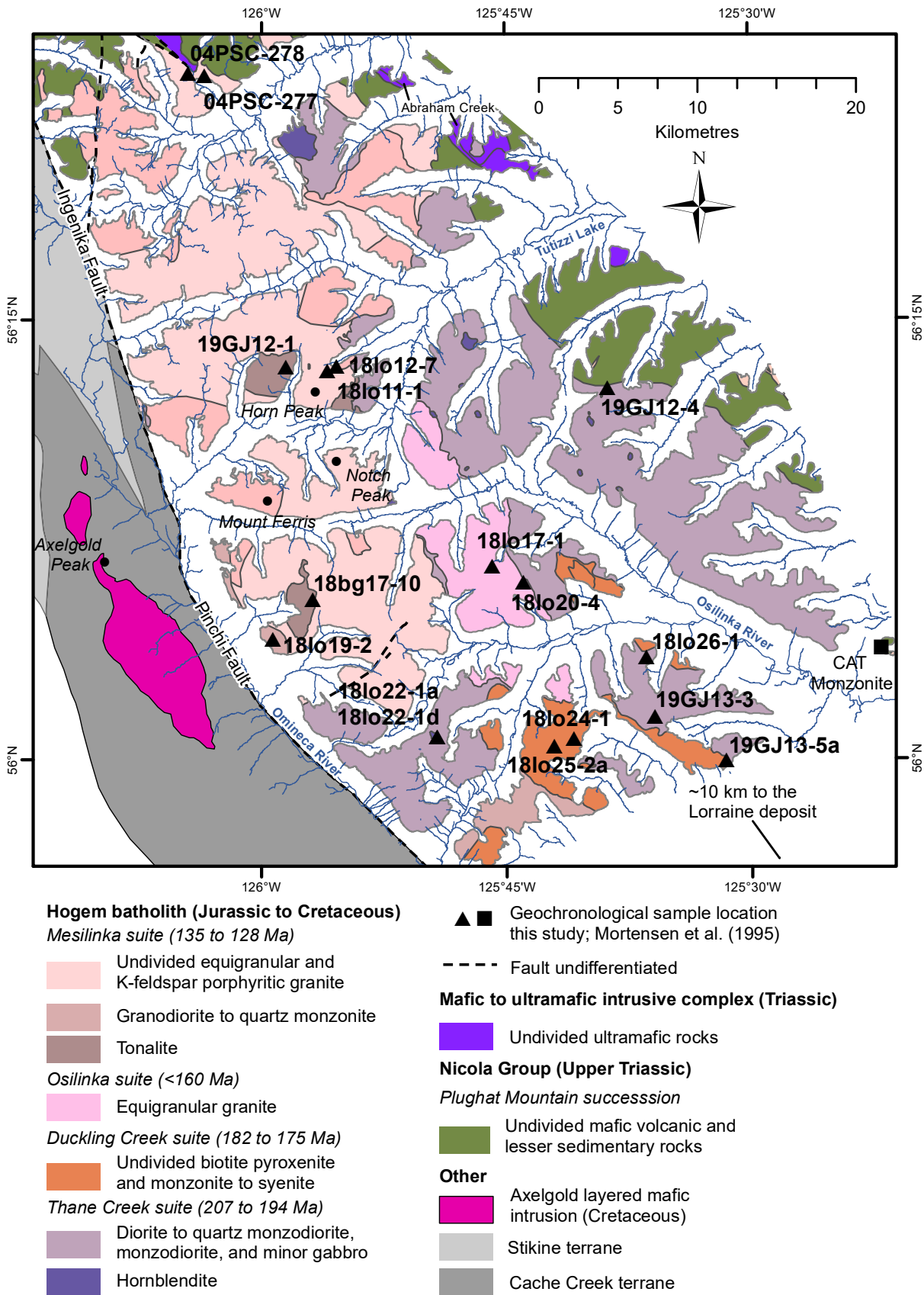
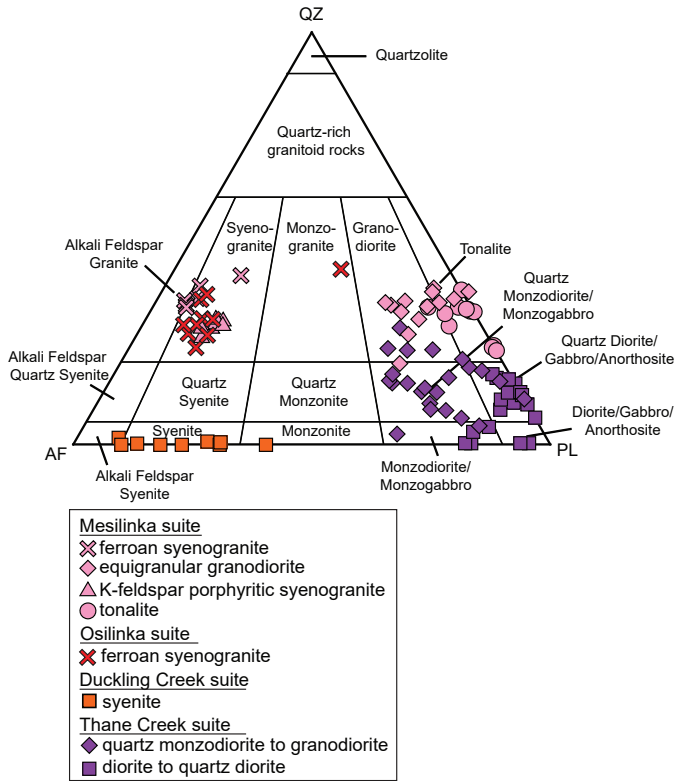


Fig. 2. Geology of northern Hogem batholith and its surroundings. The Hogem batholith is in the Quesnel terrane, which is separated from the Cache Creek and Stikine terranes by the Pinchi-Ingenika fault (dextral strike-slip). Modified after Ootes et al. (2020a).



**Fig. 3.** Quartz-alkali feldspar-plagioclase (QAP) diagram for classification of felsic igneous rocks (Le Maitre et al., 2002). Whole-rock geochemical compositions of samples from the Hogen batholith were converted to volumetric modal mineralogy using the methodology of Stanley (2017). Felsic samples from the Duckling Creek suite are mildly silica-undersaturated and plot on the feldspathoid side (not shown) of the alkali feldspar-plagioclase join.

local zones of mylonite. The Duckling Creek suite includes older biotite clinopyroxenite that is intruded by two-feldspar-bearing syenite, commonly with K-feldspar phenocrysts and local magmatic layering. In the north, the suite is weakly deformed (Ootes et al., 2019, 2020a, b), whereas in the Lorraine area to the south it is moderately to strongly deformed (e.g., Devine et al., 2014). Duckling Creek rocks are metaluminous and mildly silica undersaturated; the more felsic samples plot on the feldspathoid side of the QAP diagram (Fig. 3). Based on lower  $Al_2O_3$  and higher CaO at given  $SiO_2$ , the ultramafic rocks of the Duckling Creek suite are readily distinguished from the Thane Creek suite hornblendites (Fig. 4).

The Osilinka suite is a leucocratic medium-grained equigranular granite (Fig. 3), typically with less than 5% mafic minerals. The Osilinka suite is weakly peraluminous (Fig. 4). The intrusive rocks are deformed and although fabric development is cryptic in the granitic rocks, mafic dikes in the Osilinka suite locally contain shear fabrics (Ootes et al., 2019).

The Mesilinka suite contains at least four intrusive phases. The oldest (tonalite and granodiorite) are intruded by equigranular granite and K-feldspar porphyritic granite (Fig. 3). The suite ranges from weakly metaluminous (tonalites) to peraluminous

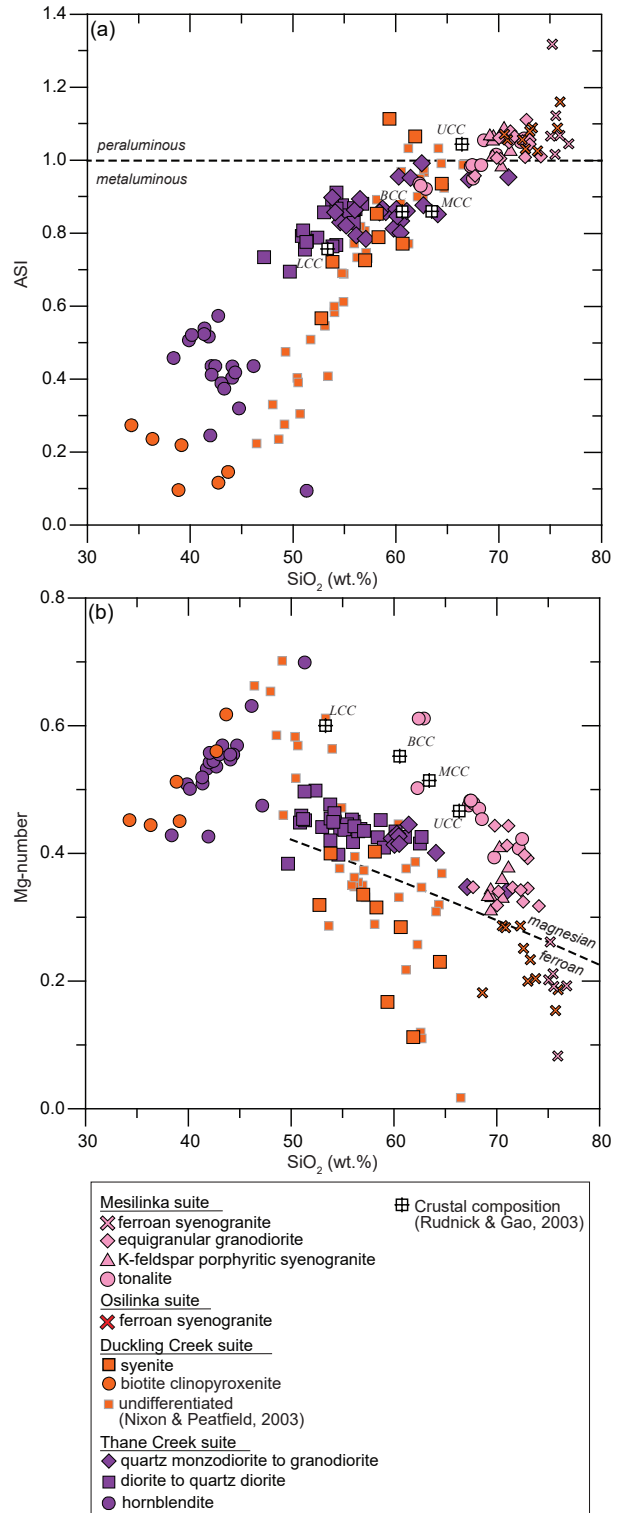


**Fig. 4.** Geochemical classification of plutonic suites of the Hogen batholith, including previously published analyses of Duckling Creek suite (Nixon and Peatfield, 2003). **a)** Aluminum saturation index ( $ASI = \text{molar } Al_2O_3 / (\text{CaO} - 1.67 P_2O_5 + Na_2O + K_2O)$ ; Shand, 1943) vs.  $SiO_2$  (wt.%). **b)** Mg-number (molar  $MgO / (MgO + FeO^{TOT})$ ) vs.  $SiO_2$  (wt.%). Magnesian and ferroan intermediate to felsic rocks are separated by the dashed line from Frost and Frost (2008). Shown for reference are the estimated compositions of lower (LCC), middle (MCC), upper (UCC) and bulk (BCC) continental crust (Rudnick and Gao, 2003).

(granite to granodiorite; Fig. 4). All the intrusive phases in the Mesilinka suite have a tectonic foliation that is defined by aligned biotite (Ootes et al., 2019, 2020a, b).

## 2.2. Previous work

Northern Hogem batholith (north of 56°N) was mapped by Armstrong (1946), Lord (1948, 1949), Armstrong and Roots (1948, 1954), Roots (1954), Irvine (1976), and Woodsworth (1976). Mapping by Ferri et al. (2001a, b), in areas to the east and northeast, focussed on the Takla Group in Quesnel terrane (referred to as the Nicola Group in this study; see discussion in Ootes et al., 2020b) and left Hogem batholith largely undivided. Schiarizza and Tan (2005a, b) mapped north of the study area and reported preliminary isotopic ages for plutonic rocks at the northern tip of Hogem batholith. Southern Hogem batholith (south of 56°N) was mapped and subdivided by Garnett (1972, 1978). Bath et al. (2014) and Devine et al. (2014) studied the Lorraine porphyry Cu-Au deposit southeast of the study area, providing isotopic ages for mineralization and host rocks. Nixon and Peatfield (2003) described rock types and presented geochemical data from the Lorraine deposit area. CGG Canada Services Ltd. (2018) presented the results of an airborne geophysical survey extending across much of the study area that includes both radiometric (K, U, Th) and magnetic data.

## 3. Methods

### 3.1. U-Pb geochronology

Samples collected in 2018 and 2019 were analyzed using laser ablation-inductively coupled plasma-mass spectrometry (LA-ICP-MS); samples collected in 2004 were analyzed using thermal ionization mass spectrometer (ID-TIMS). Table 1 summarizes the samples analyzed and preliminary results; the full analytical techniques and supporting data are in Ootes et al. (2020c).

#### 3.1.1. LA-ICP-MS

We collected unaltered rock samples weighing 5-10 kg for geochronology. Sample preparation and analysis were completed at the Canadian Centre for Isotopic Microanalysis (CCIM), University of Alberta. Approximately 1-2 kg of sample was cut, then disaggregated using the SELFRAG laboratory electronic pulse disaggregation system to yield high-quality mineral separates. Zircon separates were set in epoxy mounts and polished to expose grain mid-sections. Back-scattered electron (BSE), cathodoluminescence (CL), and secondary electron (SE) images of the zircon crystals (see Ootes et al., 2020c) were obtained using a Zeiss EVO MA15 scanning electron microscope at CCIM. These images were used to select spots for laser ablation U-Pb isotope analysis.

Zircon U-Pb isotope data were collected using laser ablation-inductively coupled plasma-mass spectrometry (LA-ICP-MS) with a RESolution 193 nm ArF excimer laser, equipped with a 2-volume Laurin-Technic S-155 ablation cell, and a Thermo Scientific Element-XR mass spectrometer. A subset of the zircon U-Pb data were collected using the laser ablation split-

stream (LASS)-ICP-MS method (e.g., Fisher et al., 2014) to simultaneously analyze U-Pb and Lu-Hf (Jones et al., 2021). All LA-ICP-MS data were reduced using Iolite software (Paton et al., 2010; Paton et al., 2011; Fisher et al., 2017). Trace element concentrations of most zircon crystals were determined during a separate analytical run in single stream or in LASS mode along with Lu-Hf (Jones et al., 2021). Not all zircon was analyzed for trace elements because of zircon grain size limitations.

After reduction, the data were filtered using trace element concentrations. Zircons with concentrations of Ca >300 ppm, Fe >300 ppm, Ti >20 ppm, and La >1 ppm were not considered in age calculations, because they may contain altered domains, or domains with mineral inclusions, which will affect the interpreted age of the sample. Zircon grains with significant common Pb were also filtered by rejecting data with  $f^{206}\text{Pb}_c$  values >1% (e.g., Vezinet et al., 2018; Ootes et al., 2020c). Zircon grains with >10% discordance, determined using the  $^{206}\text{Pb}/^{238}\text{U}$  and  $^{207}\text{Pb}/^{235}\text{U}$  ages, were also rejected. In addition to filtering the U-Pb data, the internal structures of zircon were examined using CL and BSE images. Xenocrystic or antecrystic cores were identified by the degree of roundness and crosscutting growth zones, and these grains were not used in calculating sample ages. After data filtering, individual zircon  $^{206}\text{Pb}/^{238}\text{U}$  ages were used to calculate a weighted mean  $^{206}\text{Pb}/^{238}\text{U}$  age for each sample using IsoplotR (Vermeesch, 2018). All U-Pb data are reported at the  $2\sigma$  (95.5%) confidence level.

Several samples yielded a spread in the  $^{206}\text{Pb}/^{238}\text{U}$  age data that is higher than a statistically reasonable mean squared weighted deviation (MSWD) of the weighted mean. Zircon in these samples were interpreted to be of the sample population, having passed the data reduction and filtering methods outlined above, so the spread in the zircon data was attributed to natural isotopic variation between crystals (geological scatter; Vermeesch, 2018). To reduce the spread in the data and lower the MSWD, an excess scatter constant (over-dispersion) was determined for each sample and added to the standard error of the individual analyses (Vermeesch, 2018; see sample 18lo25-2a (section 4.2.1.) for an example of filtering method results). After using excess scatter, the weighted mean  $^{206}\text{Pb}/^{238}\text{U}$  dates overlapped the concordia and non-processed weighted mean  $^{206}\text{Pb}/^{238}\text{U}$  dates, but with a reasonable MSWD. The robustness of these weighted mean  $^{206}\text{Pb}/^{238}\text{U}$  dates is shown by arbitrarily rejecting the youngest and oldest zircon dates in the sample to lower the MSWD, which yields a weighted mean  $^{206}\text{Pb}/^{238}\text{U}$  age that overlaps with the excessive scatter weighted mean  $^{206}\text{Pb}/^{238}\text{U}$  age (e.g., see sample 18lo25-2a, Fig. 7e, section 4.2.1.).

#### 3.1.2. Legacy ID-TIMS

Samples collected in 2004 were processed and analyzed soon thereafter at the Pacific Centre for Isotopic and Geochemical Research (PCIGR) at the University of British Columbia. Zircon and titanite were separated from samples

Table 1. Summary of samples and geochronological results.

Suite	Sample#	Rock type	Lat	Long	Geochronological result				Source	
					U-Pb (Ma)	Ar-Ar (Ma)	LA-ICPMS z <sup>a</sup>	hbl		
Mesiinka	04PSC-277	equigranular granite	56.3892	-126.0589						1
Mesiinka	04PSC-278	porphyritic granite	56.3905	-126.0757						1
Mesiinka	18o11-1	equigranular granite	56.221037	-125.932380			127.9±0.8			1
Mesiinka	18o12-7	porphyritic granite	56.223797	-125.923148			134.8±1.2			1
Mesiinka	19GJ12-1	tonalite	56.223775	-125.974787			134.1±0.5			1
Mesiinka	18BG17-10	tonalite	56.091248	-125.947834						1
Mesiinka	18BG17-10	tonalite	56.091248	-125.947834						1
Mesiinka	18o19-2	granodiorite	56.068745	-125.988290						1
Osiinka sheet	18o20-4	felsic porphyry	56.100984	-125.732593			162.2±2.6			1
Osiinka	18o17-1	granite	56.110442	-125.764089			159.2±4			1
Duckling Creek	18o25-2a	syenite	56.007961	-125.701574			178.9±1.3			1
Duckling Creek	18o24-1	syenite	56.012295	-125.681727				177±5		1
Duckling Creek	19GJ13-5a	syenite	55.999451	-125.526168			174.7±0.7			1
Duckling Creek	AD06-0552	vein: biotite-albite-apatite								1
Duckling Creek	MM106-9-7	leucosyenite dike			176.8±0.4					2
Duckling Creek	06FD626	vein: biotite-k-feldspar-albite-magnetite								2
Duckling Creek	06FD708	pegmatite dike			177.6±0.2					2
Duckling Creek	06FD654	K-feldspar megacrystic porphyry			178.8±0.2					2
Duckling Creek	06FD706	Equigranular monzonite			179.7±2.5					2
Duckling Creek	06FD838	Fine-grained, equigranular syenite			180.2±0.3					2
Duckling Creek	06FD709	biotite pyroxenite							181.7±1.0	2
Duckling Creek	07AB G7	syenite			178.4±0.3					3
Duckling Creek	07AB G3	rhythmically layered diopside syenite			178.6±0.2					3
Duckling Creek	07AB G2	syenite			178.7±0.3					3
Duckling Creek	07AB G5	syenite			177.3±0.4					3
Duckling Creek	07AB G1	pseudoleucite bearing feldspathic pyroxenite			178.4±0.3					3
Thane Creek	19GJ12-4	diorite	56.211666	-125.646053			206.6±0.9			1
Thane Creek	19GJ13-3	quartz monzodiorite	56.024407	-125.598711			194±1.1			1
Thane Creek	18o26-1	quartz monzodiorite	56.057991	-125.607348				202±5		1
Thane Creek	18o22-1d	diorite	56.013314	-125.820707				124±2		1
Thane Creek	18o22-1d	diorite	56.013314	-125.820707				124±1		1
Thane Creek	18o22-1a	hornblendite	56.013314	-125.820707			196.6±0.9			1
Thane Creek	FF91-5-3	CAT monzonite	56.013314	-125.820707			197.6±0.1			1
Thane Creek	06FD859	Rhonda Gabro			204±0.4					4
Notes: ± reported at 2s; <sup>a</sup> University of Alberta; <sup>aa</sup> University of British Columbia z-zircon; <sup>t</sup> titanite; <sup>hbl</sup> =hornblende; <sup>mv</sup> =muscovite										3
1-this study; 2-Devine et al. (2014); 3-Bath et al. (2014); 4-Mortensen et al. (1995)										

using conventional crushing, grinding, and Wilfley table techniques, followed by final concentration using heavy liquids and magnetic separations, then air-abrasion. Following dissolution of multi-grain zircon and titanite fractions in the presence of a  $^{233-235}\text{U}$ - $^{205}\text{Pb}$  tracer, isotopic ratios were measured using a modified single collector VG-54R thermal ionization mass spectrometer (TIMS) equipped with an analogue Daly photomultiplier. In 2020, these legacy raw data were re-reduced using the Excel-based program of Schmitz and Schoene (2007). Standard concordia diagrams were constructed, and weighted averages calculated with Isoplot (Ludwig, 2003). All errors are quoted at the  $2\sigma$  or 95% level of confidence.

### 3.2. Ar-Ar laser step-heating

This study presents  $^{40}\text{Ar}/^{39}\text{Ar}$  laser step-heating ages for single hornblende, muscovite, and biotite crystals. Samples were prepared at the British Columbia Geological Survey where they were crushed and sieved to between 100 and 250  $\mu\text{m}$  and run through a Frantz magnetic separator after which single crystals were handpicked under a binocular microscope. Full analytical techniques and supporting data are in Ootes et al. (2020c). Three of the biotite  $^{40}\text{Ar}/^{39}\text{Ar}$  laser step-heating results were also reported in Ootes et al. (2020b).

All  $^{40}\text{Ar}/^{39}\text{Ar}$  analytical work was performed at the University of Manitoba using a multi-collector Thermo Fisher Scientific ARGUSVI mass spectrometer linked to a stainless steel Thermo Fisher Scientific extraction/purification line and Photon Machines (55 W) Fusions 10.6  $\text{CO}_2$  laser. All specimens were irradiated in the cadmium-lined, in-core CLICIT facility of the Oregon State University TRIGA reactor. The duration of irradiation was 70 hours and was conducted with the Fish Canyon sanidine (28.201 Ma; Kuiper et al., 2008). Irradiated samples were placed in a Cu sample tray, with a KBr cover slip, in a stainless steel high-vacuum extraction line and baked with an infrared lamp for 24 hours. Single crystals were either fused or step heated using the laser, and reactive gases were removed after  $\sim 3$  minutes by three NP-10 SAES getters (two at room temperature and one at  $450^\circ\text{C}$ ) before being admitted to an ARGUSVI mass spectrometer by expansion. Five argon isotopes were measured simultaneously during a period of 6 minutes. Measured isotope abundances were corrected for extraction-line blanks, which were determined before every sample analysis. Each of the resulting steps have relatively small errors, and the integrated ages were calculated from the average and uncertainty by standard deviation of the best analysis.

## 4. Results

### 4.1. Thane Creek suite

#### 4.1.1. Thane Creek quartz diorite: 19GJ12-4, U-Pb zircon, 206.6 $\pm$ 0.9 Ma

The sample was taken 17.9 km east-northeast of Notch Peak (Fig. 2). It is a white and black, medium-grained, equigranular quartz diorite, and is composed of mostly plagioclase ( $\sim 62\%$ ), with about 25% equal parts of green amphiboles, with corroded

clinopyroxene cores, and brown (metamorphic?) and green biotite. The sample contains minor quartz ( $\sim 6\%$ ) and alkali feldspar ( $\sim 7\%$ ), with accessory magnetite, apatite, titanite, and epidote. Titanite occurs as rims on magnetite grains. Trace fine-grained chalcopyrite is disseminated and occurs as inclusions in magnetite.

After analysis and data reduction, two zircons were filtered out for exceeding  $\text{Ca} > 300$  ppm and  $\text{Ti} > 20$  ppm, and one zircon was rejected for  $f^{206}\text{Pb}_c > 1\%$ . Ten remaining analyses yield a weighted mean  $^{206}\text{Pb}/^{238}\text{U}$  date of  $206.6 \pm 0.9$  Ma (MSWD=1.77; probability of fit=0.07). This weighted mean is interpreted as the best estimate for the crystallization age (Figs. 5a, b).

#### 4.1.2. Thane Creek hornblende: 18lo22-1a, U-Pb zircon, CA-TIMS: 197.6 $\pm$ 0.1 Ma; LA-ICPMS: 191.4 $\pm$ 0.7 Ma

The sample was taken 18.6 km south-southeast of Mount Ferris (Fig. 2). It is a coarse-grained to pegmatitic plagioclase-bearing hornblende. Pegmatitic white hornblende-plagioclase segregations are interstitial to predominantly green hornblende. Hornblende is commonly overgrown by brown or green biotite, with biotite making up  $\sim 10\%$  of the sample. The sample contains  $\sim 5\%$  magnetite that is interstitial to amphibole and is concentrated with accessory titanite and apatite. Coarse, subhedral accessory epidote occurs in pegmatitic plagioclase segregations. Trace fine-grained chalcopyrite is disseminated through the sample.

Ootes et al. (2020b, c) report a  $197.6 \pm 0.1$  Ma zircon crystallization age, determined by chemical abrasion CA-TIMS (Fig. 5c). For LA-ICPMS, nine analyses were rejected for exceeding  $f^{206}\text{Pb}_c > 1\%$ . Thirty-three remaining zircons yield a  $^{206}\text{Pb}/^{238}\text{U}$  weighted mean date of  $191.4 \pm 0.7$  Ma (MSWD=0.87; probability of fit=0.68) (Figs. 5c, d). The discrepancy between the LA-ICP-MS weighted mean  $^{206}\text{Pb}/^{238}\text{U}$  date and the reported CA-TIMS  $^{206}\text{Pb}/^{238}\text{U}$  date ( $197.6 \pm 0.1$  Ma) may be due to differences in the calibration techniques between the LA-ICP-MS and CA-TIMS methods. Although we consider both the LA-ICP-MS and CA-TIMS U-Pb dates of the hornblende valid, the CA-TIMS date ( $197.6 \pm 0.1$  Ma) is interpreted to be more accurate and the best estimate of the crystallization age.

#### 4.1.3. Thane Creek diorite: 18lo22-1d, $^{40}\text{Ar}/^{39}\text{Ar}$ hornblende, biotite, 126-124 Ma

This sample is from 18.6 km south-southeast of Mount Ferris, 100 m east of the hornblende sample (18lo22-1a; section 4.1.2., Fig. 2). It is a 'salt and pepper', medium-grained equigranular diorite. The rock contains a moderate foliation defined by plagioclase, biotite, and amphibole. The sample is mostly clay-altered plagioclase (65%), biotite (12%), and amphibole (6%). Minor altered alkali feldspar (7%) and quartz (1-2%) are present, interstitial to plagioclase. Accessory anhedral to subhedral, fine-grained epidote, apatite, magnetite, and zircon occur with biotite. Trace fine-grained chalcopyrite is disseminated through the sample. Ootes et al. (2020b, c) report a  $196.6 \pm 0.9$  Ma zircon crystallization age, determined by CA-TIMS.

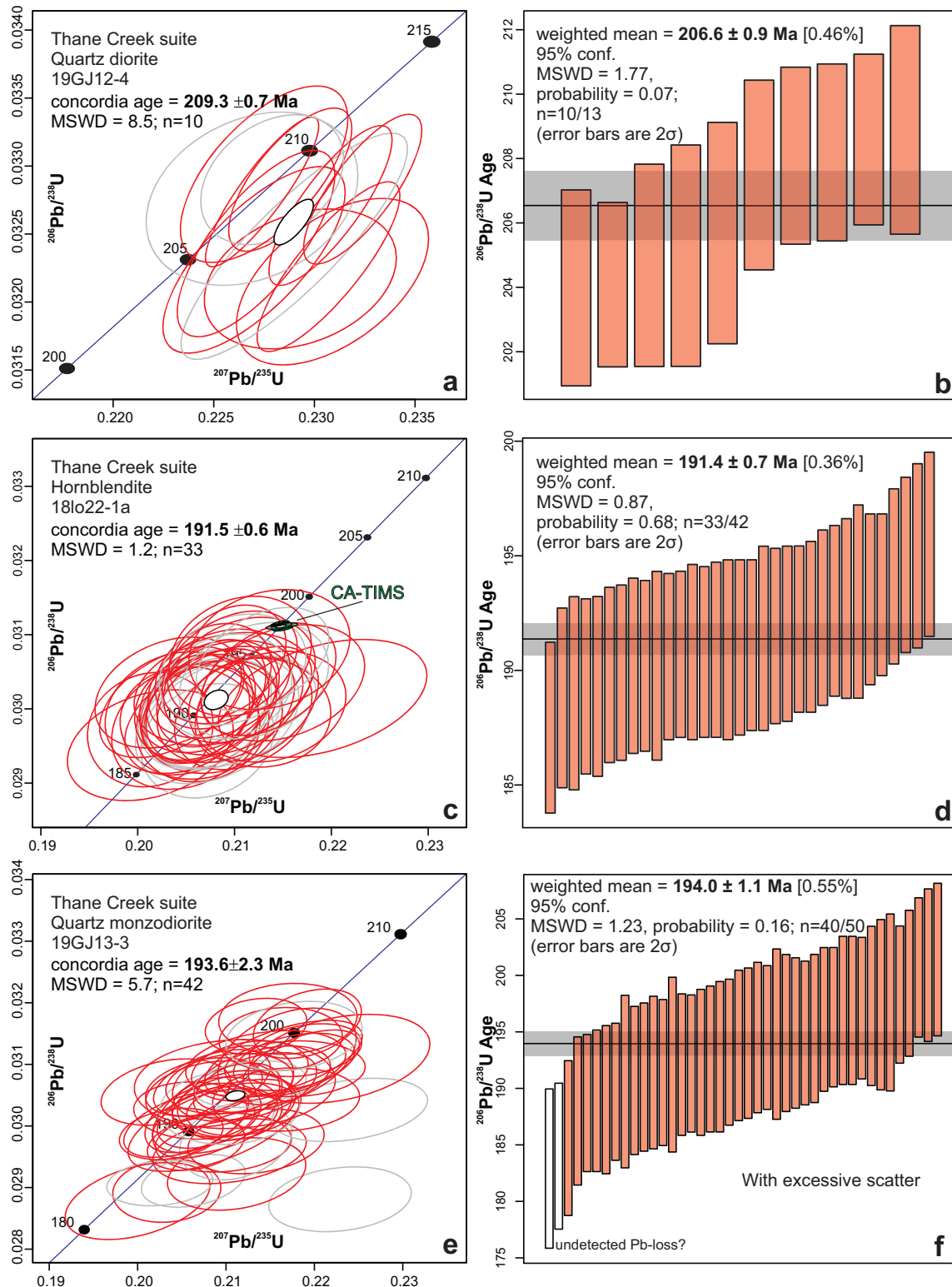


**Fig. 5.** Results of Thane Creek suite zircon U-Pb LA-ICP-MS analysis. Data used for weighted mean calculations have been filtered using the methods outlined in section 3.1.1. and Ootes et al. (2020c). Grey ellipses in concordia plots represent data that have been filtered and were not included in age calculations. Uncertainties are reported at the  $2\sigma$  or 95.5% confidence level. **a)** Concordia plot of quartz diorite sample 19GJ12-4. **b)** Weighted mean  $^{206}\text{Pb}/^{238}\text{U}$  date, interpreted as the crystallization age, of quartz diorite sample 19GJ12-4. **c)** Concordia plot of hornblende sample 18lo22-1a. Also plotted are CA-TIMS results (Ootes et al., 2020b, c). **d)** Weighted mean  $^{206}\text{Pb}/^{238}\text{U}$  date of hornblende sample 18lo22-1a. **e)** Concordia plot of quartz monzodiorite sample 19GJ13-3. **f)** Weighted mean  $^{206}\text{Pb}/^{238}\text{U}$  date of quartz monzodiorite sample 19GJ13-3, after applying excessive scatter constant (section 3.1.1.). Colourless bars passed the data filters outlined in section 3.1.1. but were not included in the weighted mean calculation due to the younger skew of these points, possibly indicating undetected Pb-loss in the zircon grains.

Two aliquots each of hornblende and biotite were analyzed by ICP-MS via laser step-heating. For biotite-aliquot 1, seven steps (C-I) released 99.98%  $^{39}\text{Ar}$  and yield an integrated  $^{40}\text{Ar}/^{39}\text{Ar}$  age of  $126 \pm 2$  Ma (Fig. 6a). For biotite-aliquot 2, six steps (D-I) released 80.23%  $^{39}\text{Ar}$  and yield an integrated  $^{40}\text{Ar}/^{39}\text{Ar}$  age of  $124 \pm 1$  Ma (Fig. 6b). For hornblende-aliquot 1, six steps (C-H) released 99.82%  $^{39}\text{Ar}$  and yield an integrated  $^{40}\text{Ar}/^{39}\text{Ar}$  age of  $124 \pm 2$  Ma (Fig. 6c). For hornblende-aliquot 2, ten steps (C-L) released 99.01%  $^{39}\text{Ar}$  and yield an integrated  $^{40}\text{Ar}/^{39}\text{Ar}$  age of  $124 \pm 1$  Ma (Fig. 6d).

#### 4.1.4. Thane Creek monzodiorite: 19GJ13-3, U-Pb zircon, $194.0 \pm 1.1$ Ma

This sample is from 25.9 km southeast of Notch Peak (Fig. 2). The sample is a ‘salt and pepper’, fine- to medium-grained, equigranular quartz monzodiorite, composed of ~40% euhedral plagioclase, ~30% poikilitic alkali feldspar, and ~15% anhedral, strained quartz. Mafic minerals make up ~10% of the sample, mainly subhedral amphibole (8%) with lesser biotite (2%). Anhedral magnetite and titanite, and euhedral apatite and zircon are accessory. Titanite occurs as ~1 mm grains and as fine rims on magnetite.

After LA-ICP-MS analyses, six zircons were rejected for  $f^{206}\text{Pb}_c > 1\%$ , two zircons were rejected for  $>5\%$  discordance. All remaining zircon passed the trace element filters, and no xenocrystic or antecrystic grains or cores were identified. An excess scatter constant of 3.99 was added to the standard error of the filtered data points to decrease the MSWD of weighted mean  $^{206}\text{Pb}/^{238}\text{U}$  date. The youngest two analyses were then rejected in order to further reduce the scatter, as they may indicate undetected Pb-loss. Forty remaining analyses yield a weighted mean  $^{206}\text{Pb}/^{238}\text{U}$  date of  $194.0 \pm 1.1$  Ma (MSWD=1.23; probability of fit=0.16). This weighted mean is interpreted as the best estimate for the crystallization age (Figs. 5e, f).

#### 4.1.5. Thane Creek monzodiorite: 18lo26-1, $^{40}\text{Ar}/^{39}\text{Ar}$ hornblende, $202 \pm 5$ Ma

The sample site is 23.2 km southeast of Notch Peak and 3.69 km north of sample 19GJ13-3 (section 4.1.4.; Fig. 2). This sample is of relatively pristine (unaltered) monzodiorite with euhedral hornblende and accessory euhedral magnetite and titanite. The sample yielded hornblende and eight steps (E-L) released 84.07%  $^{39}\text{Ar}$  and yield an integrated  $^{40}\text{Ar}/^{39}\text{Ar}$  age of  $202 \pm 5$  Ma (Fig. 6e).

### 4.2. Duckling Creek suite

#### 4.2.1. Duckling Creek syenite: 18lo25-2a, U-Pb zircon, $178.9 \pm 1.3$ Ma

Collected 22.7 km southeast of Notch Peak (Fig. 2), the sample is a pink-white, medium-grained, equigranular syenite. The sample consists of ~90% two alkali feldspars (K- and Na-bearing), with lesser clinopyroxene (~5%). Magnetite, titanite, chlorite, and zircon are accessory minerals. Titanite forms ~1 mm wide euhedral, wedge-shaped grains intergrown with clinopyroxene.

Two types of zircon were identified during mineral picking. The first type (18lo25-2a z1) are clear-pink coloured zircon fragments between 100 to 200  $\mu\text{m}$ . The second type (18lo25-2a z2) are larger grains (300 to 400  $\mu\text{m}$ ) that are brown with good crystal habit but with cores that are commonly metamict or highly fractured (see zircon CL images; Ootes et al., 2020c). Only type one zircons (z1) were considered in the U-Pb age interpretation as none of type two zircon (z2) LA-ICP-MS data passed the filters. Fourteen z1 and z2 zircons were rejected for  $>10\%$  discordance, four zircons were rejected for exceeding Fe  $>300$  ppm and/or Ca  $>300$  ppm and La  $>1$  ppm. One zircon was rejected for excessive standard error of Ca, and two zircons were rejected for high U and internal structures. An excess scatter constant of 3.11 was added to the standard error of the filtered data points to decrease the MSWD of the weighted mean  $^{206}\text{Pb}/^{238}\text{U}$  date. Twenty-two remaining type one zircons yield a weighted mean  $^{206}\text{Pb}/^{238}\text{U}$  date of  $178.9 \pm 1.3$  Ma (MSWD=1.33; probability of fit=0.15). This weighted mean is interpreted as the best estimate for the crystallization age (Figs. 7a-e).

#### 4.2.2. Duckling Creek syenite: 18lo24-1, $^{40}\text{Ar}/^{39}\text{Ar}$ hornblende, $177 \pm 5$ Ma

This sample is of coarse-grained equigranular monzonite (syenite) from the centre of the Duckling Creek suite, 23.9 km south of Mount Ferris, 1.33 km northeast of sample 18lo25-2a (section 4.2.1., Fig. 2). The sample consists of coarse K-feldspar (80%) with 15% mafic minerals. These are mostly medium-grained green clinopyroxene with lesser dark-green amphibole. Medium-grained titanite is intergrown with clinopyroxene and accessory magnetite is disseminated throughout. The sample was collected 1.33 km northeast of sample 18lo25-2a (section 4.2.1.) and was used for Ar-Ar step-heating as sample 18lo25-2a did not yield hornblende. For hornblende, four steps (F-I) released 98.45%  $^{39}\text{Ar}$  and yield an integrated  $^{40}\text{Ar}/^{39}\text{Ar}$  age of  $177 \pm 5$  Ma (Fig. 8).

#### 4.2.3. Duckling Creek syenite: 19GJ13-5a, U-Pb zircon, $174.7 \pm 0.7$ Ma

The sample was collected 31.1 km southwest of Notch Peak (Fig. 2), next to the Slide Cu-Au porphyry prospect and 7 m south of a grab sample with chalcopyrite that yielded 0.07 wt.% Cu (19GJ13-5b; Ootes et al., 2020b). The sample is a pink-white and greenish black, medium-grained, equigranular syenite. It contains alkali feldspar (~70%), with lesser amphibole (9%), plagioclase (8%), and clinopyroxene (5%). Biotite, chlorite, and magnetite combine to make up ~5% of the sample, whereas fine-grained apatite, titanite, epidote, and zircon are accessory minerals. Chalcopyrite forms rare fine, disseminated grains, and may be rimmed by titanite.

Two zircon U-Pb analyses were rejected for  $f^{206}\text{Pb}_c > 1\%$ , whereas the remaining analyses passed all data filters. Twenty-four remaining analyses yield a weighted mean  $^{206}\text{Pb}/^{238}\text{U}$  date of  $174.7 \pm 0.7$  Ma (MSWD=1.36; probability of fit=0.12). The weighted mean is interpreted as the best estimate for the crystallization age (Fig. 9).

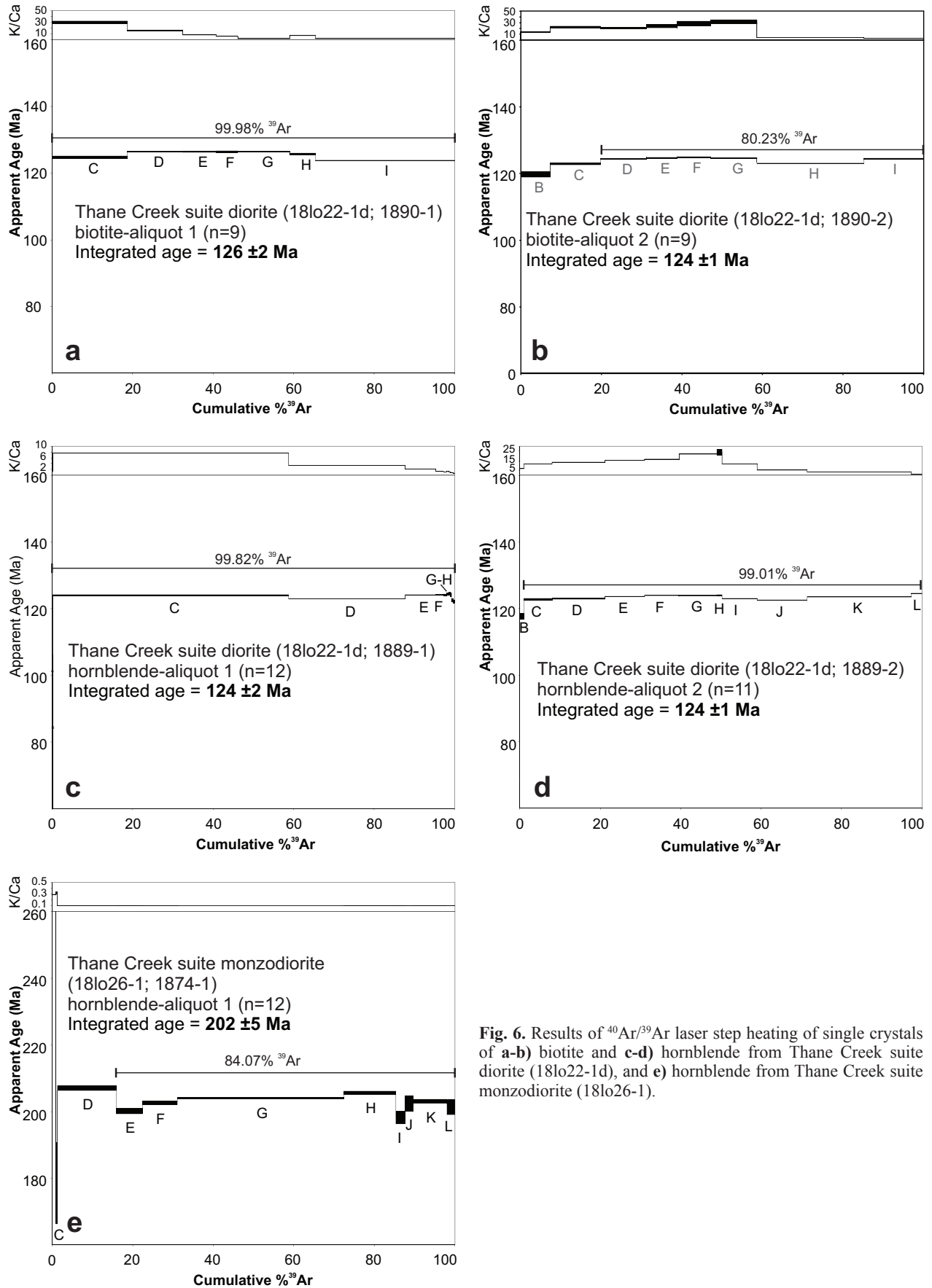


**Fig. 6.** Results of  $^{40}\text{Ar}/^{39}\text{Ar}$  laser step heating of single crystals of **a-b)** biotite and **c-d)** hornblende from Thane Creek suite diorite (18lo22-1d), and **e)** hornblende from Thane Creek suite monzodiorite (18lo26-1).

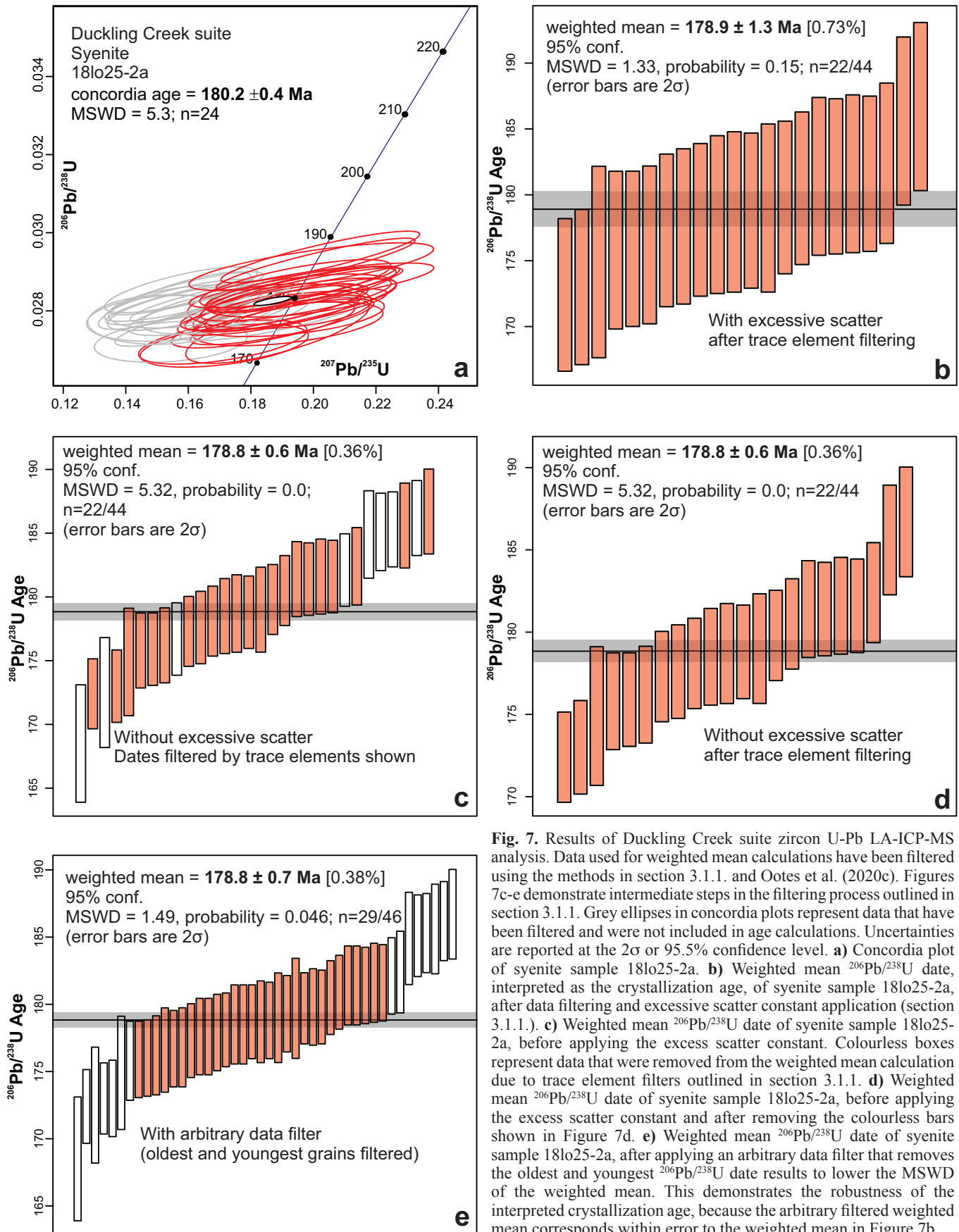


**Fig. 7.** Results of Duckling Creek suite zircon U-Pb LA-ICP-MS analysis. Data used for weighted mean calculations have been filtered using the methods in section 3.1.1. and Ootes et al. (2020c). Figures 7c-e demonstrate intermediate steps in the filtering process outlined in section 3.1.1. Grey ellipses in concordia plots represent data that have been filtered and were not included in age calculations. Uncertainties are reported at the  $2\sigma$  or 95.5% confidence level. **a)** Concordia plot of syenite sample 18lo25-2a. **b)** Weighted mean  $^{206}\text{Pb}/^{238}\text{U}$  date, interpreted as the crystallization age, of syenite sample 18lo25-2a, after data filtering and excessive scatter constant application (section 3.1.1.). **c)** Weighted mean  $^{206}\text{Pb}/^{238}\text{U}$  date of syenite sample 18lo25-2a, before applying the excess scatter constant. Colourless boxes represent data that were removed from the weighted mean calculation due to trace element filters outlined in section 3.1.1. **d)** Weighted mean  $^{206}\text{Pb}/^{238}\text{U}$  date of syenite sample 18lo25-2a, before applying the excess scatter constant and after removing the colourless bars shown in Figure 7d. **e)** Weighted mean  $^{206}\text{Pb}/^{238}\text{U}$  date of syenite sample 18lo25-2a, after applying an arbitrary data filter that removes the oldest and youngest  $^{206}\text{Pb}/^{238}\text{U}$  date results to lower the MSWD of the weighted mean. This demonstrates the robustness of the interpreted crystallization age, because the arbitrary filtered weighted mean corresponds within error to the weighted mean in Figure 7b.

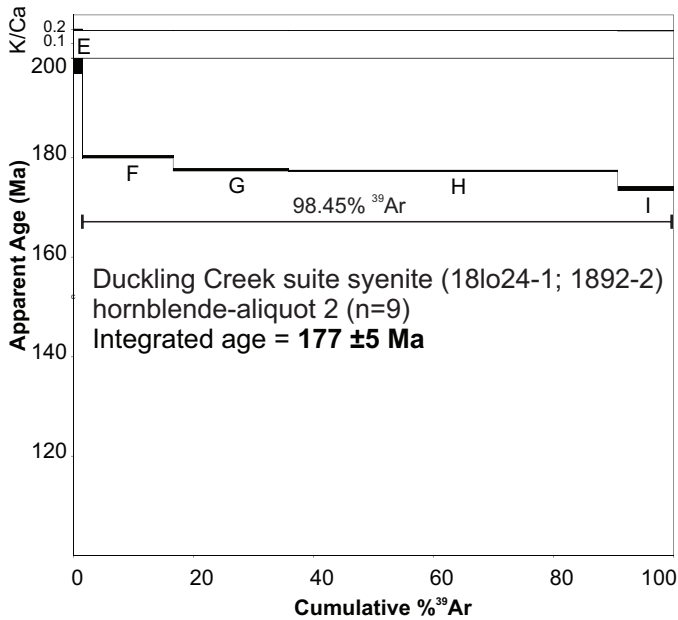


Fig. 8. Results of  $^{40}\text{Ar}/^{39}\text{Ar}$  laser step heating of a single crystal of hornblende from Duckling Creek syenite (18lo24-1).

### 4.3. Osilinka suite

#### 4.3.1. Osilinka granite: 18lo17-1, U-Pb zircon 159.2 ± 4 Ma (maximum), $^{40}\text{Ar}/^{39}\text{Ar}$ muscovite, 122 ± 5 Ma, biotite, 116 ± 1 Ma

We collected this sample 11.9 km southeast of Notch Peak (Fig. 2). The sample is of a white (leucocratic), medium-grained, equigranular granite. Strained quartz (~37%), subhedral alkali feldspar (32%), and subhedral plagioclase (26%) comprise most of the sample. Rare accessory biotite,

muscovite, and magnetite constitute less than 5% of the rock. Fine-grained biotite and magnetite occur interstitial to feldspar grains, whereas muscovite and sericite are present within feldspar cores and along grain boundaries.

Eight zircon U-Pb isotopes analyses were rejected for  $f^{206}\text{Pb}_c > 1\%$  and/or  $> 10\%$  discordance, and one zircon was rejected for  $\text{Fe} > 300$  ppm. The thirteen remaining zircon yield an approximately 30 million year spread in  $^{206}\text{Pb}/^{238}\text{U}$  dates, and are interpreted as inherited. The youngest zircon has a  $^{206}\text{Pb}/^{238}\text{U}$  date of  $159.2 \pm 4$  Ma; it is unclear if this is a magmatic or inherited zircon and therefore the  $^{206}\text{Pb}/^{238}\text{U}$  date is interpreted as the maximum crystallization age (Fig. 10a).

Both muscovite and biotite were separated from the sample and tested by laser step heating. For muscovite six steps (D-I) released 85.83%  $^{39}\text{Ar}$  and yield an integrated  $^{40}\text{Ar}/^{39}\text{Ar}$  age of  $122 \pm 5$  Ma (Fig. 11a). For biotite five steps (C-G) released 57.98%  $^{39}\text{Ar}$  and yield an integrated  $^{40}\text{Ar}/^{39}\text{Ar}$  age of  $116 \pm 1$  Ma (Fig. 11b).

#### 4.3.2. Sheet cutting Osilinka granite, 18lo20-4, U-Pb zircon, 162.2 ± 2.6 Ma (maximum)

The sample is from a flat-lying sheet, at least 4 m thick, that cuts Osilinka suite rocks, 14.01 km southeast of Notch Peak (Fig. 2). Fine-grained plagioclase and quartz make up most of the groundmass, with plagioclase phenocrysts up to 0.5 cm. Magnetite, chlorite, epidote, and calcite are accessory in the groundmass. A ~0.5 mm wide calcite-filled vein cuts the sample. Rare, ~2.5 mm wide euhedral chalcopyrite grains are in the groundmass. Eight zircon U-Pb analyses were rejected for  $f^{206}\text{Pb}_c > 1\%$  and/or  $> 10\%$  discordance. The nine remaining zircon yield an approximately 100 million year spread in  $^{206}\text{Pb}/^{238}\text{U}$  dates and are interpreted as inherited. The

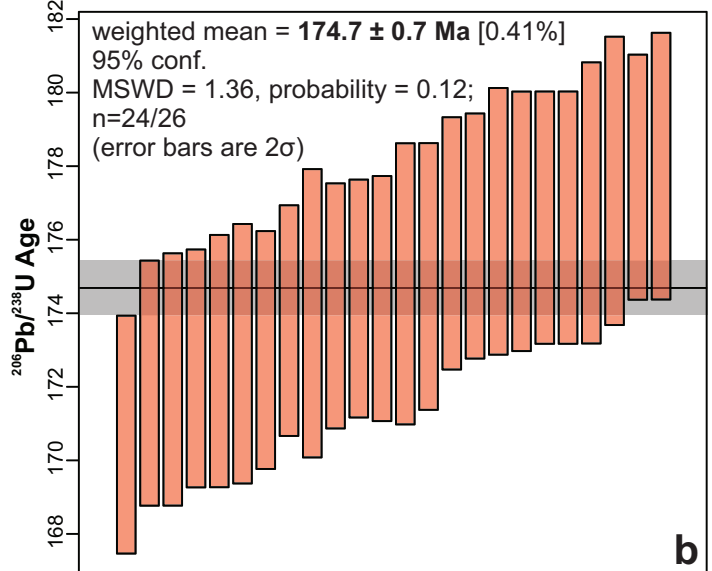
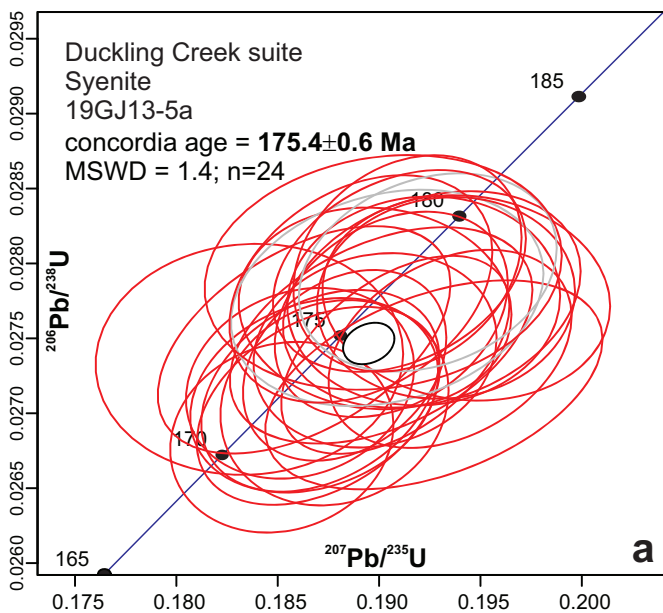
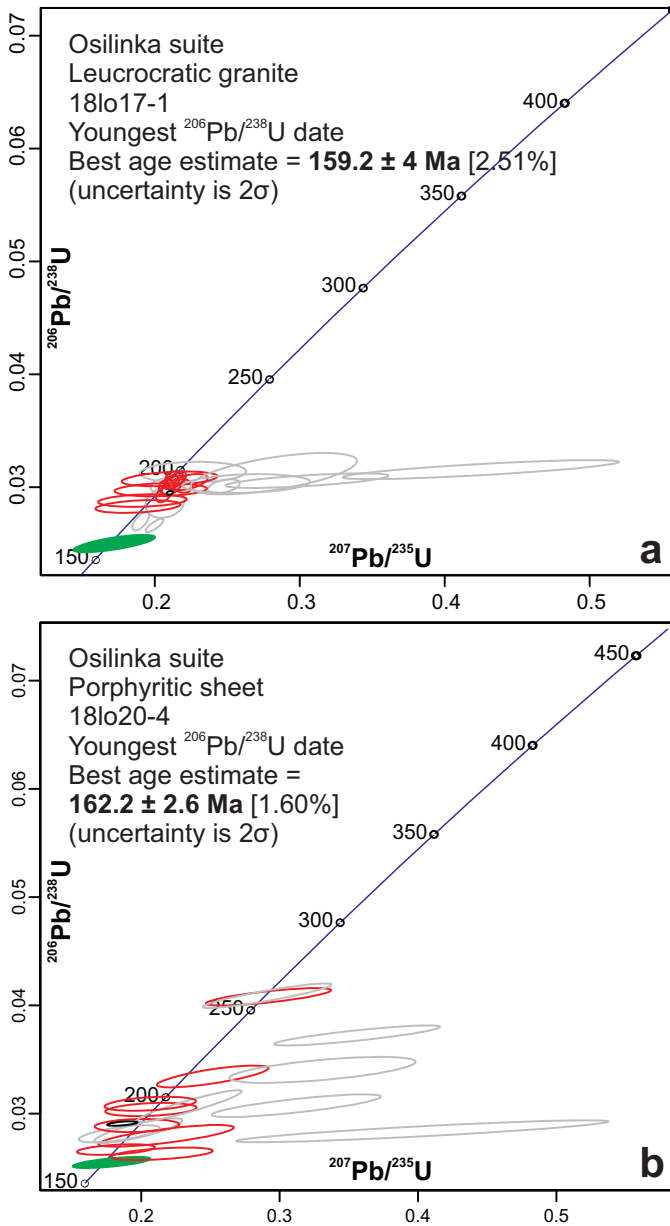
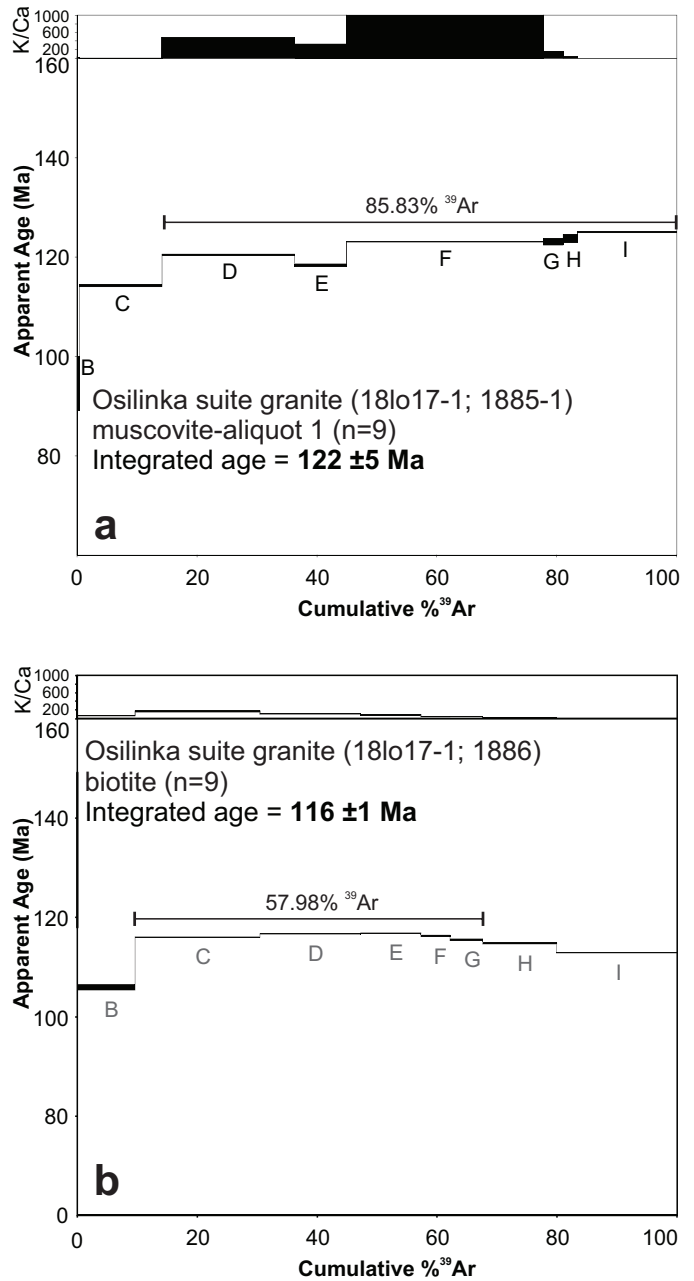


Fig. 9. Results of Duckling Creek suite zircon U-Pb LA-ICP-MS analysis. **a)** Concordia plot of syenite sample 19GJ13-5a. **b)** Weighted mean  $^{206}\text{Pb}/^{238}\text{U}$  date, interpreted as the crystallization age, of syenite sample 19GJ13-5a.



**Fig. 10.** Results of Osilinka suite zircon U-Pb LA-ICP-MS analysis. Grey ellipses in concordia plots represent data that have been filtered (section 3.1.1.) and were not included in age calculations. Uncertainties are reported at the  $2\sigma$  or 95.5% confidence level. **a)** Concordia plot of granite sample 18lo17-1. The green ellipse is the youngest zircon result, interpreted as the maximum age. Red ellipses are data that passed the data filters in section 3.1.1. and the zircon grains are interpreted as antecrysts or xenocrysts. **b)** Concordia plot of porphyritic sheet sample 18lo20-4. The green ellipse is the youngest zircon result, interpreted as the maximum age. Red ellipses are data that passed the filters in section 3.1.1. and the zircon grains are interpreted as antecrysts or xenocrysts.

youngest zircon has a  $^{206}\text{Pb}/^{238}\text{U}$  date of  $162.2 \pm 2.6 \text{ Ma}$ ; it is unclear if this is a magmatic or inherited zircon and therefore the  $^{206}\text{Pb}/^{238}\text{U}$  date is interpreted as the maximum crystallization age (Fig. 10b).



**Fig. 11.** Results of  $^{40}\text{Ar}/^{39}\text{Ar}$  laser step heating of single crystals of **a)** muscovite and **b)** biotite from Osilinka suite granite (18lo17-1).

#### 4.4. Mesilinka suite

##### 4.4.1. Mesilinka tonalite: 19GJ12-1, U-Pb zircon, $134.1 \pm 0.5 \text{ Ma}$

We collected this sample 2.45 km northwest of Horn Peak (Fig. 2). It is a grey, medium-grained, equigranular biotite-rich tonalite with a foliation defined by biotite. Equigranular granite dikes cut the tonalite at an outcrop ~50 m away. The sample is composed of slightly altered plagioclase (~50%), with lesser strained quartz (~30%) and brown and green biotite (~15%). Subhedral amphibole and magnetite, anhedral epidote, apatite, and titanite, and euhedral zircon are accessory and spatially associated with patches of biotite.

Trace element concentrations were not analyzed and not used to filter the data, because insufficient zircon remained after LA-ICP-MS U-Pb and Lu-Hf analyses and the grains were too small (<60  $\mu\text{m}$  wide) for LASS mode. Three zircon U-Pb analyses were rejected for  $f^{206}\text{Pb}_c > 1\%$ . Two analyses were rejected from the age calculation because the zircons are interpreted as xenocrysts or antecrysts due to dark cores and disrupted rim growth in CL images (Ootes et al., 2020c). In addition, the zircons have elevated  $\delta^{18}\text{O}$  values relative to the other zircons (G. Jones, unpublished data, 2021). Eighteen remaining analyses yield a weighted mean  $^{206}\text{Pb}/^{238}\text{U}$  date of  $134.1 \pm 0.5$  Ma (MSWD=1.48; probability of fit=0.09). The weighted mean is interpreted as the best estimate for the crystallization age of this sample (Figs. 12a, b).

#### 4.4.2. Mesilinka tonalite: 18bg17-10, $^{40}\text{Ar}/^{39}\text{Ar}$ biotite, $108 \pm 2$ Ma and $111 \pm 3$ Ma

The sample was collected from 6.87 km south-southeast of Mount Ferris (Fig. 2), within a body of medium-grained tonalite that contains a foliation. It consists of 65% quartz and plagioclase with 30% mafic minerals. The mafic minerals are mostly green and lesser brown (metamorphic?) biotite and lesser euhedral hornblende. Titanite is an accessory mineral.

Two aliquots of biotite were analyzed by laser step-heating. For biotite-aliquot 1, six steps (E-J) released 99.66%  $^{39}\text{Ar}$  and yield an integrated  $^{40}\text{Ar}/^{39}\text{Ar}$  age of  $108 \pm 2$  Ma (Fig. 13a). For biotite-aliquot 2, ten steps (B-M; steps E and H not included) released 99.98%  $^{39}\text{Ar}$  and yield an integrated  $^{40}\text{Ar}/^{39}\text{Ar}$  age of  $111 \pm 3$  Ma (Fig. 13b).

#### 4.4.3. Mesilinka granodiorite: 18lo19-2, $^{40}\text{Ar}/^{39}\text{Ar}$ biotite, $123 \pm 2$ Ma

This sample, a medium-grained equigranular granodiorite with biotite and minor hornblende, was collected 8.77 km south of Mount Ferris (Fig. 2). The sample yielded biotite and six Ar-release steps (B-H) released 77.07%  $^{39}\text{Ar}$ , yielding an integrated  $^{40}\text{Ar}/^{39}\text{Ar}$  age of  $123 \pm 2$  Ma (Fig. 13c).

#### 4.4.4. Mesilinka K-feldspar porphyritic granite: 18lo12-7, U-Pb zircon, $134.8 \pm 1.2$ Ma, $^{40}\text{Ar}/^{39}\text{Ar}$ biotite, $112 \pm 3$ Ma

The sample, a medium-grained K-feldspar porphyritic granite with a foliation defined by biotite was collected 2.1 km northeast of Horn Peak (Fig. 2). Clay-altered alkali feldspar phenocrysts up to 5 cm (38%), strained anhedral quartz (28%), and myrmekitic plagioclase (22%) comprise most of the sample. Biotite (10%) is 1-2 mm wide and interstitial to feldspar and quartz. Accessory minerals include zircon, magnetite, apatite, epidote, and allanite with epidote rims.

From the LA-ICP-MS results, six analyses were rejected for  $f^{206}\text{Pb}_c > 1\%$  and/or  $> 10\%$  discordance. Ten analyses were rejected for exceeding Ca  $> 300$  ppm, Fe  $> 300$  ppm, and/or La  $> 1$  ppm. One analysis was identified as a xenocryst because the CL image (zircon 49, sample 18lo12-7; Ootes et al., 2020c) shows that the zircon has a bright rounded core that is crosscut by later growth zoning. For the remaining zircon, an excess

scatter constant of 2.68 was added to the standard error of the filtered data points to decrease the MSWD of the weighted mean  $^{206}\text{Pb}/^{238}\text{U}$  date. Fourteen zircons yield a weighted mean  $^{206}\text{Pb}/^{238}\text{U}$  date of  $134.8 \pm 1.2$  Ma (MSWD=1.64; probability of fit=0.07). The weighted mean is interpreted as the best estimate for the crystallization age of this sample (Figs. 12c, d).

This sample yielded biotite and eight steps (B-I) released 99.98%  $^{39}\text{Ar}$ , resulting in an integrated  $^{40}\text{Ar}/^{39}\text{Ar}$  age of  $112 \pm 3$  Ma (Fig. 13d).

#### 4.4.5. Mesilinka equigranular granite: 18lo11-1, U-Pb zircon, $127.9 \pm 0.8$ Ma

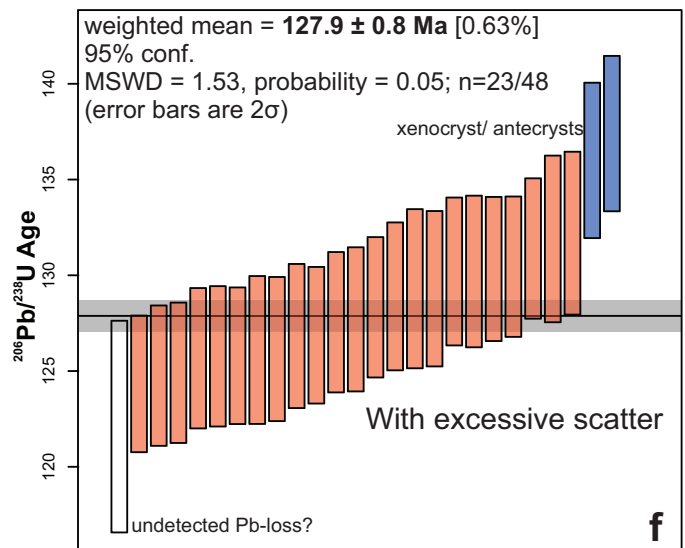
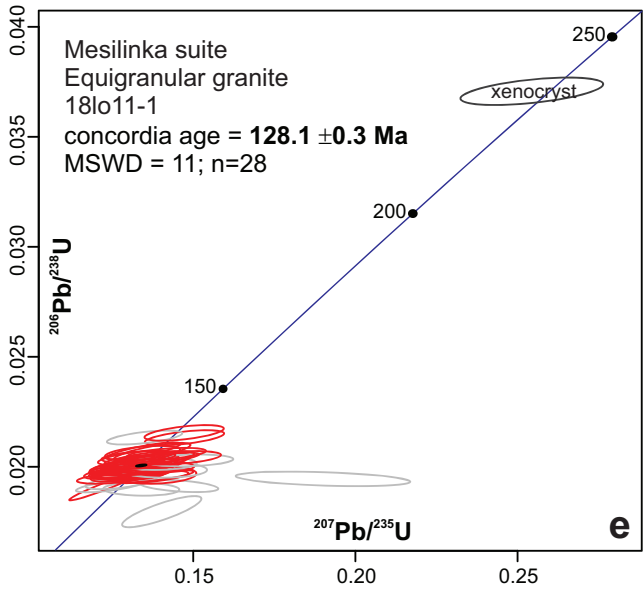
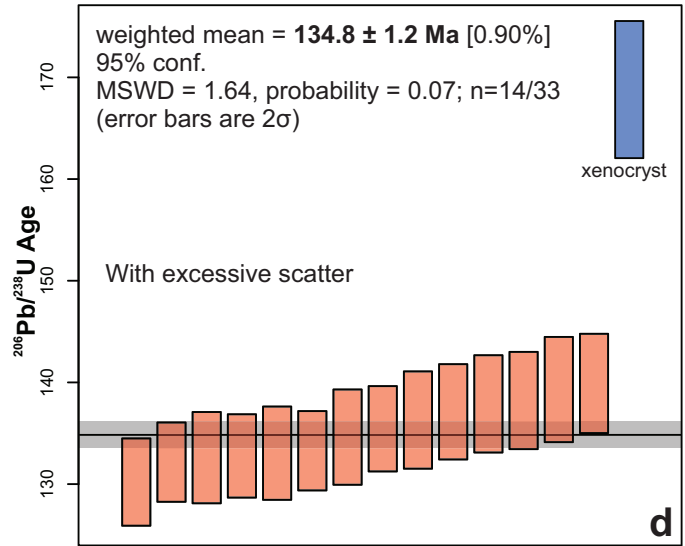
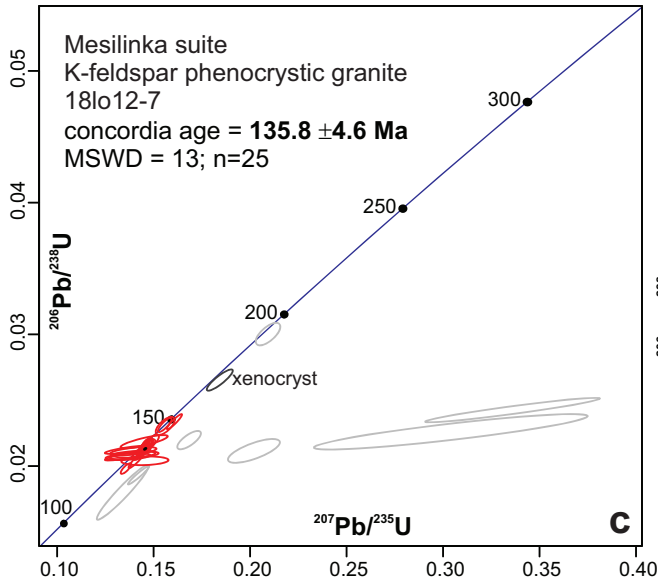
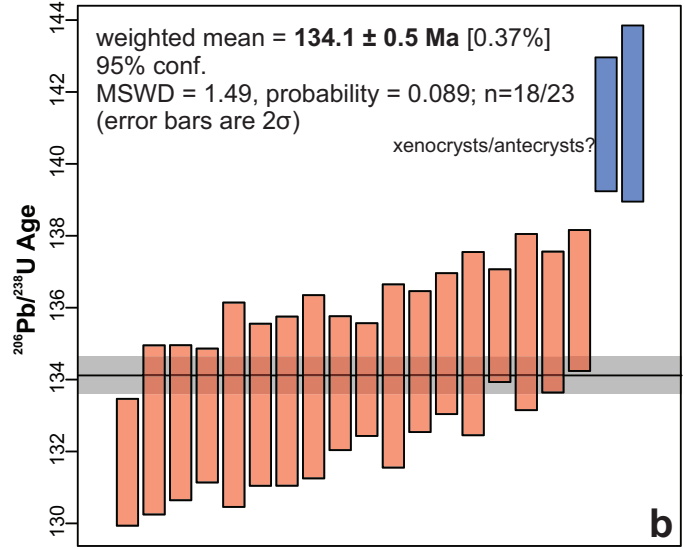
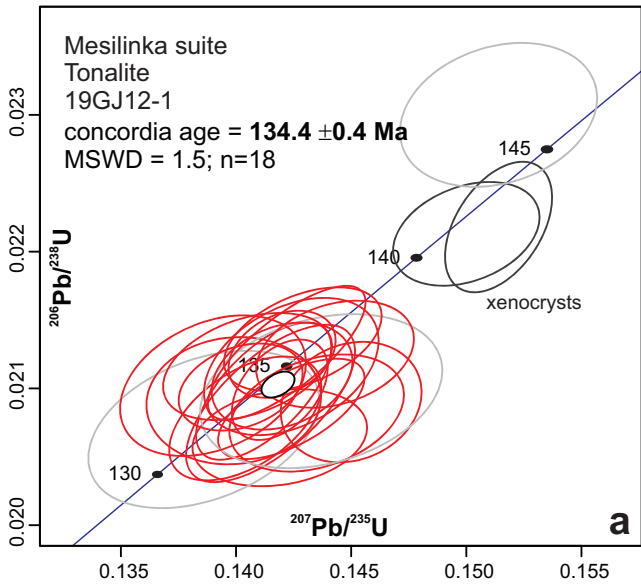
The sample, an equigranular, fine to medium-grained granite with a foliation defined by biotite was collected 1.48 km northeast of Horn Peak (Fig. 2). It consists mostly of strained fine-grained quartz (40%), anhedral medium-grained alkali feldspar (30%), and clay-altered plagioclase (25%). Accessory minerals include zircon, fine-grained muscovite, biotite, and magnetite. Magnetite may be rimmed by titanite.

Six analyses were rejected for  $f^{206}\text{Pb}_c > 1\%$  and/or  $> 10\%$  discordance. Thirteen analyses were rejected for exceeding La  $> 1$  ppm and/or Fe  $> 300$  ppm. Three zircons were rejected; one zircon (shown in Fig. 11e, not shown in Fig. 11f) and two other zircons are interpreted as antecrysts/xenocrysts because the CL images (zircons 8, 22, and 35 in sample 18lo11-1; Ootes et al., 2020c) show bright zircon cores that are crosscut by darker rims. For the remaining analyses, an excess scatter constant of 2.34 was added to the standard error of the filtered data points to decrease the MSWD of the weighted mean  $^{206}\text{Pb}/^{238}\text{U}$  date. The youngest zircon date was rejected due to possible undetected Pb-loss and large error in the  $^{206}\text{Pb}/^{238}\text{U}$  value. Twenty-three remaining analyses yield a weighted mean  $^{206}\text{Pb}/^{238}\text{U}$  date of  $127.9 \pm 0.8$  Ma (MSWD=1.53; probability of fit=0.05). The weighted mean is interpreted as the best estimate for the crystallization age of this sample (Figs. 12e, f).

#### 4.4.6. Mesilinka equigranular granite: 04PSC-277, U-Pb multi-grain titanite, $133.9 \pm 0.3$ Ma

The sample was collected from the north end of Hogem batholith, 21.5 km north-northwest of Horn Peak (Fig. 2). It is a medium-grained granite with  $\sim 55\%$  feldspar (plagioclase  $>$  K-feldspar), 25% quartz, and 20% variably chloritized mafic minerals (biotite  $>$  hornblende) and is isotropic to weakly lineated.

Single zircon and multi-grain titanite fractions were analyzed by ID-TIMS. Two titanite fractions yield a weighted mean  $^{206}\text{Pb}/^{238}\text{U}$  date of  $133.9 \pm 0.3$  Ma (MSWD=1.15; Fig. 12g), interpreted as a minimum crystallization age estimate for the granitoid, because they record cooling through the titanite closure temperature of ca. 600-650°C (Flowers et al., 2005). Three zircon fractions that give significantly younger results than the titanites and are interpreted to have suffered from Pb-loss. One zircon fraction gives older, discordant results, likely due to the presence of inherited components.



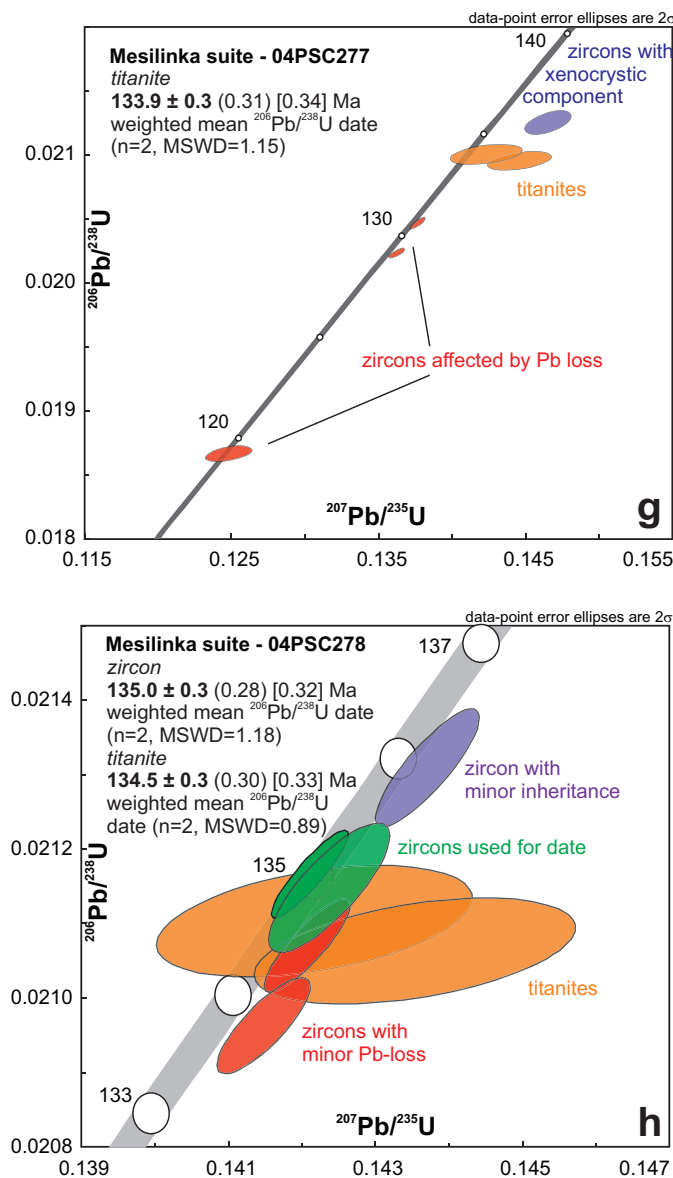


**Fig. 12.** Results of Mesilinka suite zircon U-Pb LA-ICP-MS analysis. Data used for weighted mean calculations have been filtered using the methods outlined in section 3.1.1. and Ootes et al. (2020c). Grey ellipses in concordia plots represent data that have been filtered and were not included in age calculations. Uncertainties are reported at the  $2\sigma$  or 95.5% confidence level. **a)** Concordia plot of tonalite sample 19GJ12-1. Dark grey ellipses passed the data filters in section 3.1.1., but are interpreted as antecrystic or xenocrystic zircon grains, and were not included in the concordia age calculation. **b)** Weighted mean  $^{206}\text{Pb}/^{238}\text{U}$  date, interpreted as the crystallization age, of tonalite sample 19GJ12-1. Blue bars are zircons interpreted as antecrysts or xenocrysts and were not included in the weighted mean calculation. **c)** Concordia plot of K-feldspar porphyritic granite sample 18lo12-7. The dark grey ellipse passed the data filters in section 3.1.1. but is interpreted as xenocrystic and not included in the age calculation. **d)** Weighted mean  $^{206}\text{Pb}/^{238}\text{U}$  date of K-feldspar porphyritic granite sample 18lo12-7, after applying excessive scatter constant (section 3.1.1.). The blue bar is an interpreted xenocrystic zircon and is not included in the weighted mean calculation. **e)** Concordia plot of equigranular granite sample 18lo11-1. The dark grey ellipse passed the data filters in section 3.1.1. but is interpreted as xenocrystic and is not included in the age calculation. **f)** Weighted mean  $^{206}\text{Pb}/^{238}\text{U}$  date of equigranular granite sample 18lo11-1, after applying excessive scatter constant (section 3.1.1.). The blue bars are interpreted antecrystic or xenocrystic zircons and are not included in the weighted mean calculation. The colourless bar passed the data filters in section 3.1.1. but was not included in the weighted mean calculation due to the large uncertainty and younger age, possibly indicating undetected Pb-loss in the zircon. **g)** Concordia plot of equigranular granite sample 04PSC277. Two titanite fractions were used to determine the weighted mean  $^{206}\text{Pb}/^{238}\text{U}$  date, interpreted as the crystallization age of this sample. **h)** Concordia plot of K-feldspar porphyritic granite sample 04PSC278. Two titanite and two zircon fractions yield overlapping weighted mean  $^{206}\text{Pb}/^{238}\text{U}$  dates, interpreted as the crystallization age of this sample.

#### 4.4.7. Mesilinka K-feldspar porphyritic granite: 04PSC-278, U-Pb zircon, $135.0 \pm 0.3$ Ma, U-Pb multi-grain titanite, $134.5 \pm 0.3$ Ma

The sample is from the north end of Hogem batholith, 22 km north-northwest of Horn Peak, and 1 km west of sample 04PSC-277 (section 4.4.6.; Fig. 2). The granite is coarse grained and porphyritic, with 30% K-feldspar (10% as 1 to 2 cm phenocrysts), 30% plagioclase, 20% quartz, and 20% chloritized mafic minerals (biotite >> hornblende). The sample has a strong lineation defined by elongate biotite clots and stretched feldspar and quartz grains, and a less-pronounced northeast-dipping tectonic foliation.

Single zircon and multi-grain titanite fractions were analyzed by ID-TIMS. Results for two overlapping and concordant zircon fractions give a weighted mean  $^{206}\text{Pb}/^{238}\text{U}$  date of  $135.0 \pm 0.3$  Ma (MSWD=0.18; Fig. 12h), interpreted

as a good estimate for the age of crystallization. Two slightly younger zircon fractions appear to have undergone minor Pb-loss. One zircon fraction is slightly older, likely due to the presence of inherited, or possibly or antecrystic components. Two titanite fractions yield a weighted mean  $^{206}\text{Pb}/^{238}\text{U}$  date of  $134.5 \pm 0.3$  Ma (MSWD=0.89; Fig. 12h), which overlaps with the interpreted crystallization age based on two zircon fractions and is consistent with cooling through the titanite closure temperature soon after emplacement.

## 5. Summary

Uranium-lead and  $^{40}\text{Ar}/^{39}\text{Ar}$  geochronology of Hogem batholith samples yield a range of crystallization ages from  $206.6 \pm 0.9$  to  $127.9 \pm 0.8$  Ma (Figs. 5-14; Table 1). The geochronological and geochemical attributes indicate a punctuated, protracted, and petrologically diverse intrusive

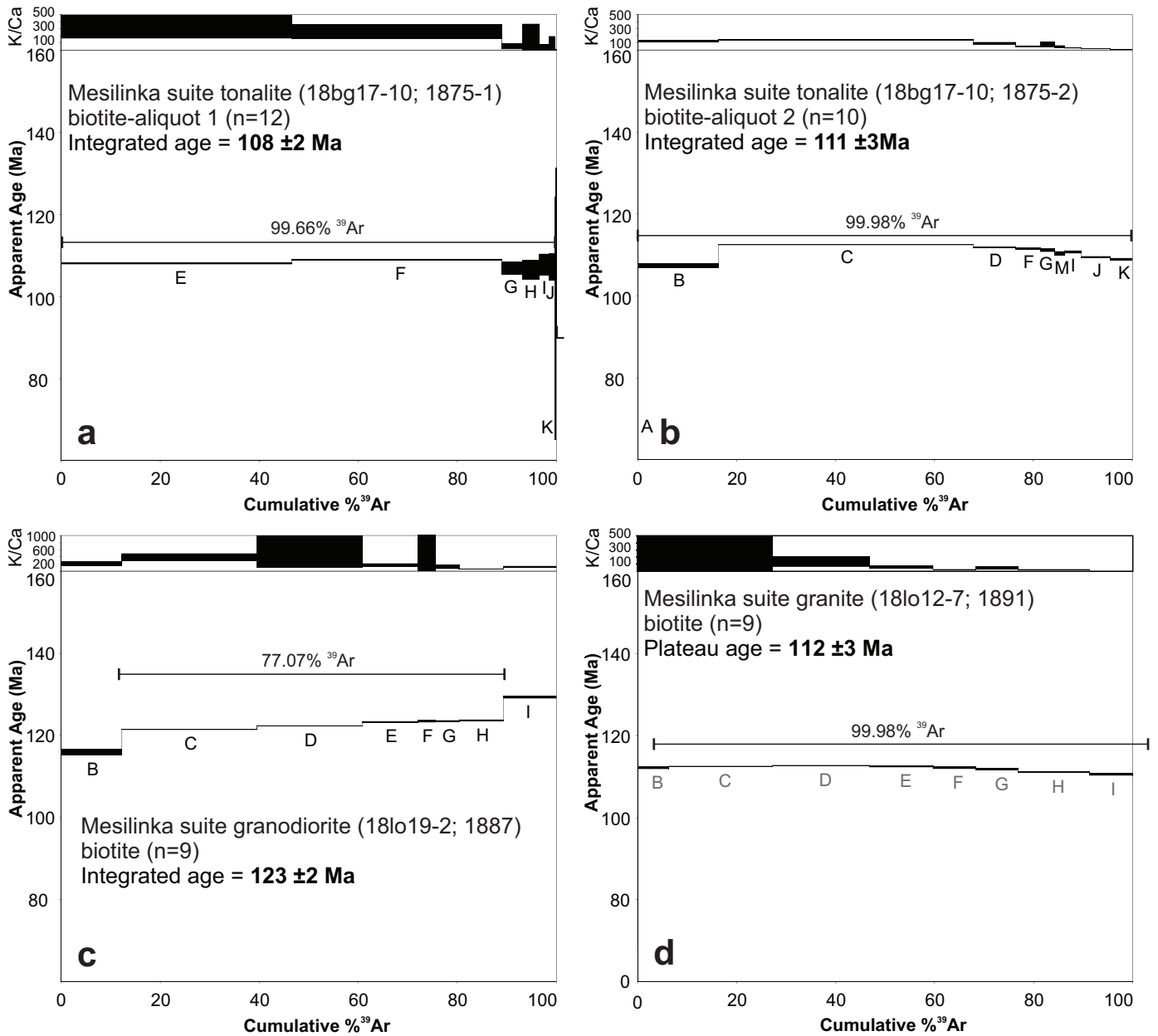


**Fig. 13.** Results of  $^{40}\text{Ar}/^{39}\text{Ar}$  laser step heating of single crystals of **a-b**) biotite from Mesilinka suite tonalite (18bg17-10), **c**) biotite from Mesilinka suite granodiorite (18lo19-2), and **d**) biotite from Mesilinka suite granite (18lo12-7).

history for the batholith (Figs. 3, 4, 14; Table 1). The Thane Creek suite crystallized between  $206.6 \pm 0.9$  and  $194 \pm 1.1$  Ma and a single  $^{40}\text{Ar}/^{39}\text{Ar}$  amphibole result from an undeformed quartz diorite phase indicates post-intrusion cooling at  $202 \pm 5$  Ma. The crystallization ages overlap an age of  $200.9 \pm 0.2$  Ma from the Rhonda-Dorothy gabbro in southern Hogem batholith (Devine et al., 2014) and a less-precise age of ca. 204 Ma from the CAT monzonite (Fig. 2, 14; Mortensen et al., 1995). The results of  $^{40}\text{Ar}/^{39}\text{Ar}$  amphibole and biotite from a deformed Thane Creek diorite indicate these minerals were reset during deformation after Duckling Creek suite emplacement ( $<175$  Ma) and underwent prolonged post-deformation cooling at ca. 125 Ma

synchronous with the Mesilinka suite (Figs. 6a-e, 14).

The Duckling Creek samples investigated in this study crystallized between  $178.9 \pm 1.3$  to  $174.7 \pm 0.7$  Ma (Figs. 7, 9, 14). A hornblende  $^{40}\text{Ar}/^{39}\text{Ar}$  age of  $177 \pm 5$  Ma, from a Duckling Creek suite syenite approximates the time of relatively rapid post-crystallization cooling (Figs. 8, 14). The full collection of results overlaps previously reported U-Pb and  $^{40}\text{Ar}/^{39}\text{Ar}$  results from the Lorraine Cu-Au deposit in southern Hogem batholith (Fig. 14; Bath et al., 2014; Devine et al., 2014). The  $174.7 \pm 0.7$  Ma zircon crystallization age result in this study is from a syenite sample that hosts Cu-mineralization (assay sample 19GJ13-5b; Ootes et al., 2020b) and is adjacent to

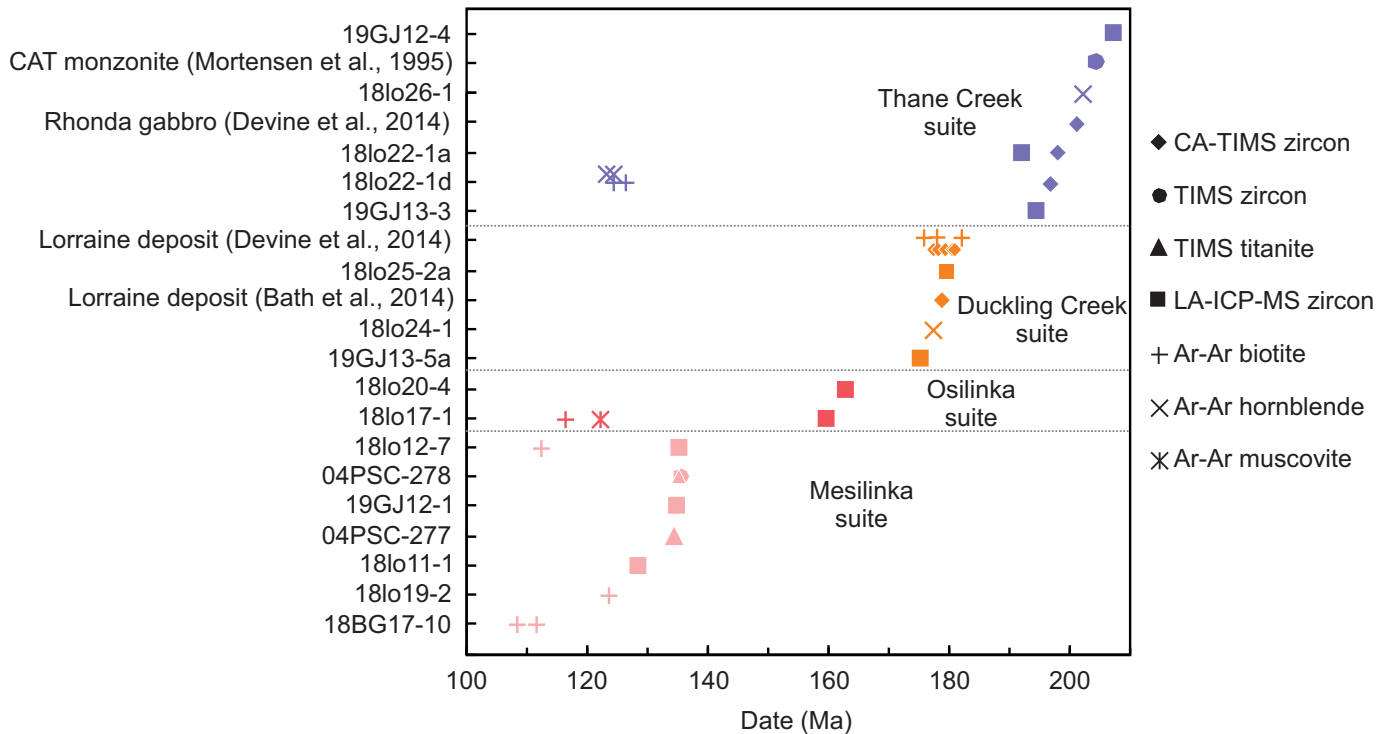


**Fig. 14.** Geochronology results of the four Hogem batholith intrusive suites. Data includes zircon U-Pb dates by CA-TIMS, TIMS, and LA-ICP-MS analysis, titanite U-Pb dates by TIMS analysis, and biotite, muscovite, and hornblende  $^{40}\text{Ar}/^{39}\text{Ar}$  dates by laser step-heating. The CAT monzonite zircon U-Pb date is from Mortensen et al. (1995). Data from Devine et al. (2014) includes CA-TIMS zircon U-Pb dates and biotite  $^{40}\text{Ar}/^{39}\text{Ar}$  dates of several samples from Duckling Creek suite phases in the Lorraine deposit area. Data from Bath et al. (2014) are represented as a single point, the average of five overlapping CA-TIMS zircon U-Pb dates of Duckling Creek suite samples from the Lorraine deposit area.

(or part of) the Slide Cu showing. This may indicate some Cu-mineralization within the Duckling Creek suite is slightly younger than at the Lorraine deposit (ca. 175 Ma; cf. 180-178.5 Ma, Bath et al., 2014; Devine et al., 2014), or may be due to results from different analytical techniques.

The Osilinka suite has a maximum crystallization age of ca. 160 Ma, estimated from the youngest zircon result of the Osilinka granite sample 18lo17-1 analysis ( $159.2 \pm 4$  Ma). A plagioclase-phenocrystic sheet cuts the Osilinka granite and yielded an overlapping U-Pb zircon date ( $162.2 \pm 2.6$  Ma). Results from  $^{40}\text{Ar}/^{39}\text{Ar}$  muscovite ( $122 \pm 5$  Ma) and biotite ( $116 \pm 1$  Ma) are interpreted as the time of post-deformation cooling (Figs. 11, 14).

The oldest tonalitic phase of the Mesilinka suite crystallized at  $134.1 \pm 0.5$  Ma and the youngest granite phase crystallized at  $127.9 \pm 0.8$  Ma (Figs. 12a-f, 14). Three Mesilinka granite ages (determined by U-Pb zircon LA-ICP-MS and multi-grain TIMS analyses) overlap at ca. 134 Ma. Two U-Pb multi-grain titanite dates, determined by TIMS, are consistent with the U-Pb zircon crystallization ages (Figs. 12g, h, 14). The tonalite is cut by the granite, and the results are best interpreted as concomitant metaluminous tonalitic and weakly peraluminous granitic magmatism, preserved as tonalite enclaves within granite intrusions (Figs. 4a, 12a-h). Four Mesilinka  $^{40}\text{Ar}/^{39}\text{Ar}$  biotite dates yield a range from  $123 \pm 2$  to  $108 \pm 2$  Ma (Figs.

13, 14). This is interpreted as a prolonged period of magmatic and post-deformation cooling following emplacement of the Mesilinka suite.

A fundamental geochemical subdivision of Hogem batholith exists between the silica-saturated Thane Creek, Osilinka, and Mesilinka suites and the mildly silica undersaturated Duckling Creek suite (0-12 wt.% normative nepheline). Despite their overlapping  $\text{SiO}_2$  concentrations, the diorites, quartz monzodiorites, and granodiorites of the Thane Creek suite ( $\text{SiO}_2=47-71$  wt.%) have significantly lower total alkali metal concentrations ( $\text{Na}_2\text{O}+\text{K}_2\text{O}=3.4-8.2$  wt.%) than the syenites of the Duckling Creek suite ( $\text{SiO}_2=53-64$  wt.%;  $\text{Na}_2\text{O}+\text{K}_2\text{O}=8.6-14.8$  wt.%). The higher  $\text{SiO}_2$  concentrations of the Mesilinka (63-77 wt.%) and Osilinka (69-76 wt.%) suites are reflected in higher relative abundances of modal quartz, although variable  $\text{K}_2\text{O}+\text{Na}_2\text{O}$  concentrations and  $\text{CaO}/(\text{Na}_2\text{O}+\text{K}_2\text{O})$  ratios result in a large compositional range between tonalite and syenogranite. Whereas the intermediate- $\text{SiO}_2$  rocks of the Thane Creek and Duckling Creek suites are metaluminous (Fig. 4a), the high- $\text{SiO}_2$  Mesilinka and Osilinka suites are weakly peraluminous ( $\text{ASI} \leq 1.2$ ) and similar to the estimated ASI of the upper continental crust (1.04; Rudnick and Gao, 2003). Samples of the Thane Creek suite are magnesian (Fig. 4b) according to the classification of Frost and Frost (2008), and clearly distinguished from the ferroan Duckling Creek

suite syenites. Although most of the samples of the Mesilinka suite are magnesian, a subset of the syenogranitic samples are ferroan and more similar to the syenogranite of the Osilinka suite (Fig. 4b). However, the two ferroan syenogranite suites are distinguished on their molar  $K/(K+Na)$  ratios; the ferrous syenogranites of the Mesilinka suite ( $K/(K+Na)=0.32-0.46$ ) are potassic relative to both the syenogranites of the Osilinka suite ( $K/(K+Na)=0.21-0.32$ ) and continental crust estimates ( $K/(K+Na) < 0.36$ ; Rudnick and Gao, 2003). In addition to the ferroan syenogranites of the Mesilinka suite, syenites of the Duckling Creek suites are also potassic ( $K/(K+Na)=0.32-0.68$ ). The remaining rocks of the Hagem batholith are relatively sodic and comparable to the continental crust composition.

The Hagem batholith contains chemically diverse igneous suites that have a punctuated and protracted intrusive history, lasting more than 80 m.y. This longevity is rare for a single batholith in the Canadian Cordillera and indicates that diverse magma sources were tapped through time. Further petrogenetic studies will help determine how each of the intrusive suites fit within the tectonic evolution of the orogen. A new finding in this study is that the Mesilinka suite (135-128 Ma) intruded during a previously documented magmatic gap in the Cordilleran orogen (Armstrong, 1988).

## 6. Economic implications

Both the Thane Creek and Duckling Creek suites host porphyry Cu-Au mineralization. The best example is the Lorraine deposit, which is hosted by Duckling Creek suite. It has an Indicated resource of 6.42 Mt at 0.62% Cu and 0.23 g/t Au and an Inferred resource of 28.82 Mt at 0.45% Cu and 0.19 g/t Au (Giroux and Lindinger, 2012). The Lorraine deposit is south of the present study area (Fig. 2; e.g., Devine et al., 2014), but equally prospective rocks are in northern Hagem batholith, as confirmed by our bedrock mapping and geochronological results (Figs. 2, 14; Ootes et al., 2020a, b, c). The Thane Creek suite hosts numerous Cu-prospects, some of which are actively being explored (e.g., Cathedral project, Naas, 2016; Top Cat, Serengeti Resources Inc., 2020), and correlative rocks host the Kwanika developed prospect south of the present study area (Serengeti Resources Inc., 2020). The results of this study confirm a similar age-relationship to the Cu-hosted Rhonda-Dorothy prospect to the south (Devine et al., 2014) and further highlight the distribution of the Thane Creek suite in Hagem batholith.

## Acknowledgments

The first author acknowledges support from the Diamond Exploration Research Training School (DERTS), which is funded by NSERC and the University of Alberta. The first author received additional funding from NSERC CGS-M and Geoscience BC. This is NRCan contribution 20200583. Reviews by F. Devine and J. Chiarenzelli helped improve the manuscript.

## References cited

- Armstrong, J.E., 1946. Aiken Lake (south half), British Columbia. Geological Survey of Canada, Paper 46-11, 1 sheet, scale 1 inch:2 miles.
- Armstrong, R.E., 1988. Mesozoic and early Cenozoic magmatic evolution of the Canadian Cordillera. In: Clark, S.P., Burchfiel, B.C., Suppe, J., (Eds.), Processes in Continental Lithospheric Deformation. Geological Society of America, Special Paper 218, pp. 55-90. <https://doi.org/10.1130/SPE218-p55>.
- Armstrong, J.E., and Roots, E.F., 1948. Aiken Lake map-area, British Columbia. Geological Survey of Canada, Paper 48-5, 46 p.
- Armstrong, J.E., and Roots, E.F., 1954. Aiken Lake, Cassiar District, British Columbia. Geological Survey of Canada, A Series Map 1030A, scale 1 inch:4 miles.
- Bath, A.B., Cooke, D.R., Friedman, R.M., Faure, K., Kamenetsky, V.S., Tosdal, R.M., and Berry, R.F., 2014. Mineralization, U-Pb geochronology, stable isotope geochemistry of the Lower Main Zone of the Lorraine deposit, north-central British Columbia: A replacement-style alkalic Cu-Au porphyry. *Economic Geology*, 109, 979-1004.
- CGG Canada Services Ltd., 2018. Geophysical survey report MIDAS high resolution magnetic and radiometric survey Search Project Phase III; Geoscience BC, Report 2018-2, 72 p.
- Devine, F.A.M., Chamberlain, C.M., Davies, A.G.S., Friedman, R., and Baxter, P., 2014. Geology and district-scale setting of tilted alkalic porphyry Cu-Au mineralization at the Lorraine deposit, British Columbia. *Economic Geology*, 109, 939-977.
- Ferri, F., Dudka, S.F., Rees, C., and Meldrum, D., 2001a. Geology of the Aiken Lake area, north-central British Columbia, NTS 94C/5, 6 and 12. British Columbia Ministry of Energy, Mines and Petroleum Resources, British Columbia Geological Survey Geoscience Map 2001-10, scale 1:50,000.
- Ferri, F., Dudka, S.F., Rees, C.J., Meldrum, D.G., and Willson, M.J., 2001b. Geology of the Uslika Lake Area, North-Central B.C. (NTS 94C/2, 3 & 4). British Columbia Ministry of Energy, Mines and Petroleum Resources, British Columbia Geological Survey Geoscience Map 2001-04, scale 1:50,000.
- Fisher, C.M., Vervoort, J.D., and Hanchar, J. M., 2014. Guidelines for reporting zircon Hf isotopic data by LA-MC-ICPMS and potential pitfalls in the interpretation of these data. *Chemical Geology*, 363, 125-133.
- Fisher, C.M., Paton, C., Pearson, D.G., Sarkar, C., Luo, Y., Tersmette, D.B., and Chacko, T., 2017. Data reduction of Laser Ablation Split-Stream (LASS) analyses using newly developed features within Iolite: With applications to Lu-Hf+ U-Pb in detrital zircon and Sm-Nd+ U-Pb in igneous monazite. *Geochemistry, Geophysics, Geosystems*, 18, 4604-4622.
- Flowers, R.M., Bowring, S.A., Tulloch, A.J., and Klepeis, K.A., 2005. Tempo of burial and exhumation within the deep roots of a magmatic arc, Fiordland, New Zealand. *Geology*, 33, 17-20.
- Frost, B.R., and Frost, C.D., 2008. A geochemical classification for feldspathic igneous rocks. *Journal of Petrology* 49, 1955-1969.
- Garnett, J.A., 1972. Preliminary geological map of part of Hagem batholith, Duckling Creek area (parts of NTS 93N/13, 14; 94C/3, 4). British Columbia Ministry of Energy, Mines and Petroleum Resources, British Columbia Geological Survey Preliminary Map 09, scale 1:50,000.
- Garnett, J.A., 1978. Geology and mineral occurrences of the southern Hagem batholith. British Columbia Ministry of Energy, Mines and Petroleum Resources, British Columbia Geological Survey Bulletin 70, 75 p.
- Giroux, G., and Lindinger, L.J., 2012. Summary report on the Lorraine-Jajay property, Omenica Mining Division, B.C. Prepared for Lorraine Copper Corp., Report 09-2012, 122 p., URL <[http://www.sedar.com/issuers/issuers\\_en.htm](http://www.sedar.com/issuers/issuers_en.htm)>, last accessed October, 2020.

- Irvine, T.N., 1976. Studies of Cordilleran gabbroic and ultramafic intrusions, British Columbia. Geological Survey of Canada, Paper 76-1A, pp. 75-81.
- Jones, G.O., Pearson, D.G., Vezinet, A., Luo, Y., Stern, R.A., Milidragovic, D., and Ootes, L., 2021. Preliminary zircon geochemistry of northern Hogem batholith, Quesnel terrane, north-central British Columbia (parts of NTS 093M/16, 093N/13, 14, 094C/03-06, 094D/01, 08). Geoscience BC Summary of Activities 2020: Minerals and Mining, Report 2021-1, in press.
- Kuiper, K.F., Deino, A., Hilgen, F.J., Krijgsman, W., Renne, R., and Wijbrans, J.R., 2008. Synchronizing rock clocks of Earth history. *Science*, 320, 500-504.
- Le Maitre, R., Streckeisen, A., Zanettin, B., Le Bas, M., Bonin, B., and Bateman, P., (Eds.), 2002. *Igneous Rocks: A Classification and Glossary of Terms: Recommendations of the International Union of Geological Sciences Subcommittee on the Systematics of Igneous Rocks*. Cambridge: Cambridge University Press.
- Lord, C.S., 1948. McConnell Creek map-area, Cassiar District, British Columbia. Geological Survey of Canada, Memoir 251, 82 p.
- Lord, C.S., 1949. McConnell Creek, Cassiar District, British Columbia. Geological Survey of Canada, A Series Map 962A, scale 1 inch:4 miles.
- Ludwig, K.R., 2003. *Isoplot 3.00: A geochronological toolkit for Microsoft Excel*. Berkeley Geochronology Center, Berkeley, 70 p.
- Mortensen, J.K., Ghosh, D.K., and Ferri, F., 1995. U-Pb geochronology of intrusive rocks associated with copper-gold porphyry deposits in the Canadian Cordillera. *Canadian Institute of Mining, Metallurgy and Petroleum, Special Volume 46*, pp. 142-158.
- Naas, C.O., 2016. Lidar surveying, ground magnetic surveying and geochemical sampling of the Cathedral property. British Columbia Geological Survey, Assessment Report 36337, 151 p.
- Nelson, J.L., Colpron, M., and Israel, S., 2013. The Cordillera of British Columbia, Yukon, and Alaska: Tectonics and metallogeny. In: Colpron, M., Bissing, T., Rusk, B.G., and Thompson, J.F.H., (Eds.), *Tectonics, Metallogeny, and Discovery: The North American Cordillera and similar accretionary settings*. Society of Economic Geologists, Special Publication 17, pp. 53-109.
- Nixon, G.T., and Peatfield, G.R., 2003. Geological setting of the Lorraine Cu-Au porphyry deposit, Duckling Creek syenite complex, north-central British Columbia. British Columbia Ministry of Energy and Mines, British Columbia Geological Survey Open File 2003-4, 24 p.
- Ootes, L., Bergen, A., Milidragovic, D., Graham, B., and Simmonds, R., 2019. Preliminary geology of northern Hogem batholith, Quesnel terrane, north-central British Columbia. In: *Geological Fieldwork 2018*, British Columbia Ministry of Energy, Mines and Petroleum Resources, British Columbia Geological Survey Paper 2019-01, pp. 31-53.
- Ootes, L., Bergen, A.L., Milidragovic, D., and Jones, G.O., 2020a. Preliminary geology of the northern Hogem batholith and its surroundings, north-central British Columbia. British Columbia Ministry of Energy and Mines and Petroleum Resources, British Columbia Geological Survey Open File 2020-02, scale 1:50,000.
- Ootes, L., Bergen, A.L., Milidragovic, D., Jones, G.O., Camacho, A., and Friedman, R., 2020b. An update on the geology of northern Hogem batholith and its surroundings, north-central British Columbia. In: *Geological Fieldwork 2019*, British Columbia Ministry of Energy, Mines and Petroleum Resources British Columbia Geological Survey Paper 2020-1, pp. 25-47.
- Ootes, L., Jones, G.O., Schiarizza, P., Milidragovic, D., Friedman, R., Camacho, A., Luo, Y., Vezinet, A., Pearson, D.G., and Zhang, S., 2020c. Geochronologic and geochemical data from northern Hogem batholith and its surroundings, north-central British Columbia. British Columbia Ministry of Energy and Mines Low Carbon Innovation, British Columbia Geological Survey GeoFile 2020-01, 21 p.
- Paton, C., Hellstrom, J., Paul, B., Woodhead, J., and Hergt, J., 2011. *Iolite: Freeware for the visualization and processing of mass spectrometric data*. *Journal of Analytical Atomic Spectrometry*, 26, 2508-2518.
- Paton, C., Woodhead, J.D., Hellstrom, J.C., Hergt, J.M., Greig, A., and Maas, R., 2010. Improved laser ablation U-Pb zircon geochronology through robust downhole fractionation correction. *Geochemistry, Geophysics, Geosystems*, 11, <https://doi.org/10.1029/2009GC002618>.
- Roots, E.F., 1954. Geology and mineral deposits of Aiken Lake map area, British Columbia. Geological Survey of Canada, Memoir 274, 246 p.
- Rudnick, R.L., and Gao, S., 2003. Composition of the Continental Crust. In: *The Crust*, Rudnick, R.L., (Ed.), *Treatise on Geochemistry* 3, pp. 1-64.
- Schiarizza, P., and Tan, S.H., 2005a. Geology and mineral occurrences of the Quesnel Terrane between the Mesilinka River and Wrede Creek (NTS 94D/8, 9), north-central British Columbia. British Columbia Ministry of Energy and Mines, British Columbia Geological Survey Paper 2005-1, pp. 109-130.
- Schiarizza, P., and Tan, S.H., 2005b. Geology of the Johanson Lake area, parts of NTS 94D/8 and 9. British Columbia Ministry of Energy, Mines and Petroleum Resources, British Columbia Geological Survey Open File 2005-4, scale 1:50,000.
- Schmitz, M.D., and Schoene, B., 2007. Derivation of isotope ratios, errors, and error correlations for U-Pb geochronology using  $^{205}\text{Pb}$ - $^{235}\text{U}$ -( $^{233}\text{U}$ )-spiked isotope dilution thermal ionization mass spectrometric data. *Geochemistry, Geophysics, Geosystems*, 8, <https://doi.org/10.1029/2006GC001492>.
- Serengeti Resources Inc., 2020. Projects overview. <https://www.serengetiresources.com/projects/projects-overview-1>, last accessed October, 2020.
- Shand, S.J., 1943. *Eruptive Rocks; Their Genesis, Composition, Classification, and Their Relation to Ore Deposits, with a Chapter on Meteorites (Revised Second Edition)*. Hafner Publishing Co., New York.
- Stanley, C., 2017. Lithochemical classification of igneous rocks using Streckeisen ternary diagrams. *Geochemistry: Exploration, Environment, Analysis*, 17, 63-91.
- Vermeesch, P., 2018. *IsoplotR: A free and open toolbox for geochronology*. *Geoscience Frontiers*, 9, 1479-1493.
- Vezinet, A., Pearson, D.G., Thomassot, E., Stern, R.A., Sarkar, C., Luo, Y., and Fisher, C.M., 2018. Electronic Supplementary Material: Hydrothermally-altered mafic crust as source for early Earth TTG: Pb/Hf/O isotope and trace element evidence from TTG of the Eoarchean Saglek Block, N. Labrador. *Earth and Planetary Science Letters*, 503, 95-107.
- Woodsworth, G.J., 1976. Plutonic rocks of McConnell Creek (94 D west half) and Aiken Lake (94 C east half) map-areas, British Columbia. Geological Survey of Canada, Paper 76-1A, pp. 69-73.

# Preliminary surficial geology of the northern Hogem batholith area, north-central British Columbia



T. Ferbey<sup>1, a</sup> and E.A. Elia<sup>1</sup>

<sup>1</sup> British Columbia Geological Survey, Ministry of Energy, Mines and Low Carbon Innovation, Victoria, BC, V8W 9N3

<sup>a</sup> corresponding author: Travis.Ferbey@gov.bc.ca

Recommended citation: Ferbey, T., and Elia, E.A., 2021. Preliminary surficial geology of the northern Hogem batholith area, north-central British Columbia. In: Geological Fieldwork 2020, British Columbia Ministry of Energy, Mines and Low Carbon Innovation, British Columbia Geological Survey Paper 2021-01, pp. 57-64.

## Abstract

The Cordilleran Ice Sheet covered the Hogem batholith area during the Late Wisconsinan glacial maximum when ice flowed east and southeast across the region from an ice divide above the Skeena Mountains. During this stage, ice-flow was independent of local topography and glaciers were able to move across valleys. However, for most of the Late Wisconsinan, ice flow was controlled by topography, as recorded by glacially streamlined or eroded landform- and outcrop-scale indicators that are commonly aligned valley parallel. Valley glaciers were not entirely controlled by local topography, flowing over low-elevation, through-valley, topographic divides, transporting glacial debris into adjacent drainages. During full-glacial conditions, glaciers deposited overconsolidated subglacial tills. During deglaciation, hummocky, and less consolidated, melt-out tills were deposited. Significant volumes of glacial meltwater flowed through the valleys during deglaciation, transporting coarse-grained sands and gravels. Much of this transport and deposition was subaerial (forming extensive outwash plains and terraces), but a component was subglacial (forming eskers) or in contact with stagnant ice blocks (producing hummocky sands and gravels). Colluvial deposits are common along the base of steep slopes and are now vegetated and stable, but talus aprons and cones are still actively being constructed. Organic deposits occur throughout the study area, mostly as narrow transition zones between tree stands and water bodies. These deposits can also be extensive along the floors of retreat-phase glaciofluvial meltwater channels. Subglacial till, the ideal sample medium for till geochemistry and mineralogy surveys in mineral exploration, is common in valley bottoms and lower hillslopes. Although bedrock is well-exposed at high elevation, small isolated outcrops are common along valley bottoms and on forested hill flanks but may be overlooked.

**Keywords:** Surficial geology, Quaternary geology, ice-flow history, Hogem batholith, Cordilleran Ice Sheet

## 1. Introduction

The Hogem batholith, which is prospective for syngenetic porphyry Cu ( $\pm$ Au, Ag, Mo) and quartz vein-hosted precious and base-metal mineralization, is in the Omineca Mountains, a remote part of north-central British Columbia (Fig. 1). In 2018, the British Columbia Geological Survey initiated a multi-year program integrating 1:50,000-scale bedrock and surficial geological mapping of northern Hogem batholith as it has not been investigated at this scale. Results from bedrock mapping, including detailed geochemical and geochronologic work to better understand the origin and timing of batholith emplacement and base- and precious-metal mineralization, are presented by Ootes et al. (2019a, b, 2020a, b) and Jones et al. (2021). Herein we present a preliminary overview of the surficial geology component by describing map units, landforms, and the ice-flow history of the area.

## 2. Setting and previous work

The northern Hogem batholith area is in north-central British Columbia, approximately 200 km northwest of Mackenzie, British Columbia (Fig. 1). Topography here consists of steep mountains with northward-facing cirques, and deep U-shaped valleys (Holland, 1976).

The Hogem batholith (Jurassic to Early Cretaceous) is a composite felsic to mafic plutonic body in Quesnel terrane.

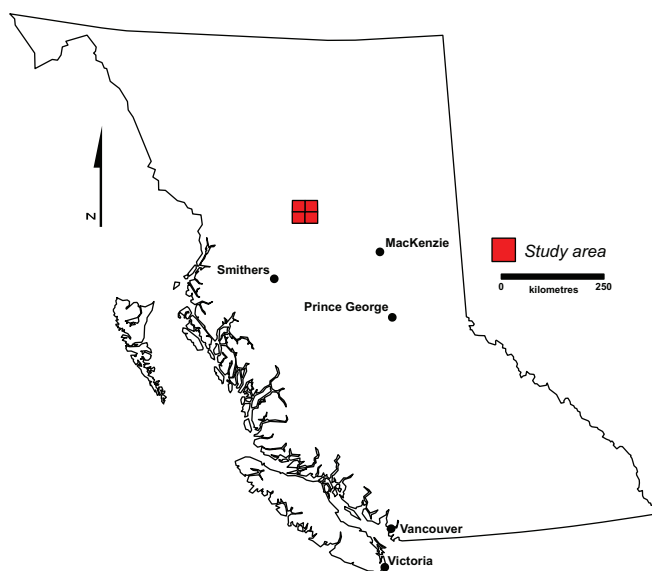


Fig. 1. Study area location.

These rocks have a high potential to host syngenetic porphyry-style Cu ( $\pm$ Au, Ag, Mo) mineralization and quartz vein-hosted concentrations of precious and base-metals. There are 112 MINFILE mineral occurrences in the study area, and an additional 19 have been discovered as part of regional

bedrock mapping by Ootes et al. (2019a, b, 2020a, b). Seventy kilometres northwest of the study area is the past-producing Kemess mine (calc-alkaline porphyry Cu-Mo-Au; MINFILE 094E 094) and 10 km south is the Lorraine developed prospect (alkalic Cu-Au porphyry; MINFILE 093N 002).

Roots (1954) and Armstrong and Roots (1954) provided detailed Quaternary geology observations while investigating the bedrock geology and mineral deposits of the Aiken Lake map-area (NTS 94C west). Plouffe (2000) studied the surficial geology and Quaternary history of the Manson River map sheet south of the present study area at 1:250,000-scale and, to the east, Rutter (1974a, b) mapped the surficial geology of the Finlay River valley at 1:125,000-scale before the flooding of Williston Lake behind the W.A.C. Bennet Dam. Ryder and Maynard (1991), Bobrowsky and Rutter (1992), Clague and Ward (2011), and Margold et al. (2013) included the area in their broader summaries of Quaternary history and Cordilleran Ice Sheet dynamics.

### 3. Methods

Before entering the field, we made preliminary surficial geology maps for NTS 094C/04, 05, 094D/01, and 08 using digital, black and white 1:40,000-scale, air photo stereo pairs. Once in the field, we modified these maps by recording observations at natural (e.g., stream cuts, gullies, up-rooted trees) and anthropogenic (e.g., road cuts, clear cuts, hand-dug pits) exposures. We traversed using truck and all-terrain vehicle in those parts of NTS 094/C04 and 05 with road access (Fig. 2). In areas without roads, we conducted short ground traverses above treeline using a helicopter for access. We made observations from the air where a helicopter was prevented from landing, either because of excessively rugged topography (at elevation) or excessive tree cover (valley bottoms). We supplemented ground observations with high resolution (<10 cm/pixel) photogrammetric DEMs generated in the field using a remotely piloted aircraft system and the structure from motion technique (Elia and Ferbey, 2020).

### 4. Surficial geology map units

The following is a preliminary summary of the major surficial geology map units of the study area. Detailed descriptions of most sediment types are from exposures in 094C/04 and 05. Observations on bedrock and colluvial units were made in all four map sheets.

#### 4.1. Bedrock

Bedrock is exposed in all topographic positions. It is most common above treeline where it forms extensive coherent exposures (Fig. 3a) or is mantled by felsenmeer consisting of frost-shattered angular fragments derived from immediately subjacent bedrock (Fig. 3b). Felsenmeer is most common in saddles, but can also occur in rounded, high-elevation, ridges or plateaus. At mid-slope positions (Fig. 3c), it can be difficult to distinguish between coherent bedrock and felsenmeer in air photos because exposures are small and discontinuous or

hidden by vegetation. Bedrock is exposed discontinuously at isolated exposures distributed along the length of valley bottoms and in adjacent benches (Fig. 3d). Bedrock outcrop below treeline is likely under-represented in surficial geology mapping because of masking by tree canopy or because exposures are too small to resolve in air photos. Nonetheless, bedrock can occur in mappable features such as modern stream banks, and glaciofluvial meltwater channels, and does occur in the stoss (up-ice) end of crag and tail ridges.

#### 4.2. Till

Till forms a cover of variable thickness in many topographic positions. At lower elevations, tills are commonly part of a thicker sediment package that obscures underlying bedrock topography. Tills are generally thinner on benches elevated above a valley, where surface topography is bedrock controlled. Streamlined tills (e.g., drumlins, flutes, crag and tails) also occur locally in the study area.

Tills in the study area contain subangular to subrounded clasts, typically pebble to cobble sizes (<10% boulders), that are set in a silty-sand matrix that typically ranges from 60 to 65% but can be as low as 20%. A massive, matrix-supported, weakly fissile, and moderately consolidated to overconsolidated variety, interpreted as a subglacial till, can be found throughout the study area (Fig. 4a). These subglacial tills locally form veneers <2 m thick overlying bedrock (Fig. 4b). The tills are commonly olive green, brown, or grey, but iron oxide staining may appear at transitions from tills to overlying B-horizon soils. Iron oxides can be restricted to individual clasts suspended in the till matrix or can be pervasive through the till matrix.

Subglacial tills of the Mesilinka River valley are predominantly sandy even though the valley appears to be underlain by mudrocks of the Takla Group (Ferri et al., 2001). This abundance of sand could represent earlier valley-fill deposits being reworked during Late Wisconsinan glacier advance and then incorporated into these tills. Alternatively, it is conceivable that unmapped crystalline intrusive or other coarse-grained rocks, that could yield sand-sized material, underlie parts of the valley. Quartz diorite rubble in a road cut near the center of Mesilinka River valley, 5 km east of Aiken Lake (Fig. 5), might point to such as yet unmapped bedrock.

Some tills have an undulating or hummocky surface expression (1 to 10 m high, 100s m long). This variety is weakly consolidated and is commonly near or adjacent to hummocky or ridged glaciofluvial sediments in valley bottoms. A sandy, weakly consolidated till is overlain by a poorly sorted, boulder-sized, glaciofluvial gravel north of Aiken Lake (Fig. 4c). We interpret these deposits to have formed by melt-out, either supraglacial or subglacial. East of Aiken Lake, tills at surface have a higher gravel content and larger clasts, but are moderately consolidated (Fig. 4d), possibly indicating subglacial deposition.

#### 4.3. Glaciofluvial

Glaciofluvial sands and gravels occur at surface in most

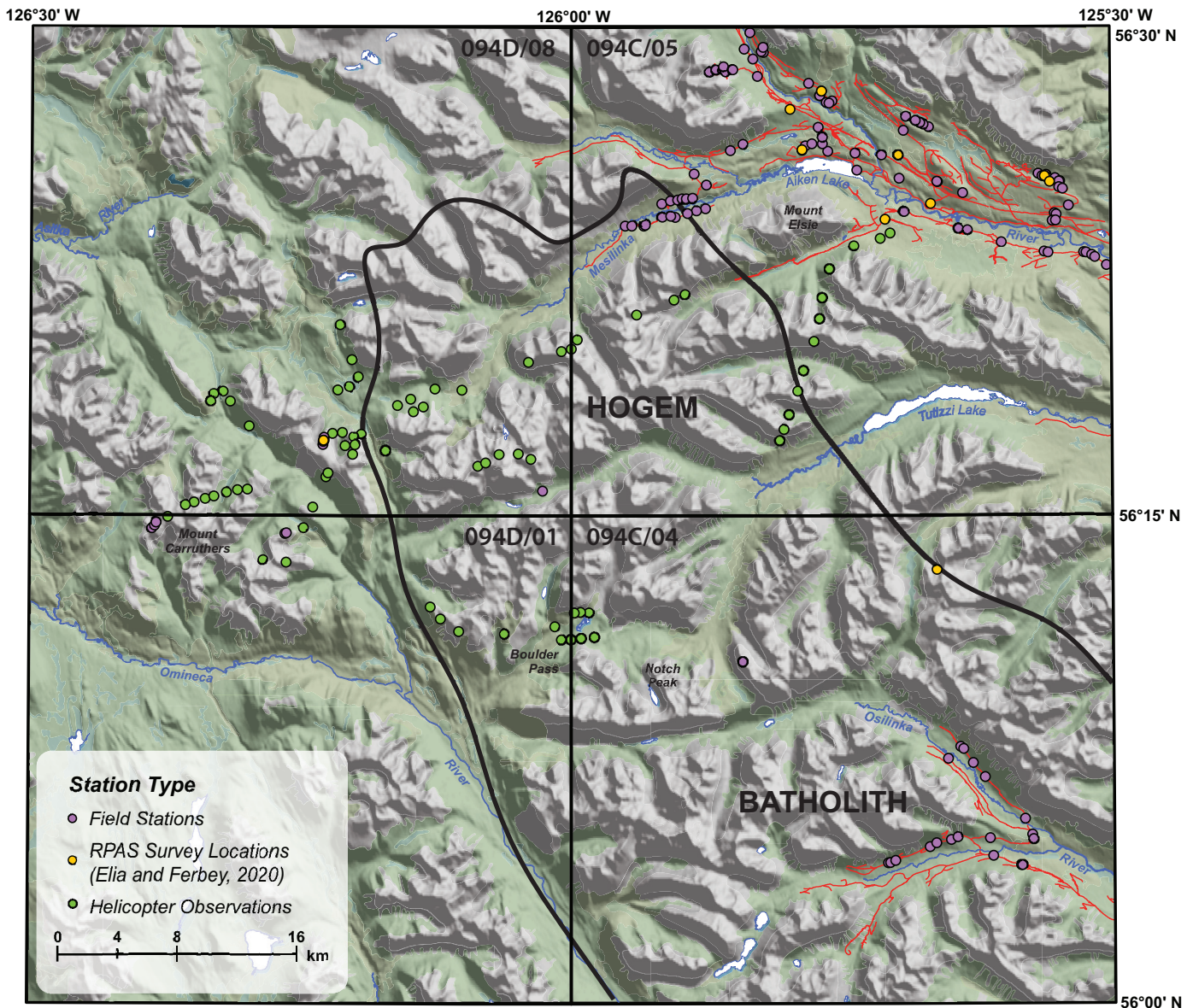


**Fig. 2.** Station types and locations. Field stations are ground observations. RPAS survey locations are where <10 cm/pixel photogrammetric DEMs were produced (see Elia and Ferbey, 2020). Helicopter observations are geolocated photographs taken from the air. The approximate extent of the Hogem batholith is after Ootes et al. (2020b).

valleys of the study area. They can extend the width of narrow, high-elevation valleys, where they are bounded by colluvial slopes, or occupy the central portions of broader valleys where they are commonly flanked by tills. These deposits can be terraced, show a hummocky or ridged (i.e., esker) surface expression, or form outwash plains or fans. Terrace gravels exposed in a 5 m road cut on the north side of Meslinke River valley, near Aiken Lake, are typical for the study area (Fig. 6). Here, a cobble to boulder gravel fines up to a pebble to cobble gravel. The gravels are predominantly clast supported but locally can be matrix supported. The matrix throughout is a silty, medium to coarse sand and clasts are subrounded to rounded. These gravels are massive but in the upper 1.5 m, oblate clasts are weakly imbricated.

#### 4.4. Colluvium

Colluvium blankets (>2 m thick) or veneers (<2 m thick) cover most slopes of this high-relief area. In many instances, these slopes are vegetated and the bedrock- or till-sourced sediment is now stable to metastable. Talus aprons or cones, consisting of loose angular pebbles and boulders accumulating directly below a steep-faced bedrock source, are the most visually prominent gravity deposits. Clasts are self-supporting and may be matrix filled or display an open framework. The lack of vegetation on these slopes indicates that talus is still forming (Fig. 7).

#### 4.5. Organics

Peat and plant material in various stages of decomposition

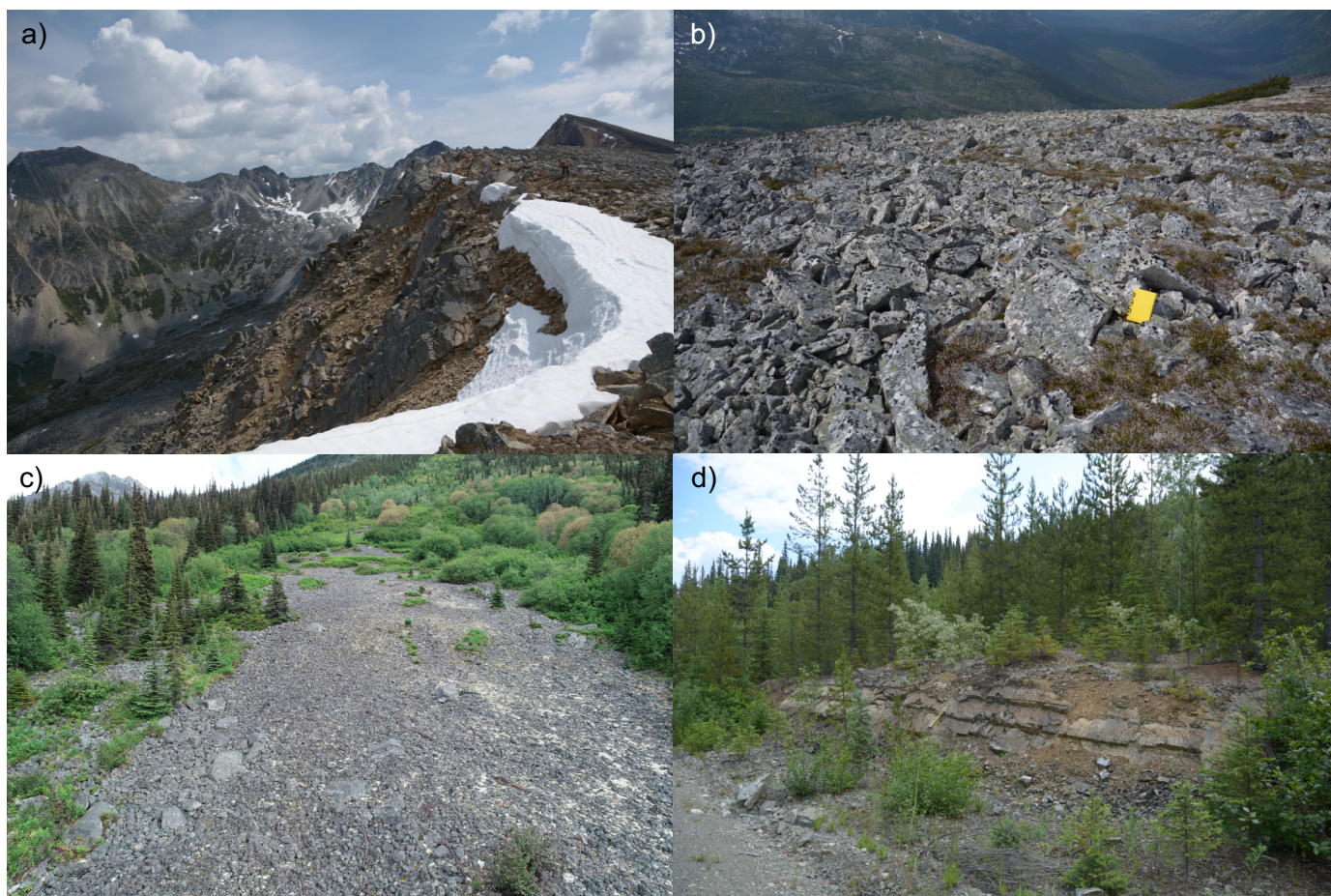


**Fig. 3.** Representative photographs of bedrock exposures. **a)** Granitic ridges of the Osilinka intrusive suite (Late Jurassic; Ootes et al., 2020b), east of Notch Peak. **b)** Felsenmeer at elevation, above immediately subjacent in-situ Osilinka intrusive suite bedrock east of Notch Peak. **c)** Felsenmeer on the southwest-facing slope of the Osilinka River valley above diorite to quartz monzonite of the Thane Creek intrusive suite (Early Jurassic, Ootes et al., 2020b). **d)** A road cut through layered mudrocks mapped by Ferri et al. (2001) as Takla Group (Upper Triassic), east of Aiken Lake on the south side of Mesilinka River valley.

are found along the shorelines of small ponds and lakes and at the margins of low-gradient streams. They form accumulations typically >1 m thick, with a planar surface expression, creating a transition zone (5 to 50 m wide) between tree stands and water bodies. Organic material also occupies the lows in hummocky, undulating, or ridged glaciofluvial terrain, or in the troughs of streamlined tills. The most extensive organic deposits are next to deglacial sands and gravels in the central portion of 094D/08, where they are in well-defined, 100- to 150 m-wide corridors that can continue for 1000s of m. In plan view, these corridors vary from anabranching to dendritic and delineate the floors of glaciofluvial meltwater systems. Today, the corridors are either abandoned or contain underfit streams.

### 5. Ice-flow history

During the most recent Quaternary glaciation (Late Wisconsinan, or marine isotope stage 2, approximately 29 to 11.7 ka), the Cordilleran Ice Sheet covered the study area (Roots, 1954; Ryder and Maynard, 1991; Clague and Ward, 2011). Ice generally flowed through the area towards the east and southeast (Fig. 8) from an ice divide over the Skeena

Mountains, ~100 km to the northwest (Ryder and Maynard, 1991; Clague and Ward, 2011). The ice sheet stage is attained once ice thickness is significantly greater than underlying topography (Kerr, 1934; Davis and Mathews, 1944); ice then flows unconstrained by topography and in the direction dictated by the surface slope of the ice sheet. Field evidence for this ice sheet stage is scarce, but 10 km northeast of Mount Carruthers, on a rounded ridge that forms the eastern boundary of a cirque basin, rat tails at 1750 m ASL are oriented towards 158° (Fig. 9). These glacially eroded features indicate that ice flow was independent of topography and that ice moved up the local slope, towards the cirque headwall. Striation data presented by Ootes et al. (2019b, 2020b), which indicate ice movement across alpine ridges (at 1700 to 2000 m ASL), confirm that the ice sheet stage was achieved in the study area. However, Roots (1954) and Ryder and Maynard (1991) considered that the ice sheet stage in this sector of the Cordilleran Ice Sheet was short lived, which would imply that inter- or cross-valley transport of glacial debris at higher elevations was minimal.

For most of the Late Wisconsinan, topography-controlled glacier flow was typical, as attested to by the well-developed

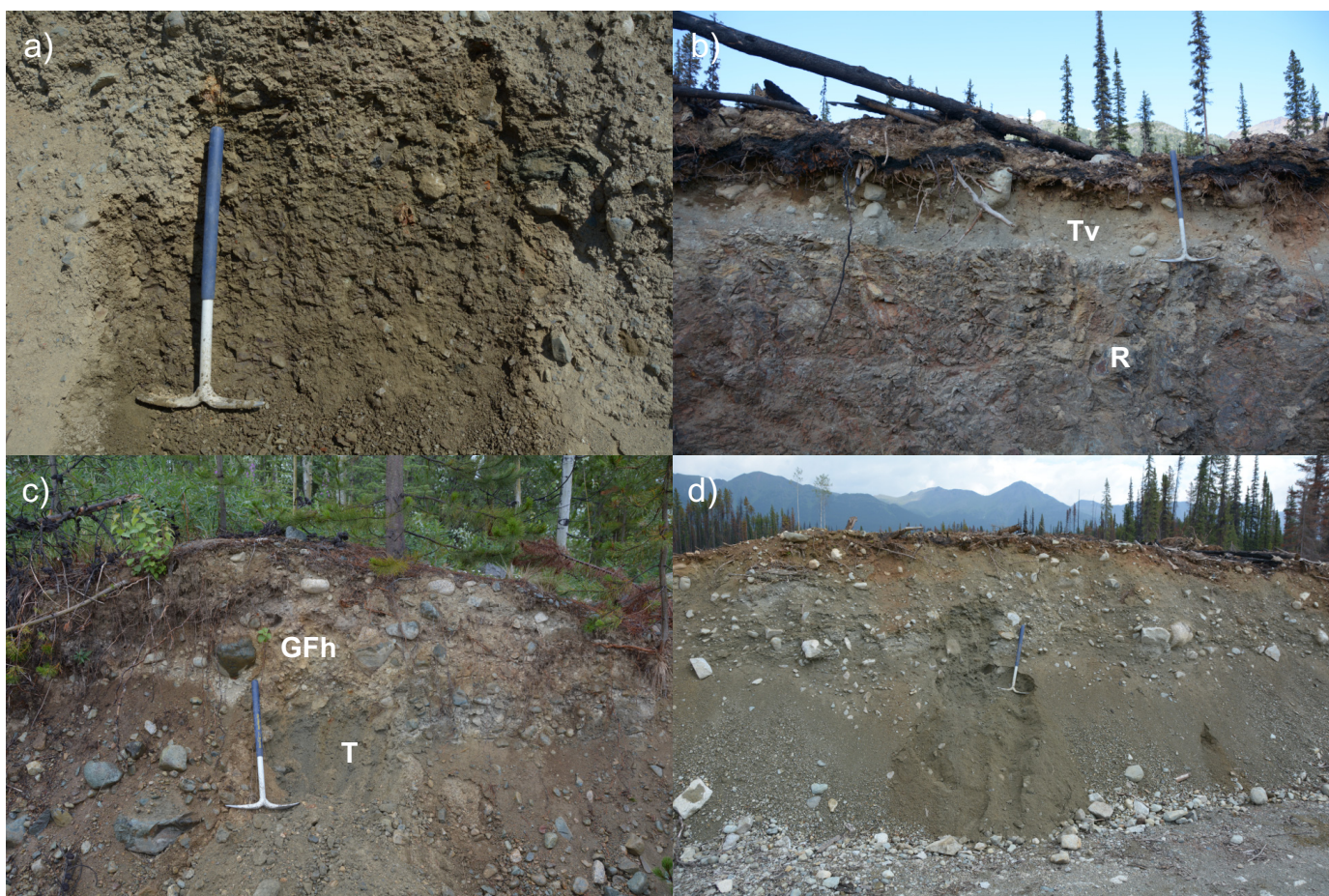


**Fig. 4.** Representative photographs of tills. **a)** A blocky, massive, overconsolidated subglacial till with a silty-sand matrix exposed on the north side of Mesilinka River valley, east of Aiken Lake. **b)** Subglacial till veneer (Tv) overlying Takla Group (Upper Triassic) mudrocks (R) northwest of Aiken Lake. **c)** A sandy, weakly consolidated, meltout till (T) overlain by hummocky glaciofluvial gravels (GFh) north of Aiken Lake. **d)** Moderately consolidated gravelly meltout till east of Aiken Lake.



**Fig. 5.** Angular blocks of quartz diorite of uncertain origin in a road cut east of Aiken Lake might signify that intrusive bodies in the Mesilinka River valley remain unmapped.



**Fig. 6.** Representative glaciofluvial terrace gravels with rounded clasts, east of Aiken Lake.

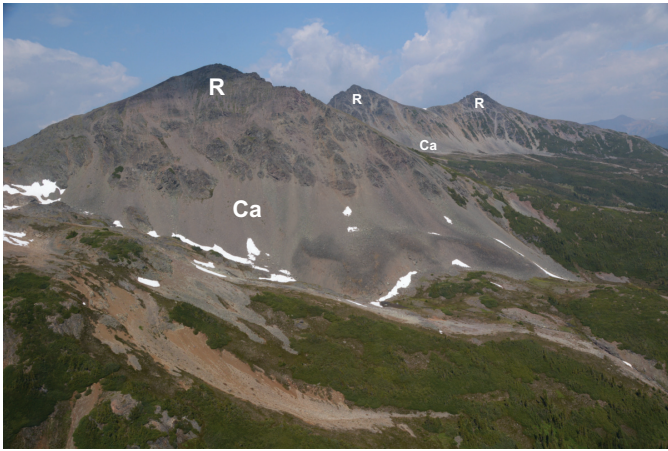
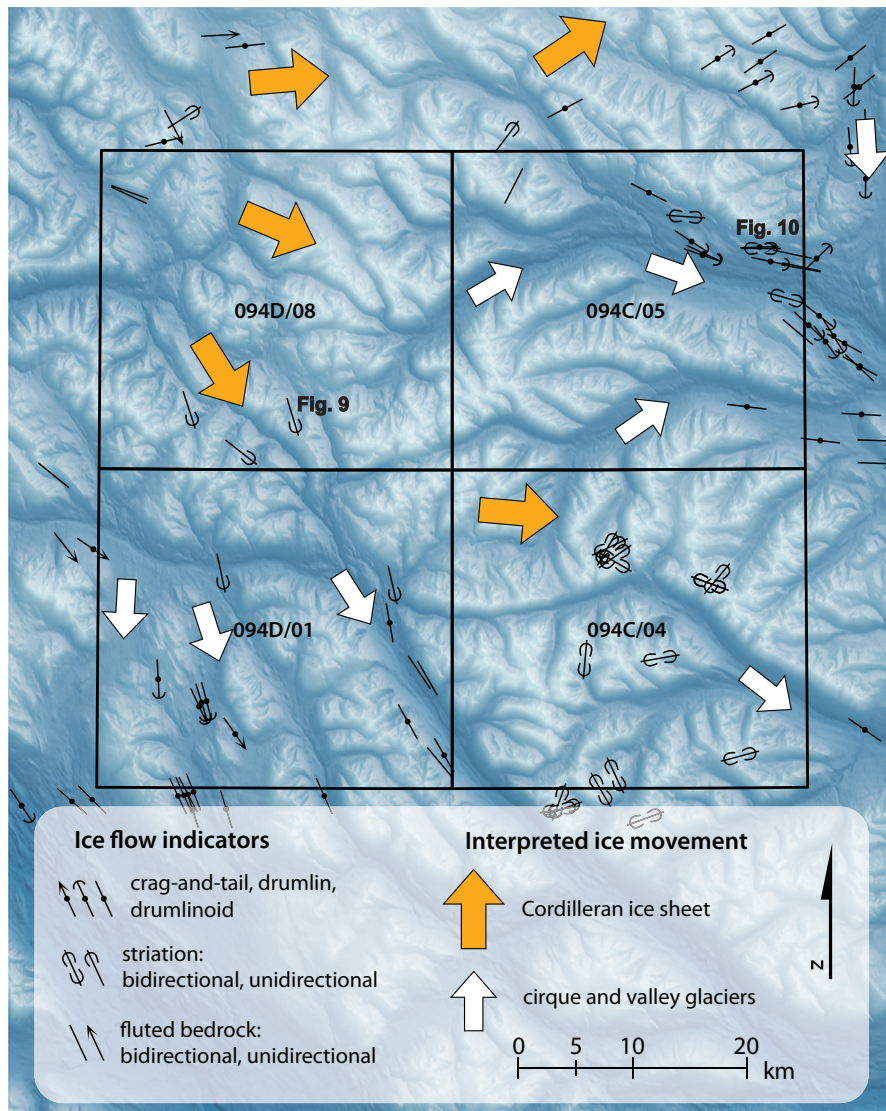


**Fig. 7.** Talus apron (Ca) and bedrock (R) on the north flank of Mount Carruthers.



**Fig. 9.** Rat tails preserved in a mafic lapilli tuff of the Asitka Group (Carboniferous to Permian). The long axes are oriented towards 158° indicating ice flow towards the cirque headwall (see Figure 8 for location).



cirques and arêtes that define the mountains of the northern Hogen batholith area. In valleys, glacially streamlined landforms such as flutes, drumlins, and crag and tail ridges are consistently oriented with valley-parallel long axes (Fig. 8). Well-developed streamlined topography (oriented towards  $095^\circ$ ) occurs in the Mesilinka River valley near the eastern side of 094C/05. Elia and Ferbey (2020) focussed on a subset of crag and tail ridges in this area for their investigation into the utility of high-resolution photogrammetric DEMs in surficial geology mapping (Fig. 10). Although outcrop-scale data like striations, rat tails, and roches moutonnées are sparse (Fig. 8) they agree with the landform record. For example, striations oriented  $259^\circ/079^\circ$  to  $270^\circ/090^\circ$  were observed on a bench on the south side of Mesilinka River valley.

The study area has a reticulate drainage pattern at a regional scale that is defined by an interconnected system of through valleys (Roots, 1954). These U-shaped valleys were cut by valley glaciers and contain subtle drainage divides that are below the treeline (Davis and Mathews, 1944). Modern fluvial systems are constrained by these drainage divides, but valley glaciers during the Late Wisconsinan were not. These glaciers flowed over these subtle divides, transporting glacial debris into neighbouring or adjacent drainages.

## 6. Summary and discussion

The Cordilleran Ice Sheet covered the Hogen batholith area during the Late Wisconsinan glacial maximum. At this time, ice flowed east and southeast through the study area from an ice divide over the Skeena Mountains,  $\sim 100$  km to the northwest. The ice sheet stage was short-lived for this sector of the Cordilleran Ice Sheet, and inter-valley transport of glacial debris at higher elevations was likely minimal. For most of the Late Wisconsinan, ice flow was controlled by topography, as recorded by landform- and outcrop-scale indicators, which are commonly aligned parallel to valleys. However, valley glaciers certainly flowed over subtle through-valley topographic divides (that are now below the tree line), transporting glacial debris into adjacent drainages.

Glaciers deposited subglacial tills as they moved through the study area and hummocky melt-out tills during deglaciation. Although subglacial tills typically have a silty matrix, local sand-rich tills above mudstones in the Mesilinka Valley suggest that pre-glacial sands were glacially reworked and redeposited. Alternatively, the sand-rich tills may reflect nearby, as yet unmapped, crystalline intrusions or other coarse-grained bedrock capable of yielding sand-sized material. Significant volumes of glacial meltwater moved through the

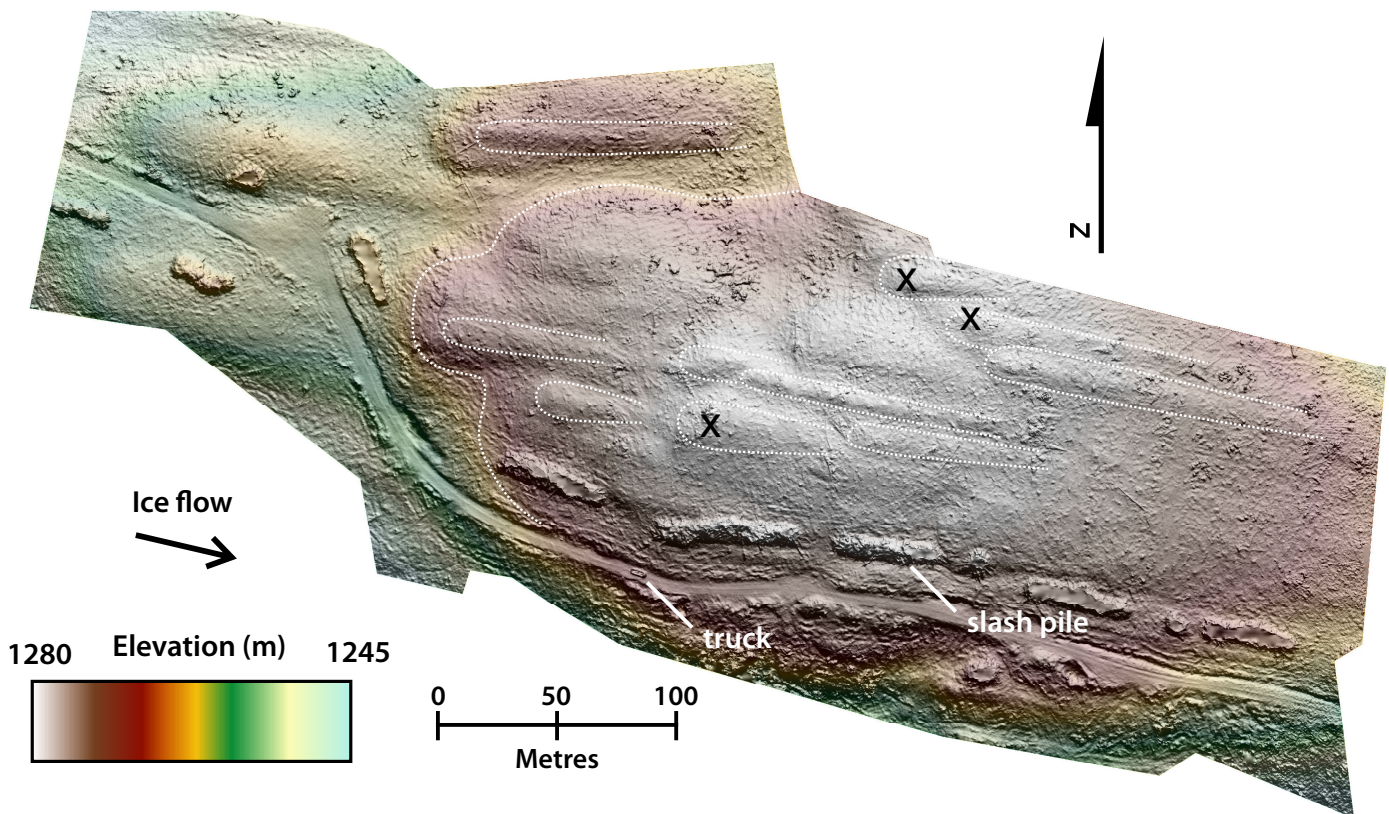


**Fig. 10.** Photogrammetric DEM of crag and tail ridges from the north side of Mesilinka River valley near the eastern boundary of 093C/05 (see Figure 8 for location). This image was generated in the field using a remotely piloted aircraft system imagery (Elia and Ferbey, 2020). These glacially streamlined ridges indicate ice flow towards the east-southeast. Bedrock outcrops observed in the field are identified by 'X'.

valleys of the study area during deglaciation, transporting coarse-grained sands and gravels. Much of this transport and deposition was subaerial (e.g., extensive outwash plains and terraces) but a component was also subglacial (e.g., eskers) or in contact with stagnant ice blocks (e.g., hummocky sands and gravels). Preliminary mapping shows that retreat-phase glaciolacustrine sediments in valley bottoms are conspicuously absent. Although some valley slopes are now vegetated and are stable, many are still actively building talus aprons and cones. Organic deposits occur throughout the study area, mostly as a transition zone between tree stands and water bodies. These deposits are also in well-defined and continuous anabranching to dendritic corridors that delineate retreat-phase glaciofluvial meltwater systems.

From a mineral exploration perspective, drift prospecting is a viable tool for assessing mineral potential in the study area. Subglacial till, the ideal sample medium for till geochemistry and mineralogy surveys, is common in valley bottoms and lower hillslopes. This glacially transported sediment is most easily observed along existing road and stream cuts but could also be sampled in hand-dug pits. Bedrock exposures are not limited to higher elevation or alpine sites. Local, discontinuous bedrock outcrop is common in valley bottoms and on hill flanks and direct prospecting and mapping are possible. Below treeline, bedrock exposures can be difficult to predict and so are typically underrepresented in surficial geology mapping. However, outcrops can be found in mappable features such as modern stream banks and glaciofluvial meltwater channels, and are found in the stoss (up-ice) ends of crag and tail ridges.

### Acknowledgments

We thank I. Grady (IGI Consulting Ltd.) for generating mapping-ready digital air photos and the Abraham family for accommodation. L. Ootes and D. Milidragovic are thanked for their insights into the bedrock geology of the Hogen batholith area. A review by A.S. Hickin improved the manuscript.

### References cited

- Arnold, H., Ferbey, T., and Hickin, A.S., 2016. Ice-flow indicator compilation, British Columbia and Yukon. British Columbia Ministry of Energy, Mines and Petroleum Resources, British Columbia Geological Survey Open File 2016-04, Geological Survey of Canada Open File 8083, scale 1:1,750,000.
- Armstrong, J.E., and Roots, E.F., 1954. Aiken Lake, Cassiar district, British Columbia. Geological Survey of Canada, Map 1030A, scale 1:253,440.
- Bobrowsky, P., and Rutter, N.W., 1992. The Quaternary geologic history of the Canadian Rocky Mountains. *Géographie physique et Quaternaire*, 46, 5-50.
- Clague, J.J., and Ward, B.C., 2011. Pleistocene Glaciation of British Columbia. In: Ehlers, J., Gibbard, P.L., and Hughes, P.D., (Eds.), *Developments in Quaternary Science*, 15, Amsterdam, pp. 563-573.
- Davis, N.F.G., and Mathews, W.H., 1944. Four phases of glaciation with illustrations from southwestern British Columbia. *Journal of Geology*, 52, 403-413.
- Elia, E.A., and Ferbey, T., 2020. Generating photogrammetric DEMs in the field from remotely piloted aircraft systems. In: *Geological Fieldwork 2019*, British Columbia Ministry of Energy, Mines and Petroleum Resources, British Columbia Geological Survey Paper 2020-1, pp. 189-200.
- Ferri, F., Dudka, S.F., Rees, C., and Meldrum, D., 2001. Geology of the Aiken Lake area, north-central British Columbia, NTS 94C/5, 6 and 12. British Columbia Ministry of Energy, Mines and Petroleum Resources, British Columbia Geological Survey Geoscience Map 2001-10, scale 1:50,000.
- Holland, S.S., 1976. Landforms of British Columbia: A physiographic outline. British Columbia Ministry of Energy, Mines and Petroleum Resources, Bulletin 48, 138 p.
- Jones, G., Ootes, L., Milidragovic, D., Friedman, R., Camacho, A., Luo, Y., Vezinet, A., Pearson, D.G., and Schiarizza, P., 2021. Geochronology of northern Hogen batholith, Quesnel terrane, north-central British Columbia. In: *Geological Fieldwork 2020*, British Columbia Ministry of Energy, Mines and Low Carbon Innovation, British Columbia Geological Survey Paper 2021-01, pp. 37-56.
- Kerr, F.A., 1934. Glaciation in northern British Columbia. *Royal Society of Canada, Transactions*, 28, 17-31.
- Margold, M., Jansson, K.N., Kleman, J., Stroeven A.P., and Clague, C., 2013. Retreat pattern of the Cordilleran Ice Sheet in central British Columbia at the end of the last glaciation reconstructed from glacial meltwater landforms. *Boreas*, 42, 830-847.
- Ootes, L., Bergen, A., Milidragovic, D., Graham, B., and Simmonds, R., 2019a. Preliminary geology of northern Hogen batholith, Quesnel terrane, north-central British Columbia. In: *Geological Fieldwork 2018*, British Columbia Ministry of Energy, Mines and Petroleum Resources, British Columbia Geological Survey Paper 2019-01, pp. 31-53.
- Ootes, L., Bergen, A.L., Milidragovic, D., and Graham, B., 2019b. Bedrock geology of Notch Peak and Ogden Creek (parts of NTS 094C/04 and 093N/13), northern Hogen batholith, Quesnel terrane, north-central British Columbia. British Columbia Ministry of Energy, Mines and Petroleum Resources, British Columbia Geological Survey Open File 2019-02, scale 1:50,000.
- Ootes, L., Bergen, A.L., Milidragovic, D., Jones, G.O., Camacho, A., and Friedman, R., 2020a. An update on the geology of northern Hogen batholith and its surroundings, north-central British Columbia. In: *Geological Fieldwork 2019*, British Columbia Ministry of Energy, Mines and Petroleum Resources, British Columbia Geological Survey Paper 2020-01, pp. 25-47.
- Ootes, L., Bergen, A.L., Milidragovic, D., and Jones, G.O., 2020b. Bedrock geology of northern Hogen batholith and its surroundings, north-central British Columbia. British Columbia Ministry of Energy, Mines and Petroleum Resources, British Columbia Geological Survey Open File 2020-02, scale 1:50,000.
- Plouffe, A., 2000. Quaternary geology of the Fort Fraser and Manson River map areas, central British Columbia. *Geological Survey of Canada, Bulletin* 554, 62 p.
- Roots, E.F., 1954. Geology and mineral deposits of Aiken Lake map-area, British Columbia. Geological Survey of Canada, *Memoir* 274, 246 p.
- Rutter, N.W., 1974a. Surficial geology and landforms of Williston Lake area (map 1), British Columbia. Geological Survey of Canada, Map 1381A, scale 1:125,000.
- Rutter, N.W., 1974b. Surficial geology and landforms of Williston Lake area (map 2), British Columbia. Geological Survey of Canada, Map 1382A, scale 1:125,000.
- Ryder, J.M., and Maynard, D., 1991. The Cordilleran Ice Sheet in northern British Columbia. *Géographie physique et Quaternaire*, 45, 355-363.

# Volcanism and geochemistry of the Kamloops Group, south-central British Columbia



Van Wagoner, N.<sup>1</sup>, Ootes, L.<sup>2</sup>, and Thomson-Gladish, J.<sup>1,3</sup>

<sup>1</sup>Thompson Rivers University, Department of Earth Sciences, Kamloops, BC, V2C 0C8

<sup>2</sup>British Columbia Geological Survey, Ministry of Energy, Mines and Low Carbon Innovation, Victoria, BC, V8W 9N3

<sup>3</sup>Archer, Cathro & Associates (1981) Limited, 1016-510 West Hastings Street, Vancouver, BC, V6B 1L8

<sup>a</sup>corresponding author: Luke.Ootes@gov.bc.ca

Recommended citation: Van Wagoner, N., Ootes, L., and Thomson-Gladish, J., 2021. Volcanism and geochemistry of the Kamloops Group, south-central British Columbia. In: Geological Fieldwork 2020, British Columbia Ministry of Energy, Mines and Low Carbon Innovation, British Columbia Geological Survey Paper 2021-01, pp. 65-88.

## Abstract

The Challis-Kamloops belt (early Eocene) includes graben-fill volcanic and sedimentary rocks that extend for about 2000 km from Challis in Idaho to central British Columbia and possibly, into southern Yukon. Mapping and sampling of the Kamloops Group in the south-central part of the belt indicates subaerial to subaqueous (lacustrine) volcanism, with volcanic facies in the type area including mega pillows, hyaloclastites, pahoehoe and aa flows, domes and phreatomagmatic cones. New geochemical data indicate that the rocks are calc-alkaline to weakly alkaline basaltic andesite to trachy-andesite, with adakitic characteristics. The major element compositions are influenced primarily by fractionation of pyroxene and olivine. The chondrite-normalized REE patterns are uniform and LREE-enriched, with relatively flat HREE patterns. The rocks have primitive mantle-normalized trace element patterns that are arc-like with positive LILE and negative HFSE anomalies. A preliminary comparison of Kamloops Group geochemistry (new and previously published data), and published data from other Eocene units (Princeton and Pentiction groups) of the Challis-Kamloops belt in south-central British Columbia indicates distinct geographic differences. The Kamloops and Princeton group melts may have been derived from the spinel-garnet transition zone in the subcontinental lithospheric mantle and influenced by slab-derived fluids, whereas the Pentiction Group shows trends toward anhydrous enrichment and may have been derived from a different source. Among the three groups there is a lateral decrease in Ba/La from west to east reflecting a declining intensity of slab-derived fluids from an Eocene subducting margin.

**Keywords:** Eocene, Kamloops Group, volcanic rocks, physical volcanology, geochemistry

## 1. Introduction

The Challis-Kamloops belt (Eocene) is a narrow (<200 km) discontinuous belt of graben-fill volcanic and sedimentary rocks that extends for about 2000 km from the Challis volcanic field in Idaho through central British Columbia and possibly as far north as southern Yukon (e.g., Dostal et al., 2001, 2003, 2019; Bordet et al., 2014). In different parts of British Columbia these rocks have been referred to by different group-level names (Fig. 1; Kamloops, Pentiction, Princeton, Ootsa Lake, Endako, Nechako Plateau, and Sloko); in southwest Yukon, the term Skukum volcanic complex is used (e.g., Morris and Creaser, 2003). Magmatism in the belt continued from ca. 56 Ma (Ypresian) to ca. 47 Ma (Lutetian; e.g., Love et al., 1998; Bordet et al., 2014). Mineralization spatially and/or temporally associated with this magmatism includes local occurrences of porphyry Cu-Mo, epithermal-Au, coal, concentrations of REE, zeolite deposits, and aggregate (e.g., Love et al., 1998). The volcanism coincides with the Early Eocene Climatic Optimum (Smith et al., 2010; Zachos et al., 2001, 2008) and may have affected local if not regional to global climate.

The present study is part of a province-wide investigation of the Challis-Kamloops belt intended to better understand the drivers of Eocene volcanism and the relationships between

volcanism, mineralization, and climate. We focus on the Kamloops Group, in the interior of south-central British Columbia (Fig. 1). Previous studies indicated that Kamloops Group volcanic rocks are mostly subaerial and lacustrine basalt to andesite flows, with lesser felsic volcanic and sedimentary rocks (Ewing, 1981a, b, c and 1982; Breitsprecher, 2002; Breitsprecher et al., 2003). Herein we present the preliminary results of mapping and sampling to more fully document the physical volcanology and geochemistry of the Kamloops Group in its type area, and to compare the geochemistry of the Kamloops Group to that of the Princeton and Pentiction groups nearby.

## 2. Setting and previous work

Magmatism in the Challis-Kamloops belt was during northeast-southwest extension of the Cordilleran orogen, which resulted in the generation of semi-isolated grabens that accumulated sedimentary and volcanic rocks (e.g., Ickert et al., 2009). Various drivers have been suggested for the volcanism, including normal arc volcanism (Morris and Creaser, 2003), subduction angle migration and plate rotation (Haeussler et al., 2003), magmatism related to a slab-tear (Breitsprecher et al., 2003; Dostal et al., 2001, 2003, 2008, 2019; Madsen et al.,

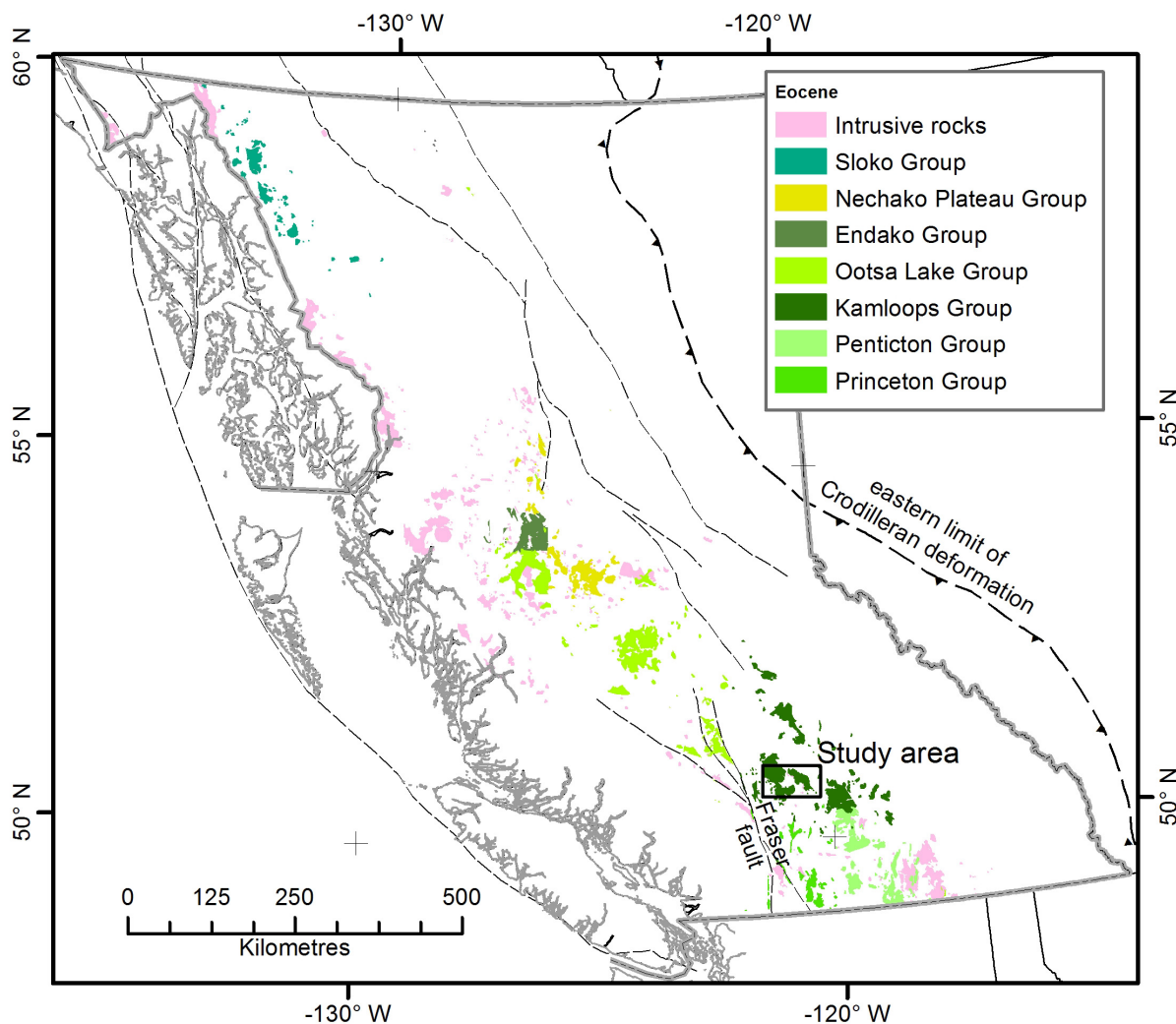


**Fig. 1.** Distribution of Eocene (ca. 56 to 47 Ma; Ypresian to Lutetian) volcanic and intrusive rocks of the Challis-Kamloops belt in British Columbia and location of study area. Grey dashed lines are Eocene dextral strike-slip faults.

2006; Ickert et al., 2009), plume-induced subduction initiation (Stern and Dumitru, 2019), and subduction termination and development of a slab gap (Bordet et al., 2014).

The Kamloops Group is an assemblage of Ypresian (ca. 52 Ma) volcanic and lesser sedimentary rocks exposed from between Cache Creek eastward to Kamloops and extending 5-10 km to the north and south (Fig. 2). The rocks mostly overlie Mesozoic basement of the Quesnel terrane with some in the east overlying North American basement. The Fraser fault (dextral strike slip) separates the Kamloops Group from the Ootsa Lake and Endako groups to the northwest (Fig. 1; e.g., Dostal et al., 2001; Bordet et al., 2014). As will be discussed further below (section 5.3.), the boundary between the Kamloops Group and the Princeton and Pentiction groups is arbitrary.

The most comprehensive studies of the Kamloops Group were by Ewing (1981a, b, c; 1982) and Breitsprecher (2002). Ewing (1981a, b, 1982) divided the Kamloops Group in its type area into the Tranquille Formation comprising the Border facies and the informal upper, middle, and lower members and the

overlying Dewdrop Formation, subdivided into nine informal members (Fig. 3). Ewing (1982) produced a 1:50,000-scale map of the type area. Ewing (1981a, b) also contributed more detailed maps of the Savona area and the McAbee fossil beds (Tranquille Formation), a British Columbia Heritage site. Breitsprecher (2002) completed local mapping in eastern exposures of the Kamloops Group and, along with Dostal et al. (2019) contributed geochemical data.

Previous mapping indicated that the Tranquille Formation comprises lacustrine to deltaic coarse arkosic-lithic wackes (Border facies), shale, tuffaceous siltstone, and tuffs that are interbedded with flows, pillowed flows and hyaloclastites (Ewing, 1981a, b; 1982). The McAbee fossil beds, included within the Tranquille Formation, contain abundant flora and fauna (e.g., Smith et al., 2010; Greenwood et al., 2005; Lowe et al., 2018a, b; Mayr et al., 2019) and have been included in the Okanagan Highlands *Lagerstätten* (Archibald et al., 2011). This *Lagerstätten*, is significant because it provides a record of the paleoecology and climate of the region during the Early

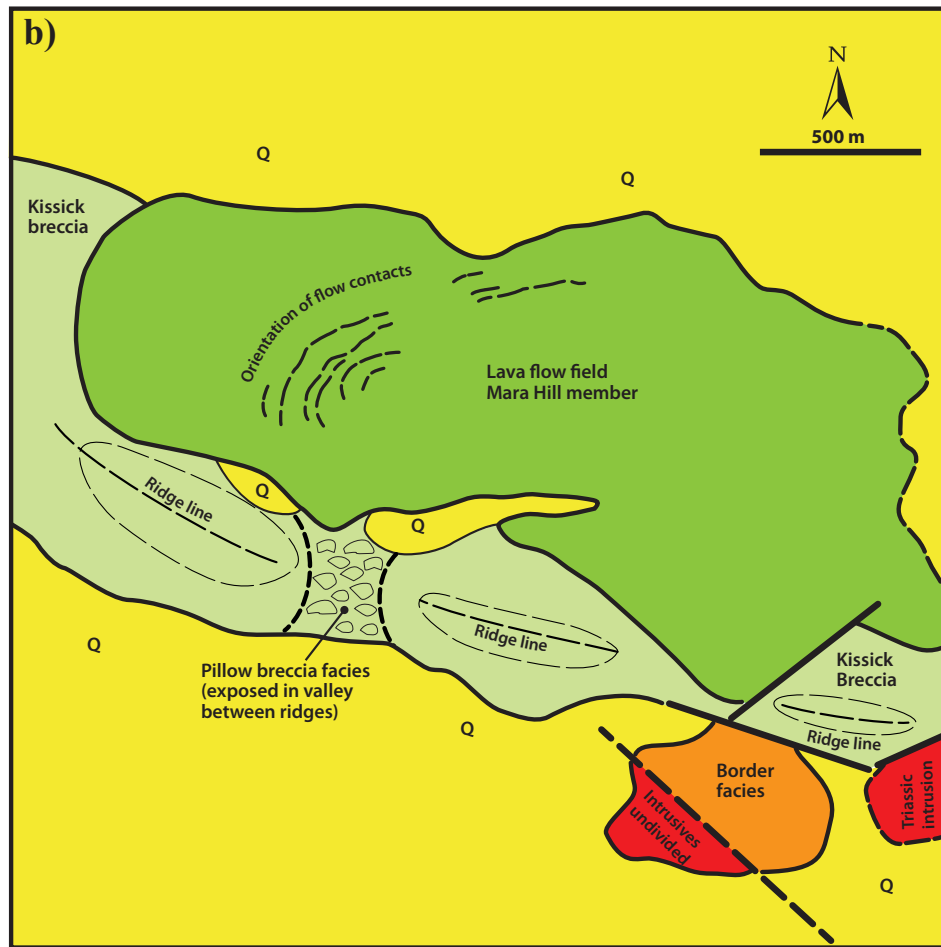
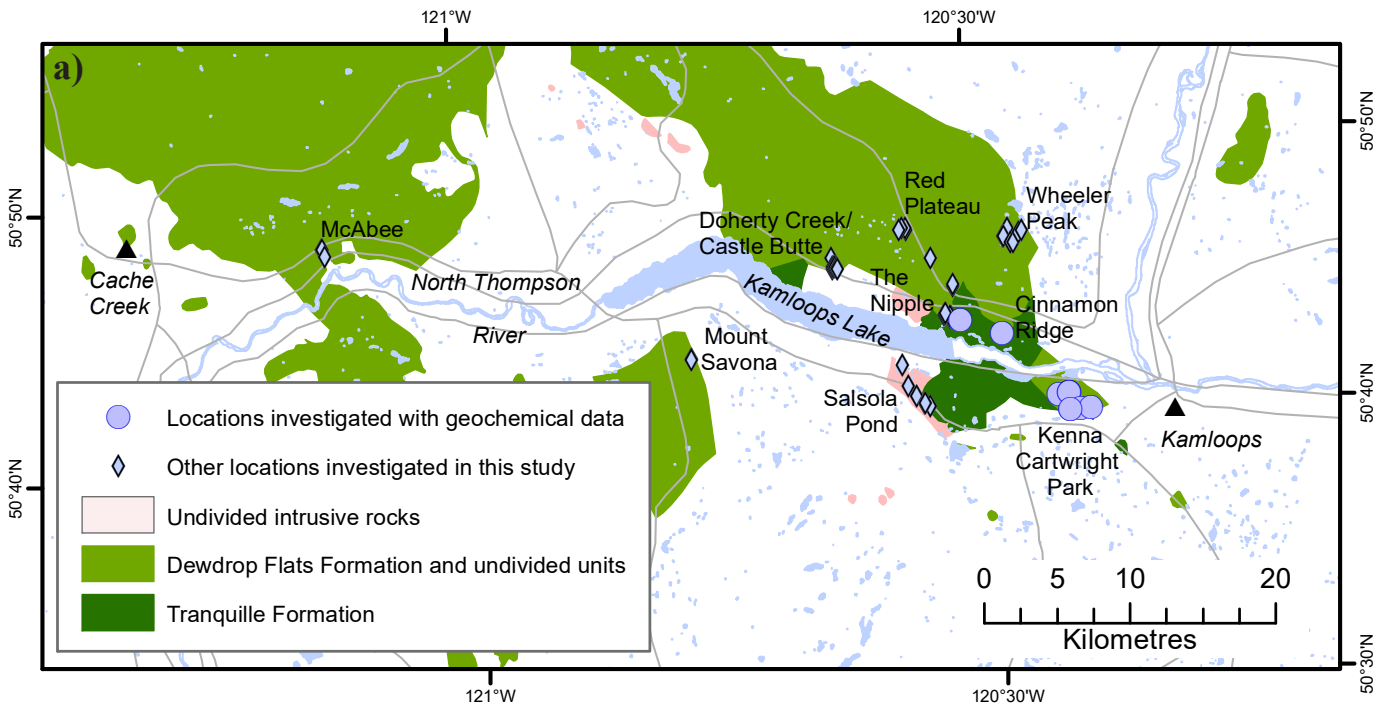


**Fig. 2. a)** Distribution of volcanic and intrusive rocks of the Kamloops Group, west of the City of Kamloops. Blue circles are locations examined in 2019 with geochemical data presented herein. Blue diamonds are locations examined in 2020. **b)** Sketch map of Kenna Cartwright Park showing the distribution of different rock units and topographic features. Q – Quaternary sediments. Modified from Ewing (1982).

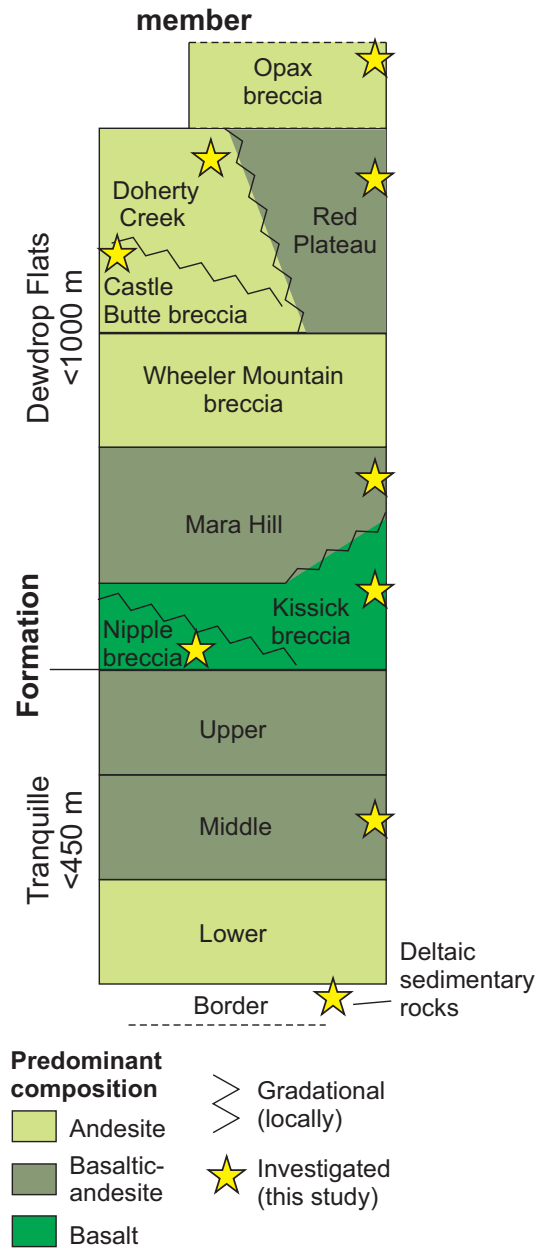


**Fig. 3.** Generalized stratigraphy of the Kamloops Group (simplified after Ewing, 1981a).

Eocene Climactic Optimum (Archibald et al., 2011; Greenwood et al., 2016; West et al., 2020). Ewing (1981a, b) correlated the McAbee beds to the “upper unit” of the Tranquille Formation based on their similar rock types. These beds were since ascribed to an unnamed member of the Tranquille Formation (Read and Hebda, 2009). The Dewdrop Formation is predominantly basaltic to andesitic sub-lacustrine to subaerial flows, flow breccias, cones, tuff rings and a composite cone (Ewing, 1981a, 1982).

**3. Field investigations of physical volcanology**

The map and field descriptions of the type area of the

Kamloops Group by Ewing (1981a, b, 1982) were used as a basis for this sampling program. In general, the rocks are well exposed in much of the area, and primary structures are well preserved, but units are laterally discontinuous and informal members of the Tranquille and Dewdrop formations include a variety of volcanic facies. The coherent flows and intrusions tend to be more resistant than the fragmental units, which tend to be more recessive and form soil-covered slopes. With the exception of volcanic glasses that have been altered to palagonite, alteration is minimal. Our sampling focussed on two parts of the Kamloops Group type area, Kenna Cartwright Park, which is underlain by the Border facies of the Tranquille Formation and the Mara Hill and Kissick members of the Dewdrop Flats Formation, and Cinnamon Ridge exposures of the middle member of the Tranquille Formation. We also examined rocks of the Kamloops Group at the Nipple, Doherty Creek/Castle Butte, Red Plateau, Wheeler Peak, Mount Savona, and McAbee localities (Fig. 2).

**3.1. Kenna Cartwright Park**

**3.1.1. The Lava flow field; Mara Hill member, Dewdrop Flats Formation**

The portion of Kenna Cartwright Park mapped by Ewing as the Mara Hill member of the Dewdrop Flats Formation (Figs. 2, 3; Ewing, 1981a, 1982) comprises a section of stacked subaerial pahoehoe flows about 210 m thick covering an area of about 2.5 km<sup>2</sup>. These flows are overlain by Quaternary sediments to the north and interfinger with monolithic basaltic breccias of the Kissick member to the south (Fig. 2b). Individual flows are 1.5 to 3 m thick, but pahoehoe toes are as thin as few cm to 10 to 20 cm, with glassy chill margins 1 to 5 cm thick (Fig. 4a). Flows are aphyric to sparsely plagioclase phyric and are sparsely vesicular (ca. 5%), with flow-aligned vesicles (2-4 cm long), and vesicle trails at the lower third of some of the thicker flows. However, some flow tops and individual flows are highly vesicular (20-30%) with spherical vesicles up to 3-4 cm in diameter. Flow features are remarkably well preserved and include small tumuli, lava tubes, pahoehoe toes, and ropy pahoehoe surfaces (Fig. 4). The concentration of these features at the top of the sequence may indicate a decline in the lava supply rate and transition to tube-fed flows (e.g., Anderson et al., 2012), or be a function of exposure.

Other lava flows are south of the Lava flow field and separated from it by outcrops of Kissick breccia and a west-northwest trending fault. Ewing (1981a) considered these flows as possibly being part of the Border facies, the unit at the base of the Tranquille Formation (Figs. 2b, 3). These lava flows are aphyric, to sparsely pyroxene and plagioclase microphyric, and massive to sparsely vesicular.

**3.1.2. Kissick breccia member andesitic breccias, Dewdrop Flats Formation**

The Kissick breccia member of the Dewdrop Flats Formation (Ewing, 1981a, 1982) forms an east-west trending ridge south of, and in contact with, the Lava flow field (Fig. 2b), where

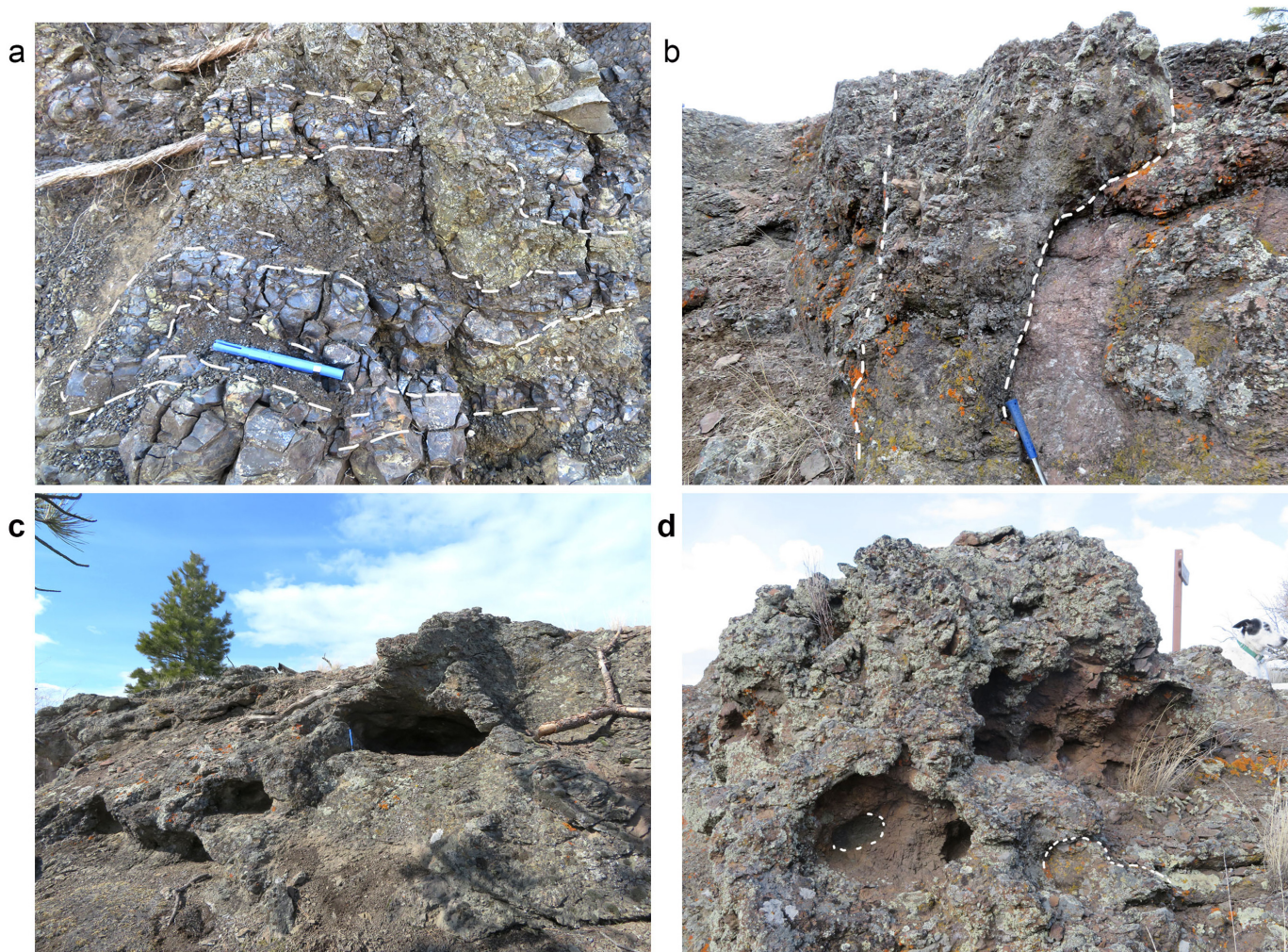


**Fig. 4.** Kenna Cartwright Park, flow features of the Lava flow field (the Mara Hill member, Dewdrop Flats Formation. **a**) Thin pahoehoe toes with vitric margins (outlined) and aphanitic interiors. The eraser tube, set inside one of the pahoehoe toes, is 13 cm long. **b**) Synvolcanic dike, or squeeze-up through a lava flow. Hammer handle is 28 cm. **c**) Drain-away tubes with a small tumulus at the top of a thick pahoehoe flow. **d**) Intermingling flow toes showing drain-away features; a budding tube or toe on the right and a filled tube inside of a larger cavity on the left. The cavity on the lower left is about 30 cm in diameter.

andesitic breccias occur stratigraphically above and below the flows. All of the breccias are monolithic but they differ in terms of volcanic structures and textures.

Where the breccia is beneath the lava flows (Fig. 2b) it is a monolithic pillow breccia, comprising bulbous pillow forms up to 40 cm (Figs. 5a-c) with partial chill margins that are brecciated such that fragments are only slightly separated and display a jig-saw fit. These broken pillow forms are mixed with a hyaloclastite of more blocky fragments ranging from a few mm to about 30 cm that appear to have been remobilized during and following fracturing (Figs. 5b, c). The breccias are clast-supported with a matrix of finer, mostly angular fragments. Beds, 0.5-1 m thick, display vague bedding defined by the alignment of elongate larger broken to more intact pillow fragments (Fig. 5a), with primary dips of about 20°. We interpret these breccias immediately beneath the Lava flow field constitute a lava-fed lacustrine delta, primarily on the

basis of the elongation and fracturing of some of the pillow-like forms, depositional dips, mix of remobilized and jig-saw fit breccias, and general similarity with deposits that have been described elsewhere (Skilling, 2002). The combination of in-situ brecciation, as indicated by the jig-saw fit of some clasts, and chaotic fragmentation and beds with primary dips suggests deposition at the topset to foreset transition. Conceivably, flows from the immediately overlying part of the Lava flow field prograded over these breccias.

Breccias above the Lava flow field at higher elevations on the ridge, are a monolithic mix of agglutinate (appearing to be deposits of more plastic ejecta) along with more angular breccias. Overall, this andesitic breccia is sparsely vesicular and aphyric, or sparsely plagioclase phyrlic. The breccias are massive, clast supported and poorly sorted with clast size ranging from 1 to 2 m in diameter down to coarse ash. Locally, hackly fractured lava bodies are surrounded by more coherent

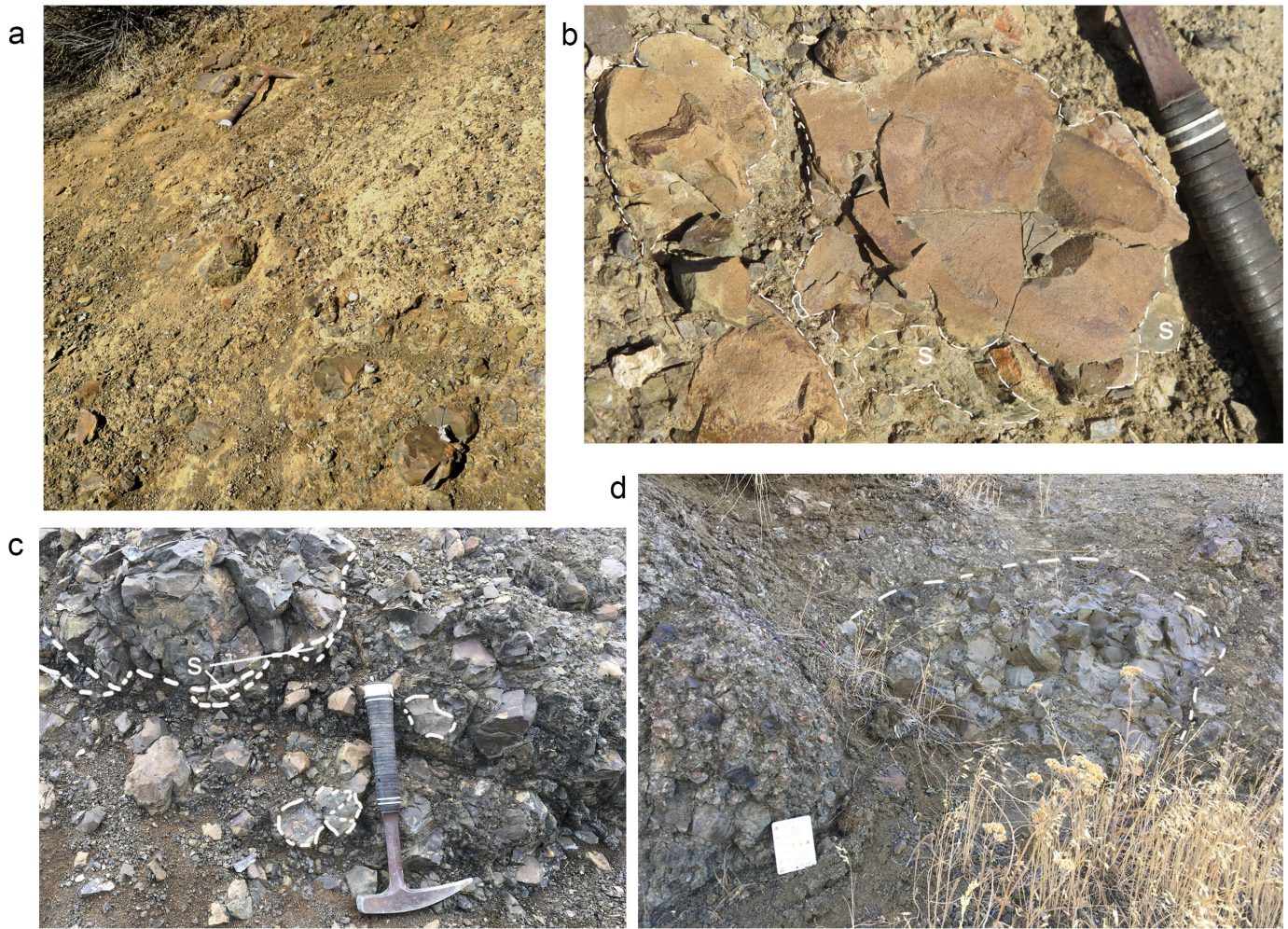


**Fig. 5.** Kenna Cartwright Park, andesitic breccias and pillow breccias of the Kissick Formation (Dewdrop Flats Formation). **a)** Lower part of Kissick Formation, monolithic pillow breccias comprising spherical and broken andesitic pillow fragments in a poorly sorted matrix of angular fine ash to block (10-15 cm) vitric and aphanitic fragments with curvilinear margins. Vague bedding (from upper right to lower left) is defined by alignment of larger and more intact pillow fragments. **b)** Lower part of Kissick Formation, a larger pillow broken into polyhedral blocks as a result of quench fragmentation and remobilized following fragmentation, as indicated by the separation along the cracks. A portion of the formerly glassy selvage (S) remains attached though most spalled off during fragmentation. **c)** Lower part of Kissick Formation, broken pillow in the upper left with partial selvage (S) in a hyaloclastite matrix, as described in a). The two smaller fragments are outlined to show the curvilinear margins and jigsaw fit of fragments. **d)** Upper part of Kissick Formation, andesitic flow lobe (outlined) internally broken into polyhedral blocks likely as a result of rapid cooling in contact with water, surrounded by a cogenetic monolithic breccia, similar to a) and c) but also containing a mix of both angular and bulbous forms, and non-vesicular to highly vesicular fragments; card is 9 cm long.

but internally fractured lava forming large pods up to 3-4 m long and 1-2 m thick. Surrounding monolithic breccias are similar to those elsewhere in the sequence but contain minor amounts of finer particles and are a mix of non-vesicular to highly vesicular fragments (Fig. 5d). Although glassy margins were not observed, the combination of deposit types resembles those formed along modern shorelines where aa flows enter a standing body of water (Yamagishi, 1991; Stevenson et al., 2012). These breccias may represent a combination of phreatic fragmentation, possibly from rootless cones, autobreccias, and hydroclastic fragmentation (e.g., Walker, 1992; Reynolds et al., 2015).

### 3.2. Cinnamon Ridge pillowed flows and hyaloclastite (Middle member, Tranquille Formation)

Pillowed flows are well exposed at Cinnamon Ridge north of the Thompson River in the Tranquille River canyon, and a canyon east of the Tranquille River (Fig. 2a). The flows form resistant mounds and hillside outcrops of closely packed pillows of various morphologies which grade laterally and vertically (in places) to abundant monolithic and altered hyaloclastite breccia. The hyaloclastites weather more easily and form gentler slopes.

The pillows are primarily aphyric and up to 2.5 m in diameter, with the large size possibly indicating high lava

fluxes (e.g., Hungerford et al., 2014). The pillows display two morphologies. In one variety, bulbous to spherical pillows become smaller upsection (Fig. 6a) and exhibit corrugated surfaces formed by expansion of the pillow after formation of the crust (Fig. 6b; see Yamagishi, 1987; Goto and McPhie, 2012), a feature that is more common in higher viscosity lavas, which cause the crust to break rather than expand with inflation (Walker, 1992). These pillows are solid, lacking central cavities, and exhibit a concentric structure defined by variations in colour and grain size (Fig. 6c). The spherical pillows are directly overlain by a thick (approximately 3 m) massive lava flow, lacking basal brecciation, suggesting either very high lava flux, or sudden draining of the lake in which the pillows formed. In the other variety, pillows are tubular and display more elliptical cross sections. These elliptical pillows exhibit radial fractures and are both filled and hollow with horizontal shelves reflecting significant inflation followed by drainage (Fig. 6d; see e.g., Hungerford et al., 2014). In both varieties, palagonitic former glassy pillow margins are well preserved, and there is little inter-pillow hyaloclastite (Figs. 6c, d).

The hyaloclastite comprises angular fine- to coarse-lapilli that were formerly glassy and now altered to palagonite, in a matrix of clays formed by alteration of the hyaloclastite. This type of hyaloclastite is formed by quench fragmentation of effusively erupting lava encountering water (e.g., Yamagishi, 1987). The field relationships indicate that the hyaloclastites are spatially and temporally related to the pillows and likely formed about the same time due to quench fragmentation of pillowed flows.

### 3.3. The Nipple

#### 3.3.1. Nipple breccia, Dewdrop Flats Formation

At the type locality, north of the east side of Kamloops Lake (Fig. 2), the Nipple volcanic breccias (Fig. 7; Ewing, 1981a), are exposed in a belt 0.25-1.5 km wide, and 3.5 km long, trending roughly N10°E with a cone-shaped edifice about 300 m in diameter near the northern extent of the exposure (the Nipple). These breccias are the most mineralogically and texturally distinct rocks in the area. In general, they are olivine and pyroxene phyric (3-15%, mostly 2-3 mm, but up to 1 cm) with plagioclase microlites (1-3%, increasing upsection), vesicular to scoriaceous, basaltic-andesite lapilli tuff to tuff breccia (Fig. 7a).

The thickest exposure of the Nipple is at the cone where the breccia is about 275 m thick. Exposures north and south of the cone are about 130 to 180 m thick. At the cone, the breccia consists primarily (98%) of lapilli- to bomb-sized clasts (75-80%) that are blocky to rounded (breadcrust to cannonball morphologies; see e.g., Alvarado et al., 2011). The breccia is clast supported with finer coarse-ash and smaller lapilli-sized particles filling spaces between the cm-scale bombs. Matrix clays are the result of in-situ alteration of smaller fragments rather than depositional (Fig. 7a). Some of the clasts exhibit internal fracturing, possibly due to impact. Rare cognate clasts are angular (Fig. 7b), but otherwise similar to the juvenile

clasts. Near the top of the exposure are larger bombs and bomb slabs, some draping the underlying breccia (Fig. 7c), and this inverse grading might signify a decrease in the explosivity as the cone evolved (e.g., Alvarado et al., 2011). Away from the cone, the pyroclastic breccias undergo a facies change to a flow breccia comprising a mix of large round, or pillow-shaped clasts up to about 10-30 cm that are internally brecciated with curvilinear fractures, and smaller blocky fragments down to coarse-ash in size (Fig. 7d) where it overlies thinly bedded and laminated tuffaceous sediments that were described by Ewing (1981a) as aquagene tuffs.

#### 3.3.2. Kissick breccias, Dewdrop Flats Formation

The Kissick breccia overlies the Nipple breccia about 2 km south of the cone where it is best exposed as part of a resistant ridge (Figs. 2, 8). The breccia is heterolithic comprising about 3-5% small, 1-4 cm angular accidental fragments of carbonate-cemented siltstone, and 95% andesitic juvenile and cognate pyroclastic fragments. The juvenile and cognate fragments, though compositionally monolithic, display a variety of morphologies ranging from ameboid (Fig. 8c) to more angular broken bomb-shaped fragments, some of which have scoriaceous cores. The matrix is poorly sorted (lapilli to coarse-ash-size) and comprises angular, non-vesicular fragments with curvilinear margins (Figs. 8d-e). In places nearby fragments show a jig-saw fit, and some display 1-3 mm thick reaction rims. The unit is very vaguely bedded, with bedding defined by the long axes of some of the larger fragments (Fig. 8d). In contrast to the Kissick member observed at Kenna Cartwright Park (Figs. 2a, 5), the breccias here are interpreted to represent emplacement of an andesitic dome or sub-volcanic intrusion. These features may record interactions of rising magma with water, causing varying degrees of magmatic and phreatomagmatic to hydroclastic and autoclastic fragmentation (see e.g., Smellie et al., 1998).

#### 3.4. Doherty Creek and Castle Butte, Dewdrop Flats Formation

The Doherty Creek member is exposed northwest of Kamloops Group type area, where it is in gradational contact with the Castle Butte member along its southern margin (Figs. 2, 3). From a distance the flows appear to form relatively continuous layers with gentle depositional dips (Fig. 9a). In detail, the flows are highly brecciated, discontinuous along strike, and intruded by northeast-trending dikes that dip steeply to the north and form distinct ridges (Fig. 9b). Near the contact with the Castle Butte member, a coherent Doherty Creek member flow about 3 m thick (Fig. 9c) changes vertically and laterally from an autobreccia to hyaloclastite breccia. The flow is aphyric, and sparsely vesicular with 1-3 mm diameter spherical vesicles comprising 5% of the flow, along with larger gas cavities 0.5 to 1 m in diameter that are filled and lined with quartz. Above this flow are several metres of coarse breccia which may be an autobreccia, similar to the Red Plateau member (section 3.5.; Figs. 9d, e). This breccia of the Doherty Creek member fines



**Fig. 6.** Cinnamon Ridge pillowed flows showing two different morphologies. **a)** Bulbous, closely packed pillows showing an overall decrease in size upward. Behind the pillows is a slump block (sb) of tube-fed pillows, tuff (t), and a dike (d). The scale bar is 1 m. **b)** Corrugated surface of a pillow likely formed by expansion of the interior of the pillow after formation of the initial crust. The smooth broken crust (bc) is on both sides of the corrugated surface. The bar scale at the tip of the walking stick is 1 cm. **c)** Concentrically zoned pillows with more elongate shapes, and minimal inter-pillow breccia. The walking stick is 1.1 m. **d)** Tubular pillows showing radial cracks, and one hollow tube (back right). The card at the bottom of the photo is 9 cm long.

along strike to the east where it was previously mapped as the Castle Butte member (Ewing, 1982). Within the Castle Butte member lakebed shales form an isolated pod about 10 by 5 m that is overlain by a felsic tuff forming a discontinuous bed 5 m thick, which in turn is overlain by fine hyaloclastite.

### 3.5. Red Plateau member, Dewdrop Flats Formation

The Red Plateau member was mapped as an upper unit of the Dewdrop Flats Formation (Fig. 3; Ewing, 1981a). Where observed at two sites near the Red Plateau (Fig. 2), this unit forms a series of andesitic flows more than 2.5 m thick. These flows are dark grey and primarily plagioclase phyric with plagioclase crystals up to 1 cm. The flows have massive, sparsely vesicular interiors, some being highly crystalline, and brecciated flow tops about 1-2 m thick (Fig. 10a). The flow top breccias comprise angular to subangular scoriaceous fragments 1-30 cm with no matrix (Figs. 10b, c). There are

sparsely disseminated sulphides in one of the flows at Wheeler Peak. The Red Plateau member covers an aerial extent of about 50 km<sup>2</sup>, which is about 25% of the type area of the Kamloops Group (Ewing, 1981a, 1982).

### 3.6. Opax breccia member, Dewdrop Flats Formation

The Opax breccia is the uppermost member of the Dewdrop Flats Formation (Fig. 3; Ewing, 1981a). It is exposed in five separate localities on hilltops, forming a roughly east-west trend, where it overlies the Red Plateau member at all except the northwest corner of the type area where it overlies the Doherty Creek member (Ewing, 1981a, 1982). The Opax breccia at Wheeler Peak (Fig. 2), is monolithic, poorly sorted, and clast supported with little matrix. Fragments are andesitic, grey, vitric to aphanitic, angular, mm to a few cm in size and internally brecciated. Some of the vitric fragments exhibit flow banding. The apparent matrix is caused by alteration,

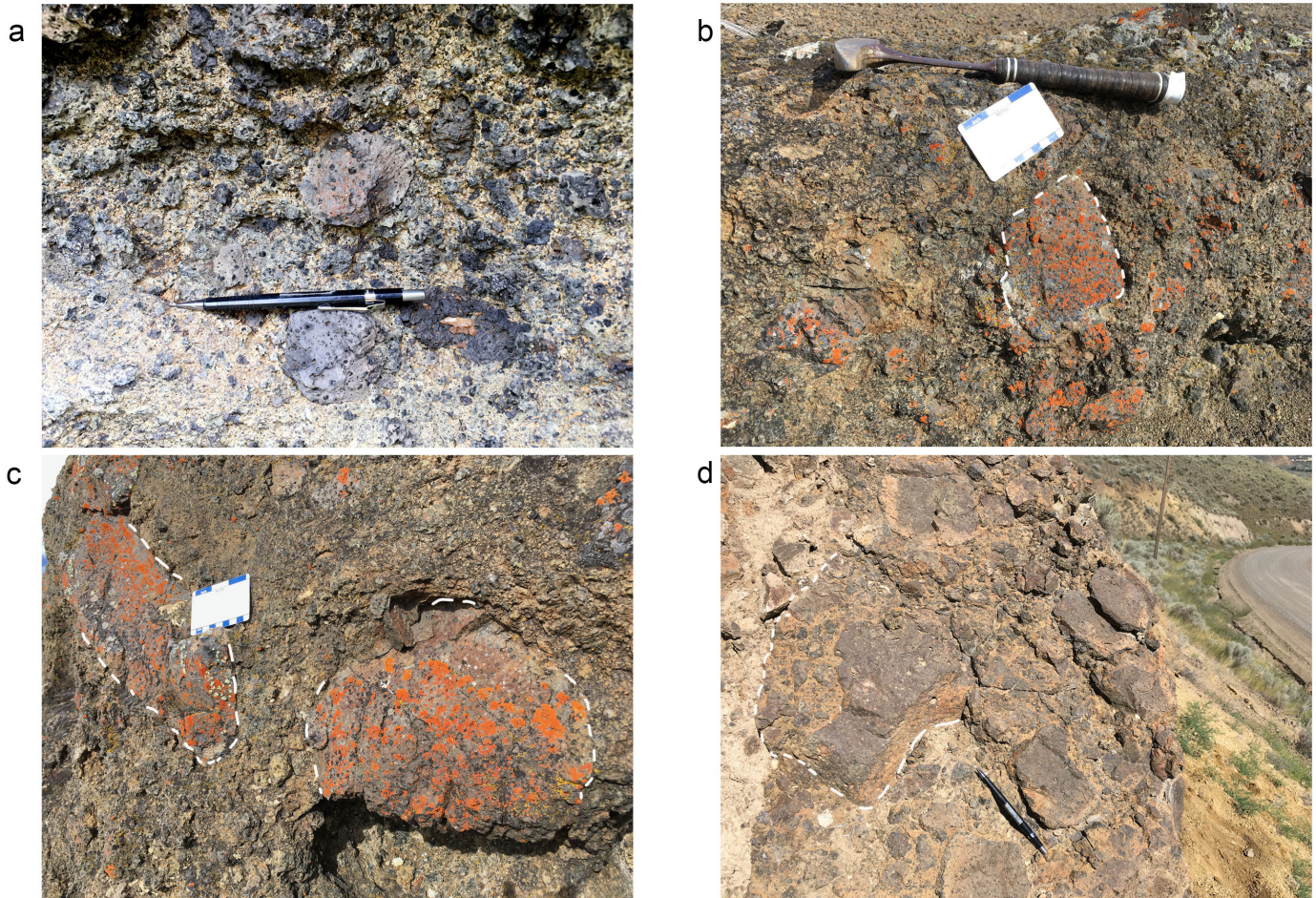


**Fig. 7.** The Nipple breccia (Dewdrop Flats Formation). **a)** Pyroclastic fragments near the base of the pyroclastic cone showing the spherical shape of some ejecta, and the variation in size of ejecta. The clay matrix is not depositional, but the result of in-situ alteration of finer vitric fragments (i.e., pseudomatrix). **b)** Angular cognate clast in the mid-portion of the Nipple breccia. **c)** Large slabs and bombs at the top of the cone. **d)** Hyaloclastite flow breccia showing one large fragment that is internally brecciated.

and alteration rims 1-2 mm thick are evident on some of the fragments (Fig. 10d). Though the area is largely barren of mineralization, finely disseminated sulphides occur in some of these rocks. Based on major element geochemistry (Ewing, 1981a, c), the Opax breccia is a trachyandesite, making it the most silicic unit in the Kamloops Group type area.

#### 4. Geochemistry

Samples for whole rock geochemistry were collected from multiple Kamloops Group exposures between 2017 and 2019 (Fig. 2). Below we summarize the results from only two sites, Kenna Cartwright Park (two flow samples from the Border facies at the base of the Kamloops Group; six samples from the Mara Hill member of the Dewdrop Flats Formation) and Cinnamon Ridge (two pillowed flows from the middle unit of the Tranquille Formation; Fig. 2). We avoided collecting from more heterolithic pyroclastic units to better enable petrogenetic interpretations. A full description of the analytical methods and the complete dataset will be presented elsewhere (Van Wagoner and Ootes, 2021).

#### 4.1. Methods

Clean, alteration-free samples were submitted to Actlabs in Ancaster, Ontario, for bulk-rock major, trace, and rare earth element analysis. At Actlabs, samples were crushed to pass 2 mm, mechanically split using a rifle splitter, and pulverized using mild steel to 95% passing 105  $\mu\text{m}$  (Code RX-2). Major element oxides were determined using inductively coupled plasma optical emission spectroscopy (ICP-OES) and trace element concentrations were determined using fusion inductively coupled plasma mass spectrometry (ICP-MS; Code 4 Lithoresearch). Measurement accuracy was determined using certified standards provided by Actlabs and blind samples of the British Columbia Geological Survey till standard.

#### 4.2. Results

Based on the total alkali-silica (TAS) diagram (re-calculated to 100% volatile-free basis), the Kamloops Group rocks are classified as andesite to dacite (Fig. 11a). The samples have 2.37 to 8.41% loss on ignition and because of the high volatile content this study relies mostly on the immobile trace elements



**Fig. 8.** The Kissick breccia (Dewdrop Flats Formation) where it overlies the Nipple breccia. **a)** At the ridge top, a typical exposure of possible sub-volcanic intrusions in the type area; in foreground are Quaternary drift deposits exposed in a road cut. **b)** Close up of a) showing sub-horizontal joints. **c)** Ameboid-shaped volcanic fragment with internal polyhedral joints. The smaller fragments in the matrix are the same composition and shape as the fragments comprising the larger form. The dark fragment near the point of the hammer is relict glass. **d)** Two tabular fragments on the right side of the photo are aligned parallel to vague bedding. The lower fragment is lighter coloured aphyric, aphanitic andesite, the upper is relict glass; both are internally brecciated. The outlined fragment displays a cusped-lobate outline, preserves a vitric margin, exhibits flow banding, and is internally fractured. **e)** Broken bomb with scoriaceous interior surrounded by breccia.



**Fig. 9.** The Doherty Creek member (Dewdrop Flats Formation) near Doherty Creek. **a)** General exposure of the Doherty Creek member. **b)** Flow breccia (fb) cut by vertical dike with near-horizontal columnar joints. **c)** Core of an aa flow surrounded by autobreccia. **d)** Close up of autobreccia showing a combination of angular and more spherical fragments and a combination of highly vesicular fragments (mostly intensely weathered) and dense non-vesicular fragments. Clay material between fragments formed by weathering of finer particles and is not depositional matrix. **e)** Breccia that has features resembling hyaloclastite, particularly fragments with curvilinear margins and internal fractures.

to classify the rocks (e.g., MacLean and Barrett, 1993). All of the rocks plot in the calc-alkaline field in a tholeiitic versus calc-alkaline discrimination diagram (Fig. 11b). They range from basalt to basaltic-andesite and trachy-andesite and are subalkaline to weakly alkaline; four of the flows from the Lava flow field are the most alkaline (Fig. 11c).

The rocks span a range of  $\text{SiO}_2$  from 59 to 66 wt.% (recalculated to 100%, LOI free; Figs. 11, 12). In general, there is an increase of  $\text{SiO}_2$  with  $\text{Na}_2\text{O}+\text{K}_2\text{O}$  (Fig. 11a), but little relationship between  $\text{SiO}_2$  and  $\text{Al}_2\text{O}_3$  (Fig. 12a). There is an inverse relationship between  $\text{MgO}$  and  $\text{SiO}_2$ , and a slight decrease in  $\text{FeO(T)}$ , and  $\text{TiO}_2$ , which is less clear. However, there is a distinct positive increase of  $\text{CaO}/\text{Al}_2\text{O}_3$  with increasing  $\text{CaO}$  (Fig. 12f). Similarly, immobile compatible elements Co, Cr, V, Ni, and Sc decrease with increasing  $\text{Zr}/\text{TiO}_2$ , used here as an indication of fractionation (Fig. 13), but the relationship with Sr is less clear. Relative to chondrite, the rocks are light-

REE (LREE) enriched ( $\text{La}/\text{Yb}_N=13-22$ ) with a relatively flat heavy-REE (HREE) pattern ( $\text{Dy}/\text{Lu}_N=1.4-1.7$ ) and no Eu anomalies (Fig. 14a). Relative to primitive mantle, all of the rocks are enriched in large ion lithophile elements (LILE), with prominent positive Ba, K, and Pb anomalies, and to a lesser extent U and Sr, and with enrichment of the LREE with respect to the HREE. High field strength elements (HFSE) Nb and Ta display negative anomalies, without distinct negative Zr or Ti anomalies (Fig. 14b).

Strontium values are relatively high, from 453-1144 ppm (Fig. 13f) and Ba ranges from 1205 to 2022 ppm, with the highest values being from the two pillowed flows. The samples are enriched in the fluid mobile LILE, compared with the less fluid mobile HFSE and REE (e.g., Ba/La; section 5.3.). Conversely, these samples have low immobile to mobile element ratios (e.g., Ce/Pb [9-11]), and immobile incompatible element ratios (e.g., Th/Yb, Nb/La; section 5.3.). Most of the

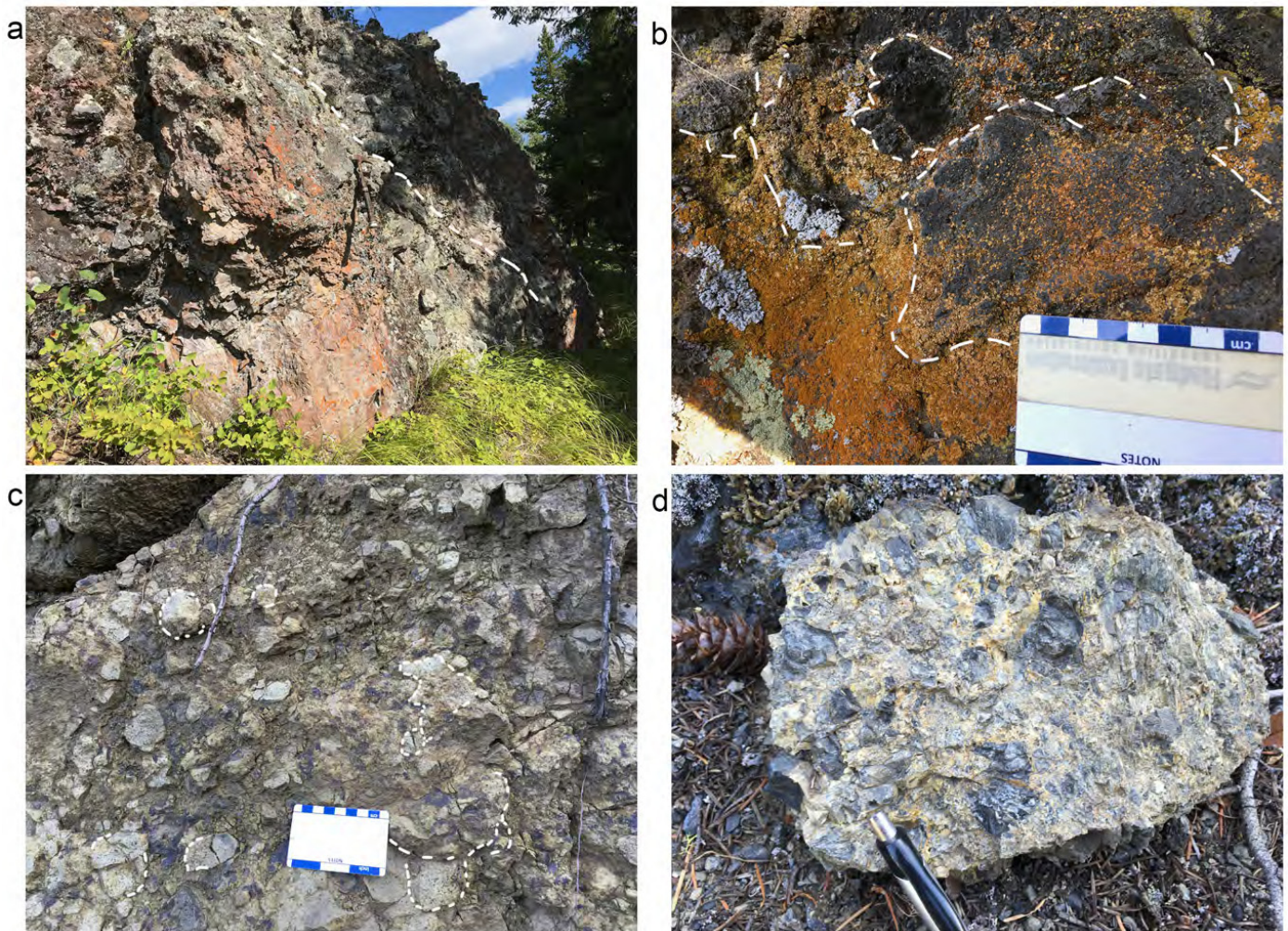


**Fig. 10.** Red Plateau member (a-c) and Opax breccia member d) (Dewdrop Flats Formation. **a**) Thick flow showing the contact (dashed white line) between the more massive part of the flow and overlying autobreccia. **b**) Highly scoriaceous flow top breccia with lichen exploiting vesicles. Fragments are angular to subspherical there is no matrix. **c**) Autobreccia that is less scoriaceous than b), with a mix of clast sizes and vesicularity. Some of the fragments are outlined to show a combination of spherical fragments lacking internal brecciation and more angular fragments that also display internal fragmentation. **d**) Opax breccia showing flow banding in some fragments and an altered matrix.

rocks have adakite-like compositions in terms of relatively high  $\text{SiO}_2$ ,  $\text{Al}_2\text{O}_3$ ,  $\text{Na}_2\text{O}$ , and  $\text{MgO}$  (Figs. 11a, 12). All have  $\text{Sr} > 400$  (Fig. 13), and all but one sample has  $\text{Sr}/\text{Y} > 40$ ,  $\text{Yb} < 1.9$ , and  $\text{La}/\text{Yb} > 20$ . Absolute values of Y are up to 22 ppm, slightly higher than typical adakites (Zhang et al., 2019).

## 5. Discussion

### 5.1. Physical volcanology

The Kamloops Group volcanic rocks include a combination of effusive and explosive volcanic rocks that preserve evidence for magma-water interaction. This includes phreatic and phreatomagmatic textures and a variety of in-situ hyaloclastites. Some of the volcanic horizons are associated with lakebed sediments and water-lain tuffs, but little evidence of peperitic breccias was observed during sampling. The sedimentary rocks and pillow basalts provide evidence of sub-aqueous volcanism, but specific relationships of the lakes to volcanic

activity remains unknown. For example, did the lakes originate solely in graben topographic lows or might some be related to lava flow dams or caldera? Forthcoming facies mapping and volcanological studies will clarify volcanic processes and the three-dimensional evolution of volcanism of the Kamloops Group, along with its extent and relationship to coeval volcanism of south-central British Columbia.

### 5.2. Fractionation trends

The variation diagrams can be used as an indication of the relative importance of fractionating phases. The positive relationship of increasing  $\text{CaO}/\text{Al}_2\text{O}_3$  to  $\text{CaO}$  (Fig. 12f) is indicative of pyroxene fractionation. The decrease of Co, Cr, and Ni with  $\text{Zr}/\text{TiO}_2$  (Fig. 13) reflects olivine and pyroxene fractionation. There is a slight decrease of  $\text{FeO(T)}$  with increasing  $\text{SiO}_2$  (Fig. 12c) and Ti with Zr (not shown) suggesting some fractionation of Fe-Ti oxides. The decrease

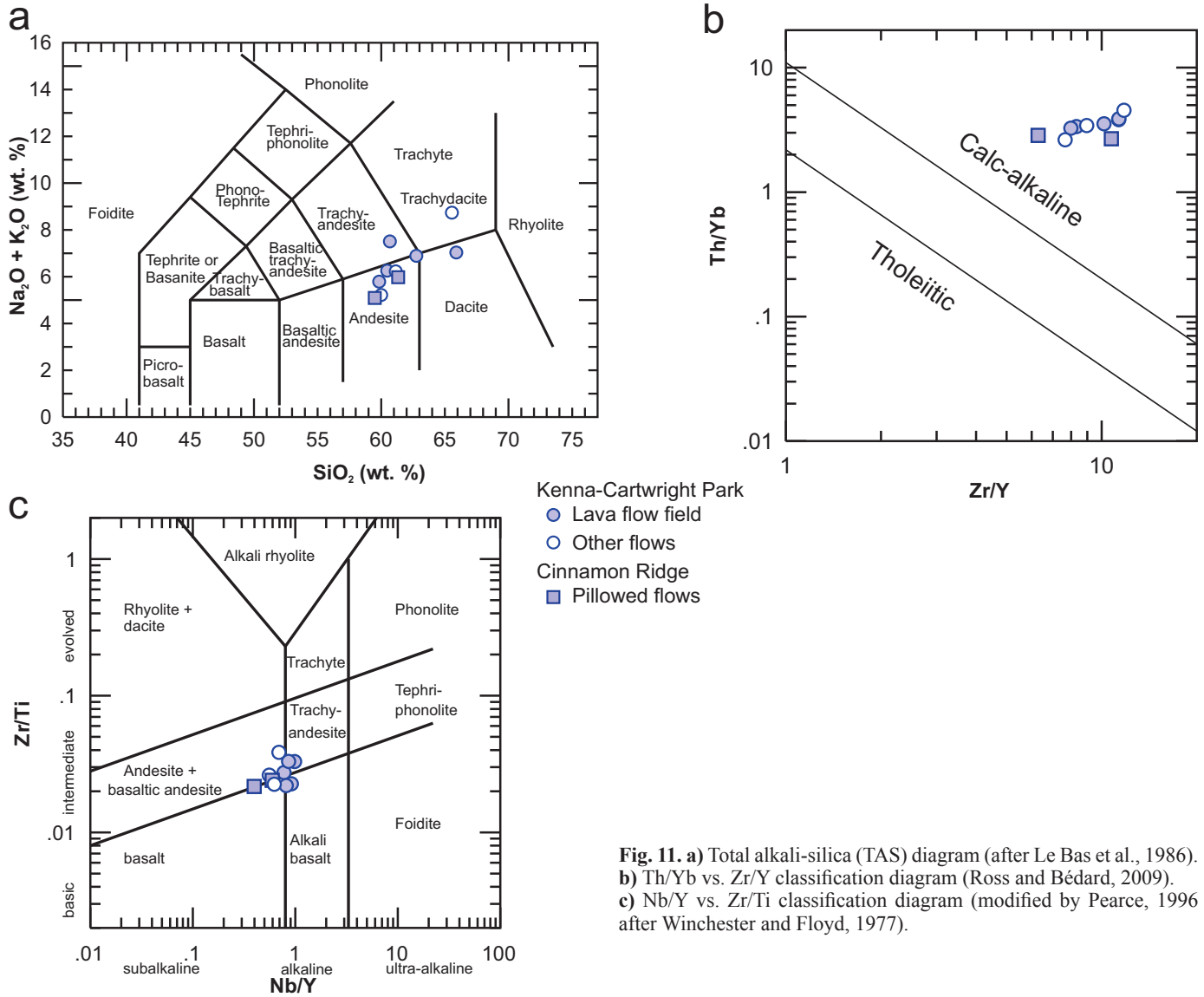


**Fig. 11.** a) Total alkali-silica (TAS) diagram (after Le Bas et al., 1986). b) Th/Yb vs. Zr/Y classification diagram (Ross and Bédard, 2009). c) Nb/Y vs. Zr/Ti classification diagram (modified by Pearce, 1996 after Winchester and Floyd, 1977).

of V with increasing Zr/TiO<sub>2</sub> (Fig. 13c) is prominent and may be partially controlled by Fe-Ti oxide fractionation. However, V also partitions into clinopyroxene and amphibole, although partition coefficients of V are influenced by oxygen fugacity, volatile phases, and temperature (Laubier et al., 2014; Wang et al., 2019; Iverson et al., 2018), as does Sc (Vander Auwera et al., 2019). The strong decrease of both Sc and V with Zr/TiO<sub>2</sub> (Fig. 13), suggests that pyroxene and probably amphibole fractionation influenced their concentrations. The lack of a strong co-variation of Al<sub>2</sub>O<sub>3</sub> with SiO<sub>2</sub> (Fig. 11a) and lack of negative chondrite-normalized Eu anomalies (Fig. 14a) indicates that plagioclase was not an important fractionating phase compared with olivine and pyroxene. The absence of a relationship between P<sub>2</sub>O<sub>5</sub> and SiO<sub>2</sub> (Fig. 12e) indicates that apatite fractionation was insignificant.

**5.3. Geochemical comparison of the Kamloops, Princeton, and Pentiction groups**

Eocene volcanic rocks in southern British Columbia are separated into the Kamloops, Princeton, and Pentiction groups (Fig. 15). However, the basis for this separation and the stratigraphic relationships between these units remains unclear. Geochemistry, paired with stratigraphic mapping, and high-precision geochronology has the potential to address this problem. Although data are sparse, particularly from the Pentiction Group (Fig. 15), some first-order comparisons can be made.

Rocks of the Pentiction Group are potassic, alkaline basaltic trachyandesites to tephriphonolites (Dostal et al., 2003). The Kamloops and Princeton groups are mostly calc-alkaline to moderately alkaline (Figs. 11b, c; Breitsprecher, 2002; Ickert et

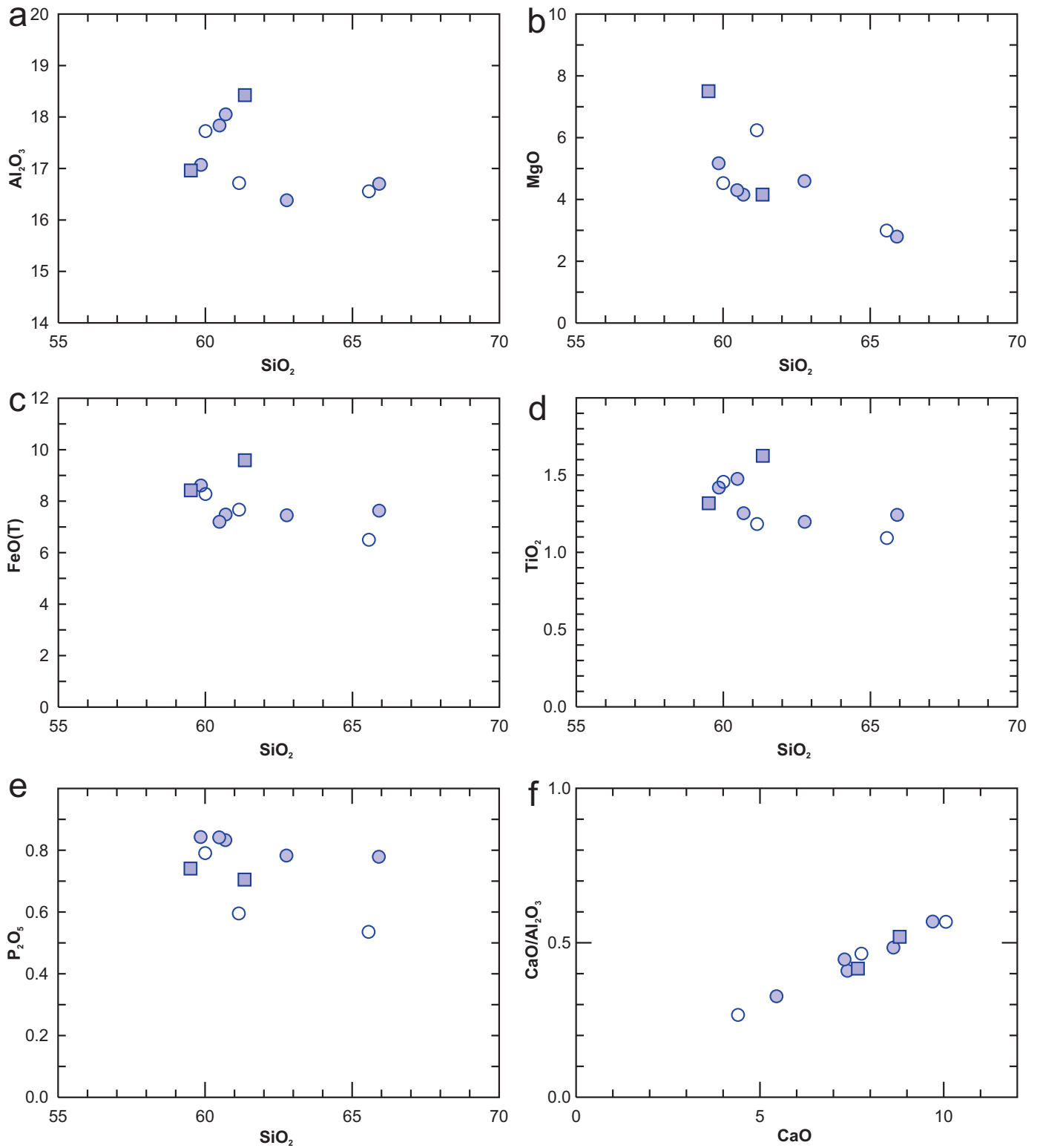


**Fig. 12.** Harker diagrams. Major elements (wt.%) are corrected to 100% volatile free.  $\text{SiO}_2$  vs. **a)**  $\text{Al}_2\text{O}_3$ , **b)**  $\text{MgO}$ , **c)**  $\text{FeO(T)}$ , **d)**  $\text{TiO}_2$ , **e)**  $\text{P}_2\text{O}_5$ , and **f)**  $\text{CaO}$  vs.  $\text{CaO}/\text{Al}_2\text{O}_3$ .

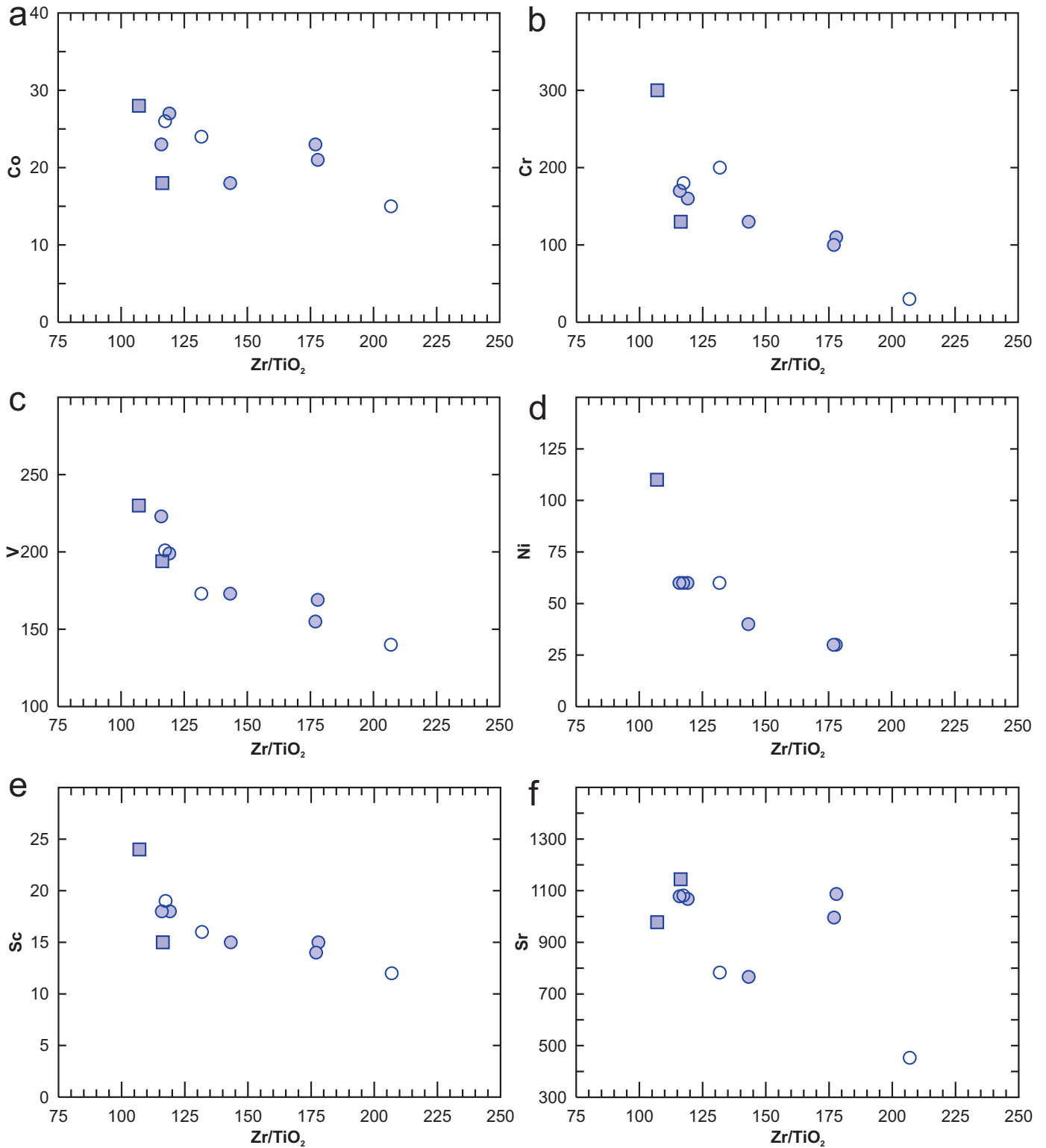


**Fig. 13.** Trace element variation diagrams. Zr/TiO<sub>2</sub> vs. a) Co, b) Cr, c) V, d) Ni, e) Sc, and f) Sr.

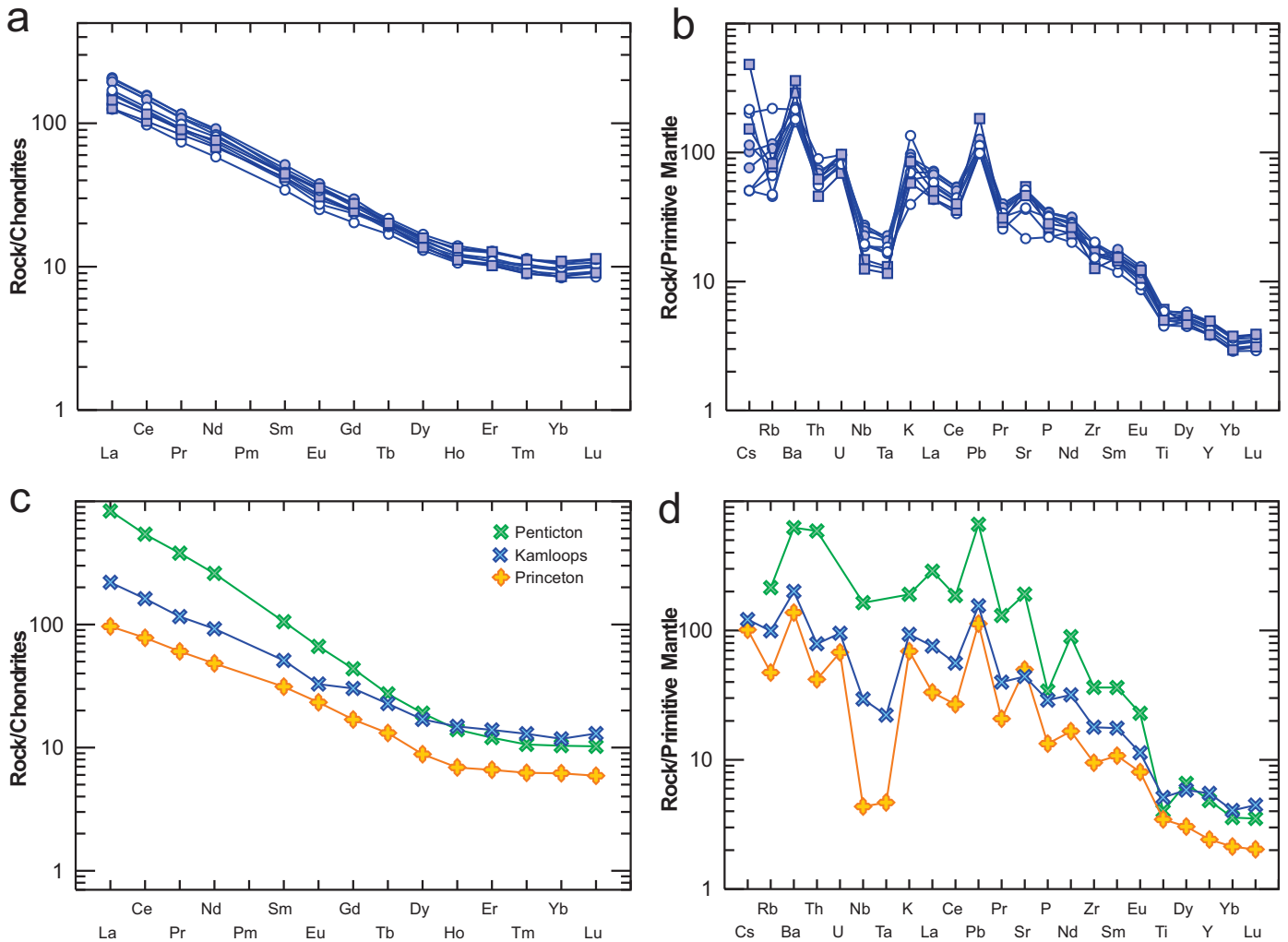


**Fig. 14.** **a)** Chondrite-normalized REE. **b)** Primitive mantle-normalized trace and REE for samples from this study. **c)** Chondrite-normalized REE and **d)** Primitive mantle-normalized trace and REE for median values (<63 wt.% SiO<sub>2</sub>) for rocks of the Kamloops, Pentiction, and Princeton Groups. Data from this study, Breitsprecher (2002), Dostal et al. (2003, 2019), and Ickert et al. (2009). Normalizing values are from Sun and McDonough (1989).

al., 2009), and both have adakitic characteristics. Rocks from all three units are LREE enriched, with flat HREE chondrite-normalized patterns, and have similar primitive mantle-normalized trace element characteristics, with the major difference being the negative anomalies of Nb and Ta that are lowest in the Princeton Group and minimal in the Pentiction Group (Fig. 14).

Trace element ratios can give an indication of the mantle source and depth of melting. Almost all the rocks from all three groups have flat HREE patterns and steep LREE patterns with some variations (Figs. 14, 16a). The REE patterns for the Kamloops Group are fairly uniform and the Princeton Group parallel, but with lower total REE and less enrichment of the LREE (Figs. 14, 16-18). The Pentiction Group has higher LREE enrichment, related to smaller degrees of partial melting (Figs. 14, 16-18). The overall LREE-enriched and flat to slightly elevated HREE patterns indicates variable amounts of garnet in the source (Fig. 16a; see Wang et al, 2002; Davidson

et al., 2007; Keskin et al., 2012; Maro and Caffè, 2016; Dostal et al., 2019).

Melts that form in equilibrium with amphibole have lower Rb/Sr and higher Ba/Rb than those that form in equilibrium with a phlogopite-bearing source (Fig. 16b; e.g., Furman and Graham, 1999; Liang et al., 2017). All of the rocks display ratios that are consistent with an amphibole-bearing source (Fig. 16b). The probable source for the Kamloops Group was amphibole-bearing lherzolite near the garnet-spinel transition, at depths of 70-90 km (Dostal et al., 2019), with consistent degrees of partial melting (Figs. 16a-c). The low Nb and other HFSE, which are depleted in the lithospheric mantle with respect to LREE, do not support an asthenospheric mantle source for the three groups (Fig. 16c; Bradshaw and Smith, 1994; Smith et al., 1999; Aydinçakir and Sen, 2013). Similarly, there is no evidence that they fall on a MORB-OIB array (Fig. 16d). The geochemical data support an origin in the subcontinental lithospheric mantle.

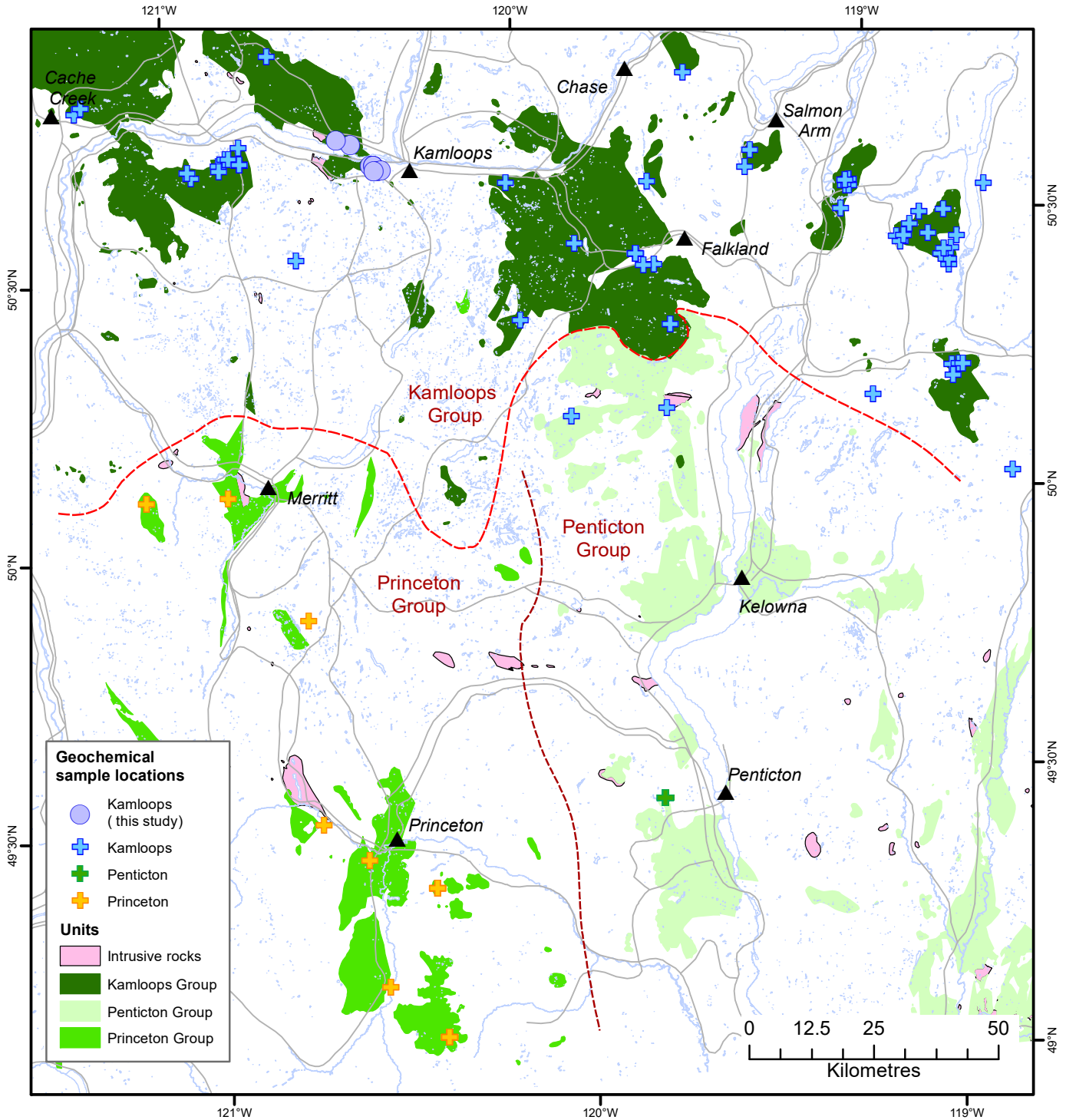


**Fig. 15.** Distribution of Eocene volcanic and intrusive rocks in south-central British Columbia. Sample locations for the Kamloops Group are from this study, Breitsprecher (2002), and Dostal et al. (2019). Princeton Group samples are from Ickert et al. (2009) and Penticton Group samples are from Dostal et al. (2003). The boundaries between the groups are shown with dashed red lines.

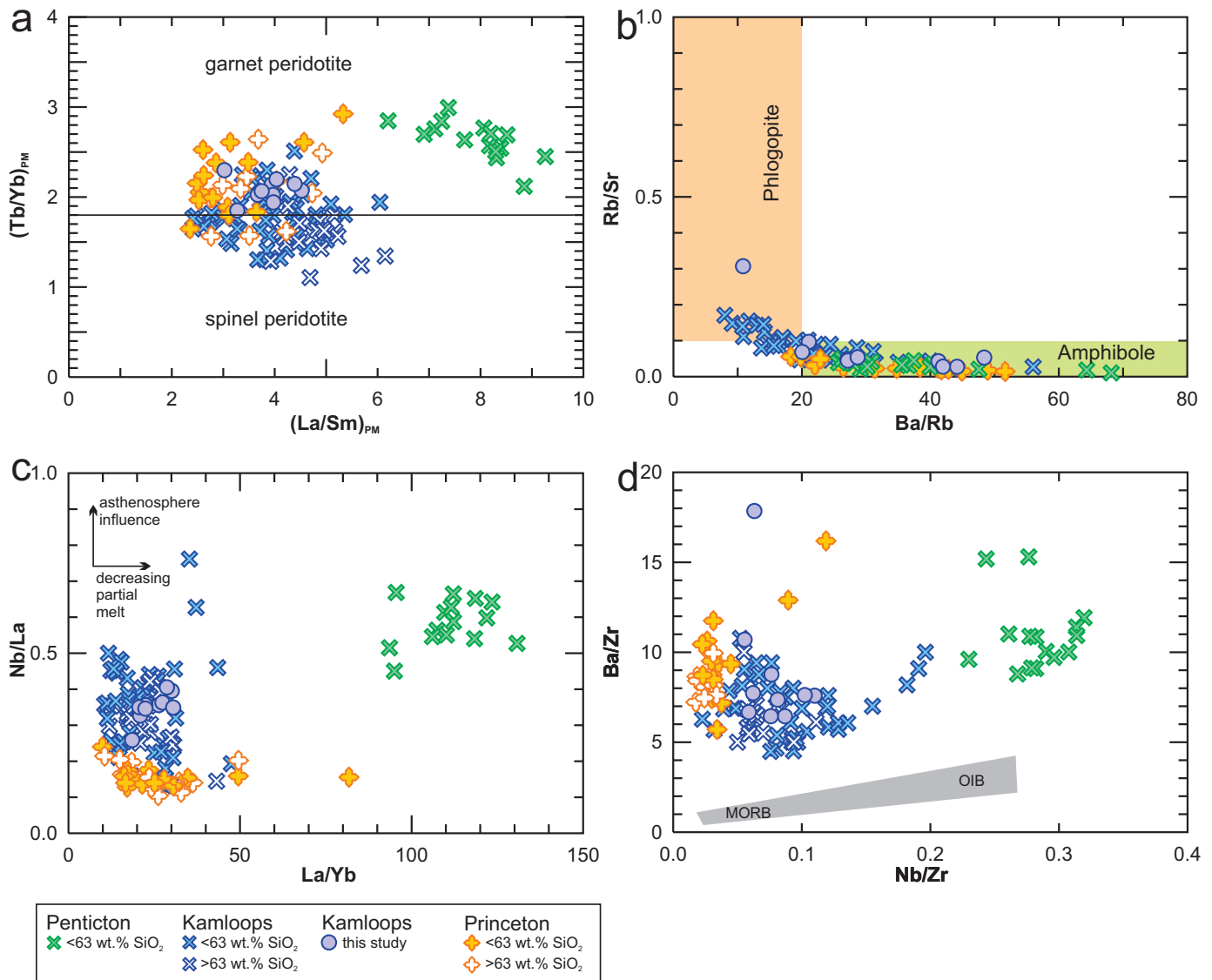


**Fig. 16.** **a**) Primitive mantle normalized  $(La/Sm)_{PM}$  vs.  $(Tb/Yb)_{PM}$ . Relative depth of melting increasing with increasing  $(Tb/Yb)_{PM}$ . Modified from Wang et al. (2002) and Dostal et al. (2019). Normalizing values from Sun and McDonough (1989). **b**)  $Ba/Rb$  vs.  $Rb/Sr$ . Phlogopite and amphibole melting fields are from Furman and Graham (1999). Only rocks with <63 wt.%  $SiO_2$  are plotted. **c**)  $La/Yb$  vs.  $Nb/La$ . Asthenosphere is characterized by  $Nb/La \sim 1.2$  (after Smith et al., 1999). **d**)  $Nb/Zr$  vs.  $Ba/Zr$ . The MORB-OIB array is from Leeman et al. (2005). Kamloops data are from Breitsprecher (2002), Dostal et al. (2019) and this study; Princeton data are from Ickert et al. (2009); Pentiction data are from Dostal et al. (2003).

The primitive mantle-normalized trace element patterns (Fig. 14d) are typical of subduction-related rocks (Dostal et al., 2003; Ickert et al., 2009). The Kamloops and Princeton groups have low  $Nb/La$  and variable  $Th/Nb$  (Fig. 17a) indicating that fluids had a role in the melt source. The Pentiction Group has high  $Nb/La$  and uniform  $Th/Nb$  (Fig. 17a) indicating less of a role by hydrous fluids in the melt source. The variable  $Ba/La$  and low  $Th/Nb$  of the Kamloops and Princeton groups further indicate a role for slab-derived fluids in the melt source, whereas the Pentiction Group is more strongly influenced by sediment contamination or sediment in the melt source (Fig. 17b; see e.g., Walker et al., 2000, 2001; Woodhead et al.,

2001). The Pentiction Group  $Ba/La$  is still relatively high and indicative of an arc affiliation (e.g., Michelfelder et al., 2013). Similarly, the Princeton and Kamloops groups trend toward  $Ba/Th$  enrichment, whereas the Pentiction Group rocks have consistently low values (Fig. 17c). The  $U/Nb$  is not affected by crystal fractionation, such that significant increases in this ratio with  $SiO_2$  can be used as an indication of crustal contamination (Fig. 17d; e.g., Krienitz et al., 2006; Dostal et al., 2019). Crustal contamination is more evident in the Princeton Group than in the Kamloops Group, but does not appear to have been significant for either unit (Fig. 17d). Overall, the Pentiction Group rocks have trace element signatures that are more

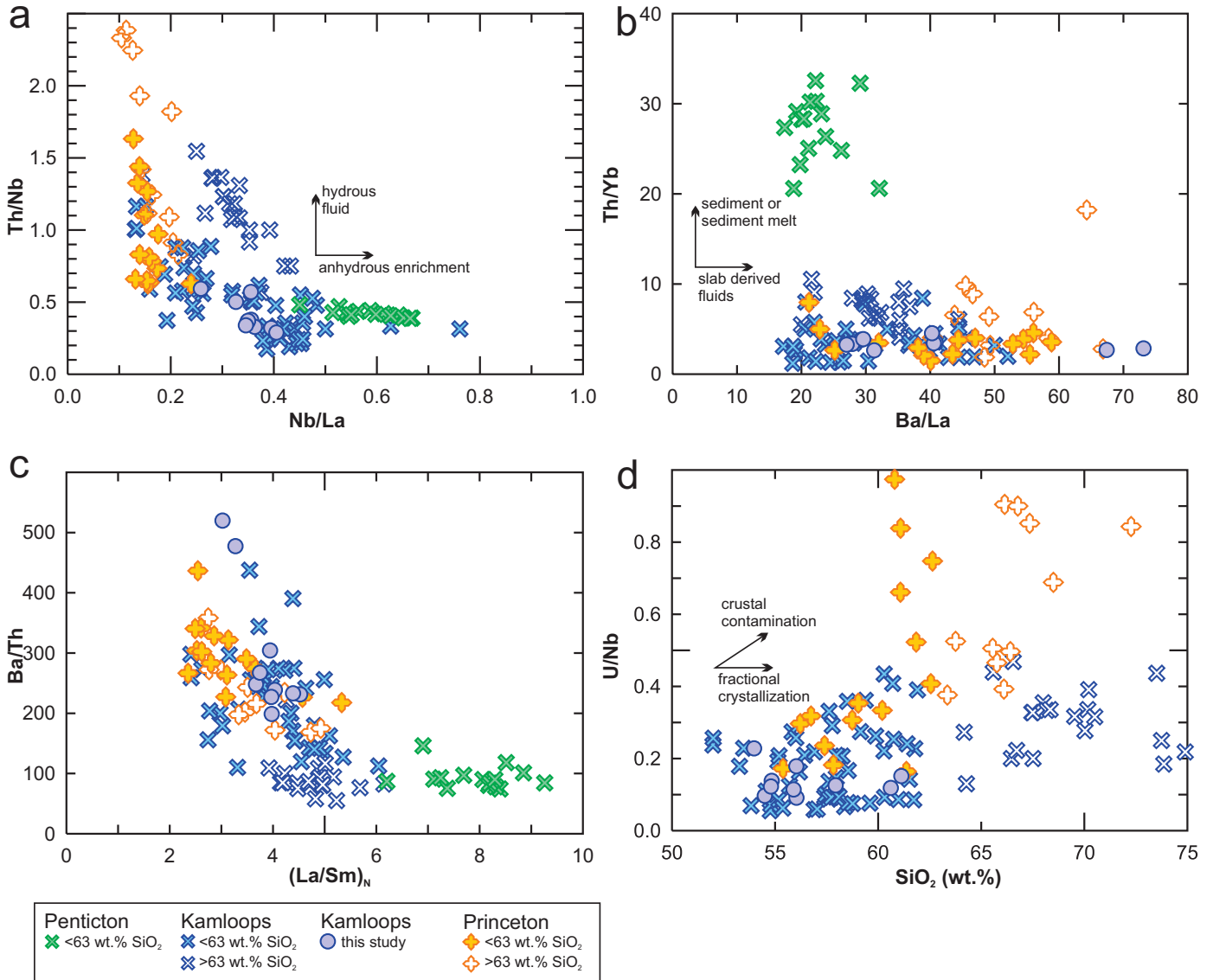


**Fig. 17.** Trace element and REE ratio diagrams. **a)** Nb/La vs. Th/Nb (Wang et al., 2016; Zhang et al., 2020). **b)** Th/Yb vs. Ba/La (Woodhead et al., 2001). **c)** Chondrite-normalized La/Sm vs. Ba/Th showing a decrease in Ba/Th with decreasing partial melting for all but the Pentiction Group. Chondrite normalizing values are from Sun and McDonough (1989). **d)** SiO<sub>2</sub> (wt.%) vs. U/Nb (Dostal et al., 2019); no U data are available for the Pentiction Group. Data sources as in Figure 16.

indicative of a mantle source influenced by anhydrous, melt induced metasomatism, whereas the Kamloops and Princeton groups reflect melting of a hydrous mantle source enriched by slab-derived fluids (Figs. 17 a-c).

Dostal et al. (2003) argued against crustal contamination as the cause of the trace and REE characteristics of the Pentiction Group and interpreted their evolved Nd and Sr isotopes to reflect melting of metasomatized Precambrian subcontinental lithospheric mantle. The adakitic compositions of the Princeton Group were interpreted by Ickert et al. (2009) to reflect partial melting of basaltic dikes in the lithosphere, with juvenile Nd isotopes indicating no role for Precambrian the subcontinental lithospheric mantle. Breitsprecher et al. (2003), Dostal et al. (2003), and Ickert et al. (2009) suggested that the source of

heat may have been upwelling asthenosphere through a slab window, or slab tear.

Figure 18 shows plots across (longitude) and along (latitude) the volcanic belts. From west to east Ba/La decreases (Fig. 18a); a similar decrease is lacking from south to north (Fig. 18b). The lateral change in Ba/La has been shown to be a good indicator of regional variations across arcs, reflecting declining intensity of fluid flux from the subducting slab (e.g., Patino et al., 2000; Michelfelder et al., 2013). From west to east Sr/Y decreases (Fig. 18c), with the highest values in the Pentiction and Princeton groups. From south to north there is a distinct decrease in Sr/Y (<100) near 50°N (Fig. 18d). Ickert et al. (2009) attributed the high Sr/Y values of the Princeton Group to melting of basaltic dikes in the lithospheric mantle whereas

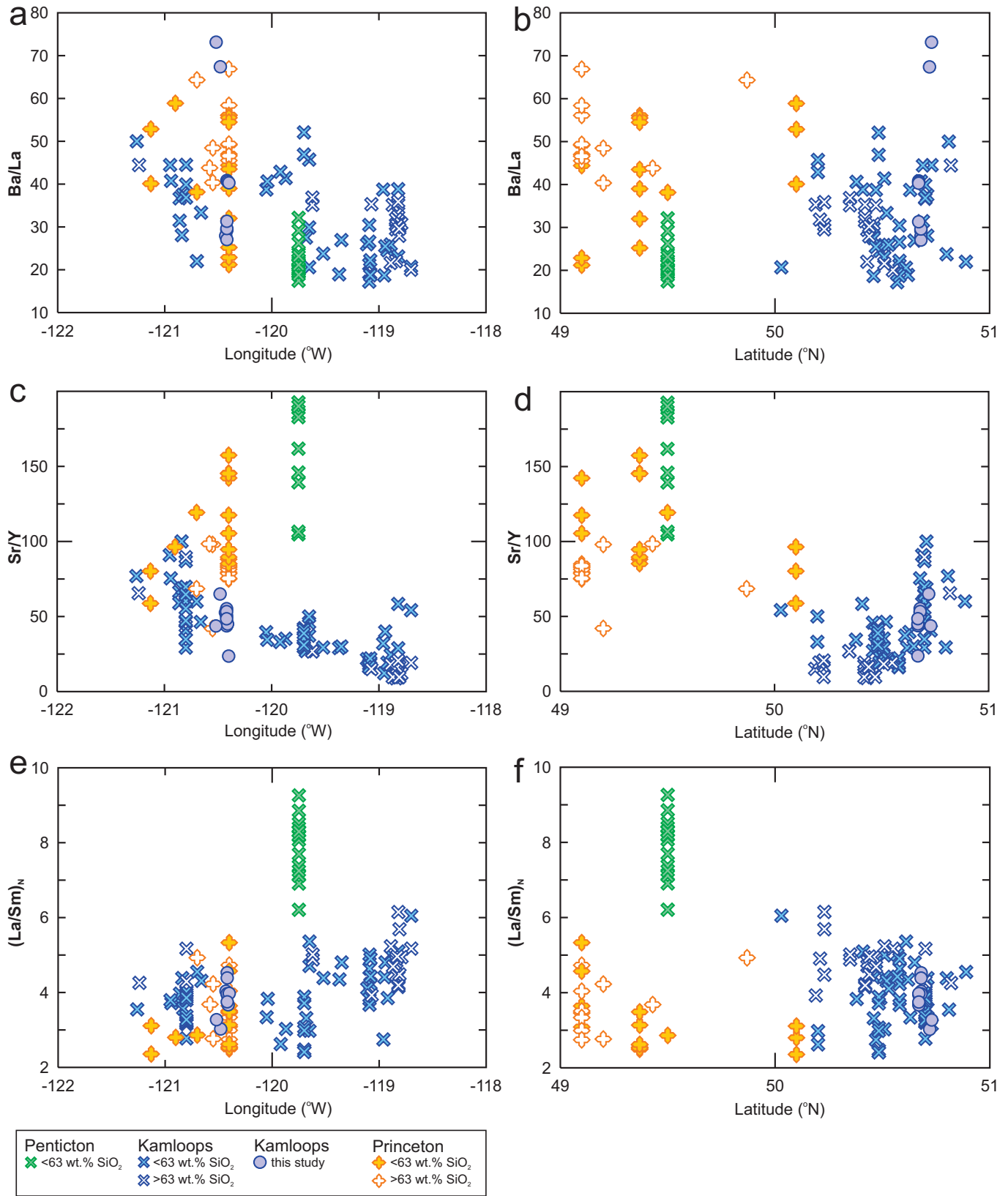


**Fig. 18.** Latitude and Longitude vs. trace element and REE ratios. **a)** Longitude and **b)** Latitude vs. Ba/La, a proxy for slab-derived fluids (e.g., Patiño et al., 2000; Michelfelder et al., 2013). **c)** Longitude and **d)** Latitude vs. Sr/Y, a proxy for adakitic volcanism (Sr/Y >40). **e)** Longitude and **f)** Latitude vs. chondrite-normalized La/Sm, a proxy for partial melt. Data sources as in Figure 16.

Dostal et al. (2003) suggested that the high Sr values are due to partial melting of a previously metasomatized Precambrian lithosphere. Chondrite-normalized La/Sm increases from west to east (Fig. 18e), but this is controlled in part by more felsic rocks of the Kamloops Group in the east; La/Sm does not decrease from south to north (Fig. 18f). Again, the Penticton Group rocks stand out and are best interpreted as reflecting different source conditions. Forthcoming geochemical data from this study will help to further evaluate these trends and guide future geochemical testing.

#### 5.4. Climatic considerations

The Early Eocene Climatic Optimum (EECO) had a warmer climate than today (Fig. 19; Zachos et al., 2001, 2008; Smith et al., 2010; Hyland et al., 2018; Anagnostou et al., 2020; Inglis et al., 2020; Stokke et al., 2020). The early onset of the EECO is marked by the Paleocene-Eocene thermal maximum (PETM; Fig. 19). Although there is evidence linking volcanism to the onset and termination of the PETM (e.g., Stokke et al., 2020), the relationship of volcanism to the overall EECO remains unclear (e.g., Anagnostou et al., 2020). The Challis-Kamloops belt is but one of a number of regions in the world that witnessed volcanism during the latest Paleocene through early Eocene (e.g., Reagan et al., 2013; Gaina and Jakon, 2019; Stokke et

al., 2020), but the potential contribution to climate fluctuations are unknown. Integrated studies of Kamloops Group volcanism will help constrain the volumes of melt production, duration, and its contribution of volatiles to the Eocene atmosphere.

#### 6. Further work

This preliminary report is part of ongoing larger study of Eocene volcanic rocks in British Columbia. Through detailed physical volcanology, including volcanic architecture and lithofacies relationships, litho-geochemistry, and radiometric age-dating, this project aims to further contribute to the following.

- Re-evaluate and clarify the nomenclature and correlations of volcanic complexes in south-central British Columbia.
- Develop a lateral and stratigraphic context for the volcanic rocks through mapping, geochemistry, and geochronology.
- Test the potential contribution of these volcanic complexes to climate change during the EECO by developing temporal, volume, and volatile flux models.
- Further evaluate the relationship of volcanism to mineralization.

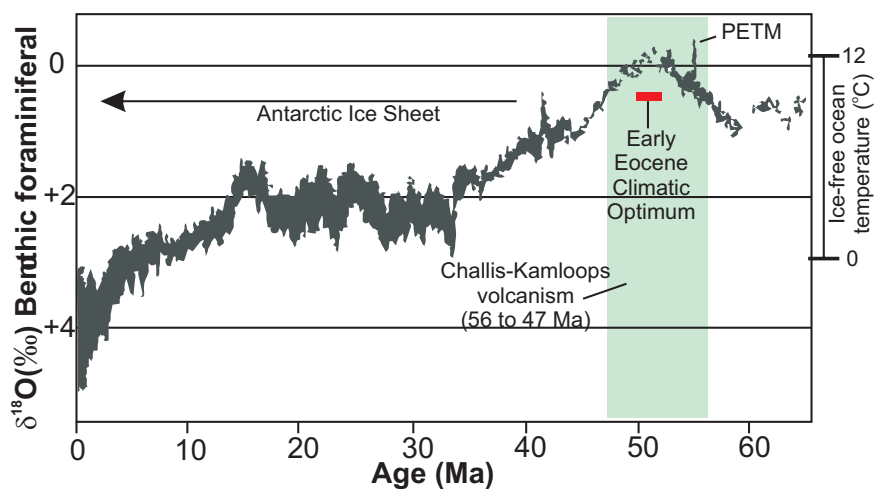


**Fig. 19.** Age vs.  $\delta^{18}\text{O}$ ‰ (Benthic foraminiferal). The  $\delta^{18}\text{O}$ ‰ values are a proxy for average sea water temperature, plotted at right, before the growth of the Antarctic ice sheet at ca. 35 Ma. The blue field shows that the Challis-Kamloops belt volcanism overlaps with the Early Eocene Climatic Optimum. PETM – Paleocene-Eocene thermal maximum. Modified from Zachos et al. (2008).

#### Acknowledgments

We are grateful to Steve Van Wagoner for field assistance and digitizing geologic maps. NVW thanks students in independent studies courses during 2017-18 who participated in studies of Kenna Cartwright Park. G. Jones assisted preparing the geochemistry figures. A review by N. Williamson improved the manuscript.

#### References cited

Aydiñakir, E., and Sen, C., 2013. Petrogenesis of the post-collisional volcanic rocks from the Borçka (Artvin) area: Implications for the evolution of the Eocene magmatism in the Eastern Pontides (NE Turkey). *Lithos*, 172-173, 98-117. <https://doi.org/10.1016/j.lithos.2013.04.007>.

- Alvarado, G.E., Pérez, W., Vogel, T.A., Gröger, H., and Patiño, L., 2011. The Cerro Chopo basaltic cone (Costa Rica): An unusual completely reversed graded pyroclastic cone with abundant low vesiculated cannonball juvenile fragments. *Journal of Volcanology and Geothermal Research*, 201, 163-177, <https://doi.org/10.1016/j.jvolgeores.2010.11.010>.
- Anagnostou, E., John, E.H., Babila, T.L., Sexton, P.F., Ridgwell, A., Lunt, D.J., Pearson, P.N., Chalk, T.B., Pancost, R.D., and Foster, G.L., 2020. Proxy evidence for state-dependence of climate sensitivity in the Eocene greenhouse. *Nature Communications*, 11, 4436.
- Anderson, S.W., Smrekar, S.E., and Stofan, E.R., 2012. Tumulus development on lava flows: insights from observations of active tumuli and analysis of formation models. *Bulletin of Volcanology*, 74, 931-946.
- Archibald, S.B., Greenwood, D.R., Smith, R.Y., Mathewes, R.W., and Basinger, J.F., 2011. Great Canadian *Lagerstätten* 1. Early Eocene *Lagerstätten* of the Okanagan Highlands (British Columbia and Washington State). *Geoscience Canada*, 38, 155-164.
- Bradshaw, T. K., and Smith, E.I., 1994. Polygenetic Quaternary volcanism at Crater Flat Nevada. *Journal of Volcanology and Geothermal Research*, 63, 165-182.
- Bordet, E., Mihalynuk, M.G., Hart, C.J.R., Mortensen, J.K., Friedman, R.M., and Gabites, J., 2014. Chronostratigraphy of Eocene volcanism, central British Columbia. *Canadian Journal of Earth Sciences*, 51, 56-103, <https://doi.org/10.1139/cjes-2013-0073>.
- Breitsprecher, K., 2002. Volcanic stratigraphy, petrology and tectonic setting of the eastern margin of the Eocene Kamloops Group, south-central British Columbia. Unpublished M.Sc. thesis, Simon Fraser University, 257 p.
- Breitsprecher, K., Thorkelson, D.J., Groome, W.G., and Dostal, J., 2003. Geochemical confirmation of the Kula-Farallon slab window beneath the Pacific Northwest in Eocene time. *Geology*, 31, 351-354, [https://doi.org/10.1130/0091-7613\(2003\)031<0351:GCOTKF>2.0.CO;2](https://doi.org/10.1130/0091-7613(2003)031<0351:GCOTKF>2.0.CO;2).
- Davidson, J., Turner, S., Handley, H., Macpherson, C., and Dosseto, A., 2007. Amphibole 'sponge' in arc crust? *Geology*, 35, 787-790, <https://doi.org/10.1130/G23637A.1>.
- Dostal, J., Church, B.N., Reynolds, P.H., and Hopkinson, L., 2001. Eocene volcanism in the Buck Creek Basin, Central British Columbia (Canada): Transition from arc to extensional volcanism. *Journal of Volcanology and Geothermal Research*, 107, 149-170, [https://doi.org/10.1016/S0377-0273\(00\)00261-4](https://doi.org/10.1016/S0377-0273(00)00261-4).
- Dostal, J., Breitsprecher, K., Church, B.N., Thorkelson, D., and Hamilton, T.S., 2003. Eocene melting of Precambrian lithospheric mantle: Alncime-bearing volcanic rocks from the Challis-Kamloops belt of south central British Columbia. *Journal of Volcanology and Geothermal Research*, 126, 303-326, [https://doi.org/10.1016/S0377-0273\(03\)00153-7](https://doi.org/10.1016/S0377-0273(03)00153-7).
- Dostal, J., Keppie, J.D., Church, B.N., Reynolds, P.H., and Reid, C.R., 2008. The Eocene-Oligocene magmatic hiatus in the south-central Canadian Cordillera: A capture of the Kula Plate by the Pacific Plate? *Canadian Journal of Earth Sciences*, 45, 69-82, <https://doi.org/10.1139/E07-062>.
- Dostal, J., Keppie, D., and Church, B.N., 2019. Generation of Eocene volcanic rocks from the Cordilleran arc of south-central British Columbia (Canada) during subduction of the Farallon and Resurrection plates and Yellowstone oceanic plateau. *Geological Journal*, 54, 590-604, <https://doi.org/10.1002/gj.3208>.
- Ewing, T.D., 1981a. Geology and tectonic setting of the Kamloops Group, south-central British Columbia. Unpublished Ph.D. thesis, University of British Columbia, 225 p.
- Ewing, T.E., 1981b. Regional stratigraphy and structural setting of the Kamloops Group, south-central British Columbia. *Canadian Journal of Earth Sciences*, 18, 1464-1477, <https://doi.org/10.1139/e81-137>.
- Ewing, T.E., 1981c. Petrology and geochemistry of the Kamloops Group volcanics, British Columbia. *Canadian Journal of Earth Sciences*, 18, 1478-1491, <https://doi.org/10.1139/e81-138>.
- Ewing, T. E., 1982., Geologic map of Tertiary rocks of the Afton-Tranquille area west of Kamloops. British Columbia. British Columbia Ministry of Energy, Mines and Petroleum Resources, British Columbia Geological Survey Preliminary Map 48, 1:50,000 scale.
- Furman, T., and Graham, D., 1999. Erosion of lithospheric mantle beneath the East African Rift system: Geochemical evidence from the Kivu volcanic province. *Developments in Geotectonics*, 24, 237-262, [https://doi.org/10.1016/S0419-0254\(99\)80014-7](https://doi.org/10.1016/S0419-0254(99)80014-7).
- Gaina, C., and Jakob, J., 2019. Global Eocene tectonic unrest: Possible causes and effects around the North American plate. *Tectonophysics*, 760, 136-151, <https://doi.org/10.1016/j.tecto.2018.08.010>.
- Goto, Y., and McPhie, J., 2012. Morphology and formation of spreading cracks on pillow lavas at Cape Grim, northwestern Tasmania, Australia. *Bulletin of Volcanology*, 74, 1611-1619, <https://doi.org/10.1007/s00445-012-0618-9>.
- Greenwood, D.R., Archibald, S.B., Mathewes, R.W., and Moss, P.T., 2005. Fossil biotas from the Okanagan Highlands, southern British Columbia and northeastern Washington State: Climates and ecosystems across an Eocene landscape. *Canadian Journal of Earth Sciences*, 42, 167-185, <https://doi.org/10.1139/e04-100>.
- Greenwood, D.R., Pigg, K.B., and DeVore, M.L., 2016. Eocene paleontology and geology of western north America. *Canadian Journal of Earth Sciences*, 53, 543-547.
- Haeussler, P.J., Bradley, D.C., Wells, R.E., and Miller, M.L., 2003. Life and death of the resurrection plate: Evidence for its existence and subduction in the northeastern Pacific in Paleocene-Eocene time. *Bulletin of the Geological Society of America*, 115, 867-880, [https://doi.org/10.1130/0016-7606\(2003\)115<0867:LADOTR>2.0.CO;2](https://doi.org/10.1130/0016-7606(2003)115<0867:LADOTR>2.0.CO;2).
- Hungerford, J.D.G., Edwards, B.R., Skilling, I.P., and Cameron, B.I., 2014. Evolution of a subglacial basaltic lava flow field: Tennena volcanic center, Mount Edziza volcanic complex, British Columbia, Canada. *Journal of Volcanology and Geothermal Research*, 272, 39-58, <https://doi.org/10.1016/j.jvolgeores.2013.09.012>.
- Hyland, E., Huntington, K.W., Sheldon, N.D., and Reichgelt, T., 2018. Temperature seasonality in the North American continental interior during the Early Eocene Climatic Optimum. *Climate of the Past*, 14, 1391-1404, <https://doi.org/10.5194/cp-14-1391-2018>.
- Ickert, R.B., Thorkelson, D.J., Marshall, D.D., and Ullrich, T.D., 2009. Eocene adakitic volcanism in southern British Columbia: Remelting of arc basalt above a slab window. *Tectonophysics*, 464, 164-185, <https://doi.org/10.1016/j.tecto.2007.10.007>.
- Inglis, G.N., et al., 2020. Global mean surface temperature and climate sensitivity of the early Eocene Climatic Optimum (EECO), Paleocene-Eocene Thermal Maximum (PETM), and latest Paleocene. *Climate of the Past*, 16, 1953-1968.
- Iverson, A.A., Rowe, M.C., Webster, J.D., and Neill, O.K., 2018. Amphibole-, clinopyroxene- and plagioclase-melt partitioning of trace and economic metals in halogen-bearing rhyodacitic melts. *Journal of Petrology*, 59, 1579-1604, <https://doi.org/10.1093/petrology/egy072>.
- Keskin, M., Chugae, A.V., Lebedev, V.A., and Sharkov, E.V., 2012. The geochronology and origin of mantle sources for late Cenozoic intraplate volcanism in the frontal part of the Arabian plate in the Karacadağ neovolcanic area of Turkey. Part 2. The results of geochemical and isotope (Sr-Nd-Pb) studies. *Journal of Volcanology and Seismology*, 6, 361-382, <https://doi.org/10.1134/S0742046312060048>.

- Krienitz, M.S., Haase, K.M., Mezger, K., Eckardt, V., and Shaikh-Mashail, M.A., 2006. Magma genesis and crustal contamination of continental intraplate lavas in northwestern Syria. *Contributions to Mineralogy and Petrology*, 151, 698-716, <https://doi.org/10.1007/s00410-006-0088-1>.
- Laubier, M., Grove, T.L., and Langmuir, C.H., 2014. Trace element mineral/melt partitioning for basaltic and basaltic andesitic melts: An experimental and laser ICP-MS study with application to the oxidation state of mantle source regions. *Earth and Planetary Science Letters*, 392, 265-278, <https://doi.org/10.1016/j.epsl.2014.01.053>.
- Le Bas, M.J., Le Maitre, R.W., Streckeisen, A., and Zanettin, B., 1986. A chemical classification of volcanic rocks based on the total alkali-silica diagram. *Journal of Petrology*, 27, 745-750.
- Leeman, W.P., Lewis, J.F., Evarts, R.C., Conrey, R.M., and Streck, M.J., 2005. Petrologic constraints on the thermal structure of the Cascades arc. *Journal of Volcanology and Geothermal Research*, 140, 67-105.
- Liang, Y., Liu, X., Qin, C., Li, Y., Chen, J., and Jiang, J., 2017. Petrogenesis of Early Cretaceous mafic dikes in southeastern Jiaolai basin, Jiaodong Peninsula, China. *International Geology Review*, 59, 131-150, <https://doi.org/10.1080/00206814.2016.1213666>.
- Love, D.A., Clark, A.H., Hodgson, C.J., Mortensen, J.K., Archibald, D.A., and Farrar, E., 1998. The timing of adularia-sericite-type mineralization and alunite-kaolinite-type alteration, Mount Skukum epithermal gold deposit, Yukon Territory, Canada; <sup>40</sup>Ar-<sup>39</sup>Ar and U-Pb geochronology. *Economic Geology*, 93, 437-462.
- Lowe, A.J., Greenwood, D.R., West, C.K., Galloway, J.M., Sudermann, M., and Reichgelt, T., 2018a. Plant community ecology and climate on an upland volcanic landscape during the Early Eocene Climatic Optimum: McAbee Fossil Beds, British Columbia, Canada. *Palaeogeography, Palaeoclimatology, Palaeoecology*, 511, 433-448, <https://doi.org/10.1016/j.palaeo.2018.09.010>.
- Lowe, A.J., West, C.K., and Greenwood, D.R., 2018b. Volcaniclastic lithostratigraphy and paleoenvironment of the lower Eocene McAbee fossil beds, Kamloops Group, British Columbia, Canada. *Canadian Journal of Earth Sciences*, 55, 923-934.
- MacLean, W.H., and Barrett, T.J., 1993. Lithochemical techniques using immobile elements. *Journal of Geochemical Exploration*, 48, 109-133.
- Madsen, J.K., Thorkelson, D.J., Friedman, R.M., and Marshall, D.D., 2006. Cenozoic to recent plate configurations in the Pacific Basin: Ridge subduction and slab window magmatism in western North America. *Geosphere*, 2, 11-34, <https://doi.org/10.1130/GES00020.1>.
- Maro, G., and Caffè, P.J., 2016. The Cerro Bitiche andesitic field: Petrological diversity and implications for magmatic evolution of mafic volcanic centers from the northern Puna. *Bulletin of Volcanology*, 78, Article 51, <https://doi.org/10.1007/s00445-016-1039-y>.
- Mayr, G., Archibald, S.B., Kaiser, G.W., and Mathewes, R.W., 2019. Early Eocene (Ypresian) birds from the Okanagan Highlands, British Columbia (Canada) and Washington State (USA). *Canadian Journal of Earth Sciences*, 56, 803-813.
- Michelfelder, G.S., Feeley, T.C., Wilder, A.D., and Klemetti, E.W., 2013. Modification of the continental crust by subduction zone magmatism and vice-versa: Across-strike geochemical variations of silicic lavas from individual eruptive centers in the Andean central volcanic zone. *Geosciences*, 3, 633-667, <https://doi.org/10.3390/geosciences3040633>.
- Morris, G.A., and Creaser, R.A., 2003. Crustal recycling during subduction at the Eocene Cordilleran margin of North America: A petrogenetic study from the southwestern Yukon. *Canadian Journal of Earth Sciences*, 40, 1805-1821.
- Patiño, L.C., Carr, M.J., and Feigenson, M.D., 2000. Local and regional variations in Central American arc lavas controlled by variations in subducted sediment input. *Contributions to Mineralogy and Petrology*, 138, 265-283.
- Pearce, J.A., 1996. A user's guide to basalt discrimination diagrams. In: Wyman, D.A., (Ed.), *Trace element geochemistry of volcanic rocks: Applications for massive sulphide exploration*. Geological Association of Canada, Short Course Notes, 12, pp. 79-113.
- Read, P.B., and Hebda, R. 2009. Geological setting and paleontology of the fossiliferous Eocene beds near McAbee, southwestern British Columbia. Online Report, British Columbia Ministry of Agriculture and Lands, 83 p., <https://www2.gov.bc.ca/gov/content/industry/natural-resource-use/fossil-management/mcabee>.
- Reagan, M.K., McClelland, W.C., Girard, G., Goff, K.R., Peate, D.W., Ohara, Y., and Stern, R.J., 2013. The geology of the southern Mariana fore-arc crust: Implications for the scale of Eocene volcanism in the western Pacific. *Earth and Planetary Science Letters*, 380, 41-51, <https://doi.org/10.1016/j.epsl.2013.08.013>.
- Reynolds, P., Brown, R.J., Thordarson, T., Llewellyn, E.W., and Fielding, K., 2015. Rootless cone eruption processes informed by dissected tephra deposits and conduits. *Bulletin of Volcanology*, 77, <https://doi.org/10.1007/s00445-015-0958-3>.
- Ross, P.-S., and Bédard, J.H., 2009. Magmatic affinity of modern and ancient volcanic rocks determined from trace-element discrimination diagrams. *Canadian Journal of Earth Sciences*, 46, 823-839.
- Skilling, I.P., 2002. Basaltic pahoehoe lava-fed deltas: Large-scale characteristics, clast generation, emplacement processes and environmental discrimination. In: Smellie, J.L., and Chapman, M.G., (Eds.), *Volcano-Ice Interaction on Earth and Mars*. Geological Society Special Publication, 202, 91-113, <https://doi.org/10.1144/GSL.SP.2002.202.01.06>.
- Smellie, J.L., Millar, I.L., Rex, D.C., and Butterworth, P.J., 1998. Subaqueous, basaltic lava dome and carapace breccia on King George Island, South Shetland Islands, Antarctica. *Bulletin of Volcanology*, 59, 245-261, <https://doi.org/10.1007/s004450050189>.
- Smith, E.I., Sanchez, A.J., Walker, J.D., and Wang, K., 1999. Geochemistry of mafic magmas in the Hurricane Volcanic Field Utah: Implications for small- and large-scale chemical variability of the lithospheric mantle. *Journal of Geology*, 107, 433-448.
- Smith, R.Y., Greenwood, D.R., and Basinger, J.F., 2010. Estimating paleoatmospheric *p*CO<sub>2</sub> during the Early Eocene Climatic Optimum from stomatal frequency of *Ginkgo*, Okanagan Highlands, British Columbia, Canada. *Palaeogeography, Palaeoclimatology, Palaeoecology*, 293, 120-131.
- Stern, R.J., and Dumitru, T.A., 2019. Eocene initiation of the Cascadia subduction zone: A second example of plume-induced subduction initiation? *Geosphere*, 15, 659-681, <https://doi.org/10.1130/GES02050.1>.
- Stevenson, J.A., Mitchell, N.C., Mochrie, F., Cassidy, M., and Pinkerton, H., 2012. Lava penetrating water: The different behaviours of pāhoehoe and 'a'ā at the Nesjhraun, Þingvellir, Iceland. *Bulletin of Volcanology*, 74, 33-46, <https://doi.org/10.1007/s00445-011-0480-1>.
- Stokke, E.W., Jones, M.T., Tierney, J.E., Svensen, H.H., and Whiteside, J.H., 2020. Temperature changes across the Paleocene-Eocene Thermal Maximum—a new high-resolution TEX<sub>86</sub> temperature record from the eastern North Sea Basin. *Earth and Planetary Science Letters*, 544, 116338, <https://doi.org/10.1016/j.epsl.2020.116388>.
- Sun, S.S., and McDonough, W.F., 1989. Chemical and isotopic systematics of oceanic basalts: implications for mantle composition and processes. In: Saunders, A.D., and Norry, M.J., (Eds.), *Magmatism in the Ocean Basins*. Geological Society of London, Special Publication, 42, pp. 313-345.
- Vander Auwera, J., Namur, O., Dutrieux, A., Wilkinson, C.M., Ganerød, M., Coumont, V., and Bolle, O., 2019. Mantle melting and magmatic processes under la Picada stratovolcano (CSVZ,

- Chile). *Journal of Petrology*, 60, 907-944, <https://doi.org/10.1093/petrology/egz020>.
- Van Wagoner, N., and Ootes, L., 2021. Geochemical data from the Kamloops Group (Eocene) volcanic rocks. British Columbia Ministry of Energy, Mines and Low Carbon Innovation, British Columbia Geological Survey GeoFile, in prep.
- Walker, G.P.L., 1992. Morphometric study of pillow-size spectrum among pillow lavas. *Bulletin of Volcanology*, 54, 459-474.
- Walker, J.A., Patiño, L.C., Cameron, B.I., and Carr, M.J., 2000. Petrogenetic insights provided by compositional transects across the Central America arc: southeastern Guatemala and Honduras. *Journal of Geophysical Research*, 105, 18949-18963.
- Walker, J.A., Patiño, L.C., Carr, M.J., and Feigenson, M.D., 2001. Slab control over HFSE depletions in Central Nicaragua. *Earth and Planetary Science Letters*, 192, 533-543, [https://doi.org/10.1016/S0012-821X\(01\)00476-9](https://doi.org/10.1016/S0012-821X(01)00476-9).
- Wang, K., Plank, T., Walker, J.D., and Smith, E.I., 2002. A mantle melting profile across the Basin and Range, SW USA. *Journal of Geophysical Research: Solid Earth*, 107, ECV 5-1-ECV 5-21, <https://doi.org/10.1029/2001jb000209>.
- Wang, J., Xiong, X., Takahashi, E., Zhang, L., Li, L., and Liu, X., 2019. Oxidation state of arc mantle revealed by partitioning of V, Sc, and Ti between mantle minerals and basaltic melts. *Journal of Geophysical Research: Solid Earth*, 124, 4617-4638, <https://doi.org/10.1029/2018JB016731>.
- Wang, X.C., Wilde, S.A., Xu, B., and Pang, C.J., 2016. Origin of arc-like continental basalts: Implications for deep-Earth fluid cycling and tectonic discrimination. *Lithos*, 261, 5-45, <https://doi.org/10.1016/j.lithos.2015.12.014>.
- West, C.K., Greenwood, D.R., Reichgelt, T., Lowe, A.J., Vachon, J.M., and Basinger, J.F., 2020. Paleobotanical proxies for early Eocene climates and ecosystems in northern North America from middle to high latitudes. *Climate of the Past*, 16, 1387-1410.
- Winchester, J.A., and Floyd, P., 1977. Geochemical discrimination of different magma series and their differentiation products using immobile elements. *Chemical Geology*, 20, 325-343.
- Woodhead, J.D., Hergt, J.M., Davidson, J.P., and Eggins, S.M., 2001. Hafnium isotope evidence for 'conservative' element mobility during subduction zone processes. *Earth and Planetary Science Letters*, 192, 331-346, [https://doi.org/10.1016/S0012-821X\(01\)00453-8](https://doi.org/10.1016/S0012-821X(01)00453-8).
- Yamagishi, H., 1987. Studies on the Neogene subaqueous lavas and hyaloclastites in southwest Hokkaido. Report of the Geological Survey of Hokkaido, No. 59, 55-117.
- Yamagishi, H., 1991. Morphological and sedimentological characteristics of the Neogene submarine coherent lavas and hyaloclastites in Southwest Hokkaido, Japan. *Sedimentary Geology*, 74, 5-23, [https://doi.org/10.1016/0037-0738\(91\)90032-9](https://doi.org/10.1016/0037-0738(91)90032-9).
- Zachos, J., Pagani, H., Sloan, L., Thomas, E., and Billups, K., 2001. Trends, rhythms, and aberrations in global climate 65 Ma to present. *Science*, 292, 686-693, <https://doi.org/10.1126/science.1059412>.
- Zachos, J.C., Dickens, G.R., and Zeebe, R.E., 2008. An early Cenozoic perspective on greenhouse warming and carbon-cycle dynamics. *Nature*, 451, 279-283, <https://doi.org/10.1038/nature06588>.
- Zhang, L., Li, S., and Zhao, Q., 2019. A review of research on adakites. *International Geology Review*, doi:10.1080/00206814.2019.1702592.
- Zhang, J., Liao, M., Santosh, M., Yang, Z., Zhang, Y., and Dai, Y., 2020. Middle Tonian calc-alkaline picrites, basalts, and basaltic andesites from the Jiangnan Orogen: Evidence for rear-arc magmatism. *Precambrian Research*, 350, 105943, <https://doi.org/10.1016/j.precamres.2020.105943>.



# Geology of the Tatogga property: Geologic framework for the Saddle North porphyry Cu-Au deposit and the Saddle South epithermal Au-Ag vein system, Iskut district, northwestern British Columbia

C.J. Greig<sup>1, 2, a</sup>, N.P. Dudek<sup>1</sup>, T.J. ver Hoeve<sup>1</sup>, T.D.M. Quinn<sup>1</sup>, G. Newton<sup>1, 2</sup>, S.A. Makin<sup>1</sup>, and R.E. Greig<sup>1</sup>

<sup>1</sup>C.J. Greig & Associates Ltd., 729 Okanagan Ave. E., Penticton, BC, V2A 3K7

<sup>2</sup>GT Gold Corp., Suite 610, 1100 Melville Street, Vancouver, BC, V6E 4A6

<sup>a</sup>corresponding author: [cjgreig1@telus.net](mailto:cjgreig1@telus.net)

Recommended citation: Greig, C.J., Dudek, N.P., ver Hoeve, T.J., Quinn, T.D.M., Newton, G., Makin, S.A., and Greig, R.E., 2021. Geology of the Tatogga property: Geologic framework for the Saddle North porphyry Cu-Au deposit and the Saddle South epithermal Au-Ag vein system, Iskut district, northwestern British Columbia. In: Geological Fieldwork 2020, British Columbia Ministry of Energy, Mines and Low Carbon Innovation, British Columbia Geological Survey Paper 2021-01, pp. 89-111.

## Abstract

Recent geologic mapping, new U-Pb zircon and Re-Os molybdenum geochronology, and an intensive drilling program provide the framework for two significant recent exploration discoveries on the Tatogga property, in the Iskut district of northwestern British Columbia. These data help to establish the Late Triassic to early Middle Jurassic evolution of host rocks, mineralization, syn- to post-mineral intrusions, and structures. Although mineralization at both the Saddle North porphyry copper-gold deposit and the Saddle South epithermal precious metals vein system is spatially related to latest Triassic to earliest Jurassic monzonitic intrusive rocks (including the Saddle North intrusive complex of the Tatogga suite), the property is underlain mainly by Upper Triassic and Lower Jurassic volcanosedimentary rocks of the Stuhini and Hazelton groups. Marine arc volcanic and related sedimentary rocks of the Stuhini Group were deposited in the Late Triassic, starting by at least ca. 224 Ma and continuing until after ca. 206 Ma, possibly from a magmatic centre near the Saddle North area. Although an abundance of hornblende-feldsparphyric volcanic rocks is typically known as a hallmark of the Hazelton Group, our work indicates that common trachyandesitic or latitic rocks with abundant very fine-grained feldspar and subordinate hornblende are part of the Stuhini Group. Between ca. 206 and 202 Ma Stuhini Group rocks were intruded by partly coeval Tatogga suite plutonic rocks. Epithermal vein mineralization at Saddle South is considered to predate emplacement of these monzonitic intrusions and thus is thought to be older than the porphyry copper-gold mineralization that is genetically related to later phases of the monzonitic Saddle North intrusive complex. As indicated by clast compositions of Hazelton Group conglomerates and a structural discordance between the Stuhini Group on the southern part of the property and the Hazelton Group to the north, the Stuhini-Hazelton transition was marked by contractional deformation, uplift, and erosional stripping (all possibly related to early movement along the Poelzer fault), as has been documented elsewhere in northern Stikinia. Following renewed arc activity and shallow-marine to subaerial deposition of Hazelton Group volcanosedimentary strata, the later stages of Hazelton Group magmatism included intrusion of Early Jurassic felsic dikes (ca. 187 to 182 Ma) in west-northwest trending swarms that cut across folds in Stuhini Group rocks. Further contractional deformation affected both the Hazelton and Stuhini group rocks in the Cretaceous, during formation of the Skeena fold-thrust belt, and may locally have reactivated earlier structures. In the Late Cenozoic, mafic dikes fed volcanic flows and tuffaceous rocks exposed in the upper Klastline River valley.

**Keywords:** Stuhini, Hazelton, Iskut, Tatogga, Saddle North, Saddle South, Klastline River, porphyry Cu-Au, epithermal Au-Ag vein, sub-Hazelton Group unconformity, Poelzer fault, Golden Triangle, GT Gold Corp.

## 1. Introduction

Stikine terrane (Stikinia) is an oceanic island arc tectonostratigraphic unit consisting of mid-Paleozoic to Middle Jurassic rocks that underlie much of western British Columbia. Stikinia is the largest of numerous allochthonous to parautochthonous terranes that were accreted to the western margin of North America by the late Middle Jurassic to form the Intermontane Belt of the Canadian Cordillera (Coney et al., 1980; Monger et al., 1982; Nelson and Colpron, 2007). Most workers accept that Stikinia was subsequently consolidated with outboard terranes of the Insular Belt to the west (Wrangell

and Alexander terranes), in the latest Jurassic to mid-Cretaceous (e.g., Gehrels et al., 1996).

In the Iskut district of northwestern British Columbia, and part of a loosely defined precious metals-rich area commonly referred to as the 'Golden Triangle', the Tatogga property (GT Gold Corp.) is underlain by Stikine terrane rocks (Figs. 1, 2). Exploration by GT Gold Corp. from 2016 to 2018 culminated in the drill discovery of significant new mineralized zones, the Saddle North porphyry copper-gold deposit and the Saddle South epithermal precious metals vein system (Greig et al., 2020). Although mineralization at both deposits is spatially

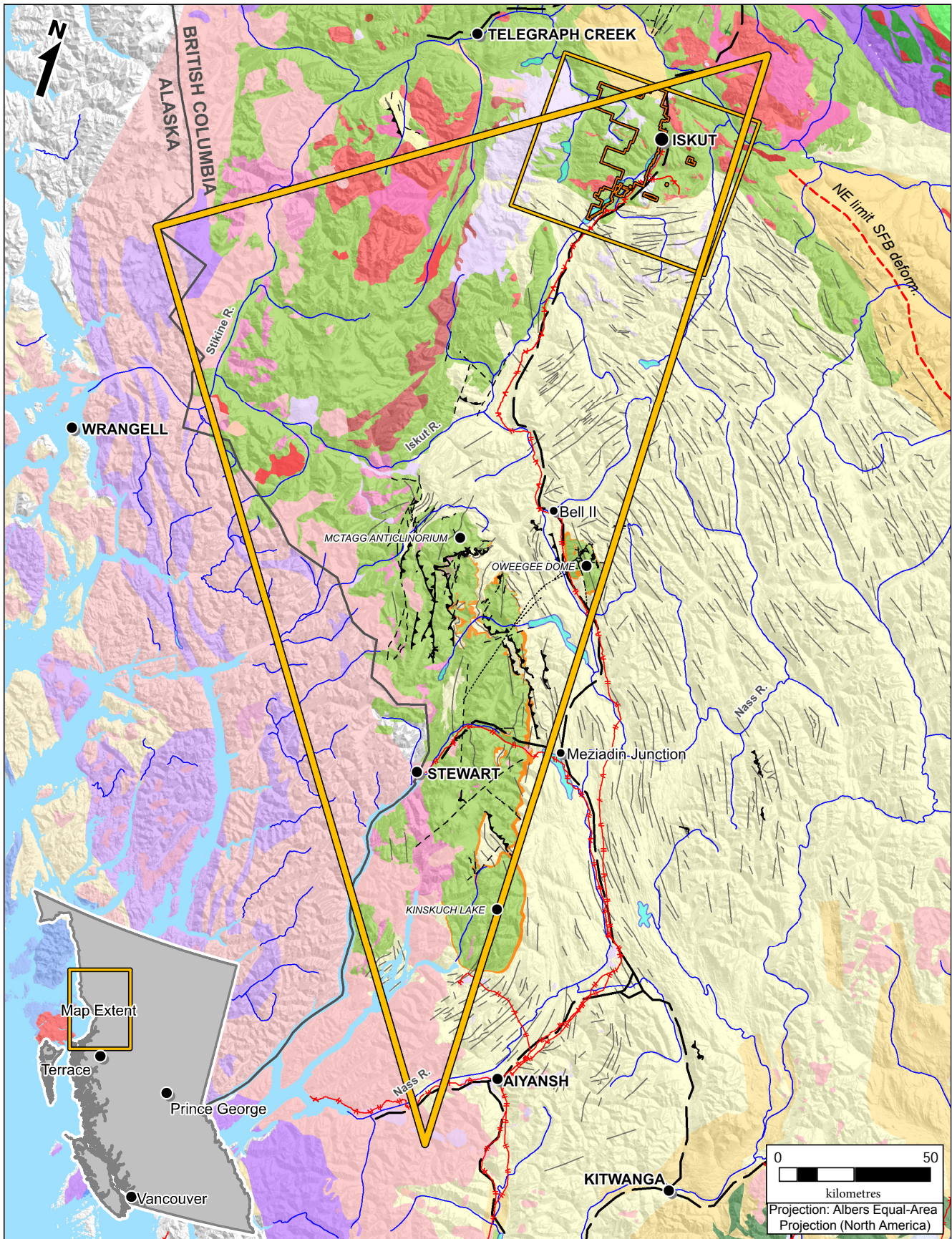


Fig. 1. Regional geology of northern Stikinia (see Figure 2 for legend).



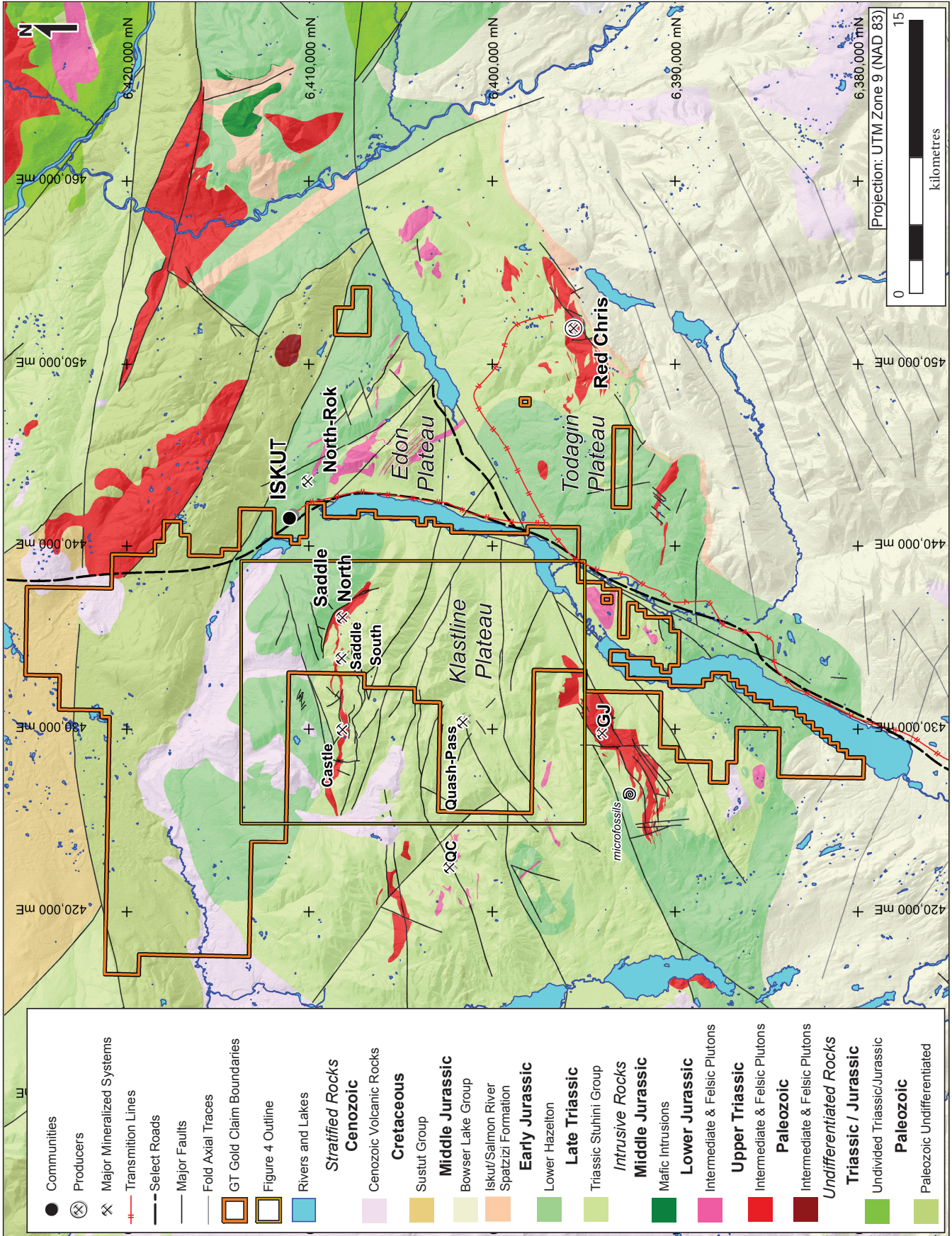


Fig. 3. Geology of the Klastline, Edon, and Todagin plateaus and Red-Chris mining camp, Iskut district.

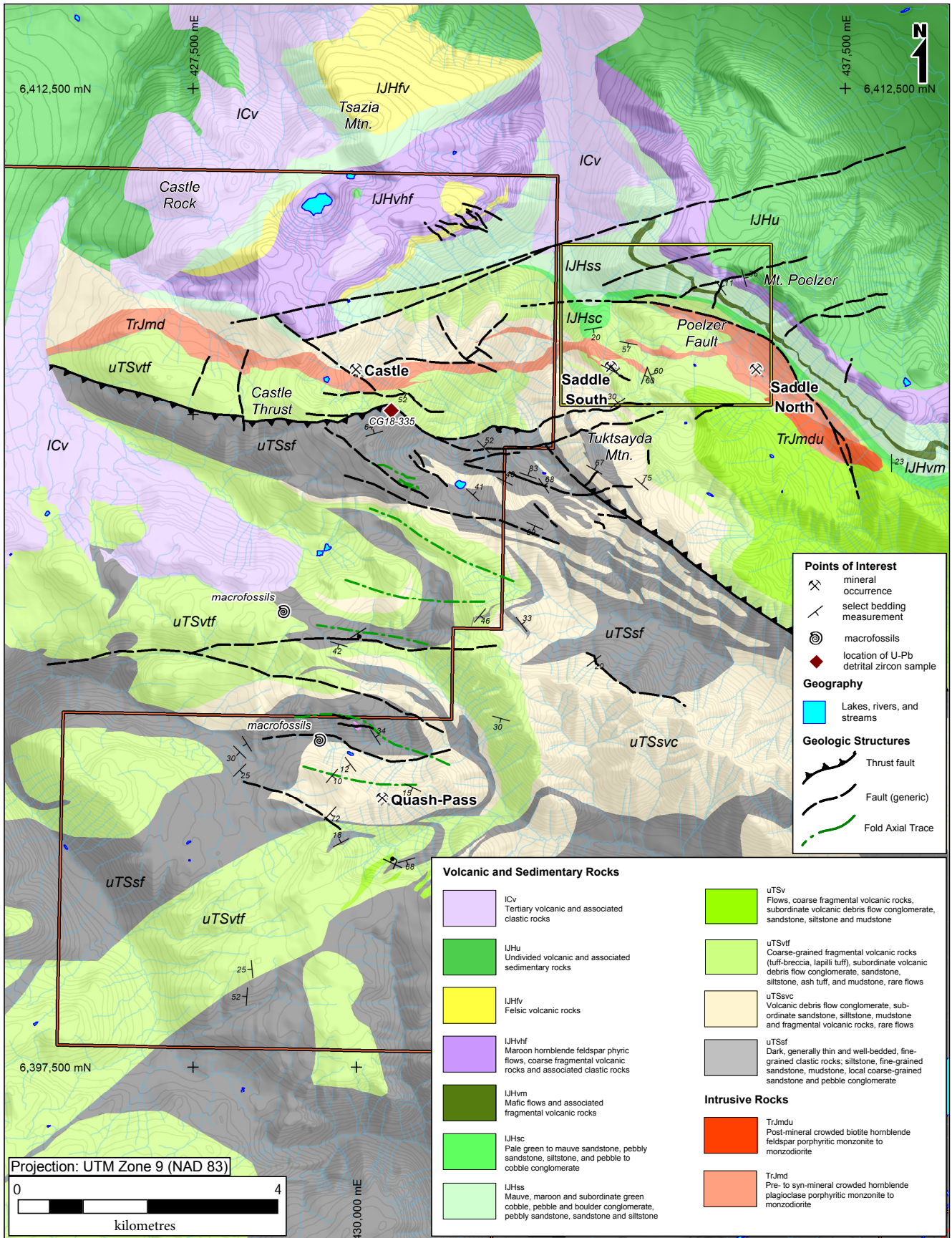


Fig. 4. Geology of the Tatogga property (geology west of northern Tatogga property after Oliver 2018).

plateaus to the north and east of the Klastline plateau, have been informally referred to as the Red suite, with individual bodies given local names, such as the Red stock (Rees et al., 2015), the Groat stock (e.g., Friedman and Ash, 1997), and the Castle stock (Bradford and Barresi, 2013). Although we favour the name Saddle intrusions, we also recognize the rationale behind, and the need for, a unifying and more regional name, such as Tatogga suite, as proposed by Nelson et al. (2018).

In the Iskut district, rocks in the upper part of the Hazelton Group commonly overlie the intrusions and their host rocks (e.g., Rees et al., 2015; Figs. 3-5). The upper Hazelton Group rocks are also commonly overlain by still younger rocks of the Bowser Lake Group (Middle Jurassic to mid-Cretaceous), or by Late Cenozoic volcanic rocks. In contrast to areas to the south, the structural grain in the region follows a more or less east-west trend (Figs. 3-5), aligned with the Skeena fold-thrust belt (mid-Cretaceous; Evenchick, 1991) and well displayed in Bowser Lake Group strata (Figs. 1-5).

### 3. Stratified rocks

#### 3.1. Stuhini Group (Upper Triassic)

Much of the Klastline Plateau south of the Saddle zones is underlain by stratified Upper Triassic to (possibly) lowermost Jurassic rocks that we assign to the Stuhini Group (Fig. 4). New geochronological data from the area suggest that these rocks range from at least ca. 224 Ma (crystallization age) to ca. 206 Ma (maximum detrital zircon age; see section 5 below; Greig et al., 2021). Assignment to the Stuhini Group is supported by Upper Triassic (Ladinian?-Norian) marine macro- and micro-fossils found locally in rocks at the southern part of the property (Unit uTSsf below; Souther, 1972; Ash et al., 1996).

Based on predominant rock types, we divided Stuhini Group rocks into four units, which may be considered as facies assemblages (Figs. 4, 5): 1) unit uTSv, with poorly-stratified coarse-grained fragmental volcanic deposits and interbedded flows; 2) unit uTSvtf, with variably well-stratified pyroclastic rocks; 3) unit uTSsvc, with well-stratified pyroclastic rocks that are interbedded with epiclastic strata; and 4) unit uTSsf, with mainly epiclastic strata. We emphasize that lithotypes interfinger, repeating in time and space, and that each of these units contains strata that are indistinguishable from the main lithotypes of the other units.

##### 3.1.1. Map units uTSv and uTSvtf

Units uTSv and uTSvtf are most common immediately south and southeast of the Saddle North deposit (Figs. 4-6). Unit uTSv includes volcanic flows (Figs. 7, 8), coarse fragmental volcanic rocks (Fig. 9) and subordinate volcanic conglomerate, sandstone, siltstone, and mudstone. Unit uTSvtf contains thickly stratified coarse-grained fragmental volcanic rocks including tuff-breccia and lapilli tuff (Figs. 9-11), subordinate volcanic conglomerate, sandstone, siltstone, ash tuff, and mudstone, and rare flows. As is common for the Stuhini Group throughout the property, both flows and fragments in

tuffaceous and conglomeratic rocks are predominantly crowded hornblende- plagioclase feldspar-phyric trachyandesite or latite with abundant fine-grained plagioclase feldspar and rarely, potassium feldspar phenocrysts (Figs. 7, 11). Also present are local pyroxene and plagioclase- pyroxene-phyric flows (Fig. 8) and spatially associated pyroxene-bearing coarse fragmental rocks (Fig. 12). Rarely, pyroxene may occur with hornblende. Modal abundance estimates of sodium cobaltnitrate-stained hand samples (Figs. 7, 11, 12) confirm that the bulk of the rocks are trachyandesitic or latitic in composition.

Map unit uTSvtf consists mainly of poorly stratified coarse fragmental volcanic rocks such as tuff-breccia and 'coarse' (average fragment >10 cm) lapilli tuff (Fig. 7). Also abundant are 'medium' (average fragment >3 <10 cm) lapilli tuff (Fig. 10), and weakly stratified, poorly sorted boulder-cobble conglomerate. Less common are 'fine' (average fragment <3 cm) lapilli tuff (Fig. 12), ash tuff, pebble conglomerate, sandstone, siltstone and mudstone; flows are also present locally. As with map unit uTSv, fragments in the tuffaceous rocks, clasts in the conglomerate, and the local flows consist predominantly of crowded hornblende- feldspar-phyric trachyandesite containing fine-grained plagioclase feldspar phenocrysts, and fine- to medium-grained hornblende phenocrysts. Also present are rare pyroxene-phyric flows and pyroxene-phyric coarse-grained fragmental rocks. These rock types may also be found locally as clasts in the tuffaceous and conglomeratic rocks.

##### 3.1.2. Map units uTSsvc and uTSsf

Map units uTSsvc and uTSsf have a greater proportion of epiclastic rocks and are typically better stratified than units uTSv and uTSvtf (Fig. 13). Unit uTSsvc consists of conglomerate (Figs. 14, 15), subordinate sandstone (Fig. 15), siltstone, mudstone (Fig. 16), trachyandesitic or latitic fragmental volcanic rocks, and rare trachyandesite or latite flows. Unit uTSsf consists mainly of generally dark, interstratified siliciclastic rocks, including fine-grained sandstone, siltstone, mudstone (Figs. 16-19), with local ash tuff, fine lapilli tuff, coarse-grained sandstone and pebble conglomerate. Pebble conglomerates and sandstones generally lack internal stratification but are arranged in repeated sharp-based fining-upward sequences (Fig. 15). Metre-scale dark grey, locally fossiliferous micritic limestone lenses are relatively common throughout. Clasts in units uTSsvc and uTSsf are similar in composition to the fragments in units uTSv and uTSvtf, consisting almost exclusively of hornblende-feldspar-phyric trachyandesite or latite with crowded fine-grained plagioclase and subordinate fine- to medium-grained hornblende phenocrysts (e.g., Fig. 14).

##### 3.1.3. Distribution and geometry

The rocks of units uTSv and uTSvtf are most abundant in the northern part of the Tatogga property where they are commonly propylitically (chlorite-epidote)- and (or) iron carbonate-altered. Together they form a northwest-trending belt hosting the mineralized zones at Saddle North and Saddle South. They also appear to be common northeast of the Quash-Pass area

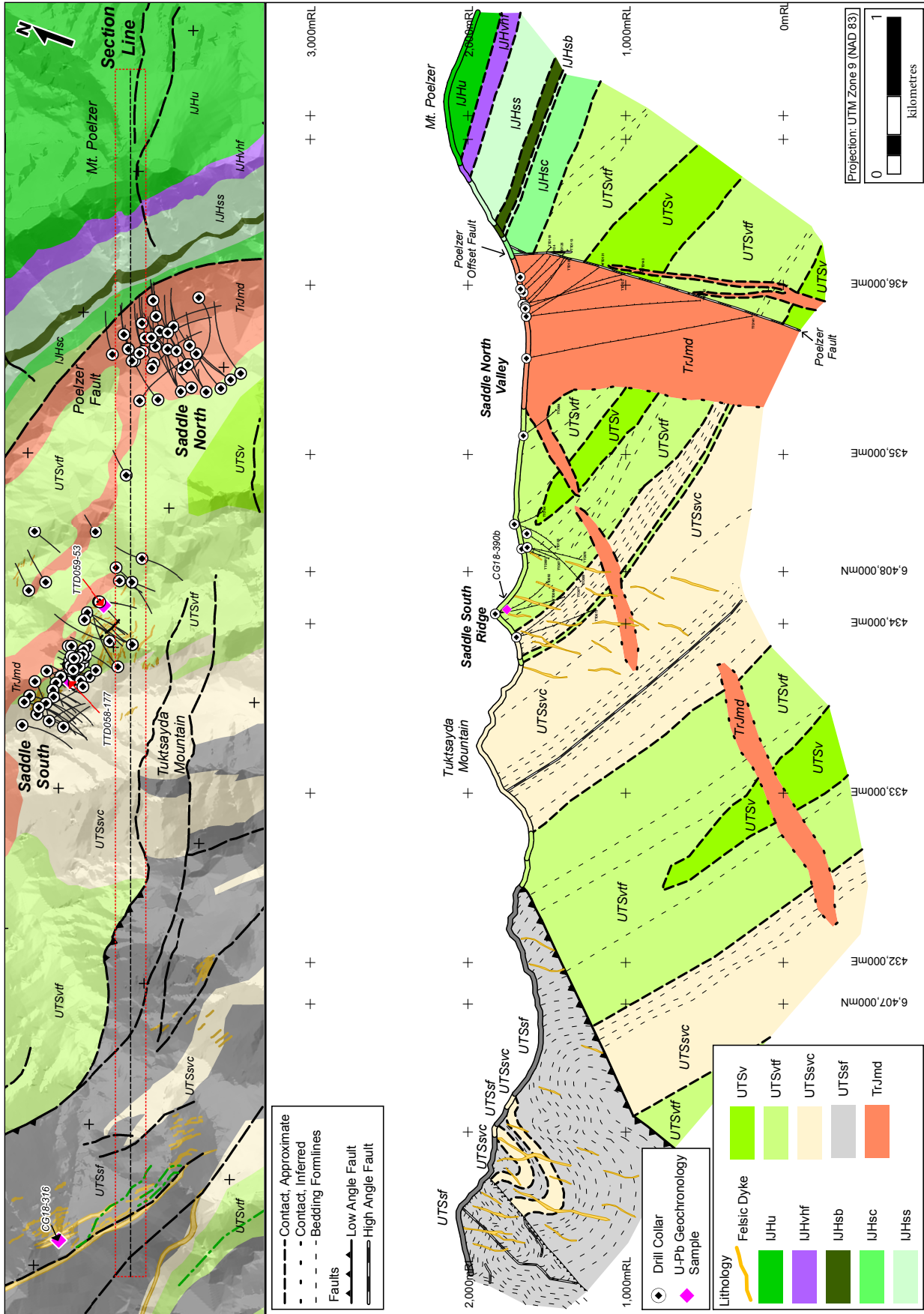
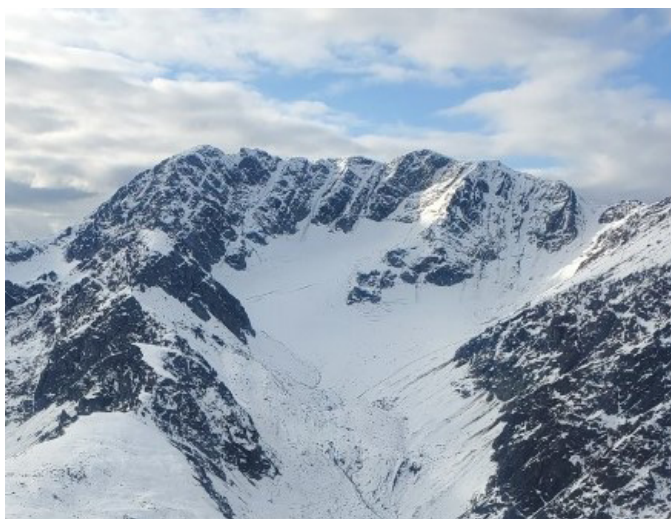
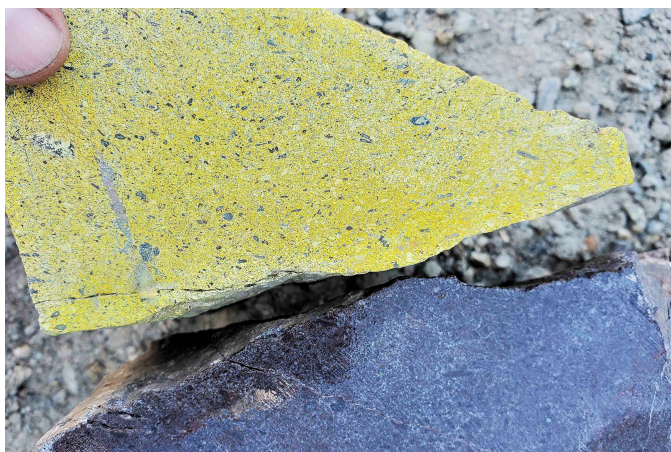


Fig. 5. Schematic cross section across the Saddle North and South mineralized zones and northern part of the Tatogga property.



**Fig. 6.** View south-southeast along and up Saddle South ridge (left) toward Tuksayda Mountain, showing northeast-dipping thickly stratified Stuhini Group fragmental volcanic rocks (unit uTSvtf).



**Fig. 7.** Stuhini Group, map unit UTSv. Crowded hornblende-feldspar-phyric trachyandesite flow, ~1.7 km southeast of Saddle North. Top stained with sodium cobaltnitrate for potassium feldspar.

(Fig. 4). Although not well stratified and lacking obvious tops indicators, on the central and the eastern part of the property the thick bedded and crudely stratified rocks of units uTSv and uTSvtf appear to define a moderately to steeply northeast dipping homocline that youngs to the northeast (Figs. 4, 5). To the southwest the coarse tuffaceous rocks are concordant with well-bedded uTSsv and uTSsf rocks. Farther west, the rocks of units uTSsv and uTSsf are commonly well folded and faulted (see section 6 below).

### 3.1.4. Environmental interpretation

As is typical of many volcanosedimentary sequences, Stuhini Group rocks in the Saddle area record the interplay of volcanism, erosion, and sedimentation repeated in time and space. Some of the coarser deposits of unit uTSv may represent a vent-proximal facies, whereas sandstones and pebble conglomerates are interpreted to represent turbiditic beds. The



**Fig. 8.** Stuhini Group map unit uTSv. Pyroxene- and feldspar-phyric basaltic trachyandesite or trachybasalt flow, ~700 m south of Saddle North.



**Fig. 9.** Stuhini Group, map unit uTSv. Medium- to coarse-trachyandesite lapilli tuff (upper) and block tuff (lower), Saddle South area.

fossils in unit uTSsf (Souther, 1972; Ash et al., 1996; Figs. 3, 4) indicate marine sedimentation in part, and the near-ubiquitous dark colours of epiclastic facies may imply relatively deep (anoxic) waters. However, rare fragmental volcanic and coarse siliciclastic rocks with red clasts and matrix, such as at immediately southwest of Mt. Tuksayda, might suggest sedimentation in an oxidizing environment and that shallow-marine conditions prevailed locally.

### 3.2. Hazelton Group (Lower Jurassic)

A distinctive well-layered volcanosedimentary sequence is exposed north of the Saddle area between Mount Poelzer and Tazsia Mountain (Figs. 4, 5 and 20); it also outcrops on the northern end of Saddle South ridge. Following Ash et al. (1997a, b) we assign these rocks to the Hazelton Group. With



**Fig. 10.** Stuhini Group, map unit uTSvtf. Medium lapilli tuff with hornblende-feldspar-phyric fragments and pyroxene-phyric fragments (green) in pale weathering groundmass, ~900 m west-southwest of Saddle North and 450 m east-southeast of Saddle South.

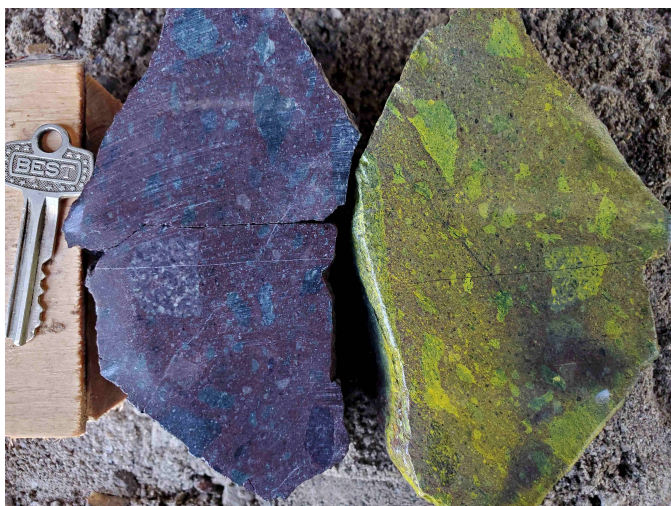


**Fig. 11.** Stuhini Group, map unit uTSvtf. Maroon and green trachyandesitic lapilli tuff (right stained with sodium cobaltnitrate for potassium feldspar); note relatively potassium feldspar-rich fragments, and possible monzonitic intrusive rock fragment (slightly coarser-grained), ~175 m north of Saddle South zone.

maroon to mauve and pale green colours, the rocks in this gently north-dipping sequence contrast sharply with the darker moderately to steeply south-dipping Stuhini Group rocks to the south suggesting an angular discordance between the two (see Fig. 5 and section 6 below). The contact is not observed at surface because it is faulted (note “Poelzer offset” fault, Fig. 5) and largely drift-covered, but the presence of an angular discordance is supported by the presence of common Stuhini Group cobbles and boulders, by pebbles and cobbles of altered rock and quartz (Fig. 21), plus an abundance of Late Triassic detrital zircon grains in basal sandstones (George et al., 2021).

Although we did not map in detail, and although the contact itself was not observed, we traversed through this section along gullies extending from the Saddle area toward the northwest-



**Fig. 12.** Stuhini Group, map unit uTSv. Maroon and green pyroxene- and feldspar-phyric basaltic trachyandesite lapilli tuff (right stained with sodium cobaltnitrate for potassium feldspar; note slight difference in potassium feldspar content between fragments and matrix), ~2 km south of Saddle North deposit.



**Fig. 13.** View to the south-southeast, looking approximately down dip at gently southeasterly dipping moderately well-stratified Stuhini Group rocks of map units uTSsv and uTSsf, on south side of valley, Quash-Pass area (see Figure 4 for location).



**Fig. 14.** Stuhini Group, map unit uTSsv. Clast-supported boulder conglomerate or pyroclastic breccia with angular fragments of moderately crowded hornblende- and feldspar phyric trachyandesite, with carbonate cement.

trending ridge that underlies Mount Poelzer (Figs. 5, 6). There the general character and a number of common rock types from the lower part of the sequence appear to have reasonable



**Fig. 15.** Stuhini Group, map unit uTSsvc. View south-southeast of moderately northeast-dipping dark grey, slightly rusty-weathering medium- to thick-bedded well-stratified and moderately well-sorted pebble conglomerate, above interbedded sandstone, siltstone and mudstone arranged in sharp-based Bouma-like fining upward sequences, ~1.5 km southwest of Saddle South.



**Fig. 16.** Stuhini Group; on right, well-bedded black mudstone (map unit uTSsf) possibly faulted against lapilli tuff on left; view to the northeast, immediately west of Tatogga property boundary, southwest of Saddle area.

along-strike continuity, given the generally well-stratified nature of the package at all scales (Fig. 21) and evident in their aeromagnetic signature and grain, which parallels their strike (Miller and Smythe, 2015). Typically maroon pebble, cobble, and rare boulder conglomerates with local well-rounded clasts (Figs. 21, 22) are particularly abundant at the base of the section on the southwest side of the creek that drains the area of the Saddle North deposit near the lower, northern end of Saddle South ridge (unit IJHsc, Fig. 4). Significantly, the conglomerates bear very common clasts that appear to have been derived from subjacent and distinctive Stuhini Group, including finely feldspar- and hornblende-phyric rocks, and less common clasts displaying a pervasive internal alteration

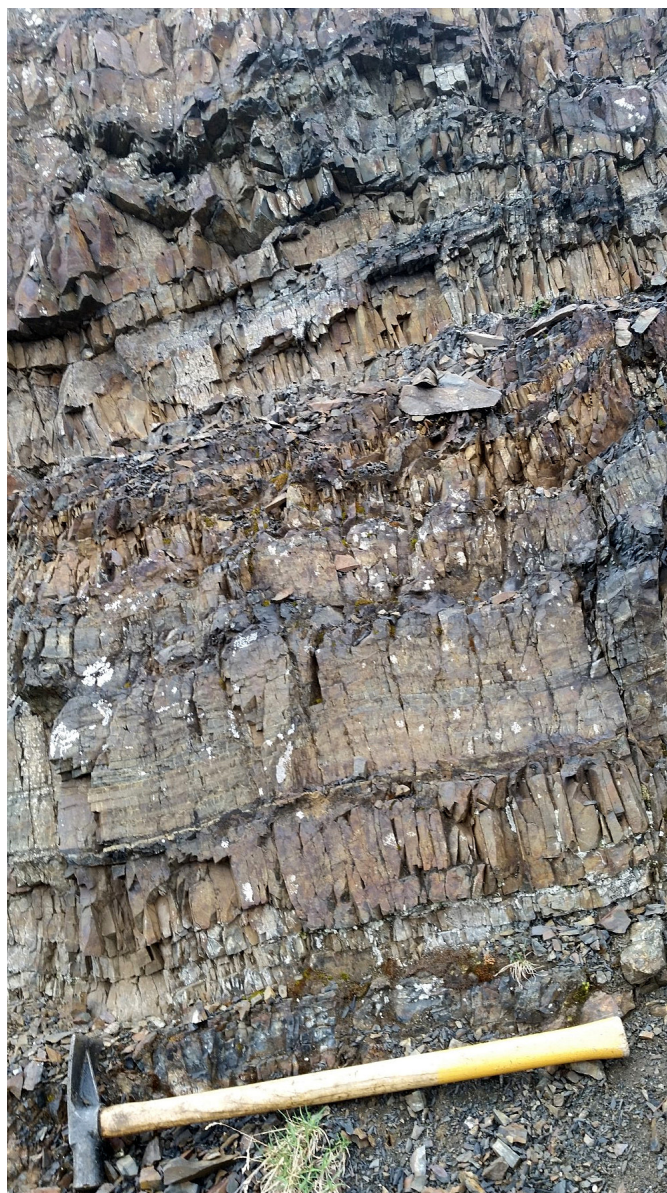


**Fig. 17.** Stuhini Group, map unit uTSsf. View to the east of fine-grained sandstones and mudstones arranged in sharp-based Bouma-like fining upward sequences and containing a steeply south-southwest dipping spaced cleavage. About 1.6 km southwest of Saddle South, immediately west of Tatogga property boundary.

similar to that found in Stuhini Group rocks hosting the Saddle area mineralized zones.

The overlying unit (IJHss) appears to be largely sedimentary and includes conglomerate, pale grey-green sandstone, siltstone, and mauve to maroon, commonly pebbly, mudstone. A sample of sandstone from this part of the section yielded a maximum depositional age of slightly younger than 190 Ma (George et al., 2021), supporting the Hazelton Group assignment. Farther upsection, on the southwest-facing slopes of Mount Poelzer, a rare layer of concretion-bearing pale green lapilli tuff is interbedded with the sedimentary rocks. Still farther upsection is a 5-10 m thick interval with limey pods and limestone layers



**Fig. 18.** Stuhini Group, map unit uTSsf. Sandstone, siltstone and silty mudstone, top stained with sodium cobaltnitrate for potassium feldspar; note that even fine-grained siliciclastic rocks are rich in potassium feldspar. Possible bioturbation structures on right side of specimen. Quash Pass area, southern Tatogga property.



**Fig. 19.** Stuhini Group, map unit uTSsf. Thinly bedded and fine-grained ash tuff and tuffaceous siltstone and sandstone. Bottom stained with sodium cobaltnitrate for potassium feldspar; many ash layers have abundant potassium feldspar. Quash Pass area, southern Tatogga property.

interbedded with laminated black siliceous mudstone and rusty weathering sandstone (Fig. 23). Also within the Hazelton Group in this area is a resistant, strongly magnetic unit of what appears to be a mafic lithology (unit IJHvm; Figs. 4, 5). It may be a finely feldspar-phyric mafic flow or, alternatively, a sill that has hornfelsed its siliciclastic wallrocks.

Overlying this largely sedimentary sequence is a section of dark purple hornblende- feldspar-rich volcanic rocks (unit IJHvhf). Most abundant are coarse fragmental volcanic rocks, tuff-breccia, and coarse lapilli tuff that interfinger with local massive flows of similar andesitic or trachyandesitic composition. Phenocrysts in these rocks include hornblende (and pyroxene?) along with distinctive medium-grained



**Fig. 20.** Hazelton Group. View west from western slopes of Mount Poelzer of gently northwesterly dipping Hazelton Group rocks underlying ridge immediately west of Tsazia Mtn. (see Figure 4), along northern parts of Tatogga and neighbouring Castle property.



**Fig. 21.** Hazelton Group, unit IJHsc. Maroon pebble conglomerate with quartz pebbles (e.g., near tip of scriber) and variably rounded and poorly sorted clasts, near Mount Poelzer, north of Saddle North deposit.



**Fig. 22.** Hazelton Group, unit IJHsc. Polymictic pebble conglomerate with abundant red mudstone clasts, stained with sodium cobaltnitrate for potassium feldspar, northern end of Saddle South ridge.



**Fig. 23.** Hazelton Group. Local limestone beds on slopes of Mount Poelzer, showing interlayering of relatively resistant cherty (orange) and recessive limestone (grey) components, north of Saddle North deposit.

tabular-blocky feldspars that locally display glomeroporphyritic textures. The volcanic rocks are overlain by maroon fine-grained mudstone to siltstone. Still farther upsection, near the top of the ridge that underlies Mount Poelzer, a variety of rock types are exposed, including maroon mudstone, quartz-eye feldspar porphyry felsic dikes and dark mafic volcanic rocks, but neither previous workers (e.g., Miller and Smyth, 2015; Ash et al., 1997a) nor the present authors have mapped these rocks in enough detail.

### 3.3. Late Cenozoic volcanic rocks

Late Cenozoic volcanic rocks (unit ICv) locally overlie both Stuhini and Hazelton groups. These rocks likely correlate with those of the Mt. Edziza volcanic complex to the west, which range in age from about 11 Ma to several hundred thousand years B.P. (Souther, 1992). In the immediate vicinity of the Tatogga property, they occur either at elevation, such as to the west at the Castle property (Fig. 4), or in valley bottoms, such as along the upper parts of the Klastline River valley, immediately north of and downstream from the Saddle area.

Although these Late Cenozoic volcanic rocks were not the focus of our mapping, local outcrops were noted from the air in the valley of the Klastline River valley near where Ash et al. (1997a) documented several small outcrops. The Cenozoic units were also mapped in abundance farther down the Klastline River valley by Souther (1972). In addition, a strong magnetic signature with a distinctive flow-like texture is apparent on regional and property-scale aeromagnetic maps, particularly of the upper Klastline River valley. The magnetic signatures and their valley-parallel grain suggest valley filling

mafic flows. The magnetic signature may indicate a volcanic vent not far downstream from the northern end of Saddle South ridge. The occurrence of the Late Cenozoic volcanic rocks both low in the valley bottoms and at much higher elevations such as along ridgetops on the Castle property suggests eruption onto a paleotopographic surface not unlike the present one.

## 4. Intrusive rocks

Numerous suites of intrusive rocks, most of which roughly follow east-west trends, cut stratified rocks at the Tatogga property. These include latest Triassic to earliest Jurassic monzonitic to monzodioritic rocks of the Tatogga suite, referred to herein as the Saddle intrusions and the Saddle North intrusive complex (units TrJmd and TrJmdu). At Saddle North, these rocks are closely associated, spatially and genetically, with porphyry copper-gold mineralization. Similarly, at Quash-Pass 6-7 km to the south, local monzonitic to dioritic rocks are associated spatially with alteration and local base- and precious metal-bearing veins. However, at Saddle South these rocks post-date precious metals mineralization. There, the monzonitic rocks occur in the immediate footwall of the steeply south-dipping mineralized zone and although they intrude the host Stuhini Group tuffaceous rocks, they do not host Saddle South-style gold- and silver-mineralized quartz-carbonate-pyrite veins, nor are they overlain by appreciable gold-in-soil geochemical anomalies which characterize the Saddle South zone at surface immediately to the south, and the westward projection of the Saddle North trend which lies not far to the north. Younger east-west trending dikes of felsic, intermediate, and mafic composition crosscut mineralization and the monzonitic rocks. These dikes are relatively abundant at Saddle South where crosscutting relationships indicate a generalized order of intrusion from felsic to intermediate to mafic. Several felsic dikes and one intermediate dike yield U-Pb zircon ages ranging from 187 to 182 Ma (Early Jurassic; see section 5 below; Greig et al., 2021), although some of the mafic dikes could be significantly younger given the regional abundance of Late Cenozoic volcanic rocks.

### 4.1. Late Triassic to Early Jurassic intrusive rocks (map units TrJmd and TrJmdu, Saddle intrusions, Tatogga intrusive suite)

In the Saddle area, stratified Upper Triassic rocks have been intruded by latest Triassic or earliest Jurassic porphyritic monzonitic and/or monzodioritic rocks with U-Pb zircon ages ranging from ca. 206 to 202 Ma (see section 5 below). These rocks are typified by the crowded fine-grained hornblende and plagioclase feldspar phenocrysts surrounded by a groundmass with potassium feldspar and minimal free quartz (Figs. 24-27). Particularly where altered, distinguishing these hypabyssal intrusive bodies from some Stuhini Group flows can be difficult. A notable feature of the intrusive rocks is the variation in the habit of amphibole, which forms either medium- to fine-grained blades or anhedral crystals that are intergrown with potassium feldspar in the groundmass of rocks crowded with fine-grained



**Fig. 24.** Saddle intrusion (Tatogga suite, unit TrJmd). Late Triassic to Early Jurassic hornblende monzodiorite porphyry bearing a few percent cognate mafic inclusions, including rectangular inclusion above finger, toward northern end of Saddle South ridge.

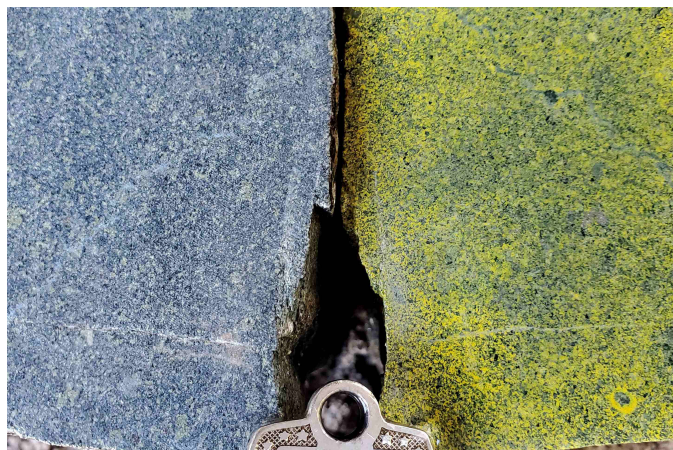


**Fig. 25.** Saddle intrusion CAP porphyry' (Tatogga suite, unit TrJmd). Well-foliated moderately quartz-sericite-pyrite altered, east side of Saddle South ridge.

ehedral plagioclase feldspar phenocrysts. Magnetite is a common accessory mineral in monzonitic and monzodioritic rocks, both in relatively unaltered variants and in more altered equivalents, such as in the core of the Saddle North mineralized system, where it occurs in veins, as replacements of amphibole and, presumably, as partly sulphide-replaced primary grains.

The most common lithology of this unit in the Saddle area is crowded fine-grained hornblende monzonite porphyry. The rocks are typically dark, although relatively fresh surfaces may be medium to dark grey; they at least locally host up to a few percent or more of cognate somewhat more mafic-rich inclusions (Fig. 24). Systematic sodium cobaltnitrate staining of samples reveals that the three main component rock-forming minerals (potassium feldspar, plagioclase, and hornblende) vary significantly in relative abundance and grain size (Figs. 25, 26). Variably overprinting styles of alteration may increase the variation in appearance and may emphasize the presence of mafic phenocrysts (Fig. 27). In more altered rocks, plagioclase feldspar is commonly sericite-altered and

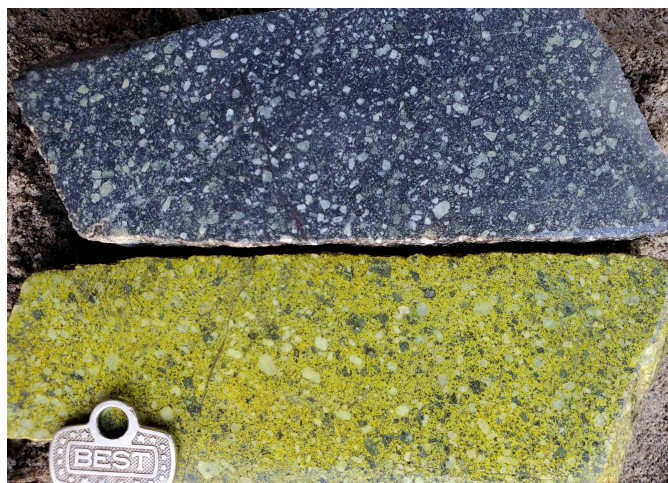


**Fig. 26.** Saddle intrusion (Tatogga suite, unit TrJmd). Fine-grained moderately altered monzonite porphyry. Hornblende (commonly epidote altered), potassium feldspar (largely in groundmass), and variably sericitized plagioclase, which is commonly pale yellow. On bottom, slab stained with sodium cobaltnitrate for potassium feldspar). From near the northern plutonic contact of monzonitic rocks that forms the northern boundary of the Saddle South mineralized zone.

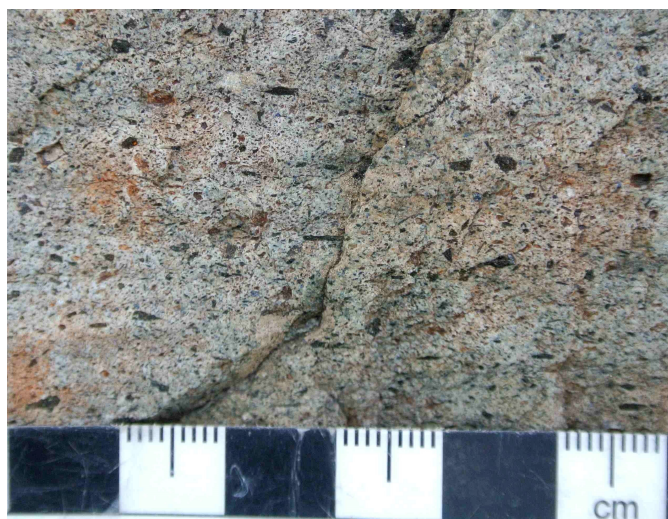


**Fig. 27.** Saddle intrusion (Tatogga suite, unit TrJmd). Crowded hornblende-pyroxene-plagioclase monzonite or monzodiorite porphyry with medium-grained epidote(?) and leucoxene-altered mafic minerals and variably sericite altered plagioclase feldspar in a groundmass of very fine-grained potassium feldspar. Bottom slab stained with sodium cobaltnitrate for potassium feldspar). North of Saddle South mineralized zone.

in stained slabs plagioclase feldspar generally takes on a pale yellow colour, likely reflecting the presence of the sericite (Fig. 26). Well-foliated varieties of the porphyritic rocks, such as the "CAP" porphyry common to the immediate footwall to north of the mineralized zone at Saddle South, and so-named in the field because of its conspicuous medium- and rarely coarse-grained amphibole, is typically quartz-sericite-pyrite altered (Fig. 27, part of map unit TrJmd). A short distance farther north and downslope from the CAP porphyry, the Saddle intrusions exposed in the cliffs immediately north of the Saddle

South zone are generally dark and fine grained. The dark tone largely appears to represent very fine-grained mafic minerals (principally amphibole), and probably magnetite, intergrown with potassium feldspar in the groundmass to the abundant fine-grained plagioclase feldspar phenocrysts. Fine-grained potassium feldspar phenocrysts may be locally abundant; rarely, potassium feldspar forms megacrysts.

At Saddle North, the exact limits of the monzonitic intrusive rocks at surface remain to be fully defined. This is largely due to the limited exposure beneath a thick cover of colluvium and till, which typically ranges from a few m to at least 25 m thick. However, the intrusion is locally well exposed, such as in the cliffs immediately north of the Saddle South mineralized zone and in the creek draining west-northwest from the Saddle North deposit area (Figs. 4, 5). Along with abundant drill intersections at Saddle North and with local drill intersections between there and Saddle South, it is clear that the monzonitic rocks coincide with an easterly linear airborne magnetic high. This suggests that they are all part of an overall east-west trending intrusive system that continues into the well-exposed intrusive trend on the Castle property to the west (Fig. 4).

#### 4.2. Early Jurassic and younger dikes

Multiple generations of m-scale, mafic to felsic dikes cut Stuhini Group stratified rocks. Most conspicuous are pale-weathering felsic dikes that occur at Saddle South and to the south and southwest and are readily visible cutting Stuhini Group rocks in cliff outcrops (Fig. 28). U-Pb zircon ages from four of these dikes range from ca. 186 to 182 Ma (see section 5 below). Although the dikes commonly take dog-leg

bends, with abrupt changes in width from as much as 10 m to as little as 0.5 m within a few m, the dikes clearly follow general west-northwest trends (Fig. 5). Dike-wall parallel flow foliation is common, particularly along contacts with country rocks. Lithophysae are commonly aligned with flow-layering and flow-folding is locally well displayed. Systematic staining and a general lack of abundant quartz phenocrysts suggests the dikes are trachydacites or high-K rhyodacites. They range from aphyric, to potassium feldspar-phyric to sparsely hornblende- plagioclase feldspar-phyric. Locally the dikes are cut by abundant veins of different compositions, including quartz, calcite and iron carbonate, but systematic geochemical sampling of the dikes at Saddle South reveals that they do not host precious metals. Although the altered and mineralized country rocks may bear a well-developed foliation, the dikes themselves typically only display a spaced or fracture cleavage.

Several suites of darker intermediate to mafic dikes commonly cut the felsic dikes. In contrast to their felsic counterparts the mafic and intermediate dikes typically have more planar contacts and may be more continuous. Only one intermediate dike, of trachyandesitic composition, has been dated and it returned a 185 Ma U-Pb zircon age that is essentially coeval with those of the felsic dikes (see section 5 below). However, contact relationships observed in drill core suggest that in general the felsic dikes are the oldest and that most of the obviously mafic dikes (very dark green, as opposed to more obviously feldspar-rich varieties of intermediate composition) are the youngest.

The intermediate dikes may contain abundant and typically aligned feldspar microlites, in a felted or trachytic texture.



**Fig. 28.** View southeast showing steeply dipping light-toned Early Jurassic felsic dikes (~185 Ma) cutting generally more gently dipping, but folded, dark-toned well-stratified Upper Triassic fine-grained sedimentary rocks of the Stuhini Group (unit uTSsf). Immediately west of northern Tatogga property; helicopter upper left for scale.

The most notable of these, the informally named “DMcg” (Dike, Mafic, coarse-grained) suite at Saddle South, somewhat resembles the older Saddle intrusions. They are generally strongly magnetic and are coarse grained only relative to other intermediate to mafic dikes on the property, which are commonly aphyric to very fine grained. The most recognizable phenocrysts in the DMcg dikes are fine- to medium-grained plagioclase feldspar laths that are commonly aligned to form a trachytic fabric, much like their finer grained counterparts. Other characteristics that help distinguish the DMcg suite in the field are the very common presence of chlorite-quartz(?)–epidote veins and a propylitic alteration assemblage (minor pyrite, very common chlorite and epidote after mafic minerals). In contrast, similar veins and alteration are generally lacking in adjacent mafic dikes.

Contact relationships suggest that most of the obviously mafic dikes (very dark green, as opposed to more obviously feldspar-rich varieties of intermediate composition) are the youngest. Like the felsic dikes, both the mafic and intermediate dikes may host numerous veinlets (most commonly calcite), but few host veins containing base or precious metals. Given the abundance of nearby Late Cenozoic volcanic rocks, including the edifice at Mt. Edziza and a probable vent approximately 2 km north of Saddle South, some of the mafic dikes are conceivably Late Cenozoic.

## 5. Geochronology

The primary goal of our geochronology program was to establish the timing of mineralization at the Tatogga property. Our approach was both direct, by using Re-Os molybdenum

geochronology on mineralized veins (three samples) and indirect, using U-Pb zircon geochronology to determine crystallization ages of interpreted mineralizing intrusions, and crystallization and maximum depositional ages of mineralized and non-mineralized wallrocks and country rocks (18 samples). The Re-Os ages were determined under contract with ALS-Global laboratories, via the University of Alberta geochronology laboratory. Molybdenite separates were analyzed by isotope dilution mass spectrometry using Carius-tube, solvent extraction, anion chromatography and negative thermal ionization mass spectrometry techniques (Selby and Creaser, 2004). The U-Pb zircon geochronology was undertaken at the Arizona Laserchron Center, Department of Geosciences, University of Arizona using laser ablation multicollector inductively coupled mass spectrometry (LA-ICPMS; Gehrels et al., 2008). Below we only summarize this work; full details are presented in Greig et al. (2021).

### 5.1. Stuhini Group

Three samples of stratified rocks from the Stuhini Group were dated. Two were collected from host hornblende-feldspar-phyric volcanic rocks intersected in drill core at the Saddle South mineralized zone (Fig. 5), and one was a detrital zircon sample collected from sandstone from unit uTSsf, approximately three kilometres west of the property boundary, on the adjacent Castle property (Fig. 4). All three samples yielded Late Triassic ages.

Sample TTD058-177m, with a crystallization age of 224.01 ± 1.1 Ma, 2σ (Fig. 29), was collected from a section of coherent grey to maroon hornblende-feldspar-phyric coherent rocks

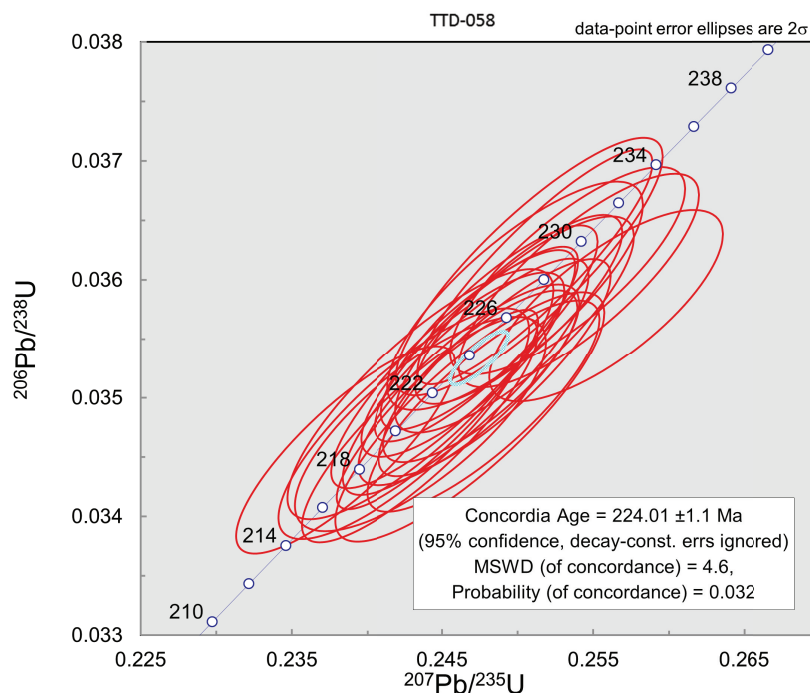


**Fig. 29.** Concordia diagram for sample TTD058-177m, Stuhini Group, unit uTSvtf, hornblende-feldspar-phyric flow, Saddle South mineralized zone.

within map unit uTSvtf. It is interpreted to be a flow, and is interlayered with tuff containing monomictic fragments that are lithologically indistinguishable from the flow. Sample TTD059-53m yielded an age of  $220.3 \pm 2.0$  Ma and was collected from a single decimetre-scale block in a hornblende- feldspar-phyric trachyandesite block tuff to the east of and upsection from TTD058-177m. The detrital zircon sample, CG18-335, was collected from a fine- to medium-grained sandstone turbiditic bed well to the west of the Saddle South mineralized zone, not far west of the western boundary of the Tatogga property (Fig. 4). The interpreted maximum depositional age of  $205.9 \pm 2.1$  Ma (Fig. 30) is based on a total of 315 analyses using 20 micron diameter laser spots.

These Late Triassic ages agree with macrofossil (Souther, 1972; Fig. 4) and microfossil (Ash et al., 1996; Fig. 3) ages reported for the Stuhini Group from elsewhere on the Tatogga property. In addition, George et al. (2021) reported Late Triassic maximum depositional ages of 206 Ma and 205 Ma for samples of sandstone collected from two locations to the southeast of the Saddle area.

### 5.2. Saddle intrusions and Saddle North intrusive complex (Tatogga intrusive suite)

We analyzed six samples from various phases of the Saddle North intrusive complex, three samples from rocks in the footwall of the Saddle South mineralized zone, and one sample from an intrusion intersected in a diamond-drill hole approximately midway between the Saddle North deposit and the mineralized zone at Saddle South. All of the samples were altered and/or mineralized to varying degrees by porphyry-style

alteration and/or vein assemblages. U-Pb zircon ages for the Saddle intrusions range from  $206.2 \pm 1.8$  Ma for the interpreted oldest phase at the Saddle North deposit, to as young as  $202.0 \pm 1.5$  Ma for the sample collected from the drill hole midway between Saddle North and the Saddle South zone.

### 5.3. Early Jurassic and younger dikes

We obtained a U-Pb zircon age of  $185 \pm 1.6$  Ma from a fine-grained intermediate composition trachyandesite dike intruding monzodiorite of the Saddle intrusions. This dike contains abundant very fine-grained lath-like plagioclase feldspar with a notable trachytic fabric and was collected from near the base of the cliffs immediately north of the Saddle South mineralized zone. We also obtained ages from four felsic dikes ranging from  $186.53 \pm 0.78$  Ma,  $2\sigma$  (sample CG18-316; Fig. 31) to  $182.35 \pm 1.6$  Ma. Similar ages are reported by George et al. (2021) for felsic dikes that intrude rocks in the upper part of the Hazelton Group west-northwest of Mount Poelzer. In contrast to the typical pale- or tan-weathering aphyric to feldspar phyric felsic dikes dated in the present study, the dikes dated by George et al. (2021) weather to shades of pink and commonly contain medium- to coarse-grained quartz eyes, which are notably absent in the dikes we dated.

### 5.4. Direct Re-Os molybdenite dating of mineralization

Three samples were collected from veins at the Saddle North deposit for Re-Os dating of molybdenite. Two of the samples yielded ages closely approximating the age of the host Saddle intrusions at  $204.2 \pm 0.9$  Ma and  $204.6 \pm 0.9$  Ma, while the other returned a significantly older age of  $207.8 \pm 0.9$  Ma. All

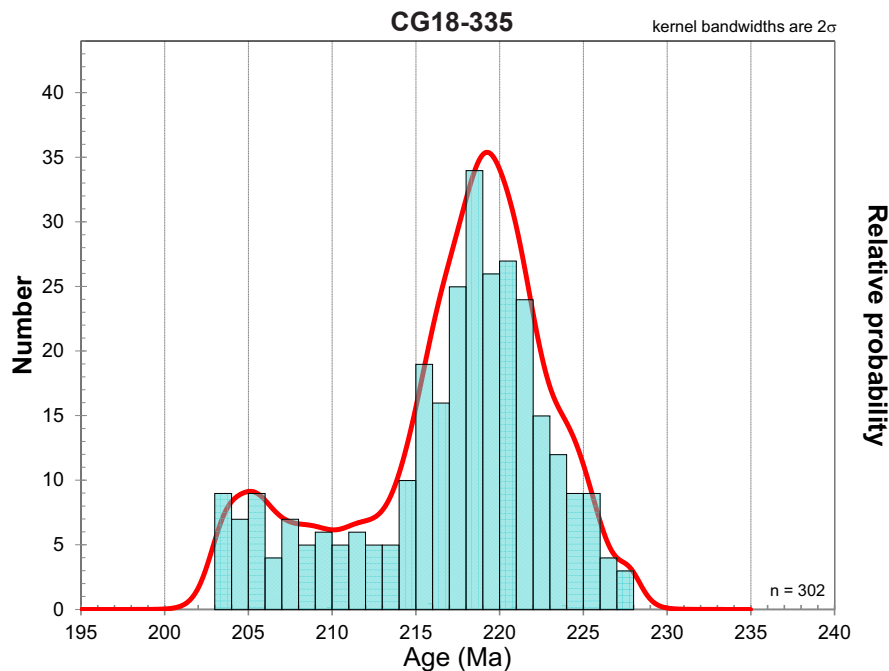


**Fig. 30.** Probability density plot for detrital zircon sample CG18-335, Stuhini Group, unit uTSsf, sandstone, approximately 3 km west-southwest of the Saddle South mineralized zone.

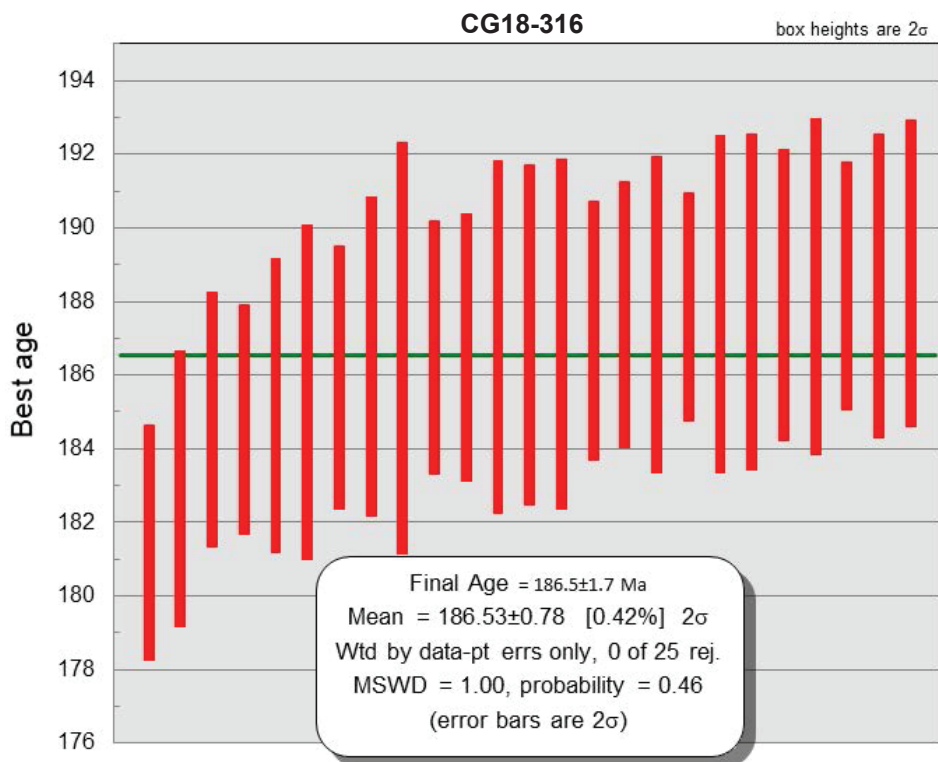


**Fig. 31.** Weighted mean diagram for age of felsic dike sample CG18-316; sample locality is from one of the light-toned felsic dikes shown in Figures 5 and 32; age calculated using the routines in Isoplot (Ludwig, 2008).

three samples were collected from calcite-quartz-chalcopyrite-pyrite veins containing sparse molybdenite hosted by well-mineralized potassically-altered phases of the Saddle North intrusive complex in the core of the deposit. Molybdenite is rarely recognized in the deposit and in the two youngest samples it occurs on slickenside surfaces that transect the veins; otherwise, all three sampled veins appear to be part of the main stage of mineralization.

## 6. Structural geology

Stratified Triassic and Jurassic rocks on the Tatogga property and adjacent areas to the west occupy two structural domains. One domain lies to the north of the Saddle area where rocks of the Hazelton Group dip gently northerly (Fig. 20), and the other lies to the south of the Saddle area where Stuhini Group rocks commonly dip moderately to steeply, either southerly or northerly, and locally display map-scale northerly vergent folds and thrusts that were developed before Early Jurassic felsic dikes were emplaced (Figs. 4-5, 32). The two structural domains correspond with the distribution of Stuhini Group rocks (southern domain) and Hazelton Group rocks (northern domain). In the immediate Saddle area, Stuhini Group host rocks dip moderately to steeply to the northeast. We consider that the structural discordance between the northern and southern domains records pre-Hazelton Group contractional deformation, in accord with Stuhini Group-Hazelton Group structural relationships and the sub-Hazelton Group

unconformity recognized elsewhere in Stikinia (e.g., Brown and Greig, 1990; Henderson et al., 1992; Greig, 2014; Miller et al., 2020).

Several of the major faults in the Tatogga area appear to have complex histories. Two of the better-understood examples serve as illustrations. The Poelzer fault, which defines the northern limit of strong porphyry mineralization at Saddle North, trends west-northwest and dips steeply south-southwest. It is not generally exposed, in large part because it has been faulted off by a younger subvertical fault (the Poelzer Offset fault, Fig. 5) but within metres of its trace in drill core, it is marked by a pervasive foliation in host rocks that incorporates mineralized veins. The foliation and veins are locally folded, and foliated rocks locally occur as rotated fragments along with pieces of mineralized veins within pyrite- and clay-rich gouge along the trace of the fault, suggesting that early ductile or semi-ductile strain was followed by brittle reactivation. The fault commonly juxtaposes well-mineralized rocks in the hanging wall with those that are intensely altered but little-mineralized in the footwall. The early more ductile to later brittle deformation may reflect only part of the fault's history. This is because the rocks in the footwall of the fault host alteration (copper-poor quartz-sericite-pyrite assemblages) and mineralization (local high-grade epithermal vein-style gold) which presumably formed at shallower depths than much of the porphyry-style potassic alteration and copper-gold mineralization common to the hanging wall, which reaches the surface in hangingwall



**Fig. 32.** View west-southwest of light-toned Early Jurassic felsic dikes cutting northerly vergent folds and thrusts in dark-toned well-stratified Upper Triassic Stuhini Group mudstone, siltstone and fine-grained sandstone (unit uTSsf), west of northern Tatogga property.

rocks. This relationship suggests significant reverse-sense offset in post-mineralization but pre-Hazelton time (i.e., before the earliest Early Jurassic).

Approximately 2-3 km to the southwest of the Saddle area are two prominent west-northwest trending reverse faults that juxtapose massive Stuhini Group rocks to the north against generally better stratified rocks to the south (Fig. 4). The fault to the west is well exposed and clearly dips to the south, with folded Late Triassic or earliest Early Jurassic rocks that we have assigned to the Stuhini Group, and that have yielded a U-Pb detrital zircon maximum depositional age of ca. 205 Ma (see section 5), in its hangingwall (Fig. 5; see also Bradford and Barresi, 2013). The fault to the east is poorly constrained, and is interpreted to juxtapose relatively thickly bedded and weakly-stratified north-northeast dipping Late Triassic rocks in the Saddle South area with rocks to the south that also dip to the north-northeast but which yield younger, Late Triassic or earliest Early Jurassic U-Pb detrital zircon maximum depositional ages (George et al., 2021).

In spite of the local complexities, structural fabrics are remarkably consistent throughout the property and in a variety of settings and rock-types, generally dipping steeply to the southwest or south-southwest (Fig. 33). In less competent rock types, a pervasive foliation is commonly developed, such as in Hazelton Group sandstones immediately northeast of and up slope from the Saddle North deposit (Fig. 34), or in sericite-rich altered volcanic or intrusive rocks marginal to

the Saddle North deposit (Fig. 35) or immediately adjacent to veins of the Saddle South mineralized vein field (Fig. 33). In more competent rocks, the fabric may be expressed as a similarly oriented south-southwest dipping fracture set. Based on reconnaissance work farther south on the property, such as near Quash-Pass, fabrics (Fig. 17) appear to be concordant with those to the north.

## 7. Discussion

### 7.1. Stuhini Group or Hazelton Group?

In contrast to other parts of Stikinia (e.g., Brown et al., 1996), Stuhini Group rocks in the Tatogga area include abundant crowded feldspar-phyric trachyandesitic to latitic volcanic rocks with abundant very fine-grained feldspar and common but subordinate hornblende phenocrysts that are set in a potassium feldspar-rich groundmass. Elsewhere, hornblende- feldspar-phyric volcanic rocks characterize the Hazelton Group and are uncommon in the Stuhini Group, which contains augite-phyric mafic volcanic rocks. On the Tatogga property and in the area of the Klastline plateau, the presence of these hornblende-feldspar-phyric examples ultimately led Ash et al. (1997a, b) to assign these rocks to the lower part of the Hazelton Group, although they had previously been assigned to the Stuhini Group (Souther, 1972; Ash et al., 1996). Furthermore, in our initial exploration in 2016 and 2017, the presence at Saddle South of common crowded hornblende- feldspar-phyric dark green to deep maroon volcanic rocks suggested to us that

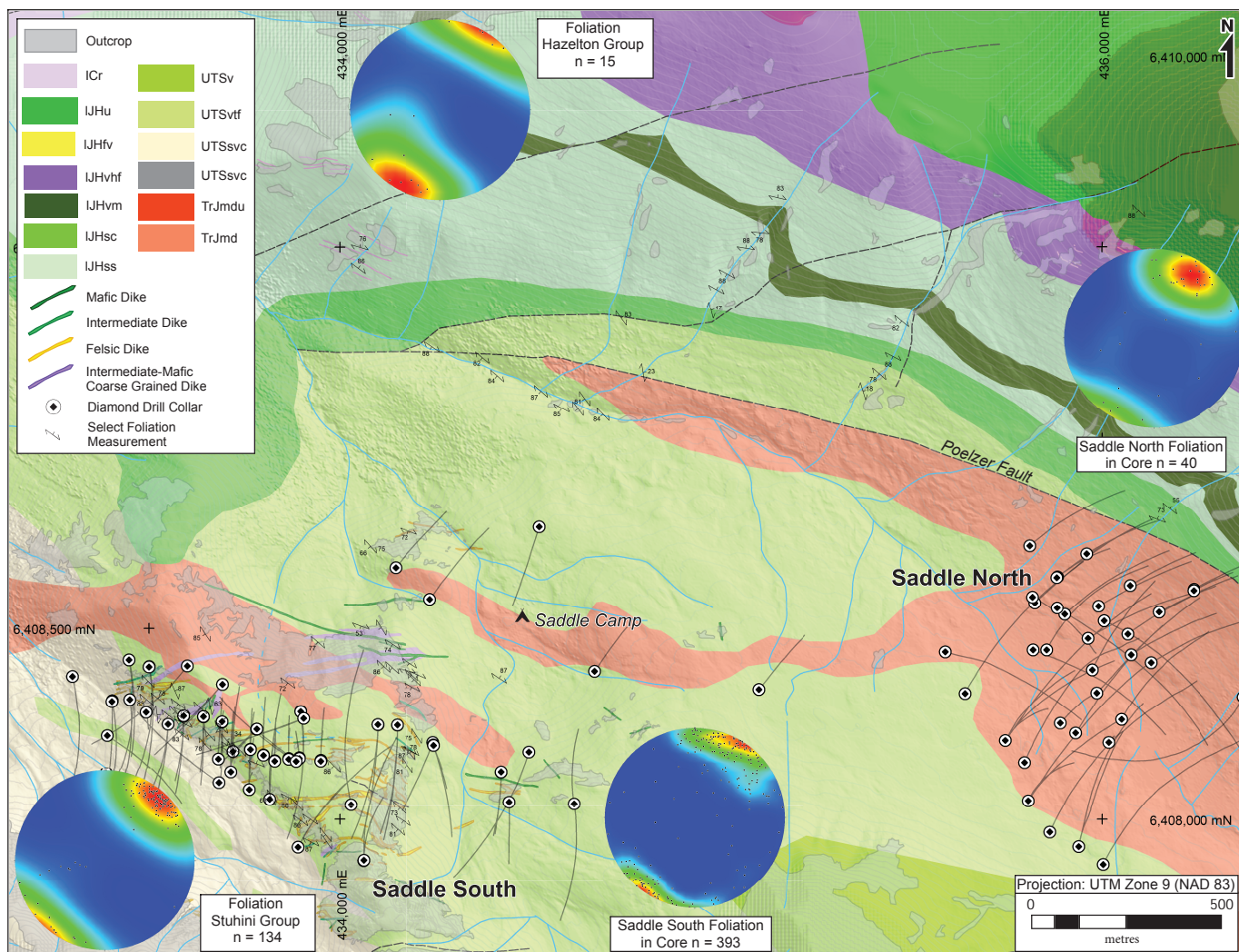


**Fig. 33.** Structural geology of the Saddle area, Tatogga property; stereoplots generated from equal area stereonet lower hemisphere projections with smoothed Kamb contouring.

the rocks hosting the mineralization indeed belonged to the Hazelton Group rather than to the Stuhini Group. However, the new Late Triassic U-Pb zircon data presented above for these hornblende- feldspar-phyric volcanic rocks in the Saddle South area indicate that they are considerably older than the lower part of the Hazelton Group of Nelson et al. (2018). We have therefore reverted to the assignments suggested by earlier mappers and consider them part of the Stuhini Group. Final resolution of the ages and assignments of rocks on other parts of the Klastline and nearby Edon and Todagin plateaus in the Iskut region awaits more detailed geochronological or paleontological work.

Clast compositions of conglomerates in the Hazelton Group and structural relationships also support assigning most of the rocks on the Klastline plateau to the Stuhini Group. Hazelton Group conglomerates contain clasts that appear to have been sourced from Stuhini Group hornblende- feldspar-phyric volcanic rocks, suggesting erosional stripping beneath the regionally developed sub-Hazelton Group unconformity. The

structural discordance between Hazelton Group rocks in the northern part of the area, which dip gently and uniformly to the north, and rocks in the south, which are commonly folded and faulted, suggests that an episode of contractional deformation separates deposition of the two units. The U-Pb zircon ages from felsic dikes that cut folded rocks in the south indicates that this contraction took place before ca. 187 Ma.

## 7.2. Intrusive rocks and mineralization

Monzonite to monzodiorite intrusions (Saddle intrusions of the regionally developed Tatogga suite) are genetically related to mineralization at the Saddle North porphyry copper-gold deposit, as indicated by the close spatial association of porphyry-style stockwork veining, potassic alteration, and elevated grades of copper and gold, with contacts of later phases of the Saddle North complex intrusive (Flynn and Kelly, 2020). U-Pb zircon data indicate that this Late Triassic to earliest Jurassic magmatic centre was active between ca. 206 and 202 Ma. The youngest dated Saddle intrusion, intersected



**Fig. 34.** Well-developed steeply southwesterly dipping foliation developed in Hazelton Group sandstone, unit IJHss; view east toward valley of Saddle North deposit on lower slopes of the ridge underlying Mount Poelzer.



**Fig. 35.** Pervasively foliated and sericite- and iron carbonate-altered medium to coarse lapilli to block tuff of the Stuhini Group, between the Saddle South and Saddle North deposits; view to ESE, with steeply SSW dipping foliation.

in a drill hole midway between the Saddle North deposit and the Saddle South mineralized zone, hosts high-temperature vein and alteration assemblages (stockwork and sheeted pyrite-chalcopyrite-magnetite quartz veins in a potassically-altered intrusive host), and two of the three Re-Os molybdenite ages from Saddle North are centred on 204 Ma, essentially coeval with the host intrusive host rocks. Intriguingly, the other Re-Os molybdenite date from Saddle North, which yielded an anomalously old age of  $207.8 \pm 0.9$  Ma, was collected from a vein in what we consider to be one of the younger intrusive phases of the Saddle North intrusive complex and deposit, with a significantly younger U-Pb zircon age ( $202.0 \pm 1.5$  Ma; Greig et al., 2021). Does this suggest that the vein sampled is a xenolith, and that an earlier porphyry mineralizing event occurred in the Saddle camp?

At the Saddle South gold-silver mineralized vein zone, the lack of mineralization in footwall intrusive rocks that are coeval and appear to be continuous with intrusions at Saddle North (Greig et al., 2021) strongly suggests that Saddle South precious metals mineralization predates the emplacement of the intrusions, and therefore likely also the porphyry copper-gold mineralizing event at Saddle North. It is probable that mineralization at Saddle South was driven by a magmatic system that is not exposed because it is older than the Saddle North intrusions and is hosted by volcanic rocks that are older still (U-Pb crystallization ages of 224-220 Ma). The presence of an anomalous Re-Os age from Saddle North also corroborates the possibility of a separate, older hydrothermal-magmatic episode and that magmatism was long-lived.

### 7.3. Structural evolution: Deformation, uplift and erosion of Stikinia in latest Triassic to earliest Jurassic

Rocks of Stikinia were subjected to two major contractional episodes, one in the latest Triassic or earliest Jurassic (e.g., Greig, 2014), and the other in the mid-Cretaceous (Skeena fold and thrust belt; Evenchick, 1991). The older deformation took place very shortly after the mineralization at Saddle North on the Tatogga property, and before emplacement of Early Jurassic felsic dikes (ca. 187 to 182 Ma), which post-date the mineralizing events at both Saddle North and Saddle South. This earlier shortening is manifested in folding and faulting of the well-bedded Upper Triassic rocks to the west of the Tatogga property, which also occurred prior to the intrusion of Early Jurassic dikes (Fig. 32). In the Saddle area, as well as elsewhere in the region, and in the Stikine terrane in general, the Upper Triassic and older rocks appear to be overlain along a regional unconformity by rocks of the Hazelton Group. The full extent and cause of this tectonic event, and the unconformity related to it, remain incompletely understood and documented, but its significance to the Saddle North deposit, and to nearby porphyry Cu-Au deposits and prospects here in northern Stikinia is clear: the rocks and mineralized zones of the Saddle area were probably uplifted and partially unroofed. This made the mineralized zones easier to explore for and may also make them easier to exploit.

Mid-Cretaceous deformation and development of the Skeena fold and thrust belt (Evenchick, 1991, 2001) apparently coincided with the arrival of outboard terranes and their collision and/or consolidation with the present-day western margin of Stikinia (Monger et al., 1982; Monger, 2014). Near the Tatogga property, the belt is best displayed to the southeast and south where it is manifested as east-west trending folds involving strata of the Middle Jurassic and younger Bowser Lake Group (Figs. 1, 3). Bowser Lake Group rocks comprise an overlap assemblage deposited during and following the accretion of Stikinia to the North American margin, and they overlie the older and more varied arc-related rocks that play host to most mineralization at both the Tatogga property and throughout northern Stikinia.

Given that Bowser basin strata largely post-dated the major metallogenic episodes in this part of Stikinia, the formation of Skeena fold belt clearly did as well, and consequently the mid-Cretaceous structural overprint on the older underlying rocks and their contained mineralized zones needs to be acknowledged and potentially accounted for. Shortening across much of the fold belt is estimated at 40-50% (e.g., Evenchick 1991, 2001; Greig and Evenchick, 1993), and therefore that shortening must also have affected the older rocks, including those on the Tatogga property. Shortening also affected deposits and their host rocks to the south in the Eskay, Sulphurets and Stewart mining camps, where this mid-Cretaceous structural overprint has been well documented (e.g., Alldrick, 1993; Bridge, 1993; Lewis, 2001; Febbo et al., 2019). In these areas, the mid-Cretaceous deformation is manifested as faults and folds and in a commonly well-developed foliation, which is best expressed in less competent rock types.

In the northwest part of Bowser basin and in the Iskut region, Skeena belt structural trends are largely east-west, which differs from the northwest-southeast trends common across much of Bowser basin (Fig. 1). All structures in rocks of the northern Tatogga property align with the east-west trends of the Skeena belt. Although structural trends to the south, such as near Quash-Pass, are perhaps less well-developed and defined, they are also more or less concordant with these regional trends, as are the faults and folds mapped on and just beyond the limits of the property. This concordance suggests that the fabrics, and possibly faults such as the Poelzer fault, which parallels the orientation of foliation across the property, likely developed in the mid-Cretaceous. However, as is the case elsewhere in this part of the northern Cordillera (e.g., the Sulphurets camp, Nelson and Kyba, 2014; Febbo et al., 2019), such structures most likely had an earlier history. Conceivably, the Poelzer fault may have had a similar earlier history, perhaps rooted in basement to Stikinia.

## 8. Conclusion

Our recent mapping and geochronologic work helps to document the geologic setting of two new discoveries in northern Stikinia, the Saddle North porphyry copper-gold deposit, and the Saddle South epithermal precious metals

vein system. The mineralized systems are closely associated spatially with east-west trending latest Triassic to earliest Jurassic crowded hornblende monzonite porphyry of the Saddle intrusions (Tatogga intrusive suite), which are similar in age and association to previously discovered mineralized systems at the nearby Red Chris mine, and at the GJ and North Rok properties. New geochronological data, along with stratigraphic and structural considerations, suggest that the rocks that host the Tatogga intrusions and which underlie much the Klastline plateau are part of the Stuhini Group (Upper Triassic), rather than Hazelton Group. The latter outcrop in the northernmost part of the Tatogga property and appear to unconformably overlie more deformed Stuhini Group rocks. In the Tatogga area, hornblende-phyric volcanic rocks are common in both the Stuhini and Hazelton groups. However, Stuhini Group rocks contain abundant very fine-grained plagioclase feldspar and are darker than the Hazelton Group, which appears to have been deposited in an oxidizing environment.

Further mapping and geochronologic studies are needed to confirm the results of our work and test our interpretations. The areas recommended for more work include the upper Hazelton Group section underlying Mount Poelzer and the northern end of Saddle South ridge, and the area south of the Saddle area, toward Quash-Pass, where further lithologic characterization and age control is necessary.

### Acknowledgments

We thank the Tahltan First Nation, on whose traditional lands the Tatogga property is situated, for their cooperation. Particular thanks go to our many local Tahltan co-workers, from both the Iskut and Tahltan Bands who, along with all the diligent geologists and geo-technicians employed on the project, contributed greatly to making the discovery and initial stages of exploration of the Saddle zones both successful and enjoyable. The management, board of directors, and employees of GT Gold Corp. are thanked for their support throughout this exciting period of exploration. Local companies, including Silver King Helicopters, Hy-Tech Drilling, Kica Catering, Rugged Edge Holdings, and Matrix Camps were contracted throughout much of the exploration and are thanked for providing excellent service under commonly difficult conditions. Pilots Darrell Adzich and Jacob Fort, drill foreman Devin Bakker, caterer Kimberly Marion, pad-builder Colin Jack, and Camp Manager Lorgen Bob are worthy of special thanks. Also worthy of thanks are reviewers JoAnne Nelson, Gayle Febbo, and Lawrence Aspler, whose thoughtful comments and thorough edits greatly improved the paper. Lastly, much credit is due to Toni and Doris Kurz of Bear Paw Ranch Resort, who provided good friendship, kind hospitality, and encouragement throughout.

### References cited

Alldrick, D.J., 1993. Geology and metallogeny of the Stewart mining camp, northwestern B.C. British Columbia Ministry of Energy, Mines and Petroleum Resources, British Columbia Geological Survey Bulletin 85, 105 p.  
Ash, C.H., Stinson, P.K., and MacDonald, R.J.W., 1996. Geology of

the Todagin Plateau and Kinaskan Lake area, (104H/12, 104G/9). In: Geological Fieldwork 1995, British Columbia Ministry of Energy, Mines and Petroleum Resources, British Columbia Geological Survey Paper 1996-01, pp. 155-174.  
Ash, C.H., MacDonald, R.J.W., Stinson, P.K., Fraser, T.M., Read, P.R., Psutka, J.F., Nelson, K.J., Arden, K.M., Friedman, R.M., and Lefebvre, D.V., 1997a. Geology and mineral occurrences of the Tatogga Lake area, NTS 104G/9NE, 16SE and 104H/12NW, 13SW. British Columbia Ministry of Energy, Mines and Petroleum Resources, British Columbia Geological Survey Open File 1997-3, scale: 1:50,000.  
Ash, C.H., MacDonald, R.W.J., and Friedman, R.M., 1997b. Stratigraphy of the Tatogga Lake area, northwestern British Columbia. In: Geological Fieldwork 1996, British Columbia Ministry of Employment and Investment, British Columbia Geological Survey Paper 1997-01, pp. 283-290.  
Bradford, J., and Barresi, T., 2013. 2013 Geological, Geochemical and Diamond Drilling Report on the Castle Property, Northwestern British Columbia. Ministry of Energy, Mines, and Petroleum Resources, British Columbia Geological Survey, Assessment Report 34551, 268 p.  
Bridge, D.J., 1993. The deformed Early Jurassic Kerr copper-gold porphyry deposit, Sulphurets gold camp, northwestern British Columbia. Unpublished M.Sc. thesis, University of British Columbia, Vancouver, Canada, 303 p.  
Brown, D.A., and Greig, C.J., 1990. Geology of the Stikine River-Yehiniko Lake area, northwestern British Columbia (104G/IIW, 12E). In: Geological Fieldwork 1989, British Columbia Ministry of Energy, Mines and Petroleum Resources, British Columbia Geological Survey Paper 1990-1, pp. 141-151.  
Brown, D.A., Gunning, M.H., and Greig, C.J., 1996. The Stikine Project: Geology of western Telegraph Creek map area, northwestern British Columbia (NTS 104G/5, 6, 11W, 12 and 13). British Columbia Geological Survey Bulletin 95, 175 p.  
Coney, P.J., Jones, D.L., and Monger, J.W.H., 1980. Cordilleran suspect terranes. *Nature*, 288, 329-333.  
Evenchick, C.A., 1991. Geometry, evolution, and tectonic framework of the Skeena fold belt, north-central British Columbia. *Tectonics*, 10, 527-546.  
Evenchick, C.A., 2001. Northeast-trending folds in the western Skeena Fold Belt, northern Canadian Cordillera: a record of Early Cretaceous sinistral plate convergence. *Journal of Structural Geology* 23, 1123-1140.  
Febbo, G.E., Kennedy, L.A., Nelson, J.L., Savell, M.J., Campbell, M.E., Creaser, R.A., Friedman, R.M., van Straaten, B.I., and Stein, H.J., 2019. The evolution and structural modification of the supergiant Mitchell Au-Cu porphyry, northwestern British Columbia. *Economic Geology*, 114, 303-324.  
Flynn, R., and Kelly, A., 2020. NI 43-101 technical report on the Saddle North copper gold porphyry project, Tatogga property, Liard Mining Division, northwest British Columbia. Internal company report prepared for GT Gold Corp. by Next Mine Consulting Ltd., 249 p. [https://www.gtgoldcorp.ca/\\_resources/tech-reports/GT%20Gold\\_Saddle%20North\\_technical%20report\\_2020%2008%2020.pdf](https://www.gtgoldcorp.ca/_resources/tech-reports/GT%20Gold_Saddle%20North_technical%20report_2020%2008%2020.pdf).  
Friedman, R.M., and Ash, C.H., 1997. U-Pb age of intrusions related to porphyry Cu-Au mineralization in the Tatogga Lake area, northwestern British Columbia (104H/12NW, 104G/9NE). In: Geological Fieldwork 1996, British Columbia Ministry of Energy, Mines and Petroleum Resources, British Columbia Geological Survey Paper 1997-01, pp. 291-297.  
Gehrels, G.E., Butler, R.F., and Bazard, D.R., 1996. Detrital zircon geochronology of the Alexander terrane, southeastern Alaska. *Geological Society of America Bulletin*, 108, 722-734.  
Gehrels, G.E., Valencia, V., and Ruiz, J., 2008. Enhanced precision, accuracy, efficiency, and spatial resolution of U-Pb ages by laser ablation-multicollector-inductively coupled plasma-mass

- spectrometry: *Geochemistry, Geophysics, Geosystems*, v. 9, Q03017, doi:10.1029/2007GC001805.
- George, S.W.M., Nelson, J.L., Alberts, D., Greig, C.J., and Gehrels, G.E., 2021. Triassic-Jurassic accretionary history and tectonic origin of Stikinia from U-Pb geochronology and Lu-Hf isotope analysis, British Columbia. *Tectonics*, in press.
- Greig, C.J., 1992. Fieldwork in the Oweegee and Snowslide ranges and Kinskuch Lake area, northwestern British Columbia. In: *Current Research, Part A, Geological Survey of Canada Paper 92-1A*, pp. 145-155.
- Greig, C.J., 2014. Latest Triassic-earliest Jurassic contractional deformation, uplift and erosion in Stikinia, NW B.C. *Geological Society of America Abstracts with Programs*, 46, p. 588.
- Greig, C.J., and Evenchick, C.A., 1993. Geology of Oweegee Dome, Delta Peak (104 A112) and Taft Creek (104 A11, 1W) map areas. *Geological Survey of Canada, Open File Map 2688*, 1:50,000 scale.
- Greig, C.J., Newton, G., Quinn, T.D.M., ver Hoeve, T., and Dudek, N.P., 2020. 2019 drilling, geophysical, and geochemical exploration program on the Tatogga property. Ministry of Energy, Mines and Petroleum Resources, British Columbia Geological Survey, Assessment Report 39131, 4168.
- Greig, C.J., ver Hoeve, T., Dudek, N.P., Greig, R.E., Quinn, T.D.M., Makin, S.A., Newton, G., Gehrels, G.E., and Creaser, R.A., 2021. U-Pb and Re-Os geochronology of the Saddle North deposit, the Saddle South mineralized zone, and the northern Klastline plateau, northwestern British Columbia. British Columbia Ministry of Energy, Mines and Low Carbon Innovation, British Columbia Geological Survey GeoFile, in prep.
- Henderson, J.R., Kirkham, R.V., Henderson, M.N., Payne, J.G., Wright, T.O., and Wright, R.L., 1992. Stratigraphy and structure of the Sulphurets area, British Columbia. In: *Current Research, Part A: Geological Survey of Canada Paper 92-1A*, pp. 323-332.
- Lewis, P.D., 2001. Structural evolution of the Iskut River area—preliminary results. Mineral Deposit Research Unit. [http://cdn.geosciencebc.com/project\\_data/GBC\\_Report2013-05/GBCR2013-05\\_full\\_map.pdf](http://cdn.geosciencebc.com/project_data/GBC_Report2013-05/GBCR2013-05_full_map.pdf).
- Ludwig, K., 2008. *Isoplot 3.6: Berkeley Geochronology Center Special Publication 4*, 77 p.
- Miller, E.A., and Smyth, C., 2015. 2014 Geological, geophysical and geochemical program, Tatogga Lake property, northwest British Columbia. Ministry of Energy, Mines, and Petroleum Resources, British Columbia Geological Survey, Assessment Report 35329, 540 p.
- Miller, E.A., Kennedy, L.A., and van Straaten, B.I., 2020. Geology of the Kinskuch Lake area and Big Bulk porphyry prospect, northwestern British Columbia: Syndepositional faulting and basin formation during the Rhaetian (latest Triassic) transition from the Stuhini to the Hazelton Group. In: *Geological Fieldwork 2019*, British Columbia Ministry of Energy, Mines and Petroleum Resources, British Columbia Geological Survey Paper 2020-01, pp. 77-99.
- Monger, J.W.H., 2014. Seeking the suture: The Coast-Cascade conundrum. *Geoscience Canada*, 4, 379-398.
- Monger, J.W.H., Price, R.A., and Tempelman-Kluit, D.J., 1982. Tectonic accretion and the origin of two metamorphic and plutonic belts in the Canadian Cordillera. *Geology*, 10, 70-75.
- Nelson, J.L., and Colpron, M., 2007. Tectonics and metallogeny of the Canadian and Alaskan Cordillera, 1.8 Ga to present. In: Goodfellow, W.D., (Ed.), *Mineral Deposits of Canada: A Synthesis of Major Deposit Types, District Metallogeny, the Evolution of Geological Provinces, and Exploration Methods*. Mineral Deposit Division, Geological Association of Canada, Special Publication 5, pp. 755-791.
- Nelson, J., and Kyba, J., 2014. Structural and stratigraphic control of porphyry and related mineralization in the Treaty Glacier-KSM-Brucejack-Stewart trend of western Stikinia. In: *Geological Fieldwork 2013*, British Columbia Ministry of Energy and Mines, British Columbia Geological Survey Paper 2014-1, pp. 111-140.
- Nelson, J., Waldron, J., van Straaten, B., Zagoresvski, A., and Rees, C., 2018. Revised stratigraphy of the Hazelton Group in the Iskut River region, northwestern British Columbia. In: *Geological Fieldwork 2017*, British Columbia Ministry of Energy, Mines and Petroleum Resources, British Columbia Geological Survey Paper 2018-1, pp. 15-38.
- Oliver, J.L., 2018. 2017 Geological, Geochemical, Induced Polarization and Airborne Magnetic Geophysical Report on the Kinaskan-Castle Property. Ministry of Energy, Mines and Petroleum Resources, British Columbia Geological Survey, Assessment Report 37464, 407 p.
- Rees, C., Riedell, K.B., Proffett, J.M. Macpherson, J., and Robertson, S., 2015. The Red Chris porphyry copper-gold deposit, northern British Columbia, Canada, igneous phases, alteration, and controls of mineralization. *Economic Geology*, 110, 857-888.
- Selby, D., and Creaser, R.A., 2004. Macroscale NTIMS and microscale LA-MC-ICP-MS Re-Os isotopic analysis of molybdenite: Testing spatial restrictions for reliable Re-Os age determinations, and implications for the decoupling of Re and Os within molybdenite. *Geochimica et Cosmochimica Acta*, 68, 3897-3908.
- Souther, J.G., 1972. Telegraph Creek map area, British Columbia. *Geological Survey of Canada Paper 71-44*, 38 p.
- Souther, J.G., 1992. The Late Cenozoic Mount Edziza volcanic complex, British Columbia. *Geological Survey of Canada, Memoir 420*, 320 p.
- Zhu, J., Richards, J.P., Rees, C., Creaser, R., DuFrane, S.A., Locock, A., Petrus, J.A., and Lang, J., 2018. Elevated magmatic sulfur and chlorine contents in ore-forming magmas at the Red Chris porphyry Cu-Au deposit, northern British Columbia, Canada. *Economic Geology*, 113, 1047-1075.





# Near-surface mercury vapour haloes in air above ore deposits and faults on Vancouver Island: Insights into buried materials in real-time?

Alexei S. Rukhlov<sup>1, a</sup>, Luke Ootes<sup>1</sup>, Adrian S. Hickin<sup>1</sup>, and Nikolay R. Mashyanov<sup>2</sup>

<sup>1</sup>British Columbia Geological Survey, Ministry of Energy, Mines and Low Carbon Innovation, Victoria, BC, V8W 9N3

<sup>2</sup>Lumex-marketing LLC, 1 lit. B, Obruchevykh Street, St. Petersburg, 195220, Russia

<sup>a</sup>corresponding author: Alexei.Rukhlov@gov.bc.ca

Recommended citation: Rukhlov, A.S., Ootes, L., Hickin, A.S., and Mashyanov, N.R., 2021. Near-surface mercury vapour haloes in air above ore deposits and faults on Vancouver Island: Insights into buried materials in real-time? In: *Geological Fieldwork 2020*, British Columbia Ministry of Energy, Mines and Low Carbon Innovation, British Columbia Geological Survey Paper 2021-01, pp. 113-143.

## Abstract

Volatile geogenic components, such as CO<sub>2</sub>, He, Rn, and Hg, form haloes in soil gas and near-surface air directly above mineral deposits. This contrasts with lithochemical, hydrochemical, and biochemical dispersion haloes that can be laterally displaced or obscured by transported overburden. Mercury vapour surveys have been used in geochemical exploration, because Hg occurs in most types of endogenic ore deposits and is highly mobile. In this study, we measured Hg vapour in air 1-50 cm above ground at 15 sites on Vancouver Island. To evaluate the effectiveness of the method across a range of settings, these sites include different types of known mineralized zones, barren rocks, and faults, both buried and exposed. The direct and continuous analysis via a portable RA-915M mercury analyzer reveals Hg vapour concentrations ranging from 0.5 to 54.4 ng·m<sup>-3</sup>. The highest Hg concentration was observed above tailings at the Bentley Au occurrence, possibly due to the amalgamation technique used for fine gold extraction between late 1800s and early 1900s. Prominent Hg vapour haloes mark shear-hosted Cu-Ag-Au sulphides at Mount Skirt (13.4x background Hg), epithermal Au-Ag-Cu at Mount Washington (8.9x background Hg), and sediment-covered polymetallic volcanogenic massive sulphide at the Lara-Coronation occurrence (4.2 to 6.6x background Hg). Basalt-hosted Cu-Ag-Au sulphide zones at the Sunro past producer are marked by weak Hg vapour anomalies relative to local background. Faults, including the Leech River fault, which was active in the Quaternary, are also marked by weak Hg vapour anomalies. The study confirms that, although the Hg level is influenced by weather, the real-time Hg vapour measurement of near-surface air can instantly delineate mineralized zones and fault structures that are buried under overburden 10s of m thick. In contrast to soil gas sampling, this simple and rapid technique can be applied to mineral exploration and geological mapping under overburden above any type of surface, including outcrops, talus, bogs, water bodies, snow, and permafrost.

**Keywords:** Mercury vapour haloes, near-surface air, real-time analysis, portable RA-915M mercury analyzer, overburden, Leech River fault, Vancouver Island, mineral exploration under cover, polymetallic volcanogenic massive sulphide, epithermal Au-Ag-Cu, shear-hosted sulphide Cu-Ag-Au, Lara-Coronation, Mount Washington Copper, Sunro, Bentley Au, Ralph

## 1. Introduction

Volatile geogenic components, such as CO<sub>2</sub>, SO<sub>2</sub>, He, Rn, and Hg, form haloes in soil gas and near-surface atmosphere directly above ore and oil and gas deposits and fault zones (e.g., Sokolov, 1956; Williston, 1968; Ovchinnikov et al., 1972; Fridman, 1975; Mashyanov, 1993; Wang et al., 2006; Utkin and Yurkov, 2010; Kalinchuk and Astakhov, 2014; Sun et al., 2017; Buttitta et al., 2020; Esbril et al., 2020; Lett et al., 2020; Xiang et al., 2020). This contrasts with lithochemical, hydrochemical, and biochemical dispersion aureoles that can be laterally displaced or obscured by transported overburden (Solovov, 1985). Because volatile geogenic species are highly mobile, they migrate to the surface from deep sources such as blind and buried ore deposits and thus form superimposed dispersion haloes.

Among atmospheric methods, Hg vapour surveys have been most useful in exploration (e.g., Sergeev, 1957; Hawkes and Williston, 1962; Fursov, 1990), geological mapping (e.g., Xiang et al., 2020), and earthquake prediction (e.g., Jin et al.,

1989; Wang et al., 2006). This is because Hg occurs in many hydrothermal ore deposit types, is highly mobile, and forms vapour haloes in soil gas and atmosphere above ore and oil and gas deposits, active faults, volcanoes, and geothermal zones (e.g., Fursov, 1970, 1983, 1990; McCarthy, 1972; Ozerova, 1975, 1986; Nriagu and Becker, 2003; Kalinchuk and Astakhov, 2014; Sun et al., 2017). Low background concentrations in the atmosphere (1.2 to 1.5 ng·m<sup>-3</sup>; Sprovieri et al., 2016) enable detecting even weak Hg emissions directly above buried ore deposits 100s of m below the surface (e.g., Krömer et al., 1981; Zonghua and Yangfen, 1981; Fursov, 1990; Zherebtsov et al., 1992; Rehn and Rehn, 1996).

In the present study, we evaluate the effectiveness of real-time Hg vapour measurement in air 1-50 cm above ground at 15 locations on Vancouver Island. These sites include different types of sediment-covered and exposed mineralized zones and faults. We use a direct and continuous analysis of ultra-low Hg concentrations in air via a portable RA-915M mercury analyzer that has a response time of one second and a detection range of

0.5-20,000 ng·m<sup>-3</sup> (Sholupov et al., 2004). Our study finds that a simple, real-time Hg vapour sampling of near-surface air can instantly delineate mineralized zones and faults that are buried under overburden 10s of m thick.

## 2. Geochemistry of mercury

### 2.1. Mercury as an indicator of endogenic processes and ore deposits

Mercury is the only metal that forms vapour haloes in soil gas and near-surface atmosphere that currently can be directly detected. Mercury readily reduces to chemically stable Hg<sup>0</sup>, which is highly volatile, actively evaporates, adsorbs, and dissolves other metals (Smirnov, 1955; Sveshnikov, 1967; Kothny, 1973; Fursov, 1983b; Schuster, 1991; Zhang and Lindberg, 1999; Gu et al., 2011; Moore and Castro, 2012). Mercury forms more than 30 minerals, including native mercury and amalgams, and concentrates in low-temperature hydrothermal minerals such as pyrite (up to 6%), tennantite-tetrahedrite (up to 21.9%), and sphalerite (up to 35%; Saukov et al., 1972). High mobility and the association with most ore deposit types make Hg vapour an ideal indicator of endogenic ore deposits and tectonic, geothermal, and volcanic activity (Kuznetsov and Obolensky, 1970; Ozerova, 1975, 1976, 1977, 1979, 1986; Babkin et al., 1976; Fursov, 1977, 1983b; Fedorchuk, 1983; Carr et al., 1984; Stepanov, 1997; Stoffers et al., 1999; Nriagu and Becker, 2003; Ryzhov et al., 2003; Rychagov et al., 2009; Yin et al., 2020).

Predicted by A.A. Saukov, ‘mercury atmosphere’ of ore deposits is the basis of Hg vapour exploration method (Saukov, 1946; Saukov et al., 1972). Along with the development of technology for direct analysis, Hg vapour surveys have been increasingly applied in exploration (Sergeev, 1957; Hawkes and Williston, 1962; Fedorchuk, 1964; Barringer, 1966, 1969; McCarthy et al., 1969, 1970; McCarthy, 1972; Fursov, 1970, 1983a, 1990; Karasik et al., 1978; Mashyanov, 1980, 1985; Krömer et al., 1981; Zonghua and Yangfen, 1981; Chengliang et al., 1989; Zherebtsov et al., 1992; Rehn and Rehn, 1996; Yasutake et al., 2011; Higuera et al., 2012; Bradshaw, 2015; Nevolko and Fominykh, 2017). Low global background in atmosphere (1.2 to 1.5 ng·m<sup>-3</sup>; Sprovieri et al., 2016) reflects low lithospheric background (45 ppb Hg; Rudnick and Gao, 2005) and enables detecting even weak Hg haloes of ore deposits and emanations through fault zones (Ozerova, 1977; Mashyanov, 1980, 1985; Jin et al., 1989; Wang et al., 2006; Kalinchuk and Astakhov, 2014; Sun et al., 2017; Xiang et al., 2020).

### 2.2. Mercury emission into the atmosphere

The global distribution of Hg in belts such as the Cordilleran orogen, which hosts more than 1,500 occurrences (e.g., Pinchi Lake ore field, British Columbia) reflects migration of Hg from the mantle along deep, linear structures (Fedorchuk, 1964, 1983; Kuznetsov and Obolenskiy, 1970; Ozerova, 1976, 1977, 1986). Some oil and gas pools in these belts have Hg resources comparable to those of Hg mines (Ozerova, 1975, 1976;

Mashyanov, 1985; Ryzhov et al., 2003). Mercury migrates to the surface mostly as Hg<sup>0</sup> vapour due to tectonic, hydrothermal, and volcanic activity (Saukov et al., 1972; Ozerova, 1977). Anomalous Hg emissions, including formation of modern Hg deposits, mark mantle plumes (e.g., Hawaii and Iceland), mid-ocean ridges, volcanic arcs, geothermal fields, and active faults (Boström and Fischer, 1969; Eshleman et al., 1971; Aston et al., 1972; Carr et al., 1974, 1975; Coderre and Steinthorsson, 1977; Ozerova, 1977; Jin et al., 1989; Stepanov, 1997; Stoffers et al., 1999; Nriagu and Becker, 2003; Rychagov et al., 2009; Kalinchuk and Astakhov, 2014). Processes such as fuel combustion (mainly coal) and artisanal gold mining are the most significant anthropogenic sources of Hg emissions into atmosphere (Higuera et al., 2012; Dalziel and Tordon, 2014; Gworek et al., 2017; Mashyanov et al., 2017; UN Environment, 2019). Elemental mercury (Hg<sup>0</sup>) vapour comprises more than 95% of the atmospheric Hg species (Sprovieri et al., 2016). Generally consistent atmospheric background can be influenced by local meteorological factors such as precipitation of Hg adsorbed on aerosols and shows significant seasonal variations (Williston, 1968; McCarthy et al., 1970; Krömer et al., 1981; Mashyanov, 1985; Dalziel and Tordon, 2014; Bradshaw, 2015).

### 2.3. On the origin of Hg vapour haloes in soil gas and near-surface air

Mercury emitted into atmosphere is diluted by turbulent diffusion and transferred with air mass movement. Hence, Hg vapour haloes (up to  $n \cdot 10^3 \times$  background Hg) occur in soil gas and near-surface atmosphere directly above ore deposits rather than forming dispersal plumes (Sergeev, 1957; McCarthy et al., 1969, 1970; Fursov, 1970, 1983a, 1990; Krömer et al., 1981; Mashyanov, 1985; Zherebtsov et al., 1992). Processes that generate Hg vapour haloes include: 1) upward diffusion-filtration of Hg along permeable zones due to the temperature, pressure, and concentration gradients, coupled with the chemical stability and high mobility of Hg<sup>0</sup> (e.g., Ozerova, 1977); 2) sublimation of Hg<sup>0</sup> from Hg-bearing minerals (e.g., Smirnov, 1955; Fursov, 1983a); 3) reduction of Hg<sup>2+</sup> to Hg<sup>0</sup> with CO<sub>2</sub>, H<sub>2</sub>, and CH<sub>4</sub> in the supergene zone (e.g., Saukov, 1946; Mashyanov, 1980, 1985); 4) ionic and cathode electrochemical reactions within ore bodies and enclosing strata (e.g., Sveshnikov, 1967; Mashyanov et al., 1995); 5) oxidation of Hg-bearing sulphides by plants and bacteria and Hg vapour transpiration from plants (e.g., Barringer, 1969; Gu et al., 2011; Bradshaw, 2015).

Soil temperature, moisture, redox potential, permeability, and organic matter are important factors that influence Hg vapour concentration in soil gas (McCarthy, 1972; Chengliang et al., 1989; Schuster, 1991; Zhang and Lindberg, 1999; Choi and Holsen, 2009; Gu et al., 2011; Yasutake et al., 2011; Higuera et al., 2012; Moore and Castro, 2012; Xie et al., 2019; Esbril et al., 2020). Chengliang et al. (1989) suggest that Hg in overburden (up to 40 m thick) over the blind Fankou Pb-Zn deposit (>200 m below the surface) in Guangdong (China) occurs mainly as free vapour and adsorbed onto soil colloids such as clays and Fe-Mn oxides. Mercury vapour haloes in soil gas are up to 40x

background Hg above the deposit (Chengliang et al., 1989). Theoretical modelling of overburden thickness and sorption and diffusion processes shows that the intensity of Hg vapour anomalies in near surface air decreases exponentially with increasing overburden thickness (Mashyanov, 1980, 1985; Sun et al., 2017). Mercury vapour anomalies in soil gas above a skarn Cu deposit buried under alluvium (up to 180 m thick) near Shanghai (China) had similar shape and intensity between the repeated surveys carried out in different seasons (Zonghua and Yangfen, 1981).

#### 2.4. Soil gas sampling versus near-surface air sampling

Because of higher Hg vapour concentration (Fursov, 1990; Zhrebtsov et al., 1992), soil gas sampling is more commonly used than near-surface air sampling (Mashyanov, 1980; Krömer et al., 1981; Yasutake et al., 2011). However, soil gas sampling is not suitable across highly variable surficial materials, outcrops, talus, wet soil, bogs, water bodies, permafrost, and snow cover (McCarthy, 1972; Mashyanov, 1985). It is also slower compared to real-time sampling of air above ground which is as rapid as a geophysical survey. In addition, Hg analyzers using gold traps to pre-concentrate Hg from soil gas have variable sample conditions depending on composition and porosity of the surficial materials. Furthermore, soil moisture strongly impacts sorption ability of the gold trap, creating concentration readings bias (Mashyanov, 1985; Zhrebtsov et al., 1992). Moreover, Hg vapour concentration in soil gas strongly depends on the time lapse between the borehole drilling and measurement, speed of drilling, depth of borehole, and sampler shape (Zhrebtsov et al., 1992; Stepanov, 1997; Sun et al., 2017). In contrast, the near-surface air measurement is free of such sampling conditions and can be more efficient (Mashyanov, 1980, 1985; Yasutake et al., 2011).

### 3. Geological setting, Vancouver Island

Vancouver Island is mainly underlain by Late Paleozoic to Early Mesozoic rocks of Wrangell terrane, with slivers of Pacific Rim and Crescent terranes along the west coast and southern tip of the island (Fig. 1; Muller, 1977; Nelson et al., 2013). Amalgamated with Alexander terrane by the Late Carboniferous, Wrangellia, now part of the Insular superterrane, accreted to inboard Intermontane terranes between Middle Jurassic and mid-Cretaceous (Nelson et al., 2013).

The oldest rocks of Wrangellia on Vancouver Island comprise volcanic and volcanoclastic strata of the Sicker Group (Middle to Late Devonian) and coeval felsic intrusions of the Saltspring plutonic suite, which record the evolution of an oceanic island arc. Intermediate to felsic volcanic rocks of the Sicker Group host significant volcanogenic massive sulphide (VMS) mineralization (e.g., Lara-Coronation, MINFILE 092B 129; Northcote and Muller, 1972; Muller, 1977; Massey, 1995; Yorath, 2005; Kelso and Wetherup, 2008; Ruks, 2015). Epiclastic sedimentary rocks and bioclastic limestone of the Buttle Lake Group (Mississippian to Early Permian) overlie the arc strata. Folded and imbricated by thrust faults, rocks of

the Sicker and Buttle Lake groups are exposed within several northwest-trending uplifts that are the result of the collision of Wrangellia with the North American margin between Middle Jurassic and mid-Cretaceous and subsequent shortening in the Eocene. The Paleozoic rocks are typically metamorphosed to greenschist facies, with amphibolite facies developed near granitoid bodies of the Island plutonic suite (Early to Middle Jurassic).

Much of Vancouver Island is underlain by younger rocks of Vancouver and Bonanza groups. The Vancouver Group (Middle to Late Triassic) consists of flood basalts of the Karmutsen Formation overlain by limestone of the Quatsino Formation. The voluminous flood basalts of the Karmutsen Formation (about 6 km thick), along with coeval mafic intrusions (Mount Hall Gabbro), mark a plume-related, oceanic plateau superimposed on the Paleozoic Sicker arc. Largely subaerial mafic to felsic volcanic and sedimentary strata of the Bonanza Group (Late Triassic to Middle Jurassic) unconformably overlie the older rocks. Together with coeval granitoids of the Island plutonic suite (Early to Middle Jurassic), they record the evolution of the Bonanza magmatic arc that overprinted Wrangellia and brought about major porphyry Cu-Mo-Au and related ore deposits (Carson, 1968; Northcote and Muller, 1972; Muller, 1977; Massey et al., 1994; Yorath, 2005). The Westcoast Crystalline complex (Paleozoic to Jurassic) underlies much of Victoria and consists of metamorphosed and partially melted host rocks that are mixed with Jurassic intrusions.

Cyclic marine and continental sedimentary sequences containing coal beds of the Nanaimo Group (Late Cretaceous) mark deposition in a broad basin along the eastern margin of Wrangellia. Strongly deformed ribbon chert, argillite, phyllite, slate, schists, and metavolcanic rocks of the Leech River (Jurassic to Cretaceous) and Pacific Rim (Triassic to Cretaceous) complexes belong to the Pacific Rim terrane. Juxtaposed against the metamorphic rocks of the Leech River complex along the Leech River fault, basalts and gabbro of the Metchosin Igneous complex (Paleocene to Eocene) underlie the southern tip of Vancouver Island. These rocks make up the Crescent (Siletz in U.S.A.) terrane, which extends more than 650 km south to Oregon and marks the Yellowstone mantle plume-related oceanic plateau accreted to the continental margin between 51 and 45 Ma (e.g., Phillips et al., 2017). The Eocene accretionary events caused folding and faulting of the Nanaimo Group and uplift, resulting in the exposure of metamorphic rocks of the Sicker Group and Westcoast Crystalline complex. The Leech River fault acted as a strike-slip fault during post-Eocene time and was active after the last glacial maximum ca. 17 ka (Morell et al., 2017).

Along the southwestern coast, the older rocks are overlain by a narrow fringe of siliciclastic rocks of the Carmanah Group (Late Eocene to Oligocene). Intermediate and felsic intrusions and related breccia pipes and pyroclastic deposits of the Mount Washington plutonic suite (Eocene to Oligocene) are associated with porphyry Cu-Mo-Au and epithermal Au-Ag-Cu mineralization (Mount Washington

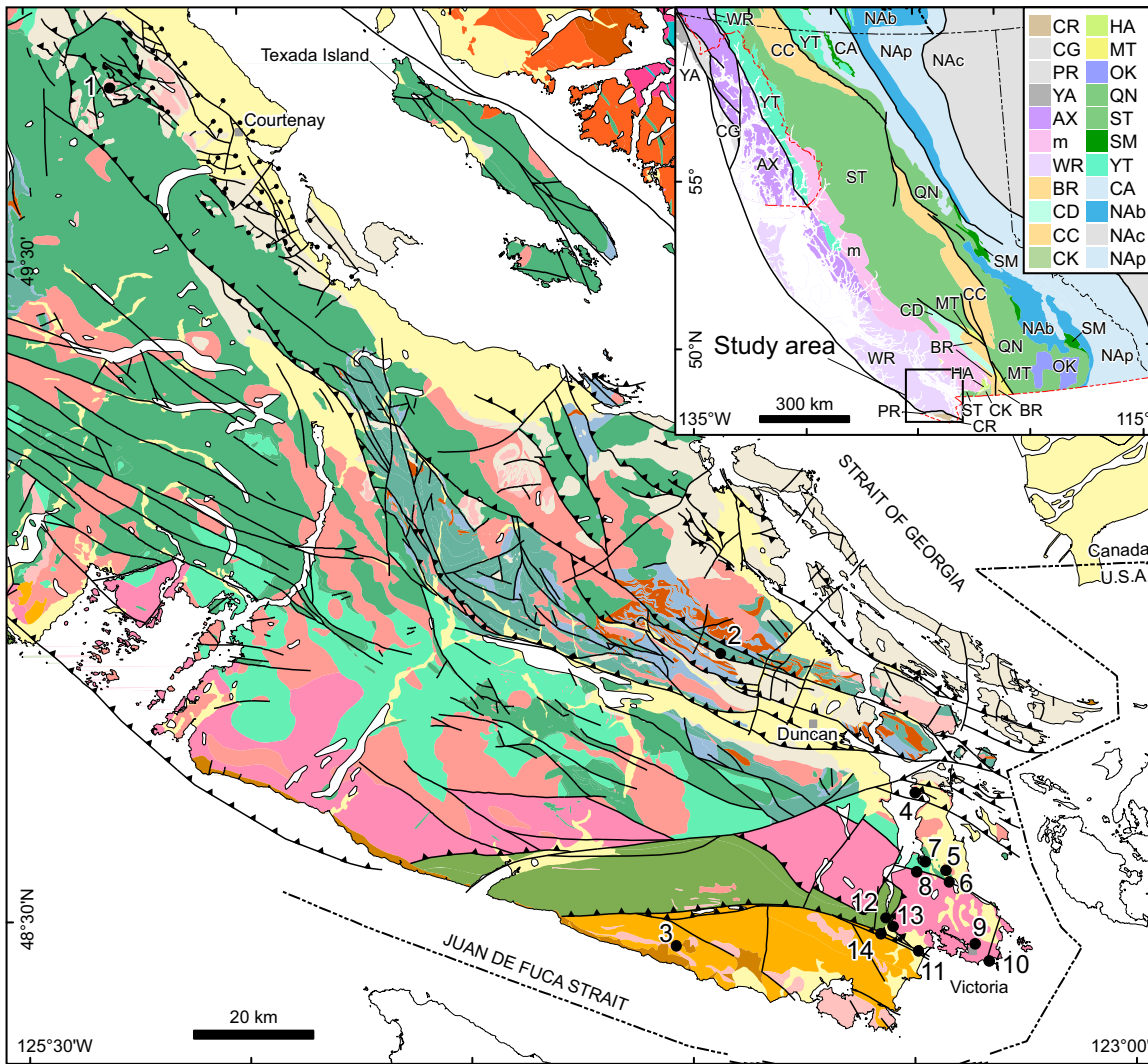


**Fig. 1.** Survey locations on southern Vancouver Island: 1 – Mount Washington; 2 – Coronation Mountain; 3 – Jordan River; 4 – Deep Cove; 5 – Bear Hill; 6 – Elk Lake; 7 – Tod Inlet; 8 – Durance Lake; 9 – downtown Victoria; 10 – Harling Point; 11 – Colwood; 12 – Goldstream; 13 – Skirt Mountain; and 14 – Sooke Hills. Geology after Cui et al. (2017, 2018) based on Clapp (1912, 1913), Erich and Blanshard (1921), Carson (1960a, b, 1968), Stevenson (1967), Guelpa and Meusy (1971), Meusy (1971), Northcote and Muller (1972), Muller (1977, 1980, 1983, 1989), Clague et al. (1982), Massey et al. (1991, 1994), Massey (1995), Wetherup (2010), Ruks (2015), and Bodnar (2017). Terrane geology after Nelson et al. (2013): Outboard terranes: CR – Crescent, CG – Chugach, PR – Pacific Rim, YA – Yakutat, WR – Wrangellia, m – Coast complex; Intermountain terranes: BR – Bridge River, CD – Cadwallader, CC – Cache Creek, CK – Chilliwack, HA – Harrison Lake, MT – Methow, OK – Okanagan, QN – Quesnellia, ST – Stikinia, SM – Slide Mountain, YT – Yukon-Tanana; Ancestral North American terranes: CA – Cassiar, NAb – Kootenay, NAp – North American platform, NAc – North American craton and cover.

Copper, MINFILE 092F 117; Domineer-Lakeview, MINFILE 092F 116). Auriferous quartz veins hosted by metamorphic rocks of the Leech River complex (Bentley Au, MINFILE 092B 067) and shear-hosted sulphide Cu-Ag-Au (Sunro, MINFILE 092C 073; Ralph, MINFILE 092B 014) also occur on southern Vancouver Island (Carson, 1960a, b, 1968; Northcote and Muller, 1972; Muller, 1977, 1989; Yorath, 2005). Most of the surficial deposits on Vancouver Island formed during or after the Fraser glaciation (Late Wisconsin; Muller, 1977; Clague et al., 1982; Yorath, 2005).

#### 4. Methods

Real-time mercury vapour ( $\text{Hg}^0$ ) mass concentrations (in  $\text{ng}\cdot\text{m}^{-3}$ ) in near-surface atmosphere (i.e. the layer of air 1-50 cm above ground) and simultaneously measured meteorological conditions were acquired during foot traversing at 15 locations on southern Vancouver Island (Fig. 1). Mercury vapour concentration in air was directly and continuously measured via a portable RA-915M differential Zeeman mercury atomic absorption spectrometer using high-frequency modulated light polarization (ZAAS-HFM; Lumex, St. Petersburg, Russia; Sholupov and Ganeyev, 1995; Sholupov et al., 2004). The instrument has a concentration detection range of 0.5 to 20,000  $\text{ng}\cdot\text{m}^{-3}$ , a response time of one second, and an analyzed air flow of 10  $\text{L}\cdot\text{m}^{-1}$ . Automatic baseline correction using a built-in, high-efficiency (>98%) sorption filter was performed every 10 minutes. Both drift and the standard deviation of zero readings are less than 2  $\text{ng}\cdot\text{m}^{-3}$ . The relative intrinsic error of the measurement is less than  $\pm 20\%$ . Mercury vapour concentrations were automatically normalized to standard temperature (20°C) and pressure (101.3 kPa). We used the average of ten consecutive readings (1 second each), which were automatically stored in the analyzer's memory. Near-surface air was analyzed for at least 20-30 seconds at each stop every 2 to 50 m along a traverse. Air was sampled 10-50 cm above ground directly through instrument's air intake inlet with a built-in dust filter, or 1-10 cm above ground via a 0.5 m long hose (20 mm diameter) attached to the air intake inlet (Fig. 2).

Meteorological parameters such as air temperature, relative humidity, absolute atmospheric (station) pressure, wind speed, and wind direction (azimuth) were simultaneously measured every 5 seconds using a Kestrel 5500 weather meter mounted on a tripod (Fig. 2). We used Garmin Glo 2 GPS-GLONASS and Garmin GPSMap 62sc receivers to acquire coordinates every 5 seconds. Relative pressure ( $P_0$ ) adjusted to sea-level (in hectopascal, hPa) was calculated according to the World Meteorological Organization's barometric formula from the absolute pressure ( $P$ ), air temperature ( $T$ ), and elevation above sea level ( $h$ ):

$$P_0 = P \cdot (1 - 0.0065h / [T + 0.0065h + 273.15])^{-5.257} \quad (\text{Eqn. 1})$$

where elevation ( $h$ ) for each data point is interpolated from the British Columbia Terrain Resource Information Mapping (TRIM) digital elevation model using GPS coordinates. Mercury vapour values of  $< 0.5 \text{ ng}\cdot\text{m}^{-3}$  (total 156 values or 1.6% of all data) due to abnormal baseline noise were discarded.



Fig. 2. Simultaneous measurement of meteorological conditions and Hg vapour concentrations in near-surface air at Harling Point, southern Vancouver Island.

#### 5. Results

Below we summarize the results of our surveys; the complete dataset is presented in Rukhlov et al. (2020). Mercury vapour survey locations include a variety of known metallic mineral occurrences, barren rocks, and faults on southern Vancouver Island (Fig. 1). Table 1 provides a statistical summary of the real-time Hg vapour data and simultaneously measured meteorological parameters (air temperature, relative humidity, relative pressure corrected to sea level, and wind speed). Appendix 1 of Rukhlov et al. (2020) provides time vs.  $\text{Hg}^0$  in air and vs. meteorological parameters, wind direction, and  $\text{Hg}^0$  in air statistical plots for each survey.

Measured Hg vapor concentrations of this study range from 0.5 to 54  $\text{ng}\cdot\text{m}^{-3}$ , averaging  $1.93 \pm 2.98 \text{ ng}\cdot\text{m}^{-3}$  ( $n=9660$ ; Table 1). The median value of  $1.40 \text{ ng}\cdot\text{m}^{-3}$  is consistent with the background Hg concentration in air of the northern hemisphere ( $1.5 \text{ ng}\cdot\text{m}^{-3}$ ; Sprovieri et al., 2016).

##### 5.1. British Columbia Geological Survey laboratory

To test the instrument, we measured air in the basement laboratory of the British Columbia Geological Survey at 1810 Blanshard Street in downtown Victoria in the presence of a benchtop laboratory mercury barometer (an undisturbed source of elemental Hg). We also took measurements in adjacent areas inside and outside of the building (Fig. 3). Our first test (July 25, 2020) revealed Hg vapour concentration up to 33  $\text{ng}\cdot\text{m}^{-3}$  near a W.M. Welch Scientific Company mercury barometer (Chicago, U.S.A.). Outside of the laboratory, 25 m away from the barometer, concentration was at the background level of  $1.4 \text{ ng}\cdot\text{m}^{-3}$ . In other areas of the laboratory, which are connected to a central heating, ventilating, and air-conditioning system, intermediate Hg vapour concentrations were observed. Measurements at the end of this study (August 28, 2020) reproduced these results (Table 1; Fig. 3). Up to 36  $\text{ng}\cdot\text{m}^{-3}$  of gaseous  $\text{Hg}^0$  was measured in the air about 2 m above the floor,

**Table 1.** Statistical summary of real-time Hg vapour concentrations in near-surface air and simultaneously measured meteorological parameters.

Parameter	N	Mean	$\sigma$	Minimum	Percentiles					Maximum
					25	50	75	87	97	
<b>All data of this study (24.07.2020-28.08.2020)</b>										
Hg <sup>0</sup> in air (ng·m <sup>-3</sup> )	9660	1.93	2.98	0.50	1.22	1.40	1.64	2.05	4.13	54.35
Air temperature (°C)	9289	19.2	3.6	12.1	15.5	19.5	22.4	23.2	24.8	30.9
Relative humidity (%)	9289	58.9	10.6	31.0	51.8	58.2	64.8	72.5	80.7	85.5
Relative pressure (hPa)	9289	1017.8	3.2	1007.2	1015.0	1018.3	1019.8	1021.0	1023.9	1025.1
Wind speed (m·s <sup>-1</sup> )	8915	0.8	0.8	0.0	0.0	0.6	1.2	1.7	2.7	6.3
<b>British Columbia Geological Survey laboratory (25.07.2020, 15:20-15:26)</b>										
Hg <sup>0</sup> in air (ng·m <sup>-3</sup> )	35	19.90	8.94	1.34	19.10	20.71	25.95	30.20	32.90	33.05
Air temperature (°C)	35	23.2	0.4	22.4	23.0	23.4	23.4	23.5	23.5	23.5
Relative humidity (%)	35	48.2	0.8	47.5	47.6	47.8	48.6	49.5	50.1	50.1
Relative pressure (hPa)	35	1022.5	0.1	1022.4	1022.4	1022.5	1022.5	1022.5	1022.6	1022.6
Wind speed (m·s <sup>-1</sup> )	na	na	na	na	na	na	na	na	na	na
<b>British Columbia Geological Survey laboratory (28.08.2020, 17:17-17:40)</b>										
Hg <sup>0</sup> in air (ng·m <sup>-3</sup> )	122	8.90	8.67	1.28	2.11	4.12	13.54	18.81	33.87	36.20
Air temperature (°C)	na	na	na	na	na	na	na	na	na	na
Relative humidity (%)	na	na	na	na	na	na	na	na	na	na
Relative pressure (hPa)	na	na	na	na	na	na	na	na	na	na
Wind speed (m·s <sup>-1</sup> )	na	na	na	na	na	na	na	na	na	na
<b>Bear Hill (28.08.2020, 13:22-14:55)</b>										
Hg <sup>0</sup> in air (ng·m <sup>-3</sup> )	490	1.24	0.17	0.72	1.12	1.24	1.37	1.45	1.58	1.81
Air temperature (°C)	490	22.7	1.5	19.8	21.6	22.3	23.7	24.4	26.1	27.9
Relative humidity (%)	490	52.9	3.7	42.8	50.1	53.3	56.1	57.0	57.9	58.5
Relative pressure (hPa)	490	1018.1	0.5	1017.0	1017.9	1018.1	1018.5	1018.7	1019.0	1019.1
Wind speed (m·s <sup>-1</sup> )	490	0.7	0.6	0.0	0.0	0.6	0.9	1.3	2.0	3.8
<b>Colwood (05.08.2020, 15:04-16:32)</b>										
Hg <sup>0</sup> in air (ng·m <sup>-3</sup> )	211	1.59	0.69	0.51	1.11	1.49	2.07	2.40	3.15	3.81
Air temperature (°C)	45	25.6	0.6	24.2	25.2	25.6	26.1	26.4	26.7	26.8
Relative humidity (%)	45	43.2	2.8	39.1	40.8	42.6	44.8	45.9	52.1	53.6
Relative pressure (hPa)	45	1012.6	2.5	1007.2	1010.7	1012.7	1014.5	1016.3	1016.8	1016.8
Wind speed (m·s <sup>-1</sup> )	45	0.9	1.0	0.0	0.0	0.8	1.3	1.7	3.5	3.5
<b>Coronation Mountain (06.08.2020, 10:38-14:06)</b>										
Hg <sup>0</sup> in air (ng·m <sup>-3</sup> )	1099	1.79	0.69	0.57	1.47	1.64	1.88	2.29	3.05	10.85
Air temperature (°C)	1099	15.3	1.3	13.0	14.4	15.1	15.9	16.6	18.5	21.6
Relative humidity (%)	1099	64.5	4.6	51.0	62.0	64.4	67.0	69.5	73.6	79.1
Relative pressure (hPa)	1099	1013.0	0.9	1010.3	1012.3	1012.6	1013.5	1014.3	1015.0	1015.4
Wind speed (m·s <sup>-1</sup> )	1099	0.7	1.0	0.0	0.0	0.0	1.1	1.8	3.6	6.3
<b>Coronation Mountain (12.08.2020, 10:19-15:49)</b>										
Hg <sup>0</sup> in air (ng·m <sup>-3</sup> )	1562	1.49	0.49	0.50	1.27	1.40	1.58	1.69	2.65	5.91
Air temperature (°C)	1562	14.8	1.1	12.4	13.9	14.9	15.6	16.1	16.9	18.2
Relative humidity (%)	1562	59.1	3.2	48.7	57.2	59.4	61.0	62.2	64.6	71.0
Relative pressure (hPa)	1562	1018.4	0.6	1016.8	1018.0	1018.4	1018.9	1019.1	1019.5	1019.8
Wind speed (m·s <sup>-1</sup> )	1562	1.1	0.9	0.0	0.4	0.9	1.7	2.2	3.1	5.2
<b>Deep Cove (27.08.2020, 13:24-15:02)</b>										
Hg <sup>0</sup> in air (ng·m <sup>-3</sup> )	519	1.27	0.19	0.78	1.16	1.27	1.38	1.46	1.60	3.06
Air temperature (°C)	519	22.6	0.9	20.3	22.1	22.7	23.2	23.6	24.2	25.0
Relative humidity (%)	519	53.0	3.2	46.4	51.0	52.5	54.4	56.5	61.1	63.6
Relative pressure (hPa)	519	1018.6	0.3	1017.8	1018.4	1018.7	1018.9	1019.0	1019.3	1019.4
Wind speed (m·s <sup>-1</sup> )	519	0.7	0.8	0.0	0.0	0.5	1.1	1.6	2.7	4.3

Table 1. Continued.

Parameter	N	Mean	$\sigma$	Minimum	Percentiles					Maximum
					25	50	75	87	97	
<b>Durance Lake (19.08.2020, 16:02-16:58)</b>										
Hg <sup>0</sup> in air (ng·m <sup>-3</sup> )	298	1.18	0.21	0.75	1.04	1.17	1.30	1.38	1.58	2.55
Air temperature (°C)	298	22.9	0.5	21.8	22.6	22.9	23.1	23.2	24.1	24.5
Relative humidity (%)	298	56.6	2.4	50.5	55.1	56.2	58.3	59.4	61.8	63.0
Relative pressure (hPa)	298	1013.4	0.4	1012.5	1013.1	1013.5	1013.6	1013.8	1014.1	1014.2
Wind speed (m·s <sup>-1</sup> )	298	0.6	0.6	0.0	0.0	0.5	1.0	1.3	1.7	2.2
<b>Elk Lake (28.08.2020, 15:39-16:07)</b>										
Hg <sup>0</sup> in air (ng·m <sup>-3</sup> )	152	1.22	0.17	0.55	1.13	1.22	1.33	1.41	1.55	1.67
Air temperature (°C)	152	20.2	0.4	19.7	20.0	20.1	20.4	20.6	21.4	21.6
Relative humidity (%)	152	63.1	2.6	56.9	61.9	63.2	65.2	65.8	67.1	67.9
Relative pressure (hPa)	152	1017.9	0.2	1017.4	1017.7	1017.9	1018.1	1018.1	1018.2	1018.3
Wind speed (m·s <sup>-1</sup> )	152	0.8	0.7	0.0	0.0	0.7	1.3	1.8	2.2	2.5
<b>Goldstream (22.08.2020, 11:50-13:23)</b>										
Hg <sup>0</sup> in air (ng·m <sup>-3</sup> )	494	4.21	8.62	0.59	1.26	1.41	1.67	3.71	34.18	54.35
Air temperature (°C)	494	19.5	0.6	18.1	19.1	19.6	19.9	20.1	20.7	21.1
Relative humidity (%)	494	59.9	5.5	49.4	55.8	58.8	63.6	67.0	71.4	73.7
Relative pressure (hPa)	494	1022.5	0.6	1020.8	1022.0	1022.3	1022.9	1023.2	1023.9	1024.2
Wind speed (m·s <sup>-1</sup> )	494	0.4	0.5	0.0	0.0	0.0	0.8	1.1	1.4	2.3
<b>Harling Point (08.08.2020, 15:23-16:19)</b>										
Hg <sup>0</sup> in air (ng·m <sup>-3</sup> )	239	1.59	0.20	1.08	1.46	1.57	1.69	1.78	2.10	2.45
Air temperature (°C)	238	16.1	1.3	12.9	15.3	15.9	16.7	17.4	19.3	21.5
Relative humidity (%)	238	73.0	4.8	56.1	71.1	74.1	75.8	77.3	81.0	85.5
Relative pressure (hPa)	238	1024.6	0.3	1024.0	1024.3	1024.8	1024.9	1024.9	1025.0	1025.1
Wind speed (m·s <sup>-1</sup> )	238	1.3	0.7	0.0	0.7	1.2	1.7	2.2	2.8	3.2
<b>Jordan River (17.08.2020, 09:57-12:51)</b>										
Hg <sup>0</sup> in air (ng·m <sup>-3</sup> )	917	1.35	0.18	0.83	1.22	1.34	1.47	1.55	1.69	1.96
Air temperature (°C)	917	19.3	1.1	17.4	18.6	19.0	19.7	20.2	22.5	24.9
Relative humidity (%)	917	78.5	3.9	62.2	77.3	79.3	80.9	81.9	83.0	84.5
Relative pressure (hPa)	917	1020.3	1.1	1018.1	1019.6	1020.1	1020.5	1021.3	1024.0	1024.5
Wind speed (m·s <sup>-1</sup> )	917	0.4	0.5	0.0	0.0	0.0	0.6	0.9	1.6	3.7
<b>Mount Washington (25.08.2020, 13:00-15:37)</b>										
Hg <sup>0</sup> in air (ng·m <sup>-3</sup> )	789	2.27	1.80	0.50	1.41	1.83	2.69	3.28	5.49	16.35
Air temperature (°C)	789	15.9	1.9	12.1	14.5	15.6	17.0	18.3	20.0	22.0
Relative humidity (%)	789	66.7	6.7	47.0	62.9	67.0	71.5	73.8	78.4	81.3
Relative pressure (hPa)	789	1015.5	1.1	1012.2	1014.7	1015.6	1016.3	1016.7	1017.2	1017.6
Wind speed (m·s <sup>-1</sup> )	625	1.2	0.7	0.3	0.6	1.0	1.6	2.1	2.8	3.9
<b>Skirt Mountain (10.08.2020, 11:43-16:15)</b>										
Hg <sup>0</sup> in air (ng·m <sup>-3</sup> )	1325	2.15	2.97	0.51	1.23	1.44	1.71	2.37	15.44	19.23
Air temperature (°C)	1325	23.4	1.5	20.7	22.3	23.2	24.2	24.9	27.0	30.9
Relative humidity (%)	1325	53.2	4.5	38.4	50.2	52.9	56.9	58.6	60.9	65.6
Relative pressure (hPa)	1325	1020.0	0.8	1018.0	1019.4	1019.9	1020.7	1020.9	1021.3	1022.1
Wind speed (m·s <sup>-1</sup> )	1325	0.5	0.6	0.0	0.0	0.4	0.8	1.1	1.7	3.4
<b>Sooke Hills (11.08.2020, 14:17-16:43)</b>										
Hg <sup>0</sup> in air (ng·m <sup>-3</sup> )	769	1.30	0.20	0.74	1.17	1.29	1.42	1.53	1.73	1.92
Air temperature (°C)	769	20.4	0.9	18.5	19.7	20.4	21.1	21.6	22.2	23.1
Relative humidity (%)	769	41.6	4.7	31.0	38.3	41.8	45.0	46.0	48.7	57.4
Relative pressure (hPa)	769	1014.1	0.7	1013.0	1013.7	1013.9	1014.4	1014.9	1015.9	1016.5
Wind speed (m·s <sup>-1</sup> )	769	1.0	0.8	0.0	0.4	0.8	1.4	1.9	2.7	5.2

Table 1. Continued.

Parameter	N	Mean	$\sigma$	Minimum	Percentiles					Maximum
					25	50	75	87	97	
<b>Tod Inlet (27.08.2020, 16:15-17:28)</b>										
Hg <sup>0</sup> in air (ng·m <sup>-3</sup> )	382	1.17	0.17	0.58	1.06	1.17	1.27	1.35	1.49	2.06
Air temperature (°C)	382	23.1	0.5	21.6	22.8	23.0	23.3	23.6	24.3	25.1
Relative humidity (%)	382	47.3	2.0	43.8	46.0	46.9	48.2	49.1	52.7	53.6
Relative pressure (hPa)	382	1017.4	0.2	1017.0	1017.3	1017.4	1017.6	1017.7	1017.9	1018.2
Wind speed (m·s <sup>-1</sup> )	382	0.7	0.7	0.0	0.0	0.5	1.1	1.5	2.4	3.4
<b>Victoria (25.07.2020, 14:56-15:20)</b>										
Hg <sup>0</sup> in air (ng·m <sup>-3</sup> )	130	1.76	0.32	1.18	1.51	1.76	1.96	2.19	2.39	2.51
Air temperature (°C)	130	22.8	0.6	21.2	22.4	22.9	23.2	23.4	23.8	24.2
Relative humidity (%)	130	48.8	1.1	46.8	48.0	48.8	49.5	50.1	51.3	51.6
Relative pressure (hPa)	130	1022.8	0.3	1022.4	1022.6	1022.7	1022.8	1023.1	1023.6	1023.8
Wind speed (m·s <sup>-1</sup> )	na	na	na	na	na	na	na	na	na	na

Real-time Hg vapour mass concentrations in near-surface air (in nanograms per cubic metre, ng·m<sup>-3</sup>) measured via a portable RA-915M Zeeman mercury atomic absorption spectrometer with high frequency modulated light polarization. Meteorological parameters simultaneously measured using a Kestrel 5500 meter. Relative pressure (in hectopascal, hPa) adjusted to sea-level (see text for details). N - number of values used to calculate the statistics;  $\sigma$  - standard deviation; na - not analyzed.

immediately near the barometer. Mercury vapour concentration gradually decreases with distance from the Hg<sup>0</sup> source. Mercury vapour concentrations in ambient air of the adjacent areas outside the laboratory, including stairwell and breezeway enclosures, were above the background Hg (1.77-5.31 ng·m<sup>-3</sup>) and diluted to background further away from the laboratory on both basement levels and immediately outside the building (Fig. 3). These results show that an undisturbed, open source of Hg<sup>0</sup> such as the laboratory mercury barometer generates a stable Hg vapour halo in the ambient air of a positively ventilated, closed area more than 25 m away from the source. Because our measurements identified an environmental exposure issue, the mercury barometer has been sealed in a plastic bag and removed to permanently ventilated chemical storage.

## 5.2. Coronation Mountain; Lara-Coronation polymetallic volcanogenic massive sulphide occurrence

The Lara-Coronation volcanogenic massive sulphide (VMS) Zn-Cu-Pb-Ag-Au occurrence is on southern flank of Coronation Mountain (Fig. 1; MINFILE 092B 129) and, with only one bedrock exposure, is mostly covered by up to 30 m of glacial sediments (Figs. 4, 5; Bodnar, 2017; Heberlein et al., 2017). We carried out surveys along a forest road, spur trails, and across a clearcut under slightly different conditions on two separate days. Air was sampled 10-50 cm above ground on August 6, 2020, following several days and nights of rain. The second survey, on August 12, 2020, sampled air 1-10 cm above ground after six days without precipitation. Air temperature was similar, but atmospheric pressure was higher and relative humidity slightly lower on August 12th compared to those on August 6th. Predominantly west-southwest wind calmed by mid-day on August 6th, whereas predominantly east-southeast wind was generally consistent on August 12th (Table 1;

Appendix 1 in Rukhlov et al., 2020).

The Lara-Coronation polymetallic occurrence comprises two lenses (up to 16 m thick) of banded and massive sphalerite, pyrite, chalcopyrite, and galena with minor tetrahedrite, tennantite, bornite, electrum, pearceite, and arsenopyrite (Northcote and Muller, 1972; Kelso and Wetherup, 2008; Wetherup, 2010; Ruks, 2015; Bodnar, 2017). The mineralization is hosted by greenschist-facies, sheared and silicified felsic and intermediate volcanic rocks of the McLaughlin Ridge Formation (Sicker Group; Middle to Late Devonian), which dip steeply northeast. Samples of massive sulphide ore yielded up to 90 ppm Hg (Kelso and Wetherup, 2008; Bodnar, 2017) that is four orders of magnitude higher than the Clarke value for the Earth's crust (45 ppb Hg; Rudnick and Gao, 2005). Associated mineralization includes chalcopyrite-pyrite stringers in silicified shear zones and pyrite-rich horizons (Figs. 5, 6).

Previous multi-media geochemical studies at Lara reported up to 460 ppb Hg in soils and up to 133 ppb Hg in vegetation (Bodnar, 2017; Heberlein et al., 2017 and references therein). However, the Hg dispersion haloes in these media are not entirely linked to the polymetallic mineralization, because anomalous Hg concentrations cluster mainly above a barren pyrite-rich horizon a few hundred metres upslope, to the northeast (Fig. 7). In contrast, anomalous Hg vapour haloes were detected in near-surface air directly above the sediment-covered Lara-Coronation VMS mineralized zones, regardless of the overburden thickness, air sampling height, soil moisture, and meteorological conditions (Figs. 8, 9). Concentrations of gaseous Hg<sup>0</sup> in air range from 0.57 to 11 ng·m<sup>-3</sup> with the median (background) value of 1.64 ng·m<sup>-3</sup> on August 6th (n=1099) and from 0.50 to 5.9 ng·m<sup>-3</sup> with the median (background) value of 1.40 ng·m<sup>-3</sup> on August 12th (n=1562; Table 1). The strongest anomalies (4 to 7x background Hg) occur above the high-grade

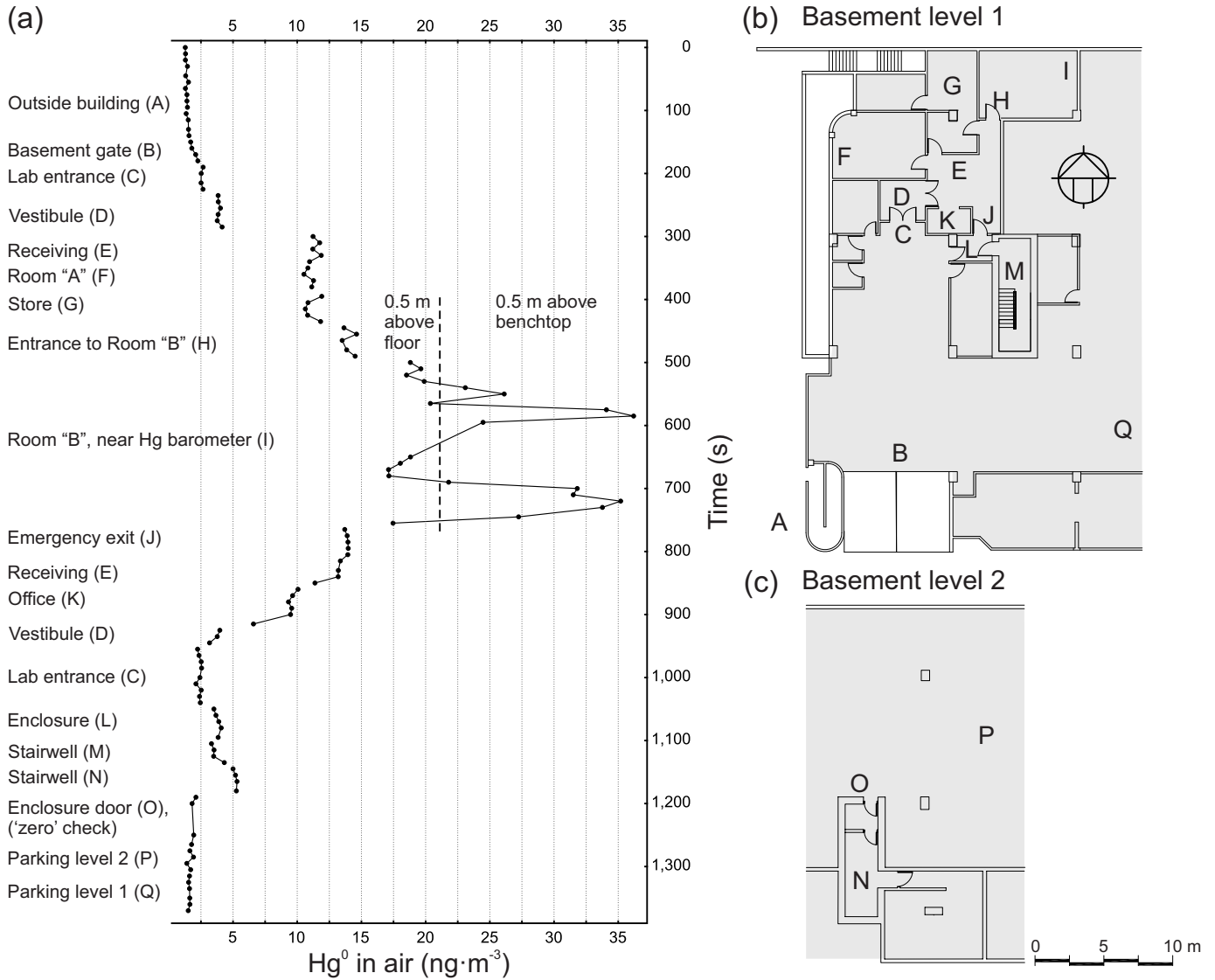


**Fig. 3.** Real-time Hg vapour concentrations in ambient air of the British Columbia Geological Survey laboratory and adjacent areas on August 28, 2020. **a)** Hg<sup>0</sup> in air (ng·m<sup>-3</sup>) vs. time (in seconds) plot. **b)** Sampling locations on basement level 1 and outside the buildings. **c)** Sampling locations on basement level 2.



**Fig. 4.** Glacigenic overburden above the Lara-Coronation polymetallic volcanogenic massive sulphide occurrence.



**Fig. 5.** Outcrop of volcanogenic massive sulphide mineralization in sheared felsic volcanic rocks of the McLaughlin Ridge Formation (Sicker Group; Late to Middle Devonian) at the Lara-Coronation occurrence.



**Fig. 6.** Closeup of chalcopyrite-pyrite stringers in a silicified shear zone at the Lara-Coronation occurrence.

ore in a flooded trench and on a nearby outcrop of mineralized volcanic rocks (Figs. 8, 9). Weaker Hg vapour haloes in near-surface air also mark polymetallic VMS zone buried under 30 m of glacial sediments, silicified shear zones with sulphide stringers, pyrite-rich horizon, and a northwest-trending thrust fault (Fig. 9). In addition, conspicuous Hg vapour emissions were measured above Nanaimo Group sedimentary rocks in the footwall of a northwest-trending thrust fault on August 6, 2020, but not on August 12, 2020 (Figs. 8, 9).

**5.3. Mount Washington; Mount Washington Copper porphyry Cu-Mo-Au and Domineer-Lakeview epithermal Au-Ag-Cu mineralization**

On the northern ridge of Mount Washington (Fig. 1), the Mount Washington Copper past producer (MINFILE 092F 117) and Domineer-Lakeview developed prospect (MINFILE 092F 116) represent porphyry Cu-Mo-Au to high-sulphidation epithermal Au-Ag-Cu mineralization (Carson, 1960a, b, 1968;

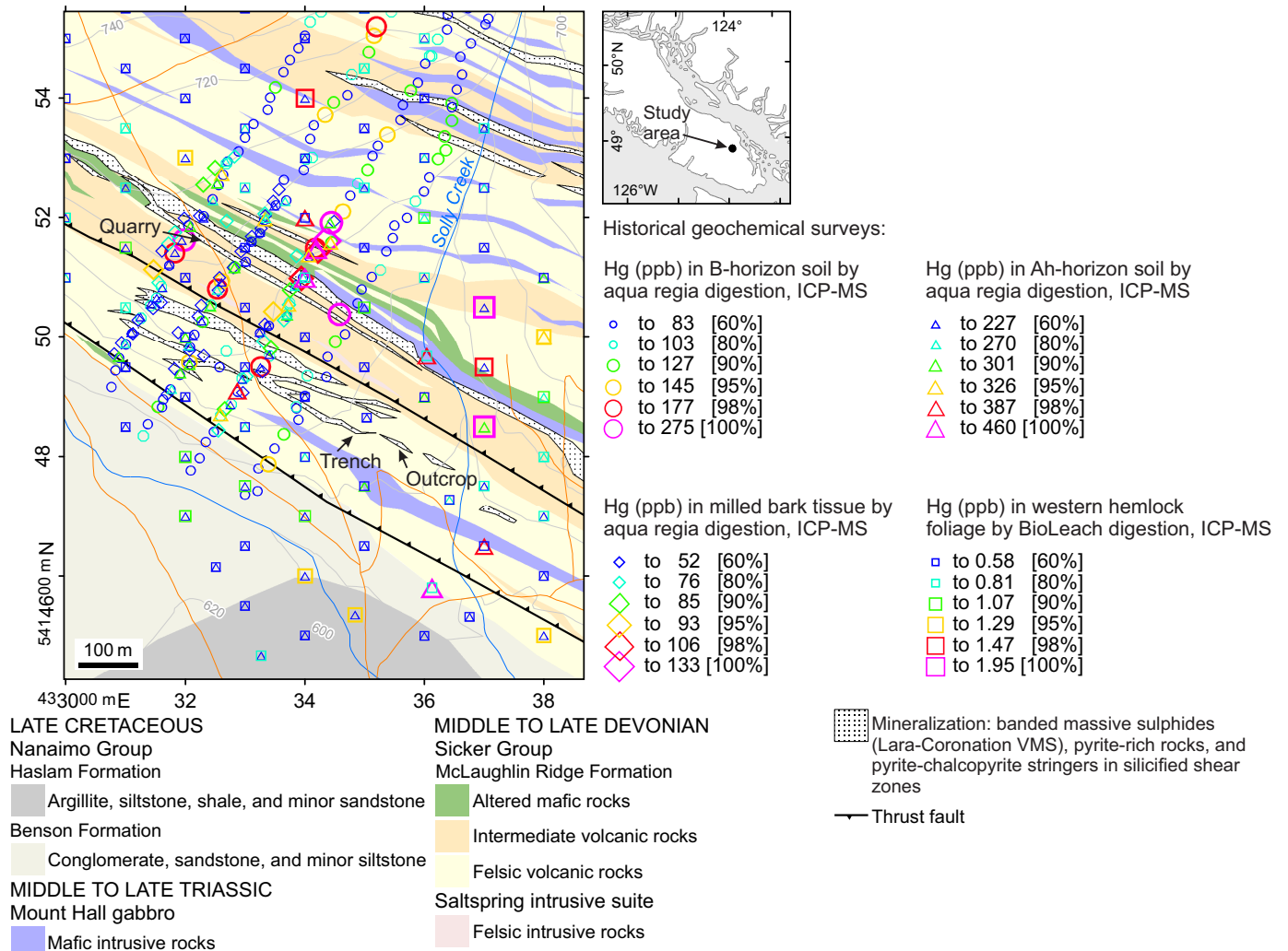


**Fig. 7.** Percentile-ranked Hg concentrations in soil and vegetation at the Lara-Coronation occurrence. Compiled geochemical data from Bodnar (2017) and Heberlein et al. (2017). Geology after Muller (1977), Massey et al. (1991, 1994), Massey (1995), Wetherup (2010), Ruks (2015), and Bodnar (2017).

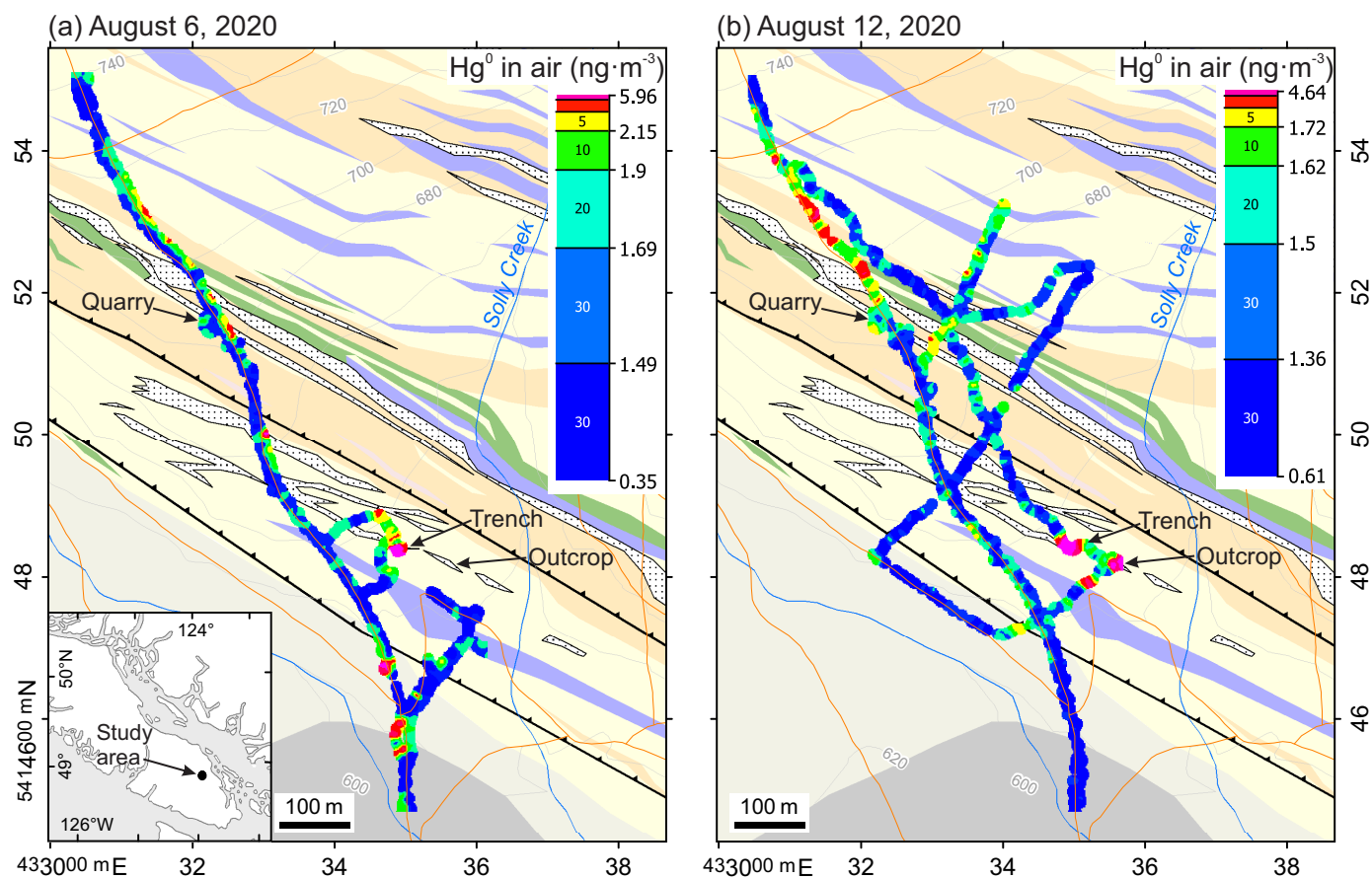


**Fig. 8.** Percentile-gridded, real-time Hg vapour concentrations ( $\text{ng}\cdot\text{m}^{-3}$ ) in near-surface air at the Lara-Coronation occurrence. Gridding interpolation based on modified inverse distance weighing method. Geology legend as in Figure 7. **a)** Hg vapour concentrations in air 10-50 cm above ground on August 6, 2020. **b)** Hg vapour concentrations in air 1-10 cm above ground sampled using a hose on August 12, 2020.

Neville, 1963; Stevenson, 1967; Northcote and Muller, 1972; McDougall, 1987; Muller, 1989; Houle, 2019). We surveyed across an open pit at Mount Washington Copper and along a trail to a trench at the Domineer zone, less than 400 m to the south (Figs. 10, 11).

The area is underlain by mafic volcanic rocks of the Karmutsen Formation (Vancouver Group; Late Triassic) that are unconformably overlain by siliciclastic rocks of the Comox Formation (Nanaimo Group; Late Cretaceous). The youngest rocks are intermediate and felsic porphyry stocks, dikes, sills, and late breccias of the Mount Washington plutonic suite and related volcanoclastic strata (Eocene to Oligocene). Detachment faults along bedding of the sedimentary and volcanoclastic rocks are offset by variably trending, high-angle faults (Muller, 1989; Houle, 2019). The late breccias host the polymetallic sulphide mineralization, which was discovered in 1940.

Both Mount Washington Copper and Domineer-Lakeview are flat-lying bodies (1-7.6 m thick). At Mount Washington Copper, a chalcopryrite-pyrite-quartz vein stockwork and disseminated sulphides continue for more than 750 m along the contact between the Comox Formation and an overlying diorite sill of the Mount Washington plutonic suite (Fig. 12). The Domineer-Lakeview zone comprises quartz-pyrite-arsenopyrite breccia

with banded sulphides, veins, and lenses within pervasive kaolinite and chlorite (outer envelope) alteration for 1.5 km along a detachment fault. Ore minerals identified at both occurrences include chalcopryrite, tetrahedrite-tennantite, arsenopyrite, realgar (Fig. 13), orpiment, bornite, covellite, chalcocite, molybdenite, arsenic, chalcostibite, sphalerite, galena, and hessite (Neville, 1963; Houle, 2019).

Mercury vapour concentrations in air 10-50 cm above ground range from 0.50 to 16  $\text{ng}\cdot\text{m}^{-3}$ , with a median (background) value of 1.83  $\text{ng}\cdot\text{m}^{-3}$  ( $n=789$ ; Table 1). Prominent Hg<sup>0</sup> haloes in near-surface atmosphere (up to 9x background Hg) mark exposed massive arsenopyrite-pyrite±chalcopryrite±realgar veins at both the Mount Washington Copper southern open pit and Domineer trench (Figs. 10, 11). Slightly elevated Hg vapour haloes (1.3-1.5x background Hg) also occur above breccia about 100 m south of the open pit. These subtle anomalies were not detected in initial measurements taken one hour earlier, although duplicated data show consistent Hg vapour concentrations elsewhere, regardless of fluctuating meteorological conditions (Fig. 11; Appendix 1 of Rukhlov et al., 2020). We attribute the discrepancy to the combined effects of wind gusts, which were up to 4  $\text{m}\cdot\text{s}^{-1}$ , increased atmospheric pressure, and decreased air temperature, which may have diluted and suppressed emission

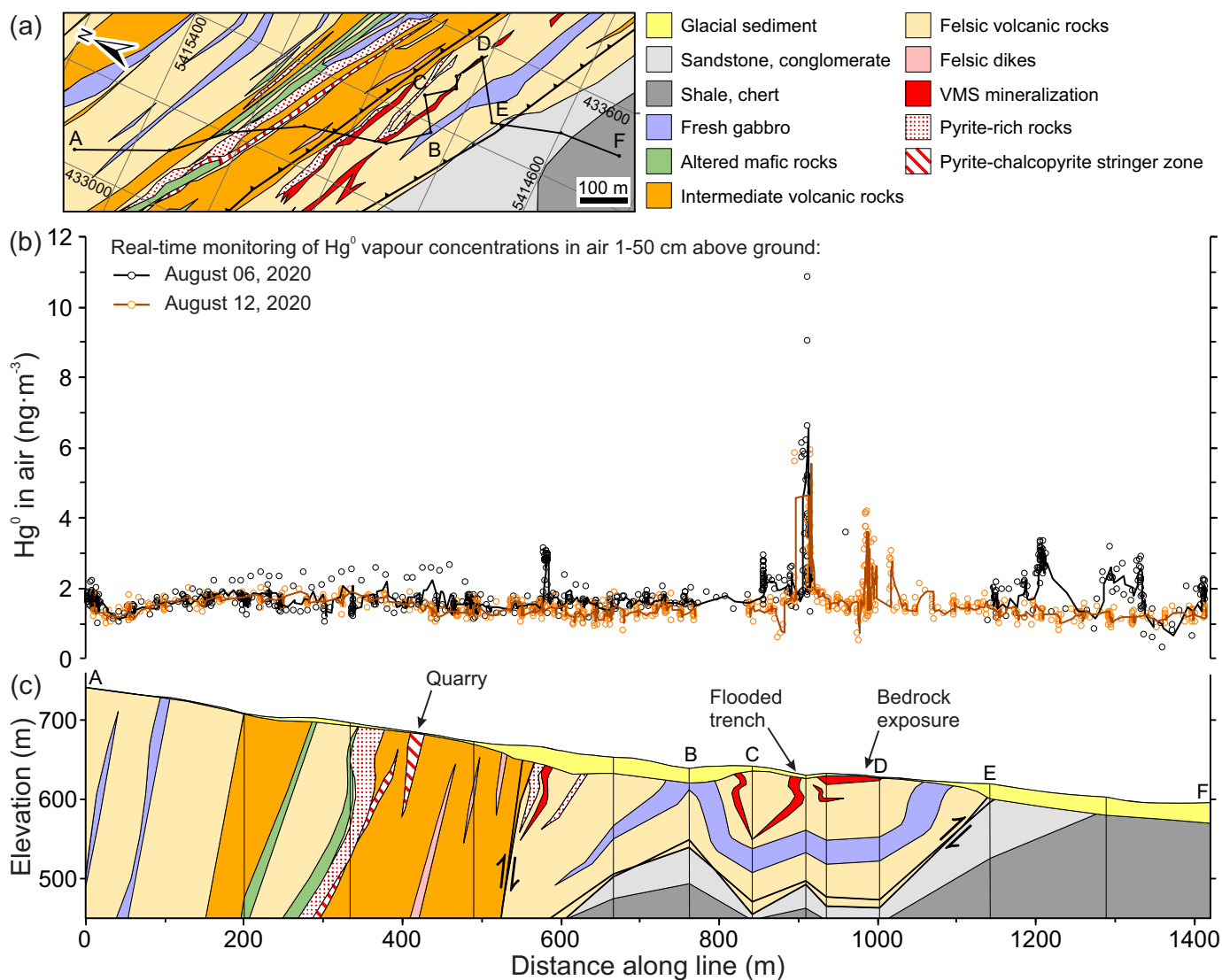


**Fig. 9.** a) Bedrock geology of the Lara-Coronation occurrence and position of section lines for b) and c); modified after Massey et al. (1991, 1994), Massey (1995), Wetherup (2010), and Bodnar (2017). b) Profile showing Hg<sup>0</sup> (ng·m<sup>-3</sup>) in near-surface air on August 6, 2020 (sampling height 10-50 cm above ground; black symbols) and August 12, 2020 (sampling height 1-10 cm above ground; beige symbols) and corresponding average curves. c) Northwest-southeast cross section; overburden thickness after Bodnar (2017).

of gaseous Hg<sup>0</sup> from the surface into the atmosphere during the initial measurements.

#### 5.4. Jordan River; Sunro Cu-Ag-Au sulphide occurrence

The Sunro occurrence is on the eastern side of the Jordan River canyon (Figs. 1, 14) and is a past-producing underground deposit (Fig. 15; MINFILE 092C 073). The deposit is hosted by basalts of the Metchosin Formation that are intruded by a steeply dipping, wide (several 100 m), medium- to coarse-grained, hornblende gabbro dike whose trend is parallel to a northwesterly fold axis in the volcanic rocks (Clapp, 1912; Brewer, 1918; Erich and Blanshard, 1921; Guelpa and Meusy, 1971; Meusy, 1971; Muller, 1977; Massey et al., 1994). Outliers of marine sandstones and conglomerates of the Sooke Formation (Carmanah Group; Eocene to Oligocene)

unconformably overlie the basalts and gabbro both to the southwest and northeast. Sulphide Cu-Ag-Au mineralization is localized in subvertical hornblendized shear zones (up to 40 m wide) in basalts adjacent to the dike. Ore minerals include mainly chalcopyrite, bornite, pyrite, and pyrrhotite, with minor native copper, molybdenite, arsenopyrite, cubanite and pentlandite. They form gash veinlets, lenticular masses, smears, and blebs (Starr and Frith, 1926; Toombs, 1951).

Mercury vapour concentrations in air 1-10 cm above ground along the traverse across the intrusive contact, several mineralized zones, and faults show a normal distribution (Appendix 1 in Rukhlov et al., 2020) and range from 0.83 to 2.0 ng·m<sup>-3</sup>, averaging 1.35 ng·m<sup>-3</sup> (n=917; Table 1). Overburden is seemingly thin (<2 m?), with bedrock exposed in steep banks and quarries along a trail to the River portal (Fig. 15). The

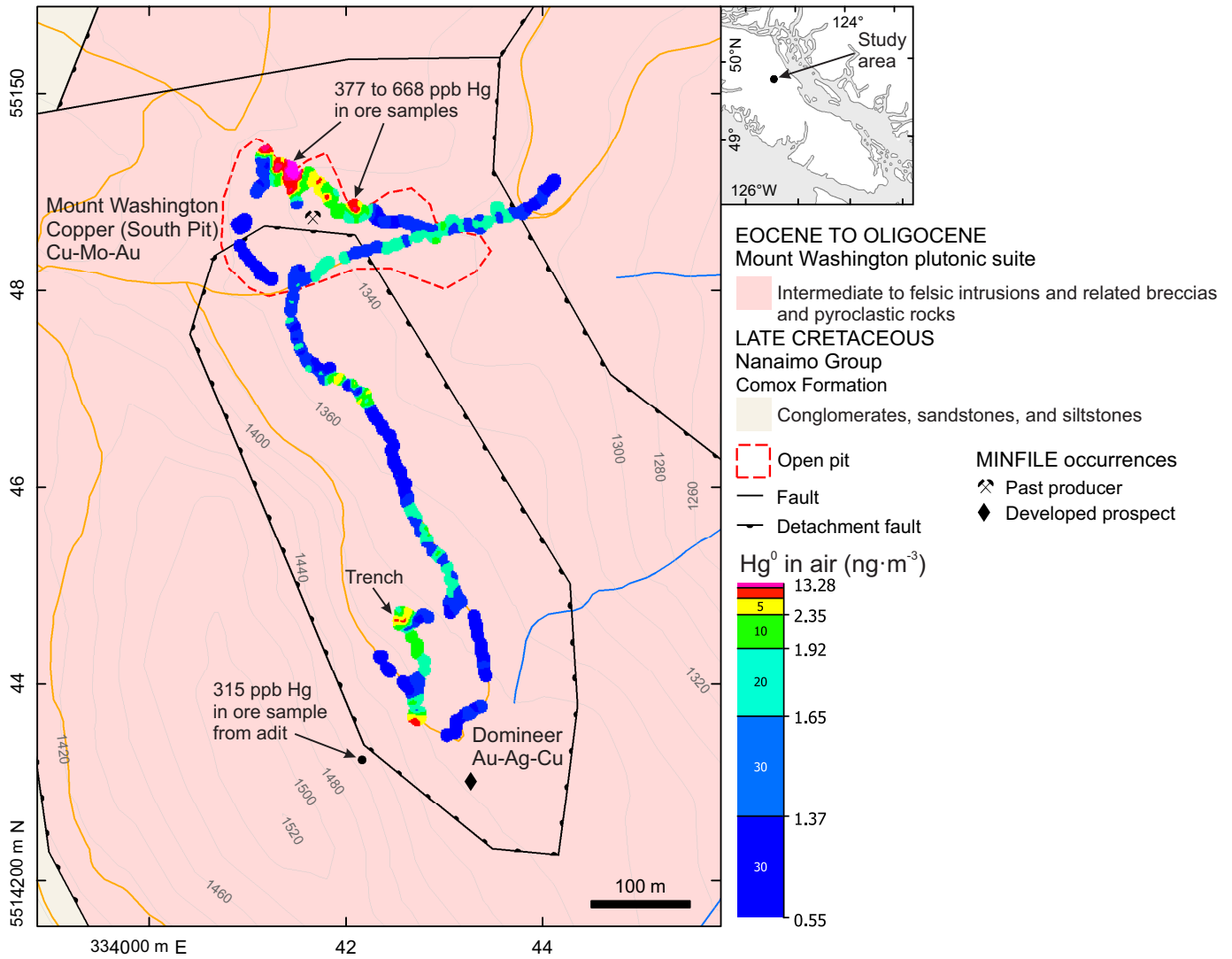


**Fig. 10.** Percentile-gridded, real-time Hg vapour concentrations ( $\text{ng}\cdot\text{m}^{-3}$ ) in air 10-50 cm above ground at Mount Washington Copper and Domineer mineralization. Gridding interpolation based on modified inverse distance weighing method. Geology after Cui et al. (2017, 2018) based on Carson (1960a, b, 1968), Stevenson (1967), Northcote and Muller (1972), Muller (1977, 1989), McDougall (1987), and Massey et al. (1994). Concentrations of Hg in ore samples from Houle (2000; 2019).

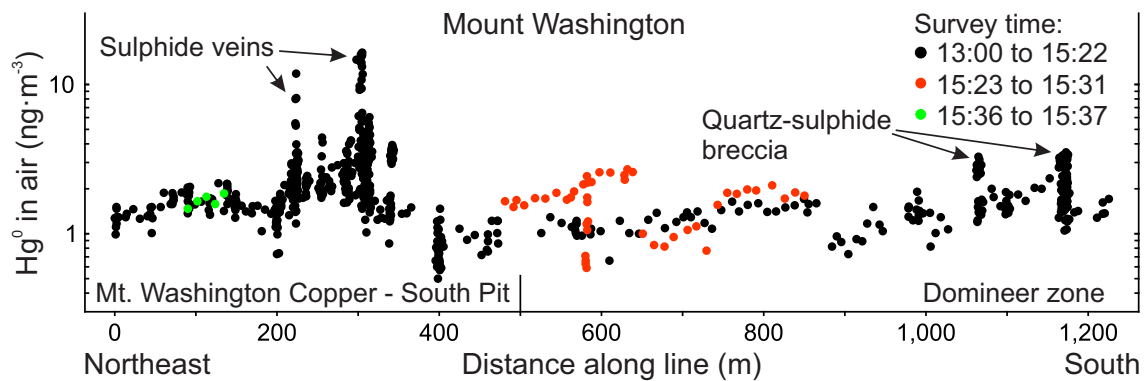


**Fig. 11.** Profile for Hg<sup>0</sup> in air ( $\text{ng}\cdot\text{m}^{-3}$ ) with respect to distance along traverse (m) for Mount Washington Copper and Domineer occurrences (see Figure 10).



**Fig. 12.** Flat-lying quartz-sulphide mineralized zone beneath dioritic sill, Mount Washington Copper.



**Fig. 13.** Realgar in quartz-sulphide mineralized zone at Mount Washington Copper.

strongest  $\text{Hg}^0$  haloes (top 5 percentile:  $1.7\text{--}2.0 \text{ ng}\cdot\text{m}^{-3}$ ) are at what appears to be intersection of the mineralized northwest-striking River fault and west-northwest Central fault, and above the intrusive contact offset by a north-south fault immediately south of the B.C. Electric Forebay reservoir (Fig. 14). Several weaker Hg vapor haloes (95<sup>th</sup> percentile:  $1.6\text{--}1.7 \text{ ng}\cdot\text{m}^{-3}$ ) also mark the Cave and Central zones and faults. Meteorological conditions were generally stable, and a spike in barometric pressure in the middle of the survey had little impact on the background  $\text{Hg}^0$  in air (Appendix 1 in Rukhlov et al., 2020).

##### **5.5. Goldstream Park area; vein gold occurrence (Bentley); Cu-Ag-Au sulphide occurrence at Skirt Mountain (Ralph)**

We conducted two surveys north of the town of Goldstream (Figs. 1, 16). One was along a trail through Goldstream Park that extends to the quartz vein Bentley Au occurrence (MINFILE 092B 067), the other along the flank of Skirt Mountain that

includes the sulphide Cu-Ag-Au Ralph occurrence (MINFILE 092B 014). Since the discovery of placer gold in the Goldstream River in 1858, the area has attracted much prospecting, with intermittent underground exploration and mining taking place until the late 1930s (Neumann, 1991; Yorath, 2005).

The Bentley Au occurrence is hosted by pervasively sheared ribbon chert, argillite, slate, phyllite, schist, and metavolcanic rocks of the Leech River complex (Jurassic to Cretaceous). An adit was driven along a quartz vein in schistose rocks and a shaft sunk upslope, about 40 m to the west (Fig. 16). The Ralph Cu-Ag-Au occurrence is hosted by interbedded silicified dacite tuff and cherty argillite of the Leech River complex that are cut by steeply dipping shear zones in the footwall of an east-dipping thrust fault that juxtaposes gneisses of the Wark-Colquitz complex (Wrangell terrane, Paleozoic to Jurassic) above the Leech River rocks (Fig. 16). The mineralization comprises en echelon lenses (0.15–1.2 m wide) of massive chalcopryrite, pyrrotite, pyrite, and chalcocite with quartz and calcite. For brief periods between 1897 and 1938, an underground mine produced 6655 kg Cu, 11.94 kg Ag, and 63 g Au (Neumann, 1991). Quaternary sediments of the Colwood delta cover bedrock in the southwestern corner of the area (Fig. 16).

Mercury vapour concentrations in air 10–50 cm above ground along the Goldstream Park traverse range from  $0.59$  to  $54 \text{ ng}\cdot\text{m}^{-3}$ , with a median (background) value of  $1.41 \text{ ng}\cdot\text{m}^{-3}$  ( $n=494$ ; Table 1). The maximum Hg vapour concentration ( $54 \text{ ng}\cdot\text{m}^{-3}$ ) is above a small pit on overgrown tailings from a nearby shaft (Figs. 16, 17a). However, air directly above the shaft shows background Hg, and only up to 3x background Hg in air at the entrance to the adit 40 m to the east (down slope). Such a strong Hg emission from the tailings suggests that Hg amalgamation might have been used to recover gold from crushed ore at the Bentley mine. Mercury amalgamation was extensively used by the mining industry between the mid-1800s and early 1900s (e.g., Higuera et al., 2012; Dalziel and Tordon, 2014). A few weak Hg anomalies ( $1.7\text{--}3.6 \text{ ng}\cdot\text{m}^{-3}$ ) also occur on a ridge immediately south of Bentley occurrence.

Concentrations of  $\text{Hg}^0$  in air 1–10 cm above ground on the western flank of Mount Skirt range from  $0.51$  to  $19 \text{ ng}\cdot\text{m}^{-3}$  with the median (background) value of  $1.44 \text{ ng}\cdot\text{m}^{-3}$  ( $n=1325$ ; Table 1). The maximum value marks an adit at the Ralph occurrence (Fig. 17b). Anomalous  $\text{Hg}^0$  haloes (up to  $5.4 \text{ ng}\cdot\text{m}^{-3}$ ) extend from the nearby oxidized tailings for more than 100 m to the southeast. Another conspicuous Hg vapour anomaly (up to  $3.9 \text{ ng}\cdot\text{m}^{-3}$ ) is 280 m to the northeast, above gneisses of the Wark-Colquitz complex in the hanging wall of the terrane-bounding thrust fault. Elevated Hg vapour haloes ( $1.9\text{--}2.4 \text{ ng}\cdot\text{m}^{-3}$ ) also highlight the thrust fault (Figs. 16, 17b). Changing weather conditions during both surveys have little effect on the anomalous Hg vapour haloes in near-surface atmosphere (Appendix 1 in Rukhlov et al., 2020).

##### **5.6. Sooke Hills and Colwood; Leech River fault and related splays**

The Sooke Hills survey, south of the town of Goldstream

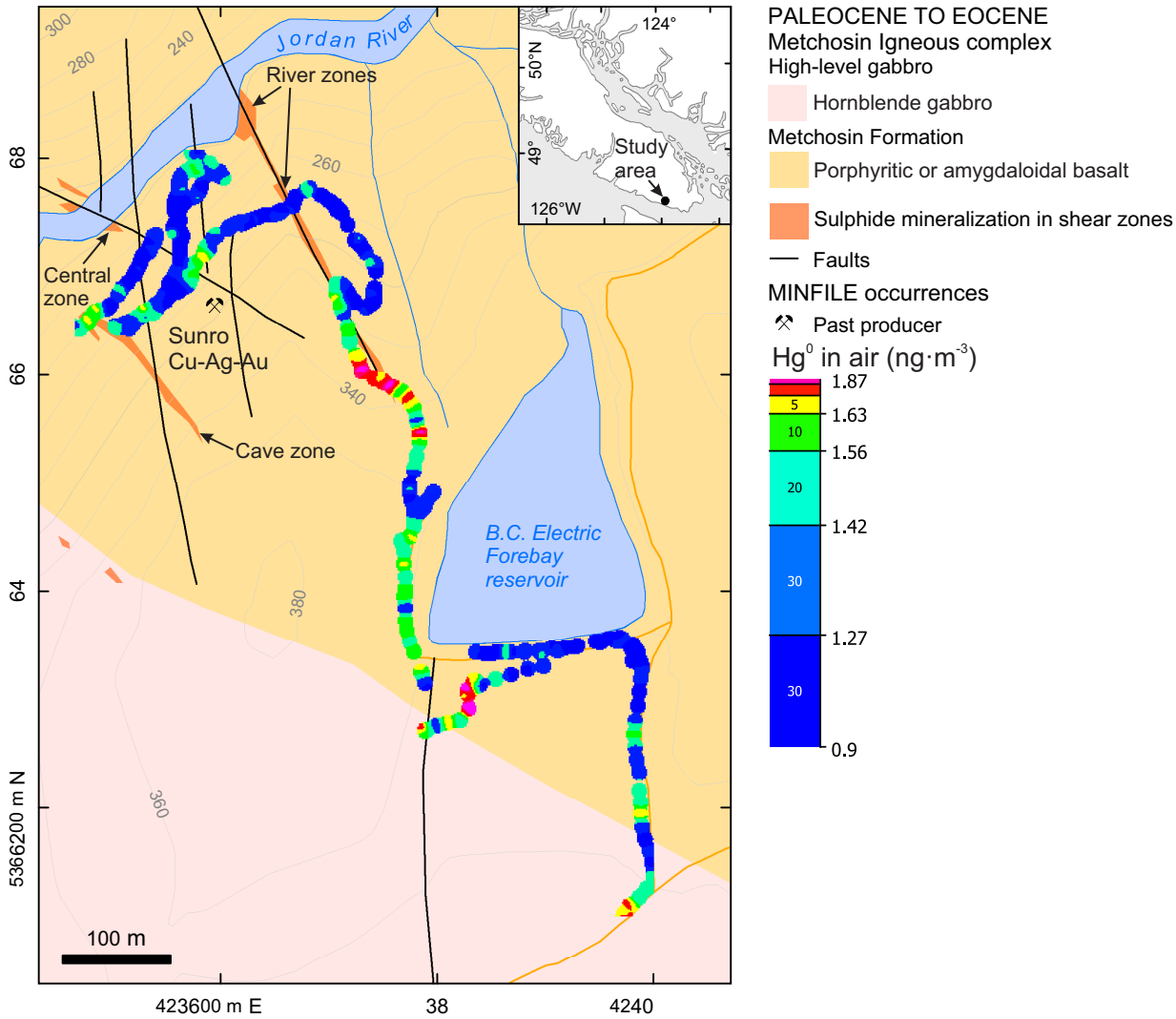


**Fig. 14.** Percentile-gridded, real-time Hg vapour concentrations ( $\text{ng}\cdot\text{m}^{-3}$ ) in air 1-10 cm above ground at the Sunro occurrence. Gridding interpolation based on modified inverse distance weighing method. Geology after Cui et al. (2017, 2018) based on Clapp (1912), Brewer (1918), Erich and Blanshard (1921), Guelpa and Meusy (1971), Meusy (1971), Muller (1977), and Massey et al. (1994).



**Fig. 15.** Sealed adit through the main ore zone (River) at the Sunro occurrence.

(Fig. 1), used the Sooke Hills Wilderness trail to traverse across the Leech River thrust fault, which juxtaposes cherty argillite, slate, phyllite, and schist interbedded with minor metavolcanic rocks of the Pacific Rim terrane (Leech River complex; Jurassic to Cretaceous) to the north against massive and pillowed basalt, basaltic hyaloclastite breccia, tuff, and rare limestone of the Metchosin Formation (Crescent terrane, Metchosin Igneous complex; Paleocene to Eocene) to the south (Fig. 18). A splay approximately 0.6 km to the southwest cuts volcanic rocks of the Metchosin Formation. Bedrock is locally exposed along the trail close to the thrusts. Metchosin Formation rocks display open folds, with fold axis trending parallel to the strike of the thrust faults. In the hanging wall, pervasively sheared Leech River complex rocks display a subvertical foliation concordant with the thrust (Clapp, 1912, 1913; Muller, 1977, 1980, 1983; Massey et al., 1994; Yorath, 2005).

Mercury vapour concentrations in air 1-10 cm above ground

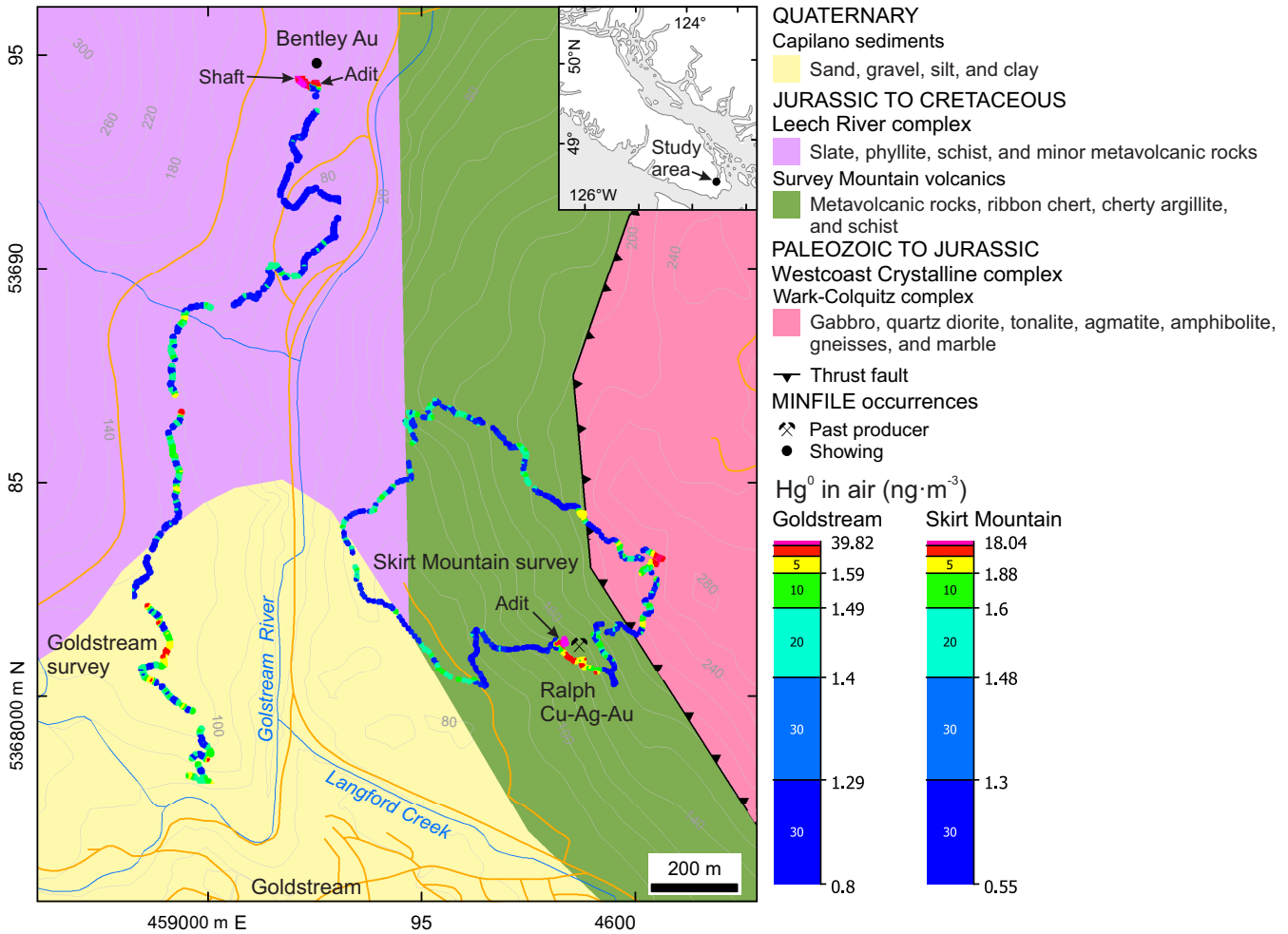


**Fig. 16.** Percentile-gridded, real-time Hg vapour concentrations (ng·m<sup>-3</sup>) in near-surface air along a trail to the Bentley Au vein occurrence in Goldstream park (sampling height 10-50 cm above ground) and on the western flank of Skirt Mountain, across the Ralph sulphide Cu-Ag-Au occurrence (sampling height 1-10 cm). Gridding interpolation is based on modified inverse distance weighing method. Geology after Cui et al. (2017, 2018) based on Clapp (1912, 1913), Muller (1977, 1980, 1983), and Massey et al. (1994).

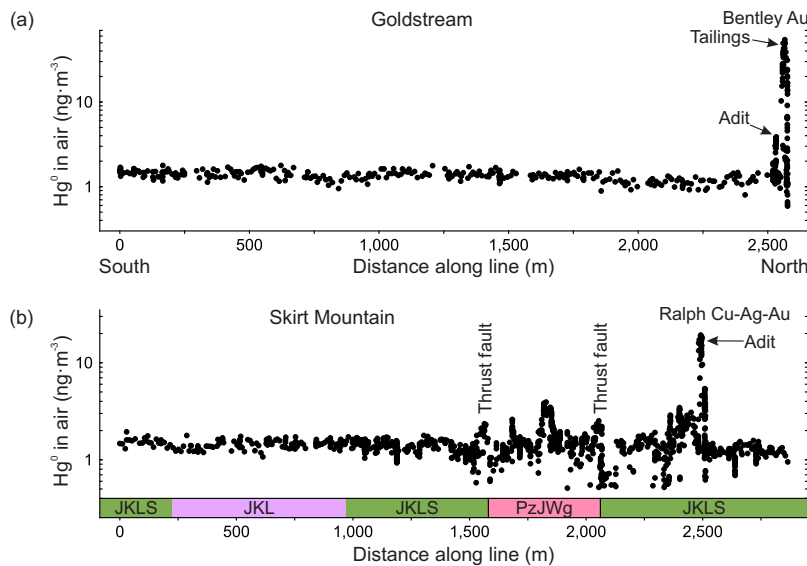


**Fig. 17.** Profiles for Hg<sup>0</sup> in air (ng·m<sup>-3</sup>) with respect to distance along traverse (m) for Goldstream Park area (see Figure 16). **a)** Goldstream Park, Bentley occurrence. **b)** Skirt Mountain; Ralph occurrence, and Wrangell terrane-Pacific Rim terrane boundary; the traverse was in a loop hence the units are repeated.

show a normal distribution (Appendix 1 in Rukhlov et al., 2020) and range from 0.74 to 1.9 ng·m<sup>-3</sup>, averaging 1.30 ng·m<sup>-3</sup> (n=769; Table 1). The top 5 percentile values (1.6-1.9 ng·m<sup>-3</sup>) highlight both the Leech River fault, which has a history of Quaternary movement (Morell et al., 2017), and its splay (Figs. 18, 19). Two anomalous Hg<sup>0</sup> haloes also occur between the Leech River fault and its splay, possibly marking additional buried splays. A positive spike in atmospheric pressure accompanied by an increased wind speed slightly suppressed the background Hg vapour concentration during the survey but did not mask the elevated Hg<sup>0</sup> emission above the Leech River fault (Appendix 1 of Rukhlov et al., 2020).

We also took measurements at Colwood, about 6 km southeast of the Sooke Hills, along roads and trails through Royal Roads University campus. Here, the along-strike continuation of the Leech River fault dips steeply northeast, juxtaposing intrusive and metamorphic rocks of the Westcoast Crystalline complex (Paleozoic to Jurassic) above basalts of the Metchosin Formation to the southwest. A subparallel splay of the Leech River fault cuts basalts of the Metchosin Formation about 0.5 km to the southwest. Sand and gravel (up to 60 m thick) of the Colwood delta (Capilano sediments; Quaternary) cover bedrock. Mercury concentrations range from 0.51 to 3.8 ng·m<sup>-3</sup>, averaging 1.59 ng·m<sup>-3</sup> (n=211; Table 1; Appendix 1 of Rukhlov et al., 2020). Values greater than 2.7 ng·m<sup>-3</sup> (90<sup>th</sup> percentile) were measured above Westcoast Crystalline complex rocks. Slightly elevated concentrations (1.7-2.3 ng·m<sup>-3</sup>) coincide with the extrapolated splay fault to the southwest.

### **5.7. Durance Lake; northwest-striking fault between Wark-Colquitz complex and Bonanza Group (Wrangell terrane)**

This survey traversed across a northwest-striking, high-angle fault that places Wark-Colquitz gneisses (Paleozoic to Jurassic) against Late Triassic to Middle Jurassic volcanic and sedimentary rocks of the Bonanza Group (Fig. 20). Wark-Colquitz gneisses are exposed south of the Durance Lake and volcanic rocks of the Bonanza Group outcrop along the northern shore of the lake (Fig. 20). Concentrations of Hg<sup>0</sup> in air 10-50 cm above ground range from 0.75 to 2.6 ng·m<sup>-3</sup>, averaging 1.18 ng·m<sup>-3</sup> (n=298; Table 1). The anomalous Hg values greater than 1.75 ng·m<sup>-3</sup> highlight the fault (Fig. 21), regardless of the minor variations in atmospheric conditions (Appendix 1 in Rukhlov et al., 2020).

### **5.8. Elk Lake; northwest-striking fault between Wark-Colquitz complex and Karmutsen Formation (Wrangell terrane)**

About 5 km southeast of the Durance Lake survey, we traversed across the continuation of the same high-angle northwest-striking fault, but where it juxtaposes Wark-Colquitz gneisses with mafic volcanic rocks of the Karmutsen Formation (Vancouver Group; Figs. 1, 22). The survey was conducted along the western shore of Elk Lake to evaluate Hg vapour emission above the bedrock units and the fault buried under a fringe (<2 m thick?) of Quaternary sediments. Mercury vapour

concentrations in air 10-50 cm above ground show a normal distribution (Appendix 1 in Rukhlov et al., 2020), ranging from 0.55 to 1.7 ng·m<sup>-3</sup> with an average value of 1.22 ng·m<sup>-3</sup> (n=152; Table 1). Some of the top 5 percentile values (>1.5 ng·m<sup>-3</sup>) occur above the buried fault, but three other spikes occur within 150 m on both sides of the fault, perhaps marking splays (Figs. 22, 23).

### **5.9. Tod Inlet; northeast-striking strike-slip fault**

This survey extends from the north shore of Tod Inlet on the western side of central Saanich Peninsula east to Quarry Lake, the site of an historical limestone quarry (Figs. 1, 24). We traversed across a northeast striking strike-slip fault that cuts mafic volcanic rocks of the Karmutsen Formation (Vancouver Group; Middle to Late Triassic), limestones of the Quatsino Formation (Vancouver Group; Middle to Late Triassic), and unconformably overlying mafic to felsic volcanic and sedimentary rocks of the Bonanza Group (Late Triassic to Middle Jurassic). Overburden thickness is less than 5 m, with bedrock locally exposed along the profile.

Mercury vapour concentrations in air 10-50 cm above ground range from 0.58 to 2.1 ng·m<sup>-3</sup>, averaging 1.17 ng·m<sup>-3</sup> (n=382; Table 1). The strongest Hg vapour halo (up to 2.1 ng·m<sup>-3</sup>) marks the sediment-covered strike-slip fault, and several weaker haloes (>95<sup>th</sup> percentile: 1.4-1.6 ng·m<sup>-3</sup>) occur above the volcanic and sedimentary rocks of the Bonanza Group and along the contact with limestone of the Quatsino Formation (Figs. 24, 25). Meteorological conditions were relatively consistent during the survey (Appendix 1 of Rukhlov et al., 2020).

### **5.10. Deep Cove; northwest-striking thrust faults**

Granitic rocks of the Saanich batholith (Island plutonic suite; Early to Middle Jurassic) and unconformably overlying siliciclastic rocks of the Nanaimo Group (Late Cretaceous) are offset by several northwest-striking thrust faults at Deep Cove on the western side of northern Saanich Peninsula (Figs. 1, 26). Air was sampled 1-10 cm above ground across the sediment-covered unconformity and one of the thrust faults and its splay, which place the granitoids exposed at Warrior Point against gently north-dipping Nanaimo Group sandstones exposed along the shore to the northwest. Concentrations of Hg<sup>0</sup> in air range from 0.78 to 3.1 ng·m<sup>-3</sup>, averaging 1.27 ng·m<sup>-3</sup> (n=519; Table 1). The top 5 percentile values (>1.53 ng·m<sup>-3</sup>) occur above granitic rocks immediately north of the thrust fault, with some 90<sup>th</sup> percentile values marking sandstones near the unconformity (Figs. 26, 27). Minor fluctuations in atmospheric conditions did not have a notable effect on Hg<sup>0</sup> in air (Appendix 1 in Rukhlov et al., 2020).

### **5.11. Bear Hill; intrusive contact between Island plutonic suite and Karmutsen Formation mafic volcanic rocks**

This survey traversed along a road and a trail to the summit of Bear Hill in central Saanich Peninsula, extending across quartz diorite and granodiorite at the southwestern margin of

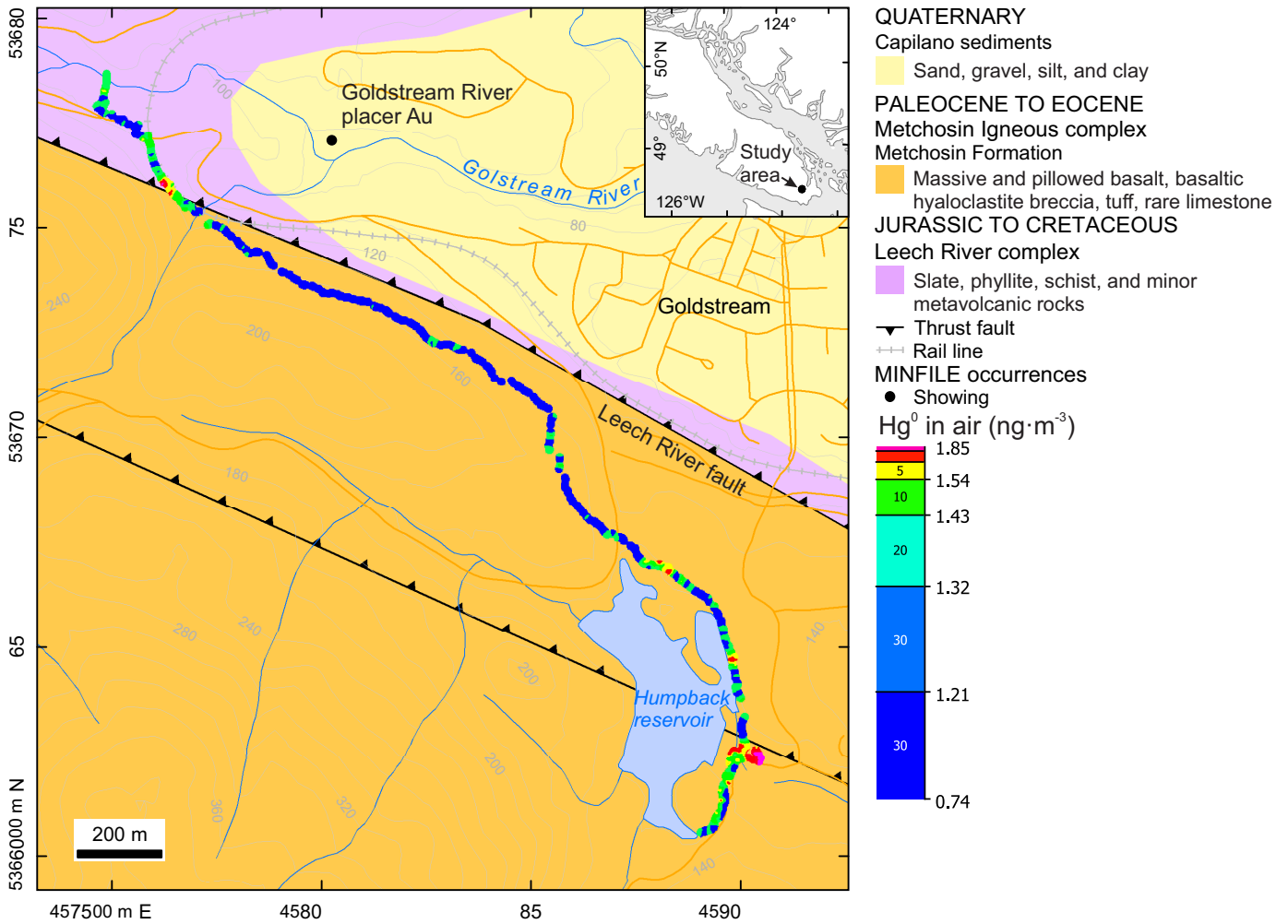


**Fig. 18.** Percentile-gridded, real-time Hg vapour concentrations (ng·m<sup>-3</sup>) in air 1-10 cm above ground at Sooke Hills. Gridding interpolation based on modified inverse distance weighing method. Geology after Cui et al. (2017, 2018) based on Clapp (1912, 1913), Muller (1977, 1980, 1983), and Massey et al. (1994).

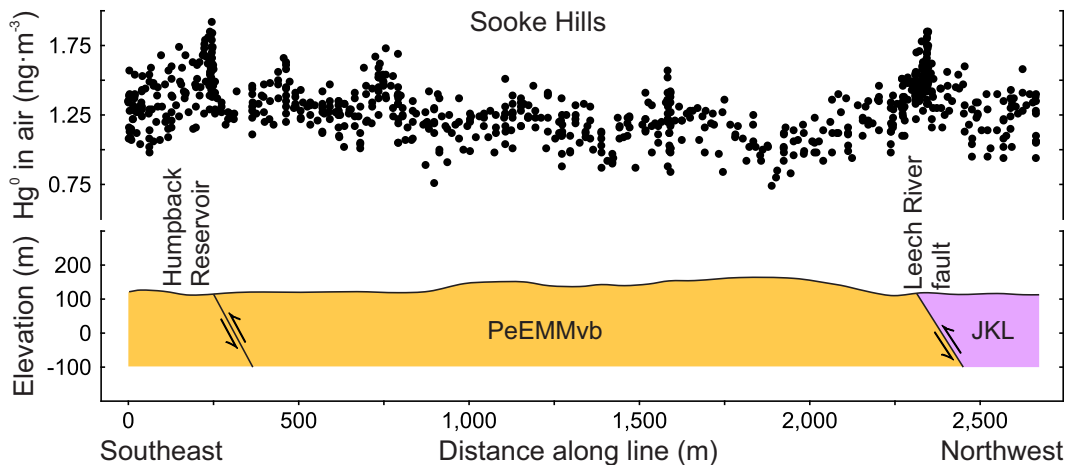


**Fig. 19.** Profile for Hg<sup>0</sup> in air (ng·m<sup>-3</sup>) with respect to distance along traverse (m) and geological cross-section at Sooke Hills (see Figure 18).

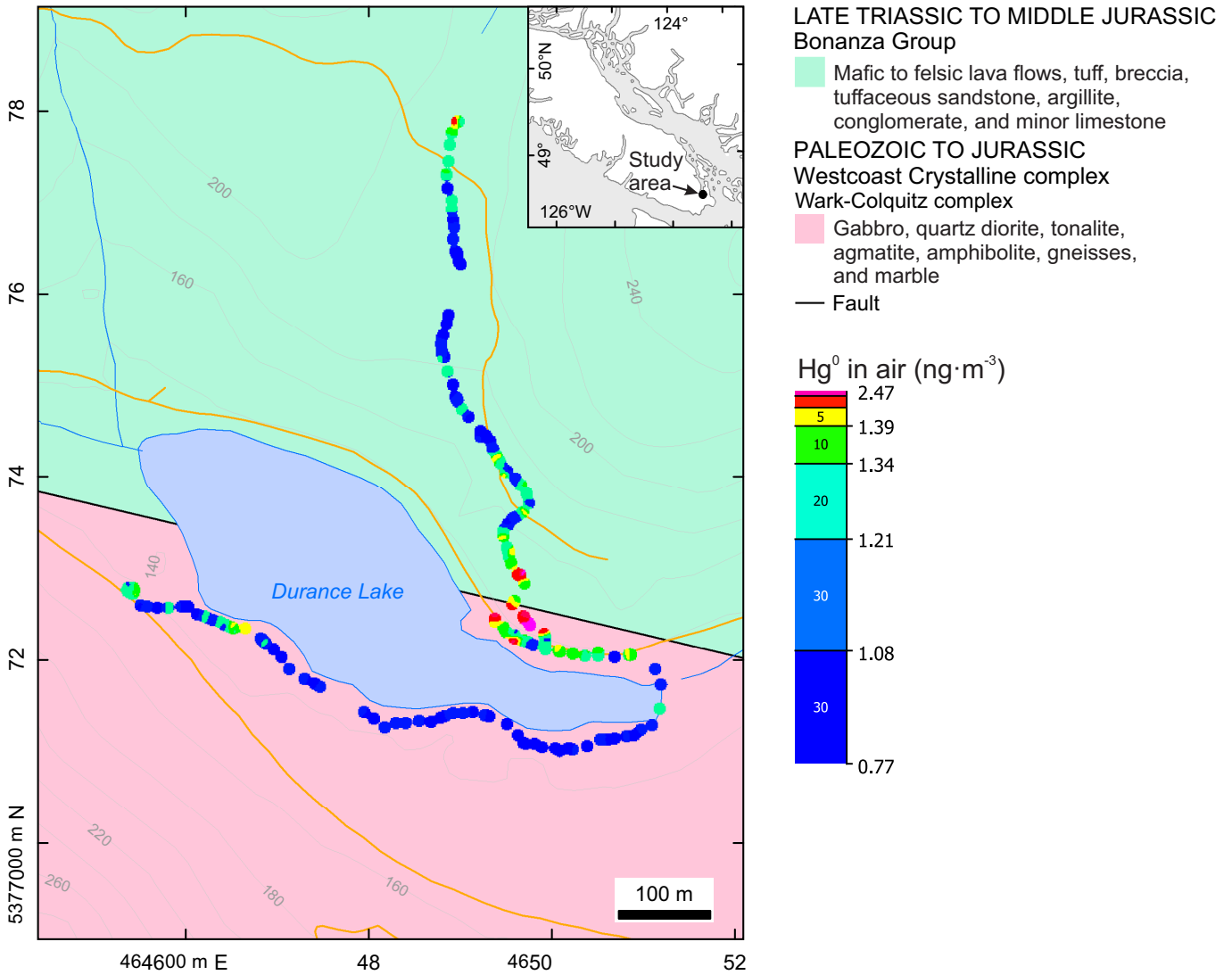


**Fig. 20.** Percentile-gridded, real-time Hg<sup>0</sup> vapour concentrations (ng·m<sup>-3</sup>) in air 10-50 cm above ground at Durance Lake, west-central Saanich Peninsula. Gridding interpolation based on modified inverse distance weighing method. Geology modified after Cui et al. (2017, 2018) based on Clapp (1912, 1913), Muller (1977, 1980, 1983), and Massey et al. (1994).

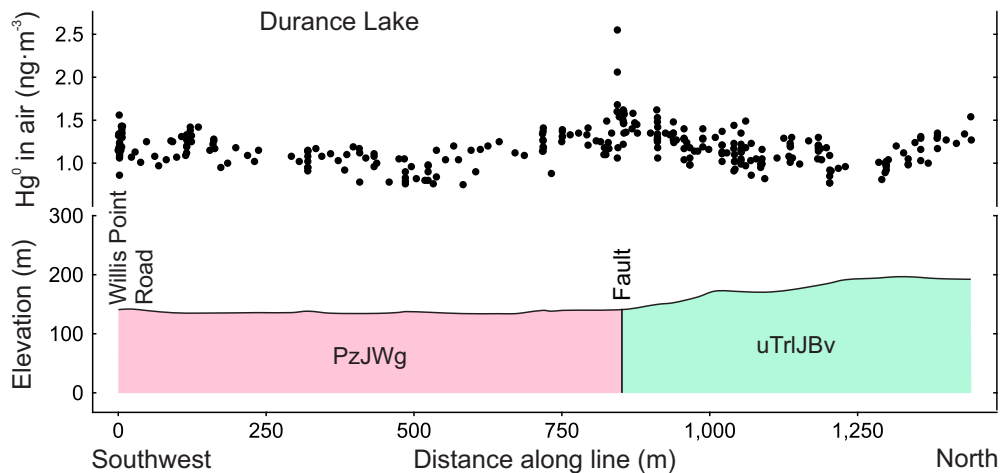


**Fig. 21.** Profile for Hg<sup>0</sup> in air (ng·m<sup>-3</sup>) with respect to distance along traverse (m) and geological cross-section at Durance Lake (see Figure 20).

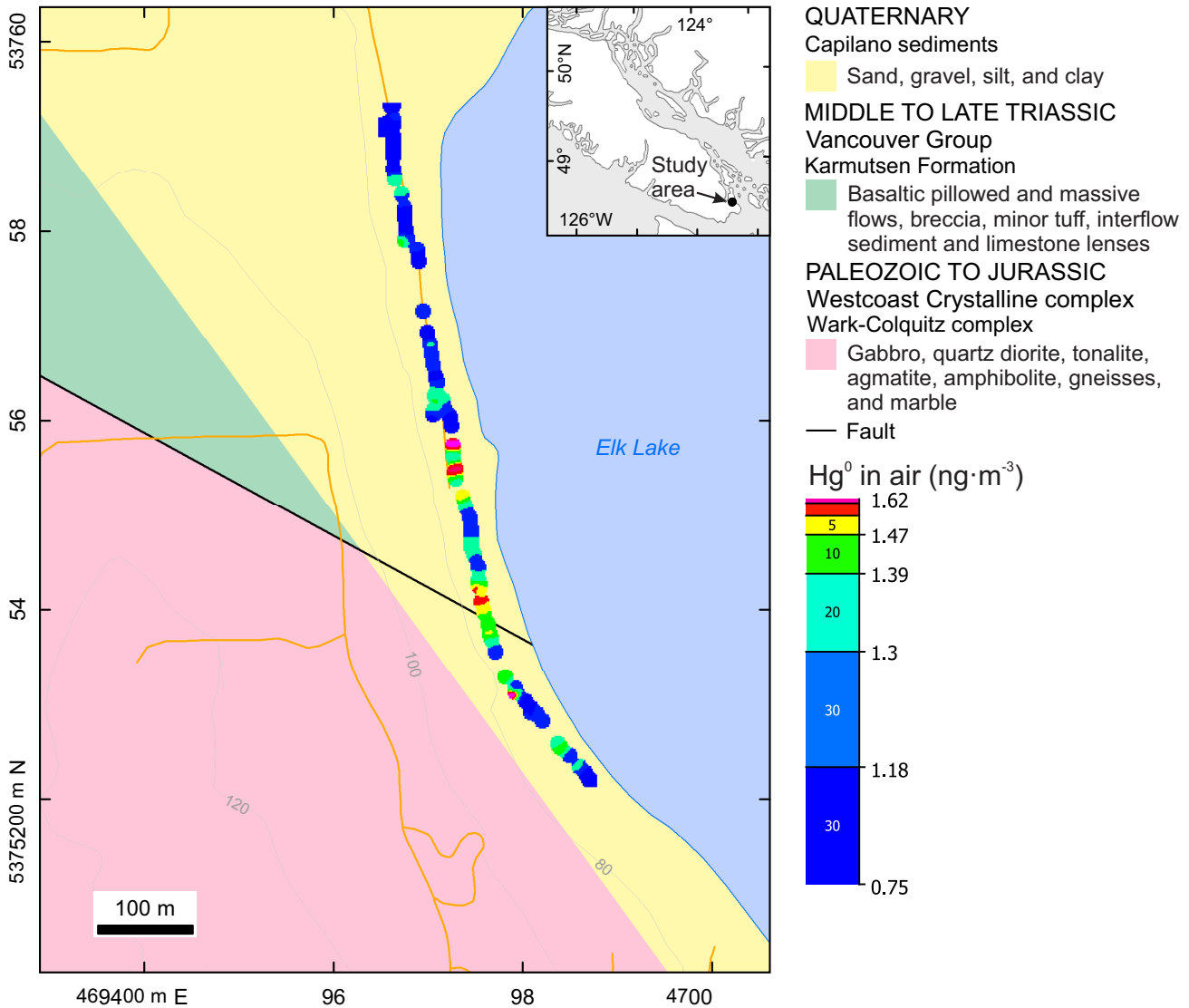


**Fig. 22.** Percentile-gridded, real-time Hg vapour concentrations (ng·m<sup>-3</sup>) in air 10-50 cm above ground at Elk Lake, central Saanich Peninsula. Gridding interpolation based on modified inverse distance weighing method. Geology after Cui et al. (2017, 2018) based on Clapp (1912, 1913), Muller (1977, 1980, 1983), and Massey et al. (1994).

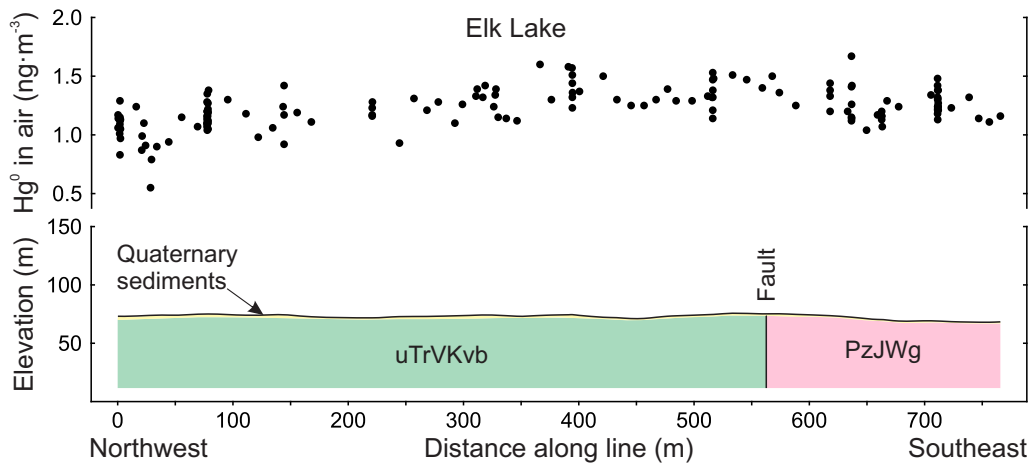


**Fig. 23.** Profile for Hg<sup>0</sup> in air (ng·m<sup>-3</sup>) with respect to distance along traverse (m) and geological cross-section at Elk Lake (see Figure 22).

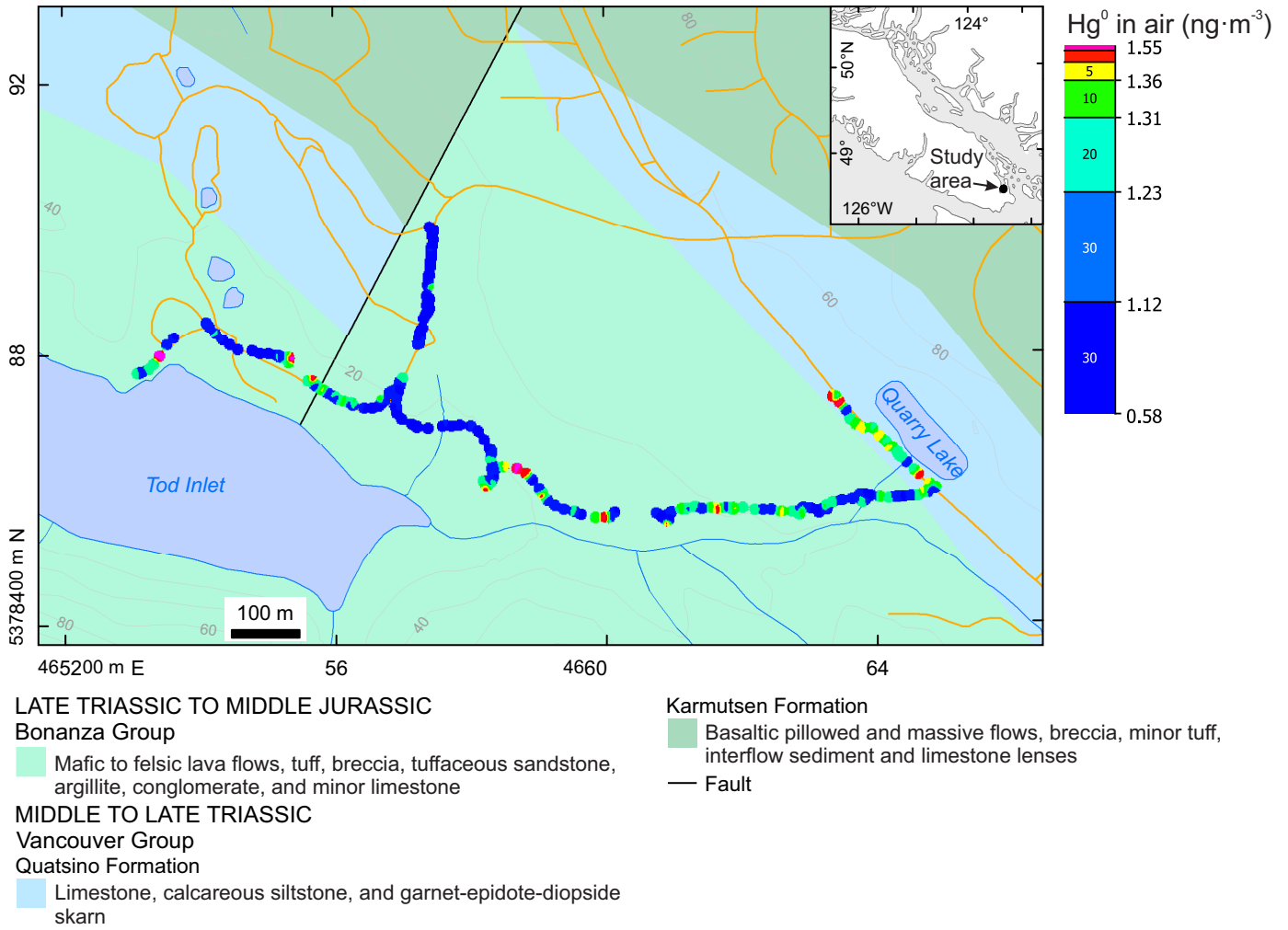


**Fig. 24.** Percentile-gridded, real-time Hg vapour concentrations ( $\text{ng}\cdot\text{m}^{-3}$ ) in air 10-50 cm above ground at Tod Inlet, west-central Saanich Peninsula. Gridding interpolation based on modified inverse distance weighing method. Geology after Cui et al. (2017, 2018) based on Clapp (1912, 1913), Muller (1977, 1980, 1983), and Massey et al. (1994).

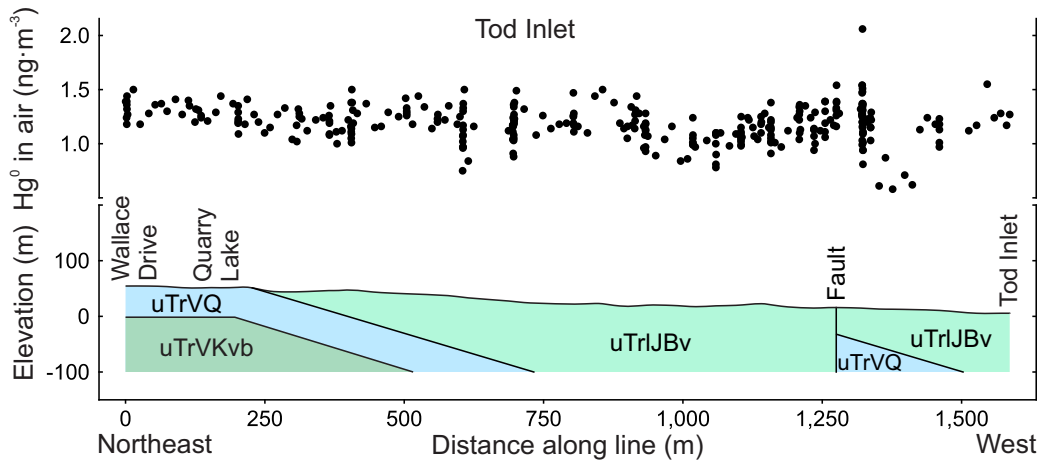


**Fig. 25.** Profile for  $\text{Hg}^0$  in air ( $\text{ng}\cdot\text{m}^{-3}$ ) with respect to distance along traverse (m) and geological cross-section at Tod Inlet (see Figure 24).

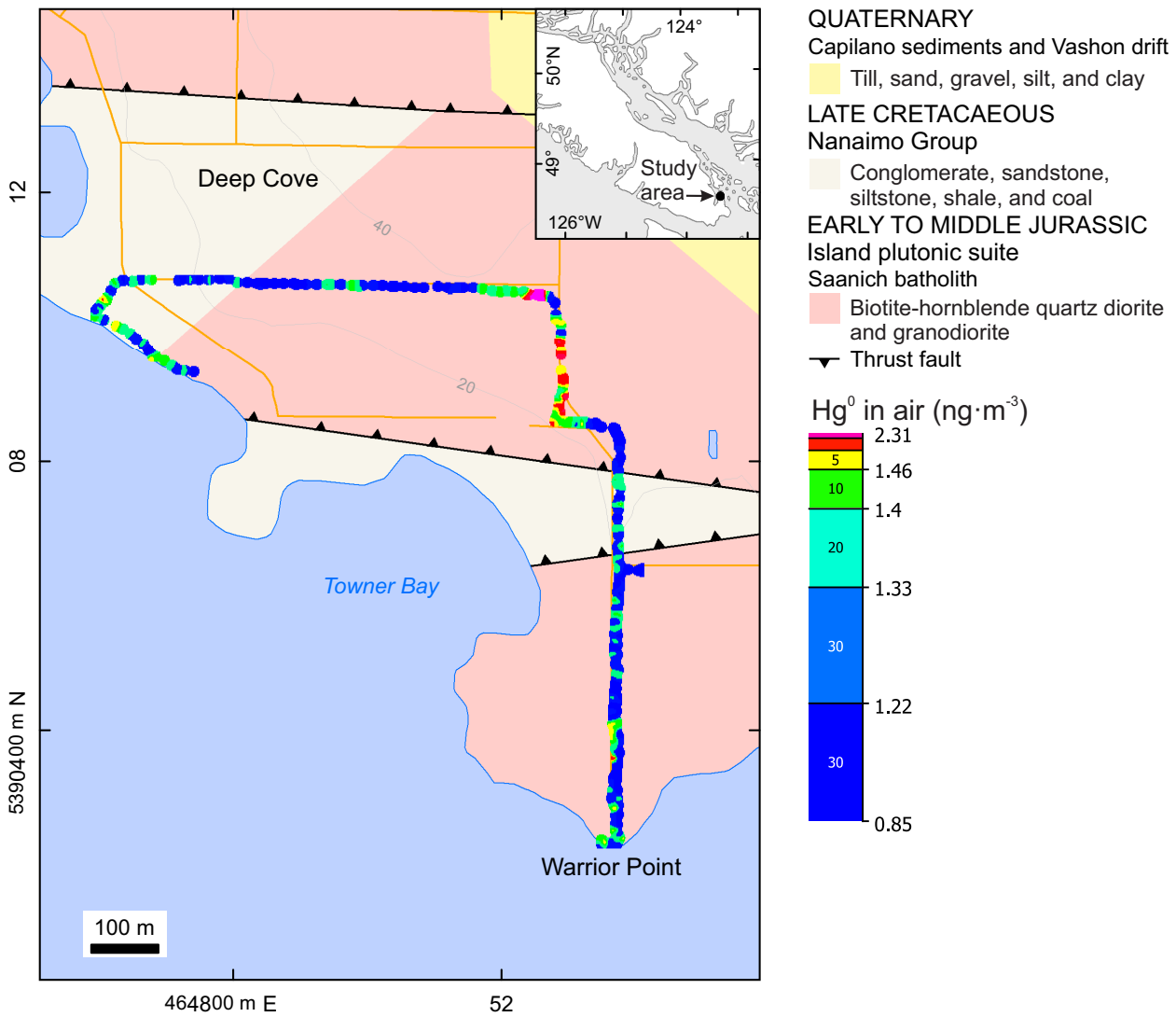


Fig. 26. Percentile-gridded, real-time Hg vapour concentrations (ng·m<sup>-3</sup>) in air 1-10 cm above ground at Deep Cove, northern Saanich Peninsula. Gridding interpolation based on modified inverse distance weighing method. Geology after Cui et al. (2017, 2018) based on Clapp (1912, 1913), Muller (1977, 1980, 1983), and Massey et al. (1994).

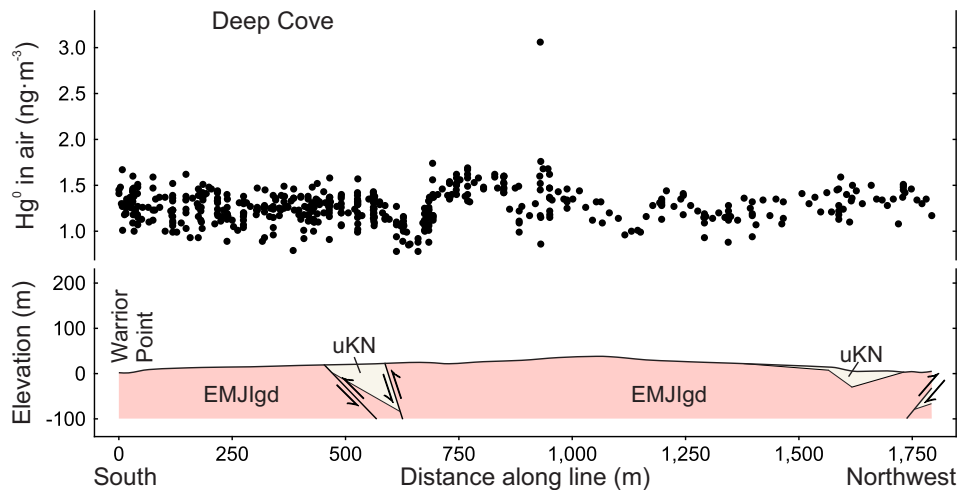


Fig. 27. Profile for Hg<sup>0</sup> in air (ng·m<sup>-3</sup>) with respect to distance along traverse (m) and geological cross-section at Deep Cove (see Figure 26).

the Saanich batholith (Island plutonic suite; Early to Middle Jurassic) that cut mafic volcanic rocks of the Karmutsen Formation (Figs. 1, 28). Although bedrock is well exposed, no volcanic rocks were observed along the trail, suggesting that the intrusive contact is farther west than portrayed on currently available maps (Figs. 28, 29). Mercury vapour concentrations show normal distribution, ranging from 0.72 to 1.8 ng·m<sup>-3</sup>, averaging 1.24 ng·m<sup>-3</sup> (n=490; Table 1; Appendix 1 of Rukhlov et al., 2020). The top 5 percentile spikes are spread for about 200 m above the granitoids exposed along the trail. Because volcanic rocks are not exposed along the survey profile, the elevated Hg emanations may mark the Saanich batholith margin. Data collected along the same traverse twice within 1.5 hrs were similar (Fig. 29), regardless of subtle changes in meteorological conditions. Changing weather might have influenced the Hg vapour concentrations. As wind speed and relative pressure decreased and air temperature increased, concentrations of Hg<sup>0</sup> in air also increased (Appendix 1 of Rukhlov et al., 2020). Therefore, the scattered elevated Hg haloes at Bear Lake might simply reflect changing meteorological conditions.

### 5.12. Central Victoria: Harling Point and downtown

At Harling Point, in the municipality of Oak Bay east of downtown Victoria, possible tectonic mélangé deposits including radiolarian chert, greywacke, mafic volcanic rocks, argillite, pebbly mudstones, and limestone clast-bearing breccias of the Pandora Peak unit (Pacific Rim terrane) are in thrust contact with Wark-Colquitz gneisses (Wrangell terrane; Rusmore and Cowan, 1985). We sampled air 1-10 cm above ground across strongly deformed rocks that are exposed in a northwest-striking shear zone. Mercury vapour concentrations in near-surface atmosphere range from 1.1 to 2.5 ng·m<sup>-3</sup>, averaging 1.59 ng·m<sup>-3</sup> (n=239; Table 1; Appendix 1 of Rukhlov et al., 2020). The terrain-bounding fault is marked by the anomalous Hg vapor haloes in excess of 1.98 ng·m<sup>-3</sup> (top 5 percentile).

To test Hg vapour levels in the urban air, we took measurements in downtown Victoria, which is underlain by intrusive and metamorphic rocks of the Westcoast Crystalline complex (Wark-Colquitz gneiss; Paleozoic to Jurassic) that are offset by northwest-striking faults and a series of northeast-striking cross-faults. Hornblende-plagioclase and quartz-feldspar gneisses and amphibolites display northwest-striking, moderately to steeply dipping foliation (Clapp, 1912, 1913; Muller, 1977, 1980, 1983; Massey et al., 1994; Yorath, 2005). Mercury vapour concentrations range from 1.2 to 2.5 ng·m<sup>-3</sup>, averaging 1.76 ng·m<sup>-3</sup> (n=130; Table 1). The area underlain by quartz-feldspar Colquitz gneiss along Mount Stephen Avenue and Haultain Street has generally higher gaseous Hg<sup>0</sup> emission (>95<sup>th</sup> percentile: 2.3-2.5 ng·m<sup>-3</sup>) compared to that underlain by amphibolite, agmatite, metadiorite, metagabbro, and hornblende-plagioclase Wark gneiss to the southwest (<2.2 ng·m<sup>-3</sup>), except for one of the three consecutive values (1.4, 1.7, and 2.4 ng·m<sup>-3</sup>) at the same location. A positive spike in relative pressure during the survey had little effect on the

measured Hg vapour concentration in near-surface air; wind speed and direction were not monitored during the survey (Appendix 1 of Rukhlov et al., 2020).

## 6. Discussion

By surveying 15 sites on southern Vancouver Island, including those with different types of mineralization (Table 2), this study evaluates the effectiveness of real-time Hg vapour sampling of near-surface atmosphere (i.e., layer of air 1-50 cm above ground) as a simple and instant technique for mineral exploration and geologic mapping in overburden-covered areas.

### 6.1. Mercury vapour haloes above mineralization

Our results show that the strongest anomalies mark auriferous quartz (Bentley Au occurrence; 38.5x background Hg) and Cu-Ag-Au sulphide veins (Ralph occurrence; 13.4x background Hg) at the Goldstream and Skirt Mountain localities (Figs. 16, 17). The highest Hg vapour concentrations in air (up to 54 ng·m<sup>-3</sup>) above a fresh pit hole in tailings at the Bentley Au occurrence indicate that amalgamation was likely used on site to recover gold. Exposed epithermal Au-Ag-Cu sulphide veins at Mount Washington (8.9x background Hg; Figs. 10, 11) and sediment-covered polymetallic VMS mineralization at the Lara-Coronation occurrence (4.2 to 6.6x background Hg; Figs. 8, 9) also have strong Hg vapour haloes. Ore samples from these occurrences contain up to 90 ppm Hg, which is four orders of magnitude higher than the average crustal abundance (45 ppb Hg; Rudnick and Gao, 2005), possibly concentrated in sphalerite and tennantite-tetrahedrite (Kelso and Wetherup, 2008; Bodnar, 2017). The Hg vapour anomalies in near-surface air above the polymetallic VMS zone buried under 30 m of glacial sediments are about 3 times weaker compared to the Hg vapour haloes above a flooded trench across the VMS mineralization at the Lara-Coronation occurrence (Table 2; Fig. 9). Other styles of mineralization such as pyrite-rich rocks and shear-hosted chalcopyrite-pyrite stringers have much weaker Hg vapour haloes compared to those of the polymetallic massive sulphides. Notably, elevated Hg concentrations in A- and B-horizon soils (up to 460 ppb) and vegetation (up to 133 ppb) are displaced from the sediment-covered VMS zones and cluster above the barren pyritic horizons in volcanic hosts up slope (Fig. 7; Bodnar, 2017; Heberlein et al., 2017). In contrast, the real-time Hg vapour haloes in near-surface air occur directly above the VMS zones and thus are better indicators of the buried mineralization. Shear-hosted, Hg-poor Cu-Ag-Au sulphides in mafic rocks (Sunro past-producer) at Jordan River are also marked by weak Hg vapour haloes in near-surface air (Fig. 14).

### 6.2. Mercury vapour haloes above faults

The terrane-bounding Leech River fault and its splay (Figs. 18, 19), thrust faults at the Lara-Coronation occurrence (Figs. 8, 9), a thrust fault at Harling Point, and other faults are marked by weak Hg vapour anomalies (1.3 to 2.2x) relative to

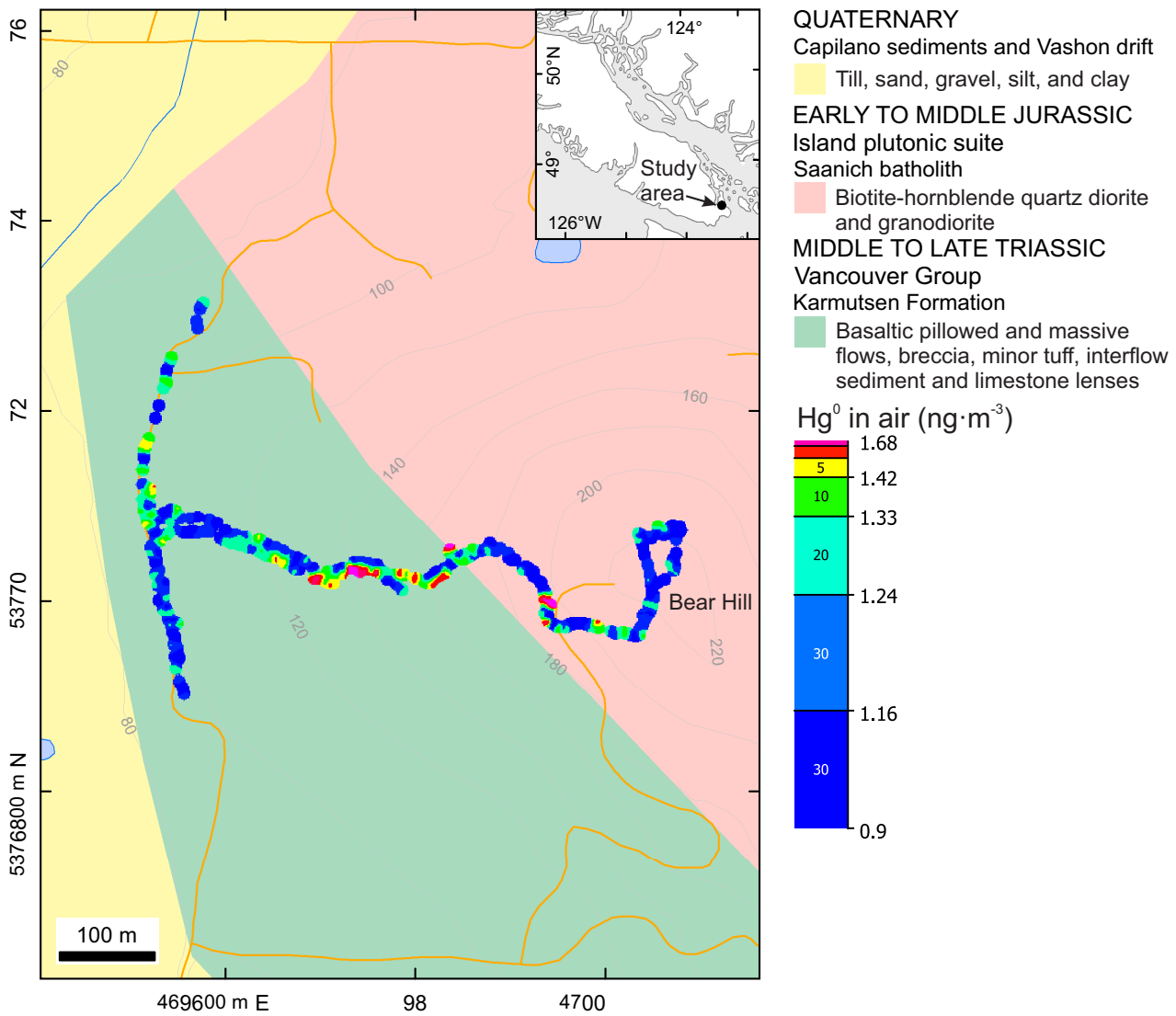


**Fig. 28.** Percentile-gridded, real-time Hg vapour concentrations (ng·m<sup>-3</sup>) in air 10-50 cm above ground at Bear Hill, central Saanich Peninsula. Gridding interpolation based on modified inverse distance weighing method. Geology after Cui et al. (2017, 2018) based on Clapp (1912, 1913), Muller (1977, 1980, 1983), and Massey et al. (1994).

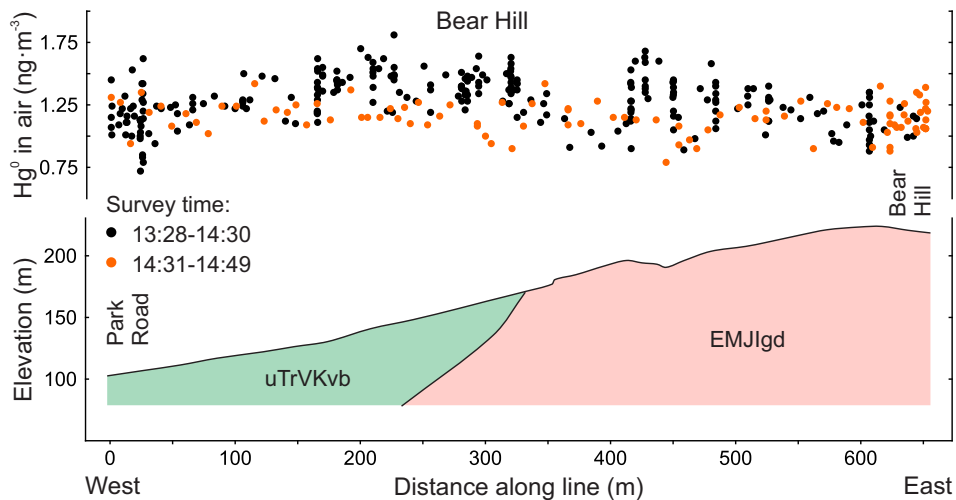


**Fig. 29.** Profile for Hg<sup>0</sup> in air (ng·m<sup>-3</sup>) with respect to distance along traverse (m) and geological cross-section at Bear Hill (see Figure 28).

**Table 2.** Summary of Hg vapour haloes in near-surface atmosphere above mineralization and other geological features.

Location	Map sheet	Survey date	Elevation above sea level (m)	Total traverse (m)	Air sampling height above ground (cm)	Geological feature	Overburden thickness (m)	Hg <sup>0</sup> in air halo contrast
Coronation Mountain*	92B/13	06.08.2020	595 to 741	1625	10-50	Volcanogenic massive sulphide Zn-Cu-Pb-Ag-Au (Lara-Coronation)	<1	6.6
	92B/13	12.08.2020	595 to 741	3182	1-10	Fulford thrust fault	30	1.9
Mount Washington	92B/13	12.08.2020	595 to 741	3182	1-10	Volcanogenic massive sulphide Zn-Cu-Pb-Ag-Au (Lara-Coronation)	<1	4.2
	92F/14	25.08.2020	1309 to 1406	1434	10-50	Fulford thrust fault	30	1.3
Jordan River	92C/08	17.08.2020	204 to 363	1948	1-10	Porphyry Cu-Mo-Au to epithermal Au-Ag-Cu (Mount Washington Copper)	20	1.3
Goldstream	92C/08	17.08.2020	204 to 363	1948	1-10	Basalt-hosted sulphide Cu-Ag-Au in shear zones (Sunro)	<2	1.5
	92B/05	22.08.2020	37 to 121	2577	10-50	Auriferous quartz vein (Bentley Au); possibly amalgamation of ore on site	0	38.5
Skirt Mountain	92B/05	10.08.2020	62 to 257	2890	1-10	Shear-hosted sulphide Cu-Ag-Au (Ralph)	0	13.4
	92B/05	11.08.2020	109 to 166	2664	1-10	Terrane-bounding thrust fault	<2	1.8
Colwood	92B/05	11.08.2020	109 to 166	2664	1-10	Leech River thrust fault	<2	1.4
	92B/06	05.08.2020	19 to 81	2514	10-50	Splay of Leech River fault	<2	1.5
Durance Lake	92B/06	05.08.2020	19 to 81	2514	10-50	Leech River thrust fault	<10?	2.0
	92B/11	19.08.2020	134 to 197	1490	10-50	Splay of Leech River fault	<60	1.5
Elk Lake	92B/11	28.08.2020	68 to 77	766	10-50	Terrane-bounding fault	<2	2.2
	92B/11	27.08.2020	5 to 55	1759	10-50	Terrane-bounding fault	<10	1.4
Deep Cove	92B/11	27.08.2020	0 to 38	1793	1-10	Strike-slip fault	<5?	1.8
	92B/11	27.08.2020	0 to 38	1793	1-10	Granodiorite near thrust fault	<10	1.4
Bear Hill	92B/11	28.08.2020	89 to 224	1224	10-50	Intrusive contact of granodiorite pluton and mafic volcanic rocks	<1	1.5
	92B/06	08.08.2020	0 to 12	389	1-10	Terrane-bounding thrust fault	0	1.6
Victoria downtown	92B/06	25.07.2020	19 to 40	1732	10-50	Intrusive and metamorphic rocks of the Westcoast Crystalline complex	<2	1.4

Mercury vapour halo contrast is defined as a ratio of the maximum concentration of Hg<sup>0</sup> in near-surface air to the background (median) Hg concentration for a given survey. \*At Coronation Mountain, wet surface was still drying during the survey on August 6<sup>th</sup>, 2020, just a few hours after the end of rain in the area for several days, compared with much drier surface on August 12<sup>th</sup>, 2020 without any precipitation between the two surveys. Weather conditions were a mix of sun and clouds during both surveys.

local background (Table 2). Mercury vapour anomalies in soil gas above modern fault zones are influenced by the fault slip rate, the degree of fault fracturing, the degree of fault locking, bedrock lithology, and overburden cover (Sun et al., 2017; Xiang et al., 2020). These factors control Hg upward migration and surface enrichment. The Leech River fault has been active after the last glacial maximum ca. 17 ka (Morell et al., 2017). Mercury vapour anomalies above it and its splays indicate that these structures serve as conduits for geogenic gases, such as has been described from elsewhere by Jin et al. (1989), Stepanov (1997), Stoffers et al. (1999), Wang et al. (2006), and Xiang et al. (2020). Other faults in the Victoria area also have associated Hg anomalies, which may indicate Neotectonic activity. Elevated Hg vapour emission (1.4 to 1.5x background Hg) also occurs above the southwestern margin of the Saanich granitoid batholith at Bear Hill (Figs. 28, 29) and above felsic rocks of the Westcoast Crystalline complex in Victoria (Table 2).

### 6.3. Meteorological effects

Air and soil temperature, soil moisture, solar radiation, and atmospheric pressure influence the emission of Hg vapour from overburden, whereas wind and turbulent movement of air both dilute and transport gaseous  $\text{Hg}^0$  escaping to the atmosphere (e.g., McCarthy, 1972; Gustin et al., 1997; Zhang and Lindberg, 1999; Xie et al., 2019). Although the mercury vapour concentrations in near-surface air measured in the present study generally show little effects of air temperature, relative humidity, and atmospheric pressure (Figs. 30a-c), minor variations of background Hg concentrations accompanied by

rapid changes in these parameters were noted at some locations (Appendix 1 of Rukhlov et al., 2020). Elsewhere, the mercury content of soil gas and air shows considerable diurnal as well as seasonal variations (e.g., Krömer et al., 1981; Dalziel and Tordon, 2014).

Wind speeds did have an effect in the present study (Fig. 30d). The diffusion of gaseous Hg in near-surface atmosphere is controlled by active turbulent mixing of air. Experimental and theoretical modelling of atmospheric diffusion show that wind can dilute, deform, shift, or destroy gaseous Hg haloes in near-surface atmosphere, with  $4 \text{ m}\cdot\text{s}^{-1}$  being the critical speed at which a gas halo becomes unstable and turns into a plume (Mashyanov et al., 1985 and references therein). In the present study, at a wind speed of about  $4.5 \text{ m}\cdot\text{s}^{-1}$ , the range of measured concentrations approached the background (median) concentration of  $1.40 \text{ ng}\cdot\text{m}^{-3}$  (Fig. 30d), consistent with the findings of other studies (Williston, 1968; McCarthy, 1972; Mashyanov, 1980, 1985; Gustin et al., 1999; Yasutake et al., 2011). In contrast, molecular diffusion of  $\text{Hg}^0$  from a static source (Hg barometer) in the closed space of the British Columbia Geological Survey laboratory generated a stable Hg vapour halo, which gradually diffused to background Hg concentrations 25 metres away from the metal source.

Rain has little influence on concentrations of gaseous  $\text{Hg}^0$  in the atmosphere, removing mainly Hg adsorbed on particulates and aerosols (Saukov, 1946; McCarthy, 1972; Mashyanov, 1985). Water bodies, bogs, snow, and permafrost do not block Hg emission into the atmosphere from underlying bedrock sources (McCarthy, 1972; Mashyanov, 1985). However, the

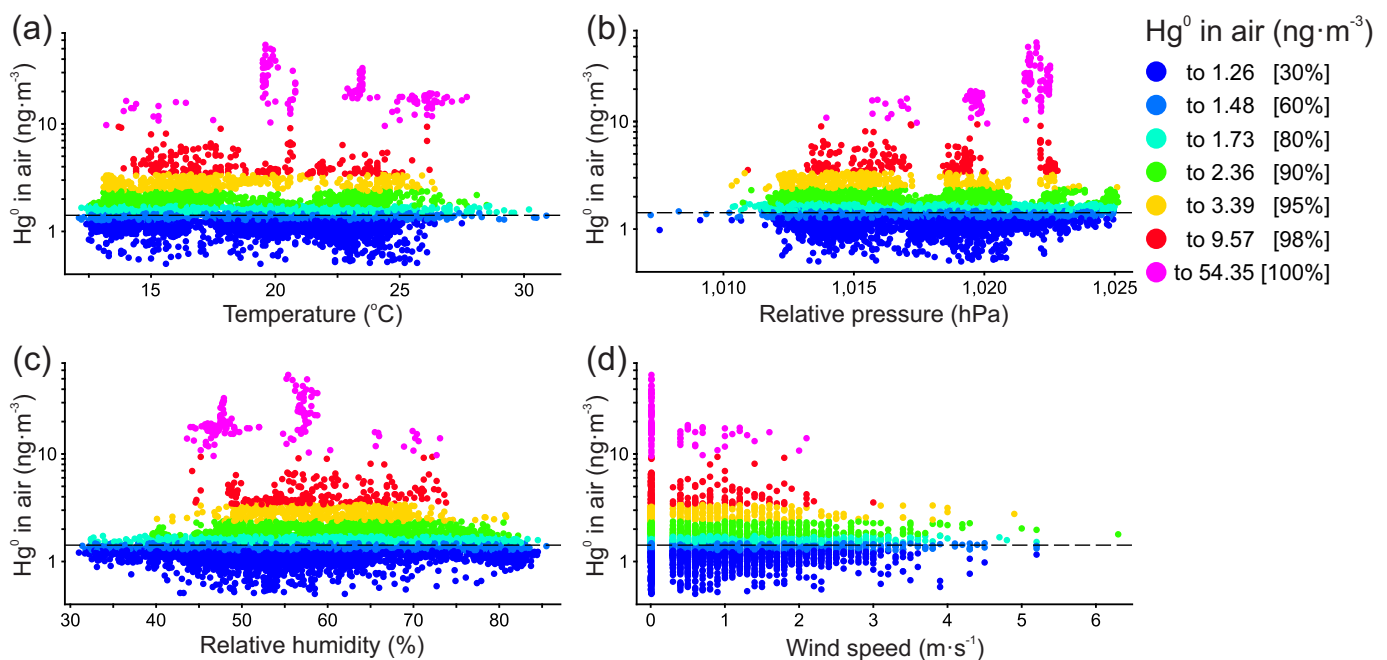


**Fig. 30.** Scatter plots of weather parameters vs. Hg vapour concentration in near-surface air for all data of this study. **a)** Air temperature ( $^{\circ}\text{C}$ ) vs.  $\text{Hg}^0$  in air ( $\text{ng}\cdot\text{m}^{-3}$ ). **b)** Relative barometric pressure at sea-level (hPa) vs.  $\text{Hg}^0$  in air ( $\text{ng}\cdot\text{m}^{-3}$ ). **c)** Relative air humidity (%) vs.  $\text{Hg}^0$  in air ( $\text{ng}\cdot\text{m}^{-3}$ ). **d)** Wind speed ( $\text{m}\cdot\text{s}^{-1}$ ) vs.  $\text{Hg}^0$  in air ( $\text{ng}\cdot\text{m}^{-3}$ ). Percentiles and median concentration of  $\text{Hg}^0$  in air ( $1.40 \text{ ng}\cdot\text{m}^{-3}$ ; dashed line) based on 9660 values.

effect of rapid changes in soil moisture is that as water fills pore space in soil, Hg temporarily accumulates in the top layer, adsorbing on soil particles. Subsequent heating and drying of the soil surface by solar radiation causes desorption and exhalation of Hg<sup>0</sup> into the atmosphere. Depending on the type and permeability of surficial materials, rapid changes in soil moisture can increase the intensity of Hg vapour anomalies (Mashyanov, 1980, 1985; Zhrebtsov et al., 1992). The effect of soil moisture might explain the variable intensity of Hg vapour haloes at the sediment-covered Lara-Coronation polymetallic VMS occurrence (Figs. 8, 9; Table 2). Mercury anomalies in near-surface air were about 1.6x stronger when the surface was still wet a few hours after the rain, compared to the intensity of the same anomalies above the dry surface following six days without rain (Fig. 9). Weather was a mix of sun and clouds, with similar air temperature, relative humidity, and wind speed, but slightly different atmospheric pressure, during both surveys (Appendix 1 of Rukhlov et al., 2020).

## 7. Conclusion

We measured real-time Hg vapour concentrations 1-50 cm above ground at 15 locations that include polymetallic VMS, epithermal Au-Ag-Cu, shear-hosted sulphide Cu-Ag-Au, auriferous quartz veins, fault structures, and barren rocks on Vancouver Island. Direct and continuous (one measurement per second) monitoring of ultra-low Hg concentrations in air was made with a portable RA-915M Zeeman mercury atomic absorption analyzer. Meteorological conditions (wind speed and direction, air temperature, relative humidity, and atmospheric pressure) were simultaneously measured using a Kestrel 5500 meter. Mercury vapour concentrations (total 9660 measurements) acquired in this study range from 0.50 to 54 ng·m<sup>-3</sup>, with a background (median) value of 1.40 ng·m<sup>-3</sup> being consistent with the global background Hg in the atmosphere. The strongest Hg emission occurs above tailings from a shaft at the Bentley Au occurrence north of Goldstream, possibly due to a mining method involving amalgamation between the late 1800s and early 1900s. Mercury vapour haloes in near-surface air (1.5 to 13.4x background Hg) mark all the mineralized zones in this study, including the Lara-Coronation polymetallic VMS buried under glacial sediments up to 30 m thick. The terrane-bounding Leech River and other faults are also highlighted by Hg vapour haloes that are 1.3 to 2.2x local background; because the Leach River fault has been active since the last glacial maximum, it is possible that some of these other faults have been as well. Wind and rapid changes in air temperature, atmospheric pressure, and soil humidity can influence the intensity of the gaseous Hg anomalies. Nonetheless, sampling of near-surface air can instantly delineate mineralized zones and faults that are buried. This simple and rapid method can be used in both regional- and property-scale exploration for ore deposits, oil and gas, geothermal zones, earthquake-hazard assessment, geological mapping, and environmental monitoring. Future detailed surveys could enhance anomaly contrasts by passive air sampling using Hg flux chambers, or by

sampling air above the disturbed, top 5-3 cm layer of surficial sediment. The mechanical disturbance of the sample site liberates Hg<sup>0</sup> adsorbed onto soil particles. In addition, sampling air under a bucket by using a hose like that of Yasutake et al. (2011) would minimize the effects of atmospheric turbulence and wind.

## Acknowledgments

We thank Lumex Instruments Canada for renting out a portable RA-915M Zeeman mercury atomic absorption spectrometer for this study, Patrick Sabourin (Lumex Instruments Canada) for technical support and discussions during the field season, and Raymond E. Lett (Emeritus Scientist, British Columbia Geological Survey) for guiding us to literature about early Hg studies in Canada. Neil Wildgust (British Columbia Geological Survey) provided support by accommodating a flexible Covid-19 safe field program. Bruce Northcote (British Columbia Geological Survey), Adam Larsen (Treasury Metals Inc.), Greg Kronstal (Mosaic Forest Management), and Don Steffler (Jordan River) are thanked for discussions about access and permits to enter private lands. We very much appreciate thorough reviews and constructive comments of Peter M.D. Bradshaw (Bradshaw Research Initiative for Minerals and Mining), and Lawrence B. Aspler (British Columbia Geological Survey).

## References cited

- Aston, S.R., Bruty, P., Chester, R., and Riley, J.P., 1972. The distribution of mercury in North-Atlantic deep-sea sediments. *Nature* 237, 125.
- Babkin, P.V., Baranov, Yu.E., Vasiliev, V.I., Demidov, N.G., Kirikilitsa, S.I., Kuznetsov, V.A., Nikiforov, N.A., Obolenskiy, A.A., Ozerova, N.A., Smirnov, V.I., Terekhova, G.A., and Fedorchuk, V.P., 1976. Metallogeny of mercury. *Nedra, Moscow*, 255 p. (in Russian).
- Barringer, A.R., 1966. Interference-free spectrometer for high sensitivity mercury analyses of soils, rocks and air. *Bulletin of Institute of Mining and Metallurgy* 75 (714), 120-124.
- Barringer, A.R., 1969. Remote-sensing techniques for mineral discovery. In: *Proceedings of the 9th Commonwealth Mining and Metallurgical Congress, Volume 1, Institution of Mining and Metallurgy*, pp. 1-42.
- Bodnar, M.M., 2017. Modelling geochemical dispersion above a buried polymetallic volcanogenic massive sulphide deposit in a recently glaciated terrain. Unpublished M.Sc. thesis, University of British Columbia, Canada, 212 p.
- Boström K., and Fischer, D.E., 1969. Distribution of mercury in East Pacific sediments. *Geochimica et Cosmochimica Acta*, 33, 743-745.
- Bradshaw, P.M.D., 2015. Sensitive mercury spectrometers for the detection of mineral deposits, airborne mercury pollution, and underground nuclear tests. Chapter 12. In: *Barringer, Back to the Future: Airborne Geochemistry and Many Related Topics, Association of Applied Geochemists*, pp. 139-148.
- Brewer, W.M., 1918. Workings on Sunloch mine, Jordan River, Victoria Mining Division. Report of Resident Engineer, Nanaimo, B.C., British Columbia Ministry of Energy, Mines and Petroleum Resources, British Columbia Geological Survey, Property File 6031, scale 1:1200.
- Buttitta, D., Caracausi, A., Chiaraluze, L., Favara, R., and Sulli, A., 2020. Continental degassing of helium in an active tectonic setting

- (northern Italy): the role of seismicity. *Scientific Reports* 10, 162.
- Carr, R.A., Jones, M.M., and Russ, E.R., 1974. Anomalous mercury in near-bottom water of a Mid-Atlantic Rift valley. *Nature* 251, 489-490.
- Carr, R.A., Jones, M.M., Warner, T.B., Cheek, C.H., and Russ, E.R., 1975. Variation in time of mercury anomalies at the Mid-Atlantic Ridge. *Nature* 258, 588-589.
- Carr, G.R., Wilmshurst, J.R., and Ryall, W.R., 1984. Mercury as a pathfinder in exploration geochemistry-Case history studies. *Journal of Geochemical Exploration* 22, 353-354.
- Carson, D.T.J., 1960a. Geology of Mount Washington, Vancouver Island, British Columbia. Unpublished M.Sc. thesis, University of British Columbia, Canada, 116 p.
- Carson, D.T.J., 1960b. Tertiary mineral deposits of Vancouver Island. *CIM Transactions Volume LXXII*, 116-125.
- Carson, D.J.T., 1968. Metallogenic study of Vancouver Island with emphasis on the relationship of plutonic rocks and mineral deposits. Unpublished Ph.D. thesis, Carleton University, Canada, 274 p.
- Chengliang, Z., Liyin, W., Yong, D., and Shengfeng, P., 1989. Distribution of trace Hg and its mode of occurrence over Fankou Pb-Zn deposit, Guangdong, China. *Journal of Geochemical Exploration* 33, 73-83.
- Choi, H.D., and Holsen, T.M., 2009. Gaseous mercury emissions from unsterilized and sterilized soils: The effect of temperature and UV radiation. *Environmental Pollution* 157, 1673-1678.
- Clague, J.J., Fulton, R.J., and Ryder, J.M., 1982. Surficial geology, Vancouver Island and adjacent mainland, British Columbia, map. Geological Survey of Canada, Open File 837, scale 1:1,000,000.
- Clapp, C.H., 1912. Southern Vancouver Island. Geological Survey of Canada, Memoir 13, 208 p., scale 1:380,160.
- Clapp, C.H., 1913. Geology of the Victoria and Saanich map areas, Vancouver Island, British Columbia. Geological Survey of Canada, Memoir 36, 143 p., scale 1:62,500.
- Coderre, J.A., and Steinthorsson, S., 1977. Natural concentration of mercury in Iceland. *Geochimica et Cosmochimica Acta* 41, 419-424.
- Cui, Y., Hickin, A.S., Schiarizza, P., Diakow, L.J., Miller, D., Nixon, G.T., Nelson, J.L., and Ferri, F., 2018. Methods to update the digital geology of British Columbia and synopses of recently integrated mapping programs. In: *Geological Fieldwork 2017*, British Columbia Ministry of Energy, Mines and Petroleum Resources, British Columbia Geological Survey Paper 2018-1, pp. 197-215.
- Cui, Y., Miller, D., Schiarizza, P., and Diakow, L.J., 2017. British Columbia digital geology. British Columbia Ministry of Energy, Mines and Petroleum Resources, British Columbia Geological Survey Open File 2017-8, 9 p. Data version 2018-04-05.
- Dalziel, J., and Tordon, R., 2014. Gaseous mercury flux measurements from two mine tailing sites in the Seal Harbour area of Nova Scotia. *Geochemistry: Exploration, Environment, Analysis* 14, 17-24.
- Erich, E.E., and Blanchard, R., 1921. Geological map of the Jordan River area, Victoria mining district, B.C., British Columbia Ministry of Energy, Mines and Petroleum Resources, British Columbia Geological Survey, Property File 6042, scale 1:12,000.
- Esbril, J.M., Higuera, P.L., Martínez-Coronado, A., and Naharro, R., 2020. 4D dispersion of total gaseous mercury derived from a mining source: identification of criteria to assess risks related with high concentrations of atmospheric mercury. *Atmospheric Chemistry and Physics*, <https://doi.org/10.5194/acp-2019-1107>.
- Eshleman, A., Siegel, M.S., and Siegel, B.Z., 1971. Is the mercury from Hawaiian volcanoes a natural source of pollution? *Nature* 233, 471-472.
- Fedorchuk, V.P., 1964. Method of Prospecting and Exploration for Concealed Mercury-Antimony Mineralization. Nedra, Moscow, 283 p. (in Russian).
- Fedorchuk, V.P., 1983. Geology of Mercury. Nedra, Moscow, 270 p. (in Russian).
- Fridman, A.I., 1975. Gas Survey in Ore Prospecting and Geological Mapping. Institute of Mineralogy, Geochemistry and Crystal Chemistry of Rare Elements (IMGRE), Moscow, 88 p. (in Russian).
- Fursov, V.Z., 1970. Mercury atmosphere of mercury deposits. *Doklady of the Academy of Sciences of the USSR, Geology Series* 194 (6), 1421-1423. (in Russian).
- Fursov, V.Z., 1977. Mercury-Indicator for Geochemical Prospecting of Ore Deposits. Nedra, Moscow, 142 p. (in Russian).
- Fursov, V.Z., 1983a. Mercury vapour method in exploration of mineral deposits. Nauka, Moscow, 240 p. (in Russian).
- Fursov, V.Z., 1983b. Mercury in rocks and ores and its sublimation temperature. *Doklady of the Academy of Sciences of the USSR* 204 (2), 451-545. (in Russian).
- Fursov, V.Z., 1990. Mercury vapor surveys: technique and results. *Journal of Geochemical Exploration* 38, 145-155.
- Gu, B., Bian, Y., Miller, C.L., Dong, W., Jiang, X., and Liang, L., 2011. Mercury reduction and complexation by natural organic matter in anoxic environments. *Proceedings of the National Academy of Sciences of the United States of America* 108, 1479-1483.
- Guelpa, J.P., and Meusy, G., 1971. Sunro mine geological map. British Columbia Ministry of Energy, Mines and Petroleum Resources, British Columbia Geological Survey, Property File 753084, scale 1:4800.
- Gustin, M.S., Taylor, Jr., G.E., and Maxey, R.A., 1997. Effect of temperature and air movement on the flux of elemental mercury from substrate to the atmosphere. *Journal of Geophysical Research* 102, 3891-3898.
- Gworek, B., Dmuchowski, W., Baczewska, A.H., Brągoszewska, P., Bemowska-Kałabun, O., and Wrzosek-Jakubowska, J., 2017. Air contamination by mercury, emissions and transformations-a review. *Water, Air, & Soil Pollution* 228, 123.
- Hawkes, H.E., and Williston, S.H., 1962. Mercury vapour as a guide to lead-zinc-silver deposits. *The Mining Congress Journal* 48, 30-35.
- Heberlein, D.R., Dunn, C.E., and Rice, S., 2017. Halogens and other volatile compounds in surface sample media as indicators of mineralization. Part 1: Lara VMS deposit, Vancouver Island, BC (NTS 092B/13). *Geoscience BC Report 2017-11*, 43 p.
- Higuera, P., Llanos, W., García, M.E., Millán, R., and Serrano, C., 2012. Mercury vapor emissions from the Ingenios in Potosí (Bolivia). *Journal of Geochemical Exploration* 116, 1-7.
- Houle, J., 2000. Unpublished description and assay data for rock samples from Mount Washington property. British Columbia Ministry of Energy, Mines and Petroleum Resources, British Columbia Geological Survey, Property File 7223, 9 p.
- Houle, J., 2016. 2015 Technical assessment report for the New Sunro property, Vancouver Island. British Columbia. British Columbia Ministry of Energy, Mines and Petroleum Resources, British Columbia Geological Survey, Assessment Report 35982, 61 p.
- Houle, J., 2019. Technical assessment report on the Mount Washington property. British Columbia Ministry of Energy, Mines and Petroleum Resources, British Columbia Geological Survey, Assessment Report 38409, 124 p., scale 1:5000.
- Jin, Y., Wu, Z., Shen, C., Wei, J., and Zhu, H., 1989. Earthquake prediction through the observation and measurement of mercury content variation in water. *Journal of Geochemical Exploration* 33, 195-202.
- Kalinchuk, V.V., and Astakhov, A.S., 2014. Atmochemical mercury dispersion aureoles over active geologic structures of northern Japan Sea area. *Geology and Geophysics* 55, 1728-1737 (in Russian).
- Karasik, M.A., Kirilitsa, S.I., and Avgitov, A.K., 1978. Methodical Recommendations for the Interpretation of Mercury Vapour Haloes

- of Mercury Deposits in Donbass. Simferopol, 140 p. (in Russian).
- Kelso, I., and Wetherup, S., 2008. Independent technical report and mineral resource estimation: Lara polymetallic property, British Columbia, Canada. NI 43-101 Technical Report, 121 p.
- Kikauka, A., 2004. Geological and geochemical report on the Sunloch claim (Sunro copper-silver-gold mine), Jordan River, B.C., British Columbia Ministry of Energy and Mines, British Columbia Geological Survey, Assessment Report 27472, 36 p., scale 1:5000.
- Kothny, E.L., 1973. The three-phase equilibrium of mercury in nature. Chapter 4. In: Kothny, E.L. (Ed.), Trace Element in the Environment. American Chemical Society, Advances in Chemistry 123, pp. 48-80.
- Krömer, E., Friedrich, G., and Wallner, P., 1981. Mercury and mercury compounds in surface air, soil gas, soils and rocks. In: Rose, A.W. and Gundlach, H., (Eds.), Geochemical Exploration 1980. Journal of Geochemical Exploration 15, 51-62.
- Kuznetsov, V.A., and Obolenskiy, A.A., 1970. Questions of the genesis of mercury deposits and the problem of sources of ore matter. *Geology and Geophysics* 4, 44-56.
- Lett, R.E., Sacco, D.A., Elder, B., and Jackaman, W., 2020. Real-time detection of bedrock mineralization and geological faults beneath glacial deposits in central British Columbia using onsite soil gas carbon dioxide and oxygen analysis by electronic gas sensors (NTS 093A/58, 093G/03). In: Geoscience BC Summary of Activities 2019: Minerals. Geoscience BC, Report 2020-01, pp. 93-100.
- Mashyanov, N.R., 1980. Experimental development of a method of prospecting for mineral deposits using gaseous mercury aureoles in atmosphere. *Vestnik of St. Petersburg (Leningrad) State University* 12, 47-55. (in Russian).
- Mashyanov, N.R., 1985. Mercury vapour survey in near-surface layer of atmosphere for prospecting of ore deposits. Unpublished Ph.D. thesis, St. Petersburg (Leningrad) State University, St. Petersburg, 201 p. (in Russian).
- Mashyanov, N.R., 1993. Atmochemical methods in geochemistry and ecology. In: Nemets, V.M., (Ed.), Methods of Analysis of Inorganic Gases, Chemistry, St. Petersburg, pp. 340-404. (in Russian).
- Mashyanov, N.R., Ilyin, Yu.T., and Ryzhov, V.V., 1995. Electrochemical decomposition of mercury-bearing sulphides - first experimental data. In: The Universities of Russia Programme, Theme 2, Geology, Volume 2, Moscow State University, Moscow, pp. 176-180. (in Russian).
- Mashyanov, N.R., Pogarev, S.E., Panova, E.G., Panichev, N., and Ryzhov, V., 2017. Determination of mercury thermospecies in coal. *Fuel* 203, 973-980.
- Massey, N.W.D., 1995. Geology and mineral resources of the Duncan sheet, Vancouver Island, 92B/13. British Columbia Ministry of Energy, Mines and Petroleum Resources, British Columbia Geological Survey Paper 1992-4, 124 p.
- Massey, N.W.D., Friday, S.J., Tercier, P.E., and Potter, T.E., 1991. Geology of the Duncan area (92B/13). British Columbia Ministry of Energy, Mines and Petroleum Resources, British Columbia Geological Survey Geoscience Map 1991-03, scale 1:50,000.
- Massey, N.W.D., Desjardins, P.J., and Grunsky, E.C. (compilers), 1994. Vancouver Island, British Columbia, (92B, C, E, F, G, K, L; 1021). British Columbia Ministry of Energy, Mines and Petroleum Resources, British Columbia Geological Survey Open File 1994-06, scale 1:250,000.
- McCarthy, Jr., J.H., 1972. Mercury vapour and other volatile components in the air as a guide to our deposits. *Journal of Geochemical Exploration* 1, 143-162.
- McCarthy, Jr., J.H., Vaughn, W.W., Learned, R.E., and Meuschke, J.L., 1969. Mercury in soil gas and air-a potential tool in mineral exploration. U.S. Geological Survey Circular 609, 16 p.
- McCarthy, Jr., J.H., Menschke, J.L., Piclin, W.H., and Learned, R.E., 1970. Mercury in the atmosphere. In: Mercury in the Environment. U.S. Geological Survey Professional Paper 713, pp. 37-39.
- McDougall, J.J., 1987. Summary report on Mt. Washington gold property. British Columbia Ministry of Energy, Mines and Petroleum Resources, British Columbia Geological Survey, Property File 885796, 23 p.
- Meusy, G., 1971. Surface geology, Sunro Mine. British Columbia Ministry of Energy, Mines and Petroleum Resources, British Columbia Geological Survey, Property File 6056, scale 1:1200.
- Moore, C.W., and Castro, M.S., 2012. Investigation of factors affecting gaseous mercury concentrations in soils. *Science of the Total Environment* 419, 136-143.
- Morell, K.D., Regalla, C., Leonard, L.J., Amos, C., and Levson, V., 2017. Quaternary rupture of a crustal fault beneath Victoria, British Columbia, Canada. *GSA Today* 27, doi: 10.1130/GSATG291A.1.
- Muller, J.E., 1977. Geology of Vancouver Island. Geological Association of Canada, Mineralogical Association of Canada, Joint Annual Meeting 1977, Field Trip 7, April 21-24, Guidebook, 54 p.
- Muller, J.E., 1980. Geology - Victoria map area, Vancouver Island and Gulf islands, British Columbia. Geological Survey of Canada, Open File 701, scale 1:100,000.
- Muller, J.E., 1983. Geology, Victoria, west of sixth meridian, British Columbia. Geological Survey of Canada, Map 1553A, scale 1:100,000.
- Muller, J.E., 1989. Tertiary low angle faulting and related gold and copper mineralization on Mount Washington, Vancouver Island (92F/11, 14). In: Geological Fieldwork 1988, British Columbia Ministry of Energy, Mines and Petroleum Resources, British Columbia Geological Survey Paper 1989-01, pp. 81-91.
- Nelson, J.L., Colpron, M., and Israel, S., 2013. The Cordillera of British Columbia, Yukon and Alaska: tectonics and metallogeny. In: Colpron, M., Bissig, T., Rusk, B.G., and Thompson, F.H., (Eds.), Tectonics, Metallogeny, and Discovery: The North American Cordillera and Similar Accretionary Settings. Society of Economic Geologists, Special Publication 17, pp. 53-109.
- Neumann, N., 1991. The geology and history of mining at Goldstream. The Geological Association of Canada, Pacific Section, British Columbia Ministry of Energy, Mines and Petroleum Resources, British Columbia Geological Survey Property File 21792, 83 p.
- Neville, B., 1963. Mineralogy of a suite of minerals from a deposit at Mount Washington, Vancouver Island, British Columbia. Unpublished Geology 409 Course Paper, The University of British Columbia, Canada, British Columbia Ministry of Energy, Mines and Petroleum Resources, British Columbia Geological Survey, Property File 600191, 11 p.
- Nevolko, P.A., and Fominykh, P.A., 2017. Orientation mercury vapour survey at the Novolushnikovskoe gold deposit (Salair Ridge). *Razvedka i Okhrana Nedr* 6, 17-20. (in Russian).
- Northcote, K.E., and Muller, J.E., 1972. Volcanism, plutonism, and mineralization: Vancouver Island. Canadian Institute of Mining, Metallurgy and Petroleum, Bulletin 65, 49-57.
- Nriagu, J., and Becker, C., 2003. Volcanic emissions of mercury to the atmosphere: Global and regional inventories. *Science of the Total Environment* 304, 3-12.
- Ovchinnikov, L.N., Sokolov, V.A., Friedman, A.I., and Yanitakii, I.N., 1972. Gaseous geochemical methods in structural mapping and prospecting for ore deposits. In: Jones, M.J., (Ed.), Geochemical Exploration 1972, Institute of Mining and Metallurgy, pp. 177-182.
- Ozerova, N.A., 1975. Mercury in gas deposits of Central Europe. *Soviet Geology* 6, 72-79. (in Russian).
- Ozerova, N.A., 1976. Some questions on geochemistry of mercury and the problem of sources of ore matter. In: Metallogeny of Mercury. Nedra, Moscow, pp. 28-41.
- Ozerova, N.A., 1977. On degassing of mercury from depths of the Earth. In: Geochemistry of Processes of Migration of Ore Elements. Nauka, Moscow, pp. 15-35. (in Russian).

- Ozerova, N.A., 1979. On mercury contents of 'through' minerals of endogenic ore deposits. In: *Geochemical Methods of Prospecting for Polymetallic Ore Deposits*. Nauka, Novosibirsk, pp. 174-181. (in Russian).
- Ozerova, N.A., 1986. Mercury and Endogenic Ore Formation. Nauka, Moscow, 232 p. (in Russian).
- Phillips, B.A., Kerr, A.C., Mullen, E.K., and Weis, D., 2017. Oceanic mafic magmatism in the Siletz terrane, NW North America: Fragments of an Eocene oceanic plateau? *Lithos* 274-275, 291-303.
- Rehn, P., and Rehn, W., 1996. Mercury vapor anomalies at the Section 30 Deposit, Twin Creeks Mine, Nevada. In: *Geology and Ore Deposits of the American Cordillera. Proceedings of the Geological Society of Nevada Symposium, Volume 30, Reno/Sparks, Nevada*, pp. 769-778.
- Rudnick, R.L., and Gao, S., 2005. Composition of the continental crust. In: Heinrich, D.H., Rudnick, R.L., and Turekian, K.K., (Eds.), *The Crust, Treatise on Geochemistry, Volume 3*, Elsevier, Amsterdam, pp. 1-64.
- Rukhlov, A.S., Ootes, L., Hickin, A.S., and Mashyanov, N.R., 2020. Supplementary data for near-surface mercury vapour haloes in air above ore deposits and faults on Vancouver Island: Insights into buried materials in real time? *British Columbia Ministry of Energy, Mines and Low Carbon Innovation, British Columbia Geological Survey GeoFile 2020-13*, 1 p.
- Ruks, T.W., 2015. Stratigraphic and paleotectonic studies of Paleozoic Wrangellia and its contained volcanogenic massive sulfide (VMS) occurrences, Vancouver Island, British Columbia, Canada. Unpublished Ph.D. thesis, University of British Columbia, Canada, 185 p.
- Rusmore, M.E., and Cowan, D.S., 1985. Jurassic-Cretaceous rock units along the southern end of the Wrangellia terrane on Vancouver Island. *Canadian Journal of Earth Sciences* 22, 1223-1232.
- Rychagov, S.N., Nuzhdaev, A.A., and Stepanov, I.I., 2009. Behaviour of mercury in the hypergene zone of geothermal deposits (southern Kamchatka). *Geokhimiya* 5, 533-542. (in Russian).
- Ryzhov, V.V., Mashyanov, N.R., Ozerova, N.A., and Pogarev, S.E., 2003. Regular variations of the mercury concentration in natural gas. *The Science of the Total Environment* 304, 145-152.
- Saukov, A.A., 1946. Geochemistry of mercury. *Academy of Sciences of the USSR, Contributions of the Institute of Geological Sciences* 74, 128 p. (in Russian).
- Saukov, A.A., Aidinyan, N.K., and Ozerova, N.A., 1972. *Studies of Mercury Geochemistry*. Nauka, Moscow, 336 p. (in Russian).
- Schuster, E., 1991. The behavior of mercury in the soil with special emphasis on complexation and adsorption processes-A review of the literature. *Water, Air, & Soil Pollution* 56, 667-680.
- Sergeev, E.A., 1957. Methods of mercurimetric investigations. In: *Geochemical Prospecting of Ore Deposits, Gosgeoltekhizdat, Moscow*, pp. 158-165. (in Russian).
- Sholupov, S.E., and Ganeyev, A.A., 1995. Zeeman absorption spectrometry using high frequency modulated light polarization. *Spectrochimica Acta Part B: Atomic Spectroscopy* 50B, 1227-1236.
- Sholupov, S., Pogarev, S., Ryzhov, V., Mashyanov, N., and Stroganov, A., 2004. Zeeman atomic absorption spectrometer RA-915+ for direct determination of mercury in air and complex matrix samples. *Fuel Processing Technology* 85, 473-485.
- Smirnov, S.S., 1955. Oxidation zone of sulphide deposits. *Academy of Sciences of the USSR, Moscow*, 332 p. (in Russian).
- Sokolov, V.A., 1956. Migration of Oil and Gas. *Academy of Sciences of the USSR, Moscow*, 352 p. (in Russian).
- Solovov, A.P., 1985. *Methods of Geochemical Exploration for Ore Deposits: Textbook*. Nedra, Moscow, 294 p. (in Russian).
- Sprovieri, F., Pirrone, N., Bencardino, M., D'Amore, F., Carbone, F., Cinnirella, S., Mannarino, V., Landis, M., Ebinghaus, R., Weigelt, A., Brunke, E.-G., Labuschagne, C., Martin, L., Munthe, J., Wängberg, I., Artaxo, P., Morais, F., de Melo Jorge Barbosa, H., Brito, J., Cairns, W., Barbante, C., del Carmen Diéguez, M., Garcia, P.E., Dommergue, A., Angot, H., Magand, O., Skov, H., Horvat, M., Kotnik, J., Read, K.A., Neves, L.M., Gawlik, B.M., Sena, F., Mashyanov, N., Obolkin, V., Wip, D., Feng, X.B., Zhang, H., Fu, X., and Ramachan, R., 2016. Atmospheric mercury concentrations observed at ground-based monitoring sites globally distributed in the framework of the GMOS network. *Atmospheric Chemistry and Physics* 16, 11915-11935.
- Starr, C.C., and Frith, O.D., 1926. Report on examination of the Gabbro mine, Jordan River, B.C. *British Columbia Ministry of Energy, Mines and Petroleum Resources, British Columbia Geological Survey, Property File 6051*, 27 p.
- Stepanov, I.I., 1997. Mercury-indicator of "hot" hydrothermal zones and dynamic processes accompanied by deformation of rocks. Unpublished D.Sc. thesis, Institute of Mineralogy, Geochemistry and Crystal Chemistry of Rare Elements (IMGRE), Moscow, 165 p. (in Russian).
- Stevenson, W.G., 1967. Geological report on the property of Mt. Washington Copper Co. Ltd. in the Nanaimo Mining Division. *British Columbia Ministry of Energy, Mines and Petroleum Resources, British Columbia Geological Survey, Property File 810035*, 43 p., scale 1:6000 and 1:31,680.
- Stoffers, P., Hannington, M., Wright, I., Herzig, P., de Ronde, C., and Party, S.S., 1999. Elemental mercury at submarine hydrothermal vents in the Bay of Plenty, Taupo volcanic zone, New Zealand. *Geology* 27, 931-934.
- Sun, X., Si, X., Xiang, Y., and Liu, D., 2017. Soil mercury spatial variations in the fault zone and corresponding influence factors. *Terrestrial, Atmospheric and Oceanic Sciences* 28, 283-294.
- Sveshnikov, G.B., 1967. *Electrochemical Processes on Sulphide Deposits*. St. Petersburg (Leningrad) State University, St. Petersburg, 160 p. (in Russian).
- Toombs, R.B., 1951. A mineralogical study of Sunloch copper ore. Unpublished Geology 409 Course Paper, The University of British Columbia, Canada, British Columbia Ministry of Energy, Mines and Petroleum Resources, British Columbia Geological Survey, Property File 600454, 22 p.
- UN Environment, 2019. *Global Mercury Assessment 2018*. The United Nations Environment Programme, Economy Division, Chemicals and Health Branch, Geneva, Switzerland, 62 p. URL: <<https://www.unenvironment.org/explore-topics/chemicals-waste>>.
- Utkin, V.I., and Yurkov, A.K., 2010. Radon as a tracer of tectonic movements. *Russian Geology and Geophysics* 51, 220-227.
- Wang, G., Liu, C., Wang, J., Liu, W., and Zhang, P., 2006. The use of soil mercury and radon gas surveys to assist the detection of concealed faults in Fuzhou City, China. *Environmental Geology* 51, 83-90.
- Wetherup, S., 2010. Structural mapping and whole rock geochemical sampling: Lara polymetallic property. *British Columbia Ministry of Energy, Mines and Petroleum Resources, British Columbia Geological Survey, Assessment Report 31578*, 42 p., 4 appendices, scale 1:20,000.
- Williston, S.H., 1968. Mercury in the atmosphere. *Journal of Geophysical Research* 73, 7051-7057.
- Xiang, Y., Sun, X., Liu, D., Yan, L., Wang, B., and Gao, X., 2020. Spatial distribution of Rn, CO<sub>2</sub>, Hg, and H<sub>2</sub> concentrations in soil gas across a thrust fault in Xinjiang, China. *Frontiers in Earth Sciences*, 8:554924. doi: 10.3389/feart.2020.554924.
- Xie, H., Liu, M., He, Y., Lin, H., Yu, C., Deng, C., and Wang, X., 2019. An experimental study of the impacts of solar radiation and temperature on mercury emission from different natural soils across China. *Environmental Monitoring and Assessment* 191, 545.
- Yasutake, A., Cheng, J.P., Kiyono, M., Uraguchi, S., Liu, X., Miura,

- K., Yasuda, Y., and Mashyanov, N.R., 2011. Rapid monitoring of mercury in air from an organic chemical factory in China using a portable mercury analyzer. *The Scientific World Journal* 11, 1630-1640.
- Yin, R., Pan, X., Deng, C., Sun, G., Yun Kwon, S., Lepa, R.F., and Hurley, J.P., 2020. Consistent trace element distribution and mercury isotopic signature between a shallow buried volcanic-hosted epithermal gold deposit and its weathered horizon. *Environmental Pollution* 259, 113954.
- Yorath, C.J., 2005. *The Geology of Southern Vancouver Island*. Harbour Publishing Co. Ltd., Madeira Park, British Columbia, 205 p.
- Zhang, H., and Lindberg, S.E., 1999. Processes influencing the emission of mercury from soils: A conceptual model. *Journal of Geophysical Research* 104, 21889-21896.
- Zherebtsov, Yu.D., Politkov, M.I., and Sikorskiy, V.Yu., 1992. *Technology of Mercurometric Prospecting of Ore Deposits*. Nedra, Moscow, 176 p. (in Russian).
- Zonghua, W., and Yangfen, J., 1981. A mercury vapor survey in an area of thick transported overburden near Shanghai, China. *Journal of Geochemical Exploration* 15, 77-92.



# Soil and till geochemical surveys at the Ace mineral property, central British Columbia



Ray E. Lett<sup>1, a</sup>, and Roger C. Paulen<sup>2</sup>

<sup>1</sup>Emeritus Geoscientist, British Columbia Geological Survey, Ministry of Energy, Mines and Low Carbon Innovation, Victoria, BC, V8W 9N3

<sup>2</sup>Geological Survey of Canada, Ottawa, ON, K1A 0E8

<sup>a</sup>corresponding author: Ray.Lett@gov.bc.ca

Recommended citation: Lett, R.E., and Paulen, R.C., 2021. Soil and till geochemical surveys at the Ace mineral property, central British Columbia. In: Geological Fieldwork 2020, British Columbia Ministry of Energy, Mines and Low Carbon Innovation, British Columbia Geological Survey Paper 2021-01, pp. 145-165.

## Abstract

A multi-media surficial geochemical survey was carried out by the British Columbia Geological Survey in 2000 to document the geochemical expression of massive sulphide and gold-quartz vein mineralization at the Ace mineral property, near Likely. Much of the bedrock on the property is concealed by lodgement (basal) till, which was deposited by a southeast to northwest ice advance, ablation till, and colluvium. Soil samples from the B-horizon soil and transitional B-C horizon, and lodgement till were collected from 85 sites and the <0.063 mm (-230 mesh fraction) was analyzed for more than 50 minor and trace elements and major oxides by three methods: modified aqua regia dissolution-inductively coupled plasma mass spectrometry; instrumental neutron activation; and lithium metaborate fusion-inductively coupled plasma emission spectroscopy. Samples were also analyzed for carbon, sulphur, and loss on ignition. Five size fractions ranging from 1-2 mm to 0.125-0.063 mm of selected till and soil samples were analyzed for 35 trace elements by modified aqua regia dissolution followed by ICP-MS.

The commodity and pathfinder metals Au, As, Bi, Co, Cu, Pb, Se, and Zn are present in higher concentrations in the <0.063 mm fraction of the basal till than in the B-horizon soil, likely because the metal content in the silt- and clay-sized fraction of till more closely reflects the chemistry of bedrock after comminution and dispersal. However, Ag and Hg have higher concentrations in the B-horizon soil where they were likely captured and concentrated by organic matter during soil formation. Till and soil size fraction analysis for metals show that Au and Pb are present in soil and till as discrete mineral grains larger than 0.063 mm. Anomalous Co, Cu, Pb, Se, and Zn concentrations in till and soil define a ribbon-shaped dispersal train along the northern edge of the survey area. The train formed from glacial erosion of mineralized bedrock, that was then transported and deposited by an east to west ice flow. This train was then subjected to post-glacial modification by colluvial processes. The trace element dispersal profiles suggest a massive sulphide source for the anomalous metals in bedrock beneath the till at the east end of the dispersal train. Potentially, other till and soil Au and As anomalies in the western and southern parts of the survey area could have been derived from unmapped, northeast-trending Au-quartz veins.

**Keywords:** Surficial geochemistry, till, B-horizon soil, Ace property, ICP-MS, drift prospecting

## 1. Introduction

Dispersal trains of minerals and rock debris in glacial sediment have long-been used to detect mineralized bedrock beneath glacially transported sediments, and the application of this concept has resulted in many successful till geochemical surveys in Canada (e.g., Hickin and Plouffe, 2017; McClenaghan and Paulen, 2018). In British Columbia, several examples have documented till geochemistry patterns related to a known mineralized bedrock source: Mount Milligan (Sibbick et al., 1996); Samatousum Mountain (Paulen, 2001); Bell Copper (Levson, 2001, 2002); Huckleberry (Ferbey and Levson, 2009; Ferbey et al., 2012); Mount Polley (Hashmi et al., 2015); and Blackwater Davidson (O'Brien et al., 1997; Averill, 2017).

Geochemical soil surveys (i.e., B-horizon soil samples) are still commonly used in for mineral exploration in British Columbia because they are faster and less labour intensive than till sampling. However, in glaciated terrain soil survey results can be misleading because the geochemical anomalies at surface typically do not overlie mineralization. Instead

anomalies reflect metal-rich till that was displaced down-ice from a bedrock source. Chemical processes are largely responsible for element dispersion in soil whereas in till, the dispersal mechanism is mechanical. Soils are also subject to other surficial post-glacial modifications such as colluvial processes, which have been shown to deform and alter the surface geometry of dispersal trains (Paulen, 2001). Numerous studies have been carried out in British Columbia to better understand the complex relationship between soil and till geochemistry and mineralized bedrock such as in the Babine porphyry copper belt (Levson, 2002), over the Galaxy property near Kamloops (Kerr et al., 1993; Lett, 2010), in the Adams Lake area (Lett, 2001) and at Mouse Mountain (Lett, 2009).

This paper describes B-horizon soil and C-horizon glacial sediment sampling on the Ace mineral property (BC MINFILE 093A 142) in the east Cariboo Lake area of central British Columbia (Fig. 1) to establish relationships between the soil and till geochemistry in an area where bedrock is mainly concealed by lodgement till, ablation till, and colluvium. The Ace mineral

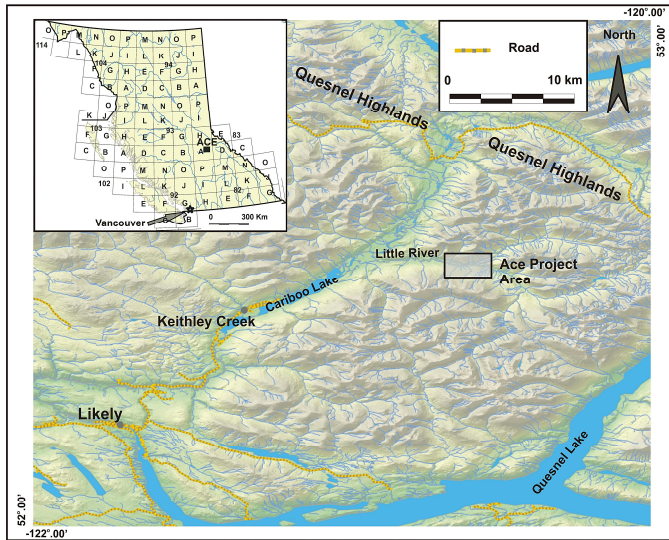


Fig. 1. Ace project location.

property was discovered in 1993 by Mr. Louis Doyle who identified gold grains in sediment panned from a creek flowing through the area. Subsequent prospecting revealed a sulphide-mineralized boulder train crossing the property for several km. Since 1993, mineral exploration identified evidence of base metal massive sulphide mineralization and gold-quartz sulphide veins hosted by Paleozoic metasedimentary and metavolcanic rocks of the Snowshoe Group (Höy and Ferri, 1998). In 2000, a detailed soil and glacial sediment sampling program directed by Peter Bobrowsky, collected 97 till and 81 B and B-C soil horizon samples from 85 sites (Bichler and Bobrowsky, 2000; Lett et al., 2005). This paper describes and presents interpretations of the soil and till geochemistry for the commodity and pathfinder elements Ag, Au, As, Cu, Co, Pb, Se, and Zn.

## 2. Survey area description

### 2.1. Physiography

The Ace property is in the Quesnel Highland, a physiographic subdivision of the Interior Plateau (Fig. 1; Holland, 1976). The property is accessible along gravel roads from the village of Likely, 34 km to the southwest. Topography reflects the erosion of a highly dissected plateau with a moderate relief. The area is drained by the Little River and its tributaries, which flow west into Cariboo Lake. Most of the sampling sites are on a glaciated, northeast-facing valley slope between a ridge to the south and the steep walled Little River valley to the north. Forest canopy species include White spruce, sub-alpine fir, Douglas fir, Lodgepole pine, and aspen with an understory of Devils Club, alder and blackberry. Depending on the surface environment and site drainage, organic, luvisolic, podzolic or brunisolic soils have formed on the glacial deposits.

### 2.2. Surficial geology

The region is blanketed by glacial sediments deposited by the Late Wisconsin Cordilleran Ice Sheet with local post-

glacial modification by Holocene colluvial processes (Bichler and Bobrowsky, 2000). Ice-flow indicators in the region surrounding the Ace property are shown in Figure 2. The limits and extent of a mineralized boulder field in the Ace study area was mapped by Bicher and Bobrowsky (2000); glacial deposit samples included basal till and ablation till (Fig. 3). The basal till has been reworked into colluvium on the steeper slopes of the Little River valley. Ablation till, identified at three sample sites to the south-east of the boulder field, may reflect englacial or supraglacial sediment deposited in the Little River valley during retreat of the ice sheet. Basal till was deposited by ice that flowed from the Cariboo Mountains towards the northwest. One ice-flow measurement of  $165^\circ$  (P. Bobrowsky, pers. comm., 2000) indicates that ice advanced from the southeast to northwest parallel to the Little River valley.

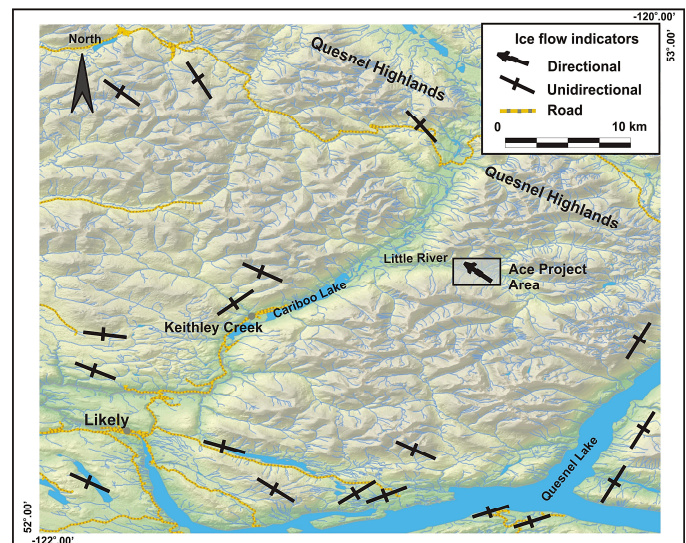


Fig. 2. Regional ice-flow indicators in the area near the Ace property (after Arnold and Ferbey, 2020; Bobrowsky, pers. comm., 2000).

### 2.3. Bedrock geology and mineralization

Tan to pale grey or green and dark grey graphitic phyllite of the Snowshoe Downey succession (lower to middle Paleozoic) underlie the Ace property (Fig. 4). Höy and Ferri (1998) suggested that these phyllites originated as fine-grained sedimentary rocks, but that green, massive chloritic phyllites visible in trenches may be metamorphosed mafic volcanic rocks. Amphibolites outcropping on the hill slope south of the area sampled were interpreted by Höy and Ferri (1998) as diorites or possibly felsic volcanic rocks. North of the Little River, bedrock consists of limestone, black phyllite, and siltstone of the Snowshoe Bralco succession and predominantly quartzite and sandstone of the Cariboo Group (Ferri and O'Brien, 2002). The contact between the Cariboo Group and the Bralco succession is a thrust fault; this thrust is cut by two northeast-trending faults that extend into the Snowshoe Downey sedimentary rocks.

Massive sulphide bodies and gold hosted in quartz veins are two deposit types suspected to be present on the Ace property

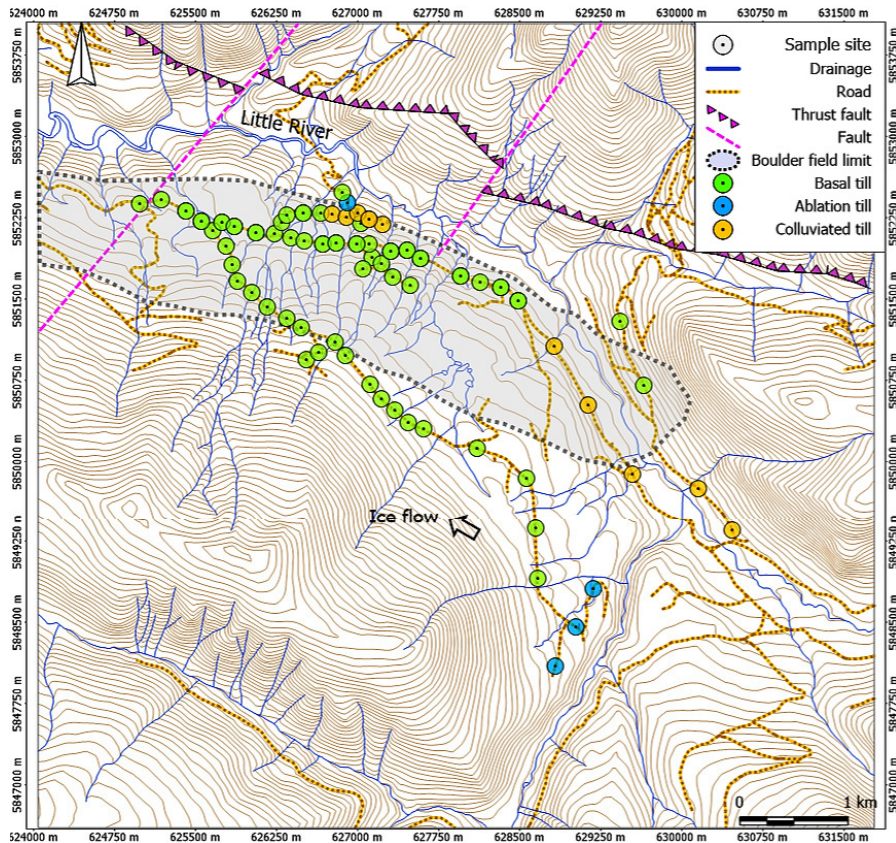


Fig. 3. Glacial sediment sample locations and types of sediment identified; extent of a mineralized boulder field from Bicher and Bobrowsky (2000).

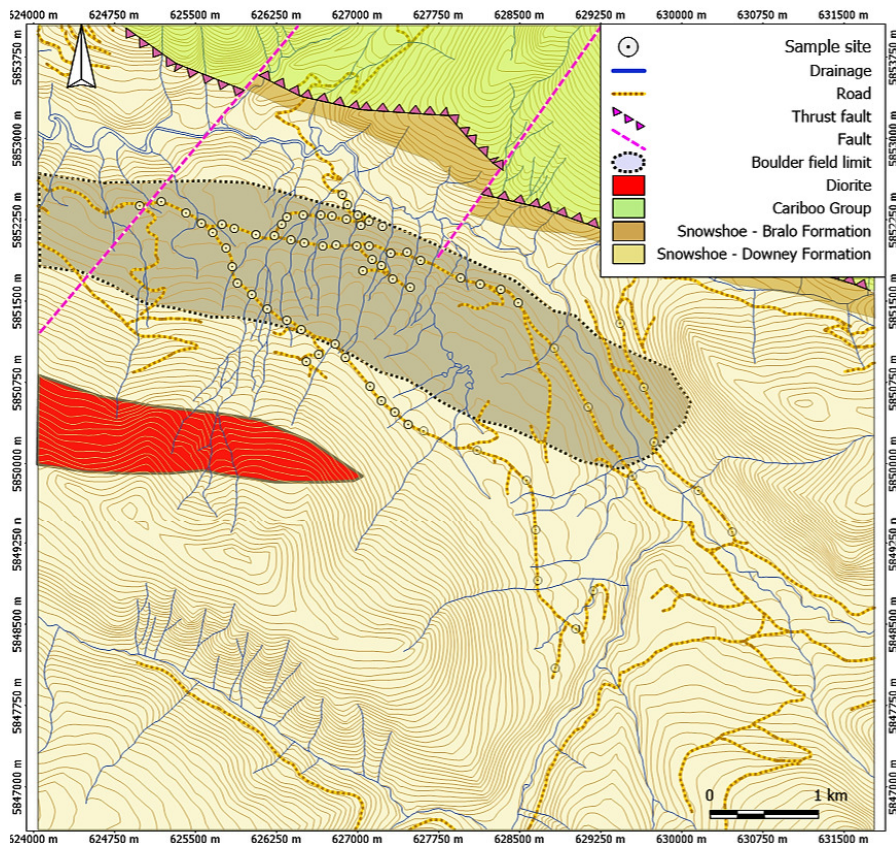


Fig. 4. Bedrock geology of the survey area (after Cui et al., 2017).

based on evidence from float samples, trench exposures, and outcrop. Massive pyrite and pyrrhotite form lenses up to 1.2 m thick in quartz-feldspar-muscovite-chlorite-biotite-garnet schists and 'felsite' interbeds (BC MINFILE 093A 142). Chalcopyrite and sphalerite have also been reported in bedrock and boulders (Höy and Ferri, 1998), but sulphide concentrations are typically less than one percent. Höy and Ferri (1998) interpreted the mineralization to be Besshi-type (Cu-Zn) volcanic massive sulphide (VMS). In addition to the massive sulphides, Au-bearing quartz veins have also been identified on the property, folded within and cross cutting the phyllites (Höy and Ferri, 1998). The veins contain native Au, cubanite, native bismuth, and tourmaline. Geochemical analysis of the vein rock shows elevated Fe, As, Au, Ag, Zn, Cu, Bi, and Te concentrations (Höy and Ferri, 1998).

### 3. Sampling, sample preparation, and analysis

Soil and the parent glacial sediment (i.e., till) were collected on the Ace property at sites between 150 to 200 m apart along the roads using a small backhoe excavator to dig a trench one m wide and several m deep (Fig. 5). After fully describing the soils and the tills upon which they were developed, samples of the B-horizon soil (0.1 to 0.6 m; mean depth 0.28 m), transition from B to C (B-C) horizon (0.2 to 1.1 m mean depth 0.61 m), and C-horizon (0.6 to 3.2 m; mean depth 1.34 m) were described and collected from the trenches for analysis at each

site. Bondar and Clegg Laboratories, North Vancouver, air dried the samples and split them into two sub-samples. One sub-sample was sieved to <0.063 mm grain size (-230 mesh) and the second sub-sample was retained as a character sample. The samples were returned to the British Columbia Geological Survey laboratory in Victoria, for addition of quality control samples before analysis at commercial laboratories.

A 0.5 gram aliquot of the <0.063 mm fraction of each sample was analyzed by Acme Analytical Laboratories Ltd., (now Bureau Veritas) Vancouver, for 37 elements including Ag, As, Au, Bi, Cd, Co, Cu, Hg, Mo, Ni, Pb, Se, Tl, and Zn by a modified aqua regia digestion (1:1:1 solution of HNO<sub>3</sub>-HCl-H<sub>2</sub>O acids) and a combination of inductively coupled plasma-mass spectrometry (ICP-MS) and inductively coupled plasma-emission spectroscopy (ICP-ES). A second aliquot of the <0.063 mm fraction (~30 g) was analyzed by Activation Laboratories, Ancaster, Ontario, by instrumental thermal neutron activation analysis (INAA) for Au and 32 elements.

Selected till and soil samples were also sieved into -10 to +18 mesh (1 to 2 mm); -18 to +35 mesh (0.5 to 1 mm); -35 to +60 mesh (0.250 to 0.5 mm); -60 to +120 mesh (0.125 to 0.250 mm) and -125 to -230 mesh (0.063 to 0.125 mm) size fraction. Samples of each of the fractions were analyzed for 37 elements including Ag, As, Au, Bi, Cd, Co, Cu, Fe, Hg, K, Mo, Ni, Pb, Sb, Se, Te, Tl, and Zn by modified aqua regia digestion (1:1:1

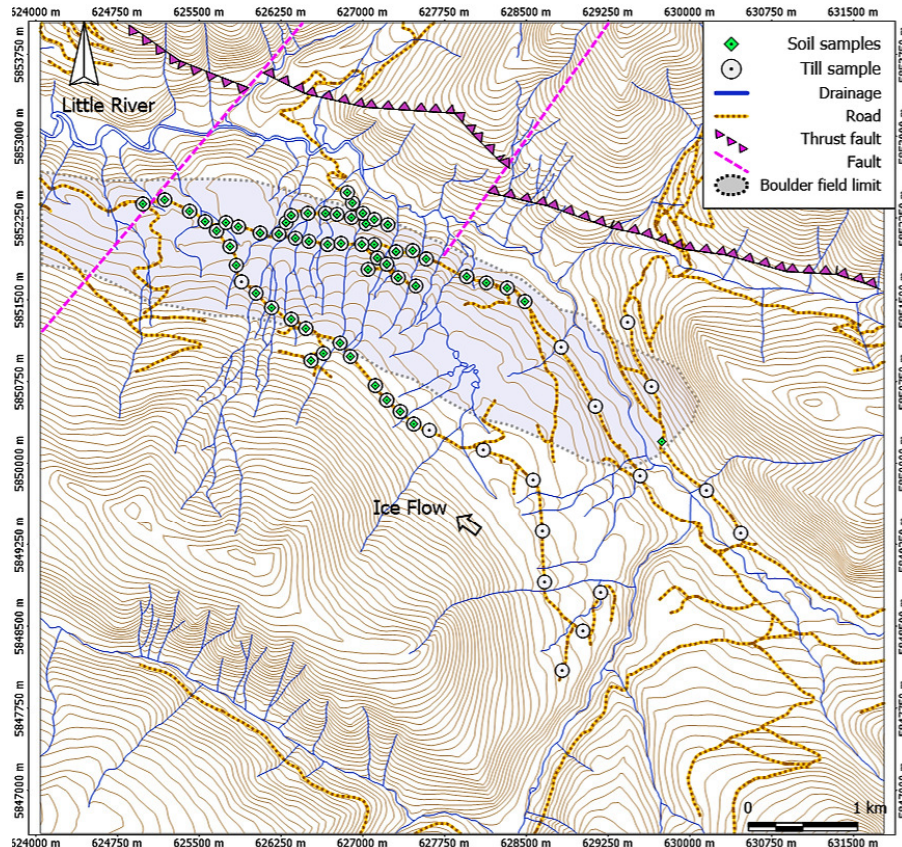


Fig. 5. Till and soil sample locations.

solution of HNO<sub>3</sub>-HCl-H<sub>2</sub>O acids) followed by ICP-MS/ES. This paper describes the geochemistry of 16 of the elements; the full dataset will be presented elsewhere (Lett and Paulen, 2021).

#### 4. Quality control measures

No reliable interpretation of geochemical data is possible unless there is an estimate of the variability, expressed as precision, introduced by the sampling and by the sample analysis. Precision of the Ace geochemical data is estimated by statistical analysis of results from the analysis of sieved duplicate samples collected at field sites, sieved duplicates prepared in the laboratory, and randomly inserted standard reference materials. Table 1 lists detection limits, mean values, and percent relative standard deviation (% RSD) for Ag, As, Au, Bi, Cd, Co, Cu, Hg, Mo, Ni, Pb, Sb, Se, Te, Tl, and Zn in six samples of the British Columbia Geological Survey in-house standard (Till 99) that were analyzed by a modified aqua regia digestion followed by ICP-MS and for Au by INAA. Except for Au, the RSD is less than 15% and the precision is considered acceptable. The greater Au precision by INAA of 12.1%, as compared with 18.7% by aqua regia-ICP-MS, reflects the larger aliquot (typically 30 g) used for the INAA analysis.

An average coefficient of variation, or CV<sub>AVR</sub>(%) calculated from a formula proposed by Abzalov (2008) provides an estimate of sampling precision from the field and laboratory duplicate data (Eqn. 1). In the formula, the terms a and b represent the analyses of the first and second of the duplicate sample pair

$$CV_{AVR}(\%) = 100 \times \sqrt{\frac{2}{N} \sum_{i=1}^N \frac{(a_i - b_i)^2}{(a_i + b_i)^2}} \quad \text{Eqn. 1}$$

and N is the number of duplicate pairs. Values can range from 0%, where duplicate pairs have identical concentrations, to an upper value above 141.21% (i.e., the square root of 2) where duplicate results exhibit maximum differences.

In Table 2, the CV<sub>AVR</sub>(%) values for each element in the <0.063 mm fraction of 15 till-soil field duplicate sample pairs analyzed by aqua regia-ICP-MS/ES and Au by INAA are sorted in order of their increasing field duplicate CV<sub>AVR</sub>(%) value (i.e., good to poor precision). Average coefficient of variation values below 15% (green) indicate good data quality, values between 15 and 30% (blue) acceptable quality, those over 30% (red) marginal to poor quality. Gold Se, Hg, Te, and Bi have marginal precision and the data for these elements should be interpreted with caution.

#### 5. Summary statistics

Tables 3, 4, and 5 list minimum, mean, median, standard deviation (SD), 3rd quartile, 80<sup>th</sup> percentile, 90<sup>th</sup> percentile, 95<sup>th</sup> percentile and maximum values for trace elements in 97 till samples, 26 B-C horizon soil samples, and 55 B-horizon soil samples. Median and 3rd quartile values in the three tables reveal that the elements can: 1) decrease from the till through the B-C horizon to the B horizon; 2) remain essentially the same; or 3) decrease. Silver, Cd, and Mo are higher in the B-horizon soil compared with till, whereas Au, Cu, As, and Zn are higher in the till (Table 6).

**Table 1.** Detection limits (DL), mean values, and percent relative standards deviations from six analyses of the British Columbia Geological Survey standard Till 99 determined by modified aqua regia digestion-ICP-MS and Au by instrumental neutron activation (INAA).

Element	DL	Mean	Pct RSD
Ag ppb ICP	2	1351	4.3
As ppm ICP	0.1	57.5	8.1
Au ppb ICP	0.2	26.6	18.7
Au ppb INAA	2	33.40	12.1
Bi ppm ICP	0.02	0.25	2.0
Cd ppm ICP	0.01	0.67	8.5
Co ppm ICP	0.1	45.0	7.4
Cu ppm ICP	0.01	168.69	2.1
Hg ppb ICP	5	377	3.3
Mo ppm ICP	0.01	0.80	5.6
Ni ppm ICP	0.1	210.6	2.8
Pb ppm ICP	0.01	209.77	2.5
Sb ppm ICP	0.02	10.64	1.9
Se ppm ICP	0.1	0.8	13.3
Te ppm ICP	0.02	0.29	5.1
Tl ppm ICP	0.02	0.10	4.9
Zn ppm ICP	0.1	357.1	6.3

**Table 2.** Average coefficient of variation (CV<sub>AVR</sub>(%)) calculated from the analysis of 15 till and B-horizon soil field duplicate samples analyzed for trace metals by modified aqua regia digestion-ICP-MS and for Au by instrumental neutron activation (INAA). The field duplicate CV<sub>AVR</sub>(%) values are sorted by increasing size. Average coefficient of variation values below 15% (in green) indicate good data quality, values between 15 and 30% (in blue), are acceptable quality and values over 30% (in red) reflect marginal to poor data quality.

Element	Field Duplicate CV <sub>AVR</sub> (%)	Analytical Duplicate CV <sub>AVR</sub> (%)
Zn ppm ICP	5.0	2.7
Tl ppm ICP	5.4	3.6
Ni ppm ICP	7.6	4.2
Co ppm ICP	8.8	4.5
Pb ppm ICP	8.8	4.4
Mo ppm ICP	9.4	4.3
Cu ppm ICP	10.0	2.4
As ppm ICP	13.3	7.4
Se ppm ICP	15.1	36.7
Hg ppb ICP	18.1	25.5
Cd ppm ICP	21.2	14
Ag ppb ICP	22.2	6.4
Sb ppm ICP	23.3	34.9
Te ppm ICP	31.9	24.9
Bi ppm ICP	41.6	5.7
Au ppb ICP	49.7	48.4
Au ppb INAA	66.1	87

**Table 3.** Statistics for trace element data for 97 till samples analyzed by modified aqua regia digestion-ICP-MS and INAA (Au).

Element	Minimum	Mean	Median	SD	3rd Quartile	80 percentile	90 percentile	95 percentile	Maximum
Ag ppb ICP	4.00	60.92	42.00	62.08	77.00	83.40	113.00	179.60	460.00
As ppm ICP	1.10	9.34	3.50	14.91	6.70	8.94	24.02	53.42	69.60
Au ppb ICP	0.60	7.36	3.50	16.15	5.70	6.64	12.28	16.06	132.40
Au ppb INAA	1.00	6.02	1.00	10.01	8.00	9.80	16.00	22.00	74.00
Bi ppm ICP	0.23	1.28	0.89	1.51	1.28	1.36	1.92	3.07	10.54
Cd ppm ICP	0.01	0.21	0.10	0.25	0.22	0.29	0.58	0.79	1.26
Co ppm ICP	13.70	30.17	27.50	10.98	34.70	36.68	41.04	50.13	76.10
Cu ppm ICP	28.70	77.66	74.94	23.42	88.35	95.35	101.61	111.85	163.80
Hg ppb ICP	5.00	19.06	17.00	9.89	24.00	25.60	30.00	33.00	60.00
Mo ppm ICP	0.36	1.84	0.95	2.49	1.73	2.30	4.05	5.65	16.69
Ni ppm ICP	37.30	65.97	64.60	16.70	72.80	77.70	91.28	96.86	113.20
Pb ppm ICP	7.25	29.57	19.04	29.52	32.34	35.01	63.09	77.30	231.55
Sb ppm ICP	0.01	0.07	0.06	0.07	0.08	0.09	0.14	0.19	0.45
Se ppm ICP	0.05	0.54	0.40	0.41	0.80	0.90	1.10	1.20	1.90
Te ppm ICP	0.01	0.07	0.06	0.04	0.08	0.08	0.10	0.16	0.24
Tl ppm ICP	0.08	0.27	0.25	0.09	0.08	0.32	0.38	0.45	0.64
Zn ppm ICP	58.70	115.40	94.90	55.35	133.90	133.94	177.44	208.85	415.90

**Table 4.** Statistics for trace element data for 26 B-C soil horizon samples analyzed by modified aqua regia digestion-ICP-MS and INAA (Au).

Element	Minimum	Mean	Median	SD	3 Quartile	80 percentile	90 percentile	95 percentile	Maximum
Ag ppb ICP	28	224	188	141	281	298	400	495	665
As ppm ICP	1.30	6.07	3.30	11.35	5.10	5.22	7.96	17.82	79.90
Au ppb ICP	0.10	5.02	1.70	15.39	2.85	3.12	4.32	18.40	109.90
Au ppb INAA	1	3	1	4	1	4	10	14	16
Bi ppm ICP	0.33	1.01	0.76	1.20	1.09	1.15	1.56	1.97	9.06
Cd ppm ICP	0.03	0.21	0.17	0.14	0.27	0.29	0.40	0.45	0.67
Co ppm ICP	7.70	18.42	17.10	6.38	21.95	23.52	26.92	30.50	38.30
Cu ppm ICP	15.24	43.17	38.21	19.35	54.92	56.33	63.76	74.35	109.62
Hg ppb ICP	7	77	75	29	90	98	113	121	158
Mo ppm ICP	0.55	1.76	1.31	1.37	2.10	2.22	3.37	4.01	8.88
Ni ppm ICP	15.4	41.5	37.7	16.9	52.8	55.5	65.9	74.9	91.2
Pb ppm ICP	10.25	21.00	16.90	13.20	21.35	23.50	36.61	49.26	74.97
Sb ppm ICP	0.01	0.07	0.06	0.05	0.09	0.09	0.12	0.14	0.32
Se ppm ICP	0.1	0.6	0.6	0.2	0.7	0.8	1.0	1.1	1.2
Te ppm ICP	0.01	0.05	0.04	0.03	0.06	0.06	0.08	0.09	0.15
Tl ppm ICP	0.08	0.15	0.15	0.04	0.17	0.17	0.20	0.22	0.23
Zn ppm ICP	38.5	104.9	92.5	47.0	119.9	132.2	153.5	200.1	295.2

**Table 5.** Statistics for trace element data for 55 B-horizon soil samples analyzed by modified aqua regia digestion-ICP-MS and INAA (Au).

Element	Minimum	Mean	Median	SD	3 Quartile	80 percentile	90 percentile	95 percentile	Maximum
Ag ppb ICP	28	224	188	141	281	298	400	495	665
As ppm ICP	1.30	6.07	3.30	11.35	5.10	5.22	7.96	17.82	79.90
Au ppb ICP	0.10	5.02	1.70	15.39	2.85	3.12	4.32	18.40	109.90
Au ppb INAA	1	3	1	4	1	4	10	14	16
Bi ppm ICP	0.33	1.01	0.76	1.20	1.09	1.15	1.56	1.97	9.06
Cd ppm ICP	0.03	0.21	0.17	0.14	0.27	0.29	0.40	0.45	0.67
Co ppm ICP	7.70	18.42	17.10	6.38	21.95	23.52	26.92	30.50	38.30
Cu ppm ICP	15.24	43.17	38.21	19.35	54.92	56.33	63.76	74.35	109.62
Hg ppb ICP	7	77	75	29	90	98	113	121	158
Mo ppm ICP	0.55	1.76	1.31	1.37	2.10	2.22	3.37	4.01	8.88
Ni ppm ICP	15.4	41.5	37.7	16.9	52.8	55.5	65.9	74.9	91.2
Pb ppm ICP	10.25	21.00	16.90	13.20	21.35	23.50	36.61	49.26	74.97
Sb ppm ICP	0.01	0.07	0.06	0.05	0.09	0.09	0.12	0.14	0.32
Se ppm ICP	0.1	0.6	0.6	0.2	0.7	0.8	1.0	1.1	1.2
Te ppm ICP	0.01	0.05	0.04	0.03	0.06	0.06	0.08	0.09	0.15
Tl ppm ICP	0.08	0.15	0.15	0.04	0.17	0.17	0.20	0.22	0.23
Zn ppm ICP	38.5	104.9	92.5	47.0	119.9	132.2	153.5	200.1	295.2

**Table 6.** Element increase/decrease from till through BC soil horizon to B soil horizon based on 3<sup>rd</sup> quartile values listed in Tables 3 to 5. The increase/decrease is shown as a shaded bar; dark blue = high concentration, light blue = low concentration. Left side of plot is till, middle of plot is B-C soil horizon, right side of plot is B-horizon soil.

Element	Till	BC Soil Horizon	B Soil Horizon
Ag ppb ICP			
As ppm ICP			
Au ppb ICP			
Au ppb INAA			
Bi ppm ICP			
Cd ppm ICP			
Co ppm ICP			
Co ppm INAA			
Cu ppm ICP			
Hg ppb ICP			
Mo ppm ICP			
Ni ppm ICP			
Pb ppm ICP			
Sb ppm ICP			
Se ppm ICP			
Te ppm ICP			
Tl ppm ICP			
Zn ppm ICP			

## 6. Element associations

A Pearson product-moment correlation coefficient matrix of Ag, As, Au, Bi, Cd, Co, Cu, Hg, Mo, Ni, Pb, Sb, Se, Te, Tl, and Zn by modified aqua regia-ICP-MS and Au by INAA for the <0.063 mm fraction of 97 till samples reveals significant positive correlations ( $>+0.65$ ) between As-Bi-Pb-Cd-Co, Zn-Cd-Mo-Pb-Se, and between Cu-Ni (Table 7). In the <0.063 mm B-C soil horizon samples (26) the most significant positive correlations ( $>+0.65$ ) are between As-Cd-Hg, Cu-Ni-Tl and Zn-Cd-Mo (Table 8) and in 55 B-horizon soil samples, the significant positive correlations ( $>+0.65$ ) are between As-Hg, Bi-Pb and Co-Ni-Tl (Table 9).

### 6.1. Elements in B-horizon soil and till size fractions

Box and whisker plots compare the range of values of Au, Ag, Cu, Pb, and Zn in till and the B-horizon soil samples sieved to 1-2 mm, 0.5-1 mm; 0.250-0.5 mm; 0.125-0.250 mm; 0.063-0.125 mm and <0.063 mm size fractions. Zinc (Fig. 6), Pb (Fig. 7), and Cu (Fig. 8) typically have higher median and outlier values in the <0.063 mm size fraction of the till samples compared with the metal content of larger size fractions. Zinc and Cu are also lower in all B-horizon soil sample fractions compared to values in the till fractions. Similar to Cu and Zn, Pb is higher in the <0.063 mm and 0.125 to 0.063 mm till sample fractions. However, the trend is reversed for the 1-2 mm, 0.5-1 mm; 0.250-0.5 mm; 0.125 mm fractions; in these, Pb is higher in the soil compared with the till. The similar Pb content of the larger grain sizes from the soil may reflect weathering of discrete Pb mineral grains from till or bedrock and their incorporation into the soil.

Most till size fractions contain more Au than the B-horizon soil size fractions (Fig. 9). However, one soil sample on the northern boundary of the survey area contains 464 ppb Au in the 1-2 mm fraction but the underlying till contains no detectable (i.e.,  $>0.2$  ppb) Au. Three till samples contain  $>48$  ppb Au in all of the fractions, which could indicate that discrete Au grains are distributed through the till (i.e., the 'nugget effect'). The Ag content is higher in all soil fractions compared with the till (Fig. 10).

### 6.2. Variation of metals in B-horizon soil and till

The spatial variation of Au, As, Cu, Pb, Se and Zn in soil and till is shown in Figures 11 to 18. These elements are common geochemical pathfinders for Cu-Pb-Zn VMS (Moon et al., 2006; McClenaghan and Peter, 2016) and can be for quartz vein-hosted Au mineralization. Till samples were collected at two depths at a number of sites. For consistency, only element values for the deeper of the two samples are plotted as a bullet symbol in the figures. B-horizon soil values are plotted as a diamond symbol. Symbol size intervals correspond to the minimum to mean value, mean to 80<sup>th</sup> percentile value, 80<sup>th</sup> to 90<sup>th</sup> percentile value, 90<sup>th</sup> to 95<sup>th</sup> percentile value and 95<sup>th</sup> to the maximum value. Unless otherwise stated anomalous values are greater than the 95<sup>th</sup> percentile.

Several till samples on a road traverse along the northern

boundary of the survey area (A-A') have anomalous Pb concentrations ( $>95^{\text{th}}$  percentile); at one site at the east end of this road, Pb concentration is 232 ppm (Fig. 11). Lead content is anomalous in both B-horizon soil and till at this site, but values decrease to less than 77 ppm to the west along a series of contiguous samples. In several of the till and B-horizon soil samples, grain size fractions  $>0.063$  mm also contain anomalous Pb contents (Fig. 11). Isolated high Pb values are in the B-horizon soil and till on two other road traverses to the south and to the west (B-B'; C-C').

The locations of anomalous Zn concentrations in till are similar to those for Pb, with the highest values in samples along the northern boundary of the survey area (A-A', Figs. 12, 13). Zinc concentrations in till decrease to the west from a peak at the east end of the road traverse. However, the highest B-horizon soil Zn value is 500 m west of the highest Zn value in till. The variation of Se concentration, a VMS pathfinder element, (Fig. 14) reveals a single till sample with higher Se ( $>1.5$  ppm) at the east end of the northern road traverse, corresponding to anomalous Pb and Zn values.

Several contiguous till samples along the northern road traverse have Cu concentrations between 95 and 111 ppm and an anomalous value ( $>111$  ppm) at the east end of the traverse (Figs. 15, 16). Isolated Cu anomalies are also in the till and B-horizon soil along the southern road traverse and at the western end of the survey area, where high concentrations of Cu, Zn and Pb in till coincide with a northeast-trending fault.

High concentrations of Pb and Zn in soil and till samples are on the western boundary of the survey area (Figs. 11-13). Element values in the three samples from this profile at the site coincident with a northeast-trending fault (Fig. 12) are listed in Table 10. Most element contents are higher in the till than in the B horizon. Silver and Hg concentrations are exceptions to this trend and are higher in the B-horizon soil.

Four till samples have anomalous Au (INAA) values ( $>22$  ppb) and three other sites contain  $>15$  ppb in the soil (Fig. 17). One site west of where road traverses A-A' and B-B' meet has anomalous Au in soil and several contiguous till samples have anomalous As (Fig. 18). Three till samples contain anomalous Au concentrations in the sizes fractions  $>0.063$  mm (Fig. 17). However, only one site on the southern road traverse has an anomalous Au content in the <0.063 mm size fractions (Table 11). One sample site on the northern road traverse contains 463 ppb Au in the 1 to 2 mm fraction of the B-horizon soil, but no Au in the <0.063 mm fraction of the soil and till.

## 7. Summary and discussion

This paper interprets data for 16 elements from till, B-C and B-horizon soil samples collected on the Ace property in central British Columbia. These elements are considered geochemical pathfinders for gold and base metal mineralization (e.g., Moon et al., 2006; McClenaghan and Peter, 2016; McClenaghan and Paulen, 2018), and significant positive correlations in the till samples could indicate precious metal (As-Sb), VMS

**Table 7.** Correlation coefficient matrix for Ag, As, Au, Bi, Cd, Co, Cu, Hg, Mo, Pb, Sb, Se, Te, Tl, and Zn analyzed by modified aqua regia-ICP-MS and Au by INAA in 97 till samples. Gold, Ag, and Hg are in ppb; other elements in ppm. The data are log transformed. Coefficients greater than +0.65 are highlighted in red.

	Ag	As	Au	Au INA	Bi	Cd	Co	Cu	Hg	Mo	Ni	Pb	Sb	Se	Te	Tl	Zn
<b>Ag</b>	1.00																
<b>As</b>	0.47	1.00															
<b>Au</b>	0.19	0.28	1.00														
<b>Au INA</b>	0.10	-0.08	0.21	1.00													
<b>Bi</b>	0.44	0.45	0.36	0.24	1.00												
<b>Cd</b>	0.37	0.49	0.25	0.20	0.51	1.00											
<b>Co</b>	0.31	0.43	0.28	0.23	0.67	0.51	1.00										
<b>Cu</b>	0.11	0.30	0.35	0.25	0.51	0.45	0.77	1.00									
<b>Hg</b>	0.26	0.23	0.24	0.01	0.26	0.29	0.27	0.07	1.00								
<b>Mo</b>	0.32	0.41	0.22	0.15	0.58	0.75	0.52	0.43	0.39	1.00							
<b>Ni</b>	0.29	0.38	0.23	0.18	0.56	0.44	0.81	0.70	0.18	0.42	1.00						
<b>Pb</b>	0.46	0.68	0.38	0.16	0.72	0.69	0.78	0.57	0.36	0.69	0.63	1.00					
<b>Sb</b>	0.28	0.55	0.30	0.15	0.26	0.63	0.29	0.40	0.17	0.44	0.22	0.50	1.00				
<b>Se</b>	0.23	0.36	0.19	0.13	0.42	0.60	0.45	0.28	0.39	0.68	0.46	0.53	0.38	1.00			
<b>Te</b>	0.42	0.41	0.32	0.18	0.71	0.51	0.67	0.61	0.23	0.57	0.55	0.66	0.27	0.38	1.00		
<b>Tl</b>	-0.16	-0.14	-0.21	-0.07	0.09	0.10	0.30	0.33	0.09	0.22	0.19	0.13	-0.02	-0.07	0.16	1.00	
<b>Zn</b>	0.32	0.46	0.22	0.21	0.53	0.79	0.61	0.51	0.19	0.76	0.57	0.78	0.49	0.53	0.51	0.09	1.00

**Table 8.** Correlation coefficient matrix for Ag, As, Au, Bi, Cd, Co, Cu, Hg, Mo, Pb, Sb, Se, Te, Tl, and Zn analyzed by modified aqua regia-ICP-MS and Au by INAA in 26 B-C horizon soil samples. Gold, Ag and Hg are in ppb; other elements in ppm. The data are log transformed. Coefficients greater than +0.65 are highlighted in red.

	Ag	As	Au	Au INAA	Bi	Cd	Co	Cu	Hg	Mo	Ni	Pb	Sb	Se	Te	Tl	Zn
<b>Ag</b>	1.00																
<b>As</b>	0.23	1.00															
<b>Au</b>	-0.09	0.31	1.00														
<b>Au INAA</b>	0.15	0.12	0.23	1.00													
<b>Bi</b>	0.16	0.30	0.29	0.16	1.00												
<b>Cd</b>	0.82	0.22	0.03	0.11	0.13	1.00											
<b>Co</b>	0.05	0.56	0.40	0.19	0.34	0.17	1.00										
<b>Cu</b>	-0.12	0.30	0.46	0.19	0.36	-0.06	0.81	1.00									
<b>Hg</b>	0.67	0.06	-0.08	0.03	0.21	0.67	-0.03	-0.20	1.00								
<b>Mo</b>	0.51	-0.19	-0.04	0.18	0.20	0.58	-0.12	-0.23	0.42	1.00							
<b>Ni</b>	0.09	0.56	0.44	0.12	0.45	0.28	0.87	0.73	0.08	0.12	1.00						
<b>Pb</b>	0.23	0.49	0.47	0.20	0.59	0.45	0.64	0.53	0.12	0.15	0.72	1.00					
<b>Sb</b>	-0.12	0.25	0.04	0.41	0.26	0.05	0.10	0.11	0.11	-0.04	0.13	0.12	1.00				
<b>Se</b>	0.40	0.09	0.00	0.01	0.27	0.49	0.07	-0.13	0.45	0.40	0.12	0.46	0.02	1.00			
<b>Te</b>	0.25	0.35	-0.04	0.11	0.63	0.22	0.20	0.03	0.39	0.30	0.34	0.42	0.29	0.46	1.00		
<b>Tl</b>	-0.09	0.17	0.29	-0.09	0.20	0.23	0.66	0.65	-0.08	0.01	0.75	0.66	-0.01	-0.06	0.12	1.00	
<b>Zn</b>	0.54	0.03	-0.01	0.14	0.09	0.70	0.24	-0.02	0.42	0.71	0.37	0.35	-0.02	0.40	0.31	0.28	1.00

**Table 9.** Correlation coefficient matrix for Ag, As, Au, Bi, Cd, Co, Cu, Hg, Mo, Pb, Sb, Se, Te, Tl, and Zn analyzed by modified aqua regia-ICP-MS and Au by INAA in 55 B-horizon soil samples. Gold, Ag and Hg are in ppb; other elements in ppm. The data are log transformed. Coefficients greater than +0.65 are highlighted in red.

	Ag	As	Au	Au INAA	Bi	Cd	Co	Cu	Hg	Mo	Ni	Pb	Sb	Se	Te	Tl	Zn
<b>Ag</b>	1.00																
<b>As</b>	0.14	1.00															
<b>Au</b>	-0.08	0.29	1.00														
<b>Au INAA</b>	0.14	0.29	0.36	1.00													
<b>Bi</b>	0.07	0.31	0.30	0.46	1.00												
<b>Cd</b>	0.57	0.29	-0.16	0.16	0.13	1.00											
<b>Co</b>	-0.06	0.21	0.17	0.06	0.01	0.12	1.00										
<b>Cu</b>	-0.07	-0.03	0.20	-0.04	-0.16	-0.08	0.70	1.00									
<b>Hg</b>	0.69	0.12	-0.12	0.06	-0.17	0.31	-0.12	-0.12	1.00								
<b>Mo</b>	0.47	0.29	-0.18	0.31	0.42	0.57	-0.24	-0.38	0.18	1.00							
<b>Ni</b>	-0.26	0.05	0.17	0.02	0.08	-0.07	0.76	0.51	-0.36	-0.30	1.00						
<b>Pb</b>	0.18	0.49	0.09	0.48	0.67	0.40	0.16	-0.08	0.02	0.44	0.18	1.00					
<b>Sb</b>	0.42	0.35	-0.01	0.25	0.20	0.55	0.16	0.04	0.37	0.37	-0.03	0.42	1.00				
<b>Se</b>	0.34	0.40	0.13	0.27	0.08	0.47	0.04	-0.10	0.36	0.33	-0.16	0.30	0.43	1.00			
<b>Te</b>	0.03	0.19	0.12	0.21	0.61	0.04	-0.05	-0.18	-0.14	0.39	0.08	0.38	0.10	0.03	1.00		
<b>Tl</b>	-0.34	-0.03	0.19	-0.03	-0.05	-0.12	0.71	0.58	-0.45	-0.36	0.77	0.09	-0.08	-0.22	-0.08	1.00	
<b>Zn</b>	0.36	0.29	0.03	0.21	0.37	0.55	0.28	-0.08	0.02	0.48	0.36	0.52	0.35	0.21	0.34	0.16	1.00

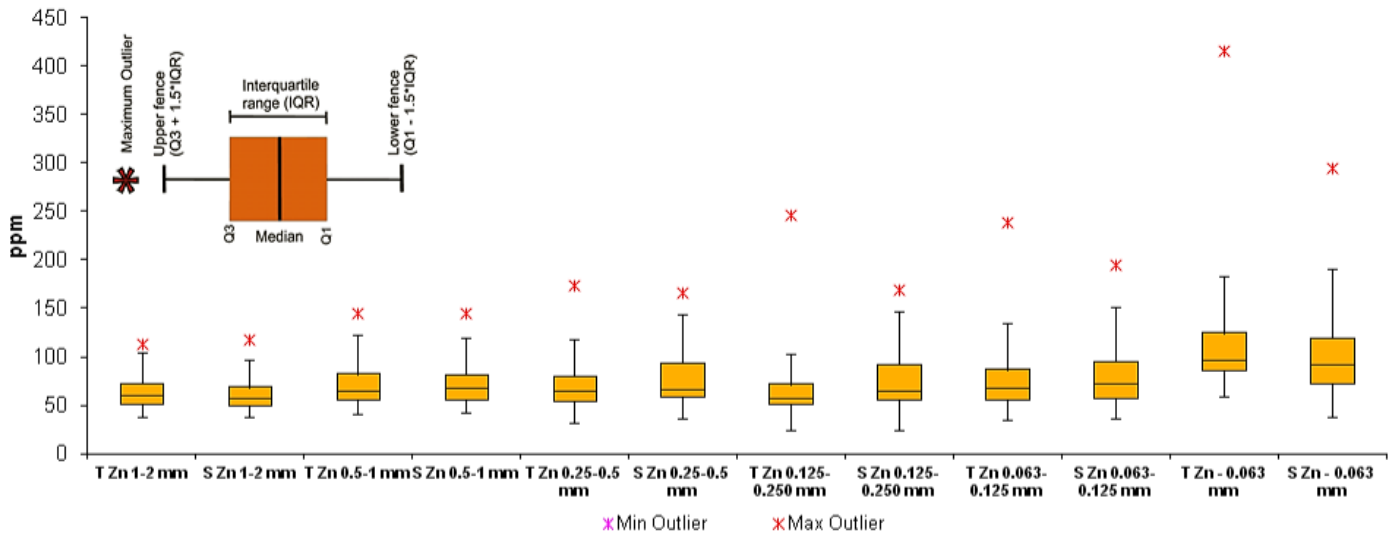


**Fig. 6.** Box and whisker plot for Zn by aqua regia-ICP-MS in till (T) and B-horizon soil (S) in size fractions ranging from 1-2 mm to <0.063 mm.

(Zn-Cd-Pb-Se), and magmatic massive sulphide (Cu-Co-Ni) mineralization. These element associations are also present, but modified, in the B-C and B-horizon soil samples. In the B-horizon soil, there is a significant correlation between Au and As that is common in Au mineralization. Selected elements in different size fractions show that Au, Cu, Pb, and Zn concentrations are generally higher in the <0.063 mm fraction of till (e.g., McClenaghan and DiLabio, 1993), whereas Ag and Hg concentrations are elevated in the B-horizon soil. The higher metal content of the <0.063 mm fraction relative to the coarser

fractions of till in this study, is commonly observed elsewhere (e.g., DiLabio, 1988, 1995). The higher metal concentrations in the finer fraction usually reflects the finer grain size of the metals in the host rocks as well as diminution of ore minerals during glacial erosion, transport, and deposition to silt and clay sized particles (e.g., McClenaghan and Peter, 2016). In experimental studies that examined the origin of the fine fraction in tills, Mäkinen (1995) observed that as the degree of sediment grinding increased, the contents of some metals (Co, Cu, Fe, Mn, Ni, Zn) decreased in comparison to the overall

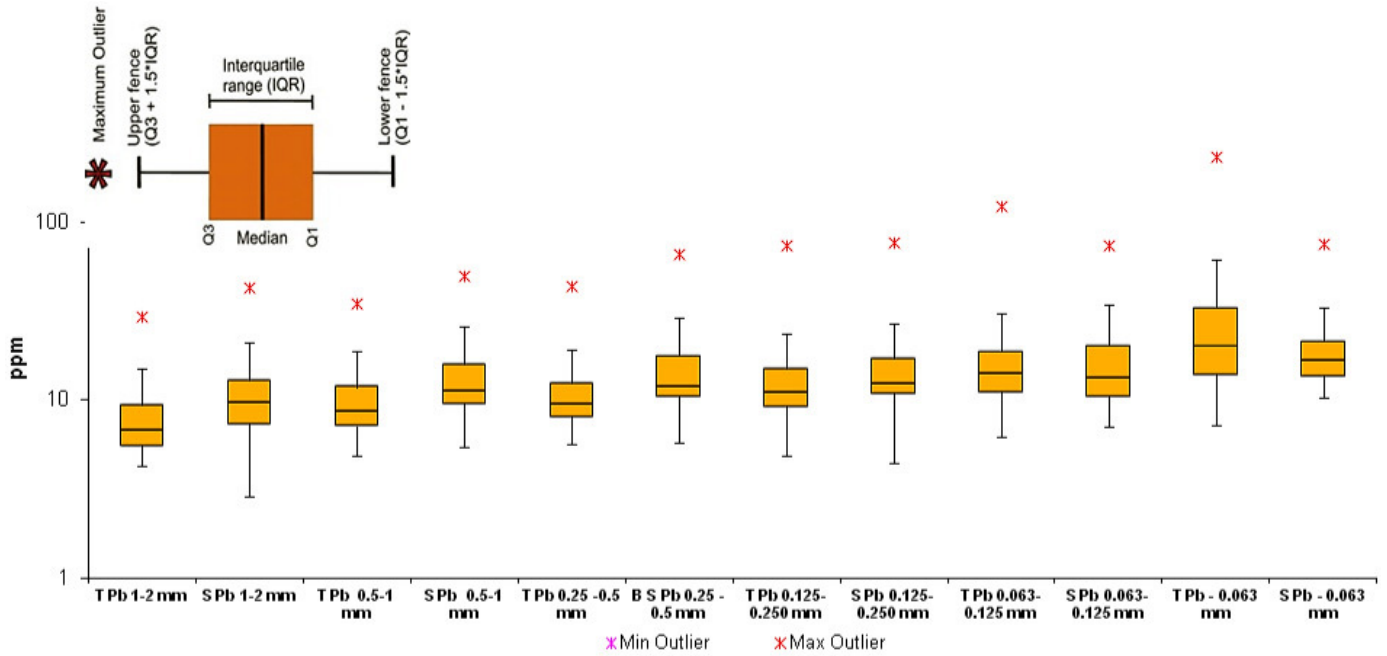


Fig. 7. Box and whisker plot for Pb by aqua regia-ICP-MS in till (T) and B-horizon soil (S) in size fractions ranging from 1-2 mm to <0.063 mm (see Figure 6 for box plot legend).

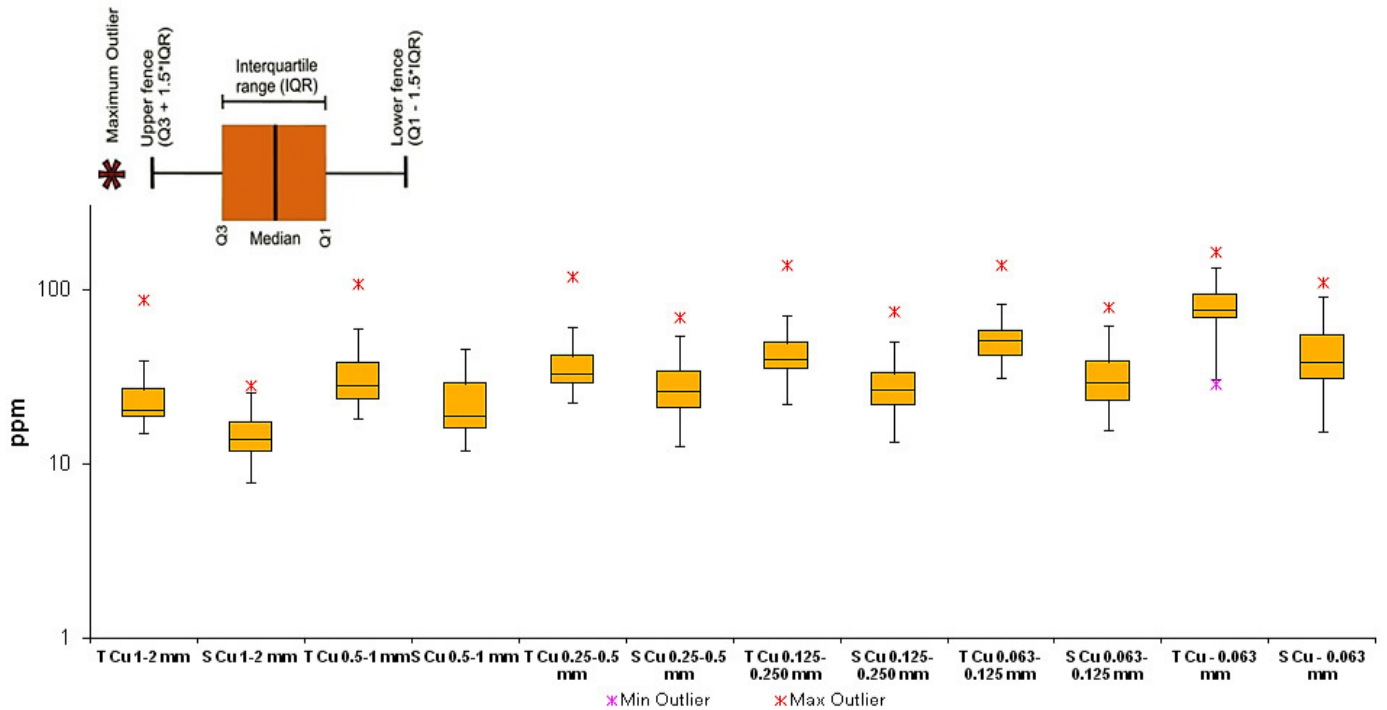


Fig. 8. Box and whisker plot for Cu by aqua regia-ICP-MS in till (T) and B-horizon soil (S) in size fractions ranging from 1-2 mm to <0.063 mm (see Figure 6 for box plot legend).

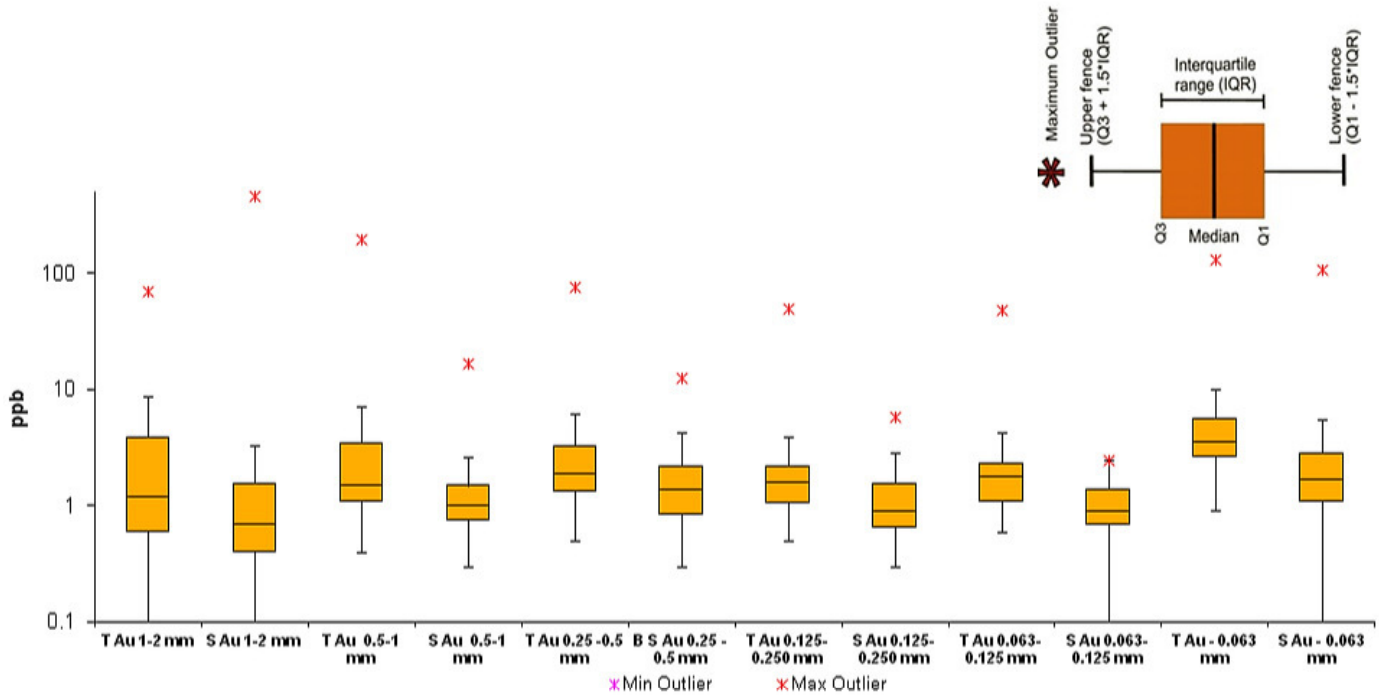


Fig. 9. Box and whisker plot for Au by aqua regia-ICP-MS in till (T) and B-horizon soil (S) in size fractions ranging from 1-2 mm to <0.063 mm (see Figure 6 for box plot legend).

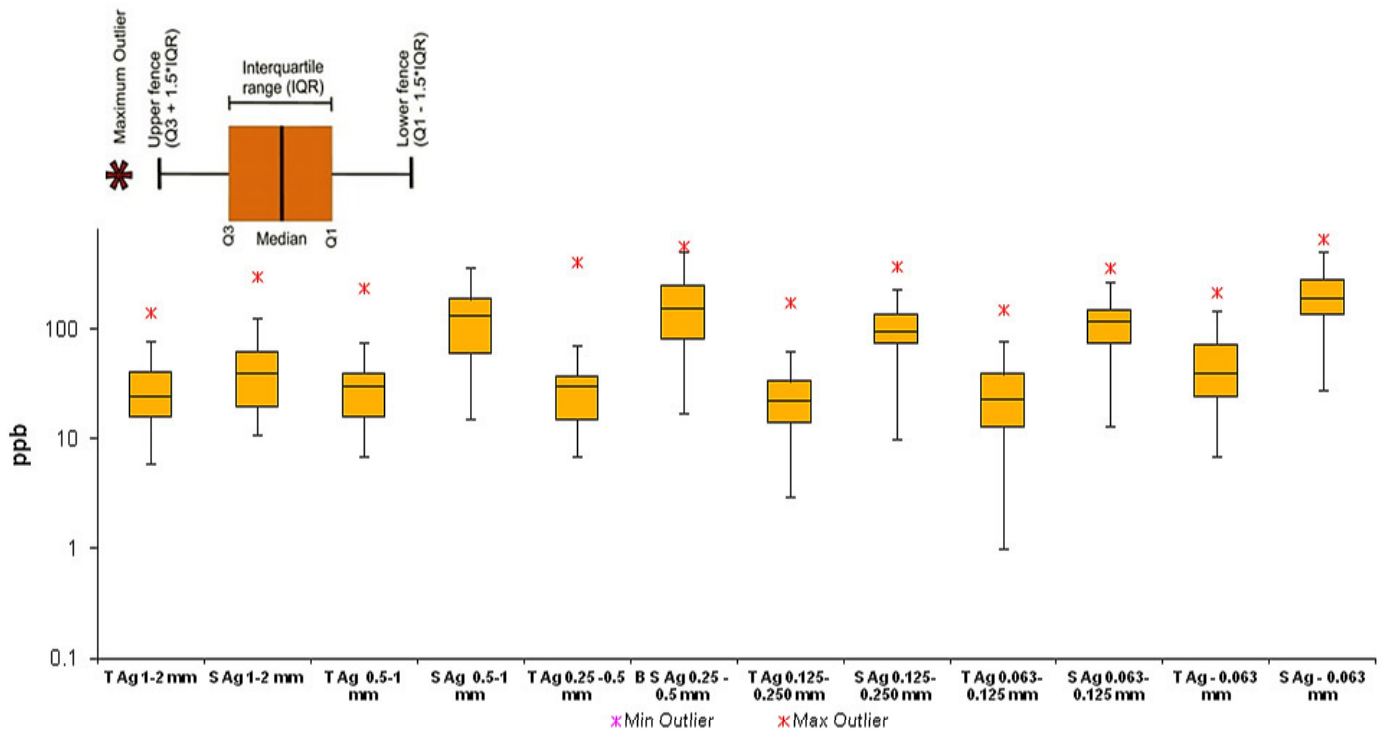


Fig. 10. Box and whisker plot for Ag by aqua regia-ICP-MS in till (T) and B-horizon soil (S) in size fractions ranging from 1-2 mm to 0.063 mm (see Figure 6 for box plot legend).

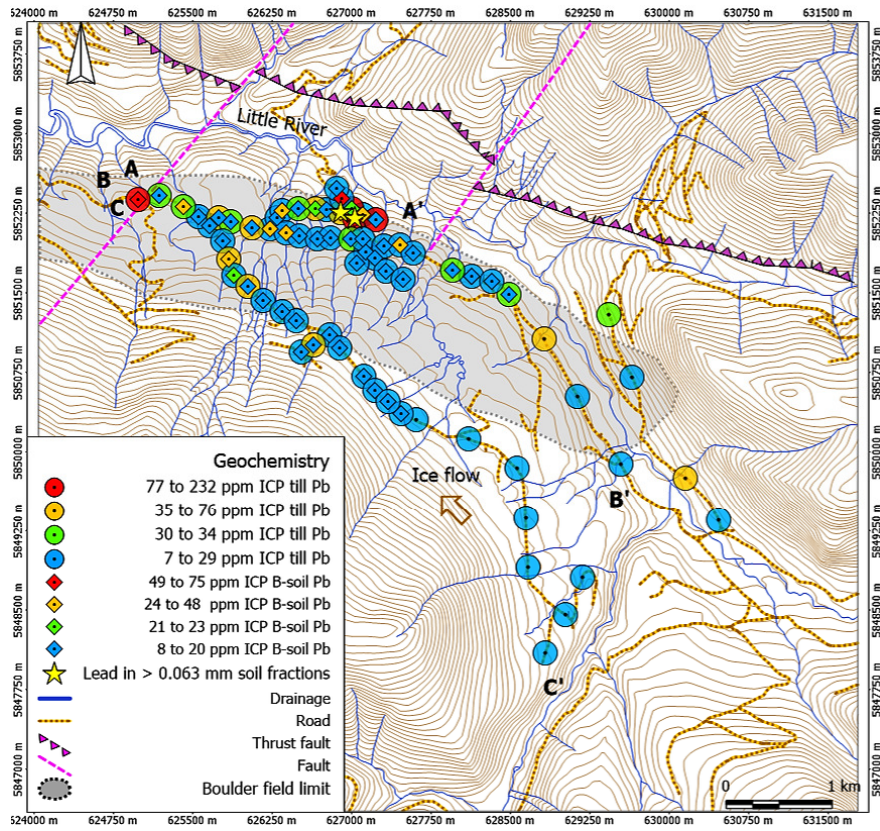


Fig. 11. Lead concentration in the <0.063 mm fraction of till and B-horizon soil determined by aqua regia-ICP-MS. A-A'; B-B' and C-C' refer to road traverses described in the text.

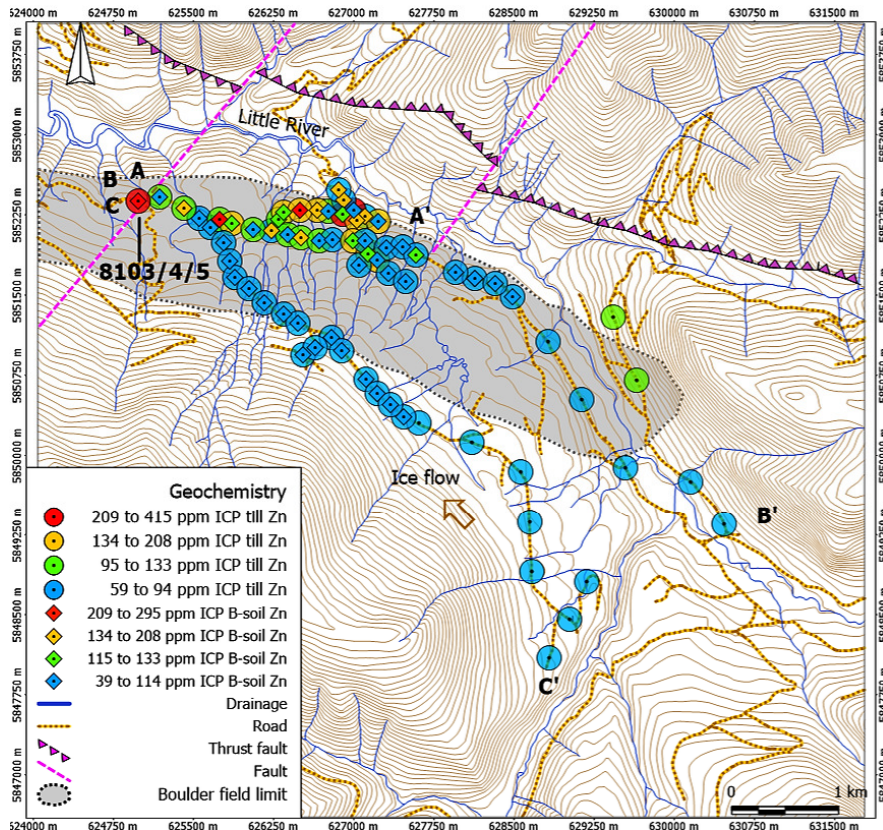


Fig. 12. Zinc concentration in the <0.063 mm fraction of till and B-horizon soil by aqua regia-ICP-MS.

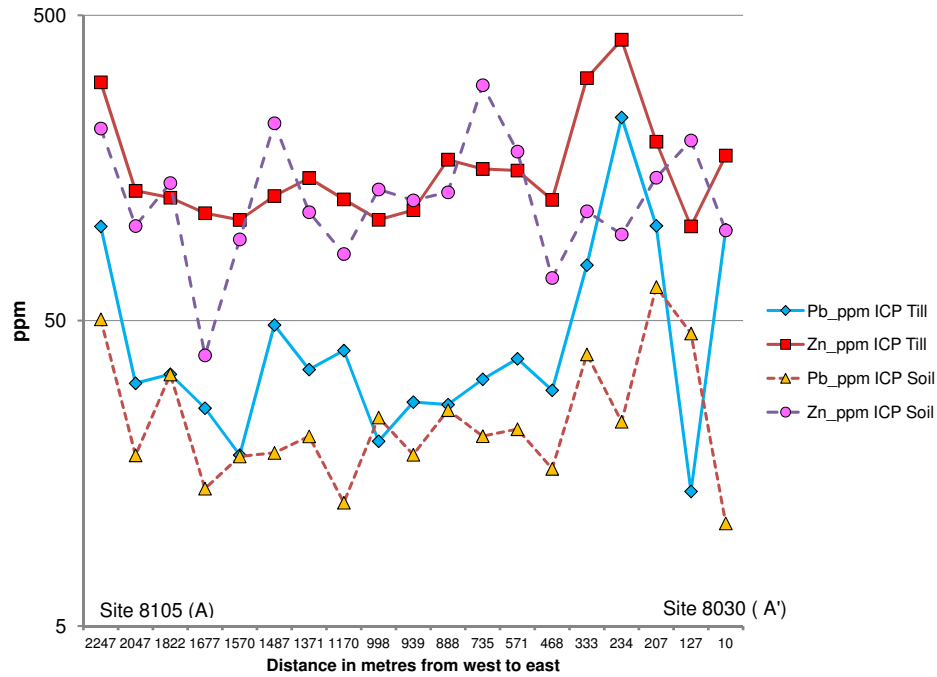


Fig. 13. Lead and Zn concentration in the <0.063 mm fraction of till and B-horizon soil determined by aqua regia-ICP-MS along the northern W-E road traverse (A-A').

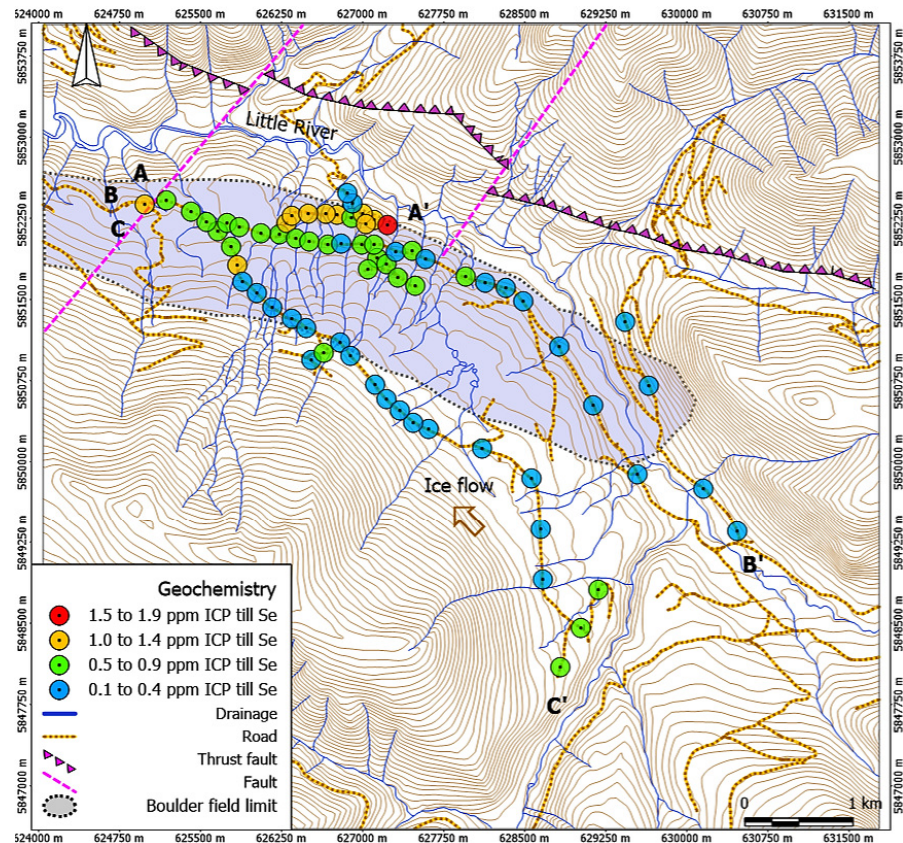


Fig. 14. Selenium concentration in the <0.063 mm fraction of till analyzed by aqua regia-ICP-MS.

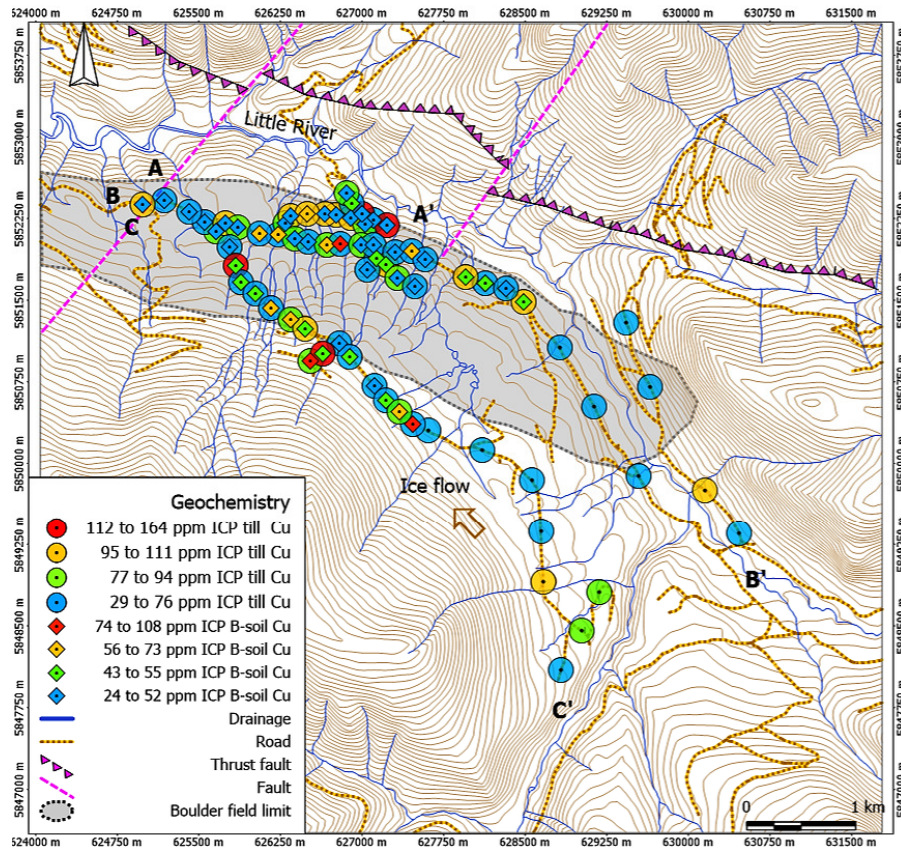


Fig. 15. Copper concentration in the <0.063 mm fraction of till and B-horizon soil analyzed by aqua regia-ICP-MS.

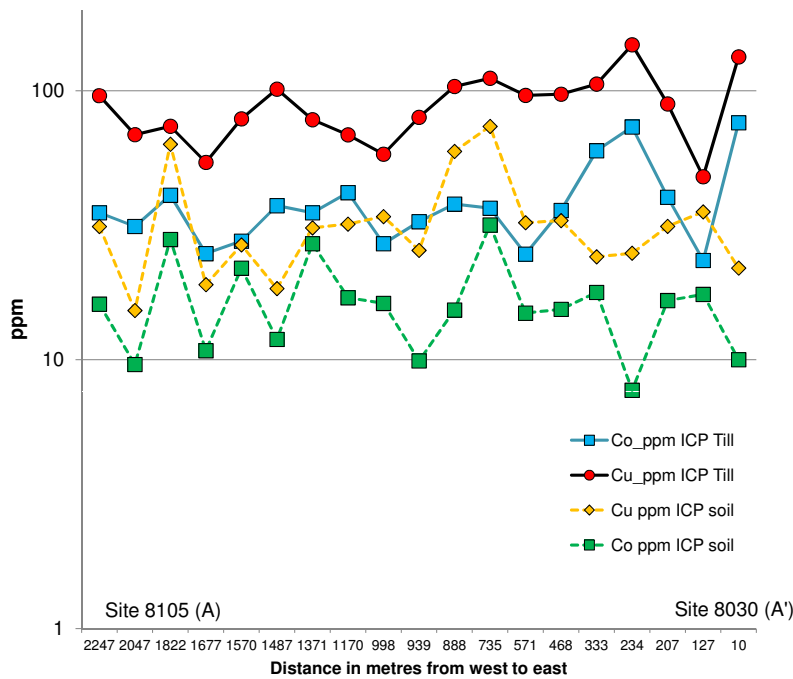


Fig. 16. Comparison of Cu and Co concentrations in the <0.063 mm fraction of till and B-horizon soil samples determined by aqua regia-ICP-MS along the northern road traverse A-A'.

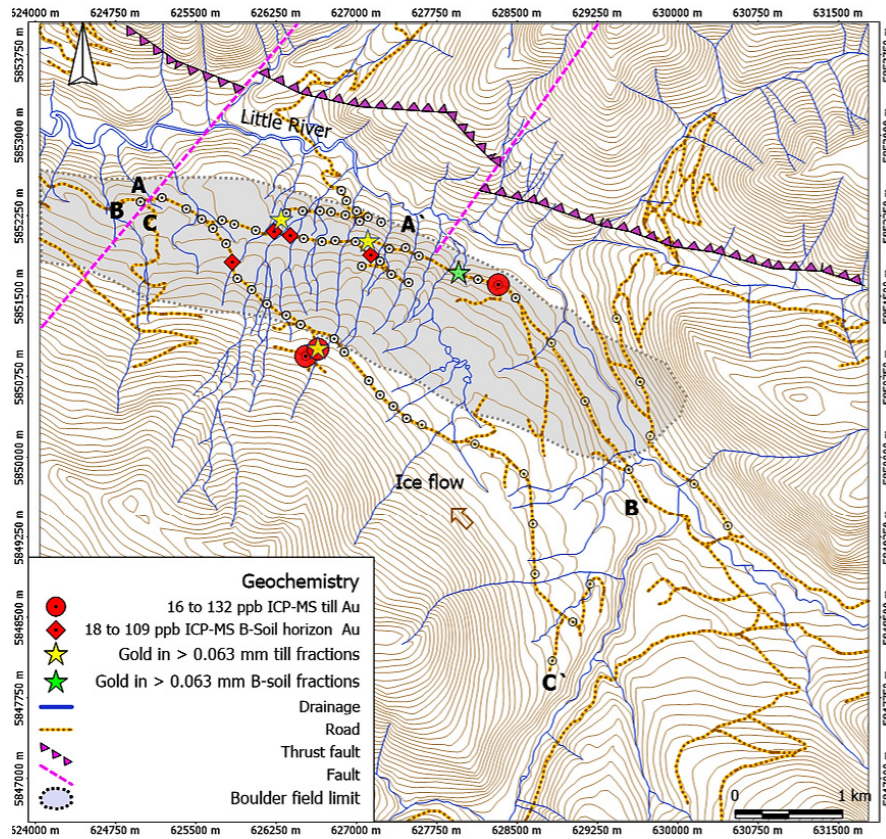


Fig. 17. Anomalous Au concentrations in B-horizon soil and till in the <0.063 mm fraction determined by modified aqua regia-ICP-MS. Sites with anomalous Au in the >0.063 mm fractions are highlighted on the map as yellow or green star symbols.

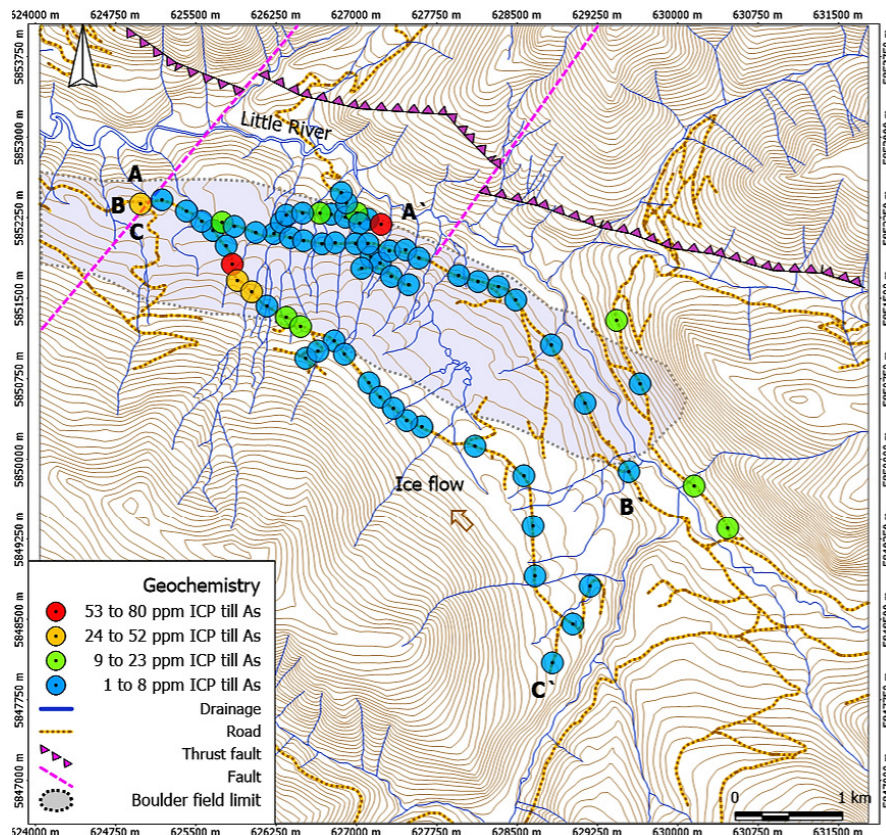


Fig. 18. Arsenic concentrations in the <0.063 mm fraction of till determined by modified aqua regia-ICP-MS.

**Table 10.** Element concentrations in B-horizon soil and till samples 8103, 8104 and 8185 at the site on the west end of the sampling transect coincident with a northeast-trending fault (see Figure 12). Silver, As, Au, Bi, Cd, Co, Cu, Hg, Mo, Sb, Se, Pb, Te, and Zn analyzed by modified aqua regia-ICP-MS and Au by INAA in the <0.063 mm fraction.

Sample Number	8103	8104	8105
Sample Depth (m)	0.1	1.2	1.85
Horizon	B-soil	Till	Till
Ag ppb ICPMS	665	82	37
As ppm ICPMS	22.3	53.3	50.3
Au ppb ICPMS	2.1	12.6	15.9
Au ppb INAA	15	1	11
Bi ppm ICPMS	1.72	2.02	2.67
Cd ppm ICPMS	0.67	0.69	0.84
Co ppm ICPMS	16.2	26.5	35.2
Cu ppm ICPMS	34.07	80.41	95.95
Hg ppb ICPMS	75	30	26
Mo ppm ICPMS	8.88	12.87	16.69
Pb ppm ICPMS	50.53	63.42	101.77
Sb ppm ICPMS	0.15	0.2	0.33
Se ppm ICPMS	1.1	1.2	1.2
Te ppm ICPMS	0.04	0.08	0.13
Zn ppm ICPMS	213	204.7	301.8

**Table 11.** Gold outlier values by modified aqua regia-ICP-MS in various size fractions of till and B-horizon soil samples shown in the box and whisker plots.

Fraction	Au Till Site	Au ppb	Au soil site	Au ppb
1.0 - 2.0 mm	8011	71	8075	463
< 0.063 mm	8011	12.2	8075	1.2
0.5 - 1.0 mm	8068	198	-	-
< 0.063 mm	8068	10.1	-	-
0.25 - 0.5 mm	8215	77	-	-
0.125 - 0.25 mm	8215	50	-	-
0.063 - 0.125 mm	8215	48	-	-
< 0.063 mm	8215	52.2	-	-

composition of the coarser fraction. Others have shown that base metals, gold, and platinum group element contents tend to be higher in the fine (<0.063 mm) till fraction (Nevalainen, 1989; Salminen et al., 1989; Shilts, 1993). Weathering of the till will release these elements into the soil where the geochemical processes active in the B-horizon soil are responsible for the ultimate trace metal anomaly size, shape, and contrast (DiLabio, 1995).

In the B-horizon soil, geochemically mobile elements (e.g., As, Cu, Co, and Zn) accumulate from meteoric water percolating downward through the soil by absorption onto clay minerals and secondary Fe and Mn oxides (McLean and Bledsoe, 1992). Depending on soil chemistry and especially pH, metals such as Cu, Zn, Ag, and Hg can preferentially complex with soil organic matter (McLean and Bledsoe, 1992). Complexing can explain the higher Ag concentrations in the 0.25 to 0.5 mm fraction

of the B-horizon soil samples through metal bonding to soil humus, a phenomenon noted by Cook and Dunn (2007). Native Au and Pb minerals are more resistant to surface chemical weathering and can exist as particles larger than 0.063 mm in till and soil. Some of the till and B-horizon soil samples in the present study have high Au and Pb concentrations in several size fractions, likely indicating the presence of the native Au and Pb-rich mineral grains.

Till samples containing >35 ppm Pb and >134 ppm Zn, along with anomalous Cu and Co, form a linear pattern aligned east-west on the northern edge of the survey area (Fig. 19). Peak metal concentrations are at the east end of this anomaly and they decrease to the west, suggesting a dispersal train of sulphide debris (Fig. 20). Conceivably, the Little River topography could have diverted the regional southeast to northwest advancing ice into the valley, resulting in east to west deposition of till.

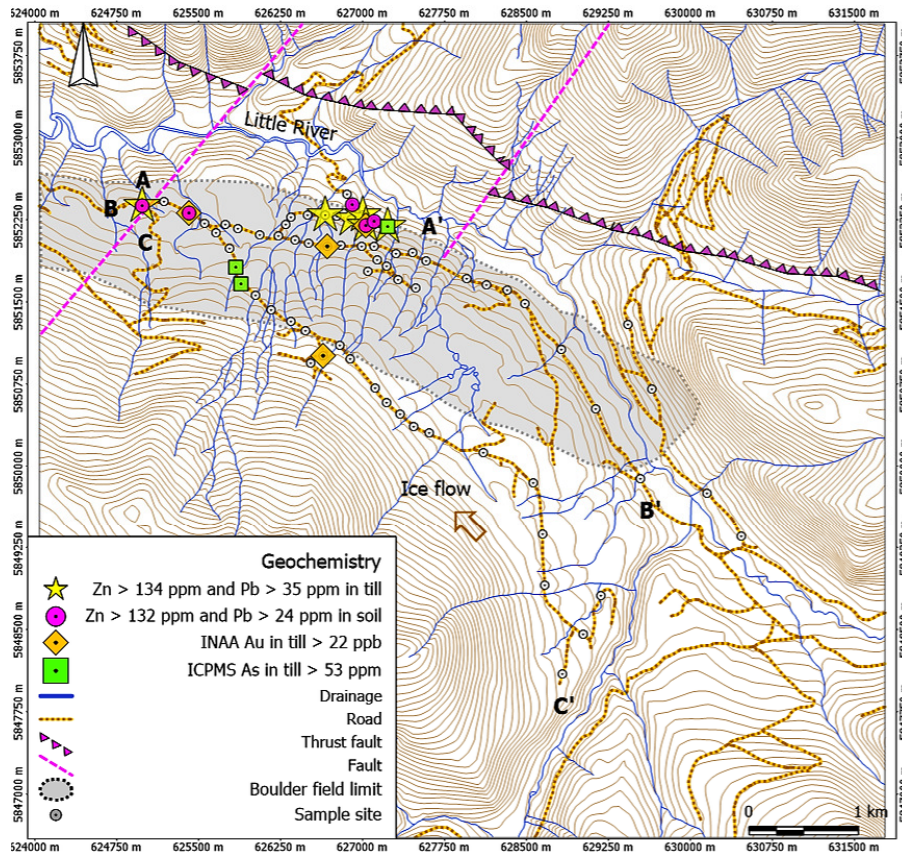


**Fig.19.** Lead and Zn values >80 percentile in the <0.063 mm fraction of till and B-horizon soil samples analyzed by aqua regia-ICP-MS. The location of anomalous Au (INAA) and As (modified aqua regia-ICP-MS) concentrations in till are indicated by yellow and green symbols.

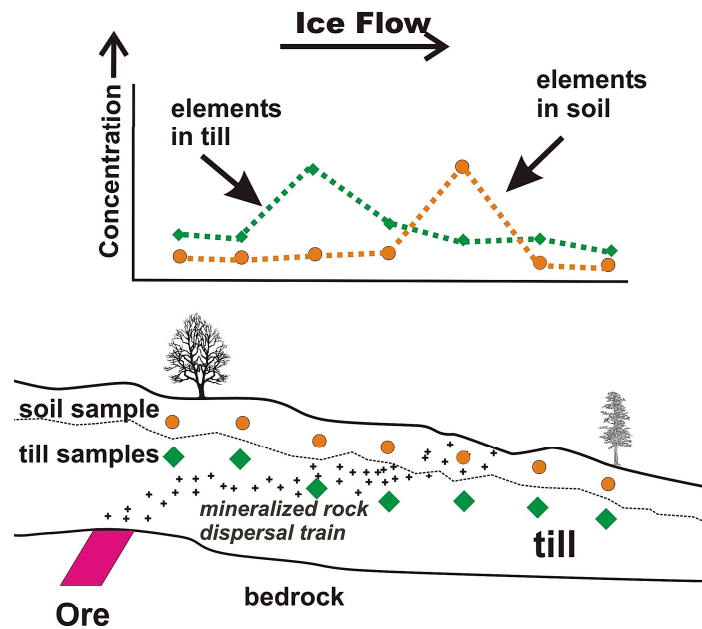


**Fig. 20.** Idealized geochemical profiles from the analysis of B-horizon soil and till samples intersecting a mineralized bedrock down-ice dispersal plume (after Drake, 1983; Miller, 1984; Hicken and Plouffe, 2017; McClenaghan and Paulen, 2018).

Separation of the Pb, Zn, Cu, and Co B-soil anomaly 500 metres to the west and down ice from the Pb-Zn-Cu-Co till anomaly is consistent with a till dispersal model described by Miller (1984) and subsequently refined by Hickin et al. (2017) and McClenaghan and Paulen (2018). However, the till at surface in this area is colluviated and the Pb-Zn B-soil anomaly trends to the north towards the Little River. Colluviation and reworking of the till may explain anomalous Pb and Au values in larger grain size fractions of the B-horizon soil and till due to the presence of discrete mineral grains.

Anomalous Ag, Au, As, Co, Cu, Pb, and Zn values with elevated Se values in the B-horizon soil and till from a site near a northeast-trending fault on the western boundary of the survey area (Fig. 11) may indicate that the structure is mineralized and is the source of the metals in the till. A geochemical profile at this site (Table 10) shows the contrast between elements such as As, Au, Bi, Cu, Co, Pb, and Zn. These are elevated in the till whereas Ag and Hg are higher in the B-horizon soil. The profile illustrates that an element signature in soil can differ from that in till and the difference should be considered when interpreting results of a geochemical survey.

Although As is a common pathfinder for Au, some till samples with anomalous Au values lack elevated As concentrations. However, individual sites along the Co-Cu-Pb-Zn till anomaly on the northern road traverse (A-A') do contain anomalous Au and As. The presence of the anomalous Au and As in this dispersal train could reflect a precious metal enrichment of the massive sulphides or a separate Au mineralized quartz vein. Several till and B-horizon soil samples with anomalous Au in the larger grain size fraction suggest the presence of large (>0.063 mm) Au grains that could have been derived from a more proximal bedrock source rather than having been entrained and transported farther down ice. Till samples with anomalous As or Au contents appear to be aligned along a northeast trend across the survey area and this could reflect the existence of mineralized Au-quartz veins related to the faults. Future work could include bulk till sampling for gold grain recovery to examine the gold grain size distribution and morphology to establish transport distance and possible bedrock source (see e.g., DiLabio, 1990; McClenaghan and Cabri, 2011).

The combination till and soil survey did not provide insights into the location of the bedrock source of the mineralized boulder train. Given that glacial transport was from the southeast, the boulders were likely transported from an unknown distance up-ice of the survey area. Additional till sampling up ice (southeast) of the current survey area would help identify the boulder train's bedrock source.

## 8. Conclusions

Till, B-C transitional horizon and B-horizon soil samples from 85 sites have been collected on the Ace property in central British Columbia and analyzed for more than 50 minor and trace elements. Based on data for 16 elements commonly considered geochemical pathfinders for Au and base metals the following conclusions are made.

- Gold, As, Co, Cu, Pb, Se, and Zn concentrations are higher in the <0.063 mm fraction of till compared to levels in the <0.063 mm of the B-horizon soil, reflecting both the nature of the mineralization in the bedrock source and the effects of comminution during glacial transport and deposition. Silver and Hg concentrations are higher in the B-horizon soil, which may reflect their preferential complexing/binding with organic matter. Data from different grain size fractions indicate that Au and Pb may also be present as larger (>0.063 mm) mineral grains in B-horizon soil and till in addition to grains that are <0.063 mm.
- Anomalous Au, Co, Cu, Pb, Se, and Zn concentrations in till and B-horizon soil outline a narrow ribbon-shaped dispersal train along the northern border of the area that was formed initially in till deposited from by ice flowing east to west and subsequently modified by gravity processes (northward displacement) on the steep hill slope to form colluvium. Trace element profiles along the anomaly axis show separation of the B-horizon soil anomaly 500 m to the west of the till anomaly. This pattern is consistent with a model of Pb-Zn-Cu sulphide transport in till from a mineralized bedrock source at the east end of the dispersal train.
- A potentially mineralized northeast-trending fault at the west end of the survey area may be the source for a Au, Cu, Co, Pb, Zn anomaly in both soil and till. The distribution of till and B-horizon soil Au-As anomalies across the survey area could also reflect the presence of northeast-trending Au-rich quartz veins.

## Acknowledgments

The authors appreciate the support and guidance from Mr. Louis Doyle (Barker Minerals) and his staff for allowing access to the Ace property and for providing an excavator. Special thanks also to Dr. Peter Bobrowsky, Geological Survey of Canada Emeritus, who conceived and designed the sampling program and supervised the field work. Assistance in the field with the sample collection and the surficial mapping by Beth Brooks, Adrian Hickin, Gloria Lopez, Ahren Bichler is most appreciated. M.B. McClenaghan (Geological Survey of Canada) and T. Ferbey (British Columbia Geological Survey) kindly reviewed drafts of the manuscript; their critiques were invaluable and helped to improve the paper.

## References cited

- Abzalov, M.Z., 2008. Quality control of assay data: A review of procedures for measuring and monitoring precision and accuracy. *Exploration and Mining Geology*, 17, 131-144.
- Arnold, H., and Ferbey, T., 2020. Ice-flow indicator database, British Columbia and Yukon. British Columbia Ministry of Energy and Mines and Petroleum Resources, British Columbia Geological Survey Open File 2020-03, 1 p.
- Averill, S.A., 2017. The Blackwater gold-spessartine-pyrolusite glacial dispersal train, British Columbia, Canada: Influence of sampling depth on indicator mineralogy and geochemistry. *Geochemistry: Exploration, Environment, Analysis*, 17, 43-60.

- British Columbia Geological Survey, 2020. MINFILE. British Columbia Ministry of Energy, Mines and Petroleum Resources, British Columbia Geological Survey. <<http://minfile.ca/>> accessed November 2019.
- Bichler, A.J., and Bobrowsky, P.T., 2000. Barkerville project: Regional till geochemistry and orientation studies. In: Geological Fieldwork 1999, British Columbia Ministry of Energy and Mines, British Columbia Geological Survey Paper 2000-01, pp. 383-396.
- Cook, S.J., and Dunn, C.E., 2007. A comparative assessment of soil geochemical methods for detecting buried mineral deposits – 3Ts Au-Ag prospect, central British Columbia. Geoscience BC Report 2007-7, 226 p.
- Cui, Y., Miller, D., Schiarizza, P., and Diakow, L.J. 2017. British Columbia digital geology. British Columbia Ministry of Energy, Mines and Petroleum Resources, British Columbia Geological Survey Open File 2017-8, 9 p.
- DiLabio, R.N.W., 1988. Residence sites of gold, PGE and rare lithophile elements in till. In: MacDonald, D.R and Mills, K.A., (Eds.), *Prospecting in Areas of Glaciated Terrain*. The Canadian Institute of Mining and Metallurgy, pp.121-140.
- DiLabio, R.N.W., 1990. Classification and interpretation of the shapes and surface textures of gold grains from till on the Canadian Shield. Geological Survey of Canada, Current Research, Paper 90-1C, pp. 323-329.
- DiLabio, R.N.W., 1995. Residence sites of trace elements in oxidized tills. In: Bobrowsky, P.T., Sibbick, S.J., Newell, J.H., and Matysek, P.F., (Eds.), *Drift Exploration in the Canadian Cordillera*, British Columbia Ministry of Energy, Mines and Petroleum Resources, Paper 1995-2, pp. 139-148.
- Drake, L.D., 1983. Ore plumes in till. *Journal of Geology*, 91, 707-713.
- Ferby, T., and Levson, V.M., 2009. The influence of ice flow reversals on the vertical and horizontal distribution of trace element values in tills, Huckleberry Mine area, west-central British Columbia. In: Paulen, R.C. and McMartin, I., (Eds.), *Application of Till and Stream Sediment Heavy Mineral and Geochemical Methods to Mineral Exploration in Western and Northern Canada*. Geological Association of Canada, Short Course Notes 18, pp. 177-183.
- Ferby, T., Levson, V.M., and Lett, R.E., 2012. Till geochemistry of the Huckleberry mine area, west-central British Columbia (NTS 93E/11). British Columbia Ministry of Energy, Mines and Petroleum Resources British Columbia Geological Survey Open File 2012-2, 56 p.
- Ferri, F., and O'Brien, B.H., 2002. Preliminary geology of the Cariboo Lake area, central British Columbia. In: Geological Fieldwork 2001, British Columbia Ministry of Energy and Mines British Columbia Geological Survey Paper 2002-1, pp. 59-82.
- Hashmi, S., Ward, B.C., Plouffe, A., Leybourne, M.I., and Ferby, T., 2015. Geochemical and mineralogical dispersal in till from the Mount Polley Cu-Au porphyry deposit, central British Columbia, Canada. *Geochemistry: Exploration, Environment, Analysis*, 15, 234-249.
- Hickin, A.S., and Plouffe, A., 2017. Sampling and interpreting stream, lake and glacial sediments for mineral exploration in the Canadian Cordillera, a review. In: Ferby, T., Plouffe, A., and Hickin, A.S., (Eds.), *Indicator Minerals in Till and Stream Sediment of the Canadian Cordillera*. Geological Association of Canada Special Paper 50, pp. 27-52.
- Holland, S.S., 1976. Landforms of British Columbia: A physiographic outline; British Columbia Ministry of Energy, Mines and Petroleum Resources, British Columbia Geological Survey Bulletin 48, 136 p.
- Höy, T., and Ferri, F., 1998. Stratabound base metal deposits of the Barkerville subterrane, central British Columbia. In: Geological Fieldwork 1997, British Columbia Ministry of Employment and Investment, British Columbia Geological Survey Paper 1998-1, pp. 13-1-13-12.
- Kerr, D.E., Sibbick, S.J., and Belik, G.D., 1993. Preliminary results of glacial dispersion studies on the Galaxy property, Kamloops, B.C. In: Geological Fieldwork 1992, British Columbia Ministry of Energy, Mines and Petroleum Resources, British Columbia Geological Survey Paper 1993-1, pp. 439-443.
- Lett, R.E., 2001. Geochemical signatures around massive sulphide deposits in southern British Columbia, Canada. In: McClenaghan, M.B., Bobrowsky, P.T., Hall, G.E.M., and Cook, S.J., (Eds.), *Drift Exploration in Glaciated Terrain*, Geological Society of London, Special Publication 185, pp. 301-321.
- Lett, R.E. 2009. Geochemical exploration pathfinders to drift covered copper-gold sulphide mineralization in Central B.C. British Columbia Ministry of Energy, Mines and Petroleum Resources, British Columbia Geological Survey Open File 2010-09, 194 p.
- Lett, R.E., 2010. Surficial geochemistry of the Galaxy porphyry copper-gold deposit, Kamloops, B.C. (NTS 92I/09). British Columbia Ministry of Energy, Mines and Petroleum Resources, British Columbia Geological Survey GeoFile 2011-12, 5 p.
- Lett, R.E., and Paulen, R.C., 2021. Soil and till geochemical surveys at the Ace mineral property, central British Columbia: Digital geochemical data. British Columbia Ministry of Energy, Mines and Low Carbon Innovation, British Columbia Geological Survey GeoFile, in prep.
- Lett, R.E., Bradshaw, P.M.D., and Doyle, L., 2005. Towards an atlas of geochemical exploration models for mineral deposits in the Canadian Cordillera. 22nd International Geochemical Exploration Symposium, Perth, Australia, Abstracts, p. 143. [https://www.appliedgeochemists.org/images/stories/IEGS\\_2005/IGES\\_Abstracts\\_FINAL\\_small.pdf](https://www.appliedgeochemists.org/images/stories/IEGS_2005/IGES_Abstracts_FINAL_small.pdf).
- Levson, V.M., 2001. Regional till geochemical surveys in the Canadian Cordillera: sample media, methods and anomaly evaluation. In: McClenaghan, M.B., Bobrowsky, P.T., Hall, G.E.M., and Cook, S.J., (Eds.), *Drift Exploration in Glaciated Terrain*, Geological Society of London, Special Publication 185, pp. 45-68.
- Levson, V.M., 2002. Quaternary geology and till geochemistry of the Babine porphyry copper belt, B.C. British Columbia Ministry of Energy and Mines, British Columbia Geological Survey Bulletin 110, 278 p.
- Mäkinen, J., 1995. Effects of grinding and chemical factors on the generation and composition of the till fine fraction: an experimental study. *Journal of Geochemical Exploration*, 54, 49-62.
- McClenaghan, M.B., and Cabri, L.J., 2011. Review of gold and platinum group element (PGE) indicator minerals methods for surficial sediment sampling. *Geochemistry: Exploration, Environment, Analysis*, 11, 251-263.
- McClenaghan, M.B., and DiLabio, R.N.W., 1993. Till geochemistry and its implications for mineral exploration: southeastern Cape Breton Island, Nova Scotia, Canada. *Quaternary International*, 20, 107-122.
- McClenaghan, M.B., and Paulen, R.C., 2018. Application of till mineralogy and geochemistry to mineral exploration. In: Menzies, J. and van der Meer J.J.M., (Eds.), *Past Glacial Environments*, Elsevier, pp. 689-751.
- McClenaghan, M.B., and Peter, J.M. 2016. Till geochemical signatures of volcanogenic massive sulphide mineralization; an overview of Canadian examples. *Geochemistry: Exploration, Environment, Analysis*, 16, 27-47.
- Miller, J.K., 1984. Model for clastic indicator trains in till. In: *Prospecting in areas of glaciated terrain 1984*, Institute of Mining and Metallurgy, London, pp. 69-77.
- McLean, J.E., and Bledsoe, B.E., 1992. United States Environmental Protection Agency ground water issue; Behavior of Metals in Soils, EPA/540/S-92/018, 25 p.

- Moon, C.J., Whateley, M.K.G., and Evans, A.M., 2006. Introduction to mineral exploration, 2nd Edition, Blackwell Publishing, 481p.
- Nevalainen, R., 1989. Lithology of fine till fractions in the Kuhmo greenstone belt area, eastern Finland. In: Perttunen, M., (Ed.), Transport of Glacial Drift in Finland, Geological Survey of Finland Special Paper 7, pp. 59-65.
- O'Brien, E.K., Levson, V.M., and Broster, B.E., 1997. Till geochemical dispersal in central British Columbia. British Columbia Ministry of Employment and Investment, British Columbia Geological Survey Open File 1997-12, 73 p.
- Paulen, R.C., 2001. Glacial transport and secondary hydromorphic metal mobilization: examples from the southern interior of British Columbia, Canada In: McClenaghan, M.B., Bobrowsky, P.T., Hall, G.E.M., and Cook, S.J., (Eds.), Drift Exploration in Glaciated Terrain, Geological Society of London, Special Publication 185, pp. 323-337.
- Salminen, R., Hartikainen, A., and Lestinen, P., 1989. Enrichment of As and S in the finest fractions of rock samples-an experimental study simulating the formation of till. *Journal of Geochemical Exploration*, 32, 287-290.
- Shilts, W.W., 1993. Geological Survey of Canada's contributions to understanding the composition of glacial sediments. *Canadian Journal of Earth Sciences*, 30, 333-353.
- Sibbick, S.J., Balma, R.G, and Dunn, C.E., 1996. Till geochemistry of the Mount Milligan area. British Columbia Ministry of Employment and Investment, British Columbia Geological Survey Open File 1996-22, 14 p.



# Appendix: British Columbia Geological Survey publications and peer-reviewed journal papers authored by BCGS staff and released in 2020

All BCGS publications are available for download, free of charge, from [www.BCGeologicalSurvey.ca](http://www.BCGeologicalSurvey.ca)

To receive notification of our latest releases email [Geological.Survey@gov.bc.ca](mailto:Geological.Survey@gov.bc.ca)



## Papers

Paper 2020-01

Geological fieldwork 2019, a summary of field activities and current research, 205 p.

Ferri, F., Jones, L.D., Clarke, G., and Hickin, A.S., 2020. British Columbia Geological Survey annual program review 2019-2020. In: Geological Fieldwork 2019, Ministry of Energy, Mines and Petroleum Resources, British Columbia Geological Survey Paper 2020-01, pp. 1-12.

Schiarizza, P., Monger, J.W.H., Friedman, R.M., and Northcote, B., 2020. Detrital zircons from the Gun Lake unit, Gold Bridge area, southwestern British Columbia. In: Geological Fieldwork 2019, British Columbia Ministry of Energy, Mines and Petroleum Resources, British Columbia Geological Survey Paper 2020-01, pp. 13-24.

Ootes, L., Bergen, A.L., Milidragovic, D., Jones, G.O., Camacho, A., and Friedman, R., 2020. An update on the geology of northern Hogem batholith and its surroundings, north-central British Columbia. In: Geological Fieldwork 2019, British Columbia Ministry of Energy, Mines and Petroleum Resources, British Columbia Geological Survey Paper 2020-01, pp. 25-47.

Steinthorsdottir, K., Cutts, J., Dipple, G., Milidragovic, D., and Jones, F., 2020. Origin and serpentinization of ultramafic rocks in dismembered ophiolite north of Trembleur Lake, central British Columbia. In: Geological Fieldwork 2019, British Columbia Ministry of Energy, Mines and Petroleum Resources, British Columbia Geological Survey Paper 2020-01, pp. 49-58.

Nott, J., Milidragovic, D., Nixon, G.T., and Scoates, J.S., 2020. New geological investigations of the Early Jurassic Polaris ultramafic-mafic Alaskan-type intrusion, north-central British Columbia. In: Geological Fieldwork 2019, British Columbia Ministry of Energy, Mines and Petroleum Resources, British Columbia Geological Survey Paper 2020-01, pp. 59-76.

Miller, E.A., Kennedy, L.A., and van Straaten, B.I., 2020. Geology of the Kinskuch Lake area and Big Bulk porphyry prospect, northwestern British Columbia: Syndepositional faulting and basin formation during the Rhaetian (latest Triassic) transition from the Stuhini to the Hazelton Group. In: Geological Fieldwork 2019, British Columbia Ministry of Energy, Mines and Petroleum Resources, British Columbia Geological Survey Paper 2020-01, pp. 77-99.

Hunter, R.C., and van Straaten, B.I., 2020. Preliminary stratigraphy and geochronology of the Hazelton Group, Kitsault River area, Stikine terrane, northwest British Columbia. In: Geological Fieldwork 2019, British Columbia Ministry of Energy, Mines and Petroleum Resources, British Columbia Geological Survey Paper 2020-01, pp. 101-118.

Nixon, G.T., Friedman, R.M., and Creaser, R.A., 2020. Late Neogene porphyry Cu-Mo( $\pm$ Au-Ag) mineralization in British Columbia: the Klaskish Plutonic Suite, northern Vancouver Island. In: Geological Fieldwork 2019, British Columbia Ministry of Energy, Mines and Petroleum Resources, British Columbia Geological Survey Paper 2020-01, pp. 119-132.

Rukhlov, A.S., Fortin, G., Kaplenkov, G.N., Lett, R.E., Lai, V.W.-M., and Weis, D., 2020. Multi-media geochemical and Pb isotopic evaluation of modern drainages on Vancouver Island. In: Geological Fieldwork 2019, British Columbia Ministry of Energy, Mines and Petroleum Resources, British Columbia Geological Survey Paper 2020-01, pp. 133-167.

Shewchuk, C., Ferbey, T., and Lian, O.B., 2020. Detecting porphyry Cu-Mo mineralization using major oxides and pathfinder elements in subglacial till, Highland Valley mine area, south-central British Columbia. In: Geological Fieldwork 2019, British Columbia Ministry of Energy, Mines and Petroleum Resources, British Columbia Geological Survey Paper 2020-01, pp. 169-187.

Elia, E.A., and Ferbey, T., 2020. Generating photogrammetric DEMs in the field from remotely piloted aircraft systems. In: Geological Fieldwork 2019, British Columbia Ministry of Energy, Mines and Petroleum Resources, British Columbia Geological Survey Paper 2020-01, pp. 189-200.

Appendix: British Columbia Geological Survey publications and peer-reviewed journal papers authored by BCGS staff and released in 2019, pp. 201-205.

## **Geoscience Map**

GM 2020-01

Mihalynuk, M.G., and Diakow, L.J., 2020. Southern Nicola arc geology. British Columbia Ministry of Energy, Mines and Low Carbon Innovation, British Columbia Geological Survey Geoscience Map 2020-01, 1:50,000 scale, two sheets.

## **Open Files**

OF 2020-01

Clarke, G., Northcote, B., Katay, F., and Tombe, S.P., 2020. Mines, mine development, selected proposed mines, and selected exploration projects in British Columbia, 2019. British Columbia Ministry of Energy, Mines and Petroleum Resources, British Columbia Geological Survey Open File 2020-01.

OF 2020-02

Ootes, L., Bergen, A.L., Milidragovic, D., and Jones, G.O., 2020. Preliminary geology of the northern Hogem batholith and its surroundings, north-central British Columbia. British Columbia Ministry of Energy, Mines and Petroleum Resources, British Columbia Geological Survey Open File 2020-02, 1:50,000 scale.

OF 2020-03

Arnold, H., and Ferbey, T., 2020. Ice-flow indicator database, British Columbia and Yukon. British Columbia Ministry of Energy, Mines and Petroleum Resources, British Columbia Geological Survey Open File 2020-03, 1 p.

OF 2020-04

Nott, J., Milidragovic, D., Nixon, G.T., and Scoates, J.S., 2020. Geology of the Polaris ultramafic-mafic Alaskan-type intrusion, north-central British Columbia. British Columbia Ministry of Energy, Mines and Petroleum Resources, British Columbia Geological Survey Open File 2020-04, 1:15,000 scale.

## **GeoFiles**

GF 2020-01

Ootes, L., Jones, G.O., Schiarizza, P., Milidragovic, D., Friedman, R., Camacho, A., Luo, Y., Vezinet, A., Pearson, D.G., and Zhang, S., 2020. Geochronologic and geochemical data from northern Hogem batholith and its surroundings, north-central British Columbia. British Columbia Ministry of Energy, Mines and Low Carbon Innovation, British Columbia Geological Survey GeoFile 2020-01, 21 p.

GF 2020-02

Han, T., and Rukhlov, A.S., 2020. Update of rock geochemical database at the British Columbia Geological Survey. British Columbia Ministry of Energy, Mines and Petroleum Resources, British Columbia Geological Survey GeoFile 2020-02, 4 p.

GF 2020-03

Nixon, G.T., Friedman, R.M., and Creaser, R.A., 2020. A new metalotect: Late Neogene porphyry Cu-Mo mineralization in British Columbia. British Columbia Ministry of Energy, Mines and Petroleum Resources, British Columbia Geological Survey GeoFile 2020-03 (poster).

GF 2020-04

Rukhlov, A.S., Fortin, G., Kaplenkov, G.N., Lett, R.E., Lai, V.W.-M., and Weis, D., 2020. Catching the tail of a golden dragon plus 60 elements in British Columbia. British Columbia Ministry of Energy, Mines and Petroleum Resources, British Columbia Geological Survey GeoFile 2020-04 (poster).

GF 2020-05

Simandl, G.J., D'Souza, R.J., Paradis, S., Spence, J., and Fitz-Gerald, W., 2020. REE in carbonates from sediment-hosted Pb-Zn deposits, southern Rocky Mountains, BC. British Columbia Ministry of Energy, Mines and Petroleum Resources, British Columbia Geological Survey GeoFile 2020-05 (poster).

GF 2020-06

Riddell, J., 2020. Evaluation of coal ash chemistry indices for predicting CSR (coke strength after reaction with CO<sub>2</sub>) for coking coals of the Rocky Mountains, British Columbia. British Columbia Ministry of Energy, Mines and Petroleum Resources, British Columbia Geological Survey GeoFile 2020-06, 18 p.

GF 2020-07

Paradis, S., Simandl, G.J., Drage, N., D'Souza, R.J., Kontak, D.J., and Waller, Z., 2020. Paleozoic carbonate-hosted deposits of the southern Rocky Mountains: A comparison. British Columbia Ministry of Energy, Mines and Petroleum Resources, British Columbia Geological Survey GeoFile 2020-07 (poster).

GF 2020-08

Han, T., and Rukhlov, A.S., 2020. Update of the provincial Regional Geochemical Survey (RGS) database at the British Columbia Geological Survey. British Columbia Ministry of Energy, Mines and Petroleum Resources, British Columbia Geological Survey GeoFile 2020-08, 3 p.

GF 2020-09

Riddell, J., and Northcote, B., 2020. Table of British Columbia coal resources, 2020. British Columbia Ministry of Energy, Mines and Petroleum Resources, British Columbia Geological Survey GeoFile 2020-09, 1 p.

GF 2020-10

Han, T., Ootes, L., and Yun, K., 2020. The British Columbia Geological Survey geochronologic database: Preliminary release of ages. British Columbia Ministry of Energy, Mines and Low Carbon Innovation, British Columbia Geological Survey GeoFile 2020-10, 4 p.

GF 2020-11

Lefebure, D.V., and Jones, L.D., (compilers) 2020. British Columbia Geological Survey mineral deposit profiles, 1995 to 2012. British Columbia Ministry of Energy, Mines and Low Carbon Innovation, British Columbia Geological Survey GeoFile 2020-11, 580 p.

GF 2020-12

Friedman, R.M., Mihalyuk, M.G., and Diakow, L.J., 2020. Geochronologic data from samples collected near Pothole Lake and Pennask Mountain (NTS 92H/15, 16) as part of the Southern Nicola Arc Project. British Columbia Ministry of Energy, Mines and Low Carbon Innovation, British Columbia Geological Survey GeoFile 2020-12, 6 p.

GF 2020-13

Rukhlov, A.S., Ootes, L., Hickin, A.S., and Mashyanov, N.R., 2020. Supplementary data for near-surface mercury vapour haloes in air above ore deposits and faults on Vancouver Island: Insights into buried materials in real-time? British Columbia Ministry of Energy, Mines and Low Carbon Innovation, British Columbia Geological Survey GeoFile 2020-13, 1 p.

## **Information Circulars**

IC 2020-01

Provincial Overview of Exploration and Mining in British Columbia, 2019. British Columbia Ministry of Energy, Mines and Petroleum Resources, British Columbia Geological Survey, Information Circular 2020-01, 132 p.

Clarke, G., Northcote, B., Katay, F., and Tombe, S.P., 2020. Exploration and Mining in British Columbia, 2019: A summary. In: Provincial Overview of Exploration and Mining in British Columbia, 2019. British Columbia Ministry of Energy, Mines and Petroleum Resources, British Columbia Geological Survey, Information Circular 2020-01, pp. 1-40.

Tombe, S.P., 2020. Exploration and mining in the Northwest Region, British Columbia. In: Provincial Overview of Exploration and Mining in British Columbia, 2019. British Columbia Ministry of Energy, Mines and Petroleum Resources, British Columbia Geological Survey, Information Circular 2020-01, pp. 41-58.

Northcote, B., 2020. Exploration and mining in the South Central Region, British Columbia. In: Provincial Overview of Exploration and Mining in British Columbia, 2019. British Columbia Ministry of Energy, Mines and Petroleum Resources, British Columbia Geological Survey, Information Circular 2020-01, pp. 75-94.

Katay, F., 2020. Exploration and mining in the Southeast Region, British Columbia. In: Provincial Overview of Exploration and Mining in British Columbia, 2019. British Columbia Ministry of Energy, Mines and Petroleum Resources, British Columbia Geological Survey, Information Circular 2020-01, pp. 95-112.

Northcote, B., 2020. Exploration and mining in the Southwest Region, British Columbia. In: Provincial Overview of Exploration and Mining in British Columbia, 2019. British Columbia Ministry of Energy, Mines and Petroleum Resources, British Columbia Geological Survey, Information Circular 2020-01, pp. 113-126.

#### IC 2020-02

British Columbia Geological Survey, 2020. British Columbia coal industry overview 2019. British Columbia Ministry of Energy, Mines and Petroleum Resources, British Columbia Geological Survey Information Circular 2020-02, 13 p.

#### IC 2020-03

British Columbia Geological Survey, 2020. British Columbia Geological Survey. British Columbia Ministry of Energy, Mines and Petroleum Resources, British Columbia Geological Survey Information Circular 2020-03, 14 p. (brochure)

#### IC 2020-04

British Columbia Geological Survey, 2020. Mineral Development Office. British Columbia Ministry of Energy, Mines and Petroleum Resources, British Columbia Geological Survey Information Circular 2020-04, 4 p. (brochure)

#### IC 2020-05

British Columbia Geological Survey, 2020. Online databases at the British Columbia Geological Survey. British Columbia Ministry of Energy, Mines and Petroleum Resources, British Columbia Geological Survey Information Circular 2020-05, 14 p. (brochure)

#### IC 2020-06

British Columbia Geological Survey, 2020. The Golden Triangle of northwestern British Columbia. British Columbia Ministry of Energy, Mines and Petroleum Resources, British Columbia Geological Survey Information Circular 2020-06, 6 p.

### **Peer-reviewed journal and volume publications**

Clennett, E.J., Sigloch, K., Mihalynuk, M.G., Seton, M., Henderson, M.A., Hosseini, K., Mohammadzaheri, A., Johnston, S.T., and Müller, R.D., 2020. A quantitative tomotectonic plate reconstruction of western North America and the eastern Pacific basin. *Geochemistry, Geophysics, Geosystems*, 20, e2020GC009117. <https://doi.org/10.1029/2020GC009117>.

Lang, J.R., Roberts, K., Galicki, M., van Straaten, B.I., and Bui, P.V., 2020. Magmatic, hydrothermal, and structural features of the Gnat Pass porphyry copper deposit, British Columbia. In: Sharman, E.R., Lang, J.R., and Chapman, J.B., (Eds.), *Porphyry Deposits of the Northwestern Cordillera of North America: A 25-Year Update*. Canadian Institute of Mining and Metallurgy Special Volume 57, pp. 324-340.

Logan, J.M., Schiarizza, P., and Devine, F., 2020. Geology, structural setting, and porphyry deposits of the Hogem batholith, northeast British Columbia. In: Sharman, E.R., Lang, J.R., and Chapman, J.B., (Eds.), *Porphyry Deposits of the Northwestern Cordillera of North America: A 25-Year Update*. Canadian Institute of Mining and Metallurgy Special Volume 57, pp. 212-227.

Nelson, J.L., and van Straaten, B., 2020. Recurrent syn- to post-subduction mineralization along deep crustal corridors in the Iskut-Stewart-Kitsault region of western Stikinia, northwestern British Columbia. In: Sharman, E.R., Lang, J.R., and Chapman, J.B., (Eds.), *Porphyry Deposits of the Northwestern Cordillera of North America: A 25-Year Update*. Canadian Institute of Mining and Metallurgy Special Volume 57, pp. 194-211.

Nixon, G.T., Scheel, J.E., Scoates, J.S., Friedman, R.M., Wall, C.J., Gabites, J., and Jackson-Brown, S., 2020. Syn-accretionary multistage assembly of an Early Jurassic Alaskan-type intrusion in the Canadian Cordillera: U-Pb and  $^{40}\text{Ar}/^{39}\text{Ar}$  geochronology of the Turnagain ultramafic-mafic intrusive complex, Yukon-Tanana terrane. *Canadian Journal of Earth Sciences*, 57, 575-600. <https://doi.org/10.1139/cjes-2019-0121>.

Ootes, L., Sandeman, H., Cousens, B.L., Luo, Y., Pearson, D.G., and Jackson, V.A., 2020. Pyroxenitic magma conduits (ca. 1.86 Ga) in Wopmay orogen and Slave craton: Petrogenetic constraints from whole rock and mineral chemistry. *Lithos*, article 105220. <https://doi.org/10.1016/j.lithos.2019.105220>.

Paradis, S., Hnatyshin, D., Simandl, G.J., and Creaser, R.A., 2020. Re-Os pyrite geochronology of the Yellowhead-type mineralization, Pend Oreille mine, Kootenay arc, Metaline district, Washington. *Economic Geology*, 115, 1373-1384. <https://doi.org/10.5382/econgeo.4720>.

van Straaten, B.I., Mostaghimi, N., Kennedy, L., Gallagher, C., Schiarizza, P., and Smith, S., 2020. The deformed Gibraltar porphyry copper-molybdenum deposit, south-central British Columbia, Canada. In: Sharman, E.R., Lang, J.R., and Chapman, J.B., (Eds.), *Porphyry Deposits of the Northwestern Cordillera of North America: A 25-Year Update*. Canadian Institute of Mining and Metallurgy Special Volume 57, pp. 547-567.

### **Contributions to partner publications**

Bouzari, F., Lee, R.G., Hart, C.J.R., and van Straaten, B.I., 2020. Porphyry vectoring within advanced argillic-altered rocks of British Columbia. In: *Geoscience BC Summary of Activities 2019: Minerals*. Geoscience BC Report 2020-01, pp. 115-130.

Castonguay, S., Ootes, L., Devine, F., and Friedman, R., 2020. Superimposed Late Cretaceous and earliest Eocene gold mineralization and deformation events along the Llewellyn-Tally Ho deformation corridor in northwest British Columbia and southern Yukon. In: Mercier-Langevin, P., Lawley, C.J.M., and Castonguay, S., (Eds.), *Targeted Geoscience Initiative 5: Contributions to the Understanding of Canadian Gold Systems*. Geological Survey of Canada Open File 8712, pp. 223-236. <https://doi.org/10.4095/326039>.

Cutts, J.A., Dipple, G.M., Hart, C.J.R., and Milidragovic, D., 2020. Assessment of the carbon mineralization potential of British Columbia by quantifying the response of physical properties to the alteration of ultramafic rocks (NTS 092H/08, 10, 093K/13, 14, 094C/05, 104I/01-16, 104N/01-16). In: *Geoscience BC Summary of Activities 2019: Minerals*. Geoscience BC Report 2020-01, pp. 137-144.

Lett, R.E., Sacco, D.A., Elder, B., and Jackaman, W., 2020. Real-time detection of bedrock mineralization and geological faults beneath glacial deposits in central British Columbia using onsite soil gas carbon dioxide and oxygen analysis by electronic gas sensors (NTS 093A/58, 093G/03). In: *Geoscience BC Summary of Activities 2019: Minerals*. Geoscience BC, Report 2020-01, pp. 93-100.

Nixon, G.T., Scoates, J.S., Milidragovic, D., Nott, J., Moerhuis, N., Ver Hoeve, T.J., Manor, M.J., and Kjarsgaard, I.M., 2020. Convergent margin Ni-Cu-PGE-Cr ore systems: U-Pb petrochronology and environments of Cu-PGE vs. Cr-PGE mineralization in Alaskan-type intrusions. In: Bleeker, W., Houlé, M.G., (Eds.), *Targeted Geoscience Initiative 5: Advances in the understanding of Canadian Ni-Cu-PGE and Cr ore systems-Examples from the Midcontinent Rift, the Circum-Superior Belt, the Archean Superior Province, and Cordilleran Alaskan-type intrusions*. Geological Survey of Canada Open File 8722, pp. 197-218.

Zagorevski, A., van Staal, C.R., Bédard, J.H., Bogatu, A., Canil, D., Coleman, M., Golding, M., Joyce, N., Lawley, C., McGoldrick, S., Mihalynuk, M., Milidragovic, D., Parsons, A., and Schiarizza, P., 2020. Paper 1: Overview of Cordilleran oceanic terranes and their significance for the tectonic evolution of the northern Cordillera. *Geological Survey of Canada Bulletin 610*, in press.

### **Database updates**

Cui, Y., Miller, D., Schiarizza, P., and Diakow, L.J., 2017. *British Columbia digital geology*. British Columbia Ministry of Energy, Mines and Petroleum Resources, British Columbia Geological Survey Open File 2017-8, 9 p. Current version 2019-12-19.

<https://www2.gov.bc.ca/gov/content/industry/mineral-exploration-mining/british-columbia-geological-survey/geology/bcdigitalgeology>.

Norris, J., and Fortin, G., 2019. Assessment report-sourced surface sediment geochemical database: Development and initial data release from the Interior Plateau. British Columbia Ministry of Energy, Mines and Petroleum Resources, British Columbia Geological Survey GeoFile 2019-04, 9 p., current version 2020-05-15.  
<https://www2.gov.bc.ca/gov/content?id=E1DC806086E34F3EB2FF4C6FDA08F427>.

Arnold, H., and Ferbey, T., 2019. British Columbia surficial geology map index. British Columbia Ministry of Energy, Mines and Petroleum Resources, British Columbia Geological Survey Open File 2019-03, current version 2020-01.  
<https://www2.gov.bc.ca/gov/content?id=9C6C634A04184AEFA75EC2816764EF9D#OF2019-03>.

Bustard, A.L., Ferbey, T., and Arnold, H., 2019. Regional- to property-scale till geochemical and mineralogical surveys in British Columbia for base and precious metals. British Columbia Ministry of Energy, Mines and Petroleum Resources, British Columbia Geological Survey Open File 2019-04, current version 2020-01.  
<https://www2.gov.bc.ca/gov/content?id=9C6C634A04184AEFA75EC2816764EF9D#OF2019-04>.

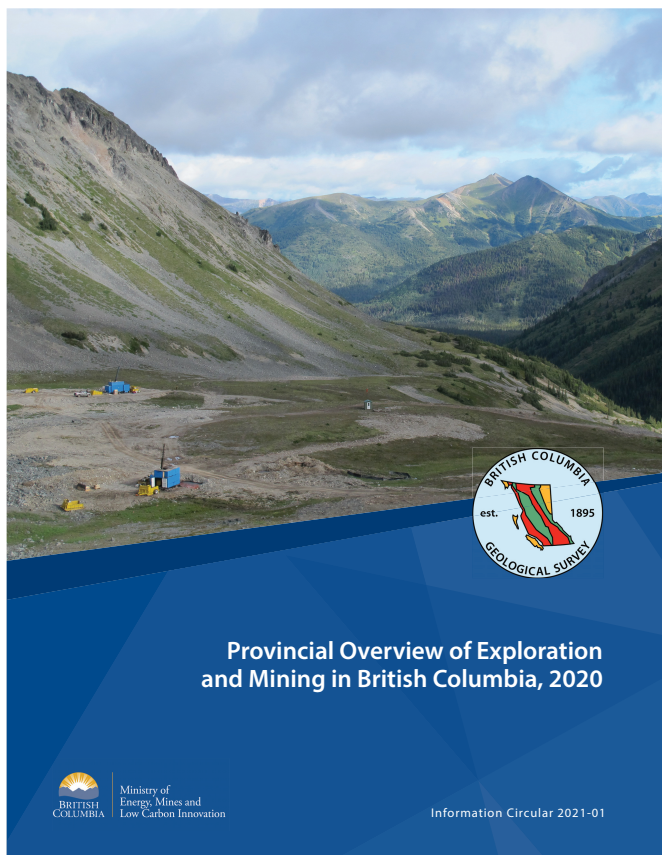
Lithochemical database, version 2020-01-20.  
<https://www2.gov.bc.ca/gov/content?id=69323EF2C5AB401BB7142E9F6617C6AF#Litho>.

Assessment Report Indexing System (ARIS) database, updated regularly.  
<https://www2.gov.bc.ca/gov/content/industry/mineral-exploration-mining/british-columbia-geological-survey/assessmentreports>.

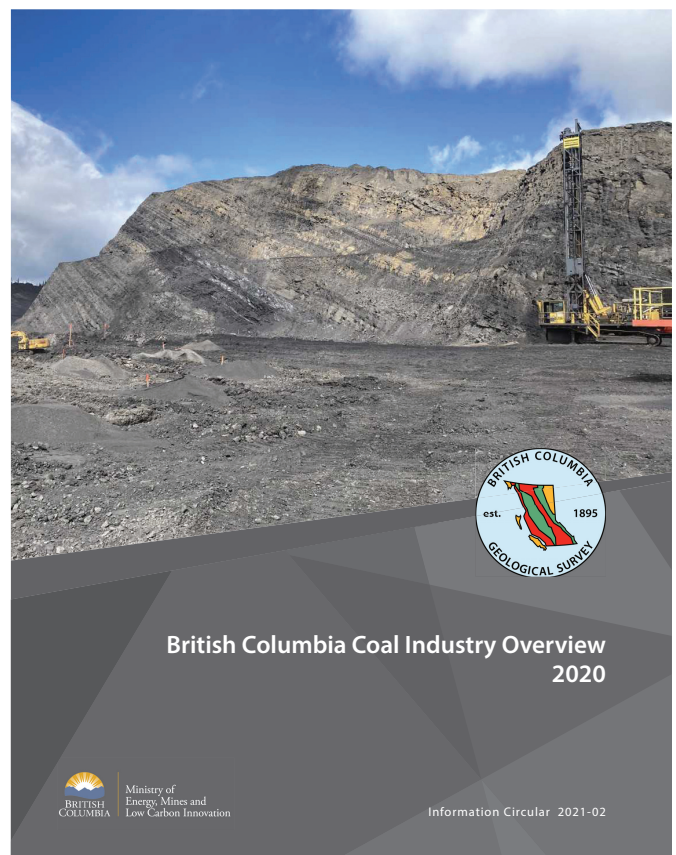
MINFILE, updated regularly.  
<https://www2.gov.bc.ca/gov/content/industry/mineral-exploration-mining/british-columbia-geological-survey/mineralinventory>.

---

Each year, the British Columbia Geological Survey publishes Geological Fieldwork, a Summary of Fieldwork and Current Research (this volume), the Provincial Overview of Mining and Exploration in British Columbia, and the British Columbia Coal Industry Overview. All British Columbia Geological Survey publications can be downloaded, at no cost, from [www.BCGeologicalSurvey.ca](http://www.BCGeologicalSurvey.ca)



Provincial Overview of Mining and Exploration in British Columbia volume, Information Circular 2021-01.



British Columbia Coal Industry Overview volume, Information Circular 2021-02.



Ministry of  
Energy, Mines and  
Low Carbon Innovation

